Università di Roma La Sapienza in union with
Università di Roma Tor Vergata and INAF

Department of Physics
PhD in Astronomy Astrophysics and Space Sciences (AASS)

Characterizing Jovian aerosols using NASA Juno and JWST infrared spectral data

PhD Thesis

Candidate:
F. Biagiotti
(XXXVIII cycle)

Supervisors:
Dr. Davide Grassi
Dr. Giuseppe Piccioni
Prof. Alessandro Mura

Rome, December 2025

A Benedetta e Teresa. Le stelle che hanno illuminato il mio cammino e che continueranno a farlo, per sempre.

Rows and flows of angel hair
And ice cream castles in the air
And feather canyons everywhere
I've looked at clouds that way

But now they only block the sun
They rain and snow on everyone
So many things I would have done
But clouds got in my way

I've looked at clouds from both sides now
From up and down and still somehow
It's cloud illusions I recall
I really don't know clouds at all

- Joni Mitchell

Abstract

The characterization of atmospheres, particularly their aerosol (clouds and hazes) content, is fundamental to understanding the thermal structure, circulation, and chemical composition of planets, including the Solar System's gas giants and distant exoplanets. Aerosols critically modulate the visible and near-infrared light from planetary bodies, often masking or weakening the gaseous absorption features that atmospheric retrievals rely upon. This challenge is exacerbated by the degeneracy of the inverse problem, where different physical aerosol properties (size, shape, composition) can yield similar observational spectra. This thesis addresses these challenges by performing the first detailed, efficient multiple scattering atmospheric retrievals of Jupiter's aerosols using a combined dataset from the Juno/JIRAM and JWST/NIRSpec missions. Jupiter, serving as a "Rosetta Stone" for gas giants, presents a complex atmosphere with uncharacterized hazes, chromophores (coloring agents), and deep-seated water clouds, whose properties defy simple thermodynamic prediction. I adopted the Planetary Spectrum Generator (PSG) for accurate multiple scattering analysis of JIRAM data, specifically targeting the solar (2-3.2 μm) and thermal (3.8-5 μm) spectral ranges, including the first successful full-range retrievals. To manage the vast data volume from both JIRAM and NIRSpec, I developed `chopper.py`, an open-source machine learning tool that exploits Principal Component Analysis (PCA) and Gaussian Mixture Models (GMM) to automatically cluster similar spectra.

My research focused on four key areas, yielding novel insights. (1) I identified and characterized over 25 Spectrally Identifiable Ammonia Clouds associated with a white turbulent vortex in the Northern Temperate Domain, providing direct evidence of pure ammonia ice in regions where it was previously not detected. (2) Global retrieval constrained the properties of the unknown contaminant materials (hazes and chromophores) responsible for the planet's colors and optical properties and confirmed their photochemical origin. (3) Spectral clustering of JIRAM and NIRSpec data revealed that the GRS is composed of two subregions—a halo and an inner oval—an undetected feature at optical wavelengths, providing new constraints on the storm's fluid dynamics and long-term stability. (4) Furthermore, a quantitative analysis of the GRS's turbulent surrounding "ripples" was performed, connecting aerosol properties to Jovian fluid dynamics and identifying these areas as potential candidates for the future search for deeper water clouds.

Collectively, this thesis work advances the state-of-the-art in Jupiter's atmosphere modeling by demonstrating the efficacy of combining accurate radiative transfer with machine learning for robust aerosol characterization, paving the way for similar analyses of Saturn, Uranus, Neptune, and exoplanets.

Contents

1 Introduction **1**

2 Planetary atmospheres and aerosols **7**
2.1 What is a planet ? . . . 7
2.2 Origin of planetary systems . . . 10
2.3 Interiors of giant planets . . . 12
2.4 Hydrostatic equilibrium of the giant planets atmospheres . . . 17
2.4.1 Lower troposphere . . . 18
2.4.2 Upper troposphere and stratosphere . . . 19
2.5 Turbulent processes . . . 20
2.6 Composition profiles and Photochemistry . . . 22
2.6.1 Methane . . . 23
2.6.2 Ammonia and Hydrogen Sulfide . . . 24
2.6.3 Water . . . 25
2.6.4 Phosphine . . . 25
2.6.5 Germane and Arsine . . . 26
2.7 Condensation processes . . . 26
2.8 Hazes . . . 33

3 Modelling planetary atmospheres with Radiative Transfer **36**
3.1 What do we observe ? . . . 36
3.2 Radiative transfer in a planetary atmosphere . . . 38
3.3 The general radiative transfer equation . . . 41
3.4 Absorption in a planetary atmosphere . . . 43
3.4.1 Line positions . . . 44
3.4.2 Line intensities . . . 47
3.4.3 Line shape . . . 48
3.4.4 Collisional Induced Absorption . . . 49
3.4.5 Line-by-Line calculations . . . 50
3.5 Scattering in a planetary atmosphere . . . 51
3.5.1 Rayleigh scattering . . . 54
3.5.2 Mie theory . . . 55
3.6 The resolution of the multiple scattering radiative transfer equation . . . 61
3.7 The Planetary Spectrum Generator and NEMESIS . . . 63
3.8 The concept of atmospheric retrievals . . . 66
3.8.1 Optimal Estimation . . . 68
3.8.2 Monte Carlo Markov Chains, MCMC . . . 70

4 A brief history of Jupiter atmosphere observations 73
4.1 Early observations (before 1850) . . . 73
4.2 Modern Astrophysics era (1850-1960) . . . 75
4.3 Space Era (1960-) . . . 76
4.3.1 Ground telescopes . . . 76
4.3.2 Space missions and a space observatories . . . 77
4.3.3 Voyager missions . . . 82
4.3.4 Galileo mission . . . 84
4.3.5 Cassini and New Horizons flybys . . . 86
4.3.6 ISO and HST . . . 87
4.3.7 The Juno mission and JIRAM . . . 88
4.3.8 James Webb Space Telescope and NIRSpec . . . 92

5 What do we know about Jupiter aerosols 95
5.1 Nomenclature and description of the Jovian atmosphere . . . 95
5.2 The Galileo Entry Probe . . . 103
5.3 Jovian spectrum across the whole wavelength range . . . 104
5.4 Effects of aerosols on the spectrum . . . 109
5.5 Retrieved aerosols structures and densities . . . 114
5.6 Retrieved clouds compositions . . . 117

6 Modeling the Juno/JIRAM spectrum with PSG 125
6.1 Adapting PSG to JIRAM . . . 126
6.2 Testing PSG with ARS . . . 126
6.2.1 Methane . . . 127
6.2.2 Ammonia . . . 129
6.2.3 Water and phosphine . . . 129
6.2.4 Germane and arsine . . . 133
6.2.5 H_2 Collision-induced absorption (CIA) . . . 133
6.2.6 Aerosols . . . 134
6.3 Simulations and retrievals of the solar range . . . 136
6.4 Choosing the cloud parametrization . . . 141
6.5 Simulations and retrievals of the thermal range . . . 145
6.6 Simulations and retrievals of the whole range . . . 147

7 The search for ammonia clouds in the Northern Temperate domain using JIRAM spectral data 151
7.1 Rationale . . . 151
7.2 Observations . . . 153
7.3 Methods . . . 157
7.4 Results . . . 160
7.4.1 NH_3 deep VMR and relative humidity . . . 171
7.4.2 Haze and main cloud particles effective radii . . . 179
7.4.3 Haze pressure level and width . . . 179
7.4.4 Main cloud pressure levels . . . 180
7.4.5 Aerosol layers densities and optical depth . . . 181
7.5 Discussion . . . 182
7.5.1 Explanation of the observed 2.73 μm shift . . . 182

7.5.2 Detection of ammonia clouds . . . 183
7.5.3 Interpretation of the vortex's nature . . . 184
7.6 Possible origin of Titan-like tholin material on Jupiter . . . 188

8 Unveil the origin of the GRS's wake ripples using JIRAM spectral data 196
8.1 Rationale . . . 196
8.2 Observations . . . 197
8.3 Methods . . . 200
8.4 Results . . . 200
8.5 Discussion . . . 212
8.5.1 ROIs as clearance regions . . . 212
8.5.2 Connection to Jovian fluid dynamics . . . 213
8.5.3 Possibility of detecting water clouds . . . 215

9 Using machine learning techniques to study Jovian clouds' global properties and the 3D structure of the GRS 217
9.1 Rationale . . . 217
9.2 Observations . . . 219
9.2.1 JIRAM data cleaning . . . 221
9.2.2 NIRSpec data cleaning . . . 223
9.3 Methods . . . 226
9.3.1 PCA step . . . 228
9.3.2 Clustering step . . . 229
9.4 Results . . . 230
9.4.1 Application to G+21 data . . . 230
9.4.2 Application to NIRSpec observations of the GRS . . . 237
9.4.3 Application to JIRAM PJ1 GRS subset . . . 241
9.5 Discussion: Identification of the GRS "halo" . . . 246

10 Conclusions 251

Chapter 1

Introduction

The quest to characterize the nature, evolution, and climate of planets—from the Solar System's gas giants to the burgeoning catalogue of exoplanets—is fundamentally contingent upon a robust understanding of their atmospheres (Seager et al., 2016; Welbanks, 2021; Roman, 2023). Within this context, aerosols—solid and liquid particles in suspension—emerge as critical factors that dictate a planetary body's thermal structure, global circulation, and chemical inventory (Kasting, 1988; Bell et al., 2024). For clarity, in this work I define clouds as larger particles ($\sim$ a few microns) formed by condensation in the lower atmosphere, and hazes as smaller particles (0.01 to 0.5 microns) formed by photochemistry by-products in the upper atmosphere.

The primary method for studying the chemical composition of planetary atmospheres is the analysis of remote sensing data (Carter et al., 2024; Roman, 2023). Spectra and images encode information about light absorbed by gases or reflected by clouds and hazes. Aerosols, in particular, fundamentally shape the visible and near-infrared spectra of planets. While their presence enables the measurable reflection of light, they also block radiation from the planetary interior, weakening or masking important gaseous absorption features. Accurate aerosol modeling is thus fundamental for obtaining physical information from remote sensing data. This is typically achieved through an atmospheric retrieval, where measured spectra are compared to simulated spectra within a Bayesian framework (MacDonald & Madhusudhan, 2017). The simulated spectra are obtained by solving the multiple scattering radiative transfer equation. The inclusion of aerosols has a huge impact on retrieval results; for instance, cloud-free retrievals often infer smaller gaseous concentrations because clouds tend to block and weaken absorption features. This effect is one manifestation of the degeneracy inherent in modeling aerosols (Barstow, 2020), where different combinations of particle size, shape, and composition can produce similar observational signals, making a unique characterization very difficult.

While atmospheric modeling remains an extremely challenging task, the wealth of available information from spectra and images is enormous. As of October 2025, studying exoplanetary atmospheres with remote sensing reflected light is the best prospect for detecting biosignatures on other habitable planets (Quanz et al., 2022). To simplify the inversion problem, well-studied planets are often used as tools for

modeling other planetary atmospheres. Jupiter, the fifth and largest planet in our Solar System, is typically considered a Rosetta Stone for gas giant planets. Its atmosphere is primarily composed of hydrogen (86 %) and helium (13 %), with minor species like methane (0.2 %) and ammonia (0.03 %)- a composition similar to those expected for Saturn, Uranus, Neptune, and many warm and cold gaseous exoplanets. With an average temperature of 125 K, its upper troposphere is dominated by cloud and haze layers, creating the dynamical and variegated visual patterns shown in Fig. 1.1.

Thermodynamically, these cloud decks are predicted to be composed of ammonia ice, ammonium hydrosulfide, and water, and to be located at layers characterized by a pressure of $\sim$ 0.7, 2, and 5 bar, respectively (Atreya et al., 1999).

Jupiter's chemical composition was mostly unveiled by the Galileo entry probe, which plunged into the atmosphere in 1995 (Seiff et al., 1997). Even if the probe entered a single point in the Jovian disk, its instrumental suite measured precise pressure and temperature vertical profiles and, via its mass spectrometer, the gaseous abundances listed above. However, the water vapor measurements indicated that the probe had entered a very dry and peculiar region, known as a "Hot Spot." Contrarly to theoretical expectations one low-density cloud deck was encountered during the descent. Consequently, the data were insufficient to characterize the nature or global variability of Jovian clouds, since the single data point represented a very peculiar atmospheric location.

Jupiter is the most studied gas giant using remote sensing visible and infrared data, owing to its size and favorable position relative to Earth. Subsequent retrieval studies of Jovian aerosols have revealed a far more complex structure than the simple thermodynamic picture (Baines et al., 2002; Sromovsky & Fry, 2010a,b, 2018; Carlson et al., 2016a; Baines et al., 2019; Braude et al., 2020; Dahl et al., 2021). Specifically, a series of fundamental challenges and open problems persist:

- Due to the problem's degeneracy and a historical lack of efficient multiple-scattering codes, results from different studies often prove difficult to compare. Identifying the precise vertical distribution, size, and density of distinct aerosol layers remains a major challenge.

- Adequately fitting visible and near-infrared data requires the introduction of an extended layer of small particles above the main cloud decks. These are not expected by condensation theory (Atreya et al., 1999), and their origin remains unclear.

- Ammonia ice, whose spectral signatures are not frequently detected (Baines et al., 2002), should produce white clouds. Yet, Jupiter displays a broad range of colorful patterns (Fig. 1.1). The material(s), known as chromophores, responsible for the planet's striking red, brown, and grey colors are believed to be embedded within the aerosols. Their exact chemical composition remains a major mystery, though candidates include elemental sulfur, phosphorus compounds, and complex organic molecules formed by photochemistry (Carlson et al., 2016a; Baines et al., 2019).

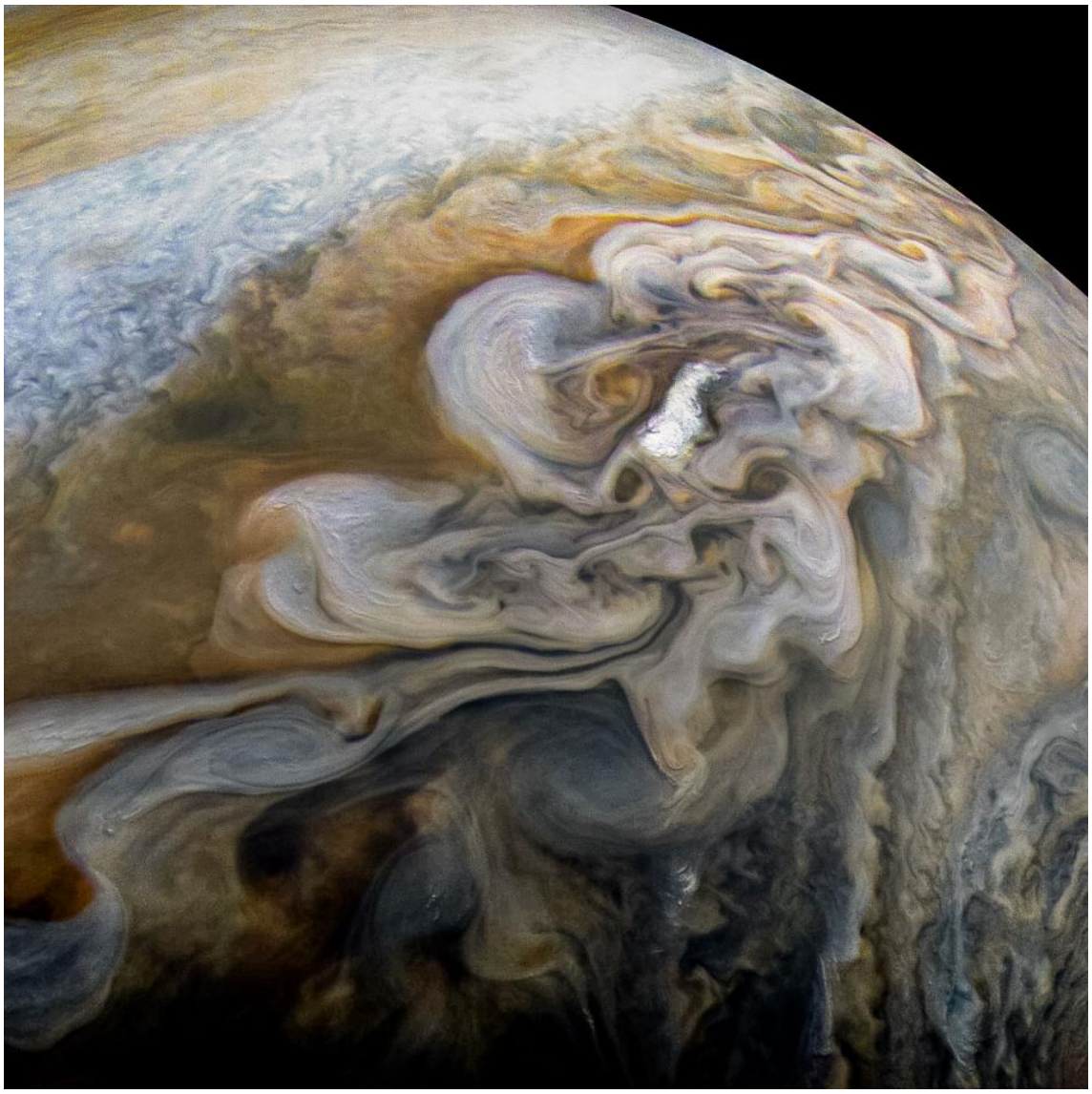


Figure 1.1: In this image taken by NASA's Juno spacecraft it is possible to observe the swirling cloud formations in the northern area of Jupiter's north temperate belt. The color-enhanced image was taken while Juno was performing its eleventh close flyby of Jupiter. At the time the image was taken, the spacecraft was about 8,186 kilometers from the tops of the clouds of the planet at a latitude of 39.9 degrees. Citizen scientist Kevin M. Gill processed this image using data from the JunoCam imager.

- The precise chemical pathways and precursors (such as ammonia, hydrogen sulfide, methane, etc., reacting under solar ultraviolet radiation and/or lightning) that lead to the formation of the different types of aerosols are not fully understood and are challenging to reproduce in laboratory experiments under Jovian conditions.

- Jupiter's atmosphere features fast, stable zonal jets and massive, long-lived storms (like the Great Red Spot and its turbulent surrounding regions), leading to intense atmospheric circulation and vertical and horizontal transport of aerosols, which vary over time and location. This makes it difficult to link a measured aerosol property to a specific formation mechanism or location.

- The detection and characterization of water clouds in Jupiter's atmosphere are particularly challenging, primarily because they are located deep beneath multiple, thicker layers of other clouds.

This thesis addresses the challenge of characterizing the nature, vertical structure, and physical properties of Jovian aerosols through the analysis of infrared spectral data acquired by the JIRAM and NIRSpec image spectrometers—pivotal instruments of the NASA Juno and JWST missions. The Juno spacecraft has been orbiting the Jovian system since 2016, and the JIRAM spectrometer has acquired tens of thousands of spectra, precisely mapping a large fraction of Jupiter's atmosphere since its first perijove (PJ1) passage. The JWST, in contrast, represents the largest space telescope ever launched, characterized by a 6.5 m primary mirror and sophisticated instruments like NIRSpec, which, via its Integral Field Unit (IFU), acquires hundreds of spectra simultaneously. As of October 2025, the combined JIRAM and NIRSpec data volumes represent the premier dataset of Jupiter observations, offering optimal spatial and spectral resolutions.
In this thesis I adopted for the first time the new, hybrid, and efficient Planetary Spectrum Generator (PSG) (Villanueva et al., 2018) to Jupiter's case, in order to perform accurate multiple scattering retrievals of JIRAM spectral data. With this approach it is possible to efficiently characterize the properties of clouds on the Jovian disk at the time of the JIRAM observations. Since retrievals of both JIRAM and NIRSpec observations can be largely time consuming, I also developed a Machine-Learning (ML) based approach to automatically clusterize large collections of spectra. For this purpose, I developed an open-source Python code named chopper.py (Biagiotti, 2025) capable to automatically classify similar spectra applying first a Principal Component Analysis (PCA) and then a Gaussian Mixture Model (GMM) clustering to the spectral collection.
My research covers the following four interconnected areas of investigation:

- Investigating the presence of spectral features associated with pure ammonia clouds in the JIRAM collection.

- Deriving global insights into the unknown haze and chromophore materials using JIRAM data.

- Assessing the possibility of detecting spectral features of deep water clouds by exploiting the JIRAM dataset.

- Characterizing the cloud properties in distinct dynamic features, including storms, vortices (such as the Folded Filamentary Regions - FFRs - in the Northern Temperate Domain), the Great Red Spot (GRS) and its turbulent surroundings, using both JIRAM and JWST data.

The thesis is organized as follows. In Chapter 2, I provide the physical and phenomenological background necessary to understand planetary atmospheres. I begin with the origin of planetary systems and the modeling of planetary internal structures, followed by a discussion of pressure-temperature profiles, volume mixing ratio profiles, and an overview of the most used condensation models for the theoretical study of clouds and hazes. Chapter 3 discusses the methodology for modeling the observed spectrum of a planetary atmosphere. I provide the necessary background on radiative transfer theory and the modern techniques used to treat the absorption and scattering of light. I detail how software packages such as PSG and NEMESIS numerically solve the multiple scattering radiative transfer equation to generate simulated spectra. The final part discusses the principles of atmospheric retrieval, providing an overview of the Bayesian frameworks of Optimal Estimation (OE) and Monte Carlo Markov Chains (MCMC). In Chapters 4 and 5, the focus shifts completely to Jupiter. Chapter 4 provides an overview of the exploration of the Jovian system, describing remote sensing observations performed by ground-based and space-based observatories and missions. This includes details about the architectures, operation principles, and noise sources of both JIRAM and NIRSpec. Chapter 5 presents the state-of-the-art on the characterization of the Jovian aerosol decks. I provide an overview of the nomenclature of Jupiter's morphological patterns, summarize the Galileo Entry Probe results, describe how clouds and hazes modify the near-infrared spectrum, and group together the latest literature results on aerosol vertical structure, optical properties, and composition.
The findings of this thesis are presented from Chapter 6 onwards. I first describe the validation tests performed to ensure PSG's adequacy for modeling JIRAM Jovian spectra. I then detail the development of the retrieval pipelines, which combine PSG with the Python codes `PyOE` (Maahn et al., 2020) and `emcee` (Foreman-Mackey et al., 2013). This chapter describes the atmospheric parameterizations considered for modeling the JIRAM solar (2-3.2 μm) and thermal (3.8-5 μm) ranges, and finally, the full range simultaneously, a task never previously performed successfully. In Chapter 7 I expand the results that have been already published in the Monthly Notices of the Royal Astronomical Sociey (MNRAS) paper *"Evidence of pure ammonia clouds in Jupiter's Northern Temperate domain from Juno/JIRAM infrared spectral data"* (Biagiotti et al., 2025d) and in the proceedings of the European Geoscience Union 2024 (Biagiotti et al., 2024a; Guillot et al., 2024a) and 2025 (Biagiotti et al., 2025b) General Assemblies and of the 2025 Europlanet Science Congress (Biagiotti et al., 2025a). This chapter describes the challenges in identifying spectral features associated with pure ammonia ice clouds in the JIRAM PJ1 dataset. I identify and focus on a candidate white, turbulent vortex—a potential Folded Filamentary Region (FFR)—within the Northern Temperate Domain. I present solar retrieval analysis results, claiming the detection of 25 Spectrally Identifiable Ammonia Clouds (SIACs) within this vortex. I show that outside the vortex, contaminant materials provide better fits than pure ammonia ice. I discuss the implications and possible origin of this vortex and, using full-range retrievals of a PJ1 JIRAM aver-

age spectrum, investigate the origin (via condensation and photochemistry) of the contaminant material modeling the surrounding regions. In Chapter 8 I expand the results that have been published in the proceedings of the 2024 Europlanet Science Congress (Grassi et al., 2024a) and of the European Geoscience Union 2025 General Assembly (Grassi et al., 2025). This chapter presents the first quantitative analysis of the turbulent regions surrounding the GRS, known as "ripples." I describe the results of the solar and thermal retrievals and discuss their connection to Jovian fluid dynamics. I also suggest that these regions are optimal candidates for the future search for water clouds on Jupiter. In Chapter 9 I expand the results that have been published in the Astronomy & Astrophysics (A&A) paper *"Machine learning spectral clustering techniques: Application to Jovian clouds from Juno/JIRAM and JWST/NIRSpec"* (Biagiotti et al., 2025e) and in the proceedings of the American Geophysical Union 2024 General Assembly (Biagiotti et al., 2024b) and of the 2024 Europlanet Science Congress (Fletcher et al., 2024). In this Chapter I discuss the technical details behind the `chopper.py` code and I describe the reduction procedures needed to be performed on both JIRAM and NIRSpec before applying any kind of clustering analysis. I discuss the results of the application of `chopper.py` on both JIRAM and NIRSpec data and I assess the adequacy of the method. I also focus on the identification of two new regions undetected at optical wavelengths. Namely, I found that the GRS appears to be composed of two subregions, a halo and an inner oval. In the Chapter I will discuss phenomenologically the consequences of this detection and its connection to the fluid dynamics of the GRS and to its long-term stability. Finally, in Chapter 10 I summarize the findings and results of this thesis work.

Chapter 2

Planetary atmospheres and aerosols

2.1 What is a planet ?

The term "planet" comes from the greek word "planetes asteres" which means "wanderer stars". In fact, in the night sky it is possible to easily distinguish a planet from a star because of their proper motion. Planets "wander" across the sky over time relative to the fixed background of stars and follow a path close to the ecliptic. In this way the ancient Greeks discovered and named Jupiter, Mars, Saturn, and Venus, the brightest planets in our solar system (i.e. the portion of the universe encompassed in a 20,000 AU sphere centered in our star, the Sun). Because of this characteristic, the planets have been the center of scientific revolutions in history. And so has been the question "What is a planet ?".
Nicolaus Copernicus was the first astronomer to propose, using the scientific method, that planets orbit the Sun. Galileo Galilei, Isaac Newton, and Johannes Kepler expanded his ideas using new physical models and observations. In particular, Kepler proposed three laws that determine the motion of the planets:

1. A planet's orbit is an ellipse where the sun is placed in one of its foci.
2. The radius vector of a planet sweeps equal areas in equal amounts of time.
3. The square of the orbital period of the planet is directly proportional to the cube of the semi-major axis of its orbit

These laws are consequences derived from the solution of the two body problem. Therefore, we can think that a planet is every object in our Solar system that follows the Kepler laws. This hypothesis is close to the correct answer, and was not discussed by the scientific community until the last decades of the 19th century, when extensive astrophysical observations became technologically feasible. In particular the discoveries of Uranus and Neptune in 1781 and 1846 helped solidify this picture. However, when the first asteroids and dwarf planets were discovered (Piazzi, 1802) and studied, it was clear that the Kepler laws were not enough to describe what a planet is.
To complicate the picture, in 1995 the astronomical and planetary communities were revolutionized by the discovery of a "planetary-mass object" orbiting the sun-like star 51 Pegasi (Mayor & Queloz, 1995). The detection was made using the radial velocity method, which is aimed to detect the tiny Doppler effect induced by the

star's reflex motion caused by the gravitational attraction of its orbiting planet. This became the very first detection of an exoplanet. Since 1995 more than 6,000 have been discovered, a large fraction of them thanks to the transit method (Charbonneau et al., 2000), which detects planets by observing the slight dimming of a star's light as a planet passes in front of it.
For these and many other reasons, we had to wait until 2009 for a proper scientific definition of what a planet is, and in reality, this is still an open topic. In its resolution B5 (IAU, 2006), the International Astronomical Union classified a planet as an object that:

1. is in orbit around the Sun;
2. has sufficient mass for its self-gravity to overcome rigid body forces so that it assumes a hydrostatic equilibrium shape, and a mass not too big to trigger nuclear fusion
3. has cleared the neighborhood around its orbit.

This definition could be expanded also to exoplanets, modifying the first point to an object that is in orbit around a main-sequence star or a stellar remnant such as white dwarfs or pulsars. This resolution became somehow controversial because it excluded Pluto from the planets, as it has not cleared its orbit. Therefore the class of dwarf planets was created for solar system objects that only satisfy the points 1) and 2).
Using this definition we can say that in our Solar System, that we define as the portion of the universe inside the Oort cloud, we can count 8 planets.

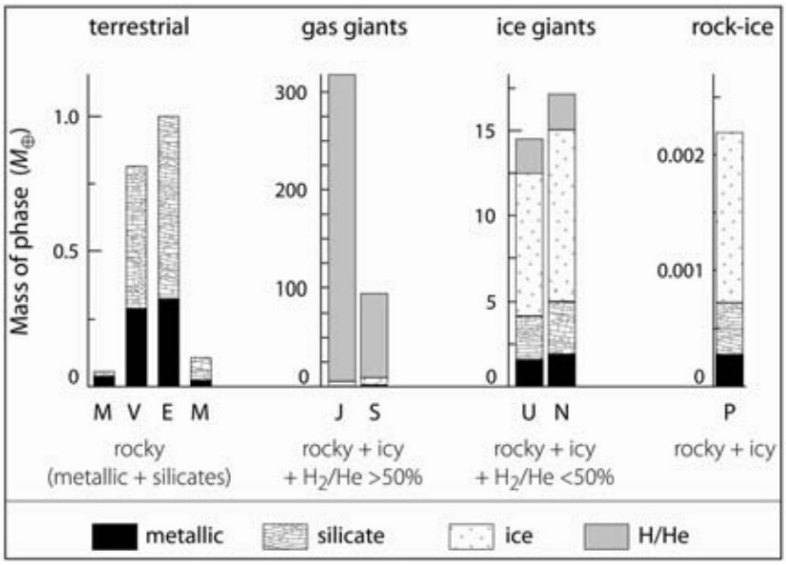


Figure 2.1: Composition of the solar system planets given in mass fractions, from Lodders (2010).

These are in order of orbital semi-major axes: Mercury, Venus, Earth, Mars, Jupiter, Saturn, Uranus, and Neptune. They are very heterogeneous in composition and physical structure. However they can be divided into three groups, see Fig. 2.1 from Lodders (2010):

- **rocky planets**: Mercury, Mars, Venus, and the Earth. They have cores and mantles composed of solid or fluid rocks (non-volatile condensates Lodders (2010)). Their surfaces are formed by different minerals and can have or not have atmosphere thin layers (i.e., gas and ice envelopes).

- **gas giant planets**: Jupiter and Saturn. Their mass is composed at >50 % by hydrogen and helium. Their atmosphere is composed at >99 % by hydrogen and helium at solar ratios. For these reasons they are usually referred to as "failed stars". They are characterized by metallic hydrogen deep layers and by thick, swirling atmospheres.

- **ice giants planets**: like Uranus and Neptune. Their mass is composed at < 50 % by hydrogen and helium. Their atmosphere is composed at >95 % by hydrogen and helium but differently from the gas giants they present higher concentrations of heavier volatile substances such as water, methane, and ammonia. Their core and internal layers are expected to be solid.

A summary of the physical properties of each planet is given in Fig. 2.2. With the discovery of exoplanets we can extend our classification to other kinds of planets:

- hot Jupiters: Gas giants (such as Jupiter) that orbit extremely close to their star, resulting in very high temperatures and short orbital periods (typically less than 10 days).

- warm Jupiters: Gas giants with bulk properties similar to Hot Jupiters but orbiting further out, where temperatures are less extreme and orbital periods are longer (roughly 10 to 100 days).

- super Earths: Planets that are more massive than Earth but significantly less massive than ice giants (like Neptune) and can be rocky or have a mixture of rock/gas. They have masses between 1 and 10 Earth masses.

- mini Neptunes: Planets that are smaller than Neptune but larger than Earth-/Super Earths (often between 2-4 times Earth's radius). They have a thick atmosphere of hydrogen/helium around a rocky core, resembling Neptune in composition but smaller.

- Young Objects (YOs): Generally refers to planets that are only a few million years old, still forming or recently formed, often still embedded in or interacting with the protoplanetary disk of gas and dust around their young host star. Studying them helps us understand planet formation processes.

We will see the origin of these worlds in section 2.2 and 2.3. Jupiter and the gas giant planets will be the main objective of this PhD thesis work aimed at characterizing their atmospheres, clouds and aerosols.

	MERCURY	VENUS	EARTH	MOON	MARS	JUPITER	SATURN	URANUS	NEPTUNE
Mass (10^{24}kg)	0.330	4.87	5.97	0.073	0.642	1898	568	86.8	102
Diameter (km)	4879	12,104	12,756	3475	6792	142,984	120,536	51,118	49,528
Density (kg/m^3)	5429	5243	5514	3340	3934	1326	687	1270	1638
Gravity (m/s^2)	3.7	8.9	9.8	1.6	3.7	23.1	9.0	8.7	11.0
Escape Velocity (km/s)	4.3	10.4	11.2	2.4	5.0	59.5	35.5	21.3	23.5
Rotation Period (hours)	1407.6	-5832.5	23.9	655.7	24.6	9.9	10.7	-17.2	16.1
Length of Day (hours)	4222.6	2802.0	24.0	708.7	24.7	9.9	10.7	17.2	16.1
Distance from Sun (10^6 km)	57.9	108.2	149.6	0.384*	228.0	778.5	1432.0	2867.0	4515.0
Perihelion (10^6 km)	46.0	107.5	147.1	0.363*	206.7	740.6	1357.6	2732.7	4471.1
Aphelion (10^6 km)	69.8	108.9	152.1	0.406*	249.3	816.4	1506.5	3001.4	4558.9
Orbital Period (days)	88.0	224.7	365.2	27.3*	687.0	4331	10,747	30,589	59,800
Orbital Velocity (km/s)	47.4	35.0	29.8	1.0*	24.1	13.1	9.7	6.8	5.4
Orbital Inclination (degrees)	7.0	3.4	0.0	5.1	1.8	1.3	2.5	0.8	1.8
Orbital Eccentricity	0.206	0.007	0.017	0.055	0.094	0.049	0.052	0.047	0.010
Obliquity to Orbit (degrees)	0.034	177.4	23.4	6.7	25.2	3.1	26.7	97.8	28.3
Mean Temperature (C)	167	464	15	-20	-65	-110	-140	-195	-200
Surface Pressure (bars)	0	92	1	0	0.01	Unknown*	Unknown*	Unknown*	Unknown*
Number of Moons	0	0	1	0	2	95	274	28	16
Ring System?	No	No	No	No	No	Yes	Yes	Yes	Yes
Global Magnetic Field?	Yes	No	Yes	No	No	Yes	Yes	Yes	Yes

Figure 2.2: Properties of solar system planets from NASA/GSFC.

2.2 Origin of planetary systems

The diversity found in the solar system planets, as described in the previous section, can be easily understood if the origin of our solar system (and of exoplanetary systems in general) is studied. In fact "the origin" branch of planetary sciences, and the "characterizing" one always walked an entangled path. The discovery of an exotic species in an atmosphere or of a very eccentric asteroid can give us new insights on how the solar system formed, and in principle, vice versa. The whole process is, therefore, iterative.

However, as often happened in science, crucial discoveries were needed to establish a theory or a model. In this case they were the first radio images of a protoplanetary disk with ALMA (ALMA Partnership et al., 2015) and the accurate estimation of hydrogen and helium in Jupiter (Niemann et al., 1996). How these measures were obtained will be explained in Chapter 4 and 5. The prevailing model for solar system formation is the nebular hypothesis (Laplace, 1796; Safronov, 1972), which posits that our system originated from a vast, rotating cloud of gas and dust known as the solar nebula. This nebula, likely a remnant of previous stellar evolution, began to collapse under its own gravity, a process potentially triggered by a nearby supernova or other disruptive event (Boss & Keiser, 2010). As the nebula contracted, it spun faster, conserving angular momentum, and flattened into a protoplanetary disk. The central region of this disk became increasingly dense and hot, eventually igniting nuclear fusion and birthing the Sun. This process, involved powerful stellar winds that cleared much of the remaining gas and dust from the inner solar system (Williams & Cieza, 2011).

Within the protoplanetary disk, and after the start of the condensation era, dust grains, initially sub-micrometric, can start colliding and sticking together through electrostatic forces, a process termed accretion (Blum & Wurm, 2008). Alternatively, the collisions can happen due to gravitational instabilities internal to the disk, as recently observed in the AB Aurigae protoplanetary disk (Speedie et al., 2024). In any case, sub-micrometer dust agglomerates into proto-planetary solids to grow into pebbles; once growth stalls due to the bouncing barrier, the pebbles undergo streaming instability, which causes their spatial concentration and gravitational collapse, leading to the formation of planetesimals. These planetesimals can continue to grow through further collisions, eventually reaching kilometer-sized dimensions. The composition of these planetesimals varies with distance from the Sun. Closer to the Sun, where temperatures were higher, only refractory materials such as metals and silicates could condense, leading to the formation of rocky planetesimals. Further out, beyond the "snow line," volatile ices like water, methane, and ammonia could also condense, resulting in icy planetesimals. This compositional gradient played a crucial role in the subsequent formation of different types of planets.

In the inner solar system, the rocky planetesimals continued to accrete, merge, or even collide, eventually forming the terrestrial planets: Mercury, Venus, Earth, and Mars. The leading hypothesis of the formation of the Moon and the Earth, called the "Theia hypothesis", suggests that the Moon formed from debris ejected after a Mars-sized object, named Theia, collided with the early proto-Earth (Wiechert et al., 2001). The formation of the gas giants, Jupiter and Saturn, in the outer solar system, followed a different pathway. The icy planetesimals in this region grew large enough to gravitationally attract and accumulate vast amounts of hydrogen and helium gas from the surrounding nebula. This rapid gas accretion led to the formation of massive, gaseous planets with thick atmospheres. The ice giants, Uranus and Neptune, likely formed later, with slower gas accretion rates due to lower nebula densities at longer orbital periods, resulting in a higher proportion of ices in their composition (Helled & Stevenson, 2017).

The dynamics of the protoplanetary disk were complex and influenced by various factors, including gravitational interactions between planetesimals and protoplanets, as well as the effects of the Sun's radiation and stellar winds. Planetary migration, driven by gravitational interactions with the residual gas and dust disk, played a profound role in shaping the final architecture of the Solar System. The Grand Tack model (Raymond et al., 2018) proposes that Jupiter initially migrated inward, perhaps as close as 1.5 astronomical units (AU) from the Sun, before reversing its path due to the growing influence of Saturn, "tacking" outward to its current orbit. This inward-outward migration is thought to have scattered planetesimals throughout the disk, contributing to the initial depletion and mixing of the inner Solar System and setting the stage for subsequent events.

This initial Grand Tack phase is separate from the widely accepted trigger of the Late Heavy Bombardment (LHB), a period of intense impacts evidenced by lunar rock samples and cratering. Following the dispersal of the gas disk, the Nice Model (Morbidelli et al., 2012; Gomes et al., 2005) provides the mechanism for the LHB itself. This model posits that the giant planets (Jupiter, Saturn, Uranus, Neptune) initially resided in a more compact configuration. The LHB is proposed to coin-

Name	Symbol	Atomic Number	Mass fraction	X/H
Hydrogen	H	1	0.738296	1
Helium	He	2	0.249524	0.08511
Carbon	C	6	0.002159	2.455×10^{-4}
Nitrogen	N	7	0.000618	6.026×10^{-5}
Oxygen	O	8	0.005355	4.571×10^{-4}
Neon	Ne	10	0.001023	6.918×10^{-5}
Sulfur	S	16	0.000339	1.380×10^{-5}
Argon	Ar	18	6.66×10^{-5}	1.549×10^{-6}
Germane	Ge	32	2.07×10^{-7}	3.89×10^{-9}
Arsenic	As	33	1.07×10^{-8}	1.950×10^{-10}

Table 2.1: Proto-solar abundances of the elements, from Irwin (2009) and Grevesse et al. (2007).

cide with the final arrangement of the giant planets approximately 600 million years after their formation, triggered when Jupiter and Saturn crossed their 1:2 mean-motion resonance. This resonance destabilized the orbits of Uranus and Neptune, causing them to rapidly migrate outward. This outward shift effectively dynamically scattered a massive, outer planetesimal reservoir (the primordial Kuiper Belt), devastating it and sending a torrent of material—the LHB—into the inner Solar System. Specifically, this period involved Neptune overtaking Uranus during their rapid migration, which was the key event that gravitationally cleared and scattered the material.
This framework—Grand Tack for early mixing/architecture and Nice Model for the late stages—is essential for understanding the Solar System's evolution. Moreover, planetary migration remains a fundamental concept to explain the origin and orbital diversity of exoplanets, particularly the existence of hot Jupiters.

Using the nebular hypothesis it is possible to compute the estimated solar system abundance for each element (Grevesse et al., 2007). These values are given in Table 2.1. Starting from them it is also possible to calculate the expected abundances of the elements in their fully hydrogenated form (Grevesse et al., 2007). These are given in Table 2.2 together with the values measured for Jupiter. The source of the data will be discussed in Chapters 4 and 5. Measuring the abundances is an important diagnostic tool to discriminate between formation histories as we will see in section 2.3.

2.3 Interiors of giant planets

In section 2.2 we saw that the nebular hypothesis can predict the composition of the planets in our solar system and, in principle, also their interior structure. Do observations align with theoretical predictions ? How is it possible to probe the interiors of a giant planet ? There are plentiful techniques, but the used are the ones that rely on measurements of : the magnetic field, the gravity planetary field, and the moment of inertia.
Regarding the magnetic field, different internal structures and internal physical con-

Molecule	$\left(\frac{X}{H_2}\right)_\odot$	$\left(\frac{X}{H_2}\right)_{\text{Jup}}$	$\left(\frac{X}{H_2}\right)_{\text{Jup}} / \left(\frac{X}{H_2}\right)_\odot$
H_2	1.0	1	1
He	0.1702	0.1702	0.92
H_2O	9.142×10^{-4}	4.9×10^{-4}	0.54
CH_4	4.909×10^{-4}	2.37×10^{-3}	4.83
Ne	1.384×10^{-5}	2.3×10^{-5}	0.17
NH_3	1.205×10^{-4}	6.64×10^{-4}	5.51
H_2S	2.760×10^{-5}	8.9×10^{-5}	3.22
Ar	3.098×10^{-6}	1.82×10^{-6}	5.87
PH_3	5.024×10^{-7}	1.2×10^{-6}	2.39
GeH_4	7.781×10^{-9}	7.0×10^{-10}	0.1
AsH_3	3.900×10^{-10}	2.2×10^{-10}	0.56

Table 2.2: Abundances of the main hydrogenated molecules in the protosolar and Jovian case as measured by the Galileo entry probe.

ditions can lead to different magnetic field patterns. Planetary magnetic fields can be measured using instruments called magnetometers or studying the distribution and energies of energetic particles in their neighbourhood.
Gravity field can give insight on the internal structure of a planet. For example an oblate spheroid (such as the earth) will have a gravity field different in direction and intensity from the one of a perfect sphere. The gravitational field U, is defined starting from the Laplace equation $\nabla^2 U = 0$. In spherical polar coordinates, Laplace's equation has a number of well-known solutions (Irwin, 2009). However in the context of planets is useful to consider the one obtained considering axial and north/south symmetries and centripetal effects (Lindal et al., 1985):

$$U(r,\Theta) = -\frac{GM}{r}\left[1 - \sum_{n=1}^{\infty} J_{2n}\left(\frac{R}{r}\right)^{2n} P_{2n}\sin\Theta\right] - \frac{1}{2}\Omega^2 r^2 \cos\Theta^2. \tag{2.1}$$

G is the gravitational constant, r the radial distance, M and R the total mass and radius of the planet, while Ω is the angular velocity induced by the planet's rotation. Θ is known as the planetocentric latitude, equal to 90° minus the real latitude. P_{2n} are the Legendre polynomials while J_{2n} are called the J-coefficients or gravity coefficients. Only the even terms are retained in the expression in virtue of the assumed symmetries. For a perfect sphere J-coefficient should be zero as they, in a few words, measure the oblateness or how much the surface gravitational field does not point directly towards the center of the planet. They can be measured by studying the acceleration of a spacecraft in the proximity of a planet or the dynamical perturbation induced on rings and satellites.
Lastly, the other parameter that has information about the mass distribution of a body is its moment of inertia C. Shapes with mass concentrated farther from the rotation axis, like a hoop, have a larger moment of inertia than shapes with mass closer to the axis, like a homogeneous disk or sphere. To measure the moment of inertia of a planet usually the so-called Darwin-Radau equation is used. This is an useful approximation that assumes the body is in hydrostatic equilibrium and shaped like an ellipsoid of revolution. The equation can read like this (Bourda &

Capitaine, 2004):

$$\frac{C}{MR_e^2} = \frac{2}{3}\left(1 - \frac{2}{5}\sqrt{1+\eta}\right), \tag{2.2}$$

where

$$q = \frac{\Omega^2 R_e^3}{GM}\,,\ \epsilon = \frac{q}{2} + \frac{3J_2}{2}\,,\ \eta = \frac{5q}{2\epsilon} - 2 \tag{2.3}$$

R_e is known as the equatorial radius. So, it is possible to know it if the angular velocity, mass, radius, and J_2 of a planet is known. For a hollow sphere C/MR_e^2 should be 2/3 while for a uniform density sphere it should be 0.4. A sphere with all the mass at its center should have a value of zero. The values of the J_{2n} and of C measured for Jupiter are given in Table 2.3 (Iess et al., 2018). The J_{2n} values suggest that Jupiter is an oblate planet, and so it can be seen as a sphere flattened at its poles and engulfed at its equator due to its rapid rotation. The C/MR_e^2 values instead indicate a significant concentration of mass towards the center of the planet. Assuming hydrostatic equilibrium, i.e. assuming a fluid where the inward force of gravity is exactly counteracted by the outward force of pressure, it is possible to use theoretical models to study how the density, pressure, temperature, and composition vary with depth for the whole planet. The results of the model can be compared to the measured values of J_{2n} and C/MR_e^2.
The generally accepted model for Jupiter interiors, see Fig. 2.3, is the one of Guillot (1999a,b), updated after the measurements of Juno (Wahl et al., 2017) (see Chapter 4). Before describing it we need to discuss briefly how energy is transported between different layers of a fluid (Grassi, 2018):

- **Radiative transfer**: it consists in the net transfer of energy from warm layers to colder ones by means of IR photons.
- **Convection**: air parcels warmed in a fluid become buoyant with respect to the surrounding environment and move upward. Their vertical motion represents an efficient mechanism for vertical transport of energy and minor fluid components.
- **Phase changes**: at certain pressures and temperatures gaseous species can condense and become liquid or solid, exchanging latent heat

Bearing this in mind, finally, Fig. 2.3 can be read as follows:

- at temperatures $>10^4$ K and at pressures 1000 GPa Jupiter presents dense core that should be composed of heavy elements. Modern Juno gravity measurements suggest that the core should be diluite (Wahl et al., 2017). In this context diluite means that the core is a "fuzzy" mix of dense, heavy elements and silicates that gradually blend into the surrounding layers.
- Above the core, for pressures below 200 GPa and temperatures below 6000 K the atmopshere is composed predominantly by hydrogen that is present in its metallic, i.e. liquid, form. This is a consequence of the change to an electron-degenerate state of pressure-ionized protons and electrons. This hydrogen "ocean" is the main driver of the planetary dynamo and responsible for the intense magnetic fields. The liquid hydrogen layer extends up to pressures

at which helium is thought to become immiscible in metallic hydrogen. As the helium separates, it's theorized that it could condense into droplets and precipitate through the metallic hydrogen layer, much as rain falling through the atmosphere on Earth, contributing to the mass concentration toward the center of the planet (Markham & Guillot, 2024).

- Above the metallic hydrogen layer an inhomogeneous layer is predicted. The term inhomogeneous is used to describe a transition zone between the states with metallic and molecular hydrogen. The nature of this internal region is still a topic of scientific discussion. Moreover, the existence of a radiative zone at these transition pressures is predicted by several models (Guillot et al., 1995; Siebenaler et al., 2025).

- At T<6000 K and at pressures < 2 GPa the hydrogen exists in its molecular phase. These are the considered boundary values for the atmosphere of Jupiter. The atmosphere then can be divided in further regions, see Fig. 2.4: (i) the troposphere roughly 1 GPa< p <10 kPa, (ii) the stratosphere 10kPa< p <0.1 Pa, (iii) the ionosphere 0.1 Pa< p <10^{-4} Pa, and lastly the (iv) exosphere for p<10^{-4} Pa. In the lower part of the troposphere heat rises from the interior and from the hypothetic radiative zone. The hotter, less dense gas rises, carrying energy with it. As it rises and cools, it becomes denser and sinks back down. This continuous cycle of rising and sinking gas creates convection currents, which efficiently transport heat outwards. This is the driver of the dynamical and turbulent processes in the upper Jovian atmosphere. It is not a case that troposphere comes from the Greek word "tropo" that means "turning".

The above discussion can be extended to Saturn and to other giant exoplanets changing the values for the pressures and temperatures (Guillot, 1999a). Since the gas giants do not have a proper surface as the solid planets, what is done usually is to define the standard isobaric surface at the pressure of 1 bar (1 bar= 10^5 Pa) and to provide altitude values referring to that specific level.
Quantitatively the interior models predict hydrogen and helium values close to the nebular hypothesis. This is confirmed by the values listed in Table 2.2. However, from the same Table it is possible to observe how methane, ammonia, hydrogen sulfide, and phosphine appear to be enriched with respect to the Solar values by a factor between 3 and 6. From these measurements the mass of heavy elements (i.e., those with mass greater than helium) it is computed to be in the range 8 $M_\oplus$ to 39 $M_\oplus$ (Saumon & Guillot, 2004), which is 1 $\pm$ 6 more than would be expected if Jupiter had a solar composition (Grevesse et al., 2007). Saturn is estimated to be even more enriched (Saumon & Guillot, 2004). Therefore the proposed hypothesis is that both of them formed by core accretion and that for Jupiter, the subsequent accretion of the gaseous H/He envelope resulted in partial or complete mixing of the core with the gas. Moreover, the larger accretion rate in the proto-Jupiter may have caused larger mixing than in the proto-Saturn (Guillot, 2004). The formation should have happened in a chemically evolved protosolar disc (Guillot & Hueso, 2006). However, the origin of Jupiter and Saturn is still an open topic in planetary sciences, that goes beyond the scope of this thesis work.

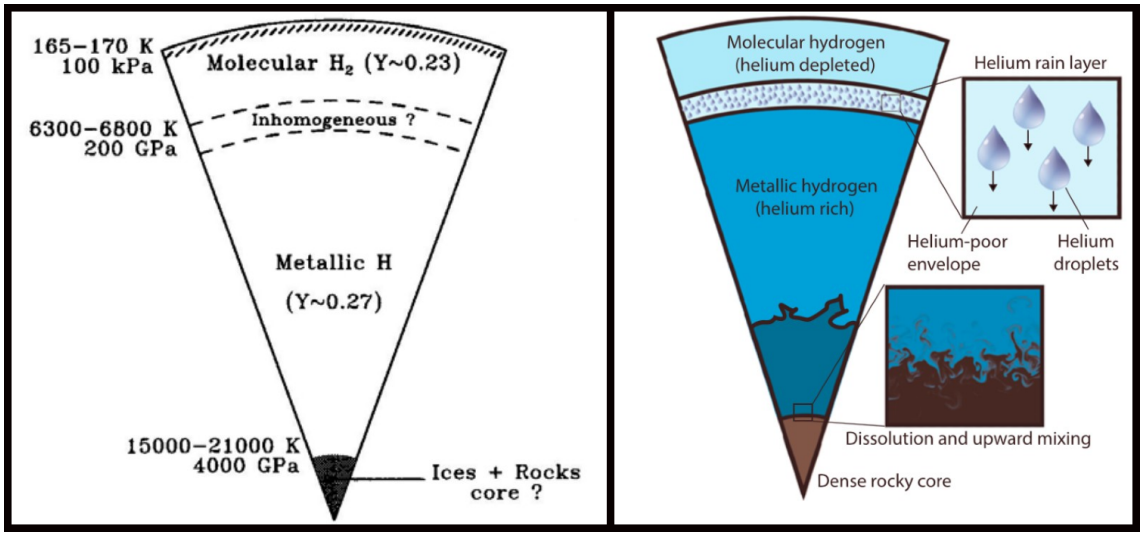


Figure 2.3: Interior models described in: Guillot (1999b) (left) and Wahl et al. (2017) (right).

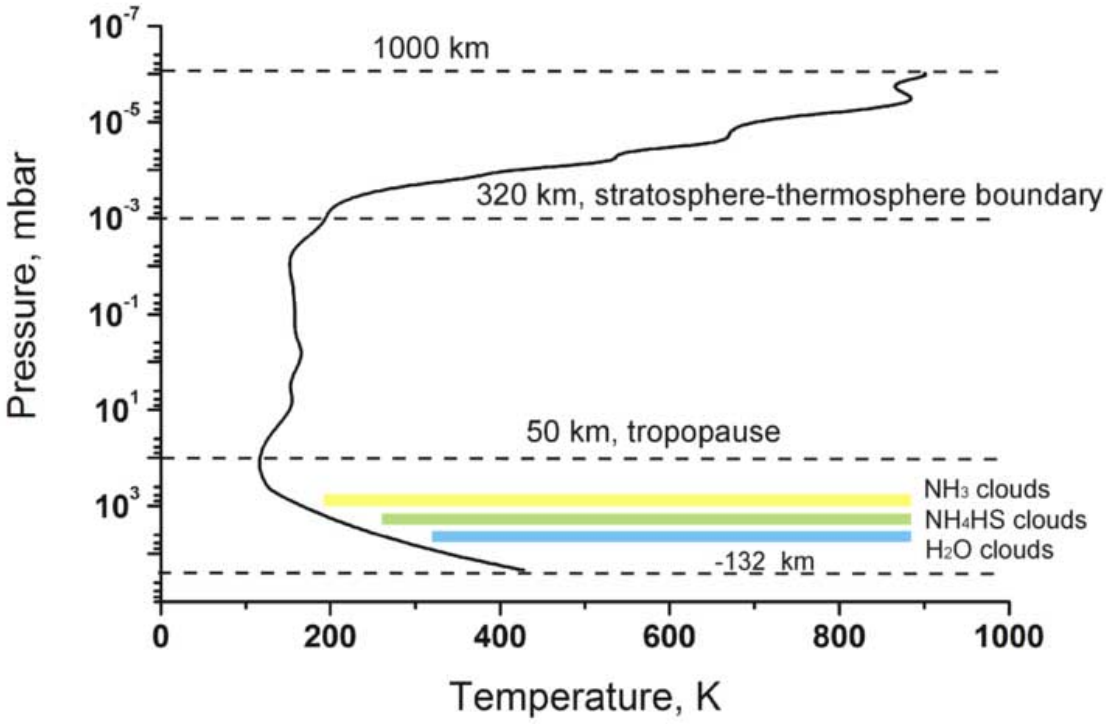


Figure 2.4: Pressure-Temperature profile measured by Seiff et al. (1997). The main condensable species are also displayed.

	J_2 $(\times 10^{-6})$	J_4 $(\times 10^{-6})$	J_6 $(\times 10^{-6})$	C/MR_e^2
Values for Jupiter	14,696.572 ± 0.014	-586.609 ± 0.004	34.198 ± 0.009	0.26393 ± 0.00001

Table 2.3: Values of J_{2n} and C/MR_e^2 measured for Jupiter by (Iess et al., 2018) and (Militzer & Hubbard, 2023).

2.4 Hydrostatic equilibrium of the giant planets atmospheres

The planetary atmospheres will be the main topic of this PhD thesis. In the previous section we saw that these are defined in giant planets as the uppermost gaseous layers in which hydrogen is mainly present in its molecular phase, together with the non-reactive helium and other volatile species (in all the phases). Due to their nature, atmospheres can be considered as a perfect physics laboratory, as well as a well-defined example of a complex system. In fact, they are characterized by their composition, density, temperature, and pressure profiles, which are determined by a complex interplay of factors, including the body's mass, gravity, temperature, and external influences such as solar radiation and impacts. In this section we will focus on the vertical profiles of the main physical parameters that characterize the intermediate part of the giant planet's atmosphere, 100 bar$< p <$0.01 bar, which encompasses both the troposphere and the stratosphere.
In order to start, we can assume that the intermediate atmosphere is in hydrostatic equilibrium and stationary along the vertical direction. In fact, visible images taken from both space missions and ground telescopes show that the horizontal winds that move the most recognizable atmospheric features over the planet's disk are much larger than the vertical ones. Therefore, to reconstruct the vertical profiles of physical quantities, we can use a layer-by-layer approach by dividing the atmosphere into different slabs. The vertical pressure difference dp across a slab of air at altitude z, of density ρ, thickness dz, and subject to a gravitational acceleration g is described by (Irwin, 2009):

$$dp = -\rho g dz. \tag{2.4}$$

At this point, we can assume that the gas in the slab behaves as an ideal gas and write:

$$\rho = \frac{\hat{m}p}{RT}, \tag{2.5}$$

where $\hat{m}$ is the mean molecular weight of the slab in g mol^{-1}, T its temperature, and R the gas constant which is equal to 8.314462618 JK^{-1} mol. Inserting Eqn. (2.5) in Eqn. (2.4) and integrating assuming a constant temperature we get the general equation that describes the vertical pressure profile of an atmosphere:

$$p = p_0 \cdot \exp\left(-\frac{z}{H}\right), \tag{2.6}$$

where H is called the atmospheric scale height of the atmosphere and is defined as $H = \frac{RT}{\hat{m}g}$. The scale height is the vertical distance over which pressure decrease of a factor e and represents an important "figure of merit" for atmospheric vertical scale. For Jupiter $H = 27$ km. Eqn. (2.6) tells us that the logarithm of pressures and altitudes are inversely proportional in an ideal isothermal atmosphere. Fig. 2.5 shows what Eqn. (2.6) should give us for the Jupiter case. I used $\hat{m} = 2.33\, g$ mol^{-1}, $g = 25\, m\, s^{-2}$, $T = 140K$, and a range of values for the altitude relative to the 1-bar level. Together to it, the real pressure-altitude profile measured by Galileo is shown (the measurement will be explained in detail in Chapter 4). It is possible to observe that the two profiles are pretty different. This is caused by the approximations made to obtain Eqn. (2.6), in particular the isothermal assumption. Real atmospheres

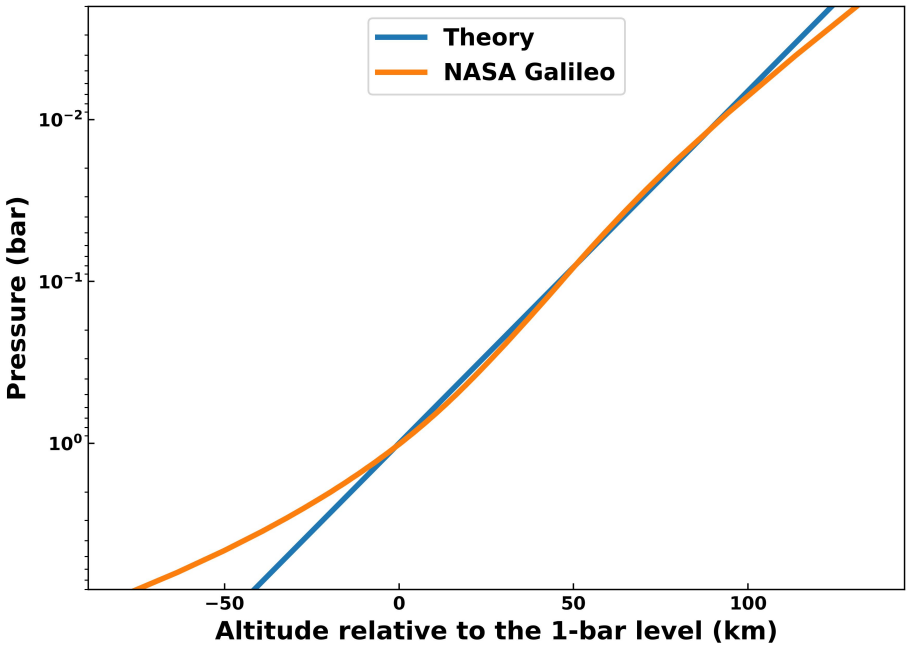


Figure 2.5: Pressure-Altitude profile measured by Seiff et al. (1997) compared to the one computed starting from Eqn. (2.6).

are known to have both pressure and temperature variable with altitude. Moreover, pressure and temperature are related to each other. Because of this, atmospheres are usually defined by pressure-temperature profiles, hereafter pT profiles. In order to treat physics more accurately it is better to divide our atmospheric region of interest in different parts: lower troposphere (p >0.4 bar), upper troposphere (0.4< p <0.1 bar), the tropopause around 0.1 bar, the lower stratosphere (0.1< p <0.01 bar), and, finally, the upper stratosphere (p <0.01 bar). In particular, the lower troposphere and the upper stratosphere are the regions were the two profiles shown in Fig. 2.5 differ the most.

2.4.1 Lower troposphere

As discussed in the previous section, in the lower troposphere convection is the dominant dynamical regime. Therefore we need to model the related vertical motion to obtain a more accurate description than Eqn. (2.6). For this purpose let's now consider a Lagrangian air parcel. The motion of the parcel of volume dV can be approximated using entropy and considering adiabatic conditions, i.e. no exchange of energy with the surrounding environment (Irwin, 2009):

$$dS = C_p \frac{dT}{T} - \left(\frac{\partial V}{\partial T}\right)_p dp = 0, \tag{2.7}$$

where C_p is the specific heat capacity. Using once again the ideal gas law ($\left(\frac{\partial V}{\partial T}\right)_p = \frac{R}{p} dp$) we can derive the adiabat pT equation:

$$T = T_0 \left(\frac{p}{p_0}\right)^{\frac{R}{C_p}}. \tag{2.8}$$

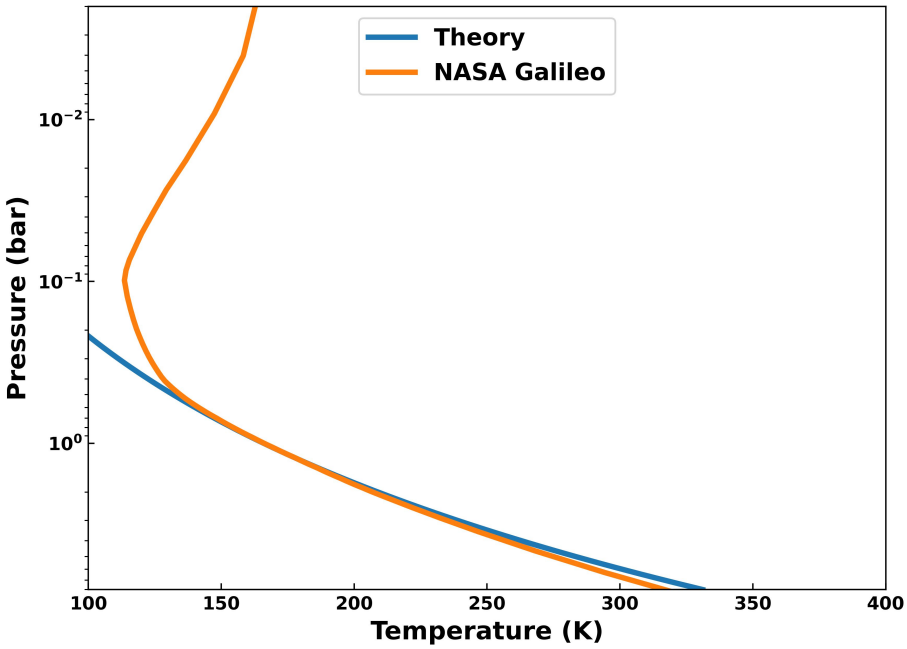


Figure 2.6: Pressure-Temperature profile measured by Seiff et al. (1997) compared to the one computed starting from Eqn. (2.8).

Using the hydrostatic equation (2.4) we can also derive an expression for the variation of temperature with altitude:

$$\frac{dT}{dz} = -\frac{\hat{m}g}{C_p} = -\Gamma_d, \tag{2.9}$$

where Γ_d is called the dry adiabatic lapse rate (DALR). The profile described by Eqn. (2.8) computed for Jovian conditions is shown together with the real one measured by the Galileo entry probe in Fig. 2.6. We can see that for pressures higher than 0.5 bar the agreement is optimal. The main conclusion is that in gas giant atmospheres similar to the one of Jupiter, the temperature increases monotonically with pressure as we probe deeper towards the interiors.
Moreover, the DALR is a quantitative measurement of the stability of convection in the atmosphere, as it was derived considering an air parcel undergoing a vertical motion. We can say that if $dT/dz <$DALR the rising parcels are cooler and denser than its surroundings and they will sink back down, indicating a stable convective atmopshere; on the other hand, when $dT/dz >$DALR rising air parcels are warmer and less dense than the air around them, therefore they will continue to rise on its own making the atmosphere unstable against convection (Schwarzschild, 1958).

2.4.2 Upper troposphere and stratosphere

From Fig. 2.4 it is possible to observe that the profile measured by the Galileo entry probe is almost constant (in temperature) for pressures lower than 0.1 bar, i.e. the tropopause. In the upper stratosphere, instead the temperature increases with decreasing pressures (i.e. increasing altitudes), a behavior commonly named as "temperature inversion". Which physical phenomena cause these effects ?
To give an answer we must introduce the concepts of gas opacity and gas optical

depth. Gas opacity, ϵ_ν defines a gas's resistance to the transmission of electromagnetic radiation. It's a quantitative measure of how much a gas absorbs and scatters radiation of a specific frequency ν per unit mass density along the path of the radiation. It is usually measured in cm^2/g. The definition of gas optical depth τ_ν is the integral of the opacity along a path ds: $\tau_\nu = \int \epsilon_\nu \rho ds$. It quantifies the attenuation of light at a specific frequency ν as it passes through the gas. It is, therefore, an adimensional quantity. I will define opacity and optical depth more rigorously in Chapter 3.
For now, let's consider a layer of opacity ϵ_ν high in the atmosphere with negligible atmospheric opacity above it. This is a good approximation for the upper atmosphere of gas giants, that as we saw in the previous subsection is thought to be mainly radiative. The atmosphere below this layer effectively emits as a black body of temperature equal to T_{bb} (see Chapter 3 for a rigorous definition). Using the Milner-Eddington equation (Atreya, 1986) we can find that the temperature of the layer T_s is:

$$T_s^4 = T_{bb}^4 \left(2 + 3\tau_{\text{IR}}\right), \tag{2.10}$$

where τ_{IR} is the infrared optical thickness between the layer and space. According to Eqn. (2.10), the temperature in the upper troposphere and stratosphere depends only on the gas optical thickness. As a consequence of the hydrostatic equilibrium, the density of gas molecules in a planetary atmosphere decrease with increasing altitude, and so it should also the gaseous opacity. Therefore, according to Eqn. (2.10) the temperature above the should tend to a constant value in the absence of other sources of heat, as observed by Galileo entry probe from lower troposphere to the stratopause (i.e. the upper limit of the stratosphere).
Looking at Fig. 2.4, we observe that above the tropopause the temperature increases. This increasing cannot be ascribed to the presence of radiative emitting gaseous species and therefore the only explanation is the presence of other energy sources. These are mainly: (i) absorption of ultraviolet radiation from the Sun via gaseous photodissociation reactions, and (ii) absorption of aerosols (see last section).

2.5 Turbulent processes

When we analyze the vertical dynamics of a complex system like the atmosphere, we cannot ignore the influence of turbulence and vertical mixing.
We define as vertical mixing a critical process that governs the redistribution of energy, momentum, and chemical species within planetary atmospheres, influencing their thermal structure, composition, and dynamics. Vertical mixing must not be confused with molecular mixing which is the movement of molecules from an area of high concentration to an area of low concentration due to their random thermal motion. While molecular diffusion operates on the scale of individual molecules, atmospheric mixing is predominantly driven by turbulent motions, or eddies, spanning a wide range of spatial and temporal scales. This turbulent mixing is often parameterized in atmospheric models as eddy diffusion, characterized by an eddy diffusion coefficient K_{zz}, measured in cm^2/s, which represents the effective diffusivity due to these unresolved turbulent motions (Prinn & Barshay, 1977). To understand what is K_{zz} we must start from the continuity equation in the vertical direction (Atreya,

1986; Yung & Demore, 1999) for a given gas species which has a number density (particles divided by a volume) n_i:

$$\frac{\partial n_i}{\partial t} + \frac{\partial f_i}{\partial z} = P_i - L_i, \tag{2.11}$$

where t is the time, f_i is the vertical flux of molecules, P_i is the chemical production rate, and L_i the chemical loss rate. Following Prandtl (1925) it is possible to solve the Eqn. (2.11) and obtain an expression for the flux of particles (Holton, 1992):

$$f_i = n_i \left[-D_i \left(\frac{1}{n_i} \frac{\partial n_i}{\partial z} + \frac{1}{H_i} + \frac{1}{T} \frac{\partial T}{\partial z} \right) - K_{zz} \left(\frac{1}{n_i} \frac{\partial n_i}{\partial z} + \frac{1}{H} + \frac{1}{T} \frac{\partial T}{\partial z} \right) \right] \tag{2.12}$$

where D_i and H_i are respectively the molecular diffusion coefficient and the atmospheric scale height of the considered species. When molecular diffusion dominates, each species tends to its own profile with its own scale height, given the dependency of H_i upon molecular weight. When eddy diffusion dominates, the gas is well-mixed and has a single bulk scale height. The pressure level where molecular diffusion becomes dominant is called homopause. The most significant difference is that molecular diffusion coefficient can be obtained using the following equation: $D_i = \frac{v_i}{3\sqrt{2} n_i \sigma_i}$, where v_i is the mean speed of the molecules of molecular weight $\hat{m}_i$, while σ_i is their cross-section.
On the contrary, the magnitude of K_{zz} varies significantly across different planetary atmospheres and even within different regions of the same atmosphere, reflecting the diverse range of dynamical processes at play. These dynamical processes include:

- Convection driven by buoyancy forces that can also lead to the formation of storms and vortices

- Shear Instabilities, i.e. fluid dynamics phenomena that arise when there are sharp differences in wind speeds or directions between adjacent layers of the atmosphere. These generate turbulence and promote mixing. These instabilities are common in regions with strong jet streams or where air masses with different velocities interact (Andrews et al., 1987). The resulting turbulence can mix momentum, heat, and chemical species, playing a crucial role in the dynamics of the middle atmosphere.

- Gravity Waves: These are oscillations that propagate through a stable, stratified fluid, with gravity acting as the restoring force. Gravity waves can be generated by various sources, including convection, flow over topography, and wind shear. As they propagate upwards, their amplitude increases with decreasing atmospheric density, and they can eventually break, depositing momentum and energy into the background flow and generating turbulence (Fritts & Alexander, 2003). Gravity wave breaking is a key driver of vertical mixing in the upper troposphere, stratosphere, and mesosphere.

However, accurately representing vertical mixing in atmospheric models remains a significant challenge. Furthermore, the spatial scales of the turbulent motions responsible for mixing are often much smaller than the resolution of global-scale atmospheric models, imposing the use of parameterizations. These parameterizations introduce uncertainties into the simulations, and improving them requires a

combination of high-resolution modeling, observational constraints, and theoretical advances. A parametrization often used for Jupiter K_{zz} is (Atreya, 1986):

$$K_{zz}(z) = K_0 \left[\frac{n_H}{n(z)}\right]^{0.5}, \tag{2.13}$$

for $p < p_{\rm tr}$, where $p_{\rm tr}$ is the pressure at the tropopause; $n(z)$ is the total number density while n_H is the number density at the homopause. For $p > p_{\rm tr}$ it is safe to assume K_{zz} =const. This holds to be consistent with observations of specific chemical species distribution across the Jovian disk (Showman & Ingersoll, 1998; Fouchet et al., 2003).

2.6 Composition profiles and Photochemistry

In Sections 2.2 and 2.3 we saw how it is possible to derive chemical composition of Jupiter starting from the nebular hypothesis and gain insights about its interiors. To verify if the composition ratios predicted by theory are confirmed by observations, it is useful to describe each chemical constituent in terms of a vertical profile that associates at each pressure (or altitude) its proportion with respect to the total volume of dry air. The so-defined profiles are called volume mixing ratio (VMR) profiles, and are therefore a-dimensional. The VMR profile of a chemical species can be highly sensitive to:

- the chemical reactions with different species occurring at given pressure and temperature values
- the phase changes occurring at given pressure and temperatures (see next section). As a result, cloud particles, either solid or liquid can be formed. In this thesis I will refer to aerosols as tiny, suspended particles of liquid or ice (or a mixture of both) in the atmosphere, typically ranging in size from a few micrometers to a few hundred micrometers. Cloud particles are aerosol particles formed through condensation, i.e. phase changes from gas to liquid or gas to solid.
- photolysis, i.e. the process where a molecule is dissociated into smaller molecules, atoms, or radicals by absorbing a photon.
- photochemistry, i.e. chemical reactions that are initiated by the absorption of light, particularly solar radiation, by atmospheric molecules and atoms
- turbulence (see previous section), strong winds, and dynamical convective events that redistribute gaseous species in space (horizontally and vertically).

A VMR profile can also be unaffected by the above listed physical phenomena, and therefore be constant throughout all the atmosphere. If so, the species is thought to be in thermodynamical equilibrium in the atmosphere. We define a species to be in disequilibrium in a planetary atmosphere if, given a pT profile, its VMR profile its different from the one expected by thermodynamical equilibrium.
In this section we will focus on the VMR profiles of the Jovian troposphere and

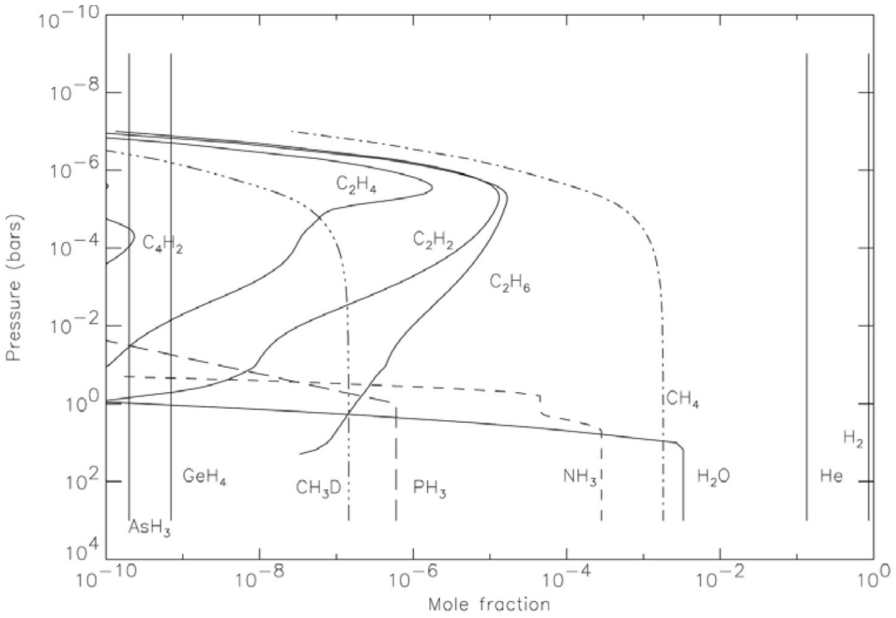


Figure 2.7: Observed and modeled abundance profiles in the atmosphere of Jupiter from Irwin (2009).

stratosphere bearing in mind that these can be easily extended to Saturn and gaseous exoplanets.

On Jupiter the chemical species all exist in their hydrogenated form. Only two species are thought to be in equilibrium: molecular hydrogen H_2 and helium He. The respective mixing ratios were measured to be 0.86 and 0.13 respectively by the Galileo mass spectrometer (see Chapter 5). Helium, being a noble gas, is highly non-reactive. On the other hand, the constant hydrogen VMR on Jupiter is a consequence of its overwhelming abundance, and the lack of significant chemical processes that would alter its concentration in the levels of our interest, i.e.: troposphere and lower stratosphere. While photochemistry does affect the upper atmosphere, the sheer amount of H_2 and its tendency to reform maintain a consistent proportion deeper down. The other species present in Jupiter atmosphere in their hydrogenated form are: methane CH_4, ammonia NH_3, phosphine PH_3, hydrogen sulfide H_2S, water H_2O, arsine AsH_3, and germane GeH_4. In the next subsections I will describe their respective VMR profiles, that are represented in Fig. 2.7. The methods used to derive these observational constraints will be described in Chapter 5.

2.6.1 Methane

The vertical profile of methane on Jupiter exhibits a near-constant volume mixing ratio (VMR) of approximately 1.8×10^{-3} throughout its deep troposphere and lower stratosphere (Atreya et al., 2003; Wong et al., 2004b). It can be considered therefore in equilibrium in the troposphere. This uniformity is primarily attributed to highly efficient vertical mixing driven by vigorous convection and turbulent motions within Jupiter's dynamic atmosphere (Ingersoll et al., 2000). This strong mixing rapidly redistributes methane, counteracting any localized variations in its concentration. Moreover methane cannot condense at pressures and temperatures of the Jovian atmosphere.

In the upper stratosphere, however, methane undergoes significant photodissociation by solar ultraviolet (UV) radiation at wavelengths shorter than 160 nm (Gladstone et al., 1996). Although the penetration of these high energy photons is inhibited by the presence of molecular hydrogen, they can nonetheless easily reach pressure levels of 0.1 mbar or lower (higher in altitude). This mainly explains the decay of the profile observable from Fig. 2.7. This photolysis initiates a complex hydrocarbon chemistry, leading to the formation of ethane (C_2H_6) and acetylene (C_2H_2) with significantly lower VMRs (around 10^{-6}) (Moses et al., 2005). These heavier hydrocarbons are subject to condensation and downward transport to warmer levels, where they can undergo thermal decomposition and reactions with hydrogen, potentially contributing to a methane recycling mechanism at deeper levels.

2.6.2 Ammonia and Hydrogen Sulfide

The vertical profiles of ammonia (NH_3) and hydrogen sulfide (H_2S) on Jupiter are significantly influenced by their condensation in the upper troposphere, leading to non-uniform distributions with altitude (Atreya et al., 2003) This is easily shown in the profiles given in Fig. 2.7. Ammonia has a constant VMR profile of 2-4$\times 10^{-4}$ in the deep troposphere (>0.8 bar), consistent with the values in Table 2.2. However, it is expected to condense into ammonia ice clouds at temperatures around 150 K (approximately 0.7 bar pressure level) (Lewis, 1969). Above this level, the gaseous ammonia abundance decreases sharply following its saturation vapor pressure curve. The saturation vapor curve is a thermodynamically defined locus of points on a phase diagram (typically pressure-temperature or temperature-entropy) that represents the conditions under which a substance exists in equilibrium between its liquid and vapor phases, with the vapor being in a saturated state.
However, observations from the Galileo probe and by the Juno MWR (see Chapter 4) and remote sensing have revealed complexities, see Fig. 2.8, that includine latitudinal depletions and variations (Li et al., 2017). These are potentially linked to deep convective upwelling and subsequent dissolution in water ice at lower temperatures, forming "mushballs" that transport ammonia deeper (Ingersoll et al., 2000; Wong et al., 2004b; Fletcher et al., 2016a; Guillot et al., 2020a,b). Above 0.1 bar the ammonia can be easily destroyed by incident energetic solar photons. Therefore usually its VMR profile is not given after this altitude or is described as rapidly decaying. Hydrogen sulfide, with a deep troposphere (>0.8 bar) VMR of roughly 3×10^{-5}, is predicted to condense at deeper levels and warmer temperatures (around 200 K, $\sim$ 2 bar) by reacting with ammonia to form ammonium hydrosulfide (NH_4SH) clouds (Lewis, 1969). Below this cloud layer, H_2S is expected to be more uniformly mixed. The Galileo probe detected H_2S at levels deeper than 1 bar (Wong et al., 2004b), supporting this general picture, although its abundance also showed variability, possibly related to the same dynamical processes affecting ammonia (Niemann et al., 1996; Wong et al., 2004b). The interplay between condensation, chemical reactions forming NH_4SH, and vigorous vertical transport results in complex vertical profiles for both NH_3 and H_2S, deviating from simple uniform mixing ratios, particularly in the cloud-forming regions of Jupiter's troposphere.

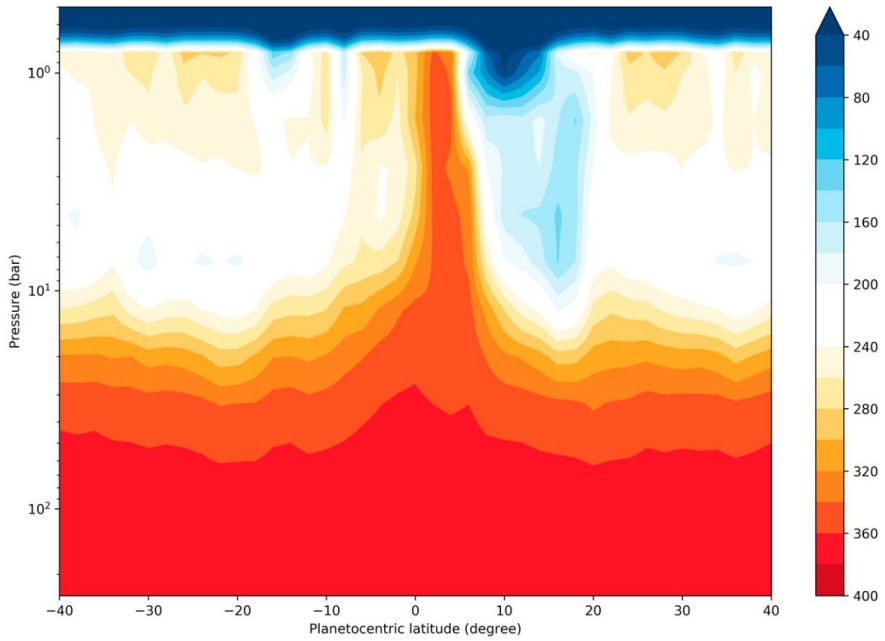


Figure 2.8: Ammonia concentration in parts per million measured by Juno/MWR Li et al. (2017).

2.6.3 Water

The vertical profile of water vapor on Jupiter is fundamentally governed by physical processes, primarily condensation and transport. At specific temperature and pressure levels corresponding to the water cloud layer (estimated to be at 5 bar from Lewis (1969)), water vapor reaches saturation and condenses into liquid water and potentially ice clouds. This condensation acts as a significant sink for water vapor in the upper troposphere, leading to the observed depletion at shallower depths. Vertical transport, driven by convection and atmospheric waves, plays a crucial role in redistributing water vapor. Upwelling motions can carry water vapor from deeper, warmer regions towards the condensation level, while downwelling motions transport drier air from above. The balance between the upward flux of water vapor and the condensation rate determines the water vapor abundance in the observable upper troposphere. While photolysis can destroy water molecules in the very upper atmosphere, its impact on the overall vertical profile in the troposphere is secondary to the thermodynamic control exerted by condensation and the dynamical influence of vertical mixing.

2.6.4 Phosphine

The vertical distribution of phosphine (PH_3) in Jupiter's atmosphere is a classic example of disequilibrium chemistry, heavily influenced by the interplay of thermodynamics and atmospheric dynamics. Thermochemical equilibrium predicts that PH_3 should be virtually absent in the observable upper troposphere, as phosphorus preferentially forms more oxidized species at lower temperatures. However, PH_3 is observed due to rapid vertical transport, primarily through convective upwelling, from Jupiter's deep, hot interior where it is thermodynamically stable (Prinn & Lewis, 1975).

This upward flux effectively "quenches" the high-temperature chemical equilibrium, carrying PH_3 to cooler, higher altitudes faster than it can be destroyed kinetically. As a result, the PH_3 volume mixing ratio exhibits a decreasing profile with altitude in the upper troposphere, reflecting the balance between the upward transport and the increasing rate of destruction processes. The primary destruction mechanism is photolysis by solar ultraviolet radiation in the upper atmosphere, which dissociates PH_3. The efficiency of vertical mixing, parameterized by eddy diffusion coefficients, plays a crucial role in determining the observable abundance of PH_3 (Fegley & Lodders, 1994). Variations in this mixing, both spatially and temporally, can lead to corresponding variations in the observed PH_3 abundance.

2.6.5 Germane and Arsine

The vertical profiles of germane (GeH_4) and arsine (AsH_3) on Jupiter are primarily governed by deep atmospheric thermochemistry and the efficiency of vertical mixing (Fegley & Lodders, 1994). Under the high temperatures prevalent in Jupiter's deep interior, germanium and arsenic are expected to be fully reduced, forming GeH_4 and AsH_3, respectively. Due to the lack of significant condensation of these species in the observable troposphere and the relatively slow chemical kinetics of their decomposition at these altitudes, their presence in the upper atmosphere depends on rapid vertical transport from the warmer, deeper layers (Prinn & Lewis, 1975). Observations, though challenging due to their low abundances (typically in the parts per billion to sub-parts per billion range), suggest a relatively constant VMR in the middle to upper troposphere, consistent with efficient upwelling overcoming slow destruction mechanisms. Photochemical destruction in the uppermost atmosphere is expected, but its influence on the bulk tropospheric abundance is limited by the strong vertical mixing.

2.7 Condensation processes

As we saw in the previous section, when a gas's VMR (Volume Mixing Ratio) profile reaches its saturation vapor curve, the gas can undergo phase changes and form liquid or solid cloud particles. This process is defined as condensation. In this section we will focus on the physical treatment of this phenomena.
To begin, it is worth noting that observations of Earth's atmosphere have shown that a gas - notably water vapour - doesn't necessarily condense just because it reaches its saturation vapor curve. In fact the presence of the so-called condensation nuclei is needed (Twomey, 1974). A condensation nucleus is a tiny airborne particle, either solid or liquid, with a typical size of a few nanometers, upon which water vapor can readily condense to form liquid water droplets. These particles possess a surface that reduces the energy barrier required for water molecules to transition from the gaseous to the liquid phase. An effective cloud condensation nucleus (CCN) is typically a hygroscopic particle. Its chemical affinity with water molecules facilitates the condensation process, enabling it to occur even at relatively low levels of water vapor supersaturation in the atmosphere. Common examples include particles of salt, dust, pollutants, and organic matter. On Jupiter this kind of CCN can exist as a result of methane photochemistry or as the result of impact of external objects

(micrometeorites, debris, etc.) (Atreya & Wong, 2005). This is still an open topic in science, so in this thesis I will assume that CCNs exist in the Jupiter atmosphere, but I won't explore their nature due to the poor quality of the observational data. Secondly, it is important to highlight the difference between cloud condensation on Earth and Jupiter. On Earth the formation of clouds is mainly driven by the solar heating of the ocean. In that way water vapor is set free in the atmosphere. It can successively rise, expand, and cool, leading to water vapor saturation and, then, condensation. On Jupiter, the formation of clouds is mainly driven by both internal heating and strong convective events (Ge et al., 2024). The first, combined with vertical mixing, can make the gas rise and cool leading to the formation of the global cloud decks. The second can transport large quantities of gas in the upper atmosphere creating dense clouds connected to vortices and storms.

Said that, now we will see how it is possible to estimate the cloud condensation levels from simple thermodynamics. The Clausius-Clapeyron equation, which governs how pressure p and temperature T vary along a phase transition, is given by (Rex & Finn, 2017; Irwin, 2009):

$$\frac{dp}{dT} = \frac{\Delta S}{\Delta V}, \tag{2.14}$$

where ΔS is the change in entropy of a certain quantity of material changing phase; and ΔV is the associated change in volume. Using again the ideal gas law we obtain:

$$\frac{dp}{dT} = \frac{Lp}{RT^2}, \tag{2.15}$$

where L is the latent heat of vaporization per mole. Assuming L to be constant we obtain:

$$\ln p_{\text{sat}} = A - \frac{L}{RT} = A - \frac{B}{T}, \tag{2.16}$$

where A and B are constants that depend on the nature of the condensing species. For ammonia, ammonia+H_2S, and water we have the following equations (Lange & Forker, 1953; Irwin, 2009):

$$p_{\text{sat, NH}_3}\,[\text{bar}] = 10^{-3} \cdot 10^{10.1883 - \frac{1633.785\,K^{-1}}{T} + 0.12490182}, \tag{2.17}$$

$$\ln p_{\text{sat, NH}_3} + \ln p_{\text{sat, H}_2\text{S}} = 34.15 - \frac{10833.6\,K^{-1}}{T}, \tag{2.18}$$

$$\ln p_{\text{sat, H}_2\text{O}_{\text{liq}}} = 14.149 - \frac{5257.2\,K^{-1}}{T}, \tag{2.19}$$

$$\ln p_{\text{sat, H}_2\text{O}_{\text{ice}}} = 17.477 - \frac{6164.65\,K^{-1}}{T}, \tag{2.20}$$

that describes their saturation vapor curves. The relative VMR curves can be obtained using this expression:

$$\text{mr}_{\text{sat}}(p, T) = \frac{p_{\text{sat}}}{p}\frac{RH}{100}, \tag{2.21}$$

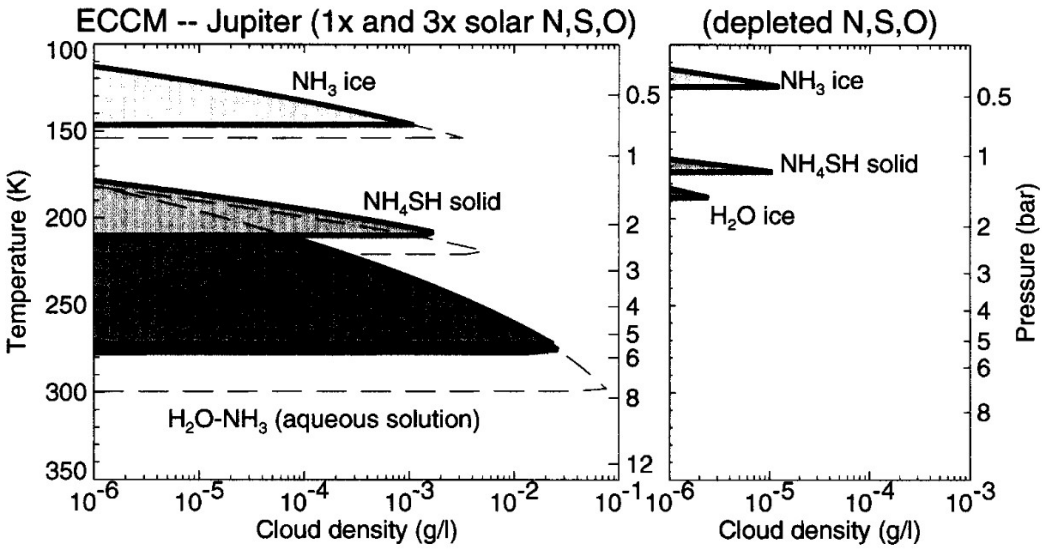


Figure 2.9: Results of Equilibrium Chemistry Condensation Models for the Jupiter atmosphere Atreya et al. (1999).

where the RH scaler parameter is defined as the relative humidity.
Based on this, the condensation levels can be estimated using the so-called equilibrium cloud condensation models (ECCMs) (Lewis, 1969; Atreya et al., 1999). First we approximate the vertical distribution of a condensable species by considering an adiabatically ascending air parcel. Condensation of the species of interest begins when the partial pressure equals the saturation vapor pressure. Further ascent and cooling lead to increased condensation, with the gaseous mixing ratio following the saturation VMR curve. If condensed particles precipitate out, the tropopause acts as a "cold trap," preventing re-evaporation and limiting stratospheric abundance. The intersection of the initial mixing ratio and the saturation VMR curve defines the cloud base level; a higher initial VMR results in a higher cloud base pressure (lower altitude), making the ECCMs highly variable on initial conditions. Considering the pT profile described in Section 2.4 and Eqn (2.17) (2.18) (2.19) (2.20) we can see that on Jupiter we expect three cloud decks:

- pure ammonia ice between 0.5-0.7 bar
- ammonium hydrosulfide at 2 bar
- water liquid/ice at 5 bar

ECCMs can also give upper limits on the expected cloud densities assuming that all the excess vapor instantaneously condenses. The physical units usually used to describe cloud densities are particles/cm^3 or g/l. In the first case we refer to number density while in the latter to bulk density. The estimated cloud profiles by Atreya et al. (1999) are shown in Fig. 2.9.

However, in reality we expect the process of condensation to be far more complex (Lunine et al., 1989). The first model that accounted for more complicated physics is the one presented in Ackerman & Marley (2001), hereafter A&M2001. This model computes the radii and densities of cloud particles by considering the

dynamic balance between the upward transport of condensable vapor via turbulent eddy diffusion and the downward removal of condensed particles through gravitational sedimentation (i.e. the process where particles suspended in a fluid settle out of the fluid due to the force of gravity acting on them). The radius of the cloud particles r is a key parameter to determine their optical properties as we will see in the next chapter. Usually, the cloud particles are approximated to follow a log-normal distribution that describes their radii (also referred as size distribution):

$$n(r) = \frac{n_0}{\sqrt{2\pi}} \frac{1}{r \ln \nu_r} \exp\left[-\frac{(\ln r - \ln r_m)^2}{2 \ln {\nu_r}^2} \right], \tag{2.22}$$

where n_0 is a normalizing constant, r_m is called the modal radius, and ν_r the variance of the distribution. From these two parameters it is possible to also define the so-called effective radius as follows:

$$r_{\text{eff}} = \frac{\int_0^\infty r^3 n(r) dr}{\int_0^\infty r^2 n(r) dr} = r_m e^{2.5 \ln {\nu_r}^2}. \tag{2.23}$$

Said this, the A&M2001 model considers a steady-state particle size distribution at each altitude where the upward flux of particles due to turbulent diffusion is balanced by the net downward flux due to sedimentation of particles of that size. This balance is mathematically expressed through a continuity equation for the number density of particles as a function of altitude and particle size:

$$-K_{zz} \frac{\partial q_t}{\partial z} - f_{\text{sed}} w_* q_c = 0, \tag{2.24}$$

where q_c is the cloud VMR while $q_t = q_c + q_v$ is the sum of q_c and of the gaseous VMR q_v of the considered condensable species. The term w_* represents the convective velocity scale. It represents a reference speed for convective motions and therefore it will be connected both to H and K_{zz}. The relation is modeled as $w_* = K_{zz}/l$, where l is called the is the turbulent mixing length which usually is considered to be $l = \text{const.} \times H$ (Rooney et al., 2022). If we approximate the eddy coefficient as (Gierasch, 1996):

$$K_{zz} = \frac{H}{3} \left(\frac{l}{H} \right)^{4/3} \left(\frac{\sigma T^4}{\hat{m} \rho C_p} \right)^{1/3} \tag{2.25}$$

where σ is the Stefan-Boltzmann constant ($\sigma = 5.67 \times 10^{-8}$ W/(m^{2}K^4)), then Eqn. (2.24) can be integrated and it rewrites as (Rooney et al., 2022):

$$q_c(z)[\text{VMR}] = q_{vs} + q_0 \exp\left(-\frac{f_{\text{sed}} z}{l} \right), \tag{2.26}$$

where q_{vs} is the constant mixing ratio of saturated vapor and q_0 a constant. Eqn. (2.26) can be easily rewritten to obtain vertical density profiles in part./cm^3 or g/l. The crucial parameter shaping the cloud density profiles is the sedimentation efficiency f_{sed}. This dimensionless parameter represents the efficiency of particle removal from a given atmospheric layer via sedimentation relative to the characteristic vertical eddy mixing scale. Physically f_{sed} can be thought of as the ratio of a characteristic sedimentation velocity to a characteristic convective velocity scale. A high

$f_{\rm sed}$ implies that sedimentation is very efficient, leading to thinner clouds with larger particles, as smaller particles are effectively removed before being mixed to higher altitudes. Conversely, a low $f_{\rm sed}$ indicates less efficient sedimentation, resulting in vertically extended clouds with smaller particles that can be lofted higher by turbulence. For Jupiter and Saturn we expect higher $f_{\rm sed}$ values than for example Hot Jupiter planets (Robbins-Blanch et al., 2022). Mathematically $f_{\rm sed}$ can be expressed as (Rooney et al., 2022):

$$f_{\rm sed} = \frac{\int_0^\infty v_{\rm sed}(dm/dr)dr}{(\hat{m}_c/\hat{m})\rho w_* q_c} = \frac{v_{\rm sed} l}{K_{zz}}, \tag{2.27}$$

where $v_{\rm sed}$ is the particle sedimentation velocity, m is particle mass, and $\hat{m}_c$ the condensate molecular weight. At this point it is possible to use an approximation for $v_{\rm sed}$:

$$v_{\rm sed} = w_* \left(r/r_{\rm sed}\right)^{\alpha_{\rm sed}}, \tag{2.28}$$

where r_w is is a reference radius, computed using the Stokes law considering w_* as the fall speed. The Stokes law for the Jupiter atmosphere can be computed starting from fluid dynamics (Young et al., 2019). Lastly, $\alpha_{\rm sed}$ is an exponent that depends on the aerodynamic drag regime, and also this can be computed using fluid dynamics and a parametrization for the Reynolds number. Plugging Eqn. (2.27) and (2.28) in Eqn. (2.22) and (2.26) it is possible to compute the effective radius of the clouds at each point in the atmosphere using this expression:

$$r_{\rm eff} = r_w f_{\rm sed}^{1/\alpha_{\rm sed}} \exp\left(-\frac{\alpha_{\rm sed}+1}{2}\ln {\nu_r}^2\right) \tag{2.29}$$

In Fig. 2.10 it is possible to observe the results of the A&M2001 model for the Jupiter case (West et al., 2007). The nature of the condensed clouds is the same as the ones predicted by ECCMs. However, it is possible to observe that the A&M2001 model predicts lower densities (around an order of magnitude) and modal radii between 1 and 10 micrometres. Therefore A&M2001 model is capable of reproducing the results of the ECCMs giving more reasonable estimates of the physical parameters as microphysics is included. Moreover, the method is extremely fast and easy to implement from a computational point of view. An example is the `virga` Python package (Rooney et al., 2022).

The "Fresh clouds" method, as detailed in Wong et al. (2015), presents an even more physically-based approach for modeling of cloud condensation by extending A&M2001, incorporating explicitly the kinetics of cloud formation within a rising air parcel. This method parameterizes the microphysical processes occurring within an updraft of a defined velocity. As an air parcel ascends and adiabatically cools, the volatile gases within it may become supersaturated before nucleation and subsequent condensation occur. With supersaturation we refer to a physical situation where the RH parameter becomes larger than 100 %. In this condition, a large number of CCNs are activated, resulting in a higher concentration of cloud droplets. However, with more droplets competing for the available vapor, the average size (radius) of individual droplets might be smaller.
The "Fresh clouds" method accounts for this supersaturation and the finite timescale

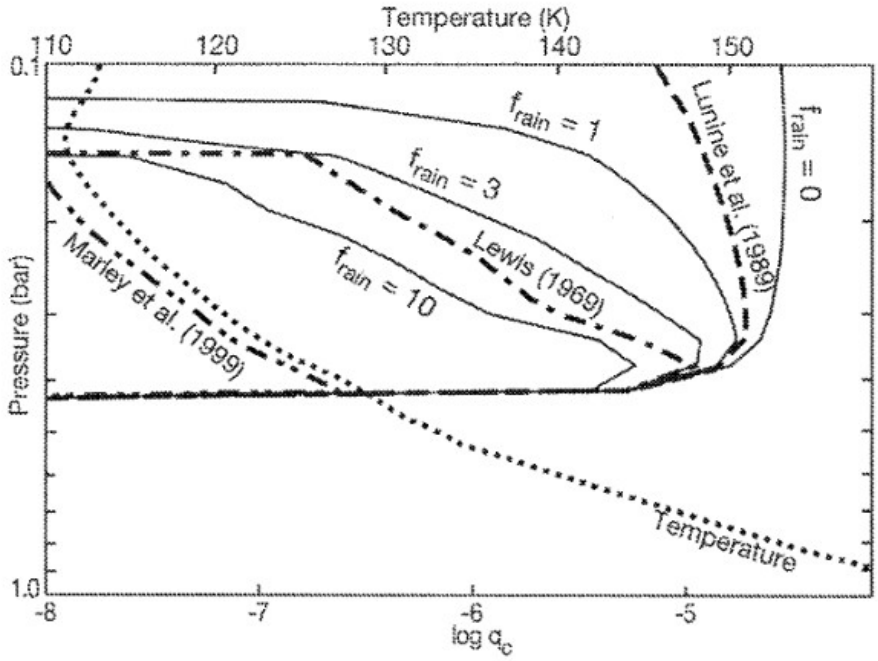


Figure 2.10: Comparison of microphysical model profiles of ammonia cloud density West et al. (2007).

required for condensation by employing parameterized formulations for nucleation rates and droplet/crystal growth as a function of supersaturation, temperature, and the availability of Condensation Nuclei (CN). Consequently, this approach can lead to the formation of clouds with distinct microphysical properties (e.g., particle size distribution, number density) and vertical density profiles compared to both ECCMs and A&M2001. The results of the model for Jupiter are displayed in Fig. 2.11. As expected, this method provides lower densities than both ECCMs and A&M2001.

It is worth to remind that in principle the formation of clouds is also highly dependent on horizontal atmospheric motion and dynamics. Strong winds for example can inhibit the whole process by reducing the amount of total available condensable gas and CCNs. In this context, General Circulation Models become very useful. They are numerical frameworks rooted in fundamental hydrodynamics and thermodynamics, employing discretized representations of planetary air masses. These models solve the governing equations of fluid flow (Navier-Stokes), energy conservation (thermodynamic equation), mass conservation (continuity equation), and radiative transfer (see next Chapter), accounting for planetary-specific forcings such as insolation, gravity, and rotation. In this context sub-grid scale processes, including turbulence and cloud microphysics, can be parameterized based on the previous discussion. For example, the work of Zuchowski et al. (2009) and Young et al. (2019) implemented the ECCMs in the framework of the Oxford Planetary Unified model System (OPUS). They found that the condensates constitute good tracers of atmospheric motion and the cloud bases are consistent with the 1D case. However, the found densities are lower of between 1 and 2 orders of magnitude with respect to the ECCMs outcomes, suggesting that horizontal motions can potentially play an important role in inhibiting cloud formation. It is important to underline that the

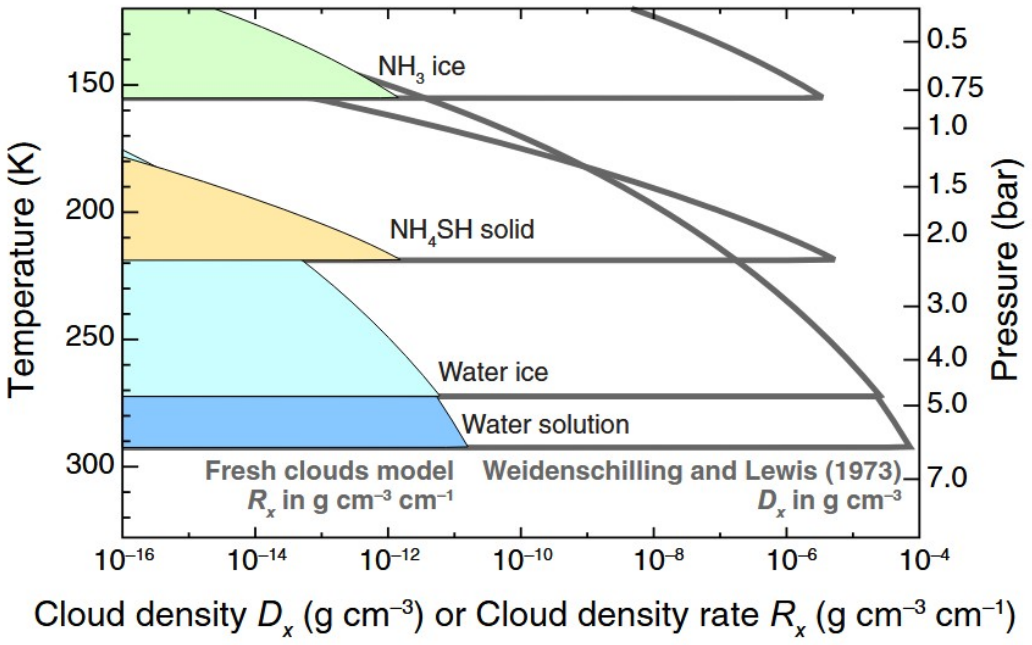


Figure 2.11: Comparison of cloud density D_x, calculated using ECCMs (grey lines) and Fresh clouds model (color), from Wong et al. (2015).

results of GCM runs usually depend strongly on boundary conditions. Therefore, this is still an open area of investigation.
I found it appropriate to provide a detailed description of the theoretical framework behind cloud formation because of their importance in the context of this thesis and for planetary atmospheres in general. As it will explained in the next chapters, clouds have a major role in driving the radiative transfer in giant planets, shaping the observed spectral radiances. They are also extremely important in the context of the energy balance of a planet. Their high albedo leads to a net cooling effect by reflecting incoming shortwave radiation. Conversely, their absorption and re-emission of outgoing longwave radiation contribute to a greenhouse warming effect. The net radiative forcing by clouds is a complex function of cloud type, altitude, fractional coverage, and microphysical properties, dictating their overall impact on planetary temperature and climate sensitivity. Understanding these intricate cloud feedbacks is crucial for accurate climate modeling. On giant planets they can also alter the pressure temperature profile. Returning to Eqn. (2.9), in the presence of condensation species it becomes (Irwin, 2009; Andrews, 2000):

$$\frac{dT}{dz} = -\Gamma_s \ , \ \Gamma_s = \Gamma_d \frac{\left[1 + \frac{1}{RT}\sum L_i x_i\right]}{\left[1 + \frac{1}{C_p T^2}\sum \frac{L_i^2 x_i}{R}\right]}, \tag{2.30}$$

where L_i is the molar latent heat of vaporization (or sublimation) of the i th condensing component and x_i is the saturated volume mixing ratio.

2.8 Hazes

In the previous section we introduced aerosols, that will be the main subject of this thesis. We also saw that condensation can lead to the formation of these solid and liquid particles in suspension. However, this is not the only process that can create aerosol particles. For example, on Earth, aerosols (as I defined them previously) are mainly composed of water ice droplets. However, there are several other sub-micron particles created in various ways. Examples include (Lohmann & Feichter, 2005):

- Fine soil and mineral particles lifted by wind, particularly in arid and semi-arid regions
- Tiny carbonaceous particles produced by the incomplete combustion of organic materials from wildfires
- Anthropogenic aerosols such as sulfates, nitrates, organic carbon, and black carbon, often formed through chemical reactions of gaseous emissions from vehicles, power plants, and industrial activities
- Fine salt particles left behind after the evaporation of sea spray
- Biological particles dispersed in the air

Usually, these particles are less influential than water clouds in the atmosphere. In fact, due to their small size, a large amount of them (in terms of number density) is usually required in order to observe their optical and physical contribution. However, in some specific physical situations (i.e. dust storms, high humidity periods) they can become dominant. From now on I will refer to those extremely small, dry aerosol particles suspended within a gaseous medium with the term haze.
In the most extreme and exotic planetary conditions we do not expect the same kind of haze that we found on Earth. In particular, on Jupiter, Saturn, and gaseous exoplanets, hazes have been inferred from observations since their discovery (Kreidberg et al., 2014). Usually the best hint about the presence of hazes is unexpected absorption (or glow) of UV or blue radiation (see Next Chapters) (Judge & Carlson, 1974; Tsubota et al., 2025; Sing et al., 2016). On the other hand, a general picture about their origin is still not clear. A reasonable explanation can be that haze particles in gaseous atmospheres are the results of the action of both photolysis and photochemistry on the minor gaseous species. This picture was consolidated by the results obtained from the Cassini Huygens mission (Matson et al., 2002; Porco et al., 2005). A key component was the Huygens probe, which detached from Cassini and became the first human-made object to land on a moon in the outer solar system when it reached Titan in 2005.
Titan, the biggest moon of Saturn, possesses a dense, predominantly nitrogen (N_2) atmosphere with a surface pressure approximately 1.5 times that of Earth's (Fulchignoni et al., 2005). A key characteristic of Titan's atmosphere is the ubiquitous presence of a thick, orange-brown haze layer that obscures its surface at visible wavelengths (Lorenz et al., 2007a,b). The Cassini-Huygens mission provided invaluable in-situ measurements of these aerosols. The Huygens probe's Aerosol Collector and Pyrolyser (ACP) experiment directly sampled aerosols at different altitudes during its descent, revealing that they are rich in carbon and nitrogen (Israël et al., 2005). All the

measurements were consistent with complex organic aerosols, formed through high-altitude photochemistry driven by solar ultraviolet radiation and Saturn's magnetospheric electrons interacting with the primary atmospheric constituents, methane and nitrogen (Waite et al., 2007). Years before the arrival of Cassini in the Saturn system, the famous American astrophysicist and science communicator Carl Sagan, designed together with his colleagues at the Cornell University fundamental laboratory works in order to study these exotic compounds (Sagan & Khare, 1979; Sagan & Thompson, 1984; Khare et al., 1984). They were able to synthesize a series of dark reddish organic solids, called tholins and to measure their optical properties. The term tholins comes from the Greek one tholós, which means "sepia ink". Since then, the term tholins indicates polymer-like materials made of repeating chains of linked subunits and complex combinations of functional groups, typically nitriles and hydrocarbons. They are therefore chains of three of the elements needed for life, C, H, and N. The Sagan and Khare experiments were repeated in the following 30 years and more, providing a very accurate and comprehensive database of tholins materials expected to be produced at Titan conditions.

Going back to Jupiter, the formation of hydrocarbon haze in the Jovian upper atmosphere is primarily driven by far-ultraviolet (FUV) photolysis of methane by solar radiation (Strobel, 1973). This initial photodissociation generates a cascade of highly reactive radicals, such as CH_3 and CH_2, which subsequently participate in a complex network of ion-neutral and radical-radical reactions see Fig. 2.12 (Atreya, 1986; Moses et al., 2005). These reactions lead to the formation of more complex hydrocarbons, including ethane (C_2H_6), acetylene (C_2H_2), and ethylene (C_2H_4), as well as higher-order polycyclic aromatic hydrocarbons (PAHs) (Friedson et al., 2002). These heavier hydrocarbons, having lower saturation vapor pressures at the cold temperatures of Jupiter's stratosphere, can undergo condensation and coagulation, forming the sub-micron sized aerosol particles that constitute the haze layers (West et al., 2007). Coagulation in atmospheric sciences is the irreversible aggregation of suspended aerosol particles upon collision, resulting in a decrease in the number concentration and an increase in the average size of the aerosol population. This process is driven by various mechanisms, including Brownian motion (random thermal motion dominant for smaller particles), turbulent shear, gravitational settling (important for larger particles with differential settling velocities), and intermolecular forces (e.g., van der Waals forces) that facilitate sticking upon contact.
The same processes may happen for the products of gaseous ammonia in the upper troposphere. However, in this case, the chemical network is not as thoroughly understood as methane's. Even less known is the chemical network including both the results of ammonia and methane photochemistries.

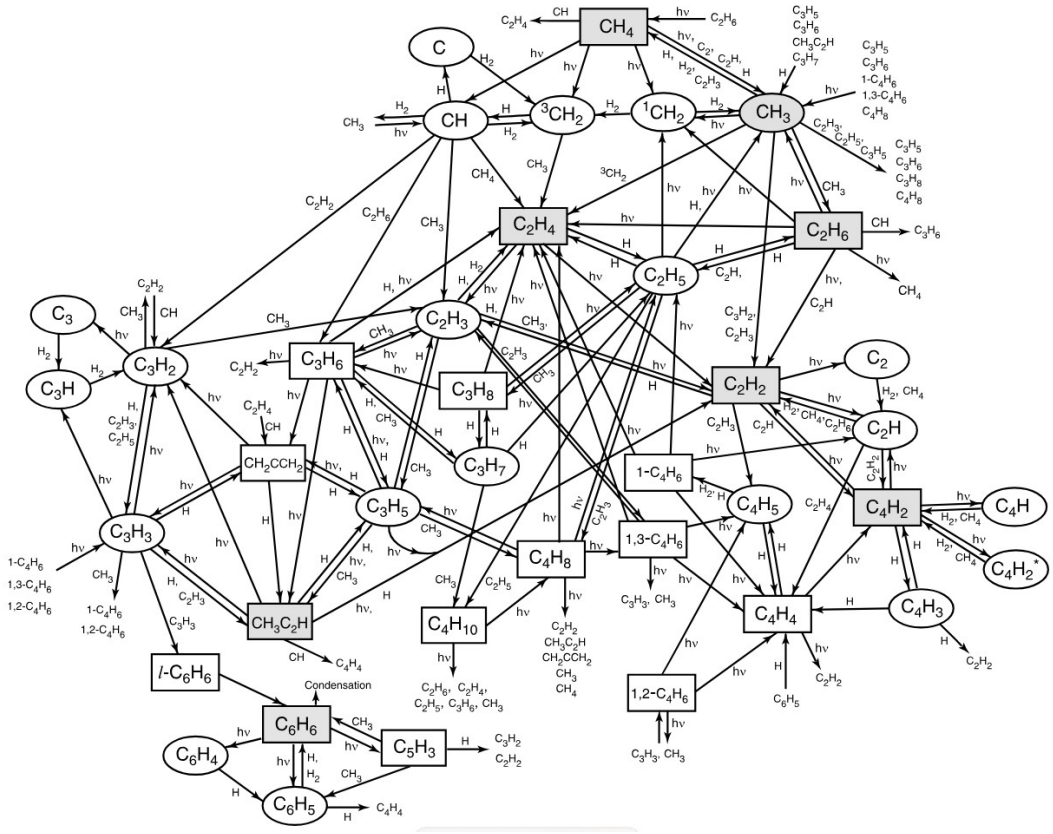


Figure 2.12: A schematic diagram illustrating the reaction pathways for forming complex hydrocarbons starting from methane photolysis (Moses et al., 2005).

Chapter 3

Modelling planetary atmospheres with Radiative Transfer

3.1 What do we observe ?

There are two methods used to study atmospheres: (1) in-situ measurements, and (2) remote-sensing observations (Hanel et al., 2003). In the first case an instrument like a probe actively measures physical and chemical properties of an atmosphere. In the second case, the physical and chemical properties of an atmosphere are inferred from comparing the measurements of an instrument to synthetic simulated data or laboratory measurements. Remote-sensing can be performed both by a spacecraft in orbit around a (or transiting in the vicinity of) planet or from ground-based or space observatories.
In this thesis work I will focus principally on the analysis of spectra and images acquired by space missions and telescopes with the aim of characterizing the upper troposphere of Jupiter.
In terms of definition an image is a digital representation of the electromagnetic radiation emanating from celestial objects or phenomena, where each pixel in the image array encodes a measured value related to the spectral radiance received by the detector within a specific spatial element and spectral band (Howell, 2000). With radiance, dI_ν, we define the measured energy dE on a determined area on the planet disk $d\Sigma$, at a given viewing solid angle $d\Omega$, in a certain interval of time dt, and in a certain frequency range $d\nu$. From a mathematical point of view it can be defined as (Hanel et al., 2003):

$$dI_\nu = \frac{dE}{dt d\Sigma d\Omega d\nu}, \tag{3.1}$$

and measured in W m^{-2} sr^{-1} Hz^{-1}. The radiance can be also measured in W/m^2/sr/μm or W/m^2/sr/cm^{-1}. In the former case the radiance is defined as the measured energy dE on a determined area on the planet disk $d\Sigma$, at a given viewing solid angle $d\Omega$, in a certain interval of time dt, and in a certain wavelength range $d\lambda$.:

$$dI_\lambda = \frac{dE}{dt d\Sigma d\Omega d\lambda}. \tag{3.2}$$

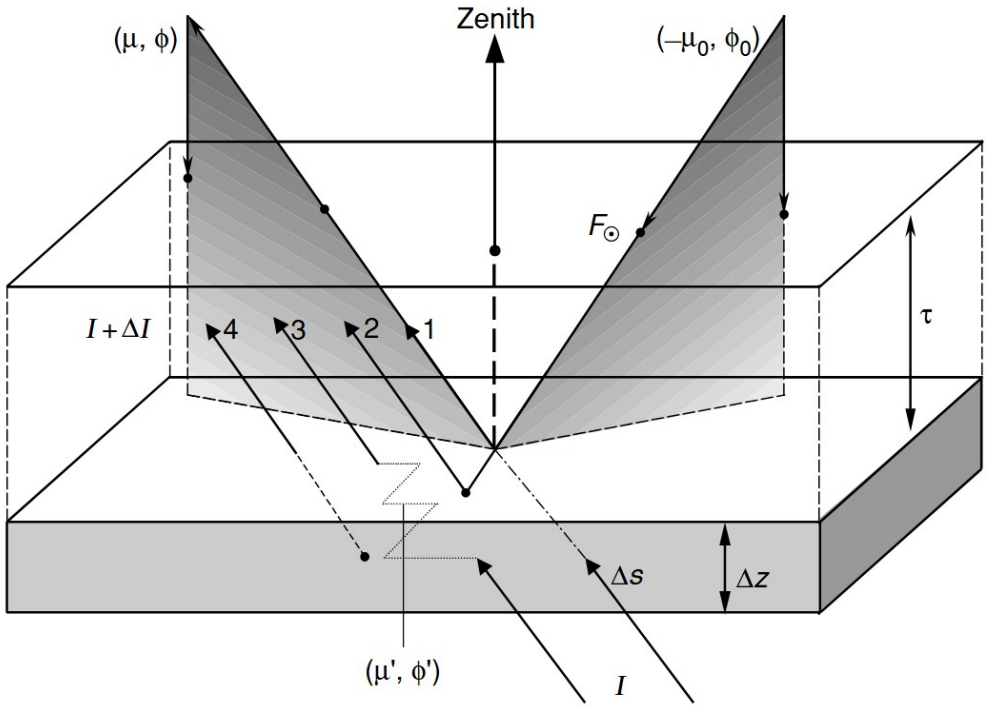


Figure 3.1: Representation of a plane paralle atmosphere from Liou (1980).

The relation between I_ν and I_λ can be obtained starting from the relation $\lambda = c/\nu$, and it can be written as

$$dI_\lambda = dI_\nu \frac{c}{\lambda^2}. \tag{3.3}$$

For its definition, the radiance is a spatial invariant, which means that it does not depend on the distance between the observer and the observed object. We then define a planetary spectrum as a representation of the radiance of electromagnetic radiation emanating from the planet as a function of wavelength or wavenumbers. From now on I will focus on radiances per unit frequency, bearing in mind that everything can be recomputed as per unit wavelength using Eqn. (3.3). I will adopt the coordinates represented in Fig. 3.1 from Liou (1980). I will assume that the atmosphere is composed of a series of plane parallel layers each of them with a thickness of dz in altitudes or dp in pressures.
I will consider a point on the planetary atmosphere that can be defined in spherical coordinates by the so-called emission angle θ and the azimuth angle ϕ, that define the observer position. The emission angle θ is measured positively from zero (the zenith) to π (the nadir). We will define $\mu = \cos\theta$ as the cosine of the emission angle. The solar radiation can enter the atmosphere at a random incidence angle θ_0 and azimuth angle ϕ_0. We will define $\mu_0 = \cos\theta_0$ as the cosine of the incidence angle. We can therefore define the solid angle element $d\Omega$ as:

$$d\Omega = \sin\theta d\theta d\phi \tag{3.4}$$

and the so-called phase φ and scattering angles θ_s:

$$\cos\varphi = \mu\mu_0 + \sin\cos\mu^{-1}\sin\cos\mu_0{}^{-1}\cos\phi \tag{3.5}$$

$$\cos\Theta = \mu\mu_0 + (1-\mu)^{1/2}(1-\mu_0)^{1/2}\cos\phi - \phi_0. \tag{3.6}$$

In terms of wavelengths I will consider the following regimes:

- UV, 0.1 $\mu m < \lambda <$0.4 μm
- visible, 0.4 $\mu m < \lambda <$0.8 μm
- NIR, 0.8 $\mu m < \lambda <$3 μm
- IR, 3 $\mu m < \lambda <$10 μm
- FIR, 10 $\mu m < \lambda <$1000 μm

In any case, it is fundamental to understand that what we observe by remote-sensing is the radiance at a certain frequency at the top of the atmosphere. This value depends on all the physical processes that happen above the pressure level at which the total optical depth (i.e. the optical depth of gas and aerosol together) at a certain frequency becomes approximately equal to the Euler's number. This criterion will become clear in the following sections.

3.2 Radiative transfer in a planetary atmosphere

Since our observables of interest are the radiances derived from images and spectra, we need to define a way to model them.
In the simplest case the radiance that we measure when we observe a planetary atmosphere can be approximated as the one emitted by a black body. A black body is an idealized object that absorbs all electromagnetic radiation incident upon it, regardless of frequency or angle. The radiance emitted by a black body is defined by the Planck function:

$$B_\nu(T) = \frac{2h\nu^3}{c^2}\frac{1}{e^{h\nu/kT}-1}, \tag{3.7}$$

where k is the Boltzmann constant ($k = 1.380649\times10^{-23}$ m^2 kg s^{-2} K^{-1}), c the speed of light ($c = 299,792,458$ m/s), and h the Planck's constant ($h = 6.62607015\times10^{-34}$ m^2 kg s^{-1}). The frequency at which the Planck function reaches its maximum value is connected to the temperature via the so-called Wien's law:

$$\nu_{\max} = 2.82\frac{kT}{h} \tag{3.8}$$

From Eqn. (3.8) it is possible to see in which wavelength range stars and planets are expected to emit more. Stars have "surface" temperatures around 10^3 K and therefore they will emit mostly in the UV/visible range of the electromagnetic spectrum. Planets have usually average temperatures around 10^2 K and therefore they will emit mostly in the NIR/IR regimes. The integration of Eqn. (3.7) on the whole frequency and solid angle ranges (i.e. the radiative flux) gives us the so-called Stefan-Boltzmann law:

$$F = \int\int I_\nu d\nu d\Omega = \sigma T^4, \tag{3.9}$$

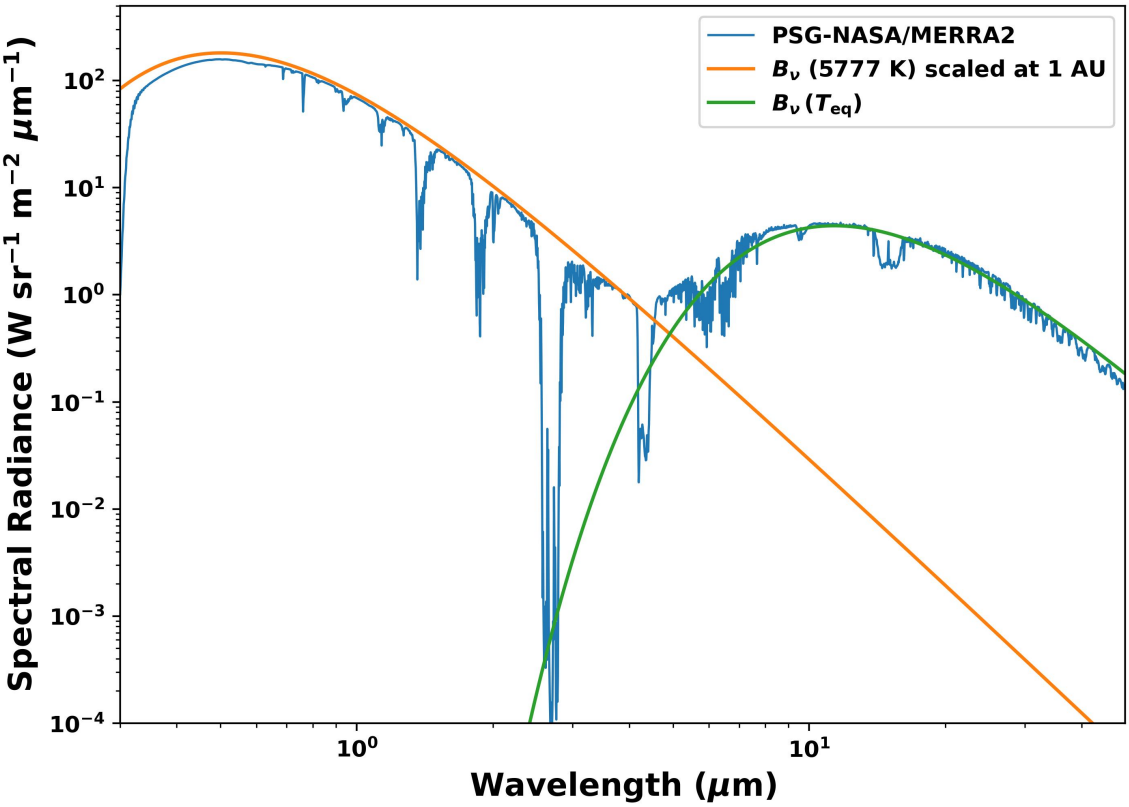


Figure 3.2: PSG simulation of Earth spectrum from NASA/MERRA2 results. Two black bodies functions representing the sunlight reflection and the thermal emission, Eqn. (3.11) are also shown.

where σ is the Stefan-Boltzmann constant already presented in the previous Chapter. Using Eqn. (3.9) it is possible to introduce the concept of equilibrium temperature of a planet, T_{eq}. This can be derived approximating the flux arriving at the top of a planet F_{top} with the thermal emitted one F_{out}. The first one can be approximated as $F_{\text{top}} = F_{\odot}(1 - A_b)\frac{\pi R_{\odot}^2}{4\pi a^2} = \sigma T_{\odot}^4(1 - A_b)\frac{\pi R_{\odot}^2}{4\pi a^2}$. $R_{\odot}$ is the Sun (or star) radius and a the semi-major axis of the planet. This geometric factor comes from the fact that the flux, contrary to radiance, is not a spatial invariant. A_b is called the mean averaged albedo and it is a real number between 0 and 1. It represents the amount of sun (or stellar) flux that is reflected by the planet. The latter term is just $F_{\text{out}} = \sigma T_{\text{eq}}^4$. Therefore, the equilibrium temperature can be written as:

$$T_{\text{eq}} = T_{\odot}\sqrt{\frac{R_{\odot}}{2a}}\,(1 - A_b)^{1/4}\,. \tag{3.10}$$

The temperature of the Sun photosphere (the outermost layer of its atmosphere) is $T_{\odot} = 5780$ K. As a consequence, Earth should have an equilibrium temperature of 255 K, while Jupiter one of 125 K. The equilibrium temperature is usually different from the real temperature of an atmosphere. For example on Earth the difference between the real and equilibrium temperature is almost 30 K, due to the presence of the greenhouse effect. For Jupiter we can see that the difference is lower, in the order of few degrees.
In Fig. 3.2 we can observe a comparison between a black body spectrum computed at a temperature equal to T_{eq}, and a synthetic spectrum generated by PSG (see

next Chapters) using the results of the NASA/MERRA2 mission (Gelaro et al., 2017; Randles et al., 2017). We can observe two major differences:

1. the Earth spectrum is non-zero for wavelengths smaller than 2 microns where we should not expect any contributions from thermal emission

2. the blackbody spectrum is smooth while the Earth spectrum appears as a black body with dips or spikes

The shape of the spectrum measured for wavelengths smaller than 2 microns resembles a blackbody at a higher temperature than the equilibrium temperature and similar to the surface of the sun, 5780 K (following Eqn. (3.8)). However, the maximum radiance emitted by a black body at 5780 K is 10^7 W/m^2/sr/μm, while in Fig. 3.2 we can observe that the maximum value is around 10^2 W/m^2/sr/μm. This is caused by the reflection of the solar radiance. In fact, the total radiance of a planet can be approximated as the sum of two black bodies:

$$I_{\nu,\,\mathrm{tot}} \simeq \mathrm{BRDF}(\theta, \phi, \theta_0, \phi_0, \nu)\frac{\pi R_\odot^2}{a^2} B_\nu(T_\odot) + B_\nu(T_{\mathrm{eq}}). \tag{3.11}$$

BRDF is called the Bidirectional Reflectance Distribution Function. From a physical point of view it is a function that describes how much of that incoming light, traveling in a specific direction, gets reflected off that point and travels in another specific direction. In the simplest case, BRDF can be approximated as BRDF=$A_b/4\pi$. This can be generalized using the following relation:

$$A_b(\theta_0, \phi_0, \nu) = \int_0^{2\pi}\int_0^{\pi/2} \mathrm{BRDF}(\theta, \phi, \theta_0, \phi_0, \nu)\mu \sin\theta d\theta d\phi. \tag{3.12}$$

Eqn. (3.11) explains the observed radiance values but not the dips and spikes. The most significant processes that shape the measured radiances (and that create the above-mentioned dips and spikes) are the same that govern the interaction between electromagnetic interaction and matter (Bohren & Huffman, 1983). In our case the electromagnetic interaction represents both the incident solar radiation and the black body radiation emitted by the planet. The matter is the gaseous and aerosol species present in the atmosphere. These processes can be listed as follows(Hanel et al., 2003):

- **absorption**: the process by which a material medium takes up the energy of incident electromagnetic radiation (photons), particles, or waves. This occurs when the energy of the incident entity matches the energy difference between two quantized energy levels within the atoms, molecules, or the bulk structure of the material (Eisberg & Resnick, 1985).

- **scattering**: the physical process where some form of radiation (e.g., electromagnetic, particle beam) is forced to deviate from its straight trajectory by one or more localized non-uniformities in the medium through which it passes (such as aerosol particles), without a net change in the total energy of the system in the case of elastic scattering (Griffiths & Schroeter, 2018).

- **emission**: the process by which matter releases energy in the form of electromagnetic radiation (photons) or other particles. This occurs when atoms, molecules, or other quantum systems transition from a higher energy state to a lower energy state (Sakurai, 1985).

The physical details behind these processes will be discussed in the Sections 3.4 and 3.5. Before doing that it is important to introduce how we mathematically describe the physical process of propagation of energy in the form of electromagnetic radiation through a medium. We call this radiative transfer, hereafter RT. We can condense all these processes into a single equation called the RT equation that will be derived in the next section.

3.3 The general radiative transfer equation

Let's consider a slab of thickness dz represented in Fig. 3.1. We want to measure the radiance emitted by the atmosphere between a level z_0 and another level z_1 (with $\Delta z = z_1 - z_0$). We are placed outside the atmosphere, observing at a certain zenith (emission) and azimuth angles, θ and ϕ. The amount of radiance that we observe is given by this equation (Hanel et al., 2003):

$$dI_\nu = dI_{\text{ext},\nu} + dI_{\text{emi},\nu} + dI_{\text{scat},\nu}. \tag{3.13}$$

Let's start from the first term $dI_{\text{ext},\nu}$ which represents the extinction of radiance. In fact, as a beam of light travels through the medium, its intensity is reduced by both absorption and scattering out of the beam. The amount of extinction along the direction s is proportional to the radiance itself and the extinction coefficient, β_{ext}, of the medium:

$$dI_{\text{ext},\nu} = -\beta_{\text{ext}} I_\nu ds = -\frac{1}{\mu}\beta_{\text{ext}} I_\nu dz. \tag{3.14}$$

The extinction coefficient and is usually measured in km^{-1}. It can be expressed as (Liou, 1980):

$$\beta_{\text{ext}} = \int_{\Delta z} \sigma_{\text{ext}} n(z) \frac{dz}{\Delta z} \tag{3.15}$$

σ_{ext} is called the extinction cross section, measured in cm^2/mol and can be defined also as $\sigma_{\text{ext}} = \sigma_{\text{ext gas}} + \sigma_{\text{ext aerosol}} = \sigma_{\text{abs}} + \sigma_{\text{scat}}$. As a result, we can also define the absorption and scattering coefficients as:

$$\beta_{\text{abs}} = \int_{\Delta z} \sigma_{\text{abs}} n(z) \frac{dz}{\Delta z} \tag{3.16}$$

$$\beta_{\text{scat}} = \int_{\Delta z} \sigma_{\text{scat}} n(z) \frac{dz}{\Delta z} \tag{3.17}$$

Therefore, $\beta_{\text{ext}} = \beta_{\text{abs}} + \beta_{\text{scat}}$. All these cross sections and coefficients are the key elements of RT; their functional forms will be given in the next two sections. The extinction coefficient can be directly connected to the optical depth defined in the previous chapter as follows:

$$\tau_\nu = \int_z^\infty \beta_{\text{ext}} dz' \tag{3.18}$$

If we assume that extinction is the sole process occurring, we obtain the so-called Beer-Lambert law:

$$dI_\nu = -\frac{1}{\mu} I_\nu d\tau_\nu \implies I_\nu(\mu) = I_0 e^{-\tau_\nu/\mu}, \tag{3.19}$$

where I_0 is the reference radiance at z_0. From this equation we can understand why a value of e in optical depth is conventionally used as a reference. If we set μ=1 we can see that if $\tau_\nu = e$, the radiance is attenuated by a factor e^{-e}, i.e. 93.3 % of the incident radiation has been extinguished by the medium through absorption and scattering. So in this thesis if $\tau_\nu > 3$ I will define the layer as optically thick, while if $\tau_\nu << 1$ as optically thin. The parameter $\mathcal{T}_\nu = e^{-\tau_\nu/\mu}$ is also called the transmittance and it can be meausred directly in some occasions, see Section 3.4.
The second term due to emission can be understood as follows. The medium itself can emit radiation, adding to the beam's radiance. The emission is characterized by the emission coefficient, J_ν, which represents the energy emitted per unit volume per unit time per unit frequency per unit solid angle. Over a distance ds, the increase in radiance due to emission is:

$$dI_{\mathrm{emi},\,\nu} = j_\nu ds. \tag{3.20}$$

Lastly we have the scattering. Radiation from other directions can be scattered into our observing beam, thus increasing the measured radiance. This contribution depends on the incident radiance from all other directions, $I_\nu^{'}$ and the scattering phase function, $P(\cos\Theta)$, which describes the probability of scattering from a random $(\theta^{'}, \phi^{'})$ into direction (θ, ϕ). Because of this definition the phase function has the following properties (Liou, 1980):

$$P(\cos\Theta) = P(\mu, \phi, \mu^{'}, \phi^{'}) \ , \quad \int \frac{P(\cos\Theta)}{4\pi} \sin\Theta d\Theta d\phi = 1 \tag{3.21}$$

The increase in radiance due to scattering into the beam from all other directions over a distance ds is:

$$dI_{\mathrm{scat},\,\nu} = \beta_{\mathrm{scat}} ds \int_0^{2\pi} \int_{-1}^{1} I_\nu^{'} \frac{P(\mu, \phi, \mu^{'}, \phi^{'})}{4\pi} d\mu^{'} d\phi^{'} = \beta_{\mathrm{scat}} ds \int_0^{2\pi} \int_{-1}^{1} I_\nu(\mu^{'}, \phi^{'}) \frac{P(\mu, \phi, \mu^{'}, \phi^{'})}{4\pi} d\mu^{'} d\phi^{'}. \tag{3.22}$$

Consequently, the phase function is a critical parameter in RT; its functional form and derivation will be detailed in the following sections. Having established this, it becomes essential to try to disentangle all the components that are masked within the final measured radiance. These are, in order:

- The radiance emitted at each z between z_0 and z_1, i.e. a black body at a temperature $T(z)$, $B_\nu(T(z))$. The part of it emitted at (μ, ϕ) will simply reach us once it will be absorbed by the gases. This contribution, therefore, is given by the term $\beta_{\mathrm{abs}} B_\nu(T(z))$.

- The incident solar radiation that was absorbed by a part of the gases and then reflected back in our viewing beam. It can be expressed as: $\beta_{\mathrm{scat}} I_{\nu,\,\odot} e^{-\tau_\nu/\mu} \frac{P(\mu,\phi,-\mu_0,-\phi_0)}{4\pi}$, where $I_{\nu,\,\odot}$ is the solar radiance at the top of the atmosphere (the one approximated with $\frac{\pi R_\odot^2}{a^2} B_\nu(T_\odot)$ in Eqn. (3.11)).

- The remaining black body radiance **not** emitted at (μ, ϕ) that can be scattered or absorbed by each layer. The same holds true for the solar radiance not reflected back at (μ, ϕ).

Therefore if we add all the contributions described in this section we obtain (Liou, 1980):

$$\begin{aligned}\frac{\Delta I_\nu(\mu,\phi)}{\Delta z} &= -\beta_{\text{ext}} I_\nu(\mu,\phi) + \beta_{\text{scat}} I_{\nu,\odot} e^{-\tau_\nu/\mu_0} \frac{P(\mu,\phi,-\mu_0,-\phi_0)}{4\pi} + \\ &+\beta_{\text{scat}} ds \int_0^{2\pi} \int_{-1}^{1} I_\nu(\mu^{'},\phi^{'}) \frac{P(\mu,\phi,\mu^{'},\phi^{'}}{4\pi} d\mu^{'} d\phi^{'} + \beta_{\text{abs}} B_\nu(T(z)) + j_\nu.\end{aligned} \tag{3.23}$$

At this point it is useful to introduce a parameter called the single-scattering albedo, ω, that is a fundamental dimensionless quantity in RT that describes the probability that a photon interacting with a particle (or a small volume of a medium) will be scattered rather than absorbed. It can be expressed as:

$$\omega = \frac{\beta_{\text{scat}}}{\beta_{\text{ext}}}, \quad 1 - \omega = \frac{\beta_{\text{abs}}}{\beta_{\text{ext}}} \tag{3.24}$$

Once we have these definitions and Eqn. (3.18), then Eqn. (3.23) can be rewritten as :

$$\mu \frac{dI_\nu(\mu,\phi)}{d\tau_\nu} = I_\nu(\mu,\phi) - J_\nu(\mu,\phi) \tag{3.25}$$

that is referred to as the general RT equation in a planetary atmosphere. $J_\nu(\mu,\phi)$ is called the source function and in the case of the planetary atmospheres is generally defined as all the contributions not connected to extinction:

$$J_\nu(\mu,\phi) = \frac{\omega}{4\pi} I_{\nu,\odot} e^{-\tau_\nu/\mu_0} P(\mu,\phi,-\mu_0,-\phi_0) \tag{3.26}$$

$$\omega \int_0^{2\pi} \int_{-1}^{1} I_\nu(\mu^{'},\phi^{'}) \frac{P(\mu,\phi,\mu^{'},\phi^{'}}{4\pi} d\mu^{'} d\phi^{'} + (1-\omega) B_\nu(T(z)) + j_\nu. \tag{3.27}$$

In general, Eqn. (3.25) should be solved for each parallel layer that composes our atmosphere, once that we define the pT, gases, and aerosol profiles.
Lastly, it is worth mentioning that all the above cited equations are valid only in local thermodynamic equilibrium (LTE) regime. In LTE, within a sufficiently small region of a medium, the matter particles (atoms, molecules, ions, electrons) have velocity distributions that are very close to a Maxwell-Boltzmann distribution, characterized by a well-defined local temperature. This implies that collisions between particles are frequent enough to maintain these equilibrium distributions, even if there are gradients in temperature, pressure, or composition across the larger system. Observations confirmed that LTE is valid for pressures larger than 1 mbar in the Jupiter atmosphere (López-Puertas & Taylor, 2001).

3.4 Absorption in a planetary atmosphere

In quantum mechanics, an energy state (or quantum state) refers to a distinct, quantized condition in which an atom, molecule, or even a subatomic particle can

exist, each characterized by a specific, discrete value of total energy. Unlike classical physics where a system can possess any continuous amount of energy, in the quantum realm, energy is "quantized," meaning it can only take on certain allowed values. These allowed energy values are often called energy levels. These can also be thought as the eigenvalues of the hamiltonian operator that defines the evolution of the atomic quantic state following the Schroedinger equation (Griffiths & Schroeter, 2018; Sakurai, 1985).
When a photon, a quantum of electromagnetic radiation possessing a discrete energy $E_\nu = h\nu$, encounters an atom or molecule residing in a lower, more stable energy state (often denoted as a ground state), absorption can occur. For this event to take place, a critical condition of energy resonance must be met: the photon's energy E_ν must be precisely equal to the quantized energy difference (ΔE) between the initial lower energy state (E_1) and a specific higher, allowed energy state (E_2) of the atom or molecule ($\Delta E = E_2 - E_1$) (Hanel et al., 2003). This principle underscores the quantum nature of light-matter interactions; only photons with the exact energy matching an allowed transition are absorbed (Bohren & Huffman, 1983).
At the same time, when an excited atom or molecule returns to a lower energy level, it releases the excess energy, often in the form of a photon with energy equal to the energy difference between the two levels. This emission can occur spontaneously or can be stimulated by the presence of external radiation at the emission frequency (Einstein, 1917). Therefore, both absorption and emission transitions should occur at precise wavelengths. Therefore each molecule can be associated to an absorption or emission spectrum where the transitions are monochromatic lines. The intensity and shape of the lines will depend on the physical conditions of the molecule. Thus, at least three factors are needed for the modeling of absorption in a planetary atmosphere:

- we need to know at which frequency the lines of a molecule are located and their so-called ground level intensity $S(\nu)$
- we need to know how to model the line broadening, $f(\nu, p, T)$
- we need to know the partition function of the molecule, $\mathcal{Q}(T)$

In the next subsections we will see how to model or obtain these terms.

3.4.1 Line positions

The position of the transition lines can be either computed using quantum field theory or measured in a laboratory. In most cases, molecules, rather than atoms, are the primary absorbers in the near-infrared (NIR) and infrared (IR) ranges of a planetary troposphere. Therefore in this discussion I will focus on them.
The starting point is the so-called Fermi golden rule (Hanel et al., 2003):

$$\mathcal{P}_{21} = \frac{8\pi^3}{h^2}|E_0|^2|R_{21}|^2 \cdot t = T_{21}t \tag{3.28}$$

which states that the probability of a molecule to transition from an energy state ψ_1 (associated to an energy E_1) to an energy state ψ_2 (associated to an energy E_2)

after time t is directly proportional to the electric dipole moment matrix R_{21} (Dirac, 1927). R_{21} can be computed once we know the electric dipole moment M as follows:

$$R_{21} = \int \psi_2^* \mathrm{M} \psi_1 dt' \tag{3.29}$$

Therefore for biatomic molecules such as H_2 or O_2, absorption cross section spectra should be null according to Eqn. (3.28), since they do not possess a dipole moment. However, this is not the case due to collisional induced absorption (CIA) as we will see later in the section.
Using efficient computer codes it is possible to compute all the transition rates (T_{ij}) and probabilities ($\mathcal{P}_{ij}$) for a wide range of energies. The intensities can be also computed referring to a ground level state (T_{i0}), i.e. fixing the energy of the ground energetic state and of the radiation field. However, this is not enough to model the whole absorption spectrum of a molecule. In particular, we will always observe lines due to the vibration and the rotational modes of the molecule, as they induce temporary changes in the dipole moment of the molecule.
Vibrational energy states refer to the quantized energies associated with the oscillatory motion of atoms within a molecule. If we imagine the chemical bonds connecting atoms as springs, therefore these springs can stretch and compress, and the atoms can bend relative to each other. These internal oscillations are not random but occur in specific patterns known as normal modes of vibration. For a non-linear molecule with N atoms, there are 3N-6 normal modes of vibration, while for a linear molecule, there are 3N-5 (rotation about the molecular axis is not considered). Each normal mode has its own set of quantized energy levels. The simplest model for molecular vibration is the quantum harmonic oscillator. In this approximation, the potential energy of the molecular bond is treated as a parabola (like an ideal spring), and the energy levels are evenly spaced (Griffiths & Schroeter, 2018; Hanel et al., 2003):

$$E_\nu = h\nu_0 \left(v + \frac{1}{2} \right). \tag{3.30}$$

ν_0 is the fundamental vibrational frequency of the bond (determined by the bond's strength and the masses of the atoms). v is the vibrational quantum number, which can take integer values 0,1,2,... On the other hand, rotational energy states refer to the quantized energies associated with the rotation of an entire molecule about main axis of inertia. Just like a spinning top, molecules can rotate, but their rotational energy should be considered quantized. The simplest model for molecular rotation is the rigid rotor. This approximation assumes that the bond lengths and angles within the molecule are fixed during rotation. The energy levels for a linear rigid rotor (like a diatomic molecule) are given by (Griffiths & Schroeter, 2018; Hanel et al., 2003):

$$E = \frac{h}{8\pi^2 I} J(J+1). \tag{3.31}$$

Here I is the moment of inertia of the molecule about the axis of rotation. The moment of inertia depends on the masses of the atoms and their distances from the axis of rotation. J is the rotational quantum number, which can take integer values 0,1,2,...Transitions between rotational and vibrational energy states involve very small energy differences, typically corresponding to the microwave or infrared

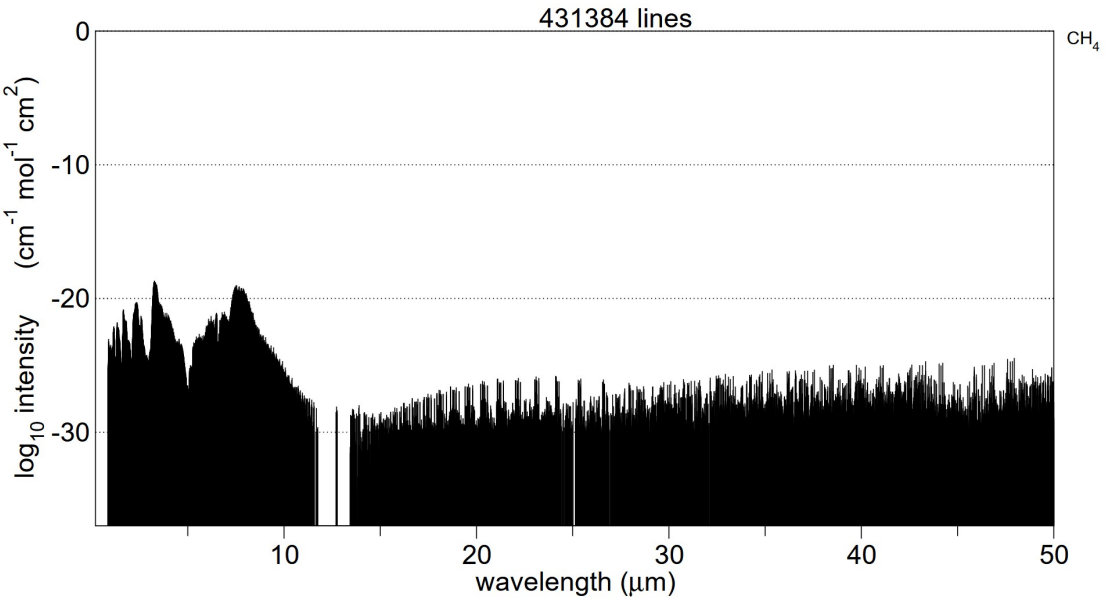


Figure 3.3: Methane abosorption spectrum from HITRAN2020 (Brown et al., 2013) considering $T = 273\,K$ and $P = 1$ bar.

regions of the electromagnetic spectrum. Given the diagnostic capabilities on the types and physical conditions of molecules in a planetary atmosphere these domains have been considered frequently to design instruments on board space missions.
In the more general case vibrational and rotational motions cannot be considered entirely independent. Transitions often involve simultaneous changes in both vibrational and rotational quantum numbers (called rotovibrational transitions). This results in a substantial increase in computational complexity. From Eqn. (3.30) and Eqn. (3.31) it is possible to observe that both vibration and rotation naturally induce the formation of a large number of, in principle infinite, lines. Therefore large computational efforts are needed to consider all the combinations of vibrational and rotational states and compute the resulting lines.
Due to the difficulties in the theoretical computations, the position of the lines pertinent to the Earth pressure and temperature have been measured by different laboratory facilities across the world in the last 50 years. For example, the National Institute of Standards and Technology (NIST) (Lovas & Tiemann, 1974) and the Cologne Database for Molecular Spectroscopy (CDMS) (Müller et al., 2001) mantain large databases of both atomic and molecular transition lines and relative intensities at Earth conditions. Similarly other databases focused on atmospheric studies have been developed such as HITRAN (Rothman et al., 2009) and Exomol (Tennyson et al., 2016). The first mostly gathers results from experimental setups while the latter is mainly known for being a theoretical database. The usual intensity unit given by these databases is cm^2 / (molecule cm). This is a transition intensity, weighted by molecule abundance. In the next subsection we will see how it is computed.
In Fig. 3.3 it is possible to see the absorption spectrum of methane from HITRAN2020 (Brown et al., 2013; Gordon et al., 2022) and the forest of lines that it can generate in the infrared.

3.4.2 Line intensities

The strengths of emission or absorption lines between an upper level, E_n , and a lower level, E_m , are given by (Einstein, 1917; Hanel et al., 2003):

$$I_{nm} = N_n A_{nm} hc\nu = N_n \frac{64\pi^4 c\nu^4}{3} |R_{nm}|^2, \tag{3.32}$$

$$I_{mn} = I_0 N_m B_{mn} hc\nu = I_0 N_m \frac{8\pi^3 \nu}{3hc} |R_{mn}|^2, \tag{3.33}$$

A_{nm} and B_{mn} are called the Einstein coefficients, while here ν is the frequency of the transitions. On the other hand, N_n and N_m are the number of molecules of the states. These can be expressed as (Hanel et al., 2003):

$$N_i = \frac{N d_i}{\mathcal{Q}(T)} e^{-E_i/kT}, \tag{3.34}$$

where N is the total number of molecules, d is called the degeneracy and $\mathcal{Q}(T)$ the partition function. Degeneracy refers to the situation where two or more distinct, measurable quantum states of a system share the exact same energy value. The partition function is a central concept in statistical mechanics that quantifies the statistical properties of a system in thermodynamic equilibrium. For a canonical ensemble (a system with a fixed number of particles, volume, and temperature T), the molecular partition function is defined as a sum over all accessible discrete energy states of a single molecule (Huang, 1987):

$$\mathcal{Q}(T) = \sum_{n=0}^{\infty} d_n e^{-E_n/kT}. \tag{3.35}$$

Therefore $\mathcal{Q}(T)$ can be also thought of as the sum of Boltzmann factors, $e^{-E_n/kT}$, weighted by their degeneracies. Using Eqn. (3.33) allows one to compute $\mathcal{Q}(T)$ for different cases. For example the partition function of the energy levels associated to the vibrations of a diatomic molecule can be expressed as (Hanel et al., 2003):

$$\mathcal{Q}_{\text{vib}}(T) = \sum_{v=0}^{\infty} e^{-h\nu_0 v/kT} = \left[1 - e^{-h\nu_0/kT}\right]^{-1}. \tag{3.36}$$

HITRAN provides partition functions for all molecular species and their isotopologues included in the database (Kochanov et al., 2016). These are specifically total internal partition sums (TIPS), which account for the statistical distribution of molecules across their various internal energy states. Rather than providing a mathematical formula for each molecule, HITRAN typically provides precomputed tables of partition function values as a function of temperature (Kochanov et al., 2016). These tables cover a wide range of atmospherically relevant temperatures (e.g., from 70 K up to 3000 K or higher, depending on the molecule and its relevance to high-temperature applications). In this way the spectral line intensity $S_{ij}(T)$ at any desired temperature T can be computed as:

$$S_{ij}(T) = I_{ij}(T_{\text{ref}}) \frac{\mathcal{Q}(T_{\text{ref}})}{\mathcal{Q}(T)} \exp\left[-\frac{-hcE_{ij}}{k}\left(\frac{1}{T} - \frac{1}{T_{\text{ref}}}\right)\right] \frac{1 - e^{-hc\nu_{ij}/kT}}{1 - e^{-hc\nu_{ij}/kT_{\text{ref}}}}, \tag{3.37}$$

once the intenisty at a reference temperature T_{ref} is known thanks to Eqn. (3.32) or (3.33).

3.4.3 Line shape

The observed spectral lines of gases are not infinitely narrow but possess a finite width, a phenomenon known as line broadening. This broadening arises from various physical mechanisms that perturb the energy levels of absorbing or emitting molecules, leading to a distribution of transition frequencies around the nominal resonant frequency. Therefore the $S_{ij}(T)$ to be considered should be the one of Eqn. 3.37 multiplied by a so-called line broadening profile f:

$$S_{ij}^{'}(\nu, T) = S_{ij}(T) f(\nu - \nu_0) \tag{3.38}$$

The functional form of profile depends on the physical mechanism leading to the broadening. These can be:

- **Doppler Broadening (Thermal Broadening)**: This intrinsic broadening mechanism arises from the random thermal motion of molecules. According to the Doppler effect, molecules moving towards an observer experience a slight increase in the perceived frequency of absorbed or emitted radiation, while those moving away experience a decrease. This results in a Gaussian-shaped line profile, where the width, called Doppler width α_D, is proportional to the square root of the kinetic temperature of the gas and inversely proportional to the square root of the molecular mass (Goody & Yung, 1989). Doppler broadening is typically dominant at low pressures and high altitudes where intermolecular collisions are infrequent. The functional form is:

$$f(\nu - \nu_0) = \frac{1}{\alpha_D \sqrt{\pi}} \exp\left[-\left(\frac{\nu - \nu_0}{\alpha_D} \right)^2 \right];\ \alpha_D = \nu_0 \sqrt{\frac{2kT}{\hat{m}c^2}}. \tag{3.39}$$

- **Pressure Broadening (Collisional Broadening or Lorentzian Broadening)**: This is the dominant broadening mechanism in the troposphere and lower stratosphere, where molecular densities are high. It results from intermolecular collisions that interrupt the absorption or emission process, shortening the effective lifetime of the energy states involved in the transition. According to the Heisenberg uncertainty principle, a shorter lifetime leads to a less precisely defined energy level, and thus a broader spectral line. Pressure broadening typically produces a Lorentzian-shaped line profile, where the line width, α, is directly proportional to the pressure and inversely proportional to the square root of the temperature (Liou, 1980). The functional form is:

$$f(\nu - \nu_0) = \frac{\alpha}{\pi(\nu - \nu_0)^2 + \alpha^2};\ \alpha = \alpha_0 \left(\frac{p}{p_0} \right) \left(\frac{T_0}{T} \right)^{\delta} \tag{3.40}$$

  where α_0 is the width at the standard pressure, p_0 (1013mb), and temperature, T_0 (273K). The index δ depends on the interacting molecular species (e.g., self-broadening, air-broadening).

- **Voigt Profile**: In most atmospheric scenarios, especially in the middle atmosphere, both Doppler and pressure broadening mechanisms are significant. The resulting line shape is a convolution of the Gaussian (Doppler) and Lorentzian

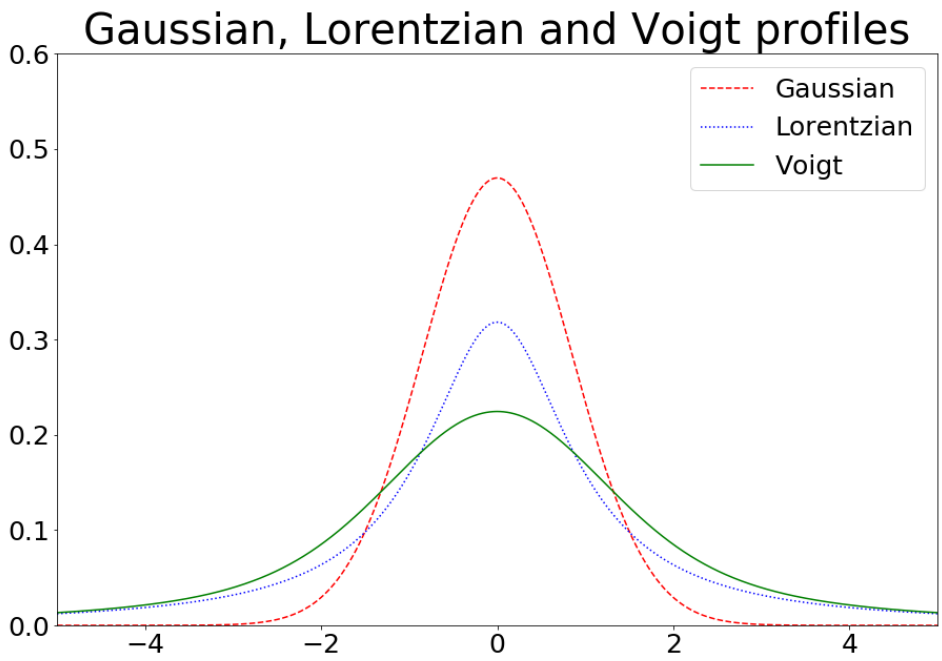


Figure 3.4: Gauss, Lorentzian and Voigt profiles describing spectral lines. Gauss and Lorentzian profiles have the same FWHM = 2, and Voigt profile is their convolution.

(pressure) profiles, known as the Voigt profile (Armstrong, 1967). This profile is more complex to compute but accurately represents the combined effects of thermal motion and intermolecular collisions. The functional form is:

$$f(\nu - \nu_0) = \frac{1}{\alpha_D \sqrt{\pi}} K\left(\frac{\nu - \nu_0}{\alpha_D}, \frac{\alpha}{\alpha_D}\right) \tag{3.41}$$

where $K(x, y)$ is called the Voigt function and is given by (Liou, 1980):

$$K(x, y) = \frac{y}{\pi} \int_{-\infty}^{+\infty} \frac{1}{y^2 + (x - t)^2} e^{-t^2} dt. \tag{3.42}$$

In Fig. 3.4 it is shown a comparison between all the above-mentioned profiles. Databases such as HITRAN provide α_D, α, and δ coefficients for a wide range of interacting molecular species.

3.4.4 Collisional Induced Absorption

Collision-Induced Absorption (CIA), also known as pressure-induced absorption, refers to the transient absorption of electromagnetic radiation by pairs or groups of interacting molecules during close-range intermolecular collisions (Irwin, 2009). From a physical perspective, the absorption in CIA arises from the induction of a transient electric dipole moment in the colliding molecular complex. As two molecules approach each other during a collision, their outer orbitals overlap and distort due to the interplay of intermolecular forces (e.g., repulsive forces at short

range, van der Waals attractive forces at longer range). This distortion leads to an instantaneous, temporary redistribution of charge within the transient molecular complex, creating a transient electric dipole moment that varies with the intermolecular separation and orientation. This induced dipole moment is inherently linked to the relative translational and internal (rotational and vibrational) motions of the colliding pair. The strength of the dipole moment strongly depends on the number density of the molecules and on the temperature (Hanel et al., 2003).
In these cases QFT computations are more feasible but their description is behind the scope of this thesis work. For Jupiter, it is fundamental to compute the CIA absorption coefficients for the H_2-H_2 case. Examples of theoretical computations can be seen in the works of Borysow (2002), Abel et al. (2011), Orton et al. (2025). However, recent laboratory measurements—such as those by Vitali et al. (2025)—have revealed discrepancies with theoretical models, indicating that the modeling of CIAs remains an open issue in atmospheric science.

3.4.5 Line-by-Line calculations

Once that the intensity lines, $\mathcal{Q}(T)$ and f are chosen for a selected molecule, its absorption cross section can be evaluated using this expression:

$$\sigma_{\text{abs}}(\lambda) = \sum_{g}^{\text{gases}} \sum_{il}^{\text{lines}} S_{il}(\lambda_i, g) f(\lambda_i, p, T, g). \tag{3.43}$$

This is usually referred to as Line-by-Line (LBL) method. In order to perform this task a series of assumptions must be made:

- We must assume that transition lines are well defined and do not overlap.
- We must assume that the absorption profile of a spectral line far away (usually named far wings, Clough et al. (1989)) from its central frequency follows the adopted line shape (Doppler, Lorentz, or Voigt).
- We must define the maximum distance (in wavenumber, cm^{-1}) from the center of a spectral line at which the line's absorption contribution is still calculated. This distance is referred as line cutoff.

In reality the far wings shapes depend strongly on the nature of the absorbing species. Moreover, a spectral line theoretically extends to infinite frequency, even if its contribution to total absorption becomes negligible far from the line center. The distance in wavenumber at which this occurs is not defined or fixed in nature. Lastly, in real dense atmospheres, the phenomenon of line mixing can occurr when the collisional broadening rate of a molecule becomes comparable to the spacing between its closely packed spectral lines (Tonkov et al., 1996). Instead of each line absorbing independently (which would lead to a simple sum of individual profiles), collisions induce inelastic transitions between the different rotational energy states. This coupling causes the spectral intensity to be transferred from the line centers to the troughs and wings of the band.
In principle every LBL calculation should account for the contributions from line mixing, far wings shape, and variable line cutoffs. However, an adequate treatment

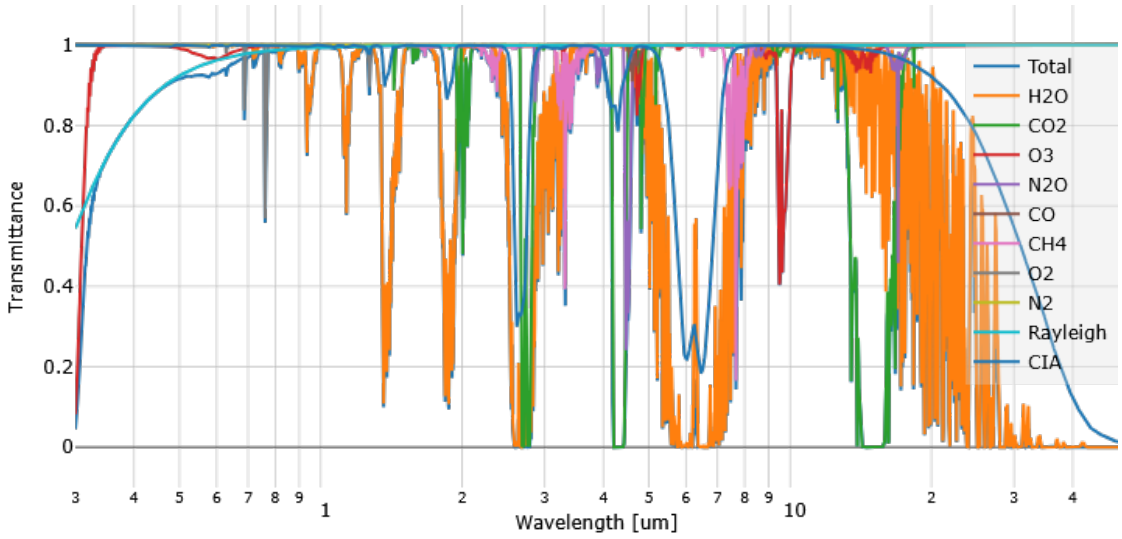


Figure 3.5: Transmittance spectra computed with PSG for the main gas species present in the Earth's atmosphere.

will increase exponentially the complexity of the problem. Therefore, the majority of the RT solvers (such as PSG or NEMESIS) assume the lines to follow the more generic Voigt profile and a line cutoff of 25 or 35 cm^{-1}. Line mixing is usually not considered or treated as a continuum. In Fig. 3.5 we can observe the transmittance spectra (see previous section) of all the species present in the Earth atmosphere computed using LBL computations. It is possible to note how they are correlated with the dips and spikes observable from the PSG generated spectrum of Fig. 3.2.

3.5 Scattering in a planetary atmosphere

When an electromagnetic wave encounters a solid or liquid particle three processes can occur:

- the wave acquires a new direction different from the incident one, this is called scattering
- the energy of the wave is absorbed totally or in part by the particle
- both the above processes together

In general any kind of scattering can be described in terms of a scattered radiance and an incident radiance:

$$I_{\text{scat}} = I_{\text{incident}} \frac{\sigma_{\text{scat}}}{R^2} \frac{P(\cos\Theta)}{4\pi} \tag{3.44}$$

that are connected by the phase function and the scattering cross-section that we introduced in the Section 3.2. R is the distance from the observer. We saw that the former describes the probability of a wave to be scattered in a given direction (μ, ϕ). We saw that one important property of the phase function is that it is normalized,

see Eqn. (3.21). Moreover in atmospheric sciences it is usually expanded in Legendre polynomials (P_l) considering the scattering angle:

$$P(\cos\Theta) = \sum_{l=0}^{N} c_l P_l(\cos\Theta), \tag{3.45}$$

$$P(\mu, \phi, \mu^{'}, \phi^{'}) = \sum_{l=0}^{N} \sum_{m=0}^{N} c_l^m P_l^m(\mu) P_l^m(\mu^{'}) \cos m(\phi - \phi^{'}). \tag{3.46}$$

Formally $N = \infty$ but in reality only a relatively limited number of terms (in the order of few tens) is usually required for practical applications.. The choice of Legendre polynomials relies on their property of forming a complete and orthogonal set of functions that are well-suited to represent angular dependences. I will come back on this later in the section.
The cross-sections depend on two optical properties of the aerosol particles: the refractive indices and the size.
Regarding the first aspect, throughout this thesis work I will assume aerosol particles to be spherical, even in reality they are tought to be irregular and well-described by complex and fractal structures (Rannou et al., 2003; Lodge et al., 2024). While these complex shapes are physically realistic, they introduce a large number of parameters (e.g., shape factors, fractal dimensions, and orientation distributions) into the light-scattering calculation. As the goal of this thesis work is to accurately model the bulk optical properties of the Jovian aerosols from single spectral measurements, the spherical particle assumption minimizes the number of required parameters while still providing a robust calculation of the ensemble's extinction, scattering, and absorption cross-sections. The choice to use spherical particles is thus a pragmatic trade-off, a methodological decision based mainly on the Occam's razor principle, not on data quantity and quality. This method is consistent with current operational standards (Rooney et al., 2022; Bell et al., 2024). The retrieved parameters, such as the effective radius, are consequently sphere-equivalent optical parameters. They are defined as the properties of an equivalent sphere ensemble that reproduces the observed optical cross-sections of the true, complex aerosol population. I acknowledge that this represents a rough approximation for solid particles, and the results are intrinsically constrained by this limitation.
The complex refractive index n of a medium is a fundamental material property that rigorously describes how an electromagnetic wave interacts with a medium and it can be expressed as:

$$n = n_0 + ik \tag{3.47}$$

where n_0 is called the real refractive index while k the imaginary or complex refractive inex. n_0 governs the directionality and intensity distribution of the scattered light. Differences in n_0 between the particle and the surrounding medium lead to refraction and reflection at the particle's boundaries. This refractive bending and internal reflection within the particle determine how much light is redirected and in which directions, influencing both the phase function and the scattering cross-section σ_{scat}. The imaginary part directly quantifies the absorption efficiency of the particle. If k is large, the particle absorbs a significant portion of the incident energy, reducing the amount of light available to be scattered. This means that,

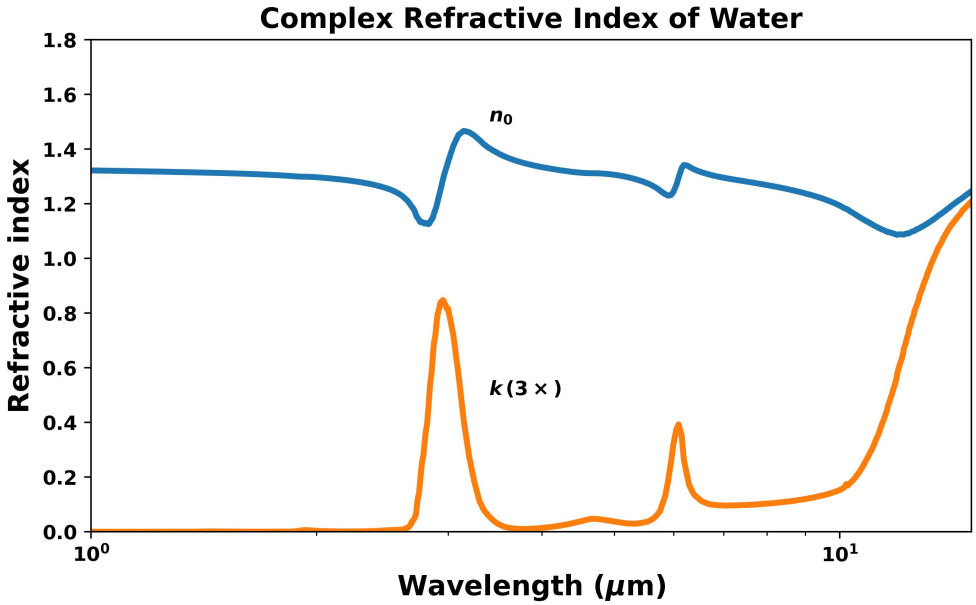


Figure 3.6: Real and imaginary refractive indexes of liquid water in the NIR and IR range.

as a rule of thumb, for a given particle size and shape, a higher k value will lead to lower scattering efficiency β_{scat} relative to the extinction efficiency β_{ext}, as more light is absorbed by the particle. The absorption of light may happen because of vibrational transitions and transitions caused by inter-molecular bounds. Usually it is very difficult to model them analytically and therefore the absorption efficiencies of scattering are usually derived once that the extinction and scattering ones are computed. In Fig. 3.6 it is possible to observe the real and imaginary parts of the liquid water refractive index as measured by Segelstein (1981). It is possible to observe that k has a huge peak around 3 μm and therefore at this wavelength we should expect a dip in the extinction cross section spectrum.
Both the real and imaginary parts are a function of wavelength or frequency. The imaginary refractive index can be measured in the laboratory thanks to the measure of the absorbance. The real part of the refractive index is then obtained thanks to the so-called Kramers-Kronig relation (Kronig, 1926; Kramers & de L. Kronig, 1928). Databases such as HITRAN list a large number of measured refractive indexes.
The functional forms of the phase functions and of the extinction and scattering cross sections (also defined as optical properties of the aerosols) strongly depends on the parameter m defined as:

$$m = \frac{2\pi r}{\lambda} \tag{3.48}$$

It is possible to define three different regimes:

- $m << 1$: Rayleigh scattering
- $m \simeq 1$: Mie theory
- $m >> 1$: geometric optics

Usually aerosol particles in planetary atmospheres have radii between 0.01 and 10 microns. Therefore in the visible and infrared spectral ranges, focus of this thesis, only the first two regimes are important and will be discussed in the following subsections.

3.5.1 Rayleigh scattering

It occurs when the aerosol particles are much smaller than the wavelength of the incident radiation. In this case absorption can be ignored and therefore we only have scattering. From the planetary atmospheres point of view, these particles can be cloud condensation nuclei, small hazes or molecules. Let the incident electric field be a plane wave in one direction, $E_i(t) = E_0 e^{-i\frac{2\pi}{\lambda}(R-ct)}$, where R represents the distance from the observer. This naturally induces an oscillating electric dipole moment in the particle that can be described as $p(t) = \alpha_P E_i(t) = \alpha_P E_0 e^{-i\frac{2\pi}{\lambda}(R-ct)}$, where α_P is a constant called polarizability. For an oscillating electric dipole, the electric field radiated at a distance R in the far-field approximation is given by the Lienard-Wiechert potentials (Liou, 1980):

$$E_{\text{rad}} = -\frac{E_0 4\pi^2 \alpha_P \sin\gamma}{\lambda^2 R} e^{-i\frac{2\pi}{\lambda}(R-ct)}, \tag{3.49}$$

γ is the angle between the scattered dipole moment p and the direction of observation. Being the intensity I_ν of an electromagnetic wave proportional to the square of the electric field amplitude, $I_\nu = |E_{\text{rad}}|^2$ and $|E_0|^2 = I_{\text{incident}}$ we can write:

$$\mathbf{I}_{\text{scat}} = \mathbf{I}_{\text{incident}} \frac{16\pi^4 \alpha_P^2}{\lambda^4 R^2} \sin\gamma^2, \tag{3.50}$$

Now we consider that the incident electric field, a vector, can always be arbitrarily decomposed into a parallel ($//$) and a perpendicular ($\perp$) component. The resulting γ angles will be, $\gamma_{//} = 90$ and $\gamma_\perp = 90 - \Theta$. Therefore as $I_{\text{scat}} = I_{\text{scat},//} + I_{\text{scat},\perp}$ and $I_{\text{incident}} = I_{\text{incident},//} + I_{\text{incident},\perp} = \frac{I_0}{2} + \frac{I_0}{2}$ we obtain (Liou, 1980):

$$I_{\text{scat}} = \frac{I_0}{R^2} \alpha_P^2 \frac{16\pi^4}{\lambda^4} \frac{1+\cos\Theta^2}{2}. \tag{3.51}$$

Using Eqn. (3.44) we can obtain an expression for the Rayleigh phase function:

$$P(\cos\Theta) = \frac{3}{4}(1+\cos\Theta^2), \tag{3.52}$$

where the 3/4 factor comes from normalization purposes, and an expression for the scattering cross-section:

$$\sigma_{\text{scat}} = \frac{\alpha_P^2 128\pi^5}{3} \frac{1}{\lambda^4}. \tag{3.53}$$

Eqn. (3.53) explicitly shows that the Rayleigh cross section strongly depends on the wavelength of the incident radiation. In particular it is very effective towards visible and UV ranges. It is a simple physical explanation of why our sky is blue.

3.5.2 Mie theory

Mie theory, also known as Lorenz-Mie theory, is a rigorous analytical solution to Maxwell's electromagnetic equations that describes the scattering and absorption of an electromagnetic plane wave by a homogeneous sphere of size comparable to the incident wavelength, arbitrary complex refractive index, and embedded in a homogeneous, non-absorbing medium (Mie, 1908; Bohren & Huffman, 1983). It provides a complete description of the interaction, including the angular distribution of scattered light and its polarization.

A monochromatic, linearly polarized plane electromagnetic wave is assumed to be incident upon a homogeneous, isotropic, and non-magnetic spherical particle. The incident electric field (E_i) can be described as a wave as we saw in the previous section. The incident wave interacts with the sphere, generating: (1) a scattered wave (E_s) that propagates outwards from the sphere, and (2) an electromagnetic wave induced inside the sphere (E_1). Since the geometry is spherical, it is natural and advantageous to express the incident, scattered, and internal electromagnetic fields in terms of vector spherical harmonics. These are a complete set of orthogonal solutions to the vector Helmholtz equation in spherical coordinates (Stratton & Chu, 1941). In particular, the general solution for the electric (E) field can be written as a superposition of two independent sets of vector spherical harmonics, often referred to as transverse electric (TE) and transverse magnetic (TM) modes, or M_{mn} and N_{mn} functions. These functions incorporate spherical Bessel functions, z_n, (for the radial dependence) and associated Legendre polynomials, Y_{mn}, (for the angular dependence):

$$\mathbf{M}_{mn} = \nabla \times (\Psi_{mn}\mathbf{R}) \ , \quad \mathbf{N}_{mn} = \frac{\lambda}{2\pi}\nabla \times \mathbf{M}_{mn} \ , \quad \Psi_{mn} = z_n\left(\frac{2\pi\mathbf{R}}{\lambda}\right) Y_{mn}(\theta,\phi). \tag{3.54}$$

Using these functions the incident, internal, and scattered fields can be expressed as follows:

$$\mathbf{E_i} = \sum_{n=0}^{\infty} E_n \left(i^n c_n \mathbf{M}_{o1n} - i^{n+1} d_n \mathbf{N}_{e1n}\right), \tag{3.55}$$

$$\mathbf{E_1} = \sum_{n=0}^{\infty} E_n \left(A_n \mathbf{M}_{o1n} - B_n \mathbf{N}_{e1n}\right), \tag{3.56}$$

$$\mathbf{E_s} = \sum_{n=0}^{\infty} E_n \left(a_n \mathbf{M}_{o1n} - b_n \mathbf{N}_{e1n}\right). \tag{3.57}$$

where E_n, c_n, d_n, A_n, B_n, a_n, and b_n are coefficients to be determined. The subscripts o and e stands for even and odd solutions. The core of the derivation lies in applying the electromagnetic boundary conditions at the surface of the sphere (at $R = r$). These conditions state that the tangential components of the electric field must be continuous across the interface (Jackson & Fox, 1999):

$$\mathbf{u} \times (\mathbf{E_i} + \mathbf{E_s}) = \mathbf{u} \times \mathbf{E_1} \tag{3.58}$$

where $\mathbf{u}$ is the unit vector normal to the sphere surface. After applying the boundary conditions, one obtains a system of linear equations for the unknown coefficients A_n,

B_n, a_n, and b_n. Solving this system for a_n, and b_n yields the expressions (Hanel et al., 2003):

$$a_n = \frac{\eta\zeta_n(\eta m)\zeta_n^{'}(m) - \zeta_n(m)\zeta_n^{'}(\eta m)}{\eta\zeta_n(\eta m)\xi_n^{'}(m) - \xi_n(m)\zeta_n^{'}(\eta m)}, \tag{3.59}$$

$$b_n = \frac{\zeta_n(\eta m)\zeta_n^{'}(m) - \eta\zeta_n(m)\zeta_n^{'}(\eta m)}{\zeta_n(\eta m)\xi_n^{'}(m) - \eta\xi_n(m)\zeta_n^{'}(\eta m)}, \tag{3.60}$$

where ζ_n are called the Riccati-Bessel fucntions and ξ_n the Riccati-Hankel fucntions as defined in Fan (2000). The prime ($'$) here denotes differentiation with respect to the argument. One of the arguments η represents the ratio $\eta = \frac{n}{n_{\text{medium}}}$. Therefore the a_n and b_n functions, also called Mie coefficients, depend strongly on the nature of the aerosol particles, on their radius, and on the chosen wavelength. Once the Mie coefficients are determined, the so-called extinction and scattering efficiencies can be calculated as follows (Hanel et al., 2003):

$$Q_{\text{ext}} = \frac{\sigma_{\text{ext}}}{\pi r^2} = \frac{2}{m^2}\sum_{n=1}^{\infty}(2n+1)\text{Re}(a_n + b_n), \tag{3.61}$$

$$Q_{\text{scat}} = \frac{\sigma_{\text{scat}}}{\pi r^2} = \frac{2}{m^2}\sum_{n=1}^{\infty}(2n+1)(|a_n|^2 + |b_n|^2), \tag{3.62}$$

As a consequence the absorption efficiency is $Q_{\text{abs}} = Q_{\text{ext}} - Q_{\text{scat}}$. The phase function can be computed as follows:

$$P(\cos\Theta) = \frac{\lambda^2}{\pi^2 r^2 Q_{\text{scat}}}(|S_1(\Theta)|^2 + |S_2(\Theta)|^2) \tag{3.63}$$

where the functions $S_1(\Theta)$ and $S_2(\Theta)$ are respectively:

$$S_1(\Theta) = \sum_{n=1}^{\infty}\frac{2n+1}{n(n+1)}\left[a_n\frac{P_n^1(\cos\Theta)}{\sin\Theta} + b_n\frac{d}{d\Theta}P_n^1(\cos\Theta)\right], \tag{3.64}$$

$$S_2(\Theta) = \sum_{n=1}^{\infty}\frac{2n+1}{n(n+1)}\left[b_n\frac{P_n^1(\cos\Theta)}{\sin\Theta} + a_n\frac{d}{d\Theta}P_n^1(\cos\Theta)\right], \tag{3.65}$$

In Fig. 3.7 it is possible to observe an example of a phase function computed by considering water ice particles of different sizes as a function of the scattering angle. The corrisponding Rayleigh phase functions are shwon as a comparison. It is possible to observe that the Mie phase function presents a strong peak in the forward direction ($\Theta = 0$). This is primarily due to diffraction. When light encounters a particle, it's diffracted around the edges of the particle, similar to how light bends around an obstacle. This diffracted light is concentrated in the forward direction. As the particle size parameter m increases, this forward scattering peak becomes narrower and more intense. As you move away from the forward direction towards larger scattering angles ($0 < \Theta < 180$), the scattering pattern becomes much more complex and oscillatory. These patterns are caused by: light reflecting off the outer surface of the particle, and/or light entering the particle, refracting, and exiting. The constructive and destructive interference of these components creates numerous peaks and valleys in the phase function curve. The number and

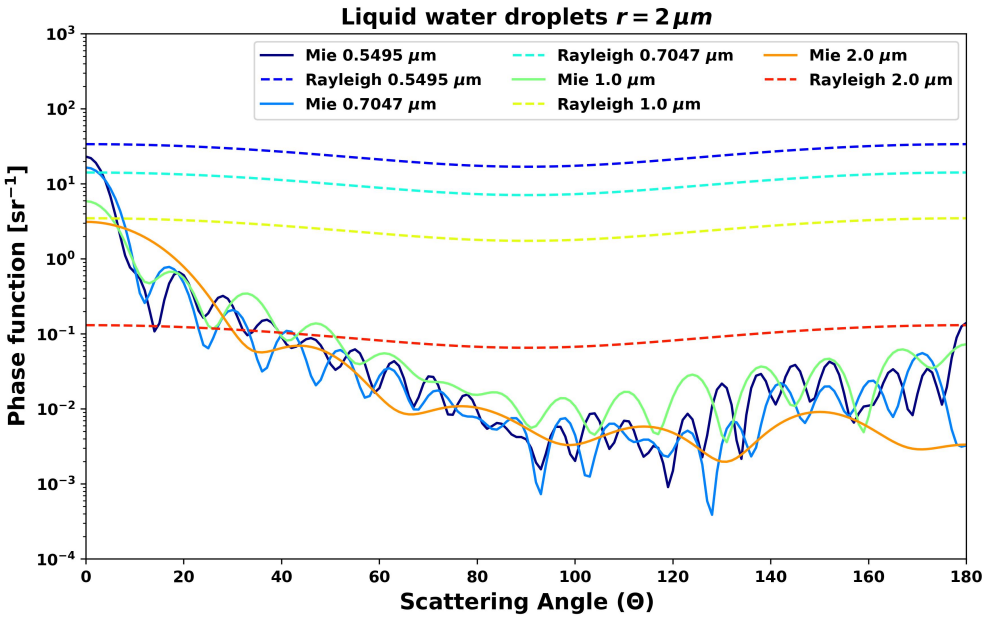


Figure 3.7: Mie and rayleigh phase functions computed considering different wavelengths and a spherical water droplet with a radius of 2 μm.

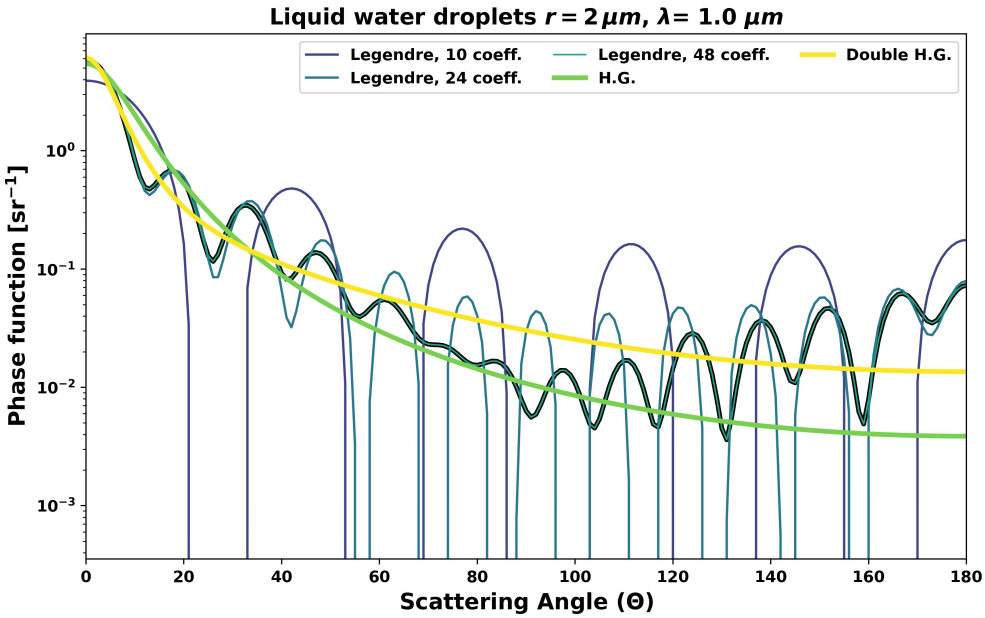


Figure 3.8: In black it is possible to observe the Mie phase functions computed at a wavelength of 1 μm considering a spherical water droplet with a radius of 2 μm. With different sequential colors the Legendre and Heyney-Greeinstein reconstructions are shown.

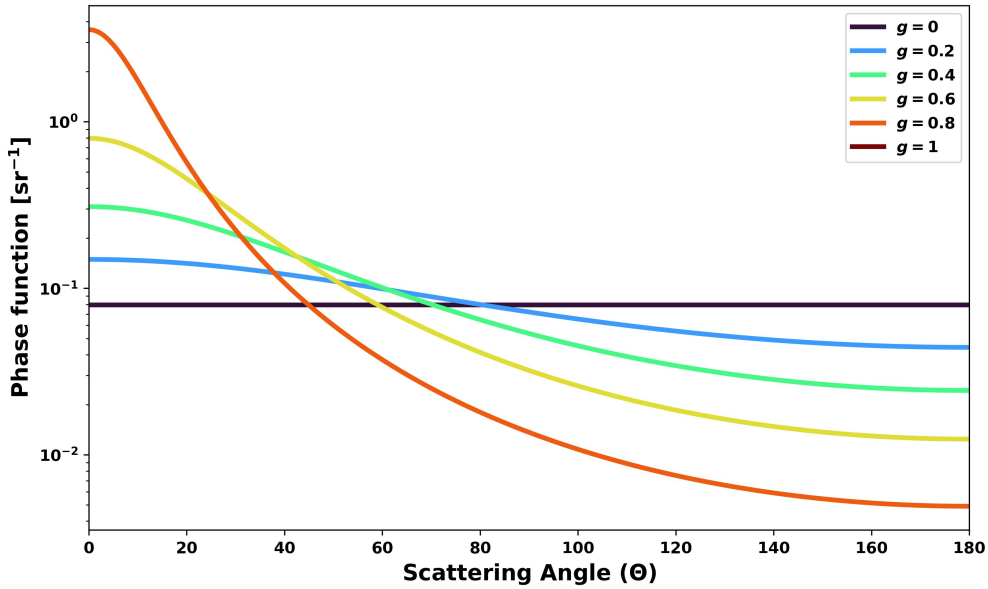


Figure 3.9: Heyney-Greeinstein function dependance on the asymmetry parameter.

sharpness of these features increase with the size parameter. Therefore, usually to represent these functions a large number of Legendre polynomials is usually used. In Fig. 3.8 it is possible to observe the comparison between a Mie-computed phase function and the relative reconstructions using 10, 24, or 48 Legendre polynomials. We can see that the reconstruction strongly depends on the number of polynomials, and it becomes closer to the truth as the number of polynomials increase. This can be a very important effect on the efficiencies of computer codes. An alternative can be the use of simplified analytical expressions. One of the most used is the so-called Henyey-Greinstein function, defined as (Henyey & Greenstein, 1941):

$$P(\cos\Theta)_{\mathrm{HG}} = \frac{1-g^2}{(1+g^2-2g\cos\Theta)^{3/2}} = \sum_{l=0}^{N}(2l+1)g^l P_l(\cos\Theta), \tag{3.66}$$

where g is called the asymmetry parameter defined as:

$$g = \frac{1}{2}\int_{-1}^{1} P(\cos\Theta)\cos\Theta d\cos\Theta. \tag{3.67}$$

From a mathematical point of view g is defined as the first moment of the phase function in $\cos\Theta$, and it can range from -1 to 1. From a physical point of view, it quantifyies the degree of forward versus backward scattering. If $g = 0$ we have isotropic scattering, where light is scattered equally in all directions. A value of $g = 1$ represents complete forward scattering, meaning all the light is scattered in the same direction as the incident beam. This usually occurs for very large particles. On the contrary, a value of $g = -1$ signifies complete backward scattering, where all the light is scattered directly back towards the source. In almost most of the cases, Mie scattering favor a $g \geq 0$. In Fig. 3.9 we can see how different values of g can modify the shape of the phase function.

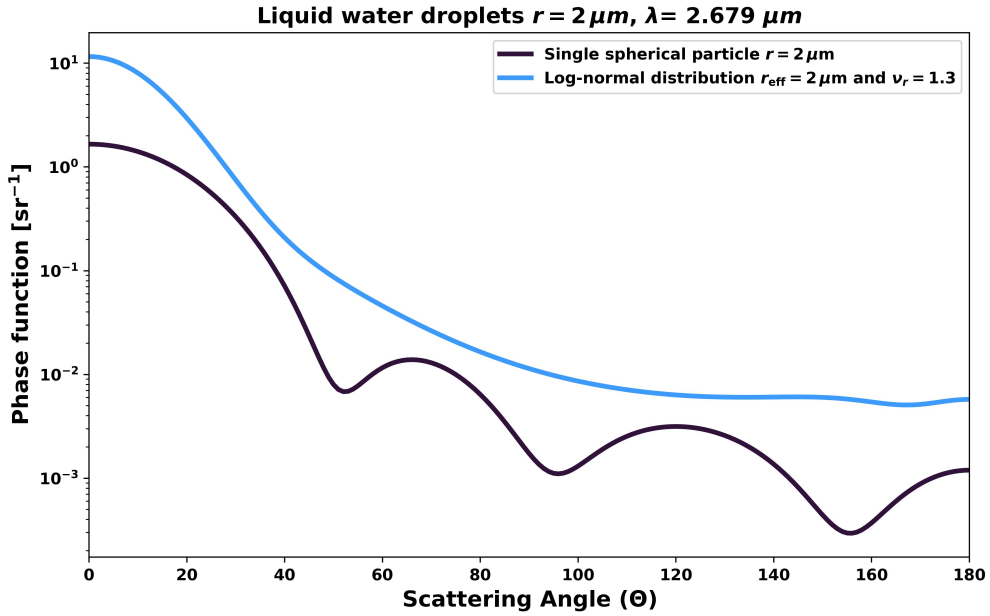


Figure 3.10: Comparison between two Mie phase functions compute considering water droplets. In dark blue it is possible to observe the case of a single sherical particle with a radius of 2 μm. In sky blue it is possible to observe the case in which a population of particles that follows a log-normal size distribution is considered.

As we saw in Fig. 3.7, however phase functions have also numerous peaks and valleys for $\Theta > 90$, i.e. in the so-called backscattering region (to not be confused with backward scattering). The Henyey-Greinstein function usually is not able to recover these patterns if they are present. Therefore, for aerosols that present huge backscattering it is better to use another function called the Double Henyey-Greinstein function defined as (Kattawar, 1975):

$$P(\cos\Theta)_{\mathrm{DHG}} = \alpha_{\mathrm{DHG}} \frac{1-g_1^2}{(1+g_1^2-2g_1\cos\Theta)^{3/2}} + (1-\alpha_{\mathrm{DHG}}) \frac{1-g_2^2}{(1+g_2^2-2g_2\cos\Theta.)^{3/2}} \tag{3.68}$$

Here α_{DHG} represents a weighting factor or mixing coefficient, where $0 \leq \alpha_{\mathrm{DHG}} \leq 1$. It determines the relative contribution of the two Henyey-Greenstein terms. The first term (with g_1) typically represents the forward-scattering component, so α_{DHG} is often close to 1. The second term (with g_2) accounts for the backscattering. The Heyney-Greeinstein functions are way more simple and can facilitate the numerical solution of the RT equation. A comparison between the Mie phase function of water droplets at 2 micron and the best fitting Heyney-Greinstein functions can be found in Fig 3.8. It is possible to observe that the Heyney-Greinstein functions can represent well the general behavior of the true Mie phase function but they cannot reproduce the valleys and the peaks. This is not a problem in real applications since distribution of particles following a log-normal size distribution are usually considered more physically realistic. As it is possible to observe from Fig. 3.10 for the case of liquid water droplets, the phase function of a population of particles is smoother than the one in the single particle case. This is due to the integration in the radial dimension considering the chosen log-normal distribution.

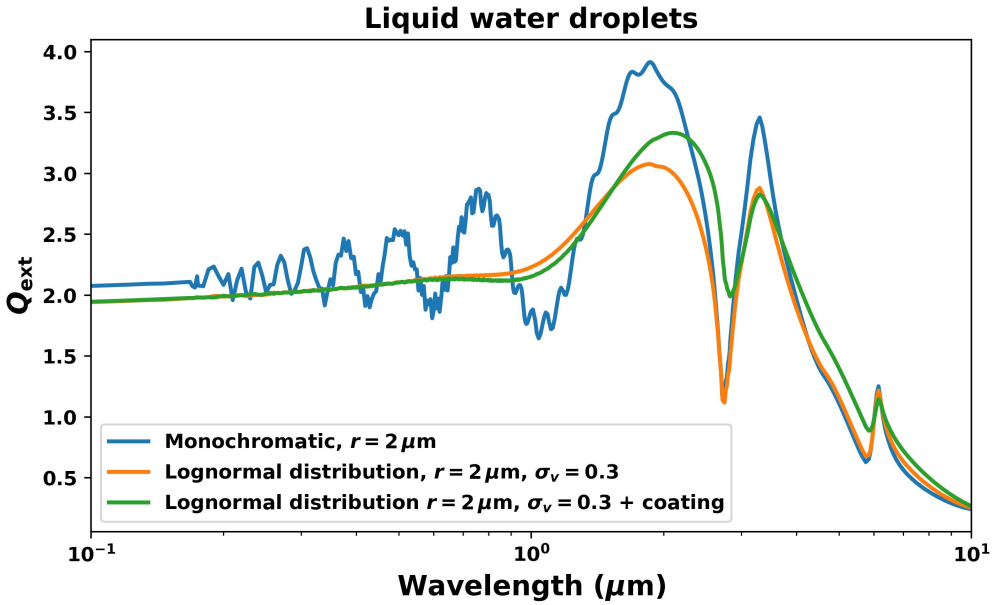


Figure 3.11: Mie extinction efficiencies computed considering: (blue) a spherical water dropet with a radius of 2 μm, (orange) a log-normal distribution of spherical water droplets, (green) a a log-normal distribution of spherical water droplets coated with ammonia.

Both the phase functions and the scattering efficiencies and the phase functions described by Eqn. (3.61) and Eqn. (3.62) must be computed with the aid of numerical methods and routines as the ones described in the fundamental works of Toon & Ackerman (1981) and Bohren & Huffman (1983). There exist a large number of Python libraries that can perform this task, such as `miepython` (Prahl, 2023) or `Py-Mie` (Rothenberg & Hisch, 2016). In the presence of a log-normal distribution of particles Eqn. (3.61), Eqn. (3.62), and Eqn. (3.63) must be integrated over the entire chosen particle size distribution. With a similar approach it is also possible to compute optical properties of particles composed by a spherical core and overlying concentrical spherical shells (coatings). The core and the coatings can be composed of different materials. In this context the parameter $\kappa = \frac{r_{\text{core}}}{r}$, defined as the ratio between the core radius and the total radius, becomes a fundamental parameter to set a further boundary condition for the integrations. In In Fig. 3.11 I compare the Mie cross sections computed considering: (1) a single spherical water ice particle with a radius of 2 μm, (2) a log-normal distribution $r_{mod} = 2\,\mu m$ and $\sigma_v = 0.3$ of water ice particles, (3) a log-normal distribution $r_{mod} = 2\,\mu m$ and $\sigma_v = 0.3$ of water ice particles coated with ammonia with a $\kappa = 60$ %. We can observe that the monochromatic (1) properties display an oscillatory behavior due to the interference between the light rays that pass through the particle (refracted and absorbed) and those that are diffracted around the particle. The presence of a distribution of particles with different sizes minimizes the oscillations. On the contrary, coating can induce new absorption features in the extinction efficiency spectra and/or weaken the original ones. In Fig. 3.12 we can observe the variation of monochromatic mie efficiencies spectra as a function of the particle size. It is possible to note three points: (1) the maximum in the Q_{ext} profiles is at wavelengths comparable to the particle size,(2) all the profiles tend to a constant value of 2 for $\lambda << r$, and (3)

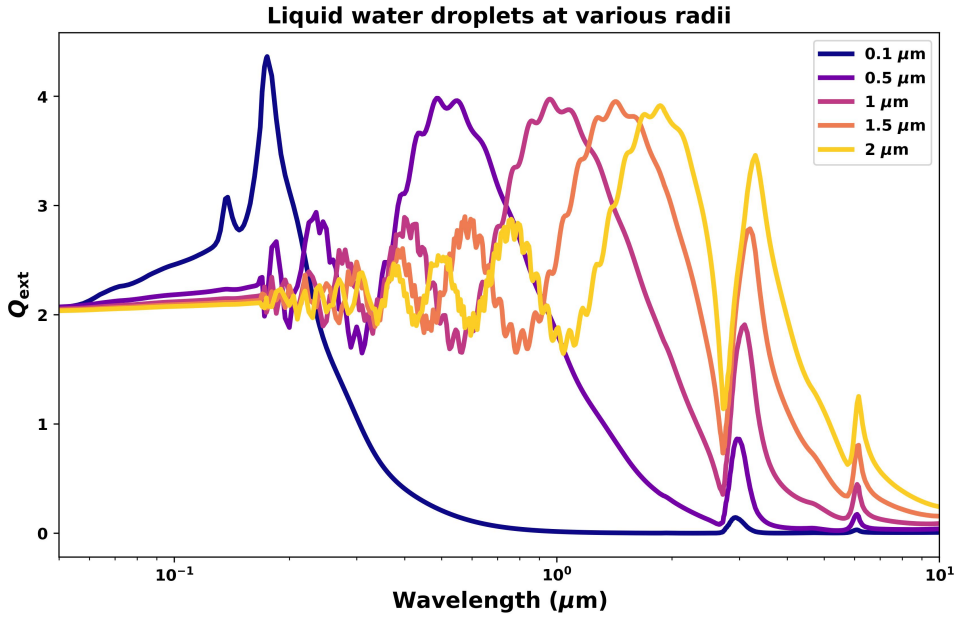


Figure 3.12: Mie extinction efficiencies computed considering spherical water droplets with different radii.

all the profiles show an absorption dip at 3 micron consistent with the imaginary refractive index of water that presents a peak there. These results show that in the NIR/IR we expect to observe scattering contributions from micron-sized particles, while in the visible the contributions from sub-micron particles become more relevant.
Lastly, from the equations derived in this section it is easy to understand that the effect of aerosol on a spectrum can be more subtle than the one of gases. We expect absorption dips only in cases where k is extremely large. In most of the cases aerosols tend to reflect and enhance the solar radiation and to flatten the spectrum (Kreidberg et al., 2014; Sing et al., 2016). I will return on this point in Chapter 5.

3.6 The resolution of the multiple scattering radiative transfer equation

To calculate the expected spectrum of a planetary atmosphere (model spectrum), the following steps are necessary:

- choose a number of parallel layers
- choose a pT profile
- choose an atmospheric composition in terms of molecules present in the atmosphere and their relative VMR profiles
- choose which aerosol species to include and their relative number density profiles and effective radii

- extract the HITRAN (or other databases) lines and the partition functions for each molecule
- compute the line intensities and partition functions for each layer
- choose a line profile and compute the cross sections for each layer
- extract the refractive indexes for the aerosol species and compute the optical properties on the basis of Mie's theory
- solve Eqn. (3.25) for each layer

There is however a problem. Eqn. (3.25) presents both the derivative and the integral of radiance. This means that Eqn. (3.23) is an integro-differential equation where the unknown variable appears also as the integration variable. It is important to note that is the presence multiple scattering that makes the RTE an integro-differential equation. Without the presence of multiple scattering the RTE can easily be solved.
Solving integro-differential equations can be challenging, and often analytical solutions are difficult to obtain. Usually an approximated numerical solution can be found using an iterative method. However, also in this case the resolution of the RTE presents several computational challenges. These include the high dimensionality of the problem, as radiance is a function of spatial coordinates (up to three), directional angles (two), and wavelength points (hundreds or thousands). The angular redistribution of scattered radiation is described by the scattering phase function, which can be highly peaked in the forward direction, demanding high angular resolution (and a large number of Legendre coefficients) in numerical schemes. Furthermore, the optical depth of the medium significantly influences the behavior of the solution and the efficiency of different numerical methods; optically thick media, where multiple scattering predominates, require robust algorithms capable of handling the diffusion of radiation.

A cornerstone in the analytical and semi-analytical treatment of radiative transfer, particularly for plane-parallel atmospheres, was laid by Subrahmanyan Chandrasekhar. In his seminal work, Chandrasekhar (1950) provided exact solutions for problems involving isotropic and Rayleigh scattering. His work also pioneered the so-called discrete ordinates method by demonstrating how the angular dependence of radiance could be discretized, transforming the RTE into a system of ordinary differential equations. While these solutions were often "exact" for the simplified physics they described, their numerical evaluation was a critical step and provided a benchmark for more general numerical methods. Chandrasekhar's insights into the mathematical structure of the RTE have profoundly influenced the development of subsequent numerical algorithms, offering a theoretical foundation and rigorous validation points.
Among the plethora of numerical techniques developed, the Discrete Ordinates Radiative Transfer (DISORT) algorithm, originally developed by Stamnes et al. (1988), has emerged as a widely adopted and highly successful method, particularly for plane-parallel, multi-layered media. DISORT approximates the integral term in

the RTE by a weighted sum (quadrature) over a discrete set of zenith angles (ordinates) and a Fourier series expansion in azimuth. This discretization converts the integro-differential RTE into a system of coupled linear ordinary differential equations. The solution of this system is typically achieved by solving an eigenvalue problem. The accuracy of the angular representation of the radiance field is determined by the number of streams (discrete ordinates) employed. DISORT is renowned for its numerical stability, accuracy, and computational efficiency for a broad range of atmospheric conditions, including those with highly anisotropic scattering and significant thermal emission. It can compute radiances at various atmospheric levels and directions, as well as fluxes. Enhancements to the original DISORT algorithm have addressed issues such as the pseudo-spherical approximation for solar beam attenuation in spherical shell atmospheres, and improvements for strongly peaked phase functions. Other prominent numerical methods include Monte Carlo techniques (O'Hirok & Gautier, 1998), which simulate photon pathways and are highly flexible for complex geometries, but can be computationally intensive to achieve low statistical noise; the Spherical Harmonics (Evans, 1998) method, which expands radiance in spherical harmonics; and the Adding/Doubling method (Hansen, 1971; Hansen & Travis, 1974), which is very efficient for vertically inhomogeneous but horizontally homogeneous layers. The choice of method often depends on the specific problem's geometry, optical properties, desired accuracy, and available computational resources, but methods like DISORT provide a robust and well-validated framework for tackling the complexities of multiple scattering in radiative transfer.
Since their developments, the algorithms of Chandrasekar and Stamnes have been modified and implemented in computer codes able to numerically solve the RTE. In the next section I will describe the two RTE solvers softwares that were used in this thesis work: the Planetary Spectrum Generator (PSG) and NEMESIS.

3.7 The Planetary Spectrum Generator and NEMESIS

The Planetary Spectrum Generator (PSG) is a sophisticated, publicly available online radiative transfer suite developed by NASA Goddard Space Flight Center (Villanueva et al., 2018). It is designed to compute planetary spectra, encompassing both atmospheric and surface contributions, across an exceptionally broad electromagnetic spectrum (from UV/Vis/near-IR/IR/far-IR to THz/sub-mm/Radio wavelengths, approximately 50 nm to 100 mm). This versatile tool enables researchers to model spectra for a diverse array of celestial objects, including solar system planets, moons, comets, asteroids, Kuiper Belt Objects (KBOs), and particularly exoplanets, as observed by various ground-based, airborne, and space-based observatories.
Technically, PSG operates by integrating state-of-the-art radiative transfer models with extensive spectroscopic and planetary databases. For high-resolution spectral computation, PSG typically employs a line-by-line (LBL) approach, where the optical depth is calculated for each discrete spectral line of atmospheric constituents, leveraging databases like HITRAN, GEISA, and JPL. For moderate spectral resolutions, it can adopt the computationally-efficient correlated-k (CK) method (Goody

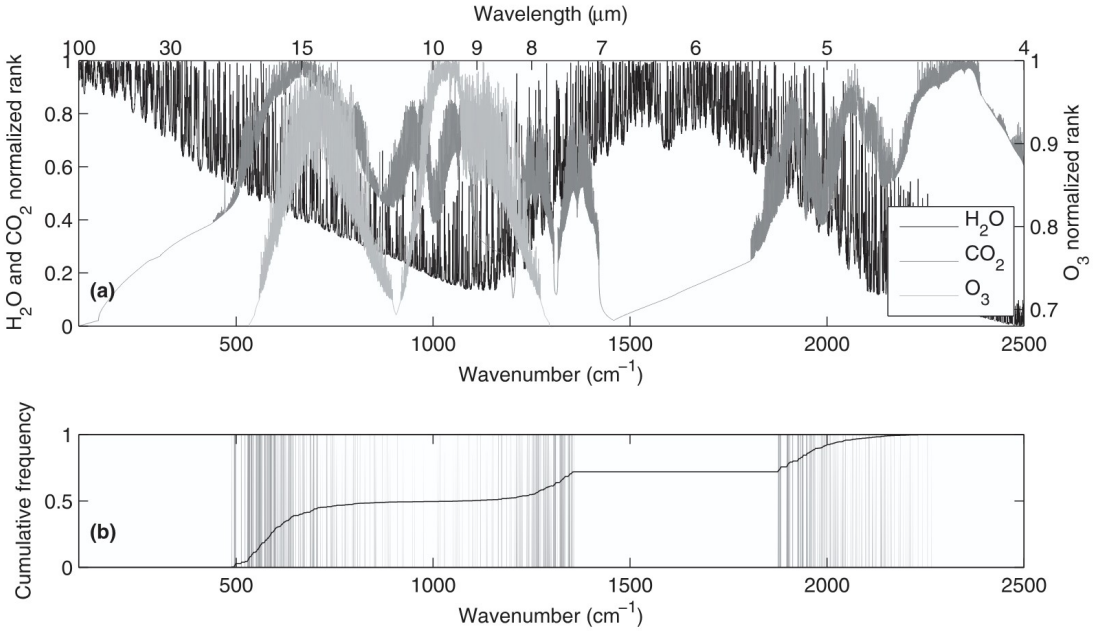


Figure 3.13: Upper panel: Normalized absorption cross sections for water, carbon dioxide, and ozone at Earth conditions from Hogan (2010). Bottom panel: the correpsonding k-distribution for water.

et al., 1989), which groups spectral lines into bins of similar absorption properties to expedite calculations. It is worth to underline that the name comes from the work of Goody et al. (1989) in which the absorbtion coefficient was named k. In this thesis I chose to use the greek letter β.

The correlated-k approach was developed to overcome the computation of the absorption coefficient by looking for the single transition lines singularly (Goody et al., 1989). In fact, as we saw, molecules can have a very large number of vibrational and rotational lines, so to compute β_{abs} accurately, in principle, a very fine wavenumber grid must be chosen. This makes numerical computations highly time expensive. If instance, we define $y = \frac{1}{\mu}\int_{z_0}^{z_1} n(z)dz$, the transmittance can be re-written as (Irwin, 2009):

$$\mathcal{T}_\nu(y) = \frac{1}{\Delta\nu}\int_{\nu}^{\nu+\Delta\nu} \exp\left(-\beta_{\text{abs}}(\nu)y\right) d\nu. \tag{3.69}$$

At this point $\beta_{\text{abs}}(\nu)$ is a rapidly varying function of frequency. Correlated-k aims to find a change of variables, $\beta_{\text{abs}}(a)$ that makes the function smooth. When performing a line-by-line computation of the transmission integral, the crucial information is the distribution of absorption values, specifically the fraction of lines exhibiting low absorption (close to 0) versus those with high absorption (close to 1). So, a reasonable choice for the change is a variable a that sorts a high-resolution normalized absorption coefficient spectrum monotonically from 0 to 1, see Fig. 3.13 (Hogan, 2010). This is called the k-distribution and must be computed one single time, since then it can be interpolated considering any frequency/wavenumber/wavelength grid. Mathematically the transmission becomes:

$$\mathcal{T}_\nu(y) = \int_0^1 \exp\left(-\beta_{\text{abs}}(a)y\right) da = \sum_{i=1}^{N_{quad}} \exp\left(-\beta_i y\right) \Delta a_i, \tag{3.70}$$

and so the integral can be computed easily choosing N_{quad} quadrature points. PSG adopts this method, and in particular, it uses the most updated k-distribution from the HITRAN database (Gordon et al., 2022).
Alternatively, PSG can also directly use gaseous cross section tables written with the same formalism of the ones adopted in the ExoTransmit database (Kempton et al., 2017).
Regarding the resolution of the multiple scattering RT equation, PSG adopts two algorithms called PUMAS and PSGDort. PUMAS (Villanueva et al., 2015) integrates the Discrete Ordinates Radiative Transfer (DORT) Algorithm in order to solve the RT equation. The strength of PUMAS is its possibility of working with a huge database of absorption coefficients, refractive indexes, and functions. It can adapt this data to work with every custom wavelength or frequency grid. The scattering modeling is implemented via PSGDORT, that adapts DISORT both to PUMAS and to the methods described in Smith et al. (2009), which also includes a correction for pseudo-spherical geometry as described by Dahlback & Stamnes (1991). In particular, PSGDort has the great advantage of working on files that contain information previously computed from Mie theory. These files can: (i) contain the single-scattering albedo, the extinction cross-section and the phase function expanded in Legendre polynomials, or (ii) contain the single-scattering albedo, the extinction cross-section, and the asymmetry parameter g. This thesis presents the first adaptation of PSG to model Jupiter's spectra in the 2–5 micron range (Chapter 6).
On the other hand, NEMESIS (Non-Linear Optimal Estimator for MultivariatE Spectral AnalySIS) is an extensively applied, open-source atmospheric retrieval code developed at the University of Oxford, designed for the quantitative analysis of observed planetary spectra (Irwin et al., 2008). Its primary function is to infer the atmospheric temperature, pressure, and chemical abundance profiles, along with aerosol/cloud properties, by fitting synthetic spectra generated from a radiative transfer model to observed spectroscopic data (see next section).
Internally, NEMESIS incorporates a fast and accurate radiative transfer scheme that explicitly solves the radiative transfer equation (RTE) for thermal emission, reflected stellar radiation, and scattered light. The code computes the monochromatic optical depth by summing the contributions from various atmospheric absorbers, typically using the correlated-k formalism. The work of Irwin et al. (2008) was one of the first where the correlated-k method was efficiently implemented numerically for the study of planetary and exoplanetary atmospheres.
Regarding the treatment of aerosols and clouds, NEMESIS can employ various scattering formalisms, including Mie theory for spherical particles, and can handle polydisperse size distributions by integrating single-particle scattering properties over predefined distributions. Multiple scattering effects are rigorously handled through advanced algorithms, often employing the doubling-or-adding method (Hansen, 1971; Hansen & Travis, 1974) or variations thereof such as the Matrix Operator Method (Plass et al., 1973). Its fundamental principle is based on the invariance principles of radiative transfer, which state that the reflection and transmission properties of a combined layer can be derived from the known reflection and transmission properties of its constituent sub-layers. The method is particularly well-suited for situations where multiple scattering is significant.

In this thesis work I used the latest version of NEMESIS as described in reference. This updated version employs correlated-k tables and methods to efficiently model the high resolution spectra of Jupiter acquired by JWST NIRSpec, see next Chapters.

3.8 The concept of atmospheric retrievals

In the previous sections I described how it is possible to model a real atmosphere using the radiative transfer formalism. The aim of this thesis work is to use these methods in order to extract physical information from infrared spectral data, i.e. real measured spectral radiances, that will be presented in Chapters 5, 6, 7, 8, and 9. In this thesis work I'm interested in comparing our data $D = \{y_n\}$ and their associated errors $\{\sigma_n\}$ with a model $\mathcal{F}$ which depends on j parameters describing the physical conditions of the atmosphere $x = x_1, ..., x_j$. Specifically, $\mathcal{F}$ is the RT solver, for example PSG or NEMESIS. In this context, it is also very important to find the best estimate for the model parameters based on the available data. To quantify the quality of the fits, we can rely on statistical functions called estimators. Two of the most used functions are the so-called chi-square (χ^2) function or goodness-of-fit function:

$$\chi^2 = \sum_{n=1}^{N} \frac{[y_n - \mathcal{F}_n(x)]^2}{\sigma_n^2}, \tag{3.71}$$

and the so-called likelihood function:

$$L = p(D|\mathcal{F}) = p(y|x), \tag{3.72}$$

where $p(y|x)$ is the probability (or probability density) of the data y occurring, given the parameters x. In the case of heteroscedastic gaussian errors the likelihood becomes:

$$L = \prod_{n=1}^{N} \frac{1}{\sigma_n\sqrt{2\pi}} \exp\left(-\left[y_n - \mathcal{F}_n(x)\right]^2 / 2\sigma_n^2\right). \tag{3.73}$$

N here is the number of data points, while heteroscedastic gaussian errors mean that every y_n value has a different error σ_n and these are assumed to be Gaussian. By using these functions we can rely on two well-known estimations: (i) the chi-squared minimization and (ii) the maximum likelihood estimation. In both cases, the minimization is concerning the model parameters x_j. In the history of mathematics and physics, two different approaches have been developed to estimate x_j from D: the *frequentist* or *classical* paradigm and the *bayesian* paradigm (Ivezić et al. (2014a)). Frequentist statistics is based on the following properties:

- It was largely developed in the 20th century by the works of Pearson and Fisher
- Probabilities refers only to the relative frequencies of events
- The model parameters x_j are fixed and unknown constants
- It doesn't rely specifically on the likelihood function

while Bayesian statistic is based on the following properties:

- It was first proposed in the 18th century by the works of the Reverend Thomas Bayes (Bayes & Price (1763)), but it was formalized lately by the works of the French mathematician Laplace. From the second half of the last century, it became widely used in scientific works.
- Computations could be time-expensive and this explains the rapid growth in the 20th century, strictly connected to the development of hardware and computers.
- Probability describes the degree of subjective belief and probability statements could be made about data, model parameters and models themselves.
- It relies on the Bayes Theorem:

$$p(A|B) = \frac{p(B|A)p(A)}{p(B)}, \tag{3.74}$$

  where p refers to probabilities; for example, $p(A|B)$ means the probability of the A event gave the B event.
- It relies specifically on the likelihood function.
- Inferences about parameters are made by studying their probability distributions.

In the frequentist approach, the parameters are the constant values that maximize or minimize a specific function, given a set of data. In the bayesian approach, we combine an initial estimate with new data to arrive at an improved estimate (VanderPlas et al. (2012a)). So, if we call our prior information about the model and the parameters I, in the case of fitting a model to data, the Bayes's Theorem, Eq. (3.74), becomes:

$$p(\mathcal{F}, x|D, I) = \frac{p(D|\mathcal{F}, x, I)p(\mathcal{F}, x|I)}{p(D|I)}, \tag{3.75}$$

or:

$$p(x|y) = \frac{p(y|x)p(x)}{p(y)}, \tag{3.76}$$

It is worth discussing the terms in Eq. (3.75). The first is $p(\mathcal{F}, x|D, I)$ which is the so-called *posterior pdf* (pdf stands for probability density function) for the model and the parameters. It can be considered as the mathematical object used to make inferences about the best-fitting parameters, i.e. the parameters that best fit the data. This object is a $j+1$-dimensional pdf in the space spanned by j model parameters x. The second term is $p(D|\mathcal{F}, x, I)$, which is the likelihood function introduced in Eqn.(3.72). The third term, $p(\mathcal{F}, x|I)$, is called the *prior* and represents all the previous knowledge that we had about the fitting parameters. The prior is independent of the data that we are analyzing and of the likelihood function. A prior that consists in a constant value, $p(x|I)$ =const., is called a flat prior. Usually, it is recommended to use priors that adopt upper and lower limits for x, so

that their integral would not diverge. The last term, $p(D|I)$, is the *probability of the data given the prior*, and it provides a proper normalization for the posterior. Therefore, a bayesian analysis should first set a prior, then compute the likelihood, and finally the posterior pdf using Eqn. (3.75). The computation of the integral $\int p(D|\mathcal{F}, x, I)p(x|I)dx$ can be highly complex, since it has to be evaluated for every combination of all the j parameters.
To obtain the best-fitting values we need to find the mean or the median of a pdf. At this point could be reasonable to ask if in the bayesian statistic the parameters are a sort of fluctuant magic numbers as if the mass of a planet that we want to determine was a distribution and not a fixed value. However, this is not what bayesian analysis says. The posterior pdf should not be understood in terms of frequencies (i.e. coin flips) but in terms of the state of our knowledge given new data and ca specific prior information. Despite the computational difficulties and conceptual ambiguities, bayesian analysis fame grew rapidly in the field of astrophysics, mostly in the fields where fitting models with a large number of parameters to the data was required. For this reason in this thesis I only used two Bayesian techniques to fit the infrared spectral data of interest. These techniques are Optimal Estimation (OE) and MonteCarlo Markov Chains (MCMC).

3.8.1 Optimal Estimation

Optimal Estimation is a method developed by Rodgers (2000) in order to generalize the more frequentist approach of chi-square minimization via the so-called Levenberg-Marquardt Algorithm.This algorith was developed independently by Kenneth Levenberg in 1944 (Levenberg (1944)) and by Donald Marquardt in 1963 (Marquardt (1963)). To describe the algorithm we first need to rewrite Eq. (3.71) using matrix notation:

$$\chi^2 = \sum_{n=1}^{N} \frac{[y_n - \mathcal{F}_n(x)]^2}{\sigma_n^2} = (y - \mathcal{F}(x))^T W (y - \mathcal{F}(x)) \ , \tag{3.77}$$

where W represents the inverse of the covariance matrix of the observations, which diagonal elements are just $W_{jj} = 1/\sigma_j^2$. The LMA is a method used to minimize the chi-squared which could be understood as a hybrid between two of the most used minimization algorithms, the Gradient Descent Method, and the Gauss-Newton Method. Both are iterative methods and their key idea is to find a perturbation h of the parameters x that minimize the χ^2 at each iteration. The process goes on until a condition of the type $|y - \mathcal{F}| < \epsilon$ is satisfied. The Gradient Descent Method (GDM) is an algorithm used to find the local minimum of a selected function. It updates the parameters by choosing h in the downhill direction, i.e. the direction opposite to the gradient of the objective function, in our case the chi-squared. This is based on the mathematical fact that the direction of the gradient could identify a local maximum, and so a function will decrease faster if it follows a direction opposite to it. So, deriving Eq. (3.77) with respect to the parameters we obtain:

$$\frac{\partial \chi^2}{\partial x} = -2(y - \mathcal{F})^T W \frac{\partial \mathcal{F}}{\partial x}. \tag{3.78}$$

Calling the gradient of the model function with J (also referred as Jacobian function), the perturbation associated with the GDM must be:

$$h_{\rm GDM} = \alpha J^{\rm T} W (y - \mathcal{F}), \tag{3.79}$$

where α is a positive constant. Instead, the Gauss-Newton Method, GNM, proposed by Karl Friedrich Gauss in 1809, essentially uses a Taylor expansion of the model function $\mathcal{F}(x+h) \simeq \mathcal{F}(x) + Jh$. Inserting it in Eqn. (3.77), we obtain:

$$\chi^2 \simeq y^{\rm T} W f + \mathcal{F}^{\rm T} W \mathcal{F} + -2 y^{\rm T} W \mathcal{F} - 2(y - \mathcal{F})^{\rm T} W J h + (hJ)^{\rm T} W J h, \tag{3.80}$$

and so deriving with respect to the perturbation h we obtain:

$$\frac{\partial \chi^2}{\partial h} \simeq -2(y - \mathcal{F})^{\rm T} W J + 2(hJ)^{\rm T} W J. \tag{3.81}$$

Consequently, the perturbation associated with the GNM must be:

$$[J^{\rm T} W J] h_{\rm GNM} = J^{\rm T} W (y - \mathcal{F}). \tag{3.82}$$

As is possible to observe, the right side of Eqn. (3.79) is equal to the right side of Eqn. (3.82), if we neglect the positive constant α. Therefore, Levenberg (1944) proposed a new iterative method where the perturbation was given by:

$$[J^{\rm T} W J + \lambda \mathbf{I}] h_{\rm LMA} = J^{\rm T} W (y - \mathcal{F}). \tag{3.83}$$

where $\mathbf{I}$ is the identity matrix and λ is called the *damping parameter*, which increases if the computed chi-squared at the $n+1$-th iteration is greater than the one computed at the n-th iteration, $\chi^2_{n+1} > \chi^2_n$. So, when we are far from the best-fitting solution, the LMA acts like the GDM, whereas when is closer like the GNM. This approach appears reasonable since the GDM is optimal to find the region in the parameter space where the local minimum of the chi-squared is located. With a reduced search space is possible to use a Taylor approximation and find the exact minimum, and that is why LMA switches from GDM to GNM. Marquardt (1963) found the same expression of Eq. (3.83), with the only exception that the damping parameter is normalized, i.e. is multiplied by diag$(J^{\rm T} W J)$ instead of the identity matrix. The numerical implementation is non-trivial; however, over the past five decades, the LMA has been widely integrated into a multitude of software packages, as the `scipy` (Virtanen et al. (2020)) and the `lmfit` (Newville et al. (2014)) Python packages.

We observed that Eqn. (3.25) depends on a great number of parameters. For example, to describe the effects of a cloud using the Mie theory we require at least 3 parameters which are: (i) the particle radius, (ii) the altitude of the clouds and its shape, and (iii) the density of the cloud. Moreover, we need to parametrize or fix the pT profile and all the gas mixing ratios. Therefore, the situation is likely to be highly degenerate, meaning that many parameters and different combinations of them could lead to similar results. In this case, the LMA is known to not perform well and therefore a Bayesian generalization is needed. The starting point is the Bayes theorem, Eqn. (3.76). In our case we can write:

$$p(y|x) = A \cdot \exp\left(-\frac{[y - \mathcal{F}(x)]^2}{2\sigma_y^2}\right) = A \cdot \exp\left(-\frac{1}{2}\xi^T S_y^{-1} \xi\right), \tag{3.84}$$

$$p(x) = A \cdot \exp\left(-\frac{1}{2}(x - x_a)^T S_a^{-1}(x - x_a)\right), \tag{3.85}$$

where we called S_y the relative covariance matrix, i.e. $S_y = \sigma_y^{\mathrm{T}}\sigma_y$, $\xi = y - \mathcal{F}(x)$, and x_a the a priori parameters values and the relative covariance matrix S_a. These values can be interpreted as the prior information and uncertainties that we have about the physical parameters that we are trying to retrieve, and can be extracted from literature or set following physical constraints. As for S_y, also S_a is often approximated as diagonal using the expression $S_a = \sigma_a^{\mathrm{T}}\sigma_a$, where σ_a will represent the standard deviation of the a-priori guess, which may be related to the confidence level that we put on the a-priori guess. As a rule of thumb, the larger σ_a is, and then the larger the parameter space will be explored. In reality the S_a matrix should also possess off-diagonal elements that represent the physical correlation between the physical parameters. In most of the cases these correlations are unknown or very difficult to parametrize and therefore S_a is approximated as diagonal. Inserting Eqn. (3.84) and (3.85) in Eqn. (3.76), and calling $K = \frac{\partial y}{\partial x}$ the Jacobian matrix, OE aims to find the best-fitting solution iteratively (Rodgers, 2000; Maahn et al., 2020):

$$x_{i+1} = x_a + (\eta S_a^{-1} + K_i^{\mathrm{T}} S_y^{-1} K_i)^{-1} K_i^{\mathrm{T}} S_y^{-1} \left[y - \mathcal{F}(x_i) + K_i(x_i - x_a)\right], \tag{3.86}$$

where η is called regularization parameter (Carissimo et al., 2005; Turner & Löhnert, 2014) and acts as a tradeoff between the a-priori values of the parameters to be retrieved and the observations in defining the updated solution. This parameter greatly stabilizes the retrieval procedure. At this point Eqn. (3.86) can be efficiently minimized using the LMA solving for the best-fitting parameters. The iteration usually stops when convergence is reached, for example Eqn. (5.29) of Rodgers (2000), or if the chi-squared (χ^2) values are lower than a certain threshold.
As for the LMA case, there exists a large number of numerical implementation of OE methods. In this thesis work I used the Python version condensed in the `PyOE` package (Maahn et al., 2020).

3.8.2 Monte Carlo Markov Chains, MCMC

Usually one of the problems of bayesian analysis is that it can be numerically intensive due to computation the integral $\int p(D|\mathcal{F}, x, I)p(x|I)dx$, which has to be evaluated for every combination of all the j parameters. This problem is noted as *marginalization*, which is a method that requires summing over the possible values of one variable to determine the marginal contribution of another. We want a posterior pdf at least for every parameter of the model, so we need to marginalize Eq. (7.5), which is a $j+1$-dimensional object, where j is the number of parameters. Quantitatively, if we are interested in the m-th parameter, the rest of the $j-1$ act like *nuisance parameters*. Indicating the nuisance parameters with $\eta = \{x_1, ..., x_{n-1}, x_{n+1}, ..., x_j\}$, the objective is computing j integrals of the type (Foreman-Mackey et al. (2013)):

$$p(x_m|D) = \int p(x_m, \zeta|D, I)d\zeta = \int \frac{1}{Z} p(x_m, \zeta|I)p(D|x_m, \zeta, I)d\zeta, \tag{3.87}$$

where Z is the normalization factor $p(D|I)$. In the previous subsection, we saw that an optimal frequentist algorithm is one that could find the minimum value of the

chi-squared efficiently. In this case, the algorithms we are interested in are the ones that can efficiently compute the integral in Eq. (3.87). A group of algorithms of this kind goes under the name of Monte Carlo Markov Chain Algorithms (MCMC). The first step that we can adopt to simplify the problem is to consider Monte Carlo Integration. The integral is discretized because is uniformly estimated sampling M random values, $X_l = \{x_{m,l}\,, \zeta_l\}$, for the parameter of interest and the nuisance parameters and then summing on all the sampled values (Ivezić et al. (2014a)):

$$p(x_m|D) \simeq \frac{V_x}{M} \sum_{l=1}^{M} p(x_{m,l}\,, \zeta_l|D, I), \tag{3.88}$$

where V_x is the integration volume. If we compare Eq. (3.88) and Eq. (3.87) we can observe that using the Monte Carlo method, we can find the posterior pdf through a "mean" where the likelihood function acts like a weight. The heart of the method is the choice of the sample generator, which in turn will regulate the algorithm's efficiency. For instance, when fitting a model with a large number of parameters, uniform sampling is not an effective choice because the integrated function can vary significantly across the integration volume. Therefore, it is preferable to adopt Markov Chains to generate the sample. A Markov Chain is a memory-less process in which the future state of a system depends only on its current state, not on the sequence of events that preceded it. So, every point X_l of a chain of values (our sample), depends only on the properties of the previous point X_{l-1}. It is worth underlining that the normalization does not depend on the parameters and therefore it is not required during the sampling. This is very important since the computation of normalization is not trivial and could be computationally intensive. One of the most famous MCMC algorithms is the so-called Metropolis-Hasting Algorithm, MHA (Metropolis et al. (1953), Hastings (1970)). Given a position X_l, the algorithm samples a proposal $l+1$ position Y using a transition distribution Q. The proposal is accepted with a probability (Foreman-Mackey et al. (2013)):

$$\mathcal{P} = \min\left(1, \frac{p(Y|D)}{p(X|D)} \frac{Q(X \to Y)}{Q(Y \to X)}\right). \tag{3.89}$$

In brief, the proposal point is accepted $X_{l+1} = Y$ if is "more probable" than the previous chain point and is rejected $X_{l+1} = X$ on the contrary. Usually, MCMC algorithms modeled on the MHA need a set of initial guesses (as for the LMA) to reduce the search region in the parameter space. Usually several steps are required to reach stability. This stage of the iteration is called *burn-in* and should be discarded from the steps used to compute the integrals, which are called *burn-out*. The above discussion about the computation of the integrals and the sample generation is only a simple introduction, as these are two of the most recent and ambitious themes in numerical analysis. A detailed discussion of this topic is beyond the scope of this work; however, the interested reader may refer to a variety of Python packages developed for MCMC analysis such as `PyMC3` (Salvatier et al. (2016)) `nautilus` (Lange (2023)), and `emcee` (Foreman-Mackey et al. (2013)). These packages uses algorithms that generalizes the MHA algorithm. In this thesis work I used `emcee` which implements a new method called affine-invariant ensemble sampler. Unlike MHA, which uses a single "walker" (i.e. a single Markov chain) to explore the parameter space,

emcee uses an ensemble of walkers. The key innovation is that the proposal step for each walker is generated by using information from the entire ensemble. This approach makes the algorithm affine-invariant, meaning its performance is not dependent on the linear transformation (scaling or rotation) of the parameter space. This is a significant advantage because it allows the algorithm to handle highly correlated parameters much more efficiently than traditional methods, which often get stuck in long, narrow "valleys" in the likelihood function.

Chapter 4

A brief history of Jupiter atmosphere observations

In this Chapter I will give the reader a brief overview of Jupiter's observations across approximately three centuries, Fig. 4.1. A particular focus will be given to the description of spectrometers, and in particular to the Juno/JIRAM and JWST/NIRSpec instruments.

4.1 Early observations (before 1850)

The history of Jupiter observations before 1850 is marked by a gradual increase in detail and sophistication, driven by advancements in telescope technology and the persistent efforts of pioneering astronomers. Ancient civilizations recognized Jupiter as a wandering star, or planet, and tracked its motion across the sky, incorporating it into their mythologies and calendars (Rogers, 1995). The invention of the telescope in the early 17th century revolutionized its study, beginning with Galileo Galilei's groundbreaking observations in 1609-1610. Galileo's Sidereus Nuncius (1610) detailed his discovery of Jupiter's four largest moons—Io, Europa, Ganymede, and Callisto—which provided strong evidence against the geocentric model of the universe and demonstrated that celestial bodies could orbit something other than the Earth. These observations not only challenged prevailing cosmological views but also established the Galilean moons as crucial subjects of study in their own right, with early astronomers meticulously recording their movements, eclipses, and occultations, contributing to the development of celestial mechanics. Following Galileo's discoveries, other astronomers, such as Giovanni Domenico Cassini and Robert Hooke, made significant contributions. Hooke is credited with discovering the Great Red Spot, a prominent feature in Jupiter's atmosphere, although its exact identity with earlier observations remains debated (Rogers, 1995; Peek, 1958; Sánchez-Lavega et al., 2024a). Cassini also observed the differential rotation of Jupiter's atmosphere, noting that different latitudes rotate at different speeds, a fundamental aspect of Jovian meteorology. Subsequent observers continued to document the planet's atmospheric features, including belts, zones, and other transient phenomena, gradually building a catalog of Jovian morphology. Early attempts to understand Jupiter's composition were largely speculative. Still, the observed features prompted questions about the planet's physical state, atmospheric dynamics,

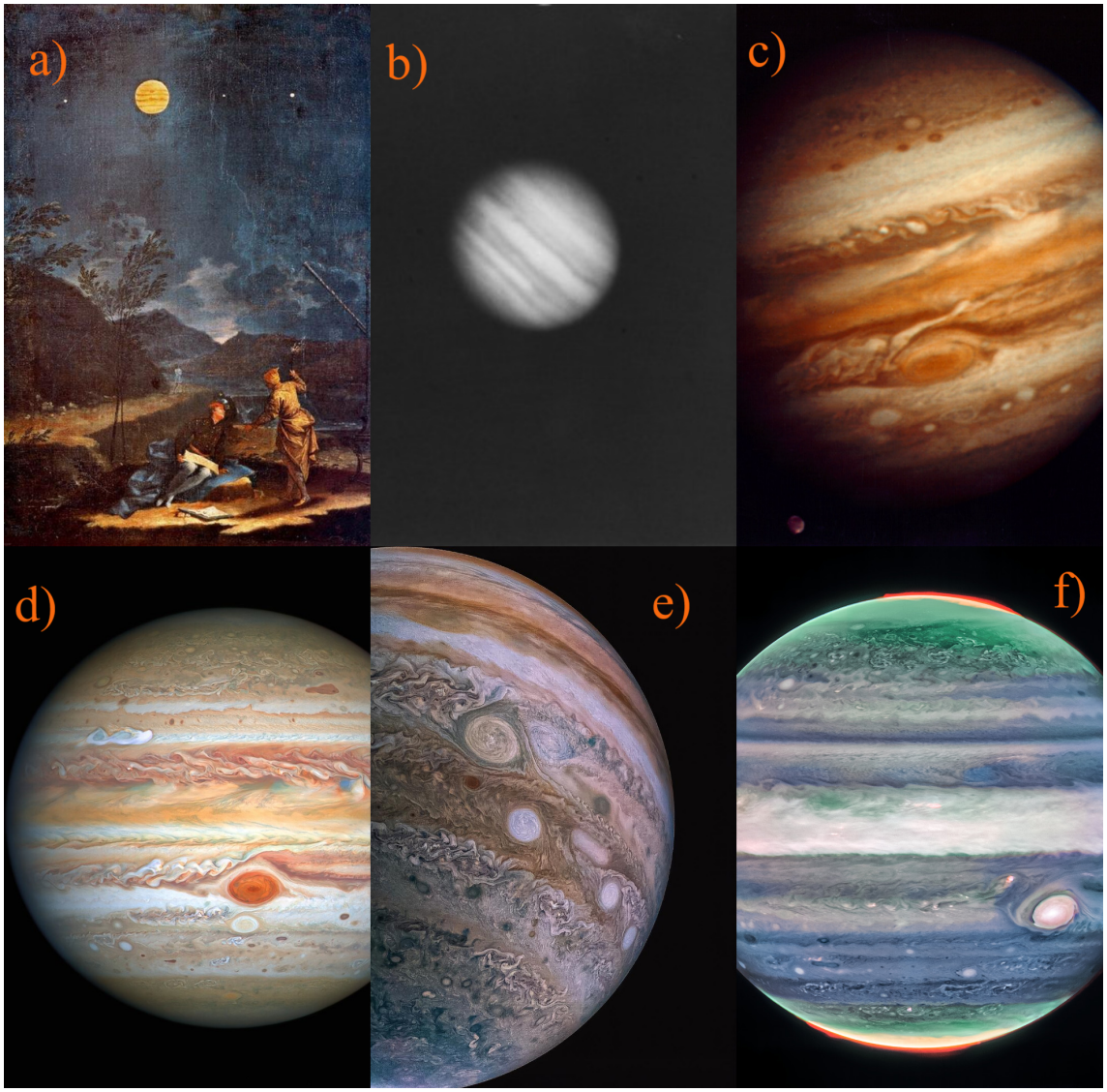


Figure 4.1: Jupiter observations across three centuries. (a) Donato Creti's painting "Astronomical Observations: Jupiter" (1711, Pinacoteca Vaticana). (b) Edward Emerson Barnard, "Jupiter", 1906-10-02 photographed with the Yerkes Observatory 40-inch refractor telescope. (c) Voyager 1 image of Jupiter and its moon Ganymede (bottom left) acquired when it was just over a month away from its closest approach to the planet in 1979. (d) Full-disk image of Jupiter captured by NASA/ESA Hubble Space Telescope on 25 August 2020. (e) Processed JunoCam image of the Jovian Southern Temperate Domain in April 2022. The image was created and color-enhanced by citizen scientist Dawson20. (f) JWST/NIRCam infrared image of the Jovian disk in July 2022.

and the nature of its surface, or lack thereof. Telescopic observations also contributed to improving the accuracy of ephemerides and refining calculations of Jupiter's orbit and its interactions with other solar system bodies. Over the centuries, improved telescopes, including achromatic lenses and larger apertures, allowed for increasingly detailed views of Jupiter, revealing finer structures in its atmosphere and moons, and setting the stage for the more sophisticated investigations of the 19th and 20th centuries.

4.2 Modern Astrophysics era (1850-1960)

The period between 1850 and 1950 represents a transformative era in the study of Jupiter, characterized by significant advancements in observational techniques, the development of new theoretical frameworks, and a growing understanding of the planet's complex atmospheric dynamics and physical properties. This epoch witnessed the transition from primarily visual observations to the dawn of modern astrophysics, laying the groundwork for the space exploration era that would follow. The mid-19th century saw a steady improvement in telescope technology, with larger aperture refractors and, increasingly, reflectors, becoming available to astronomers. These instruments offered higher resolution and greater light-gathering capabilities, allowing for more detailed observations of Jupiter's features.
The period from 1850 to 1950 saw significant advancements in how Jupiter was observed:

- **Photography**: The introduction of astronomical photography revolutionized the study of Jupiter. Photography provided a permanent and objective record of observations, overcoming the limitations of visual sketching and allowing for more accurate measurements and comparisons over time. Early photographic studies focused on capturing the planet's overall appearance, including its belts, zones, and the Great Red Spot (GRS). Astronomers like Edward Emerson Barnard and others used photographic plates to document the ever-changing morphology of Jupiter's atmosphere (Barnard, 1885).

- **Spectroscopy**: The development of spectroscopy in the late 19th century marked a crucial turning point in planetary science. This was made possible by spectrometers, i.e. instruments designed to analyze the spectral composition of light or other electromagnetic radiation. They operate by separating incoming radiation into its constituent wavelengths or frequencies and then quantitatively measuring the intensity of each component. This separation is typically achieved using dispersive elements like prisms or diffraction gratings. The separated radiation was then measured manually. The resulting measure is a spectrum, as defined in Chapter 3. A spectrometer is defined by three fundamental parameters: (1) the range in wavelength between which you can study the separated radiances, and (2) the spectral resolution, i.e. the step in wavelength at which you can separate the radiances ($\Delta\lambda$). With these two parameters it is possible to define the resolving power, RP, of a spectrometer as:

$$RP = \frac{\lambda}{\Delta\lambda} \tag{4.1}$$

By analyzing the light from Jupiter, astronomers could begin to determine its atmospheric composition. Early spectroscopic studies revealed the presence of methane and ammonia, providing the first compelling evidence that Jupiter's atmosphere was vastly different from Earth's (Wildt, 1932).

- **Radiometry**: In the early 20th century, the first measurements of emitted radiance in the IR were employed to measure Jupiter's temperature thanks to Planck's law (see previous Chapter). These measurements demonstrated that Jupiter emits more heat than it receives from the Sun, indicating the presence of an internal heat source (Menzel et al., 1926).

- **Atmospheric Dynamics**: Detailed observations of Jupiter's belts and zones revealed complex patterns of atmospheric circulation. Astronomers measured the velocities of these features, noting the differential rotation of the planet and the presence of strong jet streams. Studies of atmospheric phenomena, such as outbreaks and disturbances, highlighted the dynamic and turbulent nature of Jupiter's atmosphere (Peek, 1958).

4.3 Space Era (1960-)

4.3.1 Ground telescopes

Ground-based observations of Jupiter between 1950 and 2025 have provided a wealth of information regarding its atmospheric dynamics, composition, and thermal structure. Early investigations, carried out at observatories such as Mount Wilson and Palomar, primarily involved visual and photographic monitoring of the planet's prominent features, including zonal bands, storm systems, and the Great Red Spot. These early efforts established foundational datasets for understanding Jupiter's rotational characteristics and the long-term evolution of its visible cloud layers. The application of photoelectric photometry offered more quantitative assessments of Jupiter's brightness variations and color indices, providing initial constraints on atmospheric radiative transfer models and hinting at compositional heterogeneity within the cloud decks.
The latter decades of the 20th century and the early 21st century marked a significant advancement in ground-based Jovian studies with the deployment of sophisticated infrared (IR) instrumentation. Facilities like the NASA Infrared Telescope Facility (IRTF) on Mauna Kea became instrumental in probing the thermal emission from Jupiter's atmosphere. Infrared spectroscopy enabled the identification and quantification of key molecular species such as ammonia, methane, water, and phosphine, along with their vertical distributions within the troposphere, also due to the Texas Echelon Cross Echelle Spectrograph (TEXES) (Wong & de Pater, 2005; Fletcher et al., 2016a). Isotopic ratio measurements obtained through IR spectroscopy provided valuable insights into the planet's formation history and the conditions prevalent in the protosolar nebula. Thermal mapping at 5 micron (see next Chapter) in the infrared revealed intricate patterns of heat flux from Jupiter's interior and the temperature variations associated with its dynamic atmospheric circulation (Harrington et al., 1996). The aftermath of transient events, such as the Shoemaker-Levy

9 comet impact in 1994, was also extensively studied using ground-based IR spectroscopy, yielding information on the chemical composition of the impactor plumes and Jupiter's deep atmospheric layers (Orton et al., 1995; Griffith et al., 1997).
The advent of 8-meter class telescopes equipped with adaptive optics (AO) further revolutionized ground-based Jupiter observations. The Gemini Observatory (North and South) provided diffraction-limited imaging and high spatial resolution spectroscopy, enabling detailed studies of Jupiter's upper atmosphere. For instance, observations with the Near-Infrared Integral Field Spectrograph (NIFS) on Gemini-North have been used to map the three-dimensional thermal and compositional structure of the upper troposphere and stratosphere, revealing, for example, the vertical structure of storms and the distribution of hydrocarbons like ethane and acetylene (Fletcher et al., 2010; de Pater et al., 2010a). Gemini's high spatial resolution capabilities have also been crucial for investigating the fine-scale structure of Jupiter's polar aurorae and their relationship to magnetospheric processes (Sinclair et al., 2023).
Multi-wavelength ground-based campaigns, often integrating data from radio to infrared wavelengths, have provided a comprehensive understanding of Jupiter's atmospheric state. The Atacama Large Millimeter/submillimeter Array (ALMA) has enabled new approaches for studying Jupiter's cold upper atmosphere, allowing for high spatial resolution mapping of millimeter and submillimeter wave emissions sensitive to the distribution of gases like ammonia in the upper troposphere and stratosphere (de Pater et al., 2019a). These observations complement infrared studies, providing constraints on the vertical temperature profile and the spatial variability of key molecular constituents. Radio observations, particularly with facilities like the Very Large Array (VLA), have probed deeper atmospheric layers, revealing information about the distribution of ammonia and other condensable species below the visible clouds and tracing large-scale circulation patterns (de Pater et al., 2016). However, the microwave and radio range of the Jovian spectrum is highly contaminated by the synchotron emission produced in the Jovian magnetosphere.
The Very Large Telescope (VLT) operated by the European Southern Observatory (ESO) has also contributed significantly through its suite of high-resolution spectrographs (e.g., CRIRES, VISIR), enabling detailed analyses of Jupiter's atmospheric composition, dynamics, and thermal structure (Fletcher et al., 2010). Doppler velocimetry studies conducted with the VLT have contributed to mapping wind fields, and high-resolution spectroscopy has allowed for precise measurements of isotopic ratios. Furthermore, the VLT's AO capabilities of the SPHERES instrument have facilitated high-resolution imaging of Jupiter's Galilean moons (King & Fletcher, 2022).

4.3.2 Space missions and a space observatories

1960s was the decade that changed forever the history of humanity and of its technology. Thanks to the launch of the Sputnik in 1957 and the american moon landing, the humans understood that bringing technology to space is possible and for astrophysics very favorable. In fact, from the observational point of view, the Earth's atmosphere has always been a major challenge to observers. Its high turbulent behavior blurs and distorts the light from stars, making them appear to twinkle and

reducing the resolution of telescopes. This is called "seeing" and is due to variations in air density and temperature that refract light unevenly. Secondly, the atmosphere absorbs certain wavelengths of the electromagnetic spectrum, preventing them from reaching ground-based telescopes. This is particularly significant in the ultraviolet, X-ray, gamma-ray, and much of the infrared ranges, limiting the types of astronomical observations that can be conducted from the surface. Both these problems are still open issues regarding the problem of detecting exoplanets. In the context of (solar system) planetary ground-based observations have also other disadvantages:

- the so-called "observational windows": Due to the relative orbits of the Earth and the target planet, the latter will be favorable for observations only in particular positions of its orbit called the opposition and the quadrature. Opposition specifically refers to the configuration where a superior planet (one with an orbit farther from the Sun than Earth's) is directly opposite the Sun in the sky as viewed from Earth. This means the Earth lies roughly in a straight line between the Sun and the planet. Quadrature refers to the configuration where a celestial body, typically a planet or the Moon, appears at a right angle (90 degrees) to the Sun as viewed from Earth.

- it is possible to study the atmosphere in the infrared and visible range only on the planet day side, i.e. only the portion of the planet that is illuminated by the sunlight; in the infrared and in the microwave it is possible to study only the night side of terrestrial planets (Meadows & Crisp, 1996)

- the phase angle, important to study aerosols, is usually always close to zero for outer planets

- it is very difficult, if not impossible, to study the polar regions

Said this, in the following subsections I will list the space observatories and space missions that observed Jupiter in the space era.
From a definition point of view, a space observatory is an astronomical telescope paired (or not) with other scientific instruments placed in outer space to observe celestial objects. By orbiting above the Earth's atmosphere, these observatories overcome the significant limitations imposed by seeing and by the absorption of light by the Earth atmosphere. However, they still can target planets favorably only at the opposition and at quadrature.
A space mission is a planned and executed extra-terrestrial endeavor involving the deployment and operation of one or more spacecraft and associated ground-based infrastructure to achieve specific scientific, technological, or exploratory objectives. A spacecraft is a vehicle designed for travel and to operate in outer space. Characterized by a defined trajectory within the interplanetary medium, a space mission necessitates a rigorously engineer-integrated subsystems for power generation, thermal control, altitude determination and control, telecommunications, and propulsion to support a payload tailored to the mission's goals (e.g., scientific instruments, communication relays, human habitats).
The mission lifecycle encompasses distinct phases, including conceptualization, preliminary design, detailed design, fabrication, assembly, integration, testing, launch, in-flight operations, data acquisition and analysis, and eventual mission termination

or disposal. In the planetary sciences context a space mission can study the planet either from orbit or in situ. With the latter term I mean that the spacecraft can enter the planetary atmosphere, study it from the inside, and either be destroyed by the hot interiors or land on the surface in order to characterize it. The key elements of a spacecraft are:

- an energy generator: either a nuclear power battery or an ensemble of solar panels
- an instrument capable of two-way communication with Earth and the command center; this is typically a radio antenna and receiver, with the K and G bands (K: 18-27 GHz; G: 110-300 GHz) being the most common used
- a tracking system in order to navigate in the interplanetary medium (like a star-camera)
- a scientific payload

The scientific payload can vary from mission to mission depending on the specific science objectives. However, the primary instruments used to study planets and planetary atmospheres are:

- **magnetometer**: it is an instrument designed to quantitatively measure the strength and, in some types, the direction of a magnetic field at a specific point in space. It operates based on various physical principles (such as magnetic induction) that translate the interaction of the magnetic field with a sensing element into a measurable electrical signal.
- **energy particles detector**: Its fundamental function is to transduce the kinetic energy of incident particles into a measurable signal, providing quantitative information about their energy and potentially other characteristics like momentum, charge, mass, and trajectory. These detectors rely on various physical interaction mechanisms between the particles and the detector material, such as ionization, excitation, or scattering, followed by signal amplification and processing to yield quantifiable data.
- **mass spectrometer**: it is an instrument that measures the mass-to-charge ratio (m/z) of ions to analyze a sample's composition. Molecules are ionized and then separated by electromagnetic fields in a mass analyzer according to their $\hat{m}$. A detector records the abundance of ions at each $\hat{m}$ value, producing a mass spectrum. This spectrum identifies and quantifies the sample's components by their unique ionic masses.
- **nephelometer**: it is an instrument that measures the concentration and dimension of suspended particles in a liquid or gas by detecting the amount of light scattered by these particles
- **radar**: This is an active remote sensing instrument that works by actively sending out radio waves and then receiving the echoes that bounce back. By measuring the properties of these echoes, the radar can create detailed maps

and measure distances. Radar can also be used to characterize sub-surface deposits, measure the dielectric constant between mediums, and/or the contents of electrons or ionized species in an atmosphere.

- **radiometer**: it is an instrument that quantitatively measures te integrated electromagnetic radiation (EMR) across a specific range of the electromagnetic spectrum. By detecting and quantifying the intensity of this radiation, radiometers provide information about the source emitting the EMR, such as its temperature or composition.

- **imaging camera**: it is an instrument designed to capture and record visual information in the form of images. It exploits a lens system to focus light from a scene onto a photosensitive sensor. This sensor converts the incoming light into electrical signals, which are then processed and stored as a digital image. In astronomy the most used sensors are the Charged Coupled Devices or CCDs (Howell, 2000). Usually imaging cameras acquire images using a filter to block light from certain wavelengths and retain only the ones of interest. These filters can be narrowband or wideband and are characterized by a response function. This function is equal to 1 at the wavelength of interest and to zero at the wavelengths intended to block.

- **spectrometer**: A spectrometer serves as a foundational instrument in astronomy and planetary sciences, designed to separate polychromatic electromagnetic radiation into its constituent monochromatic components and measure their relative intensity. While early spectrometers relied on the principle of refraction via prisms, modern high-resolution, high-throughput applications are overwhelmingly dominated by diffraction grating systems, which offer superior linear dispersion and customizable spectral ranges (Kitchin, 2013). JIRAM and NIRSpec are two examples of spectrometers that work using diffraction gratings. The operation of a grating spectrometer is fundamentally governed by the principles of interference and diffraction, where the dispersive element is a precisely ruled or holographically recorded surface featuring a periodic array of grooves. The physical separation of wavelengths (λ) by a diffraction grating is described by the grating equation:

$$m\lambda = d(\sin\alpha + \sin\beta), \tag{4.2}$$

where d is the groove spacing (the distance between adjacent grooves), α is the angle of incidence of the light onto the grating, β is the angle of diffraction for the diffracted light, and m is the spectral order (an integer representing the order of interference). This equation illustrates that for a fixed incident angle α, different wavelengths will exit the grating at distinct diffracted angles β. The ability of the grating to angularly separate adjacent wavelengths is quantified by the angular dispersion (D_θ) defined as:

$$D_\theta = \frac{d\beta}{d\lambda} = \frac{m}{d\cos\beta} \tag{4.3}$$

This relationship highlights the crucial role of the groove density (inversely proportional to d) and the spectral order m in determining the dispersive

power of the instrument. In practical terms, the angular dispersion is converted into a measurable spectral separation on the focal plane of the detector array via the focal length (f) of the focusing optic. Most conventional, fixed-grating spectrometers utilize the robust Czerny-Turner configuration (Czerny & Turner, 1930). This design employs an entrance slit that defines the aperture and spectral image quality, a collimating mirror to render the incident light parallel before striking the grating, the diffraction grating itself, and a focusing mirror to image the dispersed light onto a focal plane array detector, such as a Charge-Coupled Device (CCD) or Complementary Metal-Oxide-Semiconductor (CMOS) sensor. The choice of the grating's blaze angle is paramount, as it dictates the wavelength range and diffraction order for which the grating efficiency is maximized. For a diffraction grating, the theoretical resolving power is directly proportional to the spectral order m and the total number of illuminated grooves. Maximizing resolution therefore requires a grating with a high groove density and a large illuminated area. Furthermore, the overall resolution of the instrument is often limited by the spatial size of the entrance slit, which imposes a trade-off between resolution and optical throughput (or etendue). Finally, it is worth to remark that usually in the IR to obtain a spectrum the physical phenomenon of interference is used (thanks to the so-called Fourier spectrometers), but it won't be a subject of this thesis work.

Finally, depending on the scientific case a spacecraft can be:

- **Orbiter Spacecraft**: These are designed to orbit a celestial body following a circular or elliptical path
- **Flyby Spacecraft**: These travel past a celestial body to observe it only for a brief period of time
- **Lander Spacecraft**: These are designed to land on the surface of a celestial body
- **Rover Spacecraft**: These are mobile landers used to explore the surface of a planet or moon
- **Crewed Spacecraft**: These are designed to carry humans into space

Focusing on the first point I will define that the orbiter can look to a planetary atmosphere in two different geometries, referring to Fig. 4.2 (Villanueva et al., 2018):

- **nadir observations**: In this configuration, the observer is at a defined altitude looking down to a specific latitude and longitude on the planet. In this configuration there is only one set of incidence (β in the figure but defined as θ_0 in the previous chapter) and emission angles (90 - α in the figure but defined as θ in the previous chapter) and those are relative to the observed point on the surface.
- **limb observations**: These are observation geometries in which the observer is located at a specific altitude in the atmosphere and is observing towards a specific tangent height (lowest altitude of the optical path) of the atmosphere. As a definition the emission angle is equal to zero in this case.

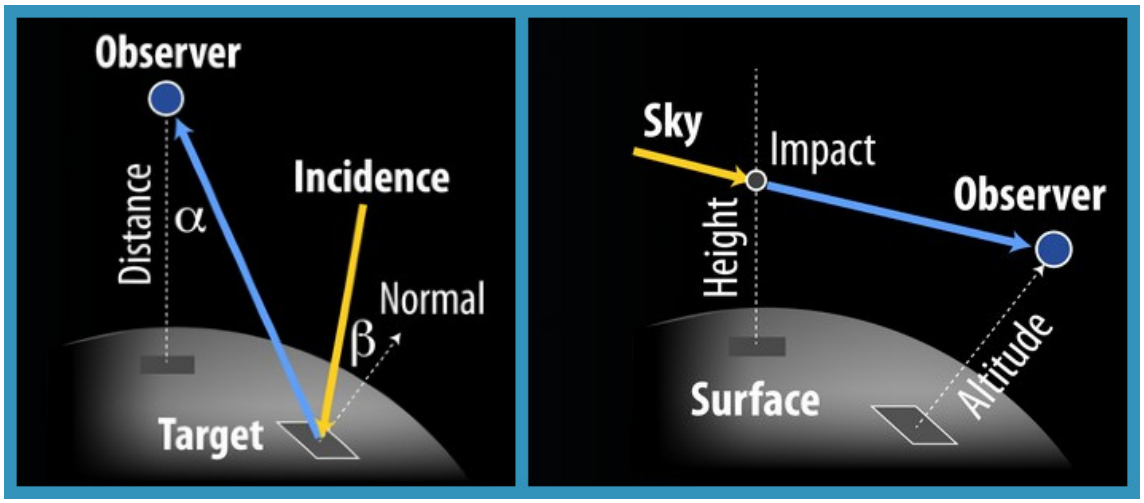


Figure 4.2: Different observations geometries of an orbiter mission.

In the previous Chapter I saw the relation that connects the emission and incidence angles to the phase angle.

On Jupiter the used coordinate system is the one defined by the System III westward-increasing longitudes and by the planetocentric latitudes. As Jupiter rotates differently at the poles than at the equator, the System III refers to any point on the Jovian disk in relation to its magnetic field, implying a rotation period of 9 hours, 55 minutes, and 29.71 seconds. On the other hand, planetocentric latitudes define the north-south position of a point on the body's surface based on the angle between the body's equatorial plane and a line drawn from the body's center to that point. In the next subsections I will focus on the imaging and spectra of the Jovian atmosphere collected by some of the space missions and space observatories in the last 50 years, see Fig. 4.3.

4.3.3 Voyager missions

The Voyager missions, see Fig. 4.4, are a pair of uncrewed American scientific probes, Voyager 1 and Voyager 2, launched by NASA in 1977 to explore the outer planets of our solar system (Kohlhase & Penzo, 1977). Their primary mission was to conduct close-up studies of Jupiter and Saturn. Voyager 2 was also designed to fly by Uranus and Neptune, making it the only spacecraft to have visited these two ice giants.
Voyager 1 executed a Jupiter flyby in 1979, significantly advancing our understanding of the Jovian system (Stone & Lane, 1979). Exploiting gravity assist maneuvers to propel them towards Saturn and beyond, both spacecrafts conducted detailed remote sensing investigations of Jupiter and its major moons. The Imaging Science Subsystem (ISS) provided unprecedented close-range images of Jupiter's atmospheric dynamics, revealing the complexity of its zonal flows and the morphology of large-scale weather phenomena, including the Great Red Spot, a persistent anticyclonic storm (Smith et al., 1979). The other instrument of interest was the Infrared Interferometer Spectrometer and Radiometer (IRIS). Thanks to a Michelson interferometry scheme (Hanel et al., 2003) IRIS achieved a spectral range from

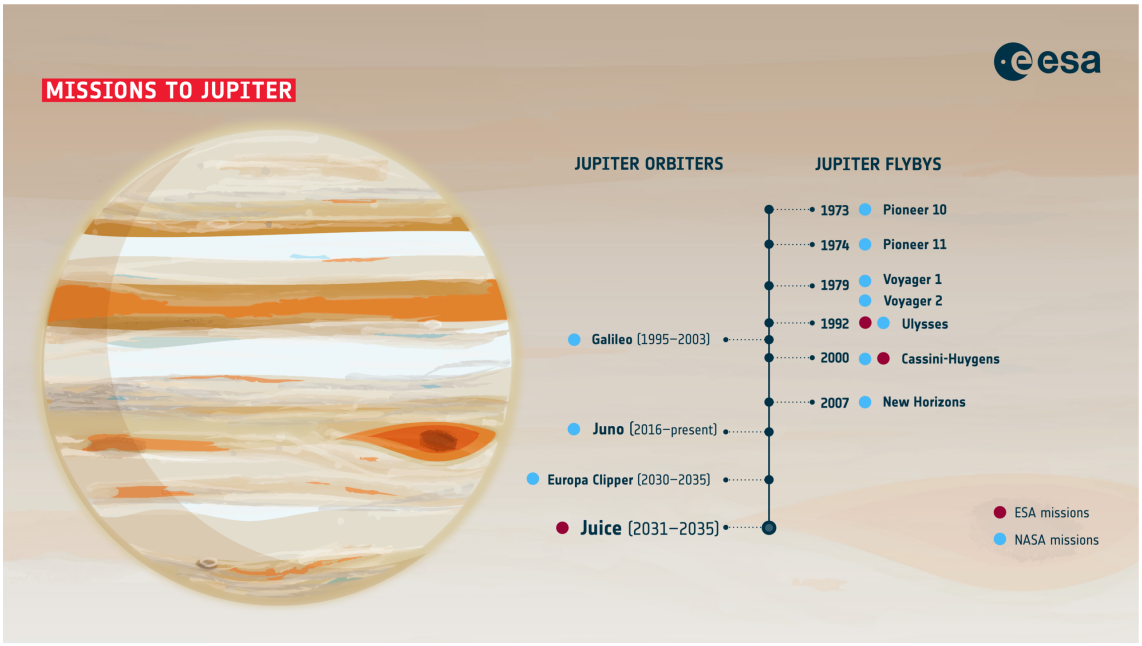


Figure 4.3: Roadmap of the hostory of Jovian system exploration.



Figure 4.4: Reproduction in a 1:1 scale of the Voyager-1 spacecraft exposed at the National Space and Air Museum at Washington DC (USA).

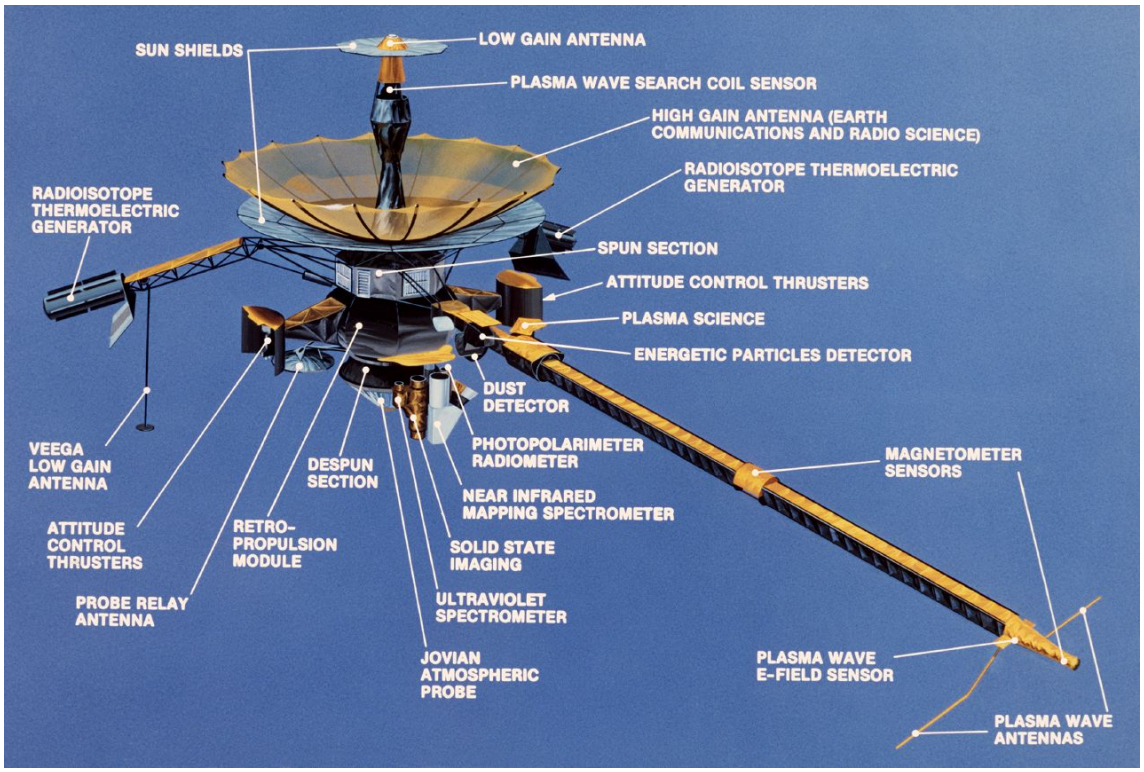


Figure 4.5: Design and instrument payload of the NASA Galileo mission.

200 to 2000 cm^{-1} with a resolution of 4.5 cm^{-1}. Thanks to IRIS it was possible to obtain accurate estimations of the concentration of minor species in the Jovian Northern Temperate Domain and the first measure of Jupiter's D/H ratio (Kunde et al., 1982). Voyager 1 notably was the first spacecraft to detect radio wave pulse-like emissions called "whistlers" (Gurnett et al., 1979). An accurate data analysis of these emissions provided the first evidence of lightning in Jupiter's atmosphere.

4.3.4 Galileo mission

The Galileo mission, Fig. 4.5, a flagship endeavor by the National Aeronautics and Space Administration (NASA), was a robotic space probe dispatched to conduct an in-depth investigation of the Jovian system (Johnson et al., 1992). Launched in October 1989 and achieving Jovian orbit in December 1995, the primary scientific objectives focused on the characterization of Jupiter's atmosphere. It was the first orbiter mission around Jupiter. A pivotal component of the mission involved the deployment of an atmospheric entry probe (Seiff & Knight, 1992), see Fig. 4.6. This descent module executed a direct plunge into Jupiter's gaseous envelope, transmitting in-situ measurements of atmospheric parameters during its terminal trajectory. The probe, equipped with a mass spectrometer and a nephelometer, was the first instrument able to precisely determine the elemental and isotopic abundances of the Jovian atmosphere, providing critical data for understanding the planet's formation and evolutionary history within the solar nebula. I will discuss the results further in the next Chapter.
The Galileo spacecraft performed 35 low-eccentricity, near-equatorial orbits of Jupiter that were used to precisely map for the first time the Jovian magnetic field. Regard-

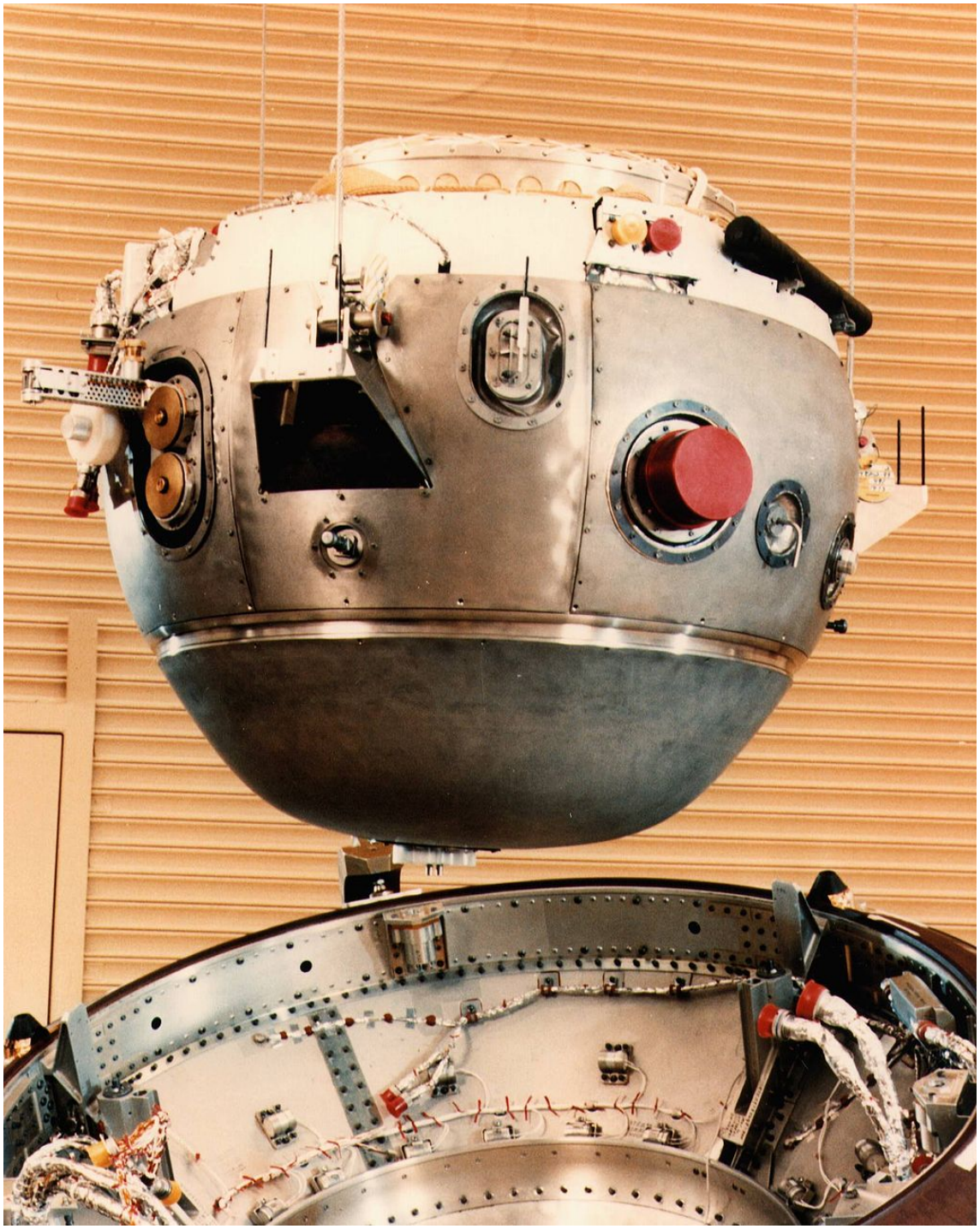


Figure 4.6: Real image of the Galileo Entry Probe prior to the launch.

ing the atmosphere, apart from the entry probe, the most important instruments were the Solid State Imager (SSI), i.e. an 800x800 pixel visible CCD camera, and NIMS spectrometer, with a spectral range between 0.7 and 5.2 micron. NIMS had a resolving power of $RP = 60$. Sadly, the Galileo mission suffered from a High Gain Antenna failure during its cruise phase. This failure limited the possibility of communicating and sending data to the science team. Consequently, the number of images was limited, and the spectra were downsampled—that is, they were transmitted to Earth with a lower resolving power. The results obtained by NIMS will be discussed in the next Chapter. The Galileo mission was the first to precisely study the Jovian atmosphere, using a probe, and the Jovian clouds, with its Solid State Imager (SSI) and Near-Infrared Mapping Spectrometer (NIMS). It also provided the first solid evidences for a subsurface on Europa (Khurana et al., 1998) and vulcanism on Io (McEwen et al., 1998).

4.3.5 Cassini and New Horizons flybys

I already introduced the Cassini spacecraft in the last section of Chapter 2. On the other hand, the New Horizons mission was a NASA space probe designed to explore the Pluto system and the Kuiper Belt (Stern, 2008). Launched in January 2006, it became the first spacecraft to conduct a close flyby of Pluto, its moons, and a Kuiper Belt object. Both Cassini and New Horizons needed to perform a close flyby of Jupiter in order to take advantage of its huge gravitational attraction and gain velocity to reach their outermost targets. Cassini performed its flyby of Jupiter on December 30 2000 (Porco et al., 2003) and arrived close to Saturn on July 1, 2004 . New Horizons did its flyby of Jupiter on February 28 2007 (Baines et al., 2007; Spencer et al., 2007) and arrived in the Pluto system July 14, 2015 (Stern et al., 2015).

Both the spacecrafts take opportunity of the flybys to test their instruments and engineering systems. However, in consideration of the Galileo antenna failure the scientists took advantage of these opportunities to capture the largest number of spectra and images possible in order to complement and improve the results obtained by NIMS. I will describe them in the next Chapter.

The most relevant instruments onboard Cassini were the Imaging Science Subsystem (ISS), the Visible and Infrared Mapping Spectrometer (VIMS), and the Composite Infrared Spectrometer (CIRS). ISS was composed of two 1024x1024 CCD cameras equipped with visible filters from 0.2 to 1.1 micron. VIMS consisted in a pair of imaging grating spectrometers designed to measure reflected and emitted radiation from atmospheres, rings, and surfaces over wavelengths from 0.35 to 5.1 microns (Brown et al., 2004). VIMS had two channels: (1) VIMS-VIS with a range of 0.35-1.05 micron and a resolution of 7.3 nm, and (2) VIS-IR with a range of 0.85-5.1 microns and a resolution of 16.6 nm. The Composite Infrared Spectrometer (CIRS) consists of dual interferometers that measure infrared emission from atmospheres, rings, and surfaces over wavelengths, to determine their composition and temperatures. The spectral resolution of CIRS was programmable, ranging from 7 to 1000 micron (1400 to 10 cm^{-1}) and to 0.5 cm^{-1} to 20 cm^{-1} (Flasar et al., 2004).

The most relevant instrument on New Horizons that performed Jupiter science was LEISA. Its name stands for Linear Etalon Imaging Spectral Array and it was one



Figure 4.7: The Hubble Space Telescope returns to orbit as an improved telescope after its second servicing mission in February 1997.

of the two main components of the Ralph instrument suite (Reuter et al., 2008), the other being the MVIC (Multispectral Visible Imaging Camera). LEISA was a short-wavelength infrared (SWIR) imaging spectrometer. It was designed to measure the spectral reflectance of surfaces (and atmospheres) in the 1.25 to 2.50 micron wavelength range with a resolving power of 300.
CIRS and LEISA were fundamental instruments that filled the gap of high spectral and spatial resolution observations between Galileo and Juno.

4.3.6 ISO and HST

The Infrared Space Observatory (ISO), a European Space Agency mission with NASA participation, was a cryogenically cooled space telescope operating in the infrared spectrum (2.5 to 240 μm) from 1995 to 1998 (Kessler et al., 1996). Its suite of four scientific instruments, including spectrometers, cameras, and a photopolarimeter, enabled detailed investigations of celestial objects through their thermal emissions and spectral signatures of molecular and atomic transitions obscured at visible wavelengths by Earth's atmosphere. In particular ISO had two spectrometers on board: (1) Short Wavelength Spectrometer (SWS) with a spectral range of 2.38-45.2 micron and a resolving power between 1000 and 2000, and (2) Long Wavelength Spectrometer (LWS) with a spectral range of 43-170 micron and a resolving power of about 200. ISO observed in the first decade of the 2010s all the solar system planets providing unprecedented high resolution full disk spectra.
The Hubble Space Telescope (HST), Fig. 4.7, a joint NASA/ESA project operational since 1990, is a multi-wavelength observatory primarily working in the ultraviolet,

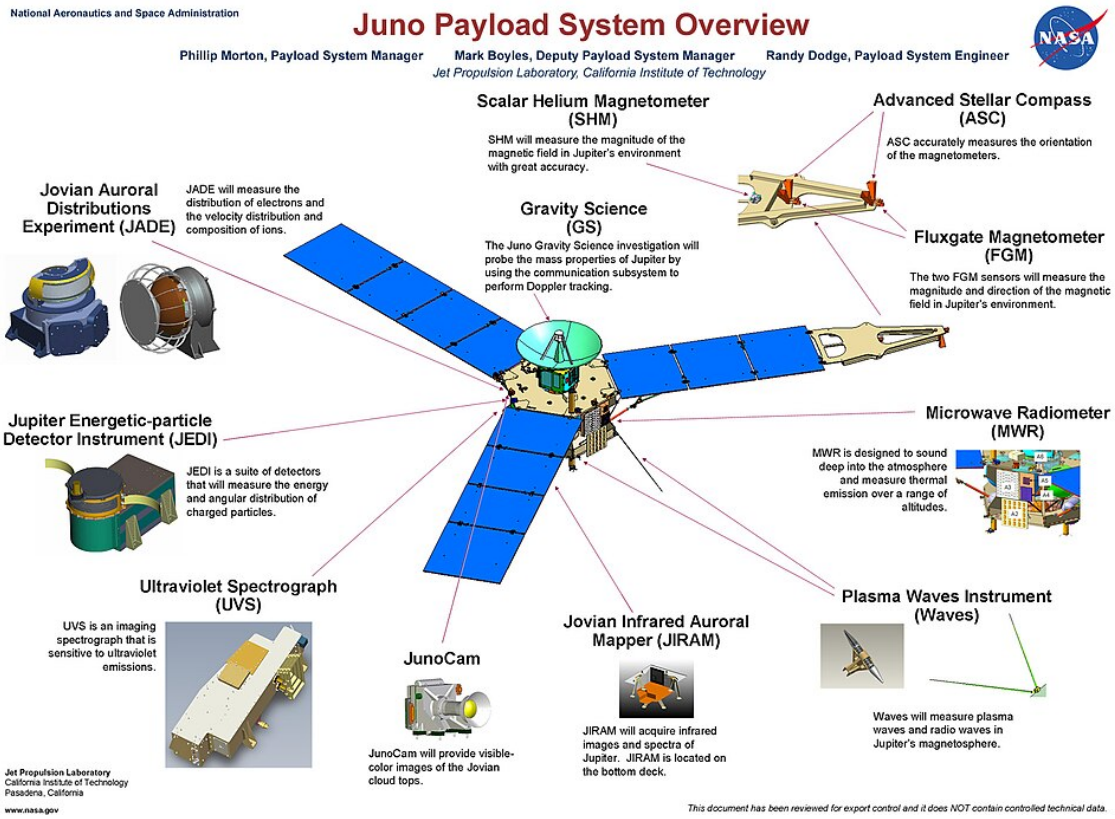


Figure 4.8: Design and instrument payload of the NASA Juno mission.

visible, and near-infrared ranges (115 nm to 2.5 μm) (Roman, 2019). In particular, the spectrometer STIS (Woodgate et al., 1998) has been the only instrument that covers the whole ultraviolet to NIR range (spectral range 0.1-1 micron) launched in space. It has a resolving power of about 10000. From the visible side of the instrumental suite, HST has had several important visible light cameras throughout its mission. The most relevant ones were the wide field cameras WF/PC and WFC3 (Sirianni et al., 2005). They were the first high resolution cameras launched to space and were equipped with a large number of filters that covered the whole UV-IR range with different passbands. The UV/VIS cameras were equipped with 2048x4096 pixels CCDs while the infrared ones with 1024x1024 pixels CMOS. This setup provided a huge FOV larger than 150x150 arcsec providing details in the resulting images of Jupiter and planetary nebulae. HST visible images were used to map the dynamics of the Jovian clouds providing precise estimates of the zonal horizontal wind patterns. STIS was frequently used to map for the first time the haze distribution and behavior for the whole disk and mostly near the polar regions.

4.3.7 The Juno mission and JIRAM

The NASA Juno mission, a component of the New Frontiers program, is the second orbiter mission dedicated to the Jupiter system (Bolton et al., 2017a,b). Launched on August 5, 2011, it arrived in the system on July 5, 2016. Notably, it was the first mission to use solar panels as a power supply while traveling past the Main Asteroid Belt.

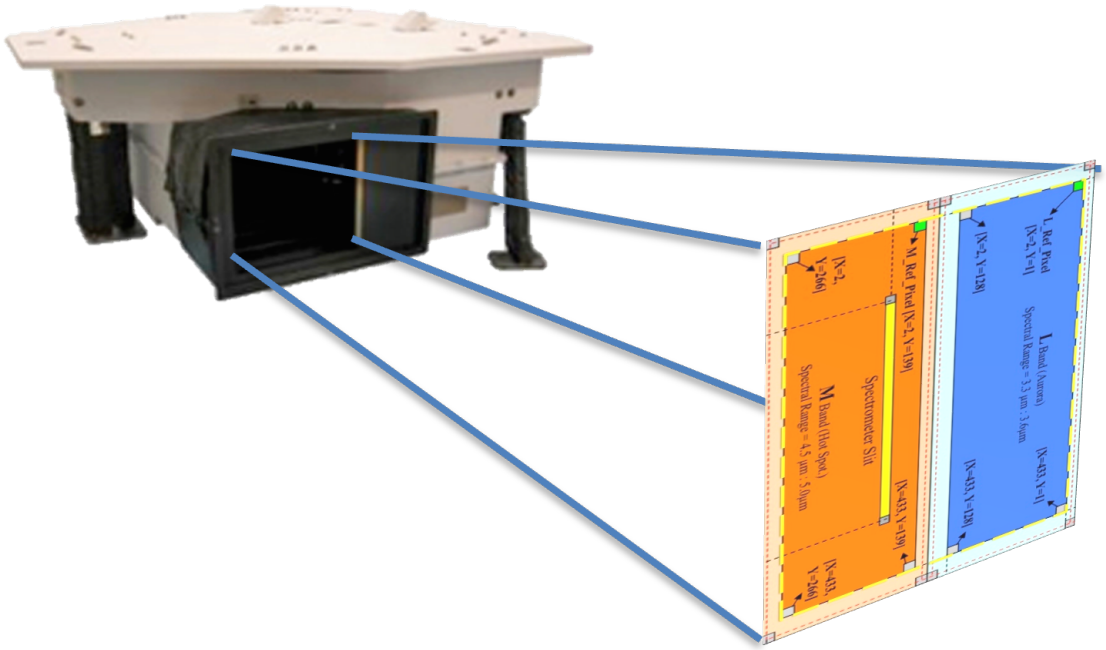


Figure 4.9: Real image of the JIRAM instrument near a sketch of its focal plane.

The most important innovation was the choice of a polar orbit with a closest approach to Jupiter (called perijove or PJ) proximal to 1.06 R_{Jup} to minimize radiation exposure. To further minimize the damage the spacecraft was designed to be rotating and spin-stabilized along one direction. Its rotation rate is approximately 2 rotations per minute (RPM). Thanks to its unique design the Juno mission was able to perform more than 70 orbits making it the third longest lived spacecraft in the outer rim of the solar system after the Voyagers. I refer to the first 35 orbits as the primary mission, the orbits from 35 to 70 to the extended mission, and the orbits after the 70th as the extended extended mission. Juno carries a suite of sophisticated in situ and remote sensing instruments, see Fig. 4.8. These include the Microwave Radiometer (MWR) (Janssen et al., 2017), the Jovian Infrared Auroral Mapper (JIRAM) for thermal mapping of the atmosphere and auroral emissions (Adriani et al., 2017), and the Magnetometer (MAG) for characterizing Jupiter's complex magnetospheric dynamics and internal dynamo (Connerney et al., 2017). Juno was the first orbiter mission of a gas giant to host a microwave radiometer. Since in the microwave domain the influence of aerosol scattering and absorption becomes less important, a radiometer can efficiently measure the brightness temperature of the atmosphere below the cloud decks. The brightness temperature (T_B) is a measure of the radiance of electromagnetic energy emanating from a source, expressed in units of temperature. Specifically, it is defined as the temperature a blackbody would need to have in order to emit the same intensity of radiation at a given frequency as the observed object. It can be directly connected to the VMR profiles of gaseous ammonia and water, see Chapter 2.
Juno was also the first mission to be equipped with a dedicated citizen science instrument, JunoCam, which was developed specifically for public outreach. It is a Push-frame imager utilizing Time-Delayed Integration (TDI) to compensate for spacecraft rotation during image acquisition (Hansen et al., 2017).

It is composed by a single simple Kodak KAI-2020 CCD imager with a resolution of 1600 x 1200 pixels equipped with four filters: red, green, blue (for true-color imaging), and a narrowband methane filter centered at approximately 889 nm for cloud height determination (Hansen et al., 2017). Furthermore, the Gravity Science experiment exploits Doppler tracking of the spacecraft's X-band and Ka-band transponders to precisely map Jupiter's gravitational field, thereby constraining models of its interior structure and the presence of a potential dilute core (Iess et al., 2018; Guillot et al., 2018; Bolton et al., 2017b).
I will now describe the JIRAM instrument that will be the focus of this thesis. JIRAM is an imaging spectrometer built and designed by the joint effort of Selex-ES (now Leonardo), ASI, and the INAF-IAPS (Adriani et al., 2017). JIRAM relies on the solid heritage derived from the Italian-made visible and near-infrared imaging spectrometers developed in the past years like VIRTIS-M aboard Rosetta (Coradini et al., 2007) and Venus Express (Piccioni et al., 2007), and VIR-MS aboard Dawn (de Sanctis et al., 2011). The optical layout is based on a modified Schmidt telescope (equivalent aperture 44mm) and thanks to a mirror system, the optical beam is divided between an imager channel and a spectrometer channel, where Hybrid Thinned HgCdTe photodiodes (CMOS) detectors are placed. The imager focal plane is divided into two equal areas defined by the superimposition of an L (centered at 3.455 μm with a 290 nm bandwidth) and an M filter (centered at 4.780 μm with a 480 nm bandwidth), see Fig. 4.9. The L-filter was designed to acquire high-resolution images of aurorae (the main goal of the instrument), as H_3^+ is expected to emit strongly at these wavelengths (Mura et al., 2018; Castagnoli et al., 2025). The spectrometer channel is able to acquire co-located imaging spectroscopy in the 2.0-5.0 μm range. The spectra are sampled in 336 points with a step of 9 nm. These characteristics have been accurately chosen to study a transition zone in Jupiter's spectra. Indeed, in all JIRAM spectra, I can observe three distinct regions:

- **a solar region**: from 2 to 3.2 μm, dominated by reflected sunlight perfect to study clouds and aerosols
- **a low-signal transition region**: from 3.2 to 4.2 μm, dominated by methane absorption in which auroral and stratospheric emission becomes dominant
- **a thermal region**: from 4.2 to 5 μm, dominated by the radiation coming from the deep troposphere

In addition to detecting auroral emissions, a primary goal of JIRAM was to characterize the Jovian atmosphere and the so-called hot spots, are regions on the disk of Jupiter where thermal radiation escapes from pressure levels (depths) larger than the average emission levels (Ortiz et al., 1998). JIRAM was able to perform a follow-up study in terms of measured radiances and of retrieval of minor species profiles (Grassi et al., 2017a). Notably, JIRAM and the Juno polar orbit enabled the discovery of a system of symmetric cyclones at both the northern and southern poles of Jupiter (Adriani et al., 2018).
As for today, the JIRAM dataset represents the more updated and complete set of spectra useful to study and model both the solar and the thermal-dominated regimes in order to clarify some of the open questions introduced in Chapter 1. The analysis of these observations are a main part of the thesis and will be described in Chapter

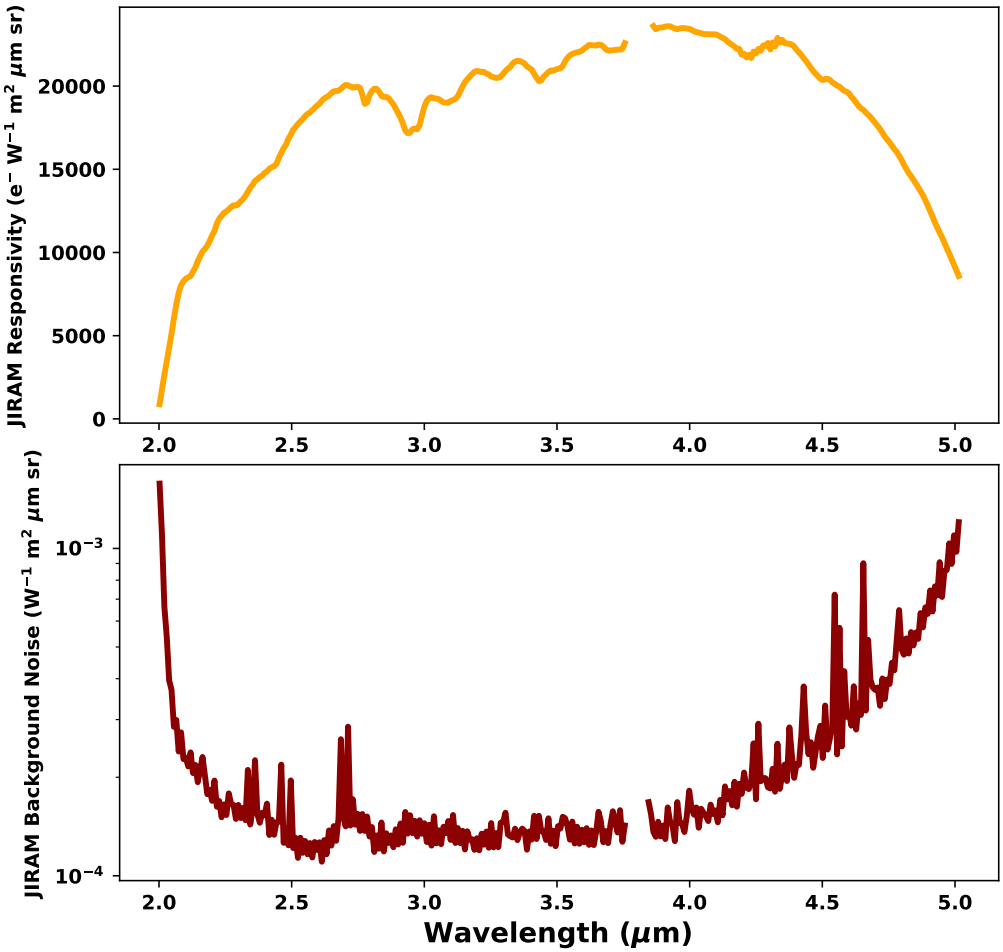


Figure 4.10: Responsivity function and thermal background noise for the JIRAM instrument as measured by Adriani et al. (2017).

6, 7, 8, and 10.

The JIRAM spectra are subject to two main source of errors: (i) photon shot noise, and (ii) thermal background b. The former arises because light is composed of photons and their arrival follows a random, statistical process, specifically Poisson statistics. The magnitude of the shot noise is proportional to the square root of the average number of detected photoelectrons in the corresponding wavelength channel. In order to compute this number, it is needed to multiply each spectrum for the so-called responsivity function, $\mathcal{R}$. It is a measure of the efficiency with which the detector converts incoming radiance into an electrical signal (and vice-versa). The background thermal noise, on the other hand, refers to the shot noise generated by the detector's own thermal environment. It represents the fundamental limit on sensitivity and can be measured once the spectrometer looks at a empty regions in the night sky. In Fig. 4.10 it is possible to observe both the JIRAM responsivity function and the JIRAM thermal background from Adriani et al. (2017). In order

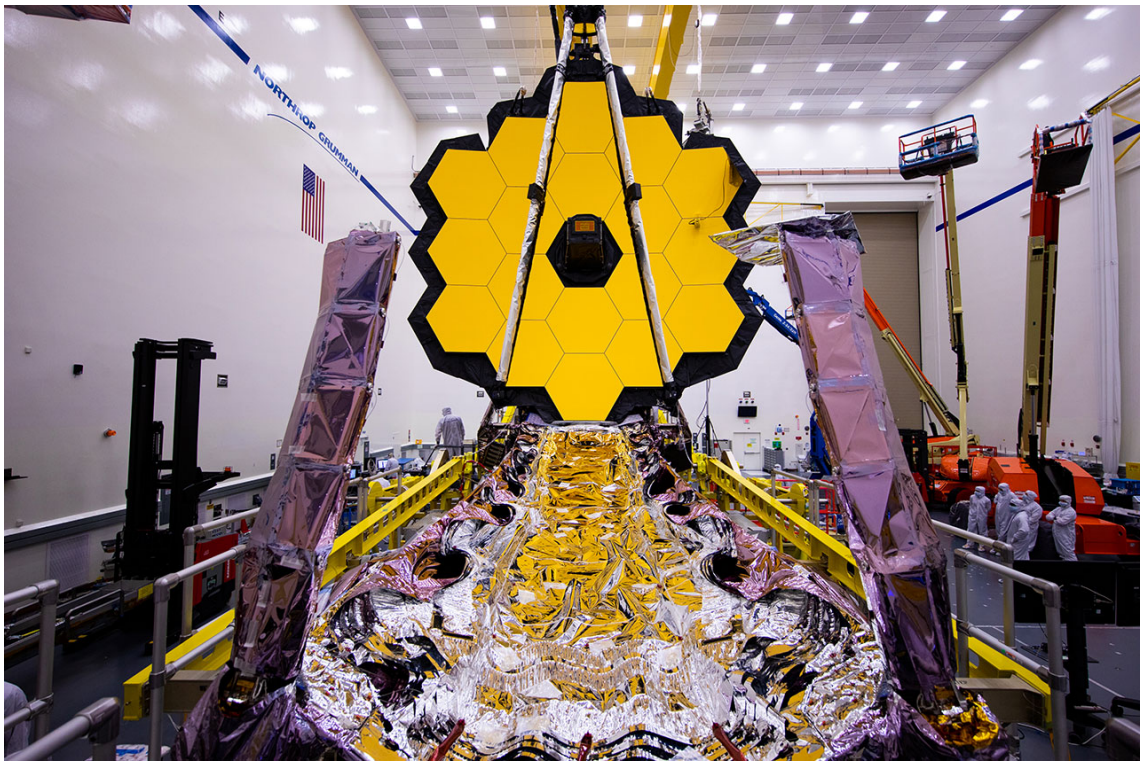


Figure 4.11: The JWST primary mirror during the test phase prior to its launch.

to obtain the final error associated to each JIRAM spectrum y_{JIRAM}, also referred to as Noise Equivalent Radiance (NER), I can use the following expression:

$$\text{NER} = \left[\left(\frac{\sqrt{\mathcal{R} \cdot y_{\text{JIRAM}}}}{\mathcal{R}} \right)^2 + b^2 \right]^{1/2} \tag{4.4}$$

Finally, even if not directly relevant to this thesis, it is worth to remark that JIRAM acquired infrared images of the lakes of lava on Io and of its paterae (Mura et al., 2024; Zambon et al., 2023) along-side the first high resolution NIR spectra of its surface (Tosi et al., 2024).

4.3.8 James Webb Space Telescope and NIRSpec

The James Webb Space Telescope (JWST) is a space-based observatory primarily designed for infrared astronomy, serving as the successor to the Hubble Space Telescope with significantly enhanced capabilities (Gardner et al., 2006). As a collaborative endeavor between NASA, the European Space Agency (ESA), and the Canadian Space Agency (CSA), JWST features a 6.5-meter diameter segmented primary mirror fabricated from beryllium and coated with gold to optimize infrared reflectivity, see Fig. 4.11. This substantial aperture, coupled with its cryogenic operating temperature of approximately 45 K, provides unprecedented sensitivity and resolution in the 0.6 to 28.5 μm range, crucial for observing faint and distant objects whose light has been redshifted into the infrared. JWST is strategically positioned in a halo orbit around the second Sun-Earth Lagrange point (L2), approximately 1.5 million kilometers from Earth, which offers a stable thermal environment and

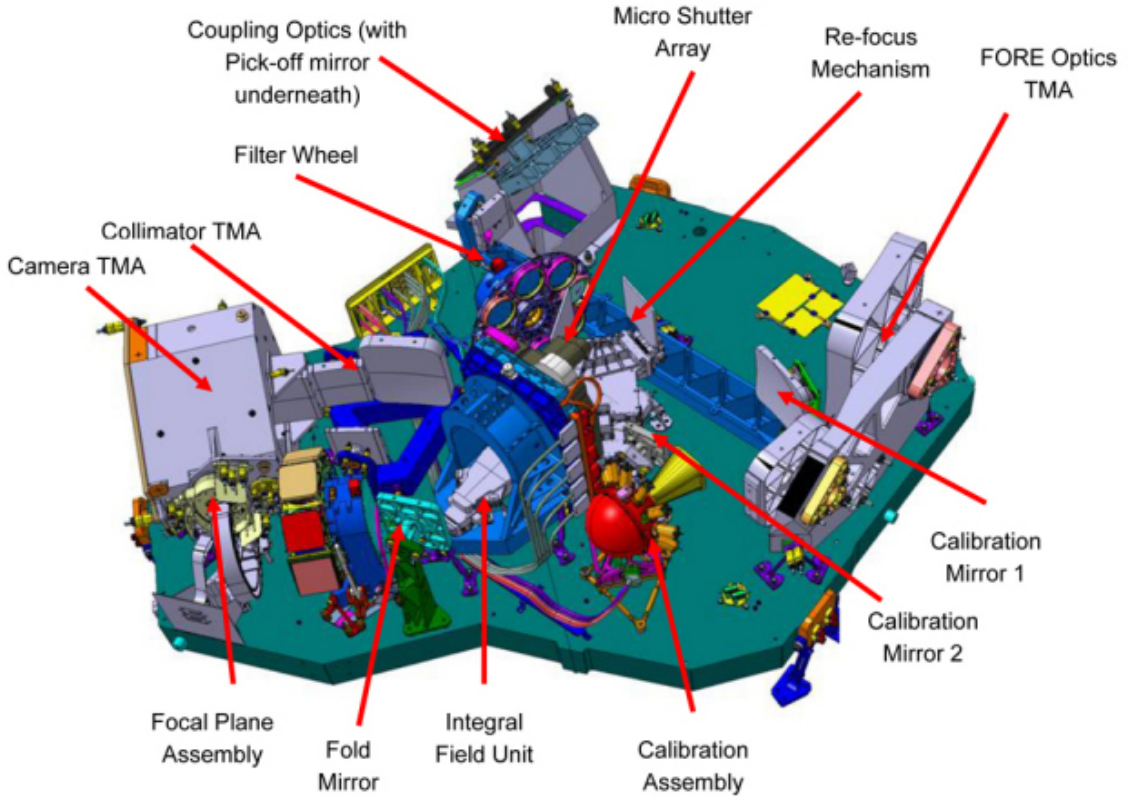


Figure 4.12: Design and optical layout of the NIRSpec instrument.

unobstructed views of the cosmos. The observatory employs a deployable five-layer sunshield,o passively cool its optics and instruments to cryogenic temperatures, essential for minimizing thermal background noise in infrared observations (Lightsey et al., 2012). The scientific payload of JWST comprises four primary instruments: the Near-Infrared Camera (NIRCam), the Near-Infrared Spectrograph (NIRSpec), the Mid-Infrared Instrument (MIRI), and the Near-Infrared Imager and Slitless Spectrograph (NIRISS). These instruments provide a suite of capabilities including high-resolution imaging, multi-object spectroscopy, integral field spectroscopy, coronagraphy for exoplanet studies, and time-series observations. In this thesis work I analyzed the data coming from NIRSpec (Jakobsen et al., 2022), see Fig. 4.12. NIRSpec was engineered by the European Space Agency (ESA) with contributions from NASA. It operates across a broad near-infrared spectrum, spanning from 0.6 to 5.3 μm. The instrument offers variable spectral resolution capabilities, selectable via its grating wheel assembly (GWA) which houses a low-resolution prism ($RP \simeq 100$), three medium-resolution gratings ($RP \simeq 1000$), and three high-resolution gratings ($RP \simeq 2700$) (Jakobsen et al., 2022). This versatility allows for both broad spectral surveys and detailed analysis of individual spectral lines. This is crucial in the context of characterizing exoplanetary atmospheres. A defining characteristic of NIRSpec is its Micro-Shutter Assembly (MSA), a innovative device containing approximately 248,000 individually addressable micro-shutters. This enables the simultaneous acquisition of spectra for up to ∼100 individual sources within a 3.4 ×3.6 arcminute field of view. The MSA significantly enhances observational efficiency for statistical studies of galaxy populations and other crowded fields. Finally,

NIRSpec also incorporates an IFU, providing spatially resolved spectroscopy over a 3×3 arcsecond field of view with a spatial sampling of 0.1×0.1 arcseconds. The NIRSpec/IFU instrument was used, together with NIRCam and MIRI, to acquire high-quality spatially-resolved spectral maps of Jupiter and of the other planets and satellites of our Solar System (Villanueva & Milam, 2023a). As part of the early-release science (ERS, PIs: de Pater & Fouchet) program 1373 (de Pater et al., 2017), six mosaic tiles were used to map the Great Red Spot (Melin et al., 2024a) and the South Polar Domain on 2022-07-27 using gratings G235H (1.66-3.17 micron range, $RP \simeq 2700$) and G395H (2.87-5.27 micron range, $RP \simeq 2700$). The analysis of these observations are a main part of the thesis and will be described in Chapter 9.

Chapter 5

What do we know about Jupiter aerosols

5.1 Nomenclature and description of the Jovian atmosphere

Jupiter's dynamic atmosphere presents a complex variety of features, the nomenclature of which is rooted in both observational morphology and inferred atmospheric dynamics, rather than a globally formalized system akin to planetary geology.
Jupiter's visible atmosphere is characterized by a remarkable system of alternating parallel bands known as "zones" and "belts." The origin of these structures are large-scale, east-west (prograde and retrograde) atmospheric wind currents, named "zonal flows" that are predominantly parallel to the planet's equator. The strength of these jet streams is latitude-dependent and strongly connected to differential rotation (Rogers, 1995). In Fig. 5.1 it is possible to observe the wind profiles (velocity against latitude) of the zonal flows inferred from JWST/NIRCam comparing two images close in time (Hueso et al., 2023). The nomenclature for these features follows a convention that labels them based on their position relative to the equator and whether they are light (zones) or dark (belts), typically moving poleward from the equator in each hemisphere.
Zones are generally brighter, wider, and typically represent regions of upwelling atmospheric gas, at least in the upper troposphere (0.7-0.1 bar). Their lighter coloration is thought to be caused by the presence of aerosols, which can condense at higher altitudes where the atmosphere is colder within the troposphere. Within zones, the dominant atmospheric motion is convective upwelling, bringing gases from deeper levels to the visible cloud tops. This convective activity can lead to the formation of bright, white, often oval-shaped anticyclonic storms. We define a cyclone as a large-scale air mass that rotates around a central area of low atmospheric pressure. As air moves toward this low-pressure center, the Coriolis effect deflects its path, causing it to rotate. An anticyclone is the opposite of a cyclone. It's a large-scale air mass that rotates around a central area of high atmospheric pressure. Air flows outward from this high-pressure center. The Coriolis effect again causes the air to rotate as it moves away. For this reason anticyclones rotate in a direction opposite to the planet's overall rotation at that latitude, while the cyclones rotate in a parallel direction.

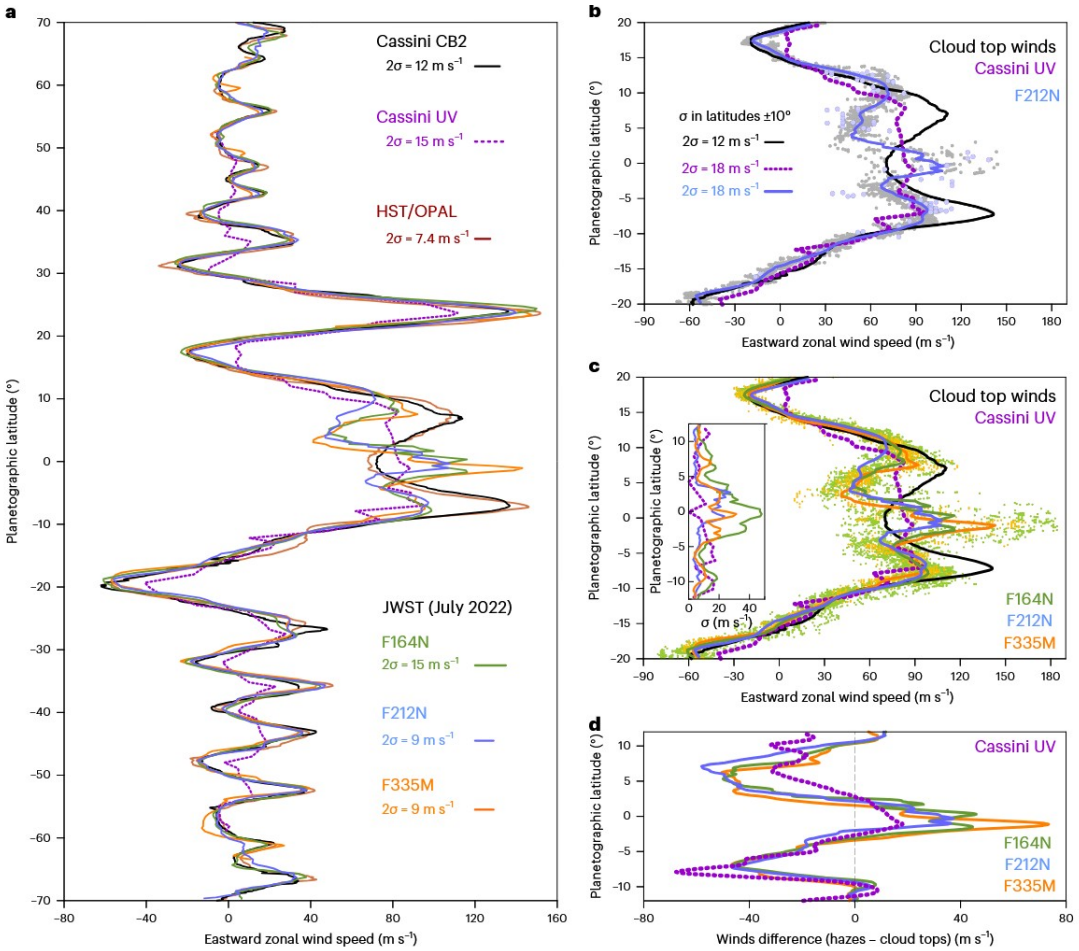


Figure 5.1: Zonal winds from JWST images are compared with zonal winds measured on Cassini UV images and on HST images (Hueso et al., 2023).

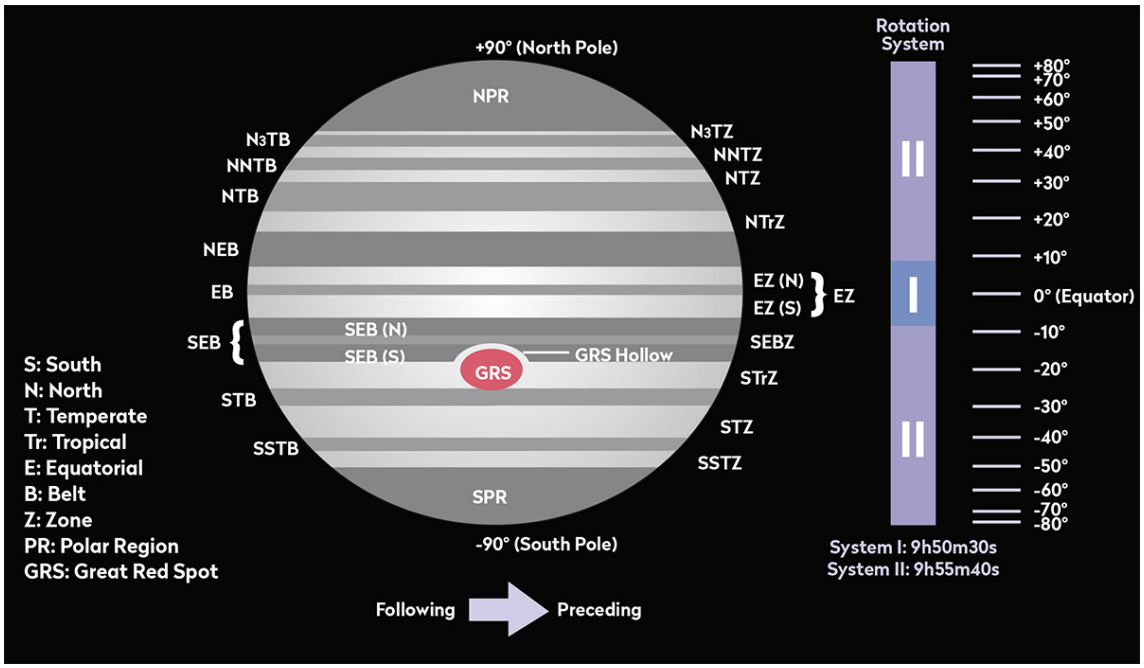


Figure 5.2: Nomenclature of the different atmospheric features on the Jovian disk.

Belts, conversely, are darker, narrower, and correspond to regions where atmospheric gas is subsiding (descending). Their darker, often reddish-brown hues are thought to be caused by the presence of complex chemical compounds. Belts are associated with lower pressure regions and exhibit cyclonic activity, including dark spots and elongated features known as "barges" that rotate in the same sense as the local planetary rotation (Sánchez-Lavega et al., 2004). From the equator poleward, and referring to Fig. 5.2, the major zones and belts in each hemisphere are:

- Equatorial Zone (EZ): A broad, usually bright zone straddling the equator, approximately from 7° S to 7° N planetocentric latitude. It is characterized by complex and often turbulent patterns of plumes, wave features, and small, bright, convective outbreaks, indicative of strong upwelling. The EZ is bordered by the prograde Equatorial Jet at its northern and southern edges (Porco et al., 2003).

- North Equatorial Belt (NEB) / South Equatorial Belt (SEB): These are typically the broadest and most prominent dark belts in each hemisphere, located directly adjacent to the EZ, generally extending from approximately 7° to 17° in each hemisphere (Fletcher et al., 2017a; Smith & Tomasko, 1984a). They are characterized by strong cyclonic shear zones and often exhibit significant outbreaks of storms, dark barges, and complex internal structures. These belts are dynamically associated with strong retrograde (westward) jet streams on their poleward edges (Gierasch et al., 1986; Simon, 1999).

- North Tropical Zone (NTrZ) / South Tropical Zone (STrZ): Bright zones situated poleward of the NEB and SEB, respectively, typically spanning latitudes from approximately 17° to 25° (Sanchez-Lavega & Quesada, 1988; Smith & Tomasko, 1984a; West, 1979). They are generally less active than the EZ but can still host smaller white ovals and turbulent features, often related to the

northward or southward extension of material from the adjacent belts. The STrZ, in particular, has historically hosted the long-lived series of vortices named "White Ovals" (Sindoni et al., 2017). They were named BC, DE, FA, and in 2020 merged into a single large vortex named Oval BA (Wong et al., 2011a, 2021a).

- North Temperate Belt (NTB) / South Temperate Belt (STB): These are the next dark belts poleward, generally from approximately 25° to 35° latitude (Hueso et al., 2017; Smith & Tomasko, 1984a). While generally narrower and less consistent in their appearance than the equatorial belts, they can still exhibit significant activity, including cyclonic storms and interactions with the white ovals within the adjacent tropical zones. The NTB is known for its sometimes dramatic outbreaks and association with powerful retrograde jets (Gierasch et al., 1986; Simon, 1999).

- North Temperate Zone (NTZ) / South Temperate Zone (STZ): Further bright zones located poleward of the temperate belts, typically approximately 35° to 45° latitude (Sanchez-Lavega & Quesada, 1988; Smith & Tomasko, 1984a). These zones are generally less active and more quiescent than their equatorial and tropical counterparts, featuring fewer large-scale convective features (Rogers et al., 2011).

- North North Temperate Belt (NNTB) / South South Temperate Belt (SSTB): Darker, often discontinuous belts at higher latitudes, ranging from approximately 45° to 55°. These belts tend to be less well-defined and more prone to dissolution or reformation, reflecting the complex and less robust zonal flows at these higher latitudes. The SSTB, for instance, often presents bright anticyclonic storms.

- North North Temperate Zone (NNTZ) / South South Temperate Zone (SSTZ): Corresponding bright zones, extending from approximately 55° to 65° latitude. These regions are generally characterized by a finer, more mottled appearance compared to the lower latitude zones, indicating weaker global convective activity.

- Polar Regions (NPR / SPR): Beyond approximately 65° latitude, the atmosphere becomes increasingly turbulent and less clearly banded towards the poles. These regions are characterized by a chaotic mosaic of smaller, often circular or oval-shaped vortices (both cyclonic and anticyclonic), and less distinct cloud features, reflecting the complex dynamics where zonal flows break down and smaller-scale convection dominates (Orton et al., 2017; Rogers et al., 2022b).

Juno MWR measurements demonstrated that both zones and belts extend deep into the planet's interior (down to 500 km, well down below the expected water condensation level) (Bolton et al., 2021). Moreover, analysis of Juno's gravity data has revealed that Jupiter's zonal flows extend thousands of kilometers deep into its molecular hydrogen envelope, reaching depths of approximately 3,000 km, or about 5 % of Jupiter's radius, and potentially as deep as 11,000 km for some equatorial

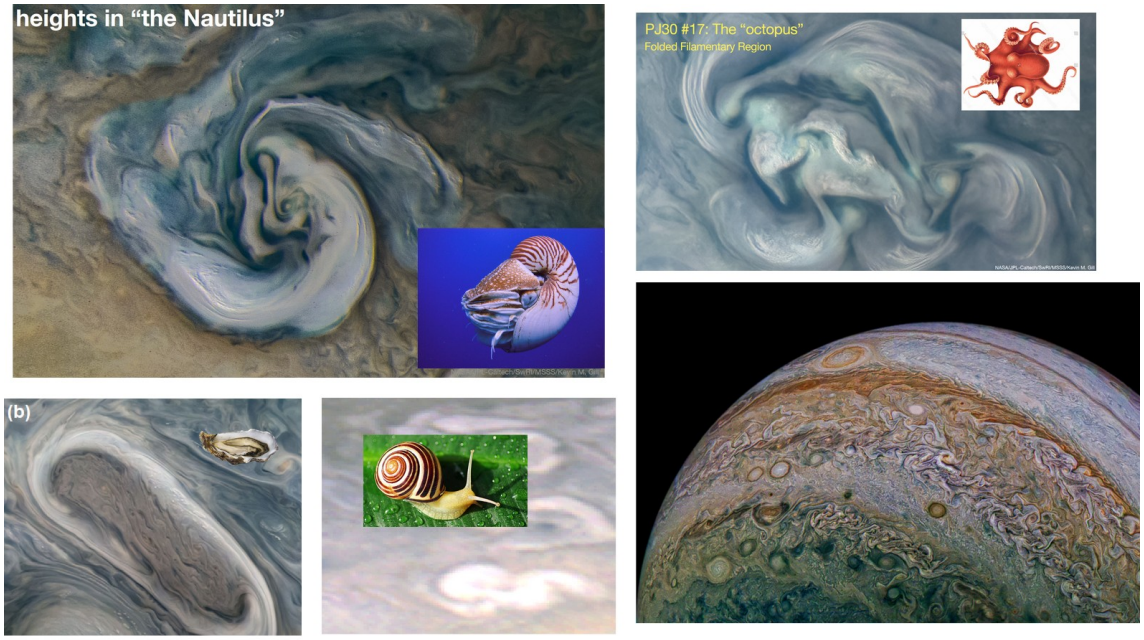


Figure 5.3: Visible images acquired by JunoCam that contain various examples of Folded Filamentary Regions in the Northen and Southern Temperate Domains.



Figure 5.4: Enhanced-color image of Jupiter’s Great Red Spot was created by citizen scientist Jason Major using data from the JunoCam imager on NASA’s Juno spacecraft.



Figure 5.5: Color enhanced JunoCam image of Jupiter's Great Red Spot and its surroundings in 2019. The image was processed by citizen scientist Kevin M. Gill.

flows (Kaspi et al., 2018). This depth is significantly greater than what was previously believed and implies that a substantial portion of the planet's interior is involved in these flows.The magnitude and latitudinal structure of these deep flows are inferred by fitting models of interior flow and density distribution to the observed gravity harmonics (Kaspi et al., 2018; Galanti & Kaspi, 2021). Ultimately, these deep-reaching zonal flows are thought to be powered by internal heat escaping from the core that drives vigorous thermal convection deep within Jupiter's fluid interior, including the metallic hydrogen layer. Theoretical models and simulations suggest that the interplay between this deep convection and Jupiter's rapid rotation (generating powerful Coriolis forces) organizes the turbulent fluid motions into these persistent, large-scale zonal jets (Christensen, 2002; Heimpel et al., 2005).
The regions between 40° and 90° and -40° and -90° are called respectively the Northern and Southern Temperate Domains. Apart from the presence of alternating zones and belts these regions are characterized by the presence of a high number of chaotic-appearing, highly-turbulent, white storm and vortex features recently named Folded Filamentary Regions (FFR) (Fletcher et al., 2022). They have been studied accurately since 2016, thanks to the good coverage provided by Juno's unique orbit. They are short lived, with lifetimes ranging from days to weeks. Because of their highly turbulent nature they can assume different forms as shown in Fig. 5.3. Some of them have been named as animals even if an IAU-approved standardized gazetteer for every atmospheric transient does not exist due to their ephemeral nature. FFRs will be the focus of Chapter 7.
Finally, approximately 22° south of its equator, Jupiter atmosphere is characterized by a colossal, persistent anticyclonic storm system named the Great Red Spot (GRS) (Sánchez-Lavega et al., 2024a), see Fig. 5.4. It is the largest known vortex in the Solar System, currently measuring roughly 16,350 km in width, although its size has significantly decreased from its peak of approximately 39,000 km in the late 19th century (Simon & Wong, 2024; Sánchez-Lavega et al., 2024a). This immense high-pressure system exhibits winds reaching speeds of up to 432 km/h at its periphery and rotates counterclockwise with a period of about 4.5 Earth days. While observations of a prominent spot on Jupiter date back to the 17th century,

notably by Robert Hooke in 1664 and Gian Domenico Cassini in 1665 (who termed it the "Permanent Spot"), recent rigorous analysis of historical data suggests that the GRS observed today is highly unlikely to be the same feature as Cassini's "Permanent Spot," which likely dissipated between the mid-18th and 19th centuries (Sánchez-Lavega et al., 2024a). The current GRS was first consistently observed in 1831, leading to an estimated minimum age of over 190 years (Sánchez-Lavega et al., 2024a). The exact origin of the GRS is still under investigation. However, recent numerical simulations do not support the hypothesis that it formed from the merging of smaller vortices or the eruption of a single, massive superstorm (Sánchez-Lavega et al., 2024a). Instead, leading hypotheses propose that the GRS most likely originated from an instability within Jupiter's intense zonal jet streams, which flow parallel to the equator and alternate direction with latitude (Sánchez-Lavega et al., 2024a). The significant north-south wind shear generated by these opposing jets—an eastward jet to its south and a stronger westward jet to its north—is considered a fundamental ingredient enabling the vortex's formation and sustained existence (Wong et al., 2021a). The absence of a solid planetary surface prevents friction that would typically dissipate such storms on Earth, contributing to the GRS's remarkable longevity (Parisi et al., 2021a). Various works have been conducted regarding the stability of the GRS, such as (Ingersoll, 1990). The general solution, coupled with gravity data, is that the GRS is a huge cylinder-like anticyclone that extends down to 100 bar (Parisi et al., 2021a). Most of these models however, considered the problem from a 2-dimensional perspective. When more sophisticated 3-dimensional models are adopted, such as in the work of Zhang & Marcus (2024), it is shown that to maintain its stability during centuries the GRS cannot possess a cylinder static shape, see Fig. 5.6. Instead, it should have a spinning-top or diamond shape extending up to more than 100 bar, see Fig. 5.7. I will come back on this in Chapter 9.

The GRS lies in between the SEB and the STB. Recent observations from HST showed that the GRS acts like a "stress ball" between these two jet streams, exhibiting oscillations in its westward drift, shape, and size within a 90-day period (Simon et al., 2024). Therefore, the GRS interacts with both the SEB and the STB. The GRS can either slightly deviate the zonal flows or block them. As a consequence, the west regions surrounding the GRS are known to be extremely dynamic, active, and turbulent. JunoCam images showed the presence of ripples, streams, vortices, and wakes, see Fig. 5.5. All of these phenomena are known to occur when a solid body, in our case the GRS, encounters a moving fluid, the SEB and STB. As demonstrated by Baines et al. (2002), the turbulent "wake" west of the GRS is a dynamic area marked by intense convective supercells and strong horizontal humidity contrasts. Their spectroscopic identification of fresh ammonia ice clouds (Spectrally Identifiable Ammonia Clouds, or SIACs) in these localized areas, particularly northwest of the GRS, provided direct evidence of active, deep convection and significant vertical uplift of material from below the main cloud decks. I will come back on this in the following sections. This finding highlights that the turbulence in these regions is not merely a superficial phenomenon but involves significant vertical transport of atmospheric constituents. Further insights into the dynamical environment of Jupiter's atmosphere, especially regarding the interaction of large-scale vortices with zonal flows, are provided in studies such as those by Vasavada et al. (1998).

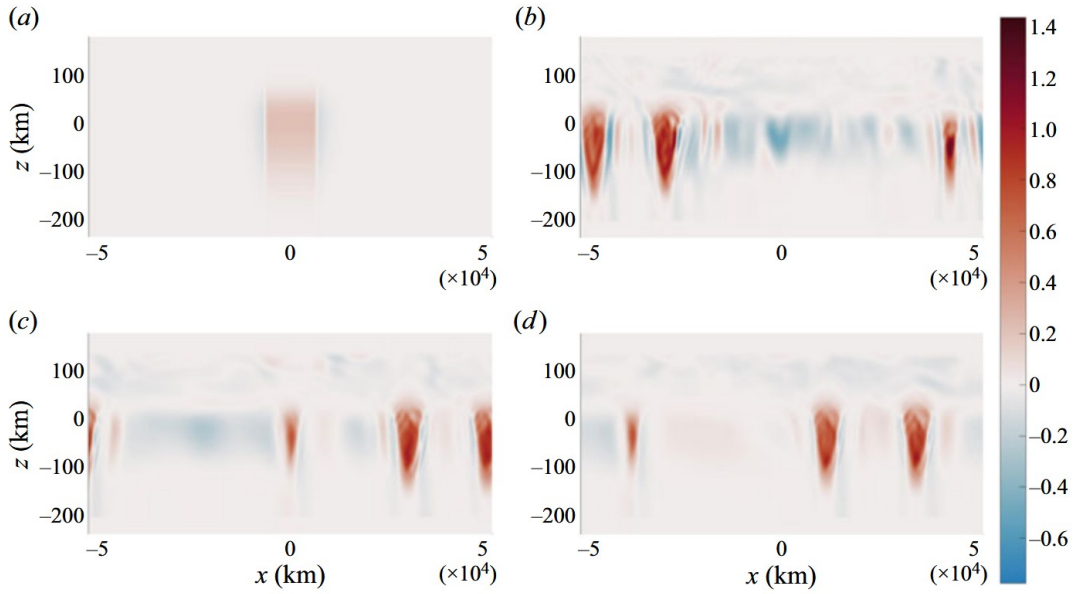


Figure 5.6: Time evolution of the GRS in the cyinder hypothesis. The letters represent various stages of the Zhang & Marcus (2024) simualtions: (a) t =0 days, (b) t =40 days, (c) t =80 days, (d) t =120 days. The colorbar represents the vertical vorticity divided for the Coriolis vector. The vorticity is a fundamental concept in fluid dynamics that measures the local rotation or "spin" of a fluid element at a specific point. From a mathematical point of view it is the curl of the velocity field vector.

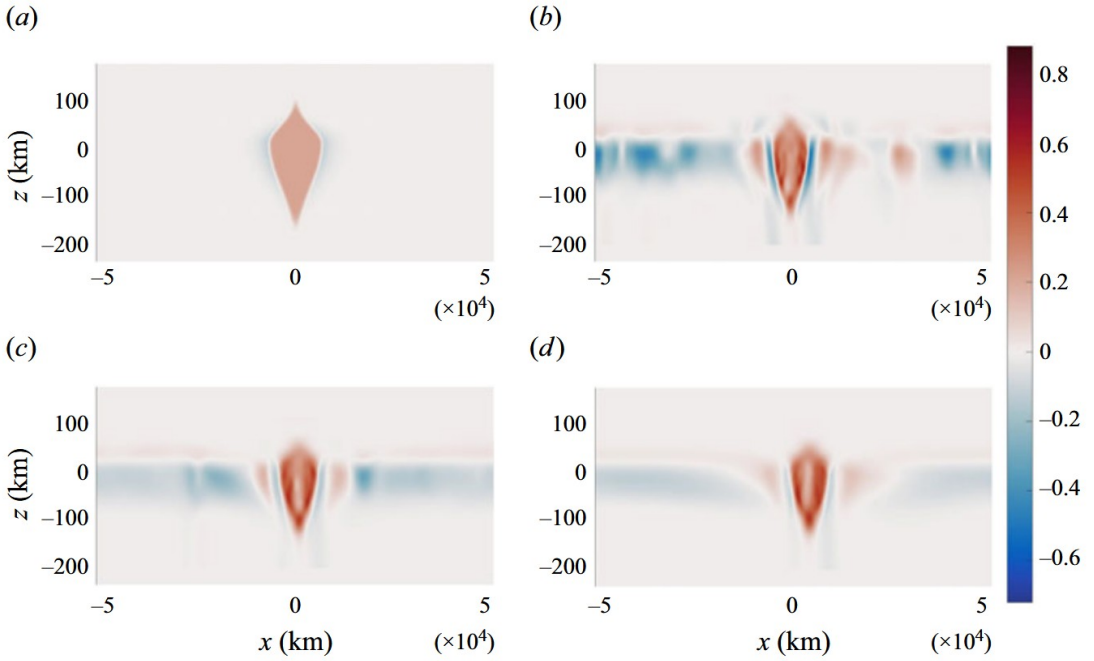


Figure 5.7: Time evolution of the GRS in the "spinning-top" hypothesis. The letters represent various stages of the Zhang & Marcus (2024) simualtions: (a) t =0 days, (b) t =40 days, (c) t =80 days, (d) t =120 days. The colorbar is the same of Fig. 5.6.

The immense size and persistence of the GRS mean it profoundly deforms the powerful eastward and westward jet streams that confine it. This interaction generates significant velocity shear, particularly where the westward jet to the GRS's north is deflected, leading to the formation of smaller-scale eddies and a cascade of energy from the large-scale vortex to smaller, more chaotic motions. These turbulent processes, named "ripples", are crucial for the transport of heat and momentum across different latitudes and depths within Jupiter's atmosphere, contributing to the planet's overall circulation and long-lived weather patterns. The continuously evolving morphology of these turbulent regions provides ongoing opportunities for understanding energy dissipation and atmospheric mixing on gas giants.

5.2 The Galileo Entry Probe

The Galileo entry probe represented a notable achievement in planetary atmospheric science, providing the first and, to date, only direct in situ measurements of Jupiter's deep atmosphere during its 58-minute descent on December 7, 1995 (Seiff et al., 1996). The entry point on the Jovian atmosphere was 6.5 degrees north latitude and 4.4 degrees west longitude, in the NEB. Its instrument suite delivered unprecedented data on the pressure-temperature profile, atmospheric composition, and aerosol distribution, challenging previous models of Jovian meteorology and formation. The Atmospheric Structure Instrument (ASI) precisely characterized the pressure-temperature profile of Jupiter's troposphere and lower stratosphere. Comprising highly accurate accelerometers, redundant temperature sensors, and pressure transducers, the ASI measured deceleration from the initial atmospheric entry point ($\sim$0.41 bar) down to approximately 24 bars, where communications ceased (Seiff et al., 1996). From these measurements, pressure was rigorously derived, and temperature was directly sensed. The data revealed a temperature increase from 143 $\pm$ 0.5 K at 0.41 bar to 427 $\pm$ 0.5 K at 23.3 bars, closely following a dry adiabatic lapse rate (1.91 $\pm$ 0.01 K/km) down to approximately 10 bars (Seiff et al., 1996). This adiabatic gradient suggested vigorous vertical mixing in the sampled region. Crucially, the ASI confirmed the presence of a "hot exosphere" at microbar levels, with temperatures exceeding 1000 K, consistent with inferences from prior remote sensing in the infrared (see Chapter 4). The Galileo pT profile has been fundamental to perform accurate atmospheric retrievals of the tropospheric properties of gas and aerosols on the basis of the data acquired by spectrometers. The Neutral Mass Spectrometer (NMS) provided definitive measurements of the hydrogen-helium-methane mixing ratios and other noble gases down to a pressure of 20 bars. The NMS, designed to quantify the molecular and atomic species by their mass-to-charge ratio, delivered a helium-to-hydrogen mole fraction of 0.156 $\pm$ 0.006, equating to a helium mass fraction of 0.238 $\pm$ 0.005 (Niemann et al., 1996). This value is notably close to the primordial, protosolar abundance, providing a key constraint for models of Jupiter's formation and internal structure, indicating efficient gravitational settling of helium has not occurred to the degree previously theorized (Niemann et al., 1996). More recent models converged to an intermediate solution, in which helium can settle substantially once it separates from hydrogen in the planet's deep interior, condensing into liquid droplets that fall toward the core (Chang et al., 2024; Markham & Guillot, 2024). Furthermore, the NMS revealed suprasolar abun-

dances of carbon (as methane, 2.9 ± 0.1 times solar), nitrogen (as ammonia, 2.9 ± 0.1 times solar), and sulfur (as hydrogen sulfide, greater than solar, indicating a substantial reservoir) (Niemann et al., 1996; Atreya et al., 2003). Moreover, also heavy noble gases like argon (2.5 ± 0.5 times solar), krypton (2.1 ± 0.5 times solar), and especially xenon (2.3 ± 0.7 times solar) were found enriched, while neon was significantly depleted (by a factor of $\simeq$ 10) and oxygen (as water) was surprisingly sub-solar, particularly below 4 bars (Niemann et al., 1996). These disparate enrichment and depletion patterns challenged simple formation models, suggesting a complex accretion history involving icy planetesimals formed at varying temperatures within the protoplanetary disk and the occurrence of complex, post-formation, depletion phenomena (Helled, 2023; Nettelmann et al., 2024; Howard et al., 2024).

5.3 Jovian spectrum across the whole wavelength range

In Fig. 5.8 it is possible to observe a Jovian spectrum from (Fletcher et al., 2023). The spectrum covers the 100 nm-0.1 cm range and it was composed using the data from different instruments, most of them being described in the previous chapter. All these instruments observed Jupiter at the quadrature in its entirety angular extension, providing so-called full-disk spectra. From 0.1 to 3.5 μm it is possible to observe that the Jovian spectrum essentially resembles the shape and intensity of the sunlight black body described in Section 3, induced by aerosol reflection, and re-scaled at 5.2 AU. In Fig. 5.9 it is possible to observe the transmittance of various chemical species in the 2-5 μm range. Comparing Fig. 5.8 with the HITRAN2020 linelists (Gordon et al., 2022) and Fig. 5.8 it is possible to observe various absorption features and bands mostly caused by:

- methane at [0.543, 0.619, 0.669, 0.725, 0.732, 0.790, 0.840, 0.862, 0.886 0.988, 1.1, 1.3, 1.4, 1.57, 1.67, 1.7, 2.1, 2.3, 2.7-2.8, 3.3-3.4,4.5-5, 7.5-8, 100-200] μm
- ammonia at [0.2, 0.552, 0.648, 0.758, 0.79, 1.0, 1.5, 1.99-2.0, 2.2, 2.9-3.1, 3.3-3.4, 4.7-5.3, 9-12, 50-60] μm
- phosphine around 200 nm and between 4 and 4.6 μm
- hydrocarbons such as acetylene or ethane below 200 nm and between 7 and 15 μm
- H3+ exotic features at [3.332, 3.408, 3.477, 3.533, 3.535] μm

At wavelengths between 200 and 600 nm the observed signal is slightly larger than the one expected by aerosol reflection only. This is caused by the contribution of hydrogen and helium molecules Rayleigh Scattering (Dalgarno & Williams, 1962). Studying the absorption features listed above with the aid of radiative transfer models it was possible to obtain estimates of the gas mixing ratios profiles presented in Section 2. The H_3^+ features are particularly interesting as they are produced in the ionosphere and upper stratosphere because of energetic particles that in turn also generate the UV and visible aurorae (Castagnoli et al., 2025).

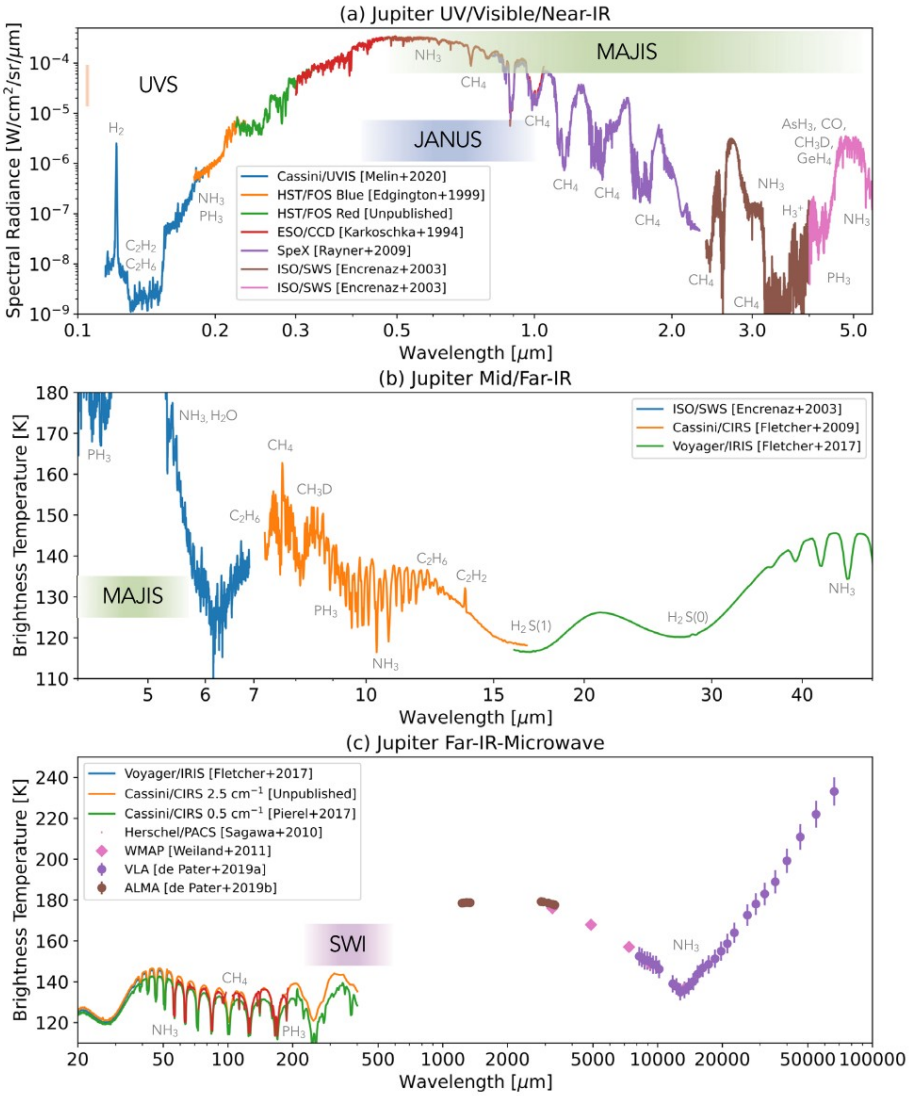


Figure 5.8: Overview of Jupiter's reflected and thermal emission spectra, with key molecular features labelled, and the approximate ranges covered by the instruments UVS, JANUS, MAJIS and SWI onboard of ESA/JUICE mission (Fletcher et al., 2023). The source of the data can be found in the legend and in the work of Fletcher et al. (2023).

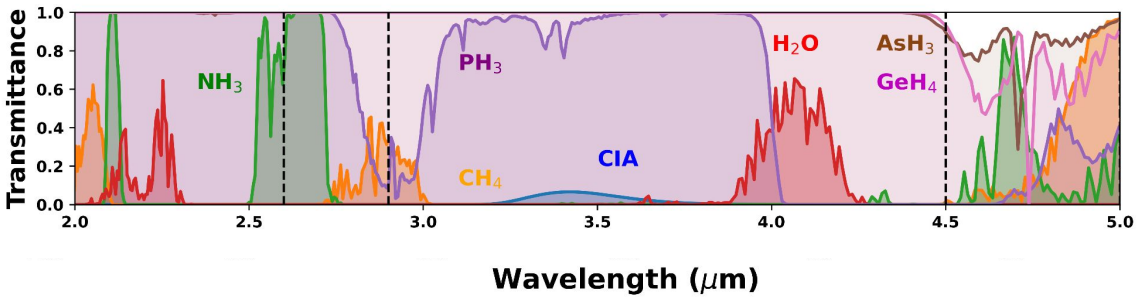


Figure 5.9: Transmittance spectra obtained with PSG between 2 and 5 μm of the gaseous species that composes the Jovian troposphere. The VMR profiles used to obtain these spectra will be defined in Chapter 6.

Particularly interesting are the [1.1-1.3], [1.5-1.62], and [2.6-2.8] μm wavelength windows, also called reflectance windows. Referring to Fig. 5.9, these windows are characterized by weak gaseous absorption, making the reflectance contribution from clouds and hazes more relevant. I will come back on this in the next section.
Describing the infrared part of the spectrum, i.e. the one at wavelengths larger than 3 micron, is far more complicated. Theoretically, in Chapter 2 we saw that a planetary atmosphere spectrum should also resemble a black body at the equilibrium temperature. For Jupiter $T_{\text{eq}} = 125K$ and Wien law tells us that its corresponding black body spectrum should peak around 24 microns. However, from Fig. 5.8 it is not possible to observe any black-body-like shape around 24 micron and neither at lower wavelengths. Why is this happening ? As we saw, Jupiter pT profile is not an isobar, but it resembles a dry adiabat that increases with decreasing altitude. Therefore, after 3 micron we observe signals only in the so-called atmospheric windows, i.e. the regions that are characterized by weak gaseous absorption by methane and ammonia, similarly to the aforementioned reflectance windows. In the atmospheric windows we observe signals that are proportional to the black bodies radiances computed at the temperature corresponding to the pressure level that is being probed. This pressure is computed by considering the gaseous opacities and finding the value at which their resulting optical depth equals one. It is possible to observe this visually in Fig. 5.10, where the unity optical depth pressure levels are shown (Sromovsky & Fry, 2018). In this context can be useful to introduce the concept of contribution function, $W(p)$ defined as:

$$W(p) = \frac{\mathcal{T}_\nu(p)}{d(\ln p)} \tag{5.1}$$

The shape of the contribution function depends strongly on the distribution and

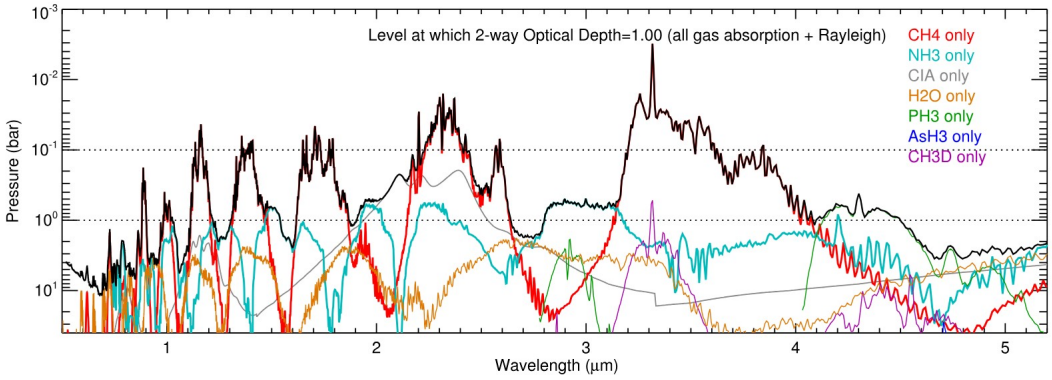


Figure 5.10: Pressure levels at which a value of 1 in optical depth is obtained in the Jovian tropsphere from Sromovsky & Fry (2018). Only the absorption from gaseous species was considered to obtain this plot.

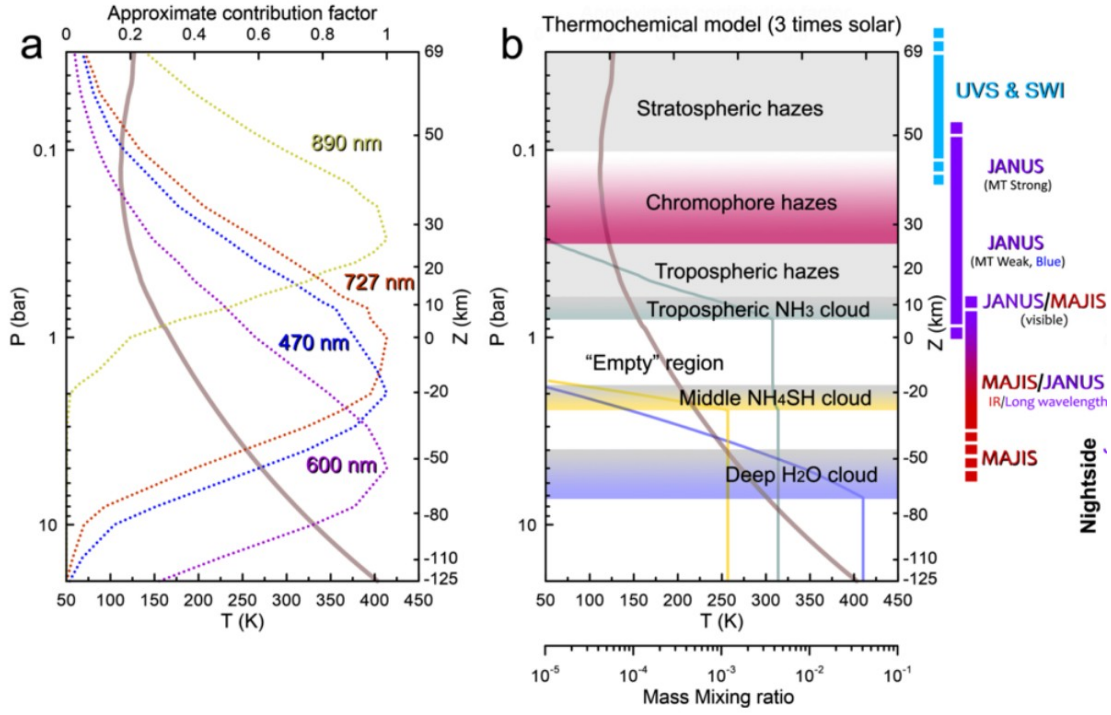


Figure 5.11: (a) Example of cloud-free contribution functions for single wavelengths from Dahl et al. (2021). (b) As a comparison, the nominal cloud structure in Jupiter from Fletcher et al. (2023).

opacity of the absorbing species. For gases usually $W(p)$ is spread in altitude, while for compact cloud decks it can be approximated with a δ-Dirac function. Because of its definition, $W(p)$ is a normalized probability distribution. Its peak indicates the atmospheric pressure level from which the majority of the radiation is emitted. It is possible to observe the optical contribution functions in the left panel of Fig. 5.11. Going back to atmospheric windows, we can identify different regions of the Jovian spectrum:

- between 4.5 and 5.5 micron (Grassi et al., 2020). Here we are probing down to the 3-4 bar level, corresponding to temperatures of 240-260 K. Because of its peculiar characteristic, this is the most used window to infer the properties of the troposphere as a whole and the structure of the clouds. Here it is possible to observe also a large number of absorption features of minor species such as water, phosphine, deuterated methane, arsine, and germane (Gordon et al., 2022). This window was crucial to study the VMR profile of minor species by means of radiative transfer models.

- between 6.5 and 15 micron (Harkett et al., 2024) and between 30 and 200 micron. Here we are probing down to the 0.5-1 bar level, corresponding to temperatures of $\simeq$ 150 K. Contrary to the 5 μm window, this window is mostly used to infer the properties of the upper troposphere and of the stratosphere. In fact, a large number of hydrocarbons are expected to show absorption features in this range and were captured by JWST MIRI (Harkett et al., 2024; Rodríguez-Ovalle et al., 2025). Because in the stratosphere the temperature gradient becomes positive (i.e. there is an inversion) these hydrocarbon lines will appear in emission rather than in absorption (Hanel et al., 2003). Further absorption features of ammonia and methane are also present in these windows.

- between 500 and 10^4 micron; here we probe very deep into the atmosphere, much deeper than the visible or even the mid-infrared. This is because, in the sub-millimiter region of the electromagnetic spectrum, the opacity of the main atmospheric constituents and even clouds becomes significantly lower. This allows radiation to escape from hundreds of bars deep in the atmosphere. This explains the black-body-like spectrum and the very large detected signal.

Particularly interesting is the region between 15 and 30 micron. Here the spectrum is particularly smooth and characterized by a Gaussian-like-bell shape. This is caused by molecular hydrogen CIA. As explained in the previous chapters, H_2 lacks a permanent dipole moment, therefore its transitions levels are induced mainly by collisional rotovibrations, see Chapter 3. The "valleys" of the aforementioned Gaussian-bell-like curve are in fact the absorption features induced by rotation, and they are named S(0) and S(1). S(0) means that the molecule is passing from J=0 to J=2, while S(1) means that it is passing from J=1 to J=3. S(0) transitions therefore are allowed only if the nuclear spins are anti-parallel (molecular state named para-H2), while S(1) if they are parallel (molecular state named ortho-H2) (Irwin, 2009). Radiative transitions between ortho and para states are highly forbidden. This means that at low temperatures, ortho-H_2 can persist for very long times, as its conversion to the lower-energy para-H_2 state is very slow unless catalyzed by collisions (e.g., on dust

grains or with H atoms) or via proton exchange reactions. The ratio of ortho-to para-hydrogen is a sensitive diagnostic of the temperature and history of the gas. That is why the 15-30 micron region of the spectrum was one of the first one studied to probe both the composition and temperature of the atmosphere (Lellouch et al., 2001). Finally, it is important to note that both NIRSpec and JIRAM observations were designed to maximize the scientific return of the data. Both instruments extensively cover the 5 μm atmospheric window and the [2.6-2.8] μm reflectance window. This capability allows them to efficiently probe the troposphere from 4 bar up to the tropopause.

5.4 Effects of aerosols on the spectrum

The presence of atmospheric aerosol has a threefold impact on the Jovian spectrum:

- they induce, enhance, and spectrally modify the reflectance peaks
- they weakens, block, and spectrally modify the radiance in the atmospheric windows thermally-emitted by deeper layers
- they can produce further absorption features

The signal observed in the reflectance windows would be zero if aerosols are not present in Jupiter's atmosphere. In fact, Rayleigh scattering can only have an impact on the <1000 nm part of the Jovian spectrum, and therefore the observed radiation between 500 nm and 3.5 μm is a large proof for the presence of clouds and aerosol species. From microphysical models, Chapter 2, we expect hazes to be submicron while clouds to be micron sized. Therefore, because of Mie theory (Chapter 3) , hazes will be more influential in the visible part of the spectrum (0.5-1 μm) while clouds in the near-infrared part (1-4 μm). The visible part of the Jovian spectrum was in fact long studied from both ground based and space observatories to investigate differences in reflectance induced by the presence of different hazes (Braude et al., 2020; Sromovsky et al., 2017a; Dahl et al., 2021). Similarly, the [1.5-1.62] and [2.6-2.8] μm windows have been used by Encrenaz et al. (1996) and Sromovsky & Fry (2010a,b) to infer the properties of clouds on Jupiter using multiple scattering atmospheric retrievals. In fact, because of the weak opacity of gaseous species, the shape and intensity of the reflectance peaks are entirely dependent on the physical parameters of the clouds and hazes. The dependence is not linear and obvious. However, it is possible to deduce some general principles:

- Denser aerosol decks will result in higher reflected signal; higher altitude aerosol layers will have the effect of enlarging or flattening the peaks. Indeed, if the aerosols are higher in the atmosphere they may cover the methane or ammonia gas layers that produce the absorption features with the result of flattening the spectrum. This has been observed also in different exoplanets (Sing et al., 2016; Kreidberg et al., 2014)
- Differences in effective radii and chemical composition result in different single scattering albedo spectra and therefore in different shapes of the reflectance peaks. This can be considered as a "second order effect". For example two

different cloud compositions may result in shifts of the maximum of the peak or in extra absorptions not explainable by gaseous species. Differences in single scattering albedo should also produce differences in colors, easily identifiable in visible images.

The effect on atmospheric windows is more straightforward. If sunlight scattering is negligible the radiance only comes from the interior of the planets. Therefore, if these signals encounter aerosol layers with different densities, and therefore different opacities, they may be weakened or blocked at all. Usually hazes do not become optically thick in non-polar regions (if yes we would not see the different atmospheric features detailed in section 5.1) therefore dense clouds may have the effect of flatten the spectrum and hide absorption features. The presence of dense clouds causes also a decrease in the measured thermal signal. In fact, only photons above the dense clouds can reach the observer and these are usually emitted at lower temeperatures and therefore lower energy with respect to the cloud-free scenario. In Fig. 5.12 it is possible to observe the effect of clouds and aerosols on the Jovian spectrum in the 2-5 μm range. The effects on reflectance and atmospheric windows has a straightforward observational consequence that was observed for the first time using Galileo data. In their work, Irwin et al. (2001) found an anti-correlation between the signals corrected for the incidence angle measured at 2.7 and 5 micron respectively, Fig. 5.13. This behavior is simply driven by the presence of a spectrally flat (or gray) cloud. If the cloud is dense the 2.7 μm signal is enhanced and the 5 μm signal is weakened. If the cloud is thin the opposite is true. This simple but yet physically meaningful relationship is a powerful tool to identify anomalous cloud structures or temporary uplifting or downwelling events.
Finally, clouds and hazes can also produce new absorption features. Albeit, due to their densities and lifetimes (usually short due to photochemistry and precipitation) these features are usually weak. To further complicate the problem these features can be at the same wavelength position of much stronger features produced by gaseous ammonia or methane. This is not a random occurrence. Indeed, for ammonia, the same covalent bonds that induce gaseous opacities are responsible also for the absorption features in the ice refractive index. Considering again the condensation models (Chapter 2) we saw that on Jupiter we expect the presence of ammonia ice, ammonium hydrosulfide and water ice. Ammonia ice has relatively sharp absorption features at 2, 2.2, 2.95, and 10.5 micron (Martonchik et al., 1984; Howett et al., 2007; Hudson et al., 2022; Wong et al., 2004a). However, at the same exact positions also gaseous ammonia absorption bands are found, making their identification rather difficult starting from spectral observations. However, many studies have aimed to accomplish this, as we will see in Section 5.6. Similarly, ammonium hydrosulfide is expected to absorb around 3.5, 5.5, and 6.85-7.1 micron (Howett et al., 2007). Water ice is expected to absorb strongly at 1.5, 2, and 3 micron (Warren, 1984). Being these regions dominated by gaseous ammonia and methane opacity, NIR spectral features of NH_4SH and H_2O ices have never been detected. It is possible to observe the refractive indexes of all these species in Fig. 5.14.

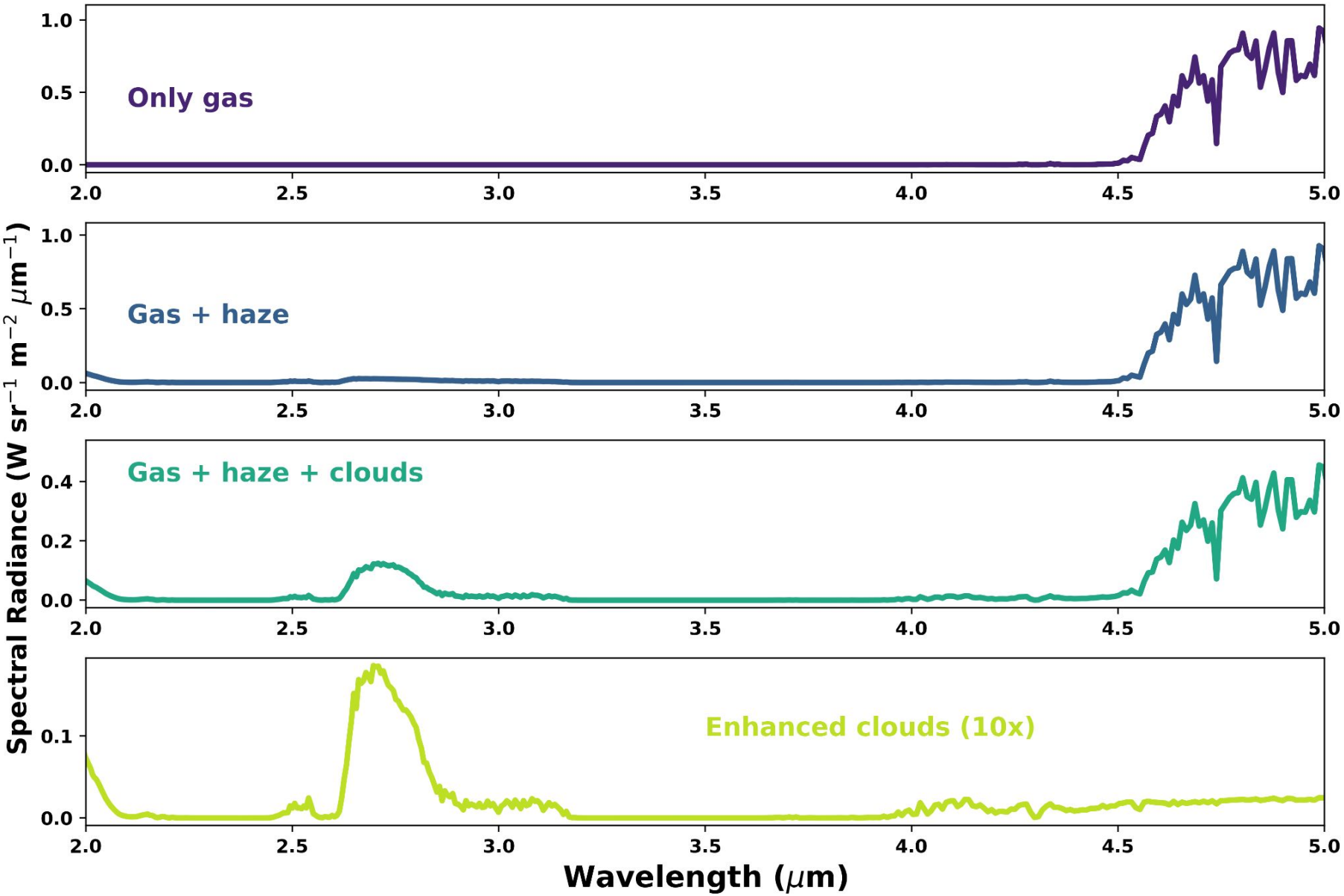


Figure 5.12: Different PSG simulations (see Chapter 6 for the details) highlighting the effect of clouds and aerosols on the Jovian spectrum in the 2-5 μm range.

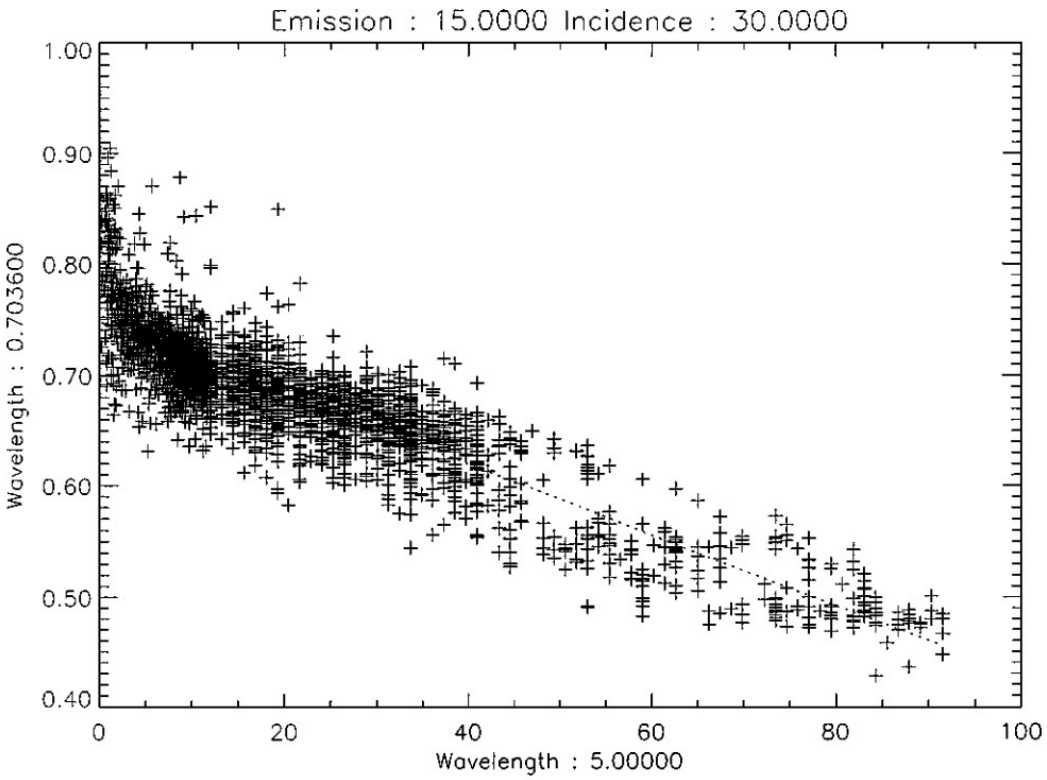


Figure 5.13: Scatter plot of BDRF (see Chapter 3) measured at 0.7036 μm against the radiance (in units of μW cm^{-2} sr^{-1} μm^{-1}) measured at 5 μm for Galileo data presented in Irwin et al. (2001).

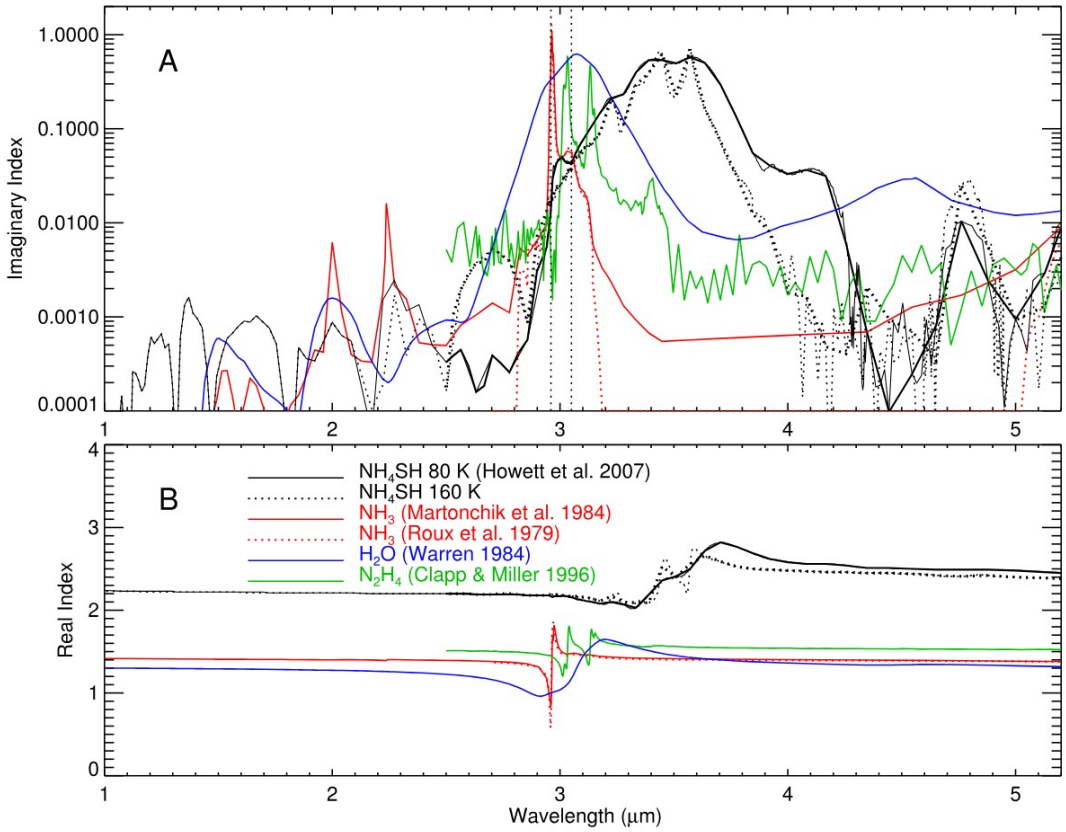


Figure 5.14: Refractive indexes of the species that are thought to condense in the Jovian troposphere, from Sromovsky & Fry (2018).

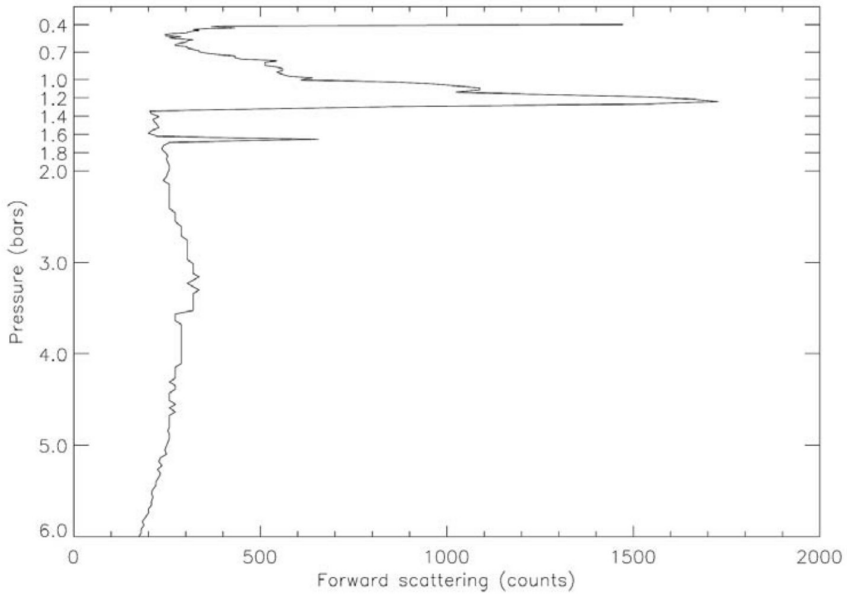


Figure 5.15: Relative cloud profile of Jupiter deduced from the Galileo probe nephelometervexperiment cloud results. From Ragent et al. (1998).

5.5 Retrieved aerosols structures and densities

The only direct measurement of clouds structures and densities in the Jovian atmosphere comes from the Galileo Entry Probe and in particular from its Nephelometer instrument. The Nephelometer (NEP) measured scattered light from a pulsed LED source in terms of reflected photons counts. Contrary to pre-mission expectations of three distinct, thick cloud decks (ammonia, ammonium hydrosulfide, and water), the NEP detected only one significant cloud layer located between approximately 1.34 and 1.63 bars, with a peak in measured counts at 1.55 bars (Ragent et al., 1998), see Fig. 5.15. This layer was relatively thin and wispy. From the number of measured counts the authors estimated the size of the cloud particles in the order of microns. Below this level, down to the maximum depth of 6 bars where NEP data was transmitted, the atmosphere was remarkably clear, with no evidence of the anticipated thick ammonium hydrosulfide or water cloud layers (Ragent et al., 1998). This finding was crucial in confirming that the Galileo probe entered a "hot spot," a dynamically warm, cloud-clear downdraft region, rather than a globally-representative atmospheric column, thus highlighting the significant spatial variability in Jupiter's cloud structure (Ragent et al., 1998; Banfield et al., 2004). Even though the probe entered a hot spot, its measurements remain the only direct ones and have served as paradigms for guiding atmospheric retrievals. Referring to Fig. 5.15 we can see that the probe detected:

- one single thin cloud around 1.3-1.4 bar and extending for about 0.04-0.08 bar
- uniform levels of counts from 0.5 to the tropopause; these counts are one order of magnitude lower than the found 1.3-1.4 bar cloud

Even if the hotspot are peculiar region, the first finding confirms that on Jupiter on Jupiter we expect thin and not extended cloud layers to be quite common, in agreement with the theoretical picture proposed by (Ackerman & Marley, 2001) that predicts high values of the $f_{\rm sed}$ parameter for Jupiter-like planets (see Chapter 2). On the other hand, the second finding hints to the presence of a some kind of haze particle distribution in the high troposphere. These haze particles should be smaller (10^{-1} μm) than the cloud particles because of the differences in measured scattered photons counts. The presence of other aerosol species other than the clouds is not predicted by any condensation theoretical model (see Chapter 2) and therefore this was one of the first pieces of evidence of the presence of photochemistry products in the Jovian atmosphere.
After the probe measurements, the only way to access information about the structure, dimension, and density of Jovian aerosols has been through retrieval from remote-sensed data (see Chapter 3). Once that a parametrization is chosen to model cloud and hazes, it is possible to infer the aerosol's properties fitting the spectra according to the Bayesian formalism However, at least two challenges arise immediately: (i) the retrieval of aerosol properties is an extremely degenerate situation, and (ii) to model the presence of aerosol, multiple scattering radiative transfer simulations are needed, and usually they require large computational capabilities.
To address this problem, usually a careful exploration of the parameters' space is required as detailed in Chapter 3. Methods such as Optimal Estimation, MCMC, and

Model	Reference	$\Delta\lambda$ (μm)	Region	Layers	$\tau^{tot}_{1\mu m}$	r (μm)	p_{base} (bar)	p_{top} (bar)
A	HST-Simon-Miller et al. (2001a)	0.3-1	NEB	1- Haze (no assumptions)	0.03 ± 0.006	0.01–0.05	0.2 ± 0.03	0.05
				2- Tropospheric cloud n.1 (no assumptions)	6 ± 1	0.6–1.2	0.97 ± 0.15	0.2
				3- Tropospheric cloud n.2 (Martonchik et al., 1984)	5.5 ± 1	0.9–3	1 ± 0.15	0.97
B	HST-Simon-Miller et al. (2001a)	0.3-1	EZ	1- Haze (no assumptions)	0.02 ± 0.004	0.01–0.05	0.24 ± 0.04	0.05
				2- Tropospheric cloud n.1 (no assumptions)	4 ± 1	0.6-1.2	0.67 ± 0.15	0.24
				3- Tropospheric cloud n.2 (Martonchik et al., 1984)	38 ± 8	0.9-3.0	0.7 ± 0.15	0.67
C	HST-Simon-Miller et al. (2001a)	0.3-1	SEB	1- Haze (no assumptions)	0.09 ± 0.003	0.01–0.05	0.24 ± 0.05	0.05
				2- Tropospheric cloud n.1 (no assumptions)	9 ± 3	0.6-1.2	0.93 ± 0.15	0.24
				3- Tropospheric cloud n.2 (Martonchik et al., 1984)	6 ± 2	0.9-3.0	1 ± 0.15	0.93
D	VIMS-Sromovsky et al. (2017a)	0.3-1	NEB	1- Stratospheric haze ($n = 1.4 + 0i$)	0.01 ± 0.004	0.01	0.05	0.04
				2- Chromophore layer (Carlson et al., 2016a)	0.19 ± 0.02	0.15 ± 0.01	0.38 ± 0.02	0.34 ± 0.02
				3- Tropospheric cloud ($n = 1.4 + 0i$)	16 ± 1	1.4 ± 0.2	3.2 ± 0.2	0.38 ± 0.02
E	VIMS-Sromovsky et al. (2017a)	0.3-1	EZ	1- Stratospheric haze ($n = 1.4 + 0i$)	0.01 ± 0.004	0.01	0.05	0.04
				2- Chromophore layer (Carlson et al., 2016a)	0.06 ± 0.01	0.12 ± 0.01	0.06 ± 0.03	0.05 ± 0.03
				3- Tropospheric cloud ($n = 1.4 + 0i$)	14 ± 1	0.59 ± 0.07	2.2 ± 0.1	0.06 ± 0.03
F	VIMS-Sromovsky et al. (2017a)	0.3-1	SEB	1- Stratospheric haze ($n = 1.4 + 0i$)	0.027 ± 0.003	0.01	0.05	0.04
				2- Chromophore layer (Carlson et al., 2016a)	0.76 ± 0.06	0.29 ± 0.02	0.49 ± 0.02	0.45 ± 0.02
				3- Tropospheric cloud ($n = 1.4 + 0i$)	25 ± 4	0.8 ± 0.2	4.9 ± 0.7	0.49 ± 0.02
G	VIMS-Sromovsky et al. (2017a)	0.3-1	GRS	1- Stratospheric haze ($n = 1.4 + 0i$)	0.004 ± 0.004	0.01	0.05	0.04
				2- Chromophore layer (Carlson et al., 2016a)	0.21 ± 0.02	0.15 ± 0.01	0.21 ± 0.01	0.18 ± 0.01
				3- Tropospheric cloud ($n = 1.4 + 0i$)	29 ± 4	1.1 ± 0.3	4.1 ± 0.6	0.21 ± 0.01
H	VIMS-Baines et al. (2019)	0.3-1	GRS	1- Stratospheric haze ($n = 1.4 + 0i$)	0.07 ± 0.4	0.25	0.05	0.04
				2- Chromophore layer (Carlson et al., 2016a)	0.19 ± 0.02	0.14 ± 0.01	0.21 ± 0.02	0.19 ± 0.02
				3- Tropospheric cloud ($n = 1.4 + 0i$)	28 ± 5	1.1 ± 0.4	4 ± 1	0.21 ± 0.02
I	VLT/MUSE-Braude et al. (2020)	0.3-1	EZ	1- Tropospheric haze ($n = 1.4 + 0i$)	0.6-1	0.1-0.5	0.3	0.1
				2- Chromophore layer (n as free parameter)	0.03 ± 0.02	0.05-0.2	0.3	0.1
				3- Tropospheric cloud ($n = 1.4 + 0i$)	25 ± 3	4.4 ± 0.1	1.5	0.6
J	VLT/MUSE-Braude et al. (2020)	0.3-1	NEB	1- Tropospheric haze ($n = 1.4 + 0i$)	0.3-0.7	0.1-0.5	0.3	0.1
				2- Chromophore layer (n as free parameter)	0.07 ± 0.02	0.05-0.2	0.6	0.3
				3- Tropospheric cloud ($n = 1.4 + 0i$)	20 ± 3	1.5 ± 0.2	1.1	0.6
K	Juno/JIRAM-Grassi et al. (2021)	2-5	SEB, EZ, and NEB	1- Tropospheric haze ($n = 1.4 + 0i$)	0.1-0.7	0.03-0.1	0.3-0.4	0.2-0.1
				2- Tropospheric cloud n.1 (Imanaka et al., 2012)	0.6-1.5	3	0.8-0.9	0.5-0.7
				3- Tropospheric cloud n.2 (Imanaka et al., 2012)	5-30	3	1.4-1.6	1-1.2
L	Dahl et al. (2021)	0.3-1	NEB	1- Chromophore layer (n as free parameter)	0.25-0.3	0.15	0.12	0.1
				2- Tropospheric cloud ($n = 1.4 + 0i$)	21-25	1-1.5	4-3	0.2

Table 5.1: Cloud and haze structures and compositions retrieved by a series of works that performed atmospheric retrievals on visible and infrared Jovian spectra. These are presented also in Fig. 5.16.

Nested Sampling are frequently used. On the other hand, as explained in Chapter 3, multiple scattering RT simulations are very demanding in terms of execution times. Therefore, the retrieval of aerosol properties in the Jovian troposphere has become feasible only with the advent of accessible adequate computational capabilities.

In Table 5.1 I summarized some of the results of literature works that addressed the retrieval of aerosol structures and densities in the Jovian troposphere. The works considered measurements from Galileo NIMS, HST, VLT/MUSE, New Horizons, ISO, JIRAM and other datasets. Some of these results are also presented in Fig. 5.16, expanded from the work of Dahl et al. (2021). The majority of these works focused either on the visible part of the Jovian spectrum or the reflection peaks. As explained earlier in this chapter, these are the wavelength ranges where it is possible to observe most of the effects of the clouds and hazes. On the other hand, the most appropriate approach to study aerosol properties is analyzing simultaneously reflection and atmospheric windows, for example the entire 1.6-5.2 micron range. In this way the properties of areosol are better constrained on the basis of both reflection and absorption properties. However, most spectral observations of the Jovian troposphere have high spectral resolution and it is computationally extremely expensive to build a retrieval system that encompasses the full near-infrared range with adequate accuracy. I will come back on this in Chapters 6 and 9.
The problem of comparing results from different literature studies are the differences in the parametrization used for clouds and hazes and the physical units. Namely, due to the degeneracy of the problem it is conceptually difficult to compare two works that used different cloud vertical profiles. Indeed, most of the time, the chosen aerosol parameterization is solely driven by data analysis and not by physics. One simple yet widely used cloud parameterization is the box, where the cloud is

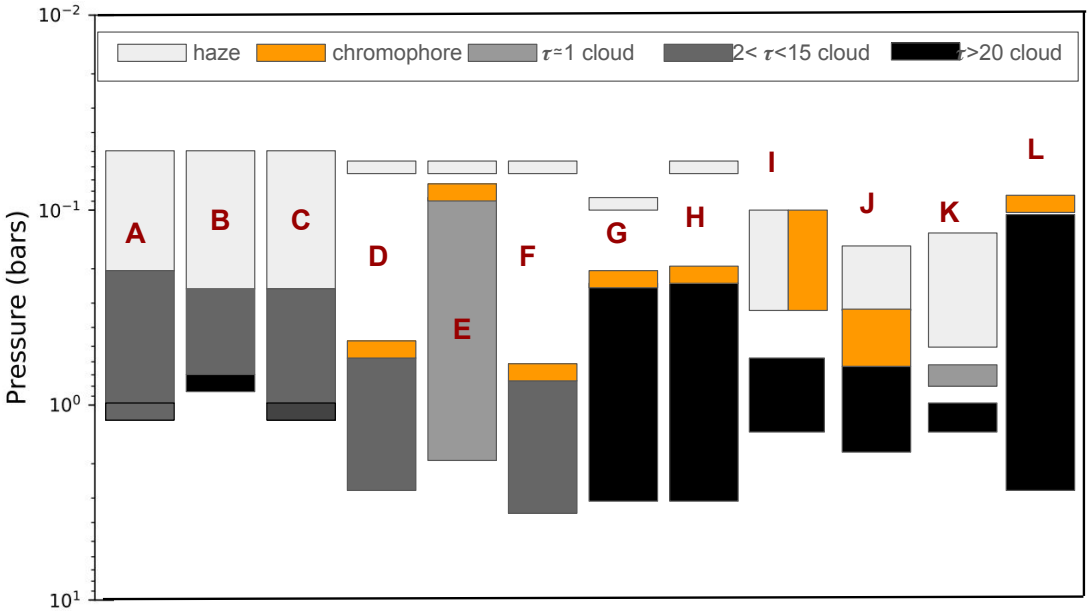


Figure 5.16: Cloud and haze structures and compositions retrieved by a series of works that performed atmospheric retrievals on visible and infrared Jovian spectra. These ar elisted in Table 5.1.

approximated with a constant vertical mixing ratio between a bottom pressure and a top pressure. As we saw earlier in this section and in Chapter 2 (Ackerman & Marley, 2001)a box cloud profile is not physical. However, the use of simple profiles can speed up the retrieval stage allowing the derivation of average properties. Another problem lies in the fact that the majority of these works present results in terms of optical depth. However, as described in Chapter 2 and 3, optical depth depends on the density, radii, and distribution of the aerosol species, parameters that should be treated separately in the retrieval process. Namely, the density of the clouds is a key parameter to be compared with theoretical models.
Nevertheless, it is possible to derive some general conclusions from the works listed in Table 5.1 and Fig. 5.16. Namely:

- small, optically thin aerosols between 0.5 and the tropopause are required in most of the works to explain the observed spectra in the visible part of the spectrum and in the 2-2.5 um region
- the retrieved cloud layers lie between 2 and 0.6 bar and are composed by micron-sized particles
- unity in optical depth (in the visible and infrared) is often reached between the 1.2 and 1.6 bar level
- the cloud layers that lie between 0.8 and 0.6 bar usually are optically thin
- there is a clear difference in the cloud top pressure levels observed in the belts and zones; this is between 10 and 20 km i.e. almost one scale height
- the clouds in the GRS can easily reach the 0.4-0.3 bar level

- in the GRS an optical depth of 1 is easily reached at the 0.5-0.4 bar level, meaning that there the clouds are extremely dense
- to explain the visible data, chromophore layers are needed (see next section)

The results of the retrieval therefore confirm that a hazy population of small particles is present in the higher Jovian troposphere, contrary to the simple picture provided by condensation models. Moreover, the occurrence of optically thin main condensation clouds (0.8-0.6 bar) is not in agreement with the upper density values predicted by ECCM and Ackerman & Marley (2001). On the other hand, the retrieved pressure levels are in a very good agreement with theoretical models. The 1.3-1.5 bar optically thick cloud deck may be the top of the NH_4SH cloud as proposed by (Guillot et al., 2024b) and (Irwin et al., 2025). I will come back on this in Chapter 7.
Particularly interesting is the case of the GRS. While the retrieved cloud structures of belts and zones are consistent with the dynamical picture presented in the first section of this chapter, the clouds present in the GRS are not. In fact, in the GRS clouds (not hazes) can easily reach the 0.4-0.2 bar level (Carlson et al., 2016a) and become optically thick (Baines et al., 2019). Also in the EZ clouds can reach these heights but they usually are optically thin (Sromovsky et al., 2017a). Therefore, the GRS has always be considered a peculiar region on Jupiter. It becomes even more peculiar once it is compared with Earth anticyclones. On Earth, anticyclones are primarily driven by radiative cooling at the top of the atmosphere and large-scale atmospheric circulation. Air in these high-pressure systems sinks and then warms adiabatically (due to compression), causing relative humidity to decrease, and leading to the evaporation of clouds and the occurrence of clearance regions at their centers. On Jupiter, the presence of anticyclones is indeed connected to optically thin clouds as observed at the poles (Adriani et al., 2020). Conversely, in the GRS we observe optically thick and high altitude clouds. The main hypothesis is that the GRS could be mainly powered by internal heat from the deep atmosphere, as it is thought to extend down to 200-300 km (Parisi et al., 2021a). As the lack of a solid surface removes the role of friction, the presence of an anomalous high pressure zone, such as the center of the GRS, has the effect of powering the convection enormously. I will come back on this in Chapter 9.

5.6 Retrieved clouds compositions

As discussed in Chapter 2, ammonia (NH_3) is often considered the main source of condensable species for Jupiter's main cloud layer (0.5-1 bar level). The other condensation species are NH_4SH around 2 bar and H_2O at 5 bar. The analysis of images and spectra of Jupiter taken from ground-based and space missions is needed to confirm or refine this picture. On the other hand, as discussed in this Chapter, the characterization of aerosols in a planetary atmosphere is a well-established challenge as they tend to flatten the signals (Kreidberg et al., 2014; Sing et al., 2016) and, most of the time, do not present sharp and easily identifiable spectral features. In the context of Jovian aerosols the NH_3 ice has the benefit of producing white clouds that should stand out with respect to the brown-orange backgrounds; moreover, as

we saw in the sections above, ammonia ice should display several strong absorption features (Martonchik et al., 1984; Howett et al., 2007; Hudson et al., 2022) in the near and mid-infrared and this led to several research works aimed to identify them. Early ground-based observations (Orton et al., 1982), however, did not report the detection of absorption features in the far infrared, at 9.4 and 26 microns, and the works by Carlson et al. (1993) and de Pater et al. (2001) pointed out that the ammonia condensation should happen at pressure levels lower than 600 mbar. Also Galileo-NIMS observations showed that clear spectral features connected to the occurrence of pure ammonia clouds (expected near 2 microns and 3 microns, Howett et al. (2007), two regions dominated by the gaseous ammonia absorption) are absent in most of the cases (Irwin et al., 2001), with the exception of particularly dynamic regions that cover less than 2% of the globe (Baines et al., 2002). These rare regions containing SIACs were thought to be formed by fresh ammonia that persists less than two days in the atmosphere, and that is transported from the deep troposphere to the cloud level by convective uplifting events. The SIACs found in the NIMS data show clear 2 micron anomalies, see Fig. 5.17, which are correlated to an anomalously low signal in the [2.6-2.8] μm window, that is connected to cloud reflection. This finding was supported also by the subsequent work of Wong et al. (2004a) that detected the further signature in the mid-infrared near 10 microns in the CIRS data.

The following observations confirmed that pure ammonia ice clouds on Jupiter are quite rare. In particular, observations from the Infrared Space Observatory (ISO) (Brooke et al., 1998; Sromovsky & Fry, 2010a) and Cassini-VIMS (Sromovsky & Fry, 2010b) demonstrated that a better fit of the 2.5-3.1 micron region (and mostly of the [2.6-2.8] μm window) is achieved when particles of both NH_4SH and NH_3 were included in the main cloud layer (at 0.5-0.9 bar), with the predominant opacity provided by NH_4SH, see Fig. 5.18. This picture was later criticized as NH_4SH is not expected to be present in its solid form at pressures lower than 1 bar. Nevertheless, it was one of the first work that used multiple scattering retrievals to study the [2.6-2.8] μm window and it demonstrated that ammonia ice particles cannot provide a good enough fit to the observed data.

Using observations from New Horizons/LEISA in the 1-2.5 micron range (Sromovsky & Fry, 2018) also detected evidence for the presence of SIACs in small regions near the equator and with the same characteristics of the ones detected by Galileo, see Fig. 5.19 and 5.20. Making use of precise multiple scattering retrievals, the authors found that these further SIACs are best fitted by an extended (between the 3 and 0.3 bar levels) optically thick NH_3 cloud and with an effective radius close to 3 microns, see Fig. 5.21.

Exploiting the optimal spectral resolution between 2 and 5 microns of the JIRAM image spectrometer, it has been possible to investigate whether the Juno data are in agreement with the findings of previous missions and if they confirm the rarity of NH_3 ice clouds. The work of Sindoni et al. (2017) studied a particular region of the southern hemisphere of Jupiter, the SSTZ, in the solar-dominated region of the JIRAM range (2.5-3 μm). They found that the best fit is achieved when a hydrazine haze, a main cloud deck of NH_3 particles with a coating of tholins, and a deep cloud made of NH_4SH are invoked, see Fig. 5.22. Grassi et al. (2021) repeated the analysis in a wider spectral range (2-3.2 μm) and for a large collection of

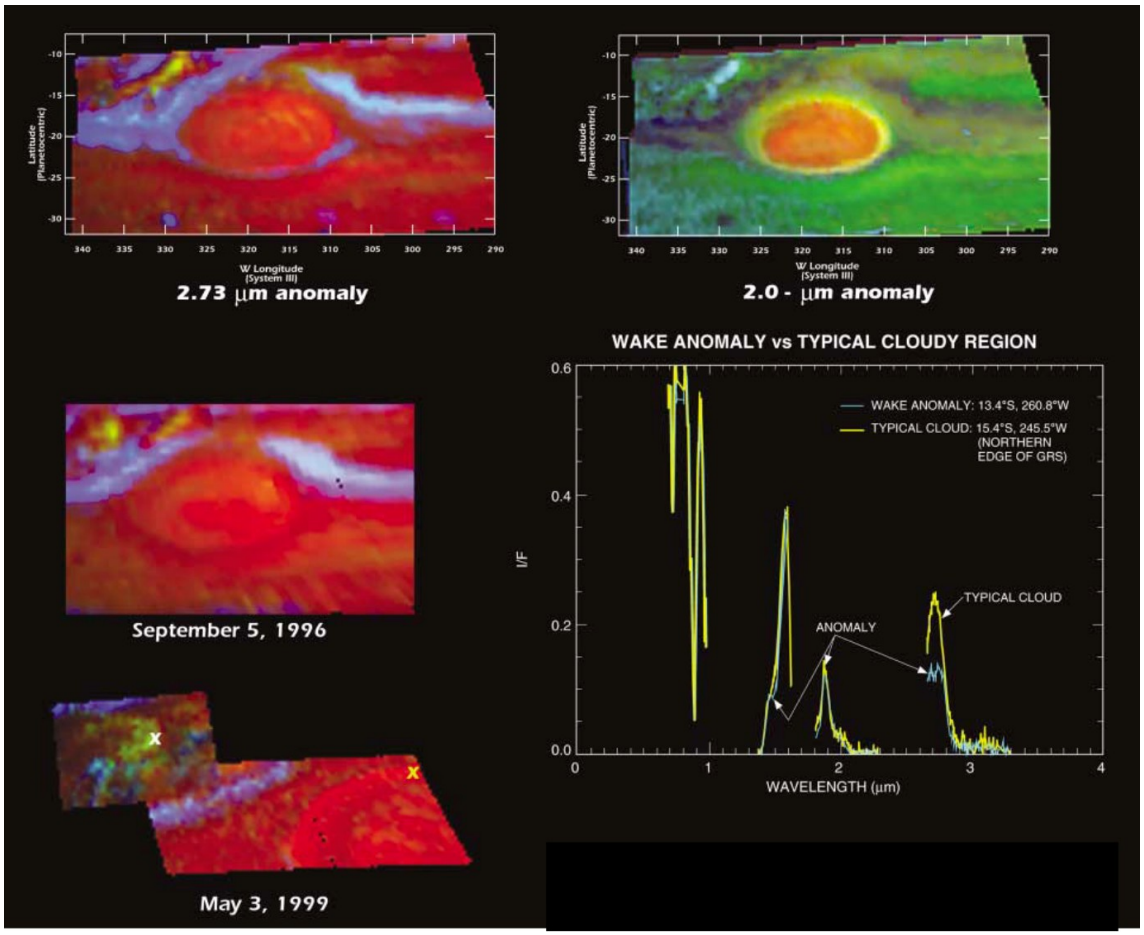


Figure 5.17: Left column: Representative images of the turbulent wake anomaly as observed during the first 28 orbits of the Galileo mission. Yellow denotes clouds that are both bright in the 1.6-μm continuum band (red), implying they are optically thick, and bright in the 1.60-μm/2.74-μm reflectivity ratio (green), implying anomalously dark reflectivity at 2.74 μm. Right top image: same as the left column but here pale-white aqua denotes clouds that simultaneously (1) are optically thick (green), (2) exhibit a large band depth between 1.94 and 2.00 μm (blue), implying anomalously dark reflectivity at 2.00 μm, and (3) are at relatively high altitude, as indicated by their relatively bright appearance in the 2.05-μm H_2 absorption band (red). Middle right panel: a spectrum of an anomalous feature (cyan) compared to a spectrum (yellow curve) of a cloud at the northern edge of the GRS that resides near the same level in the upper atmosphere. Bottom right panel: Comparison of the observed spectrum in terms of reflectivity with a spectrum of ammonia ice (yellow) and gaseous ammonia. All the images are taken from Baines et al. (2002).

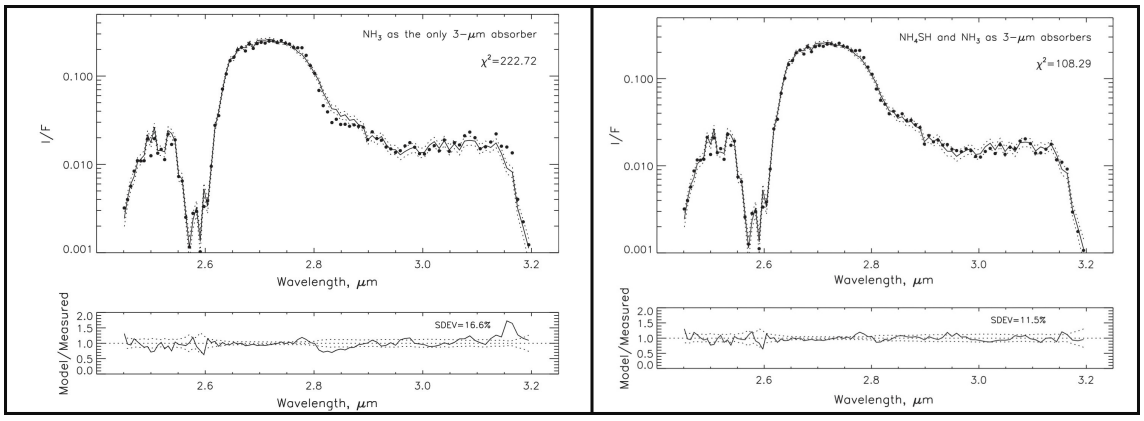


Figure 5.18: Left: ISO spectrum from Sromovsky & Fry (2010a) compared with the best-fitting model with ammonia ice clouds. Right: ISO spectrum from Sromovsky & Fry (2010a) compared with the best-fitting model where clouds are composed both of ammonia ice and NH_4SH. It is possible to note that the fit is significantly improved with respect to the right panel.

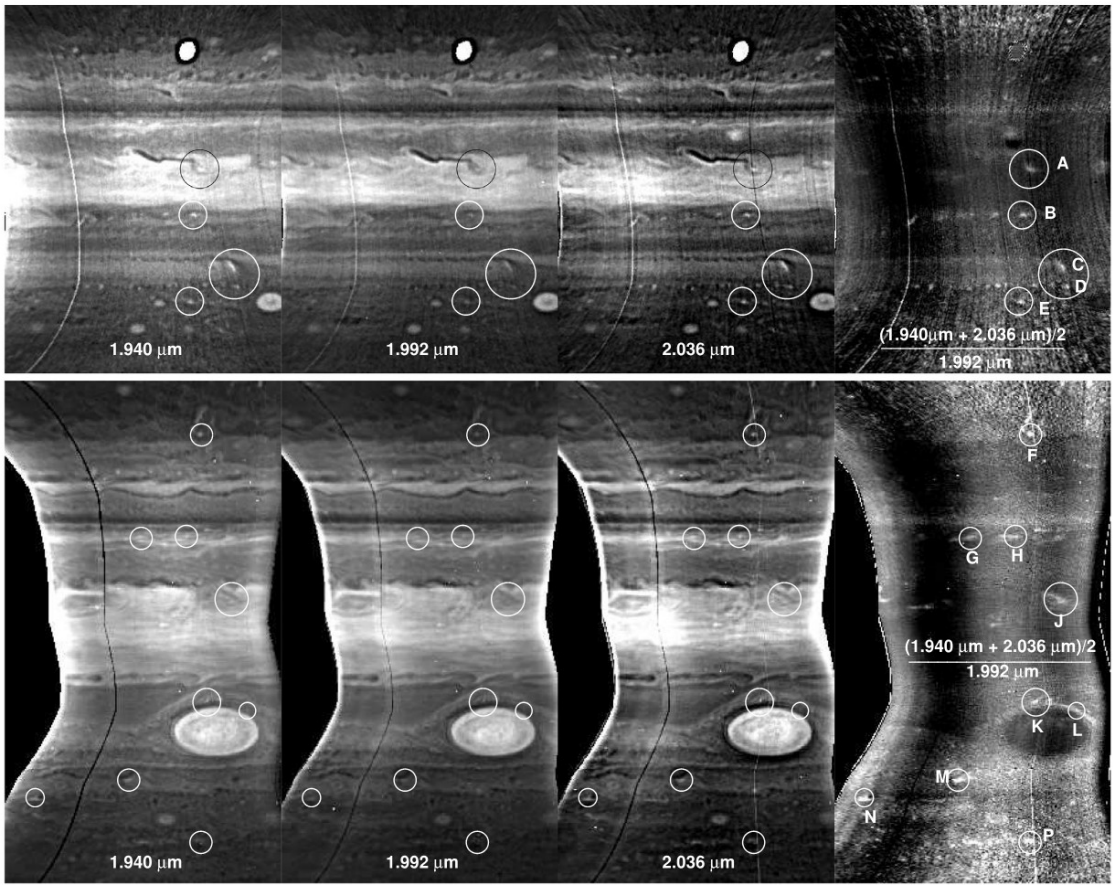


Figure 5.19: LEISA images of the Jovian disk at three wavelengths from Sromovsky & Fry (2018). The first and third columns are maps taken at 1.94 μm and 2.036 μm, outside the NH_3 ice absorption band. The second column is composed by maps taken at 1.992 μm, near the 2 μm NH_3 ice absorption peak. Images in the 4th column display the ratio of the absorbing I/F to the mean I/F of the non-absorbing adjacent wavelengths, making absorbing features bright. Circles locate features exhibiting absorption typical of pure NH_3 ice, i.e. SIACs.

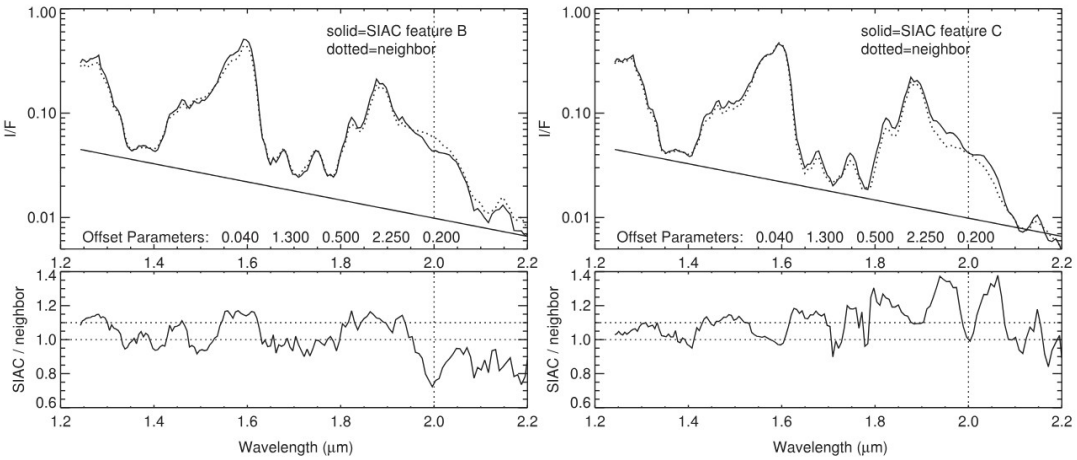


Figure 5.20: LEISA spectra (Sromovsky & Fry, 2018) of the SIACs B and C identified in Fig. 5.19.

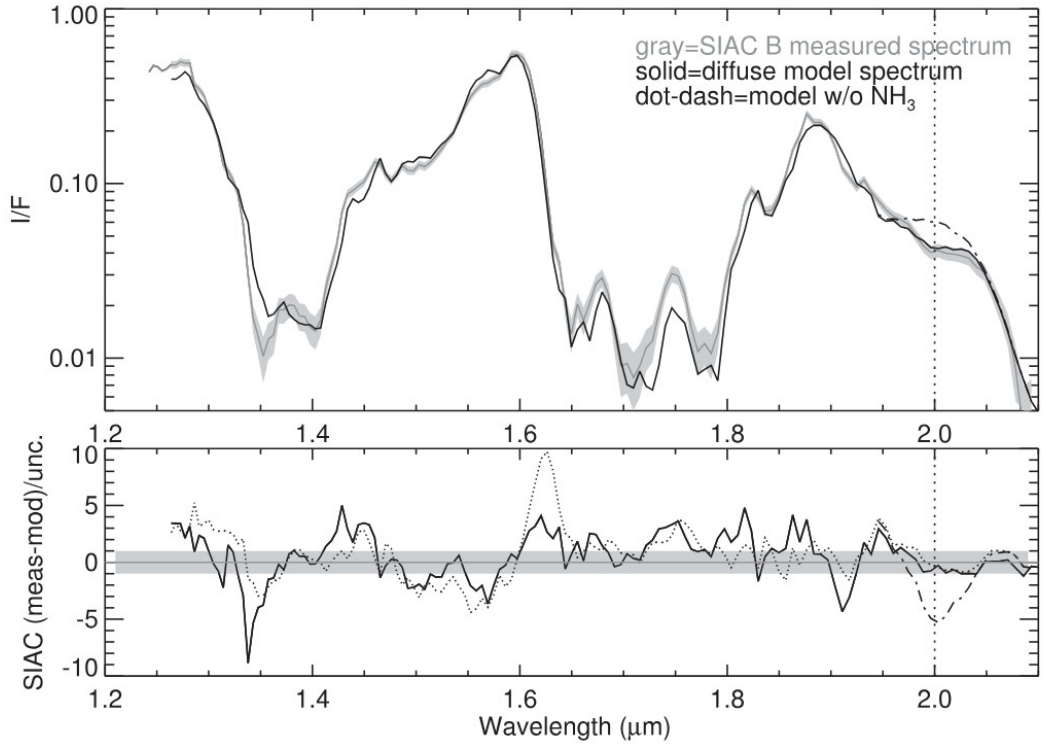


Figure 5.21: In light grey it is showed a LEISA spectrum of the SIAC B region identified in Fig. 5.19. It is compared with the results of multiple scattering retrievals that do (solid) and do not (do-not) consider the presence of pure ammonia ice clouds (Sromovsky & Fry, 2018). It is possible to note that the best-fitting model is the one considering pure ammonia ice clouds, particularly in the 1.8-2.2 μm range, i.e. a reflectance peak.

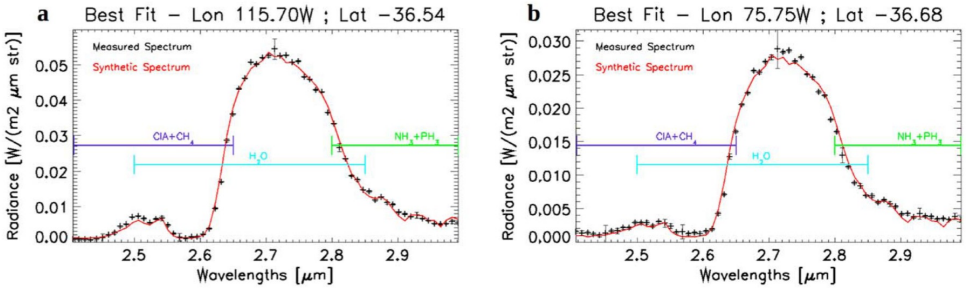


Figure 5.22: The black dots and the red line represent the JIRAM measured mean spectrum and the best fit synthetic spectrum obtained by Sindoni et al. (2017) considering ammonia-coated Imanaka et al. (2012)-tholins with different core-to-coating ratios (see Chapter 3). The spectrum in the (a) panel was taken inside the first White Oval, while the one in the (b) panel in the surrounding regions of the Ovals.

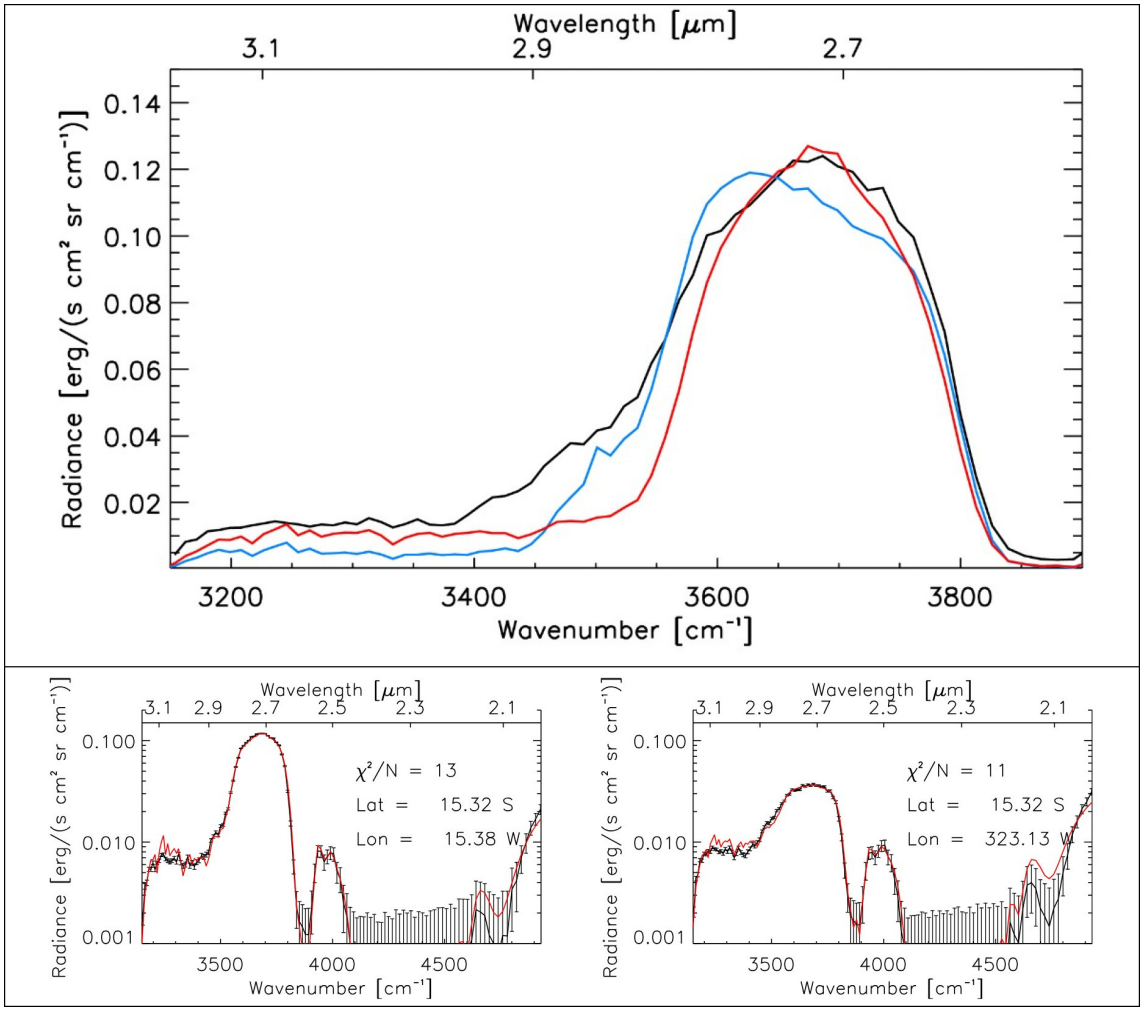


Figure 5.23: Top panel: JIRAM spectrum averaged over the South Tropical Zone (in black), comapred to synthetic spectra obtained considering ammonium hydrosulfide (blue) and pure ammonia ice (red) clouds. Both the materials do not provide good agreement. Bottom panels: JIRAM spectra (in black) from Grassi et al. (2021) compared to the best-fitting spectra obtained considering clouds composed of Imanaka et al. (2012) tholins.

spectra that covers all the jovian globe in longitude and the [-30,20] degrees range in latitude. There, in most circumstances, reasonable fits are obtained using just a pure reflecting tropospheric haze and two cloud decks made of tholins from Imanaka et al. (2012), see Fig. 5.23. It should be stressed that neither of the two studies claim that true Titan-like tholins are actually present in the Jovian atmosphere but that they just represent a very good approximation of the optical properties of the unknown amorphous material that should be present in Jupiter's clouds. Notably, these materials are exppected to bear the N-H and C-N bonds (Grassi et al., 2024b). The origin of this material is still unknown but should be connected to the chemical reactions between methane, gaseous ammonia, and the hydrocarbon products of photochemistry in the upper troposphere and the stratosphere (Atreya & Wong, 2005; Atreya, 2010; Kalogerakis et al., 2008; Carlson et al., 2016a). I discuss this further in Chapter 7. Undoubtedly, without invoking the presence of clouds composed of materials with optical properties similar to Titan's tholins in the 2-3.5 μm range, it is very difficult to fit the main reflection peak in the JIRAM data. This result is consistent with the main conclusion of the Sromovsky & Fry (2010a) study, which showed that accurately modeling the ubiquitous 3 μm feature observed with ISO is very difficult when using only clouds composed of pure ammonia ice. It is also noteworthy that neither did visible observations of the Jovian atmosphere report the detection of spectral features associated with ammonia clouds.

As ammonia ice or ammonia hydrosulfide particles should produce bright white clouds, the red/orange color of many features like the Great Red Spot (GRS) has long been puzzling. In order to explain this, the occurrence of an unknown chromophore material able to absorb UV and blue light was hypothesized (West et al., 2007). Carlson et al. (2016a) measured the transmission spectrum and imaginary part of the refractive index for the materials resulting from chemical reactions between photolyzed NH_3 and C_2H_2 in the 0.4-0.9 μm range. The resulting radiative transfer simulations were consistent with HST and Cassini's observations of the GRS. In these simulations, the measured chromophore was applied as a coating on existing cloud particles. Later, Sromovsky et al. (2017a) considered the same set of refractive indices and were able to obtain excellent fits of Cassini/VIMS visible spectra for different belts and zones, demonstrating that the Carlson et al. (2016a) material can possibly represent a nearly universal chromophore on Jupiter. Baines et al. (2019) was able to obtain excellent fits also of the VIMS spectra of the GRS, using the Carlson et al. (2016a) chromophore as a thin haze on top of the main cloud decks, see Fig. 5.24. This cloud model has been named "Crème brûlée" model, see Models G and H in Fig. 5.16. However, due to the lack of laboratory measurements in the near-infrared range (Carlson et al. (2016a) refractive indexes are given for λ <900 nm) it was impossible to confirm whether the Carlson et al. (2016a) chromophore could also fit JIRAM spectra adequately.

To summarize, the general picture regarding the presence of ammonia ice clouds is still unclear even after decades of ground-based and space exploration. These clouds are expected by theory but only rarely observed. Moreover, the search for these elusive clouds pointed out that most of the time to model typical regions of Jupiter the presence of contaminants or coated particles is needed, meaning that they are characterized by clouds composed, at least in part, of unknown materials not predicted by equilibrium condensation chemistry.

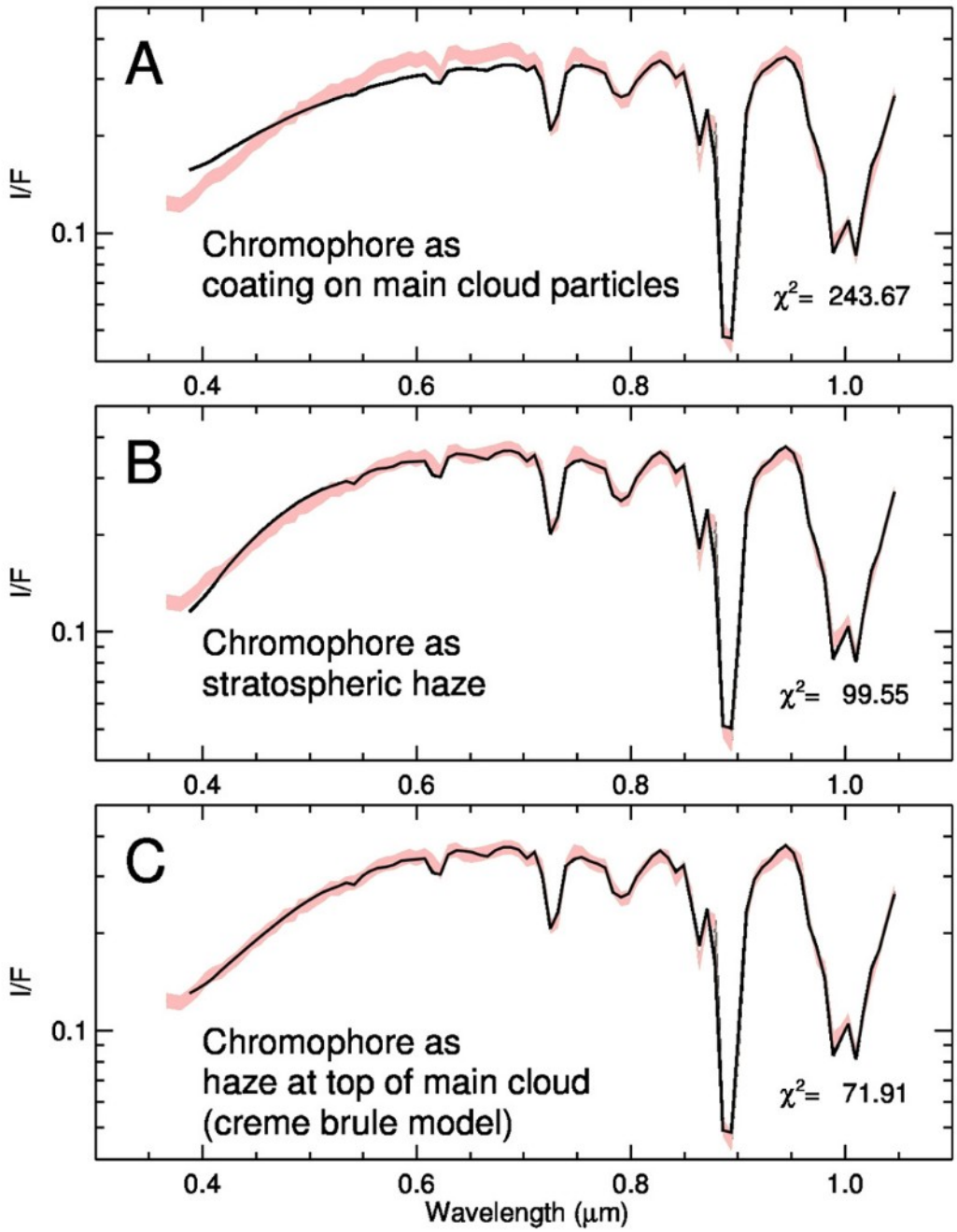


Figure 5.24: Spectral fits of a VIMS near-central-meridian GRS core spectrum from Baines et al. (2019) for a variety of cloud morphologies. (A): a coating of Carlson et al. (2016a) chromophore overlying a core of conservative scattering particles; (B): the Carlson et al. (2016a) chromophore restricted to a stratospheric haze layer at 40 mbar, several tenths of a bar above the GRS cloud, which itself is composed of conservatively scattering aerosols; (C): a layer of Carlson et al. (2016a) chromophore particles overlying a layer of conservatively scattering aerosols, informally known as the crème brûlée model.

Chapter 6

Modeling the Juno/JIRAM spectrum with PSG

In this chapter I summarize the analysis I performed in order to adapt the Planetary Spectrum Generator to model Juno/JIRAM spectra. Prior to this thesis work, JIRAM data were modeled with the following radiative transfer codes:

- ARS, developed by Nikolai Ignatiev, with minor adaptations by Davide Grassi (Ignatiev et al., 2005; Grassi et al., 2010)
- GRANADA, developed at Instituto de Astrofísica de Andalucía by Funke et al. (2012)
- KOPRA, developed at Institut für Meteorologie und Klimaforschung (Stiller et al., 1998)
- NEMESIS, developed by Patrick Irwin, Leigh Fletcher and Nick Teanby at University of Oxford (Irwin et al., 2008)

ARS was used to perform atmospheric retrievals of the solar and thermal wavelength regions separately (Grassi et al., 2010, 2021). NEMESIS was used by Melin et al. (2022) to attempt to perform atmospheric retrievals of the whole JIRAM range but the presented results were not fully conclusive. KOPRA and GRANADA instead were used to model only the 3.1-3.4 um region of the JIRAM spectrum focusing on non-LTE and auroral emission (see previous Chapter) (Castagnoli et al., 2025). With respect to the codes listed above, PSG has the advantage of being an open source code continuously monitored by a large community of users from different fields of planetary sciences. It is largely documented and has many advantages in dealing with modern problems in radiative transfer, as I discussed in Chapter 3. Therefore I chose it as the reference code for this PhD thesis. As far as I know, this thesis work represents the first attempt to use PSG to model actual measured Jovian spectra both in its solar-reflected and thermal regimes. The methods described here can be easily generalized to the case of Jupiter-like planets orbiting other stars outside our solar system.

6.1 Adapting PSG to JIRAM

PSG is largely documented and an extensive number of examples are available on its website. PSG can work both online or remotely thanks to the aid of so-called configuration files (cfg.txt). These are ASCII files in which the user can describe:

- the object of the simulation and its physical properties: it can be any object from asteroids to exoplanets
- the geometry of the simulation: nadir, observatory or limb as discussed in Chapter 4
- the structure of the atmosphere in terms of: the number of considered layers, the pressure-vs-temperature and gaseous volume mixing ratio profiles, the spectral database to use (HITRAN, ExoMol, or others), the aerosol species to consider and their optical properties
- the properties of the surface: in terms of (BDRF) bi-directional reflectance
- the properties of the output spectrum: in terms of units, range, resolving power and/or simulated associated noise

To adapt PSG to JIRAM I used an example template that simulates the reflected Jovian spectrum in the 0.5-0.9 μm range at the same resolving power of HST. I first verified that the physical properties (in terms of radius, mass, and surface gravity) were updated to the latest results from Juno gravity data. Therefore I changed the template in order to consider nadir observations and wrote a simple python script that can change the atmospheric VMR profiles automatically in the cfg.txt file. Since Jupiter does not have a defined surface I simply checked that the surface properties in terms of pressure and temperature were consistent with the deepest defined layer. Lastly, I modified the wavelength range to 1.9-5.1 μm and set the resolving power to a value >450. The choice for these parameters will be clear in the next sections. An example of a PSG cfg.txt file adapted to JIRAM can be found in the Appendix.

6.2 Testing PSG with ARS

As a first step I verified that the PSG simulations are consistent with the ARS (Ignatiev et al., 2005) radiative transfer code. I chose it as ARS was extensively used and designed to analyze Jupiter spectra acquired by JIRAM in the past years (Grassi et al., 2010, 2017b, 2020, 2021). Testing a new RT code in relation to others is a well-established technique in the field and has been used extensively in the context of exoplanets. An example can be found in the CUISINES initiative (Villanueva et al., 2024). In order to proceed, a simple model atmosphere is first considered. Starting from the same inputs, two different RT codes should give consistent results. If differences arise, it is possible to analyze whether this issue arises from the adopted RT algorithms or, for example, or from the spectroscopic databases. Notably, the latter case has been highlighted as one of the main sources of degeneracies and uncertainties in the field of atmospheric retrievals (Niraula et al.,

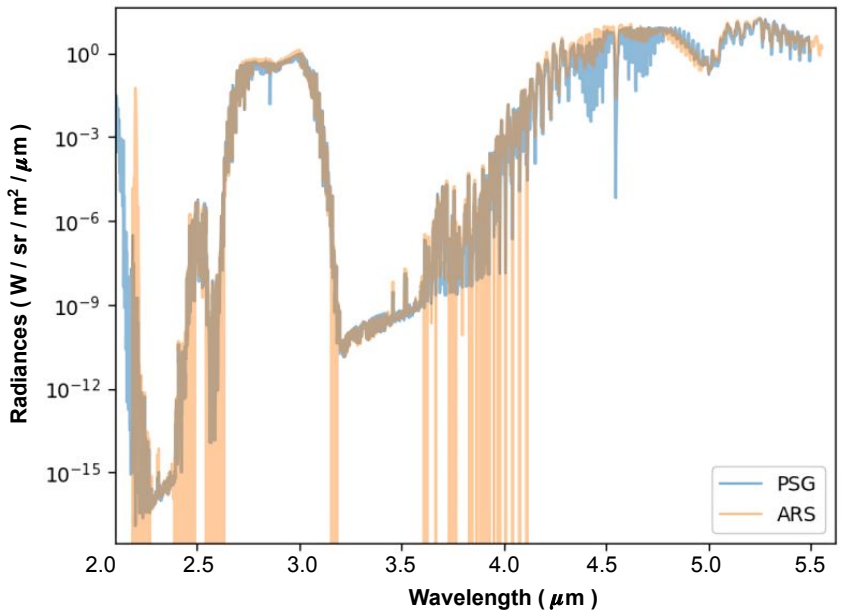


Figure 6.1: Comparison between synthetic spectra computed using ARS and PSG considering an atmosphere where methane is the only optically active species.

2022). In the following subsections I will summarize the tests that I performed in order to verify that the spectral data used by PSG were adequate to model JIRAM spectra. PSG uses correlated-k tables generated from the latest HITRAN data release, HITRAN2020 (Gordon et al., 2022). PSG's correlated-k tables cover a broad wavelength range from 0.2 μm to 100,000 μm. The tables are computed on a grid of various temperatures and pressures to account for atmospheric variations. 20 temperature points and 17 pressure points are used in the precomputation of these tables, ranging from 40 K to 2000 K and from 1 μbar to 100 bar. On the contrary, ARS uses custom-made correlated-k tables computed considering the exact points of the required pT profile. ARS allows for easy inclusion of data from different sources, such as HITRAN2016 (Gordon et al., 2017) and ExoMol. To perform the tests I used the pT profile presented in Braude et al. (2020).

6.2.1 Methane

I tested a simple atmosphere composed only of methane with a constant VMR profile of 0.00181. Since methane is the species that most affects the JIRAM spectrum (exception made for H_2 CIA) I performed simulations in the whole 2-5 μm range. For ARS I created correlated-k tables using the data presented in HITRAN16 for both CH_4, $^{13}CH_4$, and CH_3D. In ARS I considered isotopologues ratios of 0.994, 0.0108, and 0.00021 from Lellouch et al. (2001). In PSG instead the considered ratios are 0.9888, 0.0107, and 0.00045, equal to the Earth case.

In Fig. 6.1 I show the comparison between ARS and PSG simulations considering the full JIRAM range. It is possible to observe that overall there is a good agreement for λ <4.6. The most relevant discrepancies are observed in the 2.0-2.2, 3.7-4.0, 4.4-4.55, and 4.6-4.9 μm wavelength windows. The observed differences are thought to be caused by the differences in the amount of considered CH_3D. The 3.7-4.0,

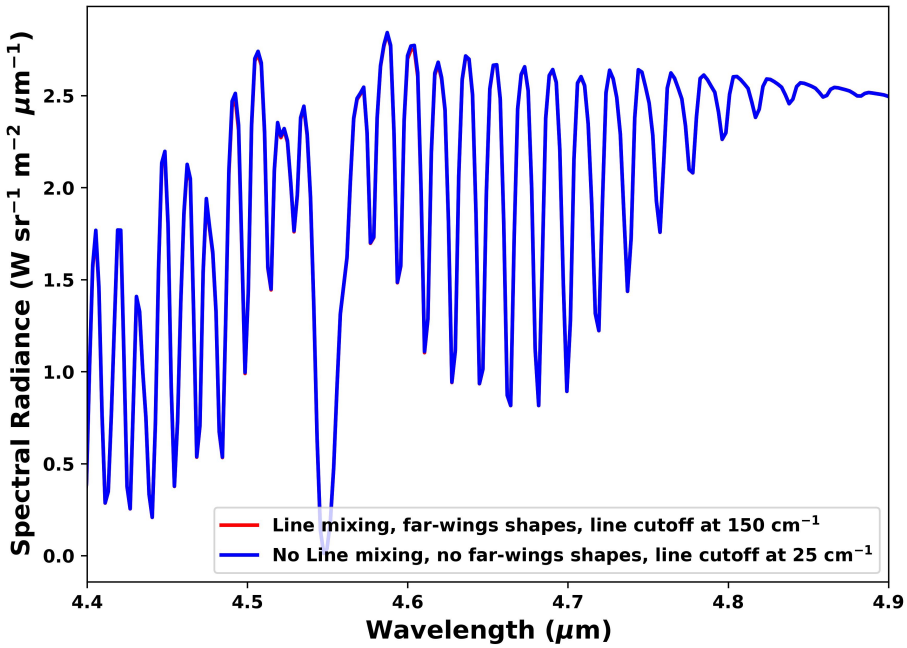


Figure 6.2: Comparison between two synthetic spectra computed using ARS. Methane is the only optically active species. In blue ARS uses the PSG options, i.e. no specific line mixing or far-wing shapes and a line cutoff at 25 cm^{-1}. In red ARS considers Tran et al. (2006) line mixing, Hartmann et al. (2002) far-wing line shape shape, and 150 cm^{-1} line cutoffs.

and 4.4-4.55 μm windows are usually characterized by low radiation values and therefore the observed differences are negligible for my purposes. On the contrary, PSG simulations differ the most from the ARS ones in the 4.6-4.9 μm region and these differences must be accounted for. I first investigated if these discrepancies could be explained by the introduction of methane line mixing (Tran et al., 2006), far wing lineshape for H_2 broadened CH_4 infrared transitions (Hartmann et al., 2002), and broader line cutoffs (see Chapter 3). In fact, PSG does not consider specific line mixings for each species. It also considers a standar Voigt profile for the line shape with line cut-off at 25 cm^{-1}. In Fig. 6.2 it is possible to observe that, at spectral resolutions close to the JIRAM case, the introduction of Tran et al. (2006) line mixing, Hartmann et al. (2002) far-wings shape, and 150 cm^{-1} line cutoffs, do not induce significant changes in the simulated radiances with ARS in the 4.4-49 μm region. Therefore, this cannot be the source of discrepancies between ARS and PSG. In this region, there is an important CH_3D absorption feature as reported by (Brown et al., 2013; Gordon et al., 2022) and in fact the PSG curves are lower in signal than the ARS ones, as it consider a higher concentration of deturated methane. It is possible to observe that CH_3D is the cause of the discrepancies in Fig. 6.1 once that I use the same isotopologues ratio both in PSG and ARS. This has been done in Fig. 6.3. It is possible to observe that the ARS simulation with Jovian isotopologues ratios produce a larger signal than the ARS simulation with terrestrial ratios. When terrestrial ratios are used both in PSG and ARS the discrepancies in the 4.4-4.9 μm range disappear. In the end, the test was useful to demonstrate that PSG internal correlated-k tables are adequate to model JIRAM data once that the difference in the isotopologues ratios is taken in account at thermal wavelengths. I did that using custom cross-section tables as I will explain in the following subsections.

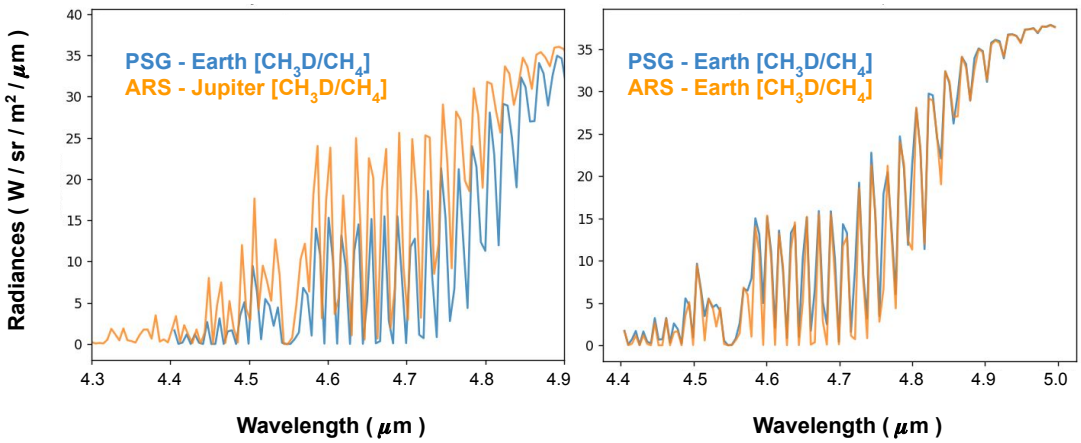


Figure 6.3: Left: comparison between ARS and PSG synthetic spectra considering an atmosphere where methane is the only optically active species. ARS uses custom correlated-k table built considering Jovian isotopologues ratios (Lellouch et al., 2001). PSG uses its own internal correlated-k tables. Right: same as the left panel, but the ARS spectrum is computed using correlated-k tables built considering Earth isotopologues ratios.

6.2.2 Ammonia

I tested a simple atmosphere where ammonia with a constant VMR profile of 400 ppm represent the only optically active component. Also ammonia affects both the solar and thermal part of the Jovian spectrum. In this case I performed simulations in the 2-3.4 μm and 4.4-5 μm ranges separately. In ARS I used the correlated-k tables used also in Grassi et al. (2021) derived from ExoMol data before 2020. In Fig. 6.4 and 6.5 I show the comparison between ARS and PSG simulations in both the solar and thermal ranges. It is possible to appreciate a very good agreement between the results of two codes. The only differences in radiances arise in the 2.4-2.5 μm range. However, this is to be ascribed to a previously unreported absorption band that was eventually included in the latest HITRAN2020 data release. Therefore I verified that it is safe to use PSG internal correlated-k tables in the whole JIRAM range.

6.2.3 Water and phosphine

I tested two simple atmospheres composed of: (1) water with a constant VMR profile of 20 ppm being the only optically active component and (2) phosphine with a constant VMR profile of 1 ppm being the only optically active component. Both water and phosphine present prominent absorption features in the thermal range (see previous Chapter), and therefore I only considered the 3.6-5 μm for the tests. As for ammonia, for ARS I used the correlated-k tables used also in (Grassi et al., 2021) derived from ExoMol data before 2020 and HITRAN2016. In Fig. 6.6 and 6.7 I show the comparison between ARS and PSG simulations. For

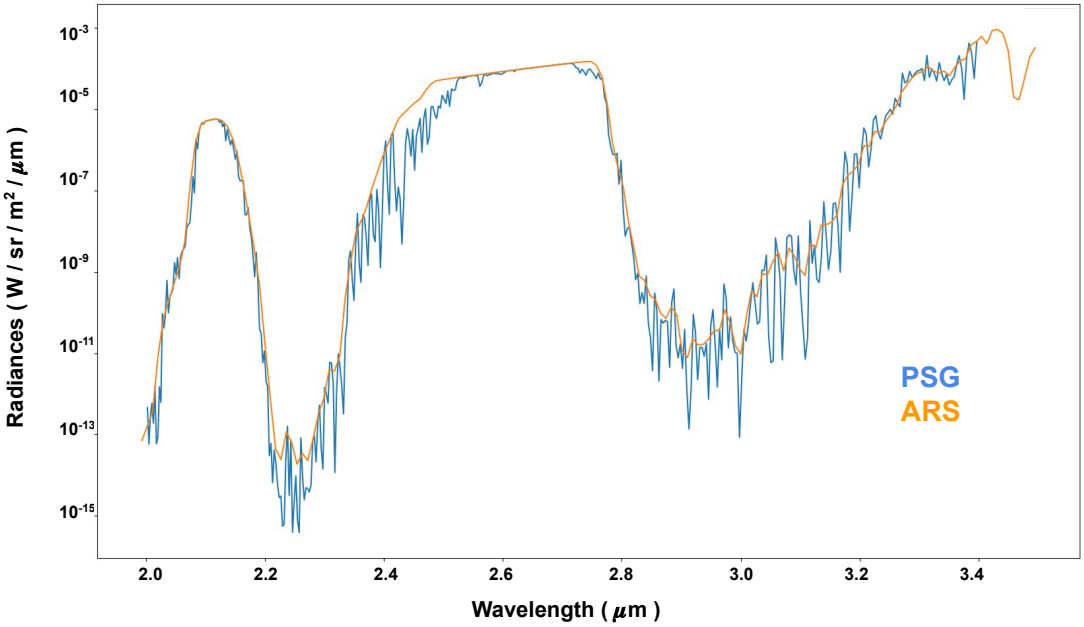


Figure 6.4: Comparison between synthetic spectra computed using ARS and PSG considering an atmosphere where ammonia is the only optically active species. It is possible to note an overall good agreement between the two curves even if the spectral resolution of the two simualtions is not the same.

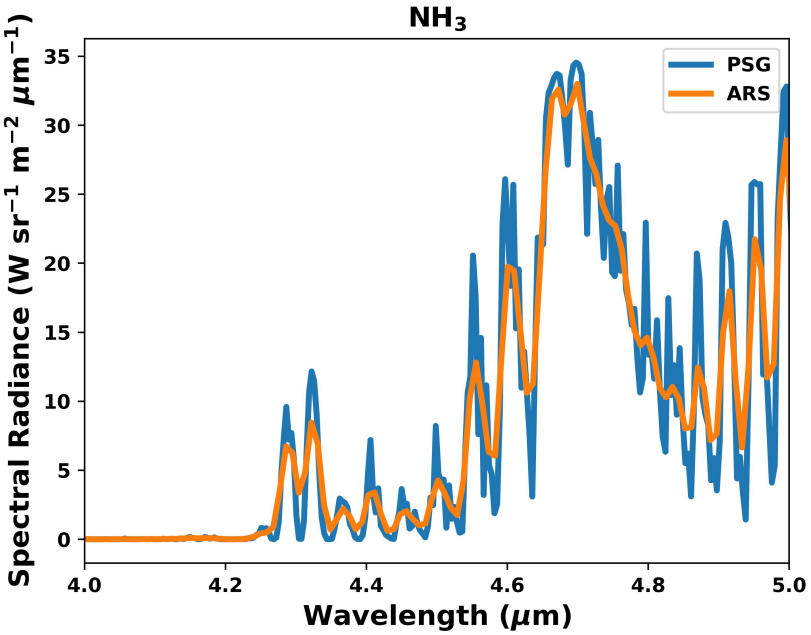


Figure 6.5: Comparison between synthetic spectra computed using ARS and PSG considering an atmosphere where ammonia is the only optically active species. It is possible to note an overall good agreement between the two curves even if the spectral resolution of the two simualtions is not the same.

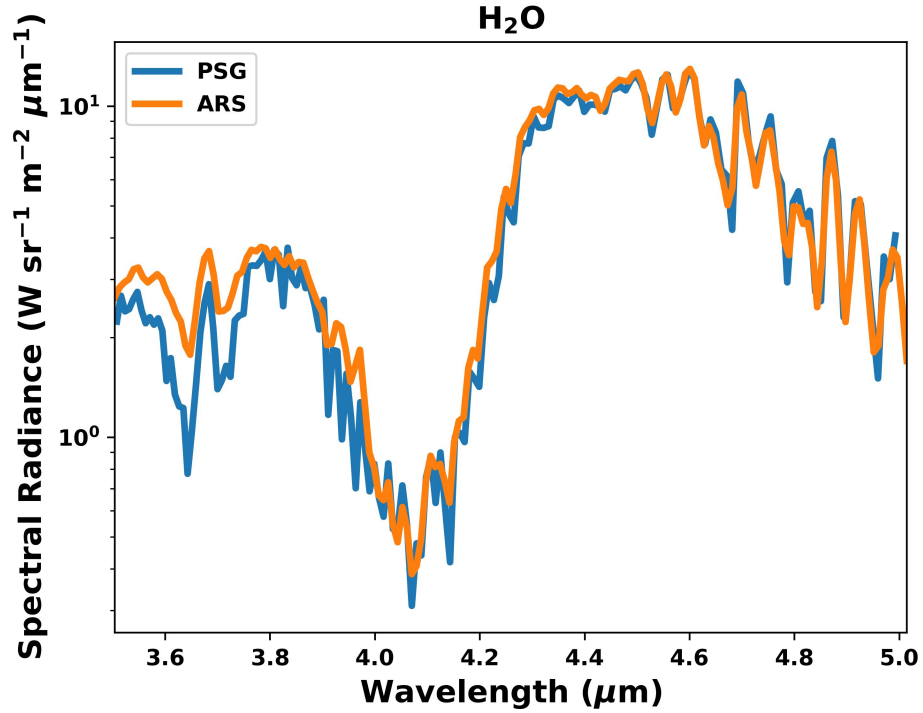


Figure 6.6: Comparison between synthetic spectra computed using ARS and PSG considering an atmosphere where water is the only optically active species.

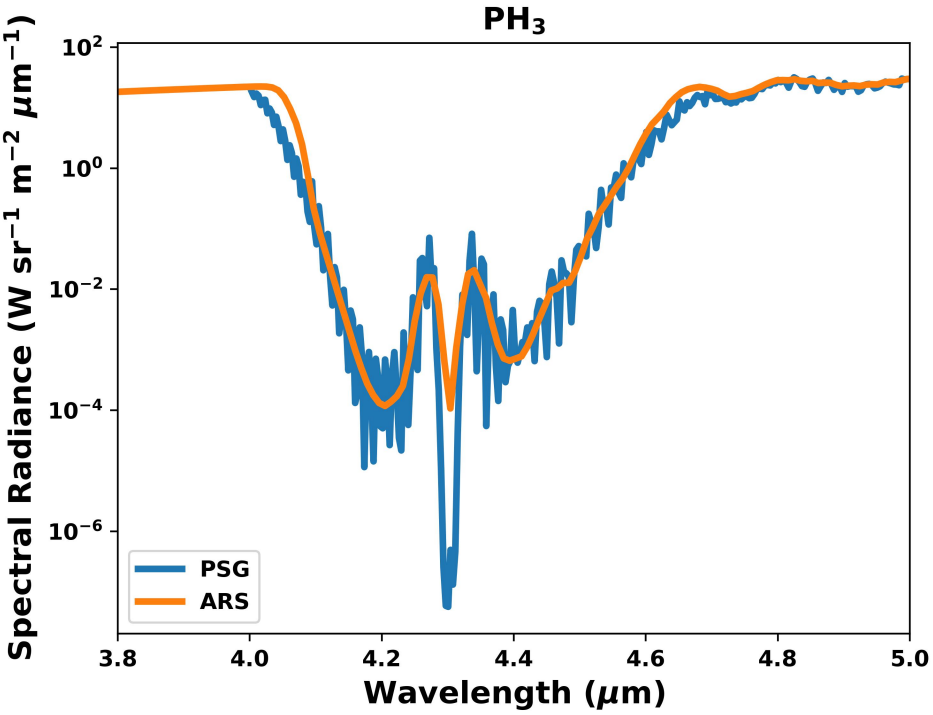


Figure 6.7: Comparison between synthetic spectra computed using ARS and PSG considering an atmosphere where phosphine is the only optically active species. The spectral resolution of the two simualtions is not the same.

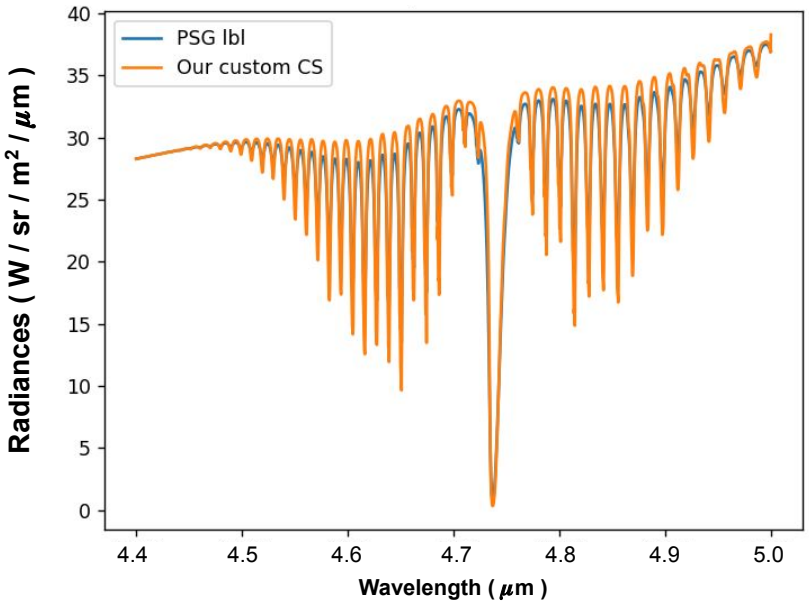


Figure 6.8: Comparison between two different PSG simulation considering an atmosphere where germane is the only optically active species. One simulation (blue) was performed using internal PSG linelists. The other (orange) using custom-made cross sections computed using ars k.

water I observe a very good agreement. The only observed difference in radiances is between 3.5 and 3.8 μm. This is induced by changes in the HITRAN releases and because of the so-called water continuum, considered by PSG. Water vapor continuum absorption, often parameterized by models such as MT-CKD (Mlawer-Tobin-Clough-Kneizys-Davies) (Mlawer et al., 2023), refers to the self-collisional broadening and the intermolecular component of the total absorption coefficient of water vapor that varies smoothly with wavelength across broad spectral regions. It is defined as the absorption that remains after accounting for the contributions of individual, spectroscopically well-defined discrete absorption lines (rotovibrational transitions) within a specific spectral cut-off (e.g., typically beyond ± 25 cm^{-1} from line centers). The physical mechanisms underlying this continuum are not yet fully elucidated from first principles but are generally attributed to a combination of far wings and CIAs. PSG accounts for it by means of an empirical model and this induces the lower signals in the d 3.5-4 μm transmittance window (White et al., 1978). Notably, this effect is usually not considered in ARS simulations of Jupiter's atmosphere. Therefore I verified that it is safe to use PSG internal correlated-k tables for water in the JIRAM range.
For phosphine there is a substantial disagreement in the line intensities. However, HITRAN2020 PH_3 data substantially revised and updated the datasets present in ExoMol, and available in ARS. Therefore I trust the latest results based and more recent laboratory work and I decided to consider PSG internal correlated-k tables for phosphine in my simulations.

6.2.4 Germane and arsine

These were the only two species that were not possible to test against ARS. The reasons were mainly two:

- ARS was optimized to work with tables from different outdated and obsolete databases (like GEISA and ExoMol before 2016). The new releases from HITRAN2020 and ExoMol greatly improved the resolution and precision of absorption coefficients for both GeH_4 and AsH_3 and therefore it was no-sense to use ARS as a comparison.

- PSG does not have internal correlated-k tables for both arsine and germane. It has only the option of working with lines from HITRAN2020 in the case of germane.

Therefore I proceed as follows. I considered the linelists from HITRAN2020 for germane and the ones from ExoMol for arsine. Using the arsk routine of ARS package, I computed the absorption coefficients for a series of points that encompasses the pT range of the Braude et al. (2020) profile. These data were consequently converted into cross-sections and listed in two separate tables readable by PSG. I decided to proceed with two separate tables since both germane and arsine concentrations will be treated as free parameters in the retrieval stage. In order to verify that these tables work correctly, I tested a simple atmosphere with GeH_4 with a constant VMR profile of 0.6 ppb being the only optically active species. In PSG I first used the internal HITRAN2020 linelists data and performed a line-by-line simulation. I then used my custom-made cross section tables. The results are shown in Fig. 6.8. It is possible to observe that there is a very good agreement between the two simulations verifying that it is safe to use my custom-built cross-section tables.

6.2.5 H_2 Collision-induced absorption (CIA)

I tested a simple atmosphere composed only of hydrogen and helium with constant VMR profiles of 0.864 and 0.136 respectively. Usually, CIA opacities are computed starting from theoretical or laboratory-measured binary coefficients tables; it is relatively straightforward to implement results from different works inside ARS. In the past ARS worked using the theoretical tables of Borysow (2002). However, to perform the tests I created new opacity tables starting from the more recent works of Abel et al. (2011) for H_2-H_2 CIA and Abel et al. (2012) for H_2-He. However, these tables are given up to 200 K. Therefore the opacities for T<200 K were extrapolated from the Abel et al. (2011, 2012) data using the experimental constraints given by Vitali et al. (2025). According to the PSG handbook (Villanueva et al., 2022), also PSG implements cross-section tables for H_2-H_2 and H_2-He CIA derived from Abel et al. (2011, 2012) works. In Fig. 6.9 it is possible to observe the final comparison between ARS and PSG. There is a clear difference in radiances for the entire range. In particular PSG curves are lower in radiance, implying that they are overestimating CIAs opacities. This can be very important and risky in the context of multiple scattering models. In fact, overestimated CIA opacities can result in overestimated cloud densities. Indeed, if the opacity in the atmosphere is higher than expected

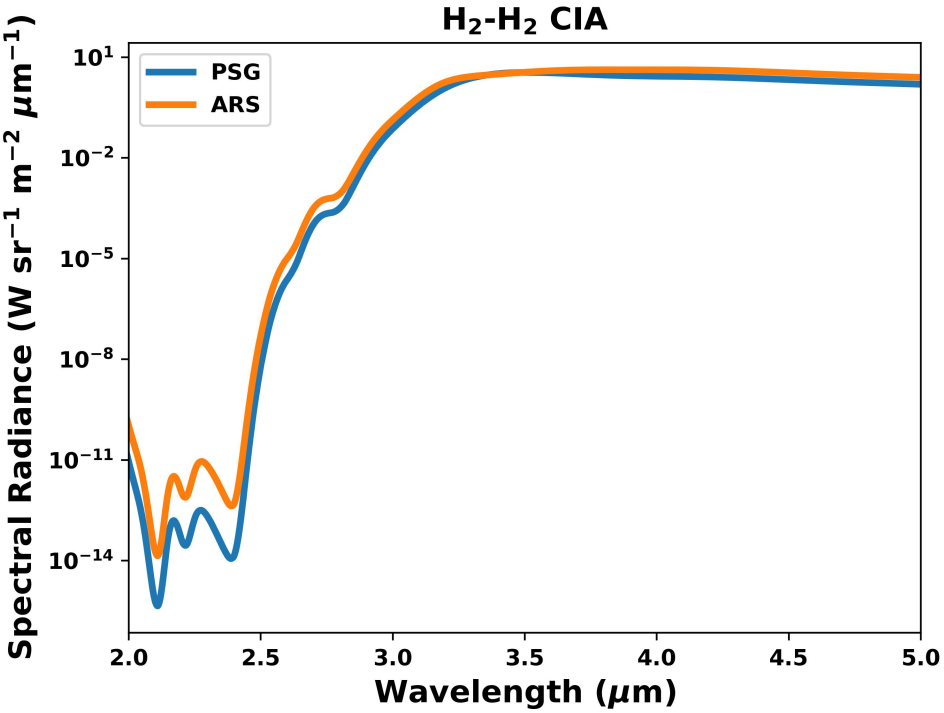


Figure 6.9: Comparison between synthetic spectra computed using ARS and PSG considering an atmosphere where hydrogen and helium are the only optically active species. PSG simualtions were performed using its internal cross sections tables.

I also need more cloud particles to achieve a given value of reflected radiance. After a careful investigation I found the ultimate cause of PSG overestimated CIAs opacities. The problem arises from the internal cross-section tables. Since the Abel theoretical data stop at 200 K, the PSG internal tables treat each atmospheric layer at T<200 K as if the corresponding CIAs' opacity was the one of a layer at T=200 K. I reported the bug to the developers and the issue is currently being addressed. Therefore to model JIRAM spectra with PSG I needed to insert the custom ARS-derived cross-section tables for H_2-H_2 and H_2-He CIAs, as in the case of germane and arsine. Doing so, the comparison between PSG and ARS is almost perfect, see Fig. 6.10. Hydrogen and helium are well-mixed in the Jovian atmosphere as for methane. Therefore while creating the cross-section tables I also added an opacity contribution that accounts for the difference in isotopologues ratios between Earth and Jupiter (see above subsection). In this way it is also possible to account for extra-CH_3D absorption.

6.2.6 Aerosols

Finally I also tested an atmosphere composed only of a uniform haze deck with a constant retractive indices of n=(1.4,0.0001i) (constant in wavelegth) and a log-normal size distribution with an effective radius of 0.2 μm. To compute the Mie-derived optical properties I used a python routine that generalizes the Bohren & Huffman (1983) calculations. In Fig. 6.11 I show the comparison between ARS and PSG. The agreement is almost perfect and it was expected as both the radiative

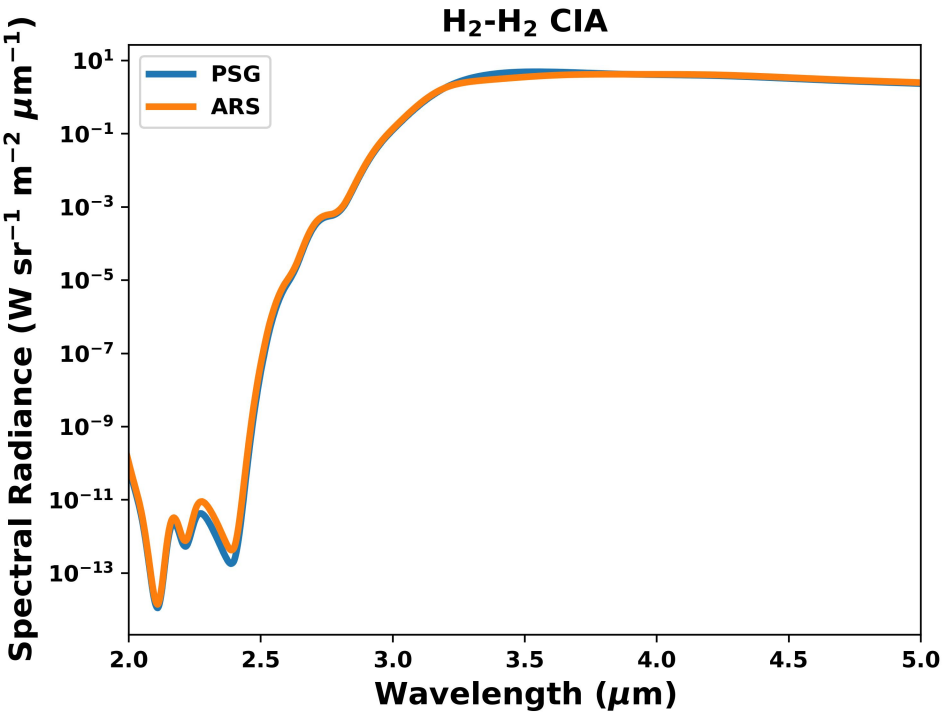


Figure 6.10: Comparison between synthetic spectra computed using ARS and PSG considering an atmosphere where hydrogen and helium the only optically active species. PSG simualtions were performed using custom inserted cross sections tables built considering the experimental results of Vitali et al. (2025).

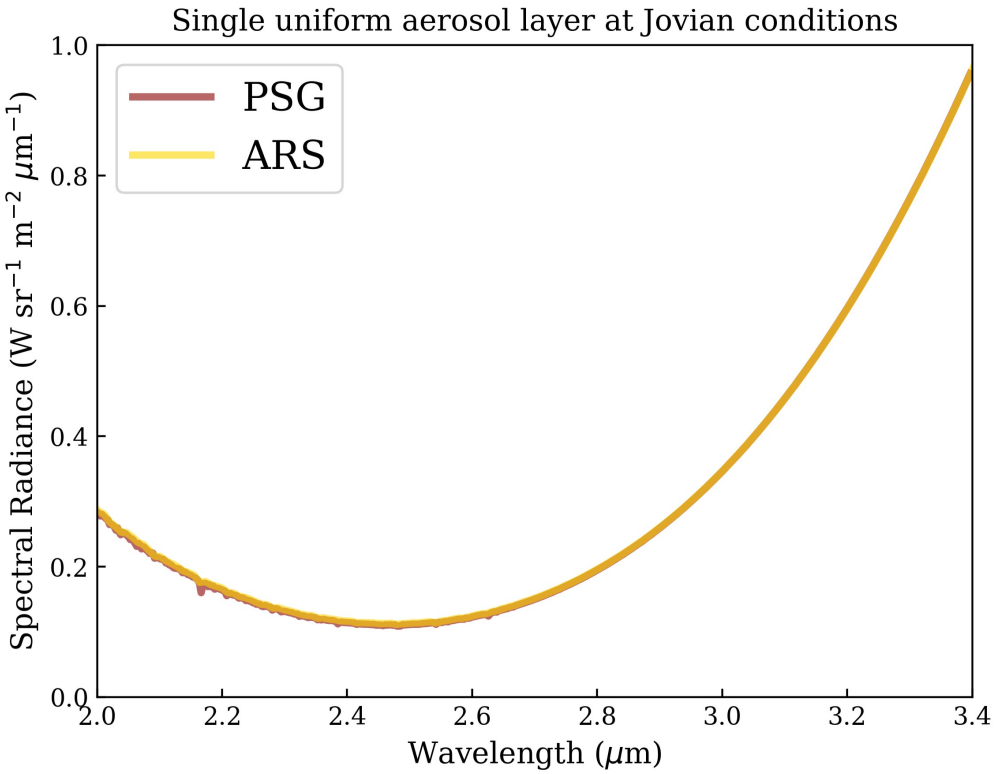


Figure 6.11: Comparison between synthetic spectra computed using ARS and PSG considering an atmosphere where a n=(1.4,0.0001i) aerosol deck is the only optically active species.

transfer suites implement DISORT (see Chapter 3).

6.3 Simulations and retrievals of the solar range

Once I verified that PSG treats correctly both the gas opacities and the multiple scattering computations, I pursued an atmospheric parametrization to be inserted in an atmospheric retrieval code. In this section I will focus on the 2-3.2 μm range that, as seen in Chapter 5, has been often considered to infer cloud and hazes properties. In section 6.5 I will describe the parametric description of the atmosphere adopted to treat the thermal range (4-5 μm) and in the final one the work done to converge on a single model atmosphere that can be useful to describe the whole JIRAM range. The model atmosphere that I considered encompasses the following items, see Fig. 6.12:

- a fixed pressure temperature profile extrapolated from Braude et al. (2020). The model atmosphere is considered to be composed of 98 plane-parallel layers. It covers the 8-0.1 bar range in pressures.
- constant mixing ratio profiles for H_2, He, and CH_4. The values were assumed to be respectively 0.86, 0.13, and 0.00181 as measured by the Galileo entry probe (Niemann et al., 1996).
- a variable mixing ratio profile for gaseous NH_3. Following Irwin et al. (1998), the profile is defined by two parameters: a deep volume mixing ratio (VMR)

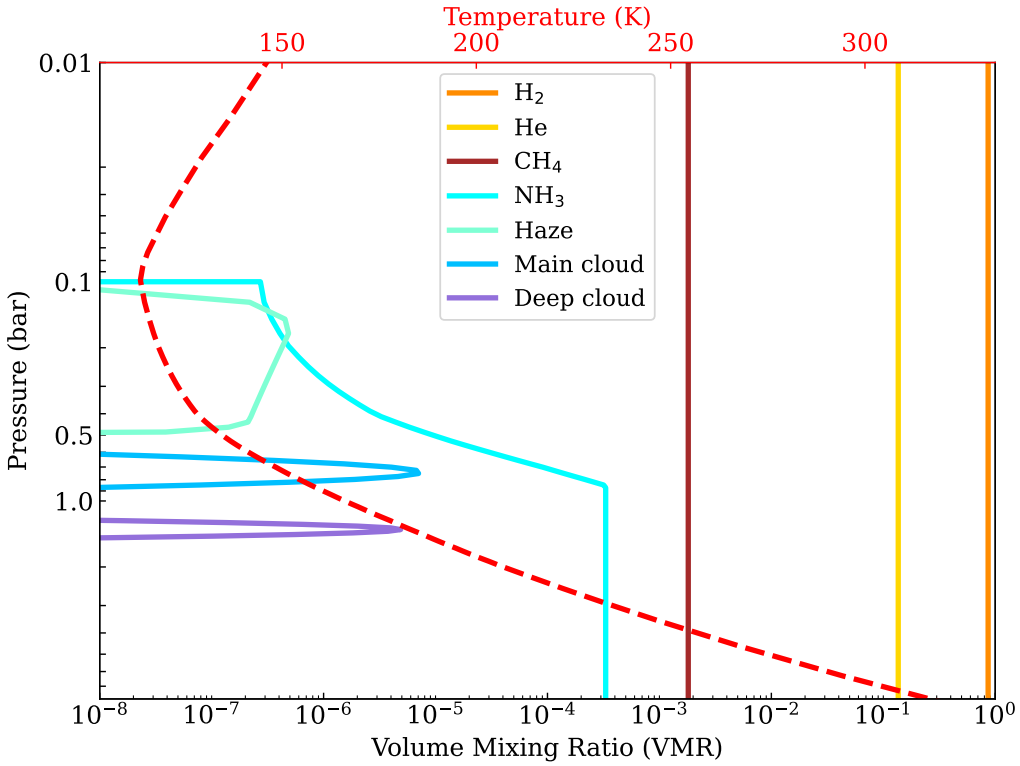


Figure 6.12: Gaseous and aerosols vertical profiles used to model JIRAM data in the solar range. The H_2, He, and CH_4 are held fixed. All the other profiles represents are parametrized as explained in the text. The considered pT profile is showed using a red dashed line.

and a relative humidity (RH). Once the saturated vapor pressure profile for ammonia is computed from the equation presented in Chapter 2, the expected mixing ratio can be computed as follows:

$$\mathrm{mr}_{\mathrm{sat}}(p,T) = \frac{p_{\mathrm{sat}}(T)}{p}\frac{\mathrm{RH}}{100}. \tag{6.1}$$

The considered mixing ratio profile is defined as:

$$\mathrm{mr}_{\mathrm{NH_3}}(p,\mathrm{VMR},\mathrm{RH}) = \begin{cases} \mathrm{VMR} & \text{if } \mathrm{mr}_{\mathrm{sat}}(p,T) > \mathrm{VMR} \\ \mathrm{mr}_{\mathrm{sat}}(p,T) & \text{if } \mathrm{mr}_{\mathrm{sat}}(p,T) < \mathrm{VMR} \end{cases} \tag{6.2}$$

- a slab-like tropospheric pure-reflecting haze. The profile has four free parameters, to be adjusted during the fit procedure: the effective radius of the haze in microns (r_h), the central pressure level in bar (p_h), the width of the slab in bar (w_h), and the number density of the haze expressed in part/cm^3 (N_h). The so-defined profile assumes a constant number density in altitude per unit volume between $p_h + \frac{1}{2}w_h$ and $p_h - \frac{1}{2}w_h$. It is important to remark that a constant number density profile does not result in a constant volume mixing ratio profile, since the mixing ratio profile depends on the atmospheric density. Following (Sromovsky & Fry, 2010b) I considered this haze to be composed of a material with a refractive index of (1.4,0). The optical properties and the Heyney-Greeinstein asymmetry parameter (see Chapter 3) were computed using a Mie-based code[1] in Python that implements the methods from Bohren

[1] https://github.com/nasapsg/scattering

& Huffman (1983). A log-normal size distribution with a variance of 0.3 was considered. Since I will always consider log-normal populations of particles throughout the thesis, the Heyney-Greeinstein approximation is robust. In fact, as seen in Chapter 3, populations of particles tend to flatten the ripples in the phase function and in the Mie efficiencies.

- a main cloud layer with a Gaussian number density vertical profile. In order to replicate a profile similar to the computations of Atreya et al. (1999) and to the measures of the Galileo mission nephelometer (Ragent et al., 1998), I decided to use a fixed FWHM of 0.04 bar. The profile has three free parameters, to be adjusted during the fit procedure: the effective radius of the cloud, in microns (r_C), the pressure level of the cloud deck (p_C), and the maximum number density, expressed always in part/cm^3 (N_C). The parameter p_C can be considered as the mean (in pressure levels) of the Gaussian, whose maximum value (in number density) is constrained by N_C. The composition of this cloud, i.e. the refractive index, must be fixed prior to the retrieval in order to compute the optical properties and insert them in PSG.

- a deep cloud layer with a Gaussian number density vertical profile. I considered a fixed FWHM of 0.04 bar and a fixed effective radius of 1 μm. The reason of this choice will be discussed in the next section. The composition was chosen to be either Imanaka et al. (2012) tholins or a simple gray cloud n =(1.4, 0). This profile has two free parameters: the pressure level in bar (p_D) and the number density in part/cm^3 (N_D). Also in this case the optical properties were computed using the same Mie-based code cited above considering a log-normal size distribution with a variance of 0.3.

All the parameters listed above are considered using their corresponding logarithmic values (natural logarithm for pressures and common logarithm otherwise). This approach greatly stabilizes the retrieval stage that I will describe in the following paragraphs.
Using the Python packages `PyOE` (Maahn et al., 2020) and `emcee` (Foreman-Mackey et al., 2013) and the PSG API I wrote a fully pythonic retrieval code that consists in different steps:

1. **Reading**. The code reads the input JIRAM spectrum and the corersponding viewing conditions, in terms of incidence, emission, and phase angles.

2. **Creating a template .cfg file**. The code prepares the .cfg file, as described in the first section of this chapter. Namely, it modifies the parts that define the properties of the RT simulation, such as number of streams, number of Legendre decomposition polynomials, resolving power and spectral range. I always decided to use six streams and a decomposition in 99 Legendre terms, that represents the maximum number supported in PSG. Choosing a high number of Legendre terms can make the simulations longer but it avoids problems in representing the phase function accurately as showed in Chapter 3. This part of the code also selects the spectral databases or custom input cross-section table to be adopted.

3. **Geometry**. Starting from the template .cfg file the code modifies the parts containing the viewing angles and inserts the ones relative to the considered JIRAM spectrum. In this way, a so-called geo-template is created.

4. **Atmosphere setting**. In this part of the code it is possible to set the considered model atmosphere as described in the previous section. Namely, the code defines: the number of atmospheric layers, the pT profile, the Python-functions that describe the gases mixing ratios, and the Python-functions that define the aerosol densities.

5. **Define the write_cfg function**. This function is the core of the retrieval. It rewrites the rows of the geo-template in order to insert the atmosphere layers. In order to perform this task, it adopts the functions defined in the previous point. In the solar case, therefore, write_cfg is a function of the free parameters defined above in the section (e.g., the haze and cloud effective radii, the ammonia relative humidity, etc.). The output of the function is a new cfg.txt file that was created starting from a set of input parameters.

6. **Define the forward model**. This is just a function that depends on a series of free variables (that in the previous step were the parameters of write_cfg). This function uses write_cfg in order to write a cfg.txt file. Then it calls the PSG remote operation API and starts a multiple scattering radiative transfer run. Eventually, it reads the PSG output file and returns a spectrum. This spectrum is provided in a wavelength range larger than the JIRAM one and at much higher spectral resolution. This choice of settings was driven by the fact that the PSG synthetic spectrum must be convoluted with the actual JIRAM responsivity function, as defined in Adriani et al. (2017) and in Chapter 4. Therefore a broader range and a higher resolving power than JIRAM are needed to avoid errors caused by interpolation or convolution.

7. **Define the error estimator function**. It is an ancillary function that estimates the JIRAM Noise Equivalent Radiance or NER starting from the input spectrum. The NER function is a quadratic sum of the photon shot noise that goes as the square-root of the measured signal, and of thermal noise as defined in Adriani et al. (2017) and explained in Chapter 4.

8. **Perform the retrieval**. Once that setting is complete it is possible to run the retrieval. This can be done either according to an Optimal Estimation algorithm or using a MCMC approach. In the former case, the PyOE package is adopted, defining the a priori values, the a priori covariances , the regularization parameter, and the convergence criterion required by the Bayesian formalism, see Chapter 3. I decided to always use a value between 5 and 10 for the regularization parameter after a series of preliminary tests. In the other approach, the MCMC, it is needed to define the priors, the likelihood function, and the chain' properties required by the Markov Chains formalism, see also Chapter 3. In any approach, it is also needed to set the convergence criterion. This can easily be represented by a threshold value on the Chi squared or be represented by a further parameter.

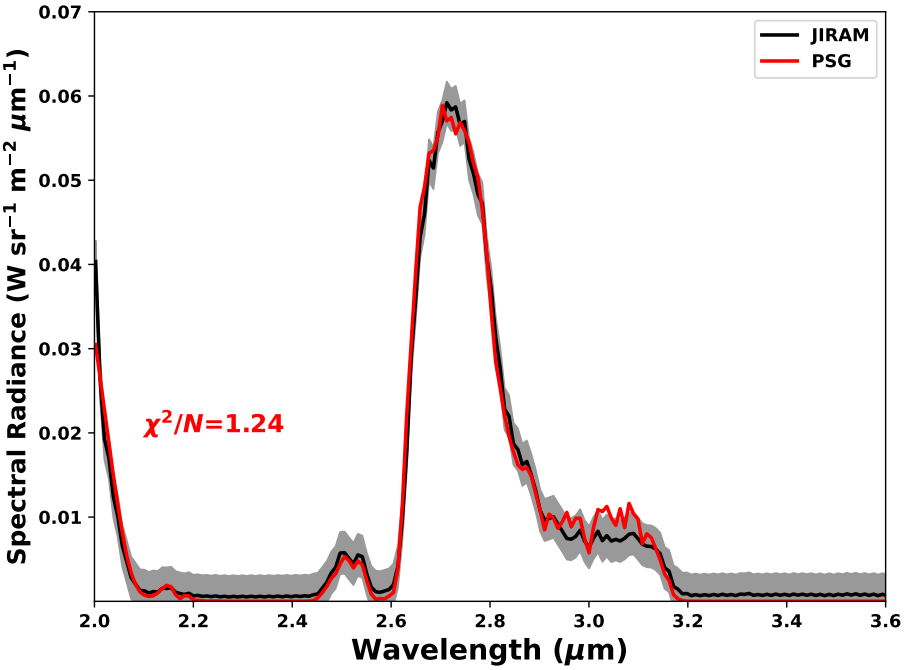


Figure 6.13: Comparison between a real JIRAM spectrum (black) and the PSG best-fitting model (red) obtained after an OE retrieval.

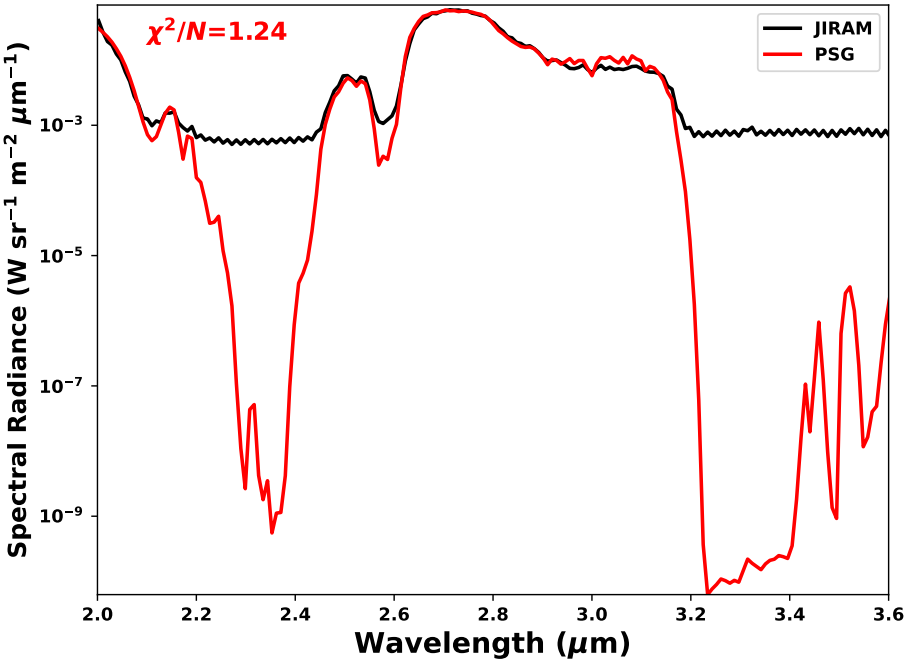


Figure 6.14: Same as Fig. 6.13 but using log-scale for the measured radiances.

The modular approach adopted in my pipeline makes it easily changeable and extendable to other ranges or instruments.
In Table 6.1 I list and summarize the parameters used to model JIRAM spectra in the solar range. I also list the standard a-priori values and uncertainties (as defined in Chapter 3) chosen starting from the literature results presented in Chapter 5. In Fig. 6.13 it is possible to observe the results of a retrieval of a typical JIRAM spectrum in the solar range. I chose the main cloud to be composed of Titan's tholins as measured by Imanaka et al. (2012) in order to follow the findings of Grassi et al. (2021) and Sindoni et al. (2017). To compute the optical properties a log-normal distribution with a variance of 0.3 and an effective radius of 2.5 μm was considered. The fit looks quite good in the linear scale as shown by the relative chi-square value. The main reflectance peaks are well fitted and explained by the chosen aerosol parametrization. However, if the log scale is used for the radiance values, as in Fig. 6.14, it is possible to note some second-order discrepancies in different regions: (1) near 2 μm, (2) between 2.2 and 2.4 μm, (3) between 2.55 and 2.6 μm, (4) between 2.9 and 3.1 μm, and (5) after 3.2 μm. Between 2.9 and 3.1 μm it is possible to probe the stratosphere of Jupiter. In this window the PSG simulations seem to be higher than the JIRAM signal meaning that I lack of an absorber that can either be identified in the hydrocarbon species predicted by Moses et al. (2005) or by the presence of a further **absorbing** stratospheric haze as suggested by Park et al. (2024). However, as the inclusion of this absorber would lead to a negligible improvement in the fitting quility, and as I am mainly interested in characterizing the Jovian troposphere, I decided to not include any further stratospheric aerosol species.
In the other afore-mentioned windows the JIRAM data show a strange plateau in signal that cannot be described by any cloud of gas species. In fact, the large discrepancies are induced by the presence of a straylight, i.e. a spurious light that reaches an optical system's focal plane through a path other than the intended one. This straylight was already identified in Tosi et al. (2024) in the case of observations of the icy moon Ganymede. In that case, it was removed using a sigmoid fit of the raw data. In the Jupiter case removing the straylight it is far more complex and it is still an open topic in the JIRAM team at the time this thesis has been written. This thesis work contributed to the identification of the problem and in the first raw estimate of the straylight background expected for JIRAM, that is $10^{-3}\,W sr^{-1} m^{-2} \mu m^{-1}$. Under this threshold JIRAM data cannot be considered as reliable.

6.4 Choosing the cloud parametrization

As described in Chapter 5, clouds and aerosols are the main driver of spectral shape and intensity in the 2-3.2 μm range. However, the physical effects of clouds in a multiple scattering atmosphere are very degenerate, i.e. different cloud structures could lead to similar simulated spectra (see Chapter 3). Therefore, prior to choosing the cloud parametrization discussed in the previous section I performed a series of tests that I will summarize in this section. I investigated the role of the cloud parametrization on the resulting retrievals. The cloud structure eventually adopted in my analysis (a haze + two thin clouds) and detailed above was indeed

Parameter	Symbol	x_a	σ_a	Reference
Logarithm (10) of the haze's effective radius	$\log r_h$	-0.5 (0.316 μm)	0.5	
Logarithm (10) of the main cloud's effective radius	$\log r_C$	0.5 (3.16 μm)	0.5	
Logarithm (10) of NH_3 deep VMR	$\log \mathrm{NH}_{3VMR}$	-3.48 (331 ppm)	0.1	Li et al. (2017)
Logarithm (10) of NH_3 deep relative humidity	$\log \mathrm{NH}_{3RH}$	1.7 (50 %)	0.20	Flasar et al. (2004), Fletcher et al. (2016a)
Logarithm (e) of the haze's pressure level	$\ln p_h$	-1.2 (0.3 bar)	0.5	Simon-Miller et al. (2001a), Sromovsky & Fry (2010
Logarithm (e) of the haze's width	$\ln w_h$	-1.5 (0.22 bar)	0.4	Grassi et al. (2021)
Logarithm (10) of the haze's density	$\log N_h$	2 (100 part./cm^3)	1	Sindoni et al. (2017), Grassi et al. (2021)
Logarithm (e) of the main cloud's pressure level	$\ln p_C$	-0.1 (0.9 bar)	0.5	Sindoni et al. (2017), Grassi et al. (2021)
Logarithm (10) of the main cloud's density	$\log N_C$	1.6 (40 part./cm^3)	1	Sindoni et al. (2017), Grassi et al. (2021)
Logarithm (e) of the deep cloud's pressure level	$\ln p_D$	0.2 (1.22 bar)	0.5	Braude et al. (2020)
Logarithm (10) of the deep cloud's density	$\log N_D$	2 (100 part./cm^3)	1	Sindoni et al. (2017), Grassi et al. (2021)

Table 6.1: Retrieval parameters. Their meaning, symbols, a priori values (x_a), and standard deviation of the a priori (σ_a) are given in the first colums. In the last colums the references used to set the values are listed.

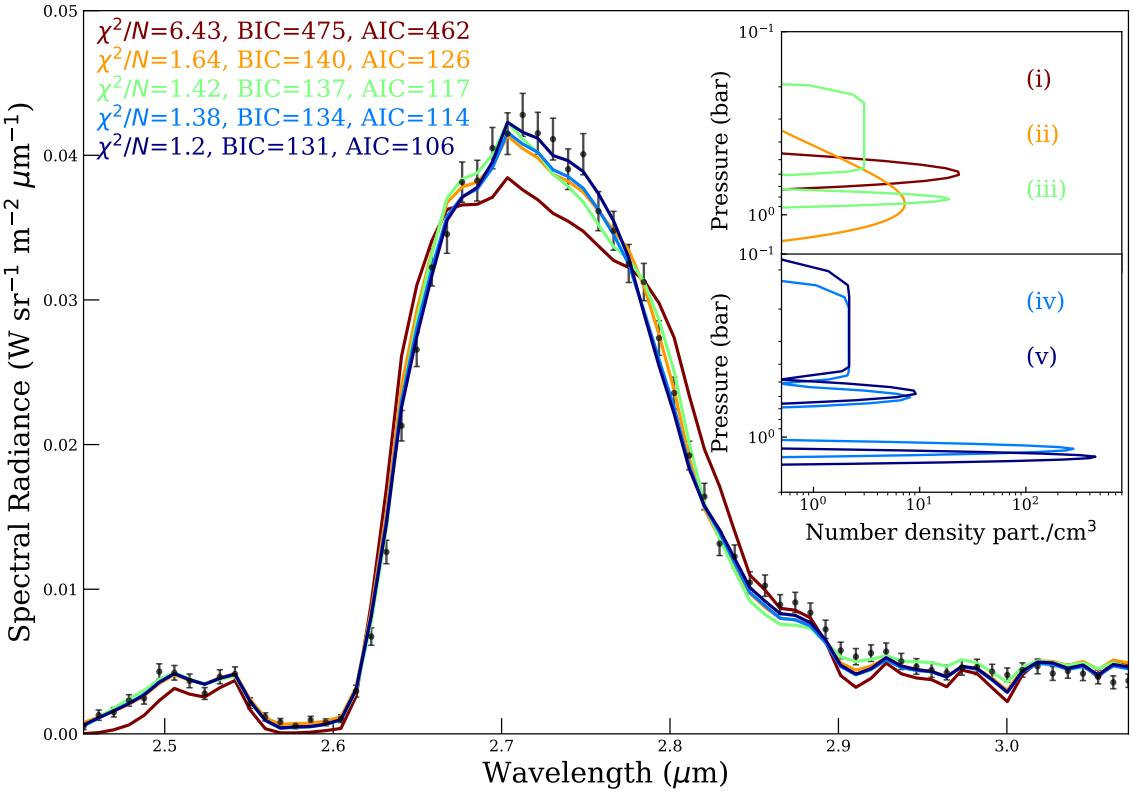


Figure 6.15: Comparison between different PSG/OE retrievals on a JIRAM test spectrum, obtained varying the aerosol parametrization. In the sub-panels it is possible to observe also the best-fitting aerosol's profiles with the same color scheme of the best-fit models.

selected after a preliminary assessment aimed to mitigate the high degeneracy of retrieval results when multiple scattering is involved. Focusing on a typical JIRAM spectrum from Grassi et al. (2021) and Sindoni et al. (2017), I tested Optimal Estimation retrievals using five different cloud structures (see Fig. 6.15): (i) a single tholin Gaussian cloud, constrained to not become wider (FWHM) than 0.2 bars (red curves), (ii) a single Gaussian tholin cloud with no constraints on its width (orange curves), (iii) a single fixed-width (Atreya et al. (1999)-like) gaussian tholin cloud and a pure reflecting haze (green curves), (iv) the "final" cloud structure, but with the number density of the deepest cloud considered fixed (sky blue curves), and (v) the "final" cloud structure (dark blue curves). In Fig. 6.15 it is possible to observe the best-fitting OE retrievals of the test JIRAM spectrum and the best-fitting cloud profiles in each case. The haze + two clouds structure is indeed the one that provides the lowest chi-squared value, justifying its adoption for the bulk of my analysis. It is worth to remark that a very similar structure was found to fit very well visible data from VLT/MUSE (Braude et al., 2020).
Notably, this sensitivity test proved to be extremely informative also on other aspects. Firstly, each aerosol structure is consistent with the others, suggesting that the main source of reflectivity in the 2.5-3 μm range should lie between 0.6 and 1 bar, but requiring, at the same time, an extended layer of particles between 0.5 bar and the tropopause. Secondly, the (ii) and (iii) structures both provide a similar fit quality and reflect the degeneracy between the cloud extension and its number density. This means that it is very difficult to distinguish between a single largely extended cloud (from 2 to 0.1 bar) and a haze layer combined with a thin denser cloud. This degeneracy is unbreakable from JIRAM data alone, so I decided to be guided by physics and theoretical predictions. Indeed, it is physically plausible that an extended layer of small particles may lay in the upper troposphere in virtue of the photochemistry processes in the upper Jovian atmosphere, consistently with my "final" structure. Moreover, Jupiter is expected to have very high values of the sedimentation parameter - i.e. compact and not-extended clouds - (Ackerman & Marley, 2001) contrary to, for example, the extreme hot Jupiter planets (Robbins-Blanch et al., 2022). Compact clouds were also predicted by equilibrium condensation models (Atreya et al., 1999) and measured in the peculiar regions called hot spots by the Galileo nephelometer (Ragent et al., 1998). Lastly, it is worth discussing the role of the deeper cloud that is mandatory to obtain higher reflectivity and achieve better-fit quality in the [2.7-2.75] μm range. This physically means that the main cloud layer is not completely optically thick but that some radiation can pass through, to reach a deeper deck and be reflected and added in this way to the total observed radiation budget. However, in the JIRAM solar range we are not sensitive to the optical properties (i.e. how this cloud reflects the light as a function of wavelength) of this deep cloud. We, instead, are sensitive to its pressure level and in te amount of reflected (or blocked) radiation. The second effect is regulated both by the effective radius, the vertical extension, and the density of the clouds in a degenerate combination. Therefore, in my solar retrievals I decided to fix both the radius and the vertical extension of the deep cloud to values consistent with the theoretical computations of Ackerman & Marley (2001).

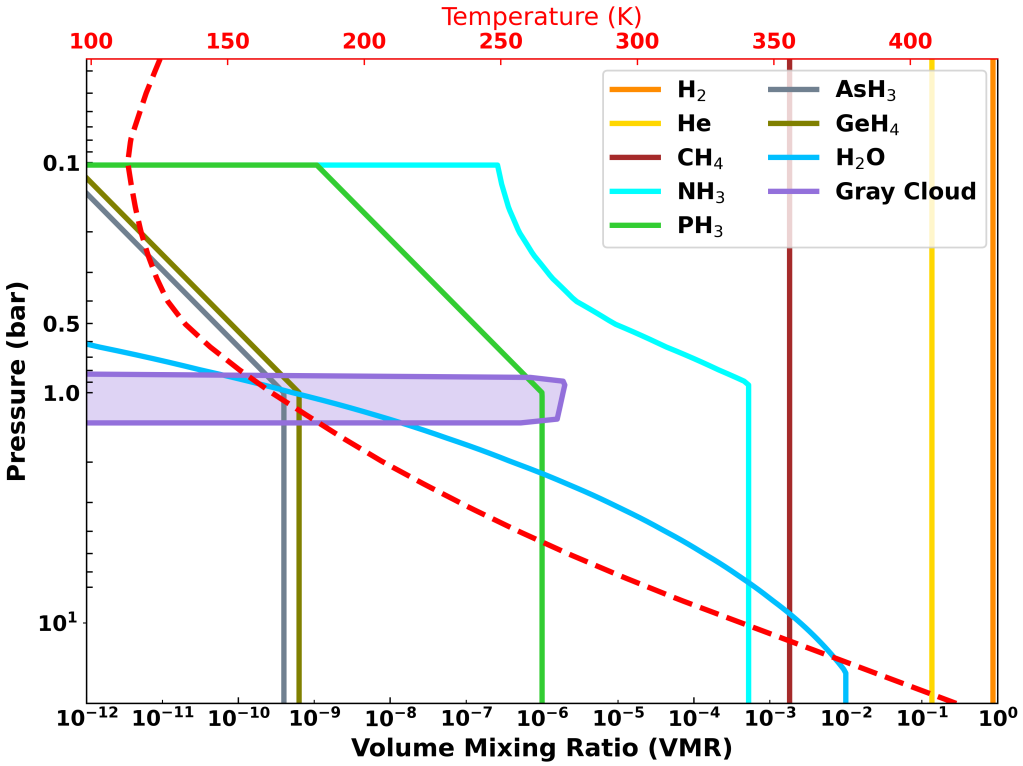


Figure 6.16: Gaseous and aerosols vertical profiles used to model JIRAM data in the thermal range. The H_2, He, and CH_4 are held fixed. All the other profiles represents are parametrized as explained in the text. The considered pT profile is showed using a red dashed line.

6.5 Simulations and retrievals of the thermal range

As we saw in Chapter 5, in the solar range we are highly sensitive to the presence of clouds and of ammonia. In the thermal range clouds are still a very important driver for the signal level, as they may block and absorb the black body emission from the interiors. However, from this act of "blocking" it is possible to infer constraints mainly on total opacity, which in turn depends in a degenerate way on both mass and effective radius. Therefore, in the thermal range, it is very difficult to have a sense of the vertical structure of the clouds. Similarly, we are mostly sensitive to deep mixing ratios of the minor atmospheric constituents because of the contribution functions discussed in Chapter 5. The term "deep" refers to pressures >0.8 bar. Moreover, the presence of gaseous species in the upper troposphere is regulated by precise physical phenomena such as condensation and photochemistry. Therefore, the best way to proceed in order to model the thermal range is to consider as a starting point the results of solar range retrievals. Namely, initial guesses from the solar range allows one to constrain the vertical structure of the aerosols and the presence of gaseous ammonia in the upper troposphere, two key parameters that shape the Jovian spectrum. In order to perform simulations and retrieval of the JIRAM thermal window I adopted the following model atmosphere, following the initial analysis of Grassi et al. (2020), ultimately derived from Irwin et al. (1998). The retrieval scheme is exactly the same as the one described in the previous section. The model atmosphere can be described as follows, see Fig. 6.16:

- a fixed pressure temperature profile, extrapolated from Seiff et al. (1997). The model atmosphere considers a stack of 171 plane-parallel layers. spanning over the 22-0.01 bar range .

- fixed mixing ratio profiles for H_2, He, and CH_4, as explained in the section 6.3.

- variable gaseous ammonia and water profiles, modeled by a deep volume mixing ratio (VMR) and a relative humidity (RH) and that were introduced in section 6.3. These free parameters can vary during the retrievals but the ammonia-related ones are constrained to be consistent with the values obtained from the solar retrievals; to do so the iteration is either accepted or rejected if the retrieved VMR_{NH3} and RH_{NH3} values are consistent, within the uncertainities, with the ones obtained from the solar range retrievals.

- variable profiles for phosphine (PH_3), germane (GeH_4) and arsine (AsH_3). The vertical mixing ratio profiles are approximated as constant and equal to a deep volume mixing ratio (VMR) value until a pressure level of 0.7 bar, which will be referred to as the "knee pressure level". For pressures lower than the knee pressure the profiles decay following a constant fractional scale height (FSH) of 0.25 . The knee pressures and FSH are considered as fixed, in order to cope with the high degeneracy of the problem. These are chosen to be consistent with the retrievals of Grassi et al. (2020) and Fletcher et al. (2016a) that studied large regions on the Jupiter disk

- a single gray cloud. "Gray" term is used to indicate that cloud's optical properties are assumed as independent from wavelength (i.e. constant over the considered spectral range) during the radiative transfer stage. The cloud has a single scattering albedo of 0.7-0.8 and an asymmetry parameter of 0.3-0.4, chosen to be consistent with Giles et al. (2017). Its vertical number density profile is approximated as a slab and has four free parameters, to be adjusted during the fit procedure: the effective radius of the haze in microns (r_g), the central pressure level in bar (p_g), the width of the slab in bar (w_g), and the number density of the cloud (assumed uniform in altitude inside the slab), expressed in part/cm^3 (N_g). This gray, slab-like cloud covers the pressure levels of the main and deep clouds presented in the previous subsection. These parameters are constrained to reproduce a similar total aerosol optical depth as the one derived from the solar range retrievals. For this purpose, at the end of each retrieval iteration the total column optical depth is computed considering the retrieved cloud structure, and the extinction coefficient at 3 μm (the latter as estimated considering an ω=0.8, g=0.3, and the retrieved radius). At this point, the iteration is either accepted or rejected if the computed optical depth value is consistent, within the uncertainities, with the one obtained from the solar range retrievals.

It is worth reminding that the haze is not expected to have a significant contribution in the thermal range (Drossart et al., 1998) and therefore it was not considered in my model atmosphere.
In summary my model atmosphere has a total of 11 free parameters. I listed them and the relative a priori standard values and uncertainties in Table 6.2. Contrary

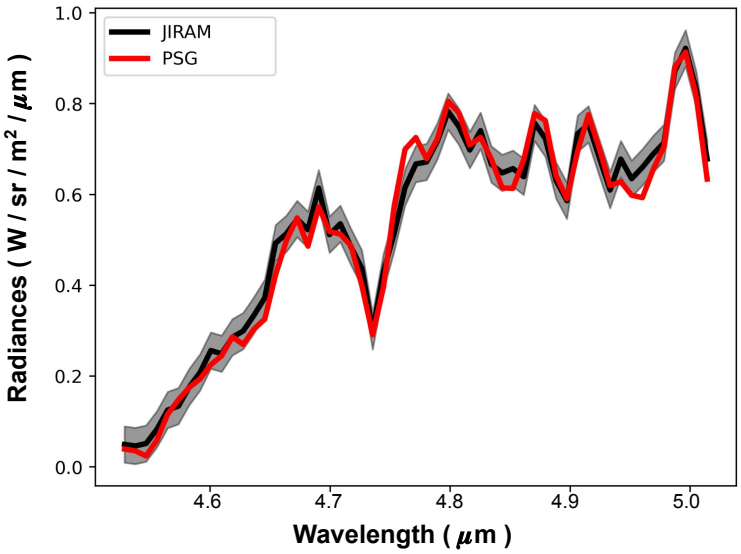


Figure 6.17: Comparison between a real JIRAM spectrum (black) and the PSG best-fitting model obtained after an OE retrieval.

to the solar case where the chi square can be considered as a good convergence indicator, the thermal retrievals are considered to be converged when a threshold level of 0.12 of the quality parameter q, defined as (Grassi et al., 2020):

$$q = \sum_{n=1}^{N} \left| \frac{\mathcal{F}_n - y_n}{\mathcal{F}_n} \right| \cdot \frac{1}{N \cdot 100}, \tag{6.3}$$

is reached.
It is worth to stress that during my retrievals PSG simulations of JIRAM data included a full treatment of multiple scattering. This is a significant improvement with respect to the algorithm presented in Grassi et al. (2020), where the much simpler two-stream approximation was considered. In Fig. 6.17 it is possible to observe the results of a retrieval of a typical JIRAM spectrum.

6.6 Simulations and retrievals of the whole range

Using the methods already described in Sections 6.3 and 6.5 it was straightforward to build a pipeline able to both simulate JIRAM data in the entire wavelength data and subsequently perform a retrieval.
Regarding the atmospheric parametrization, I used the same pT profile and gaseous profiles described in Section 6.5. I find adequate to use the same aerosol structure introduced in Sections 6.3 and 6.4, i.e. a slab-like haze and two Gaussian shaped clouds. However, in order to fit the entire JIRAM range it is needed to let the width of the two Gaussians, namely w_C and w_D, to be two further free parameters. In the same way also the radius of the deep cloud, r_D, is set to be a free parameter.
Why is this happening ? In the solar range we are mostly sensitive to the reflectance of solar radiation which is largely induced by the main cloud. The reflectance depends strongly on the composition of the cloud and its effective radius, and secondly

Parameter	Symbol	x_a	σ_a	Reference
Logarithm (10) of NH_3 deep VMR	$\log NH_{3VMR}$	-3.48 (331 ppm)	0.5	Li et al. (2017)
Logarithm (10) of NH_3 deep relative humidity	$\log NH_{3RH}$	1.7 (50 %)	0.5	Flasar et al. (2004), Fletcher et al. (2016a)
Logarithm (10) of H_2O deep VMR	$\log H_2O_{VMR}$	-2 (0.01)	0.5	Li et al. (2020a)
Logarithm (10) of H_2O deep relative humidity	$\log H_2O_{RH}$	1 (10 %)	0.5	Fletcher et al. (2016a)
Logarithm (10) of PH_3 deep VMR	$\log PH_{3VMR}$	-6 (1 ppm)	1	Li et al. (2017)
Logarithm (10) of AsH_3 deep VMR	$\log AsH_{3VMR}$	-9.5 (0.3 ppb)	1	Li et al. (2017)
Logarithm (10) of GeH_4 deep VMR	$\log GeH_{4VMR}$	-9.3 (0.5 ppb)	1	Li et al. (2017)
Logarithm (10) of the gray cloudeffective radius	$\log r_g$	0.3 (2 μm)	0.5	Giles et al. (2017)
Logarithm (e) of the gray cloud pressure level	$\ln p_g$	-0.2 (0.8 bar)	0.5	Giles et al. (2017), Grassi et al. (2020)
Logarithm (e) of the gray cloud width	$\ln w_g$	-1.5 (0.22 bar)	0.5	Grassi et al. (2020)
Logarithm (10) of the gray cloud density	$\log N_g$	0.7 (5 part./cm^3)	1	Giles et al. (2017), Grassi et al. (2020)

Table 6.2: Retrieval parameters. Their meaning, symbols, a priori values (x_a), and standard deviation of the a priori (σ_a) are given in the first colums. In the last colums the references used to set the values are listed, together with the median retrieved uncertainties.

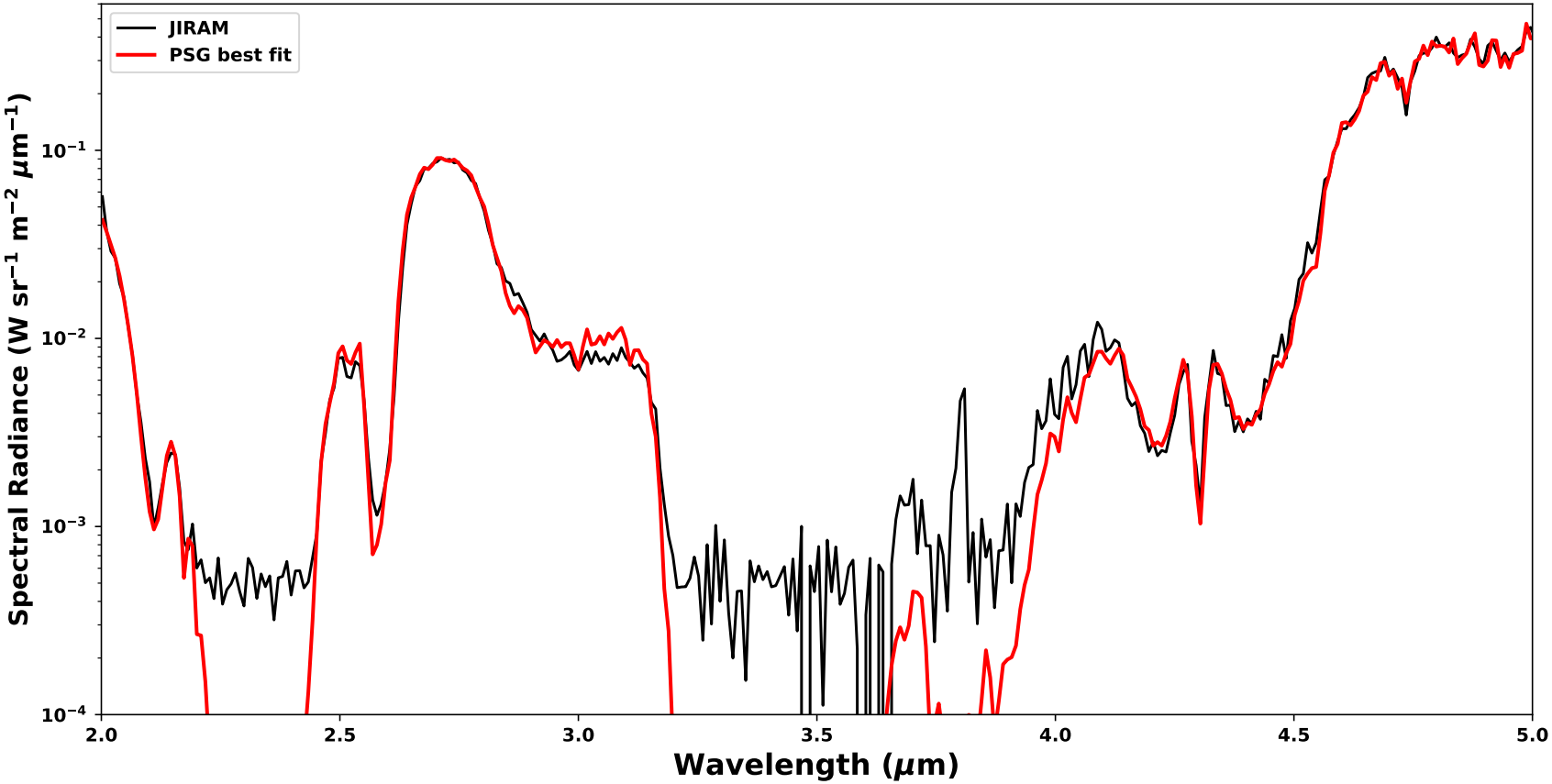


Figure 6.18: Comparison between the JIRAM mean spectrum of the SEB (black) and the PSG best-fitting model obtained after an OE retrieval.

on a degenerate combination of its density, and width. In particular, the density and the width are known to be strongly correlated. Therefore it was reasonable to fix the clouds width to reasonable values expected by theory to perform solar retrievals. The introduction of the thermal range can provide a further constraint that can provide a separate estimation of the density and effective radius of clouds. In this way, it is possible to extract an estimate of the clouds width from the retrievals. In the end, the adoptedatmospheric parametrization exploited to model the whole entire JIRAM range consists of 18 free parameters, namely r_h, r_C, r_D, p_h, w_h, N_h, p_C, w_C, N_C, p_D, w_D, N_D, NH_{3VMR}, NH_{3RH}, H_2O_{VMR}, H_2O_{RH}, PH_{3VMR}, AsH_{3VMR}, and GeH_{4VMR}. Because of the large number of free paramaters the only way to accurately explore the parameter space is through MCMC. Therefore, I never used OE to perform full range retrievals of JIRAM data in this thesis work. However, the use of MCMC makes the convergence time become significantly high.
In Fig. 6.18 it is possible to observe the results of a retrieval of a JIRAM spectrum that represents the mean of the SEB observations during the PJ1. To perform the fit I considered the deep cloud as gray ($n = (1.4, 0i)$) and the main cloud as composed of Imanaka et al. (2012) tholins. I will come back on this in the last section of Chapter 7.

Chapter 7

The search for ammonia clouds in the Northern Temperate domain using JIRAM spectral data

7.1 Rationale

As discussed in Chapter 2, equilibrium condensation models predict the existence of pure ammonia cloud decks around 0.5-0.7 bar in the Jovian atmosphere (Atreya et al., 1999). However, we also saw in Chapter 5 that when atmospheric retrievals are applied to visible and infrared spectral data it is very difficult to obtain reasonable fits if ammonia clouds are invoked. Most of the spectral features of ammonia ice, expected at 2, 3, and 11 μm (Howett et al., 2007) are very difficult to detect and measure. Although at the same wavelengths we should expect also the gaseous ammonia absorption features, even at higher spectral resolution the ammonia ice spectral features were difficut to be observed (Harkett et al., 2024) on the Jovian disk. On the contrary mixtures of pure ammonia and ammonium hydrosulfide (Sromovsky & Fry, 2010a) or Titan's tholins (Sindoni et al., 2017; Grassi et al., 2021) seem to provide better fits. This is reasonable as ammonia ice clouds should produce white clouds while the Jovian disk in the visible is mostly reddish, orange, and grey. The only excpetion is represented by white bright vortex and storm features that usually cover less than $< 2\,\%$of the whole Jovian disk. Here the spectral features of pure ammonia ice were detected by Baines et al. (2002) and Sromovsky & Fry (2018). This hold two fundamental questions: (1) are pure ammonia ice detectable only in correspondence of strong convective events ? (2) If pure ammonia ice is not the main component of Jovian clouds, what is the unkwnown material that compose them ? In order to answer to both of them, in this Chapter I investigated if the data collected by JIRAM in its first perijove passage contain the spectral features of ammonia and how can I use them to obtain constraints and insights on the true nature of the Jovian clouds.

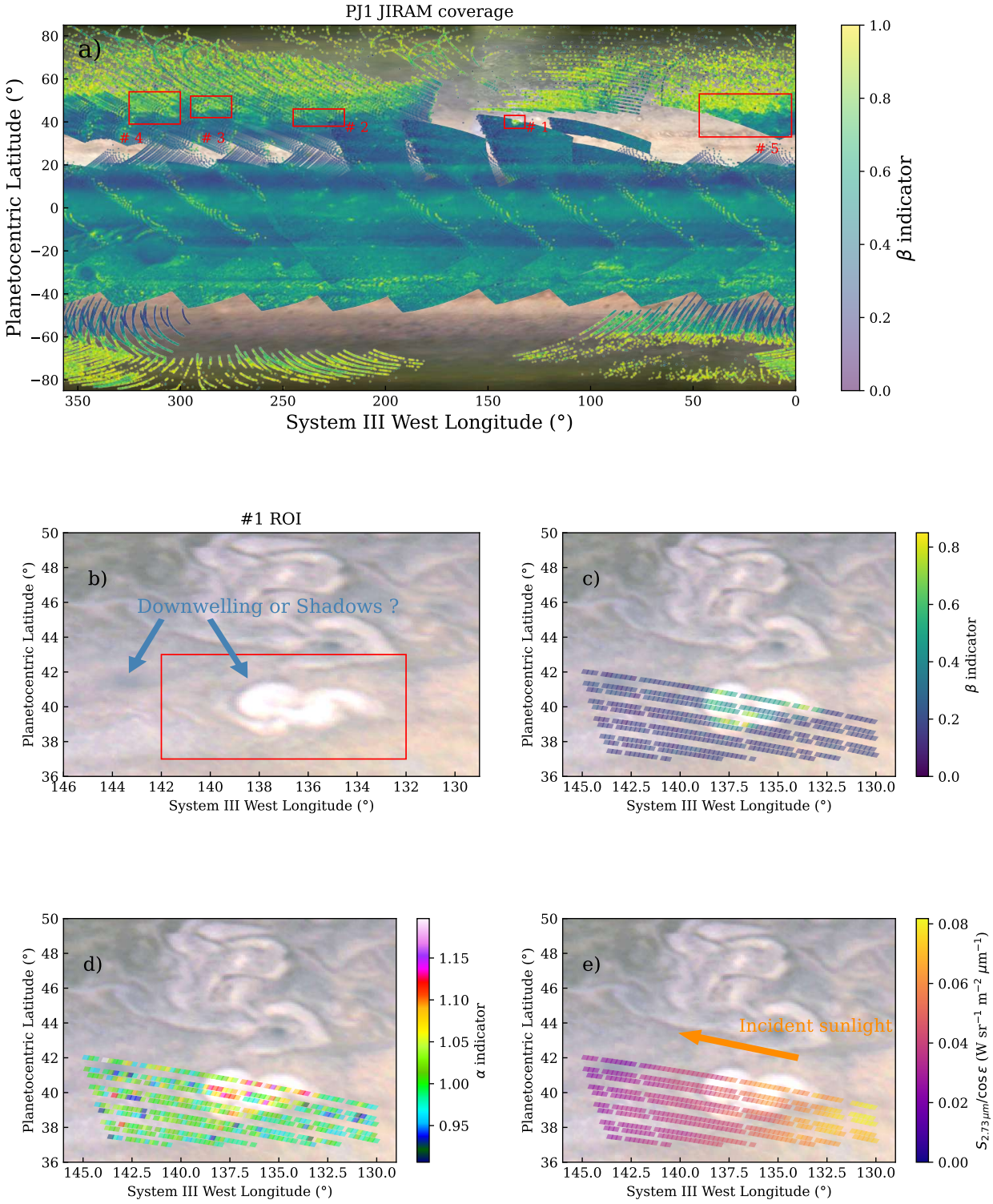


Figure 7.1: Spatial distribution of JIRAM spectra considered in this work and their characteristics. (a) β indicator, Eqn. 7.2, computed using all the JIRAM PJ1 collected and non-corrupted spectra. Five regions of interest (ROIs), where the values seem to form a pattern, are highlighted with red boxes. (b) Zoom on the #1 ROI. (c) β indicator distribution for the #1 ROI. (d) α indicator distribution for the #1 ROI. (e) Signal measured by JIRAM at 2.73 μm corrected for the cosine of the emission angle. For all the panels, the background is a global map created from visible images acquired by the JunoCam.

7.2 Observations

In the work described in this Chapter and also in the following ones I will focus on the JIRAM data collected during the first perijove passage, herafter PJ1, as it is the one with the best spatial coverage. In particular, it was possible to map most of the Jovian disk as it is possible to observe in Fig. 7.1a. In this context, it is also useful to look at the spatial coverage achieved by JunoCam images during the PJ1 passage, that proved sufficient to produce a global mosaic of Jupiter[1], which was already used in Grassi et al. (2021). The composite mosaic was obtained using JunoCam's images acquired with Blue (450-500 nm), Green (500-600 nm), and Red (600-800 nm) filters (Hansen et al., 2017). A portion of this mosaic serves as a reference background in the present analysis. To account for the different acquisition times of JIRAM and JunoCam over the areas of interest—separated by a few hours—and the drift of atmospheric features caused by zonal winds, a manual longitude shift was applied to the JunoCam mosaic coordinates. This shift was determined by minimizing the positional differences between the darker features in JunoCam images (assumed, in most cases, to be regions with thinner upper clouds) and the brighter spots observed in JIRAM infrared (M-filter) images, acquired simultaneously with JIRAM spectral slits.

As I was interested in precisely mapping a possible storm or vortex, I decided to use only the PJ1 data and its optimal spatial resolution for this work. These data were acquired between 2016 August 25 and August 26. The spectra have been corrected for the presence of spikes caused by encounters with energetic particles in the jovian environment (or cosmic rays). I used a modified version of the standard algorithm presented in Whitaker & Hayes (2018) to correct the spectral regions below λ <4.5 μm. Although the method is no longer effective above this limit - because of the frequent gaseous absorption features- my analysis remains nevertheless unaffected since in this Chapter I was interested mainly in the solar reflected signal, in order to retrieve the aerosol properties.

To select a collection of spectra I decided to consider two different and independent spectral indicators, called respectively α and β. They are defined as:

$$\alpha = \frac{\overline{S}_{[2.98-3.02]\,\mu\mathrm{m}}}{\overline{S}_{[2.94-2.98]\,\mu\mathrm{m}}}, \tag{7.1}$$

$$\beta = \frac{S_{4\,\mu\mathrm{m}}}{S_{2.96\,\mu\mathrm{m}}}, \tag{7.2}$$

where the notation S_λ indicates the radiance value in W μm^{-1} sr^{-1} m^{-2} at a reference wavelength λ, while the notation $\overline{S}_{[\lambda_1,\lambda_2]}$ indicates the mean of the radiances of all the channels between λ_1 and λ_2. Both the indicators are expected to be sensitive to the presence of possible high-altitude ammonia ice clouds. The α indicator should be higher if the signal in the [2.94-2.98] μm range is lower, exactly at the position where the absorption feature of NH_3 ice is expected (Howett et al., 2007). The β indicator was selected starting from Fig. 5.8 and 5.12 (Sromovsky &

[1]https://britastro.org/section_information_/jupiter-section-overview/results-from-juno-2016-2017-perijoves-1-10/junocam-at-perijove-1-map-of-the-planet

Fry, 2018). The 4 μm and 2.97 μm wavelengths are characterized by a similar transmission weighting function and therefore they should probe the same pressure level; however, as said for the α indicator, the ammonia clouds are expected to strongly absorb at 2.96 microns. This means that I should get the same value of this indicator almost everywhere on Jupiter, with the exception of regions with absorbing aerosols at 2.96 μm or anomalous high-altitude clouds. In Fig. 7.1 I present the β indicator for all the PJ1 spectra. I note that it is low (< 0.4) for almost all the zones and belts. However, it is possible to note that the indicator is slightly higher in correspondence of the zones, as expected for uplifting regions. The higher values are reached in four regions of interest (ROIs) in the northern hemisphere, marked by red boxes. It is also possible to note that in general higher values are reached in the polar regions. However, in most circumstances this behavior is caused mainly by the extreme observing conditions. In fact, in the polar regions, where an emission and/or incidence angle $> 80°$ or $< 10°$ is easily reached, the β indicator can not be easily compared to equatorial, sub-observer regions, given the enhanced role of multiple scattering. In this Chapter I focused on the ROI #1 for different reasons: (i) in this region the JunoCam images show the occurrence of two vortices that appear similar (both in shape, size, and latitude location) to the "Nautilus" convective storm presented in Guillot et al. (2024a); (ii) this is the first work in literature in which the JIRAM data of these relatively high-latitude regions are analyzed, and, moreover, I wanted to focus on a transition-case between the belts and zones structures and the subpolar regions. The vortex, see Fig. 7.1b, has a "snail-like" form, and a characteristic white color. Both these qualitative characteristics are a hint that we are dealing with a strong convective event that may have brought fresh ammonia in the upper troposphere, i.e. a candidate folded filamentary region (see Chapter 5). In Fig. 7.2 it is possible to compare ROI #1 against a larger fraction of the Jovian disk, both captured by JunoCam.

In total, the number of selected spectra for the #1 ROI are 433. Fig. 7.1c and 7.1d show the patterns of the β and α indicators. Fig. 7.1e shows the signal at 2.73 μm (where the maximum of solar reflected radiation in the JIRAM spectral range is expected), roughly corrected for the emission angle. From the same figures it is also possible to note that the sun illuminates the scene from the right side. This is possibly the cause of the shadow region that can be noted in the left of the snail-like vortex in Fig. 7.1b. Lastly in Fig. 7.3 it is possible to observe the geometrical observing conditions for each of the spectra in the collection.

Moving to spectral data, Fig. 7.4 shows two example spectra in the reflected solar radiation region, one inside and the other outside the vortex. I note that with respect to the spectrum outside the vortex, the inner spectrum exhibits both a shifted solar reflected peak and a weak absorption dip near 2.95 μm. The latter spectral distortion is expected in the presence of pure ammonia ice clouds and was largely discussed in the literature. On the other hand, the displaced reflection peak was not mentioned before in literature (Baines et al., 2002; Sromovsky & Fry, 2018). Indeed, Baines et al. (2002) noted a deficiency in the 2.73 μm channel of NIMS (see Chapter 5) for the candidate SIAC spectra but did not report a change in the spectral shape. In fact, NIMS took and transmitted spectrally sparse data, due to the severe cuts in data volume demanded by the failure of the primary antenna. Probably, this observation has become possible with the improved spectral resolution of JIRAM,

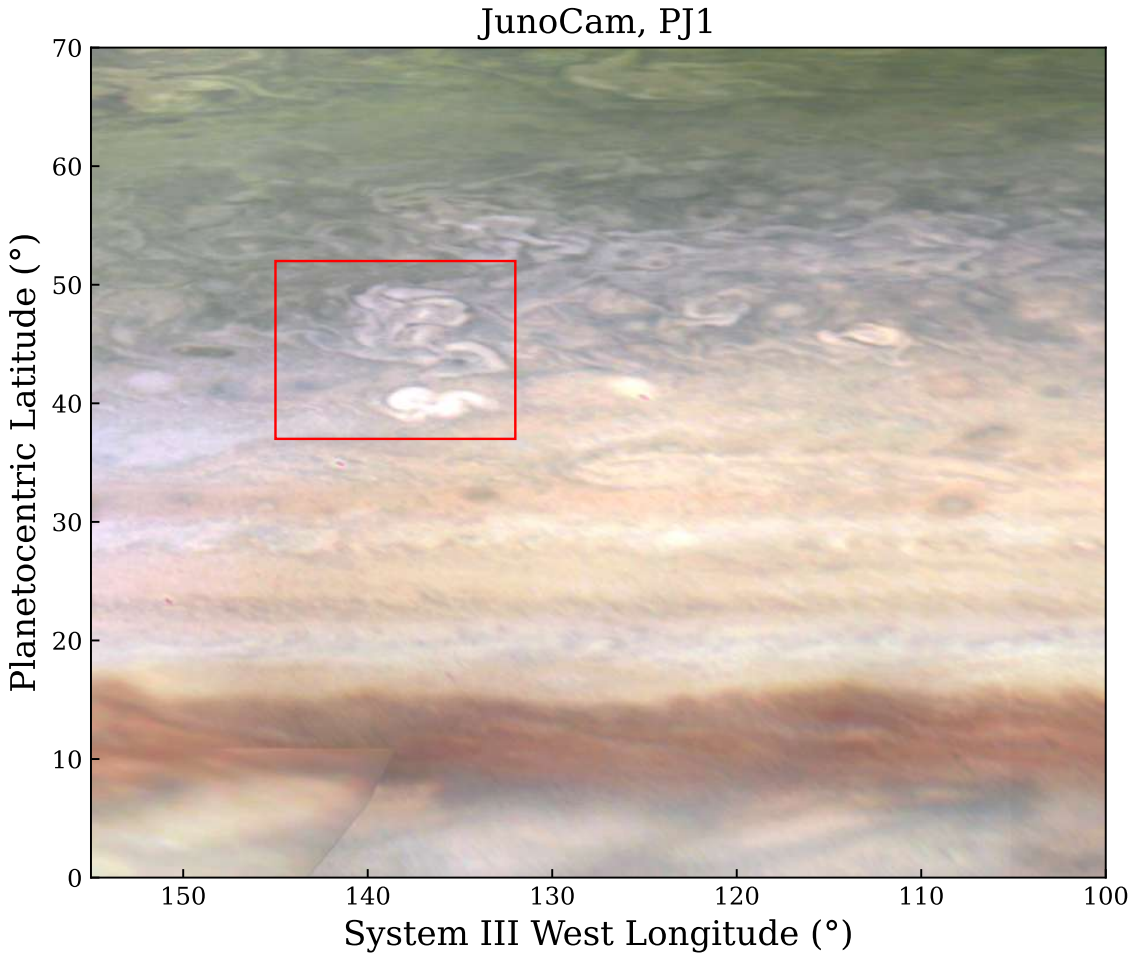


Figure 7.2: The snail-like white vortex structure (the brighter feature) and its sorroundings (red box) captured by Juno Cam, in context with the rest of the Jovian Northern hemisphere.

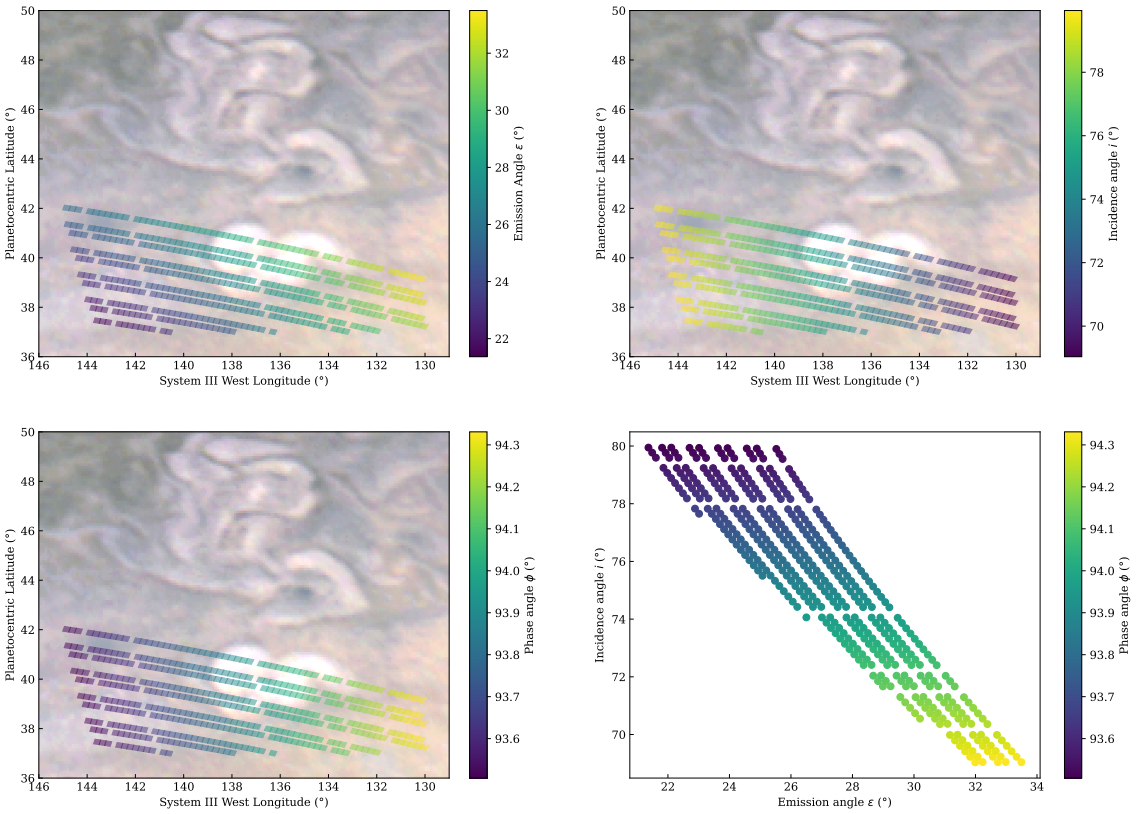


Figure 7.3: Geometry of the JIRAM observations presented in this work. In the first three panel in a clocwise order the JIRAM coverage of the #1 ROI is shown, and the color of each pixel represents (a) the emission, (b) incidence, and (c) phase angles of the observations. The last panel, (d), show the relation between the above mentioned angles.

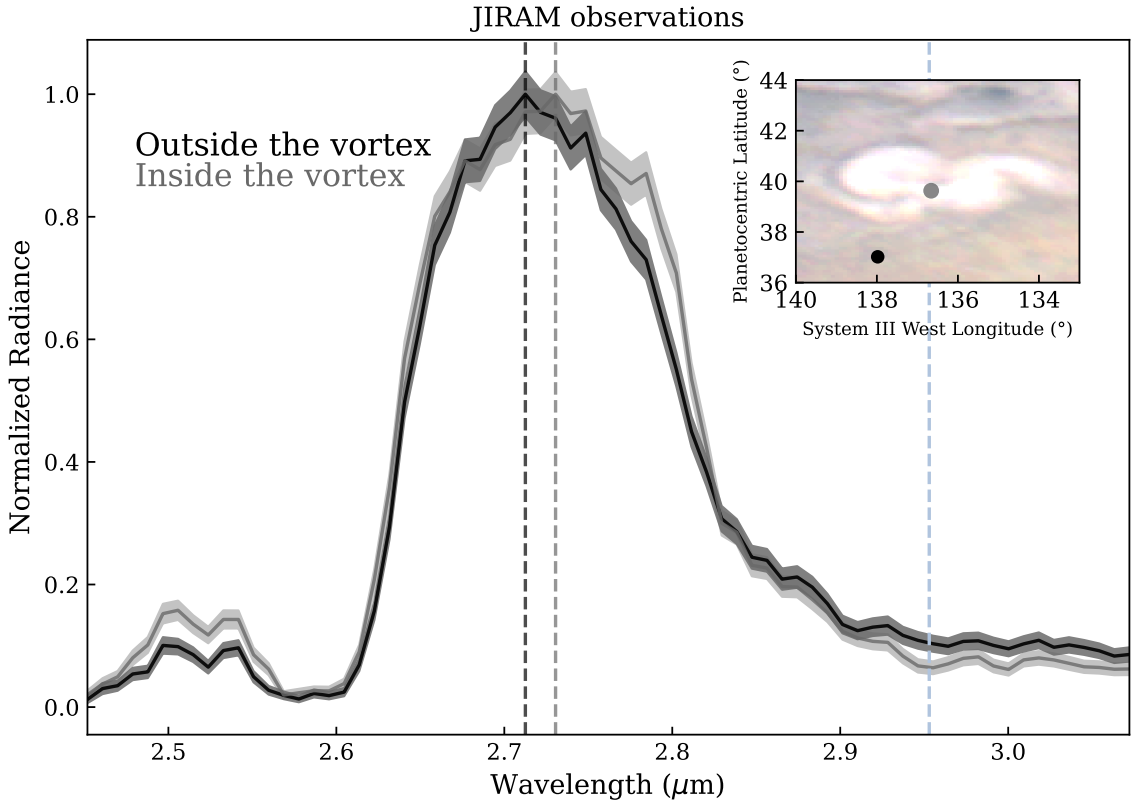


Figure 7.4: An example of two JIRAM spectra in the 2.5-3.1 μm range. The black spectrum was collected outside the white vortex structure, while the gray one inside, as it is possible to observe in the sub-panel. The spectra are normalized for visualization purposes. The location of the maximum of the reflection peak is indicated with dashed lines (black and gray), as the location of the expected absorption feature caused by pure ammonia ice (sky blue).

and thanks to the good quality of the transmitted data. The spectral dichotomy presented in Fig. 7.4 can be connected to the difference in color, and so in single scattering albedo, observed also in the JunoCam visible images. In fact, at these wavelengths the gas opacities of methane and ammonia are rather low, making the contribution from the aerosol layers more significant. In order to perform a more quantitative assessment, a complete retrieval is required. This is the subject of next section.

7.3 Methods

In order to perform the retrievals of the data selected in the previous section I used the methods described extensively in Chapter 6. I only performed retrievals in the 2.5-3.1 μm region of the JIRAM spectrum. This choice is justified by the presence of contaminating straylight and as I am interested in characterizing the main cloud deck that I suppose is the main reason of why we are seeing different reflectance peaks inside and outside the vortex. In particular I used four different compositions for the main cloud:

1. Tholin particles with refractive indexes from Imanaka et al. (2012), following the previous works of Grassi et al. (2021) and Sindoni et al. (2017); it is worth

Model N.	Haze	Main Cloud	Deep Cloud
1	n=1.4, k=0	Tholins (Contaminant), Imanaka et al. (2012)	Tholins (Contaminant), Imanaka et al. (2012)
2	n=1.4, k=0	Pure ammonia ice, Hudson et al. (2022)	Tholins (Contaminant), Imanaka et al. (2012)
3	n=1.4, k=0	50 % ammonia-coated tholins	Tholins (Contaminant), Imanaka et al. (2012)
4	n=1.4, k=0	85 % ammonia-coated tholins	Tholins (Contaminant), Imanaka et al. (2012)

Table 7.1: Summary of the aerosol compositions used in the four different model atmospheres considered to fit JIRAM data.

stressing that Titan's tholins are used as an approximation of a real unknown contaminant material (see Chapter 5);

2. Pure ammonia ice particles with refractive indexes from Hudson et al. (2022);

3. Imanaka's tholin cores coated with ammonia ice with a core-to-total-radius ratio ($\gamma = \frac{r_{\text{core}}}{r_{\text{total}}}$) of 50 %;

4. Imanaka's tholin cores coated with ammonia ice with a core-to-total-radius ratio ratio ($\gamma = \frac{r_{\text{core}}}{r_{\text{total}}}$) of 85 %.

To compute the optical properties as a fucntion of the wavelength and of the effective radius, I used a Mie-based code for the 1) and 2) cases, while for 3) and 4) I used the `py-mie` python package[2], which is a python wrapper of the Fortran methods developed by Toon & Ackerman (1981). The py-mie computations were also validated against the BART code[3]. A log-normal distribution with a variance of 0.3 was considered.

It is worth to briefly discuss why I chose to use these different main cloud compositions. Galileo and ISO data suggested that a 3 μm absorber aerosol was needed to explain the observed reflectivity (Sromovsky & Fry, 2010a). This absorption feature is strictly connected to chemical species bearing the N-H bond. In fact, referring to Fig. 7.5, it is possible to observe that species such as ammonia NH_3 (Hudson et al., 2022), ammonium hydrosulfide NH_4SH (Ferraro et al., 1980), hydrazine (Clapp & Miller, 1996), and Titan's tholins (Sagan & Khare, 1979; Imanaka et al., 2012) all present imaginary refractive indexes that become larger as we approach 3 μm. However, also species like water (Warren, 1984) present a similar behavior. Nevertheless, at the 0.5-1 bar level only ammonia and contaminant materials similar to Titan's tholins can form and sustain in the solid form. The former is formed thanks to moist convection and condensation, while the latter is the final product of photochemistry in the upper troposphere that may coagulate and accrete. In fact, 'tholins' should be intended as poorly characterized materials made of repeating chains of linked sub-units and complex combinations of functional groups - (typically nitriles and hydrocarbons) - that should bear both the N-H and C-N bonds (Sagan & Khare, 1979). The latter one may play a role to explain the limb-darkening maps at 5 μm obtained fom JIRAM data (Grassi et al., 2024b). In principle, a tholin-like contaminant material can also act as a coating for previously-formed ammonia particles, masking their characteristics and optical features. Water ice particles can be present at these pressure levels only due to extremely strong convective storms (Guillot et al., 2020a).

[2]https://github.com/darothen/py-mie
[3]https://www.ugr.es/ aquiran/codigos.htm

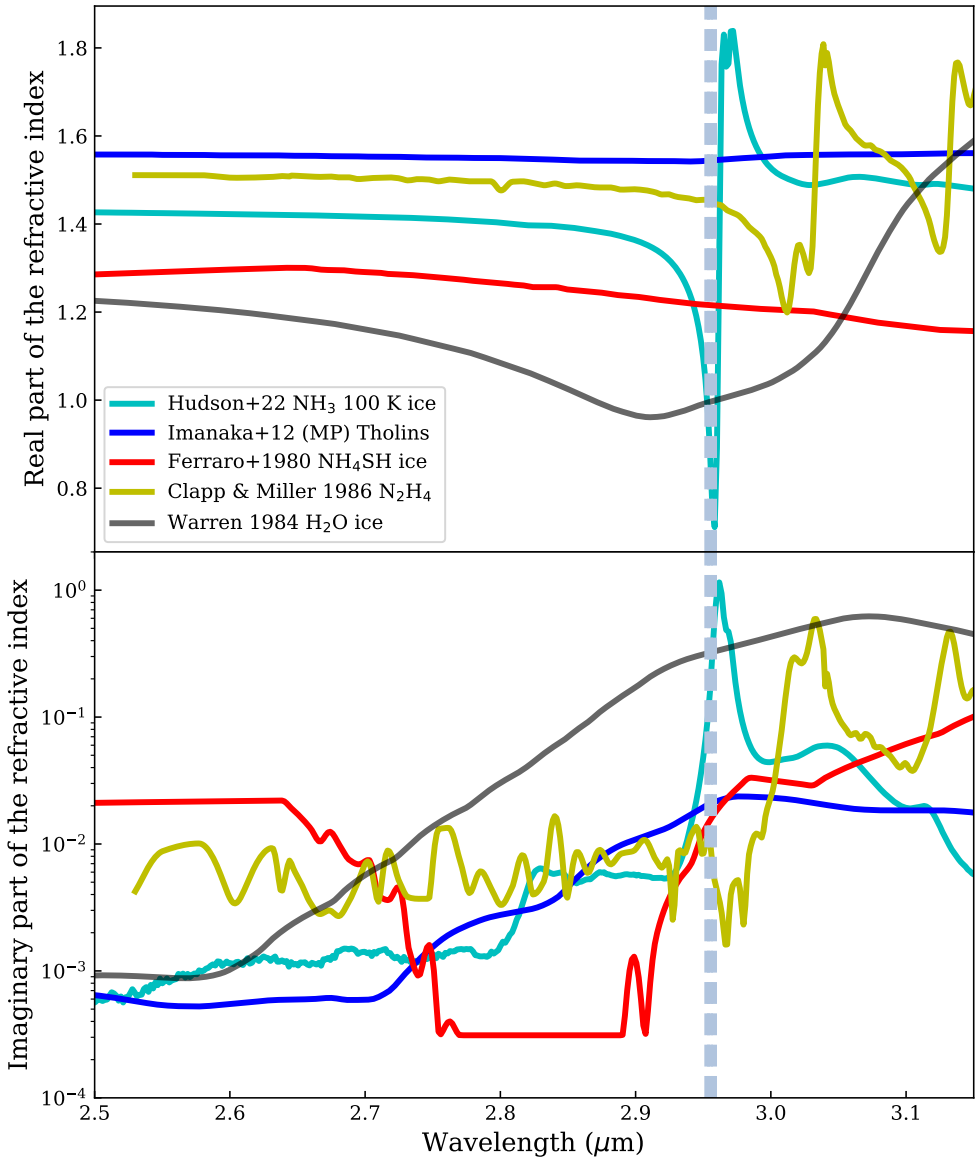


Figure 7.5: Refractive indexes of the putative 3-μm absorbers materials in Jovian clouds.

For the reasons explained above, I only decided to focus on tholins, pure ammonia ice particles, and ammonia-coated tholin particles. The optical constants used to compute pure ammonia ice optical properties are the ones presented in Hudson et al. (2022). I decided to use this dataset instead of the ones presented in Howett et al. (2007) or Martonchik et al. (1984) for two main reasons: (i) this dataset is most recent and is derived from laboratory measurements that adopts the most advanced technology, and (ii) it presents explicitly optical constants for crystalline particles at 100 K, a temperature closer to the Jovian atmosphere with respect to the 80 K of Howett et al. (2007).
Examples of the optical properties computed for a log-normal distribution of spherical particles with $r_{\text{eff}} = [1, 2, 3]\,\mu$m and variance set to 0.3 considering the selected aerosol species is given in Fig. 7.6, 7.7, and 7.8. It is possible to observe that both tholins and pure ammonia present decreasing single scattering albedo and increasing asymmetry parameters going from 2.5 μm towards 2.95 μm. However, the curves for pure ammonia always include the classical absorption signature at 2.95 μm, marked by a dashed line. The optical properties of ammonia-coated tholins at $\gamma = 50\,\%$ and $\gamma = 85\,\%$ have intermediate characteristics between pure ammonia and 'pure' tholins, as expected. This is consistent with the idea that tholin-like material can mix, after precipitating, with pre-existing ammonia particles, masking their spectral features. A detailed view of the 2.60-2.90 μm region for the single scattering albedo profiles is presented in the middle panel of Fig. 7.8. I note that the different species present very different behaviors. In particular, the pure ammonia and $\gamma = 50\,\%$ ammonia-coated tholins profiles seem to decay less rapidly toward longer wavelengths than the $\gamma = 85\,\%$ ammonia-coated tholins and pure tholins ones. The phenomenon is stronger for effective radii between 2 and 3 micron.

Regarding the retrieval stage, I ran PSG using the Nadir observing mode and giving as inputs for each spectrum the relative viewing conditions (emission, incidence, and phase angles represented in Fig. 7.3). The retrieval strategy follows the so-called Occam razor principle. I decided to first perform the retrievals for each spectrum in the dataset considering Model 1, as this one is considered to be the simplest model that can fit the typical Jupiter's spectra as seen by JIRAM. Then, for the spectra with which Model 1 retrieval did not converge, or converged with a high chi-squared value, I decided to perform Models 2,3, and 4 retrievals, to verify if relaxing assumptions on cloud compositions can get lower chi-squared values.

7.4 Results

The atmospheric retrievals converged for 419 spectra on a total of 433 when only Model 1 (main clouds composed of tholins) was considered. The number rises to 423 when all the Models are used. In Tab. 7.2 it is possible to observe the retrieved parameters inside and outside the vortex obtained performing two separate weighted means. Aerosols properties have never been retrieved for regions at these latitudes, now easily accessible thanks to the Juno mission's orbit. Moreover, these retrieved parameters can be considered as the very first attempt to spectrally model a vortex in a folded filamentary region of Jupiter. All the free parameters are well-constrained by the fit, as it is possible to observe by comparing the retrieved uncertainty to the a-priori one, last column of Tab. 7.3. The parameters more difficult to constrain are

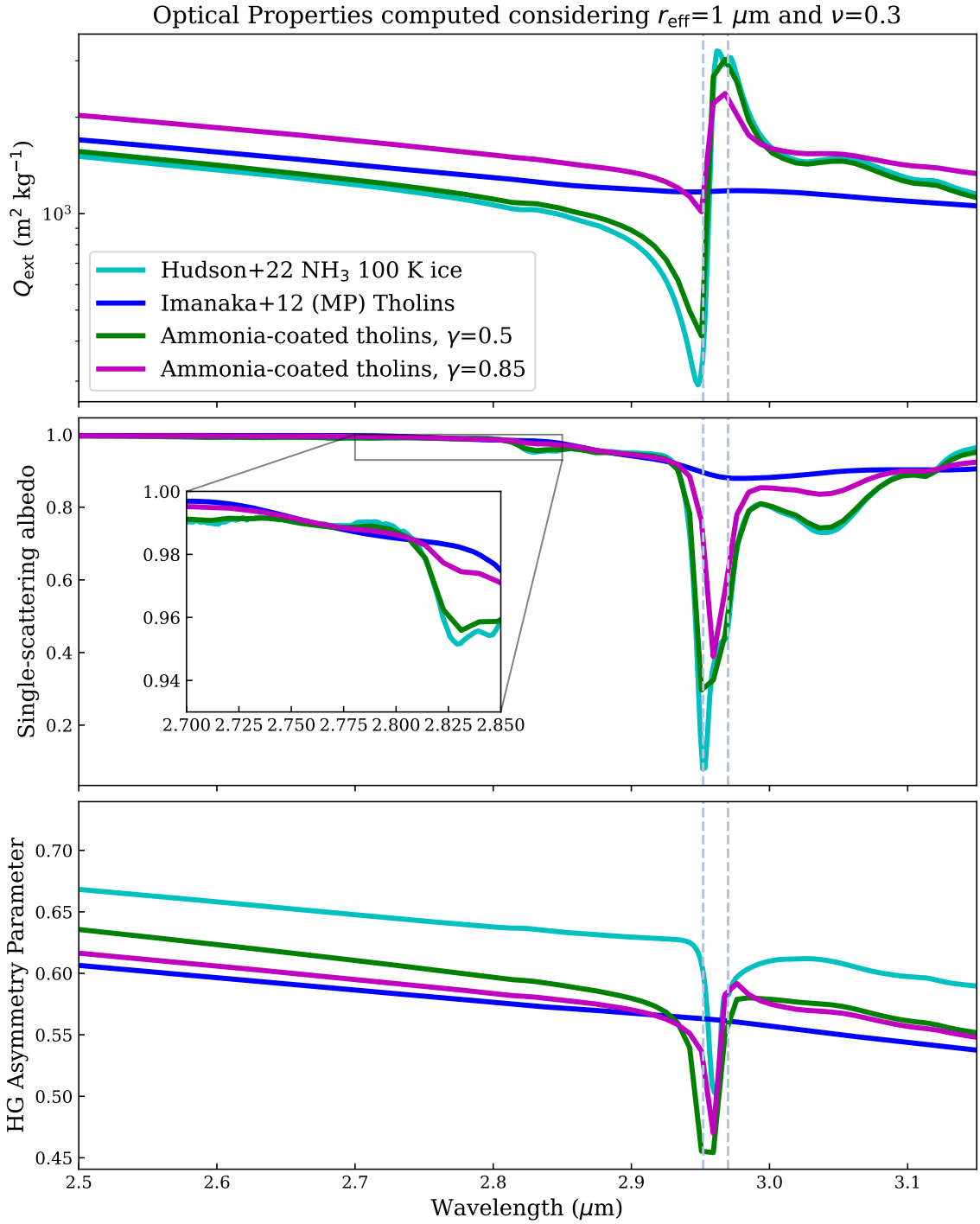


Figure 7.6: Optical properties of the four different aerosol species considered in this work: tholins, pure ammonia ice, and ammonia-coated tholins with different core-to-radius parameter (γ). The properties are computed considering a log-normal distribution of particles with an effective radius of 1 μm and a variance of 0.3.

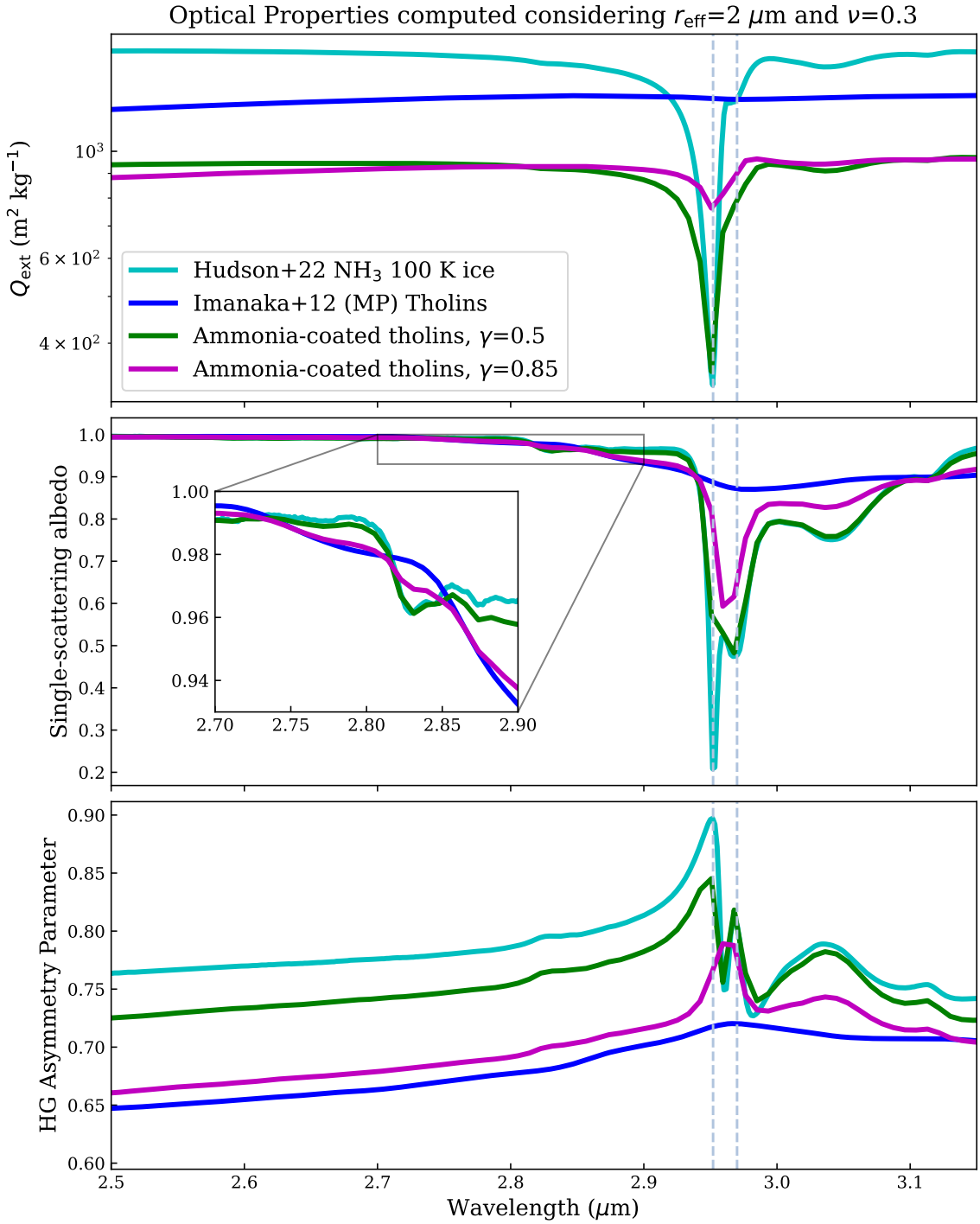


Figure 7.7: Optical properties of the four different aerosol species considered in this work: tholins, pure ammonia ice, and ammonia-coated tholins with different core-to-radius parameter (γ). The properties are computed considering a log-normal distribution of particles with an effective radius of 2 μm and a variance of 0.3.

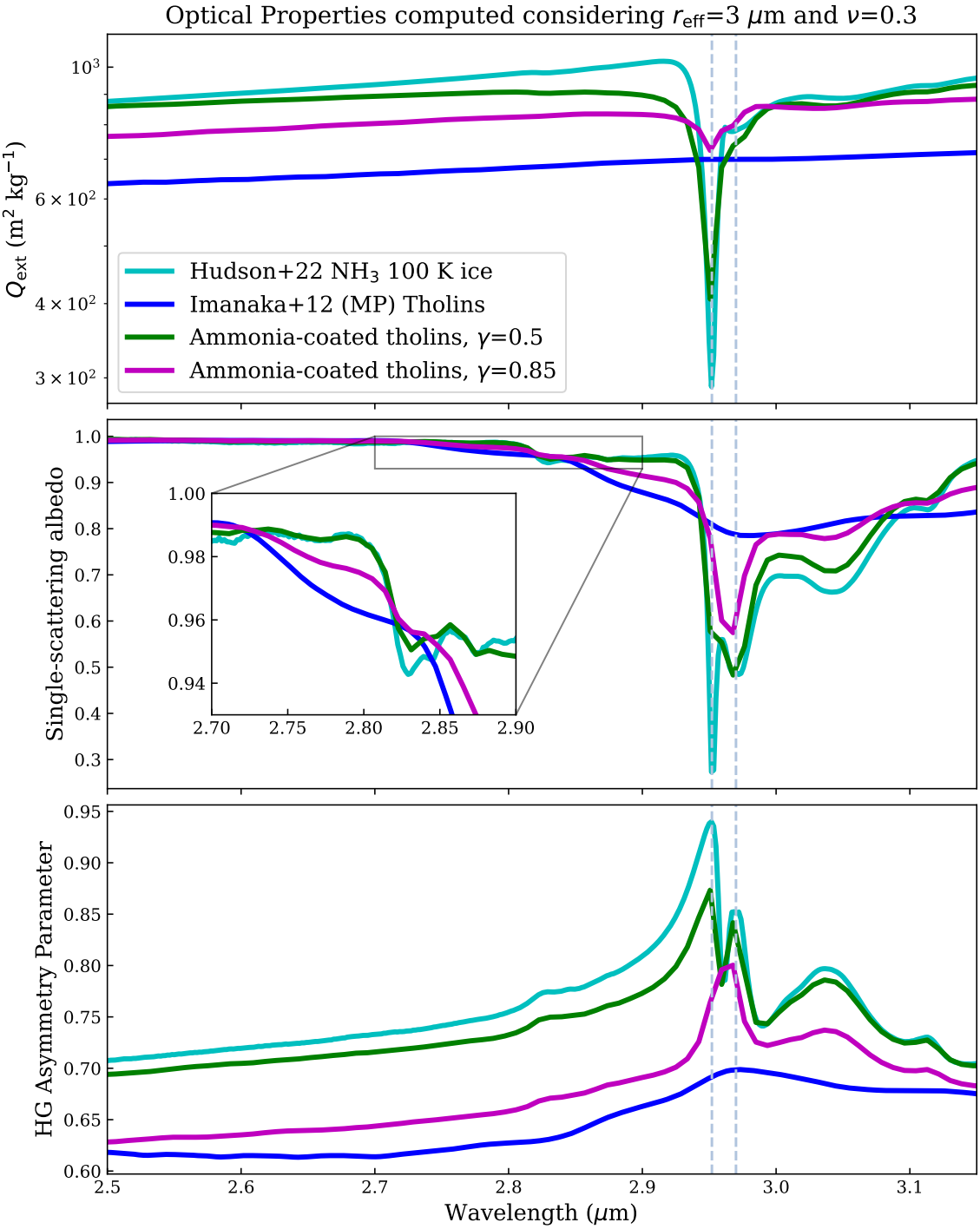


Figure 7.8: Optical properties of the four different aerosol species considered in this work: tholins, pure ammonia ice, and ammonia-coated tholins with different core-to-radius parameter (γ). The properties are computed considering a log-normal distribution of particles with an effective radius of 3 μm and a variance of 0.3.

Parameter	Unit	Outside the vortex	Inside the vortex
r_h	μm	0.34 ± 0.02	0.24 ± 0.03
r_C	μm	3.02 ± 0.11	2.79 ± 0.20
NH_{3VMR}	ppm	328 ± 10	331 ± 27
NH_{3RH}	%	39 ± 2	53 ± 6
p_h	bar	0.32 ± 0.01	0.25 ± 0.02
w_h	bar	0.22 ± 0.01	0.23 ± 0.03
N_h	part./cm^3	126 ± 35	128 ± 94
p_C	bar	0.60 ± 0.01	0.60 ± 0.01
N_C	part./cm^3	9 ± 1	19 ± 3
p_D	bar	1.23 ± 0.04	1.33 ± 0.17
N_D	part./cm^3	386 ± 23	268 ± 66

Table 7.2: Retrieved parameters considering respectively regions outside and inside the white vortex. The values are obtained through a weighted mean.

Parameter	σ_a	$\bar{\sigma}_{\mathrm{ret}}$
$\log r_h$	0.5	0.13
$\log r_C$	0.5	0.09
$\log \mathrm{NH}_{3VMR}$	0.1	0.095
$\log \mathrm{NH}_{3RH}$	0.20	0.13
$\ln p_h$	0.5	0.20
$\ln w_h$	0.4	0.35
$\log N_h$	1	0.78
$\ln p_C$	0.5	0.09
$\log N_C$	1	0.20
$\ln p_D$	0.5	0.20
$\log N_D$	1	0.18

Table 7.3: Retrieval parameters and their relative standard deviation of the a priori (σ_a). In the last columns the median retrieved uncertainties are given

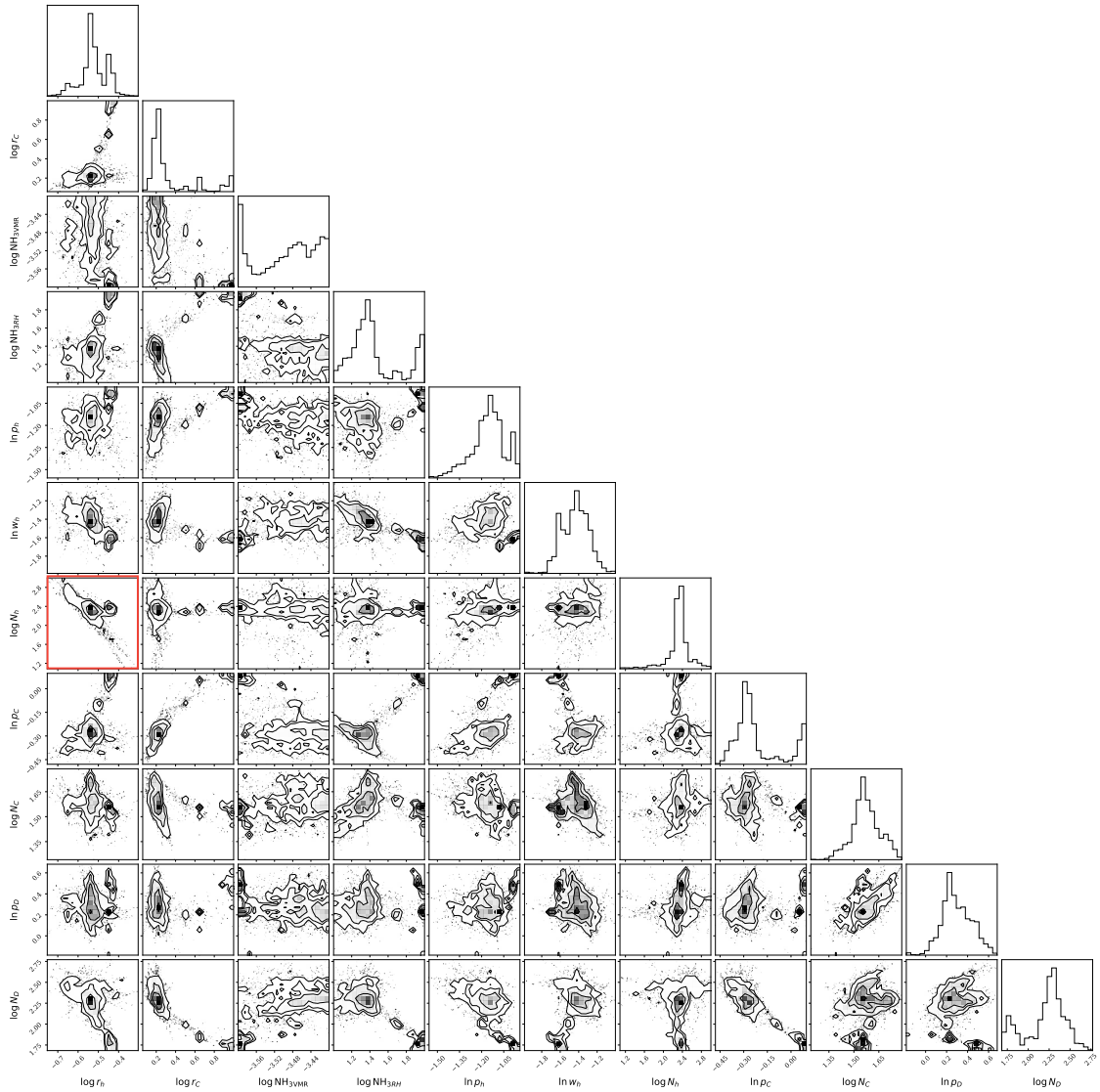


Figure 7.9: Posterior distribution of the retrieval paramters after a MCMC fit of a JIRAM test spectrum outside the vortex. The red box highlight the existing correlation between the haze's particles effective radius and density.

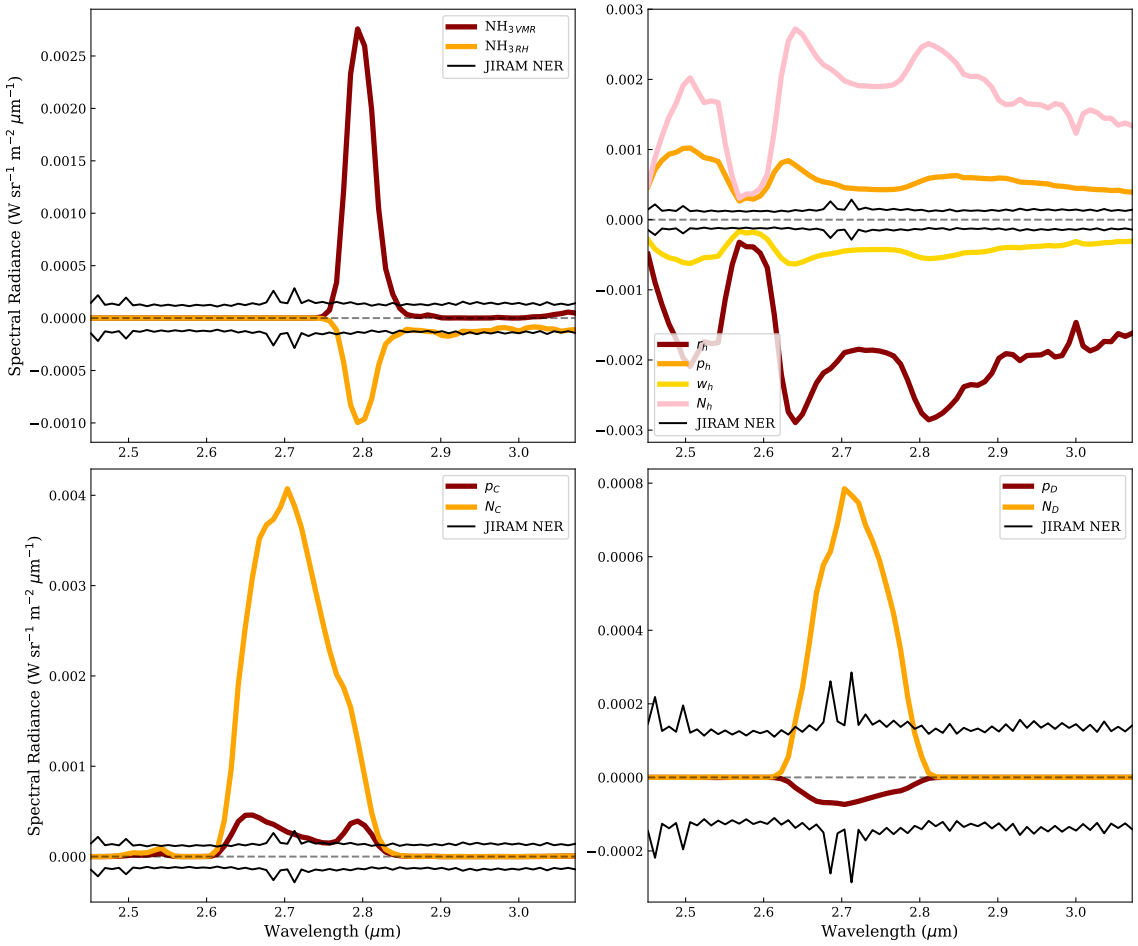


Figure 7.10: Spectral variations corresponding to a perturbation of $0.1 \cdot \sigma_a$ in the retrieval parameters. These curves also represent the Jacobians after the first OE iteration. Note the different vertical scales.

the gaseous NH_3 deep mixing ratio and the haze densities. Indeed, this behavior was largely expected. In fact, the deep mixing ratio can not be well sounded in this region because of the very dense clouds. On the contrary, the haze density in the infrared is strongly correlated with the haze effective radius. In fact, the spectral effects of the haze are not as strong as in the visible, because the extinction cross-section of the haze peaks at wavelengths similar to the effective radii ($\simeq$ 0.1-0.4 μm), and decreases strongly towards longer wavelengths. So, the hazes act as a flat scatterer layer in the JIRAM spectral range. This in turn implies that there is an unbreakable correlation between the density and the effective radius. In fact, equally fitting models can be obtained with large density and small effective radius or vice versa, as both the parameters are fundamental to derive the haze extinction efficiency. I verified this behavior by performing an independent analysis using a Monte Carlo Markov Chains approach (MCMC), as implemented by the `emcee` python package (Foreman-Mackey et al., 2013). For this test, a typical spectrum outside the vortex was considered, and the results are shown in Fig. 7.9. It is possible to observe that: (i) the posterior distributions of the parameters are consistent with the values derived with optimal estimations, (ii) the haze's density and effective radii distributions are clearly anti-correlated, since they follow a straight line.
Going back to sensitivity to other parameters, the pressure level and density of the deeper cloud were not constrained and remained stuck at the a-priori values when the main cloud deck became optically thick. Lastly, in Fig. 7.10 it is also possible to observe the Jacobians of the first iteration, that provide the sensitivity of the retrieval to the elements of state vector (i.e. free retrieval parameters) for a JIRAM test spectrum outside the vortex. From that figure I note that the spectral shape of the reflected peak is mostly sensitive to the main cloud deck, while the deeper one acts to increase the measured signal. So, in this spectral range we are not sensitive to the composition of the deepest cloud but only to its pressure level and density. The choice of the tholin contaminants, therefore, is only conservative and driven by the findings of Grassi et al. (2021).

Fig. 7.11 presents the Model 1 (main clouds composed of tholins) best fit of the two example spectra introduced in Section 2. I note that Model 1 can model very well the spectra outside the snail-like white vortex, but not the one inside, where the retrieval is systematically poorer. This is easily observable in Fig. 7.12a that shows the resulting chi-square values of the retrievals performed using only Model 1. The poor fit quality is caused by the occurrence of shifted reflectance peaks and/or of spectral absorptions near 2.95 μm. Neither of these two features can be reproduced by clouds made of tholins. For this reason, I also tested retrievals using Models 2,3, and 4 on the spectra inside the vortex. The resulting chi-square map is shown in Fig. 7.12b. There I note that inside the vortex the quality of the fit is greatly improved if pure ammonia ice or ammonia-coated tholin cloud decks are considered. In Fig. 7.13 it is possible to see which model provides the best fit for all the spectra in the set. From the same figure, I note that:

- most of the spectra inside the vortex are better reproduced considering Models 2,3, and 4,
- the spectra that do not display any shift in the reflectance peak but show the 2.95 μm absorption feature are, in most of the cases, best-reproduced by tholin

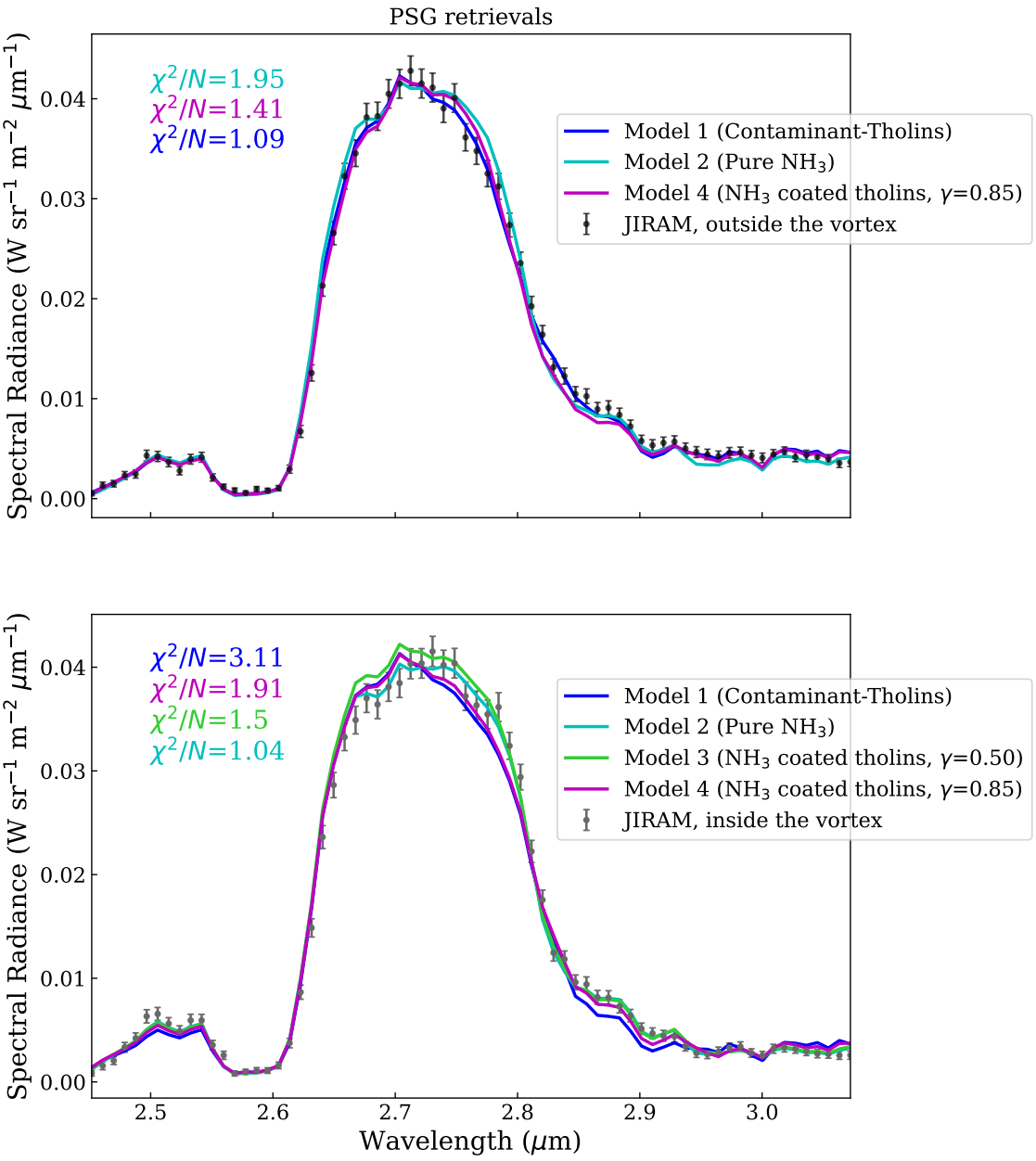


Figure 7.11: Example of two best-fit PSG/OE retrievals and corresponding statistical indicators. *Upper panel*: black JIRAM spectrum presented in Fig. 9.3. *Bottom panel*: gray JIRAM spectrum presented in Fig. 7.4. The best-fitting models follow the same color convention presented in Fig. 7.8.

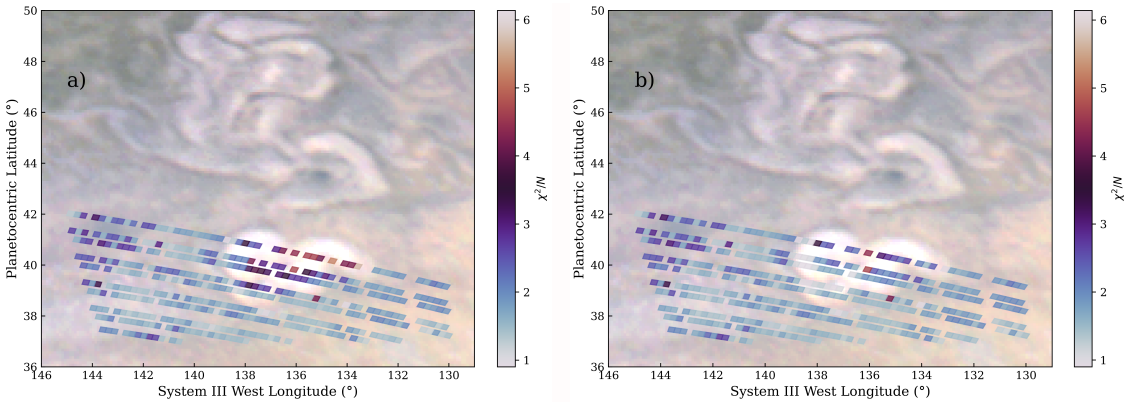


Figure 7.12: (a) χ^2/N maps obtained considering only Model 1 atmospheres during the retrieval stage. (b) χ^2/N maps obtained considering all the four Model atmospheres during the retrieval stage.

particles coated with ammonia, with a core/total ratio of 85 % (upper right panel),

- the spectra that display moderate shift in the reflectance peak and a 2.95 μm absorption are, in most of the cases, best-reproduced by tholin particles coated with ammonia, with a core/total ratio of 50 % (bottom left panel),
- the spectra that present a strong shift in the reflectance peak and a 2.95 μm absorption are in most of the cases best-reproduced by pure ammonia ice particles (bottom right panel).

The choice of the best-fitting model was performed considering the difference between the BIC indicators that are defined as:

$$\mathrm{BIC} = \chi^2 + N_x \ln N \ , \tag{7.3}$$

where N_x is the number of parameters of the model and N the number of datapoints. I only considered the BIC as all the different models that I used to fit JIRAM data have the same number of free parameters. The chi-square and BIC values for the spectra modeled using all four models are given in Tab. 7.5. The BIC is an useful indicator as can be connected to the Bayes Factor using the following expression: (Patra et al., 2017)

$$\mathcal{B}_{12} = \exp\left(\frac{\mathrm{BIC}_2 - \mathrm{BIC}_1}{2}\right) \tag{7.4}$$

The Bayes factor is a fundamental measure in Bayesian statistics that quantifies the strength of evidence provided by the data in favor of one statistical model or hypothesis compared to another. In its most general form, the Bayes factor is the ratio of the marginal likelihoods of the data under two competing models, M_1 and M_2:

$$\mathcal{B}_{12} = \frac{p(D|M_1)}{p(D|M_2)} \tag{7.5}$$

using the same notation used in Chapter 3. For example, a Bayes factor of $\mathcal{B}_{12} = 5$ means that the observed data are 5 times more likely to occur under model M_1 than

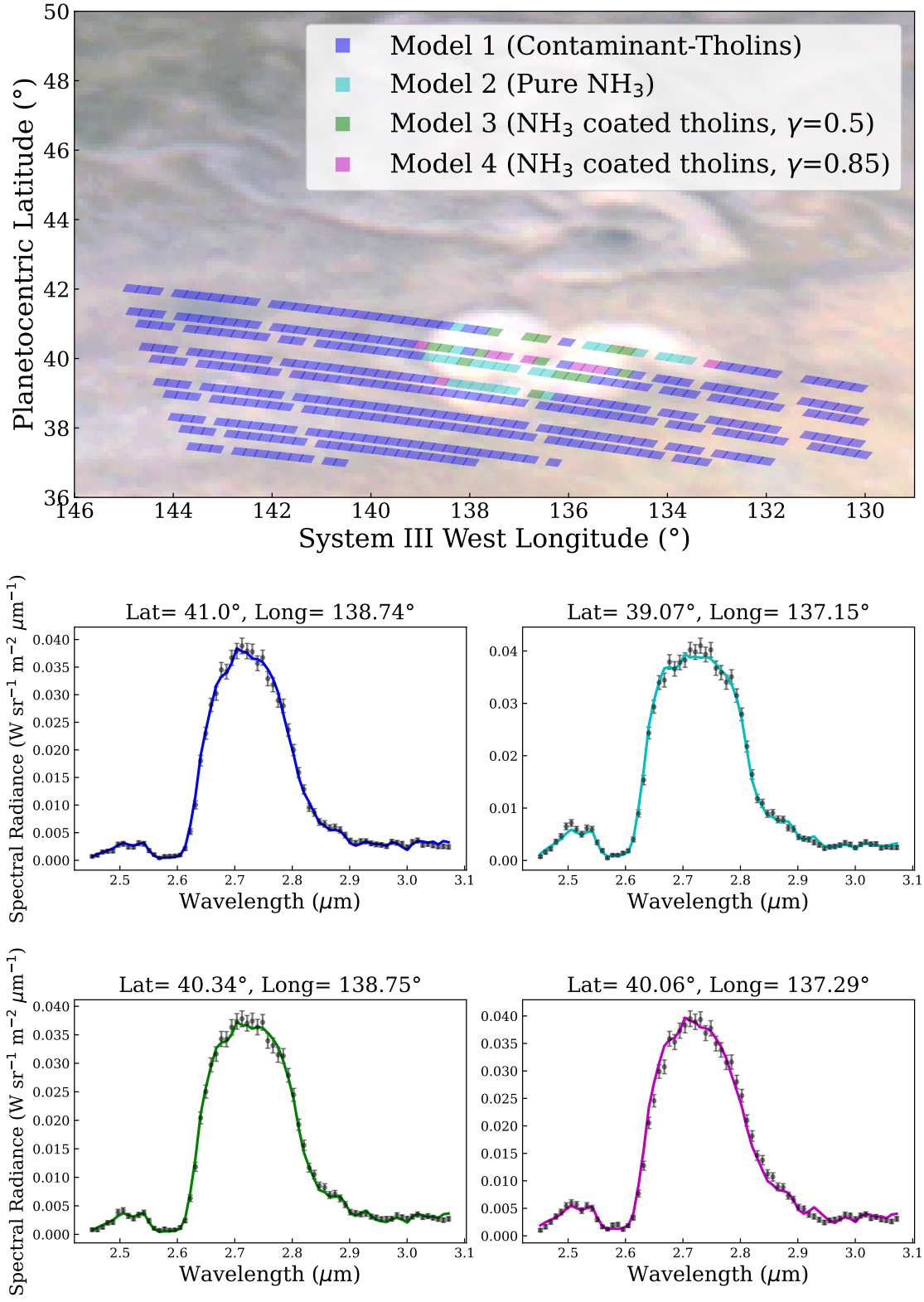


Figure 7.13: *Upper panel*: JIRAM coverage of the #1 ROI where the color of each pixel represents the Model atmosphere that provide the lowest χ^2/N retrieval. Bottom panels: four examples of best-fitting retrievals for each Model atmosphere.

under model M_2. In contrast, a $\mathcal{B}_{12} = 0.2$ means that the data are 5 times more likely under M_2 than under M_1. Therefore, a BIC difference > 10 indicates that the evidence favoring the lower BIC model against the other is quite strong (Cornish & Littenberg, 2007). Looking at the values of ΔBIC presented in Tab. 7.5, I note that 25 spectra inside the vortex are best-reproduced by pure ammonia ice clouds (Model 2), while 15 spectra are best-reproduced by 50 % ammonia-coated tholins clouds (Model 3). For 38 of these spectra the Model 2 and 3 are favored with respect to Model 1 by ΔBIC larger than 20-30 in most of the cases. This, in turn, implies that a total of 38 pixels covering Spectrally Identifiable Ammonia Clouds have been detected thanks to JIRAM in the PJ1 phase of the NASA Juno Mission. A total of 9 spectra are instead best-reproduced by tholin particles coated with ammonia, with a core/total ratio of 85 % (Model 4), and so identified as peculiar spectra. In this case, however, not all the fits provide ΔBIC larger than 20-30. The remaining 374 spectra of the dataset are best-reproduced by tholin clouds (Model 1). Tab. 7.4 presents the retrieved parameters for the SIACs and peculiar spectra. The JIRAM spectra of the identified SIACs together with their best-fitting PSG synthetic spectra are represented in Figures 7.14, 7.15, and 7.16.
Once the best-fitting model has been identified for each spectrum in the dataset, it is possible to derive maps of the retrieved physical parameters. These are presented in Fig. 7.17, 7.18, and 7.19, and discussed in the following subsections.

7.4.1 NH_3 deep VMR and relative humidity

It is possible to observe the retrieved gaseous ammonia deep VMR in Fig. 7.17a. The values vary from a minimum of 300 $\pm$ 70 ppm to a maximum of 342 $\pm$ 80 ppm. The mean uncertainty value is 74 ppm, therefore the variations observed in 7.17a are not significant. Since in this wavelength interval we are not very sensitive to the deep atmosphere and we are studying cloudy regions, the values have to be taken with caution. Bearing this in mind, my results are in good agreement and are consistent at the 1σ-level with the results from MWR (Li et al., 2017) at the same planetocentric latitudes. A correlation with the snail-like vortex seems to be not evident, nor any longitude or latitude trend.
It is possible to observe the gaseous ammonia relative humidity values in Fig. 7.17b. The values can vary from a minimum of 32 $\pm$ 9 % to a maximum of 63 $\pm$ 13 %. The mean uncertainty value is 11 %. This is the first measure of gaseous ammonia relative humidity from Juno's data at these latitudes and it is in good agreement both with Cassini/CIRS results (Achterberg et al., 2006) and with ground-based TEXES measurements (Fletcher et al., 2016b). Differently from the deep vmr, the relative humidity displays a longitudinal trend anti-correlated to the 2.73 μm signal. This may be connected to the effect of the incident solar radiation, which in turn may be linked to ammonia's destruction efficiency. Higher anomalous values are reported inside the vortex, suggesting a correlation between the presence of SIACs and higher relative humidity. It is worth to underline that the pixels that show the higher values in both Fig. 7.17a and b, are the same pixels for which the retrievals using Model 2 (pure ammonia ice) and Model 3 (50 % ammonia-coated tholins) converged with the lowest reduced chi-square values.

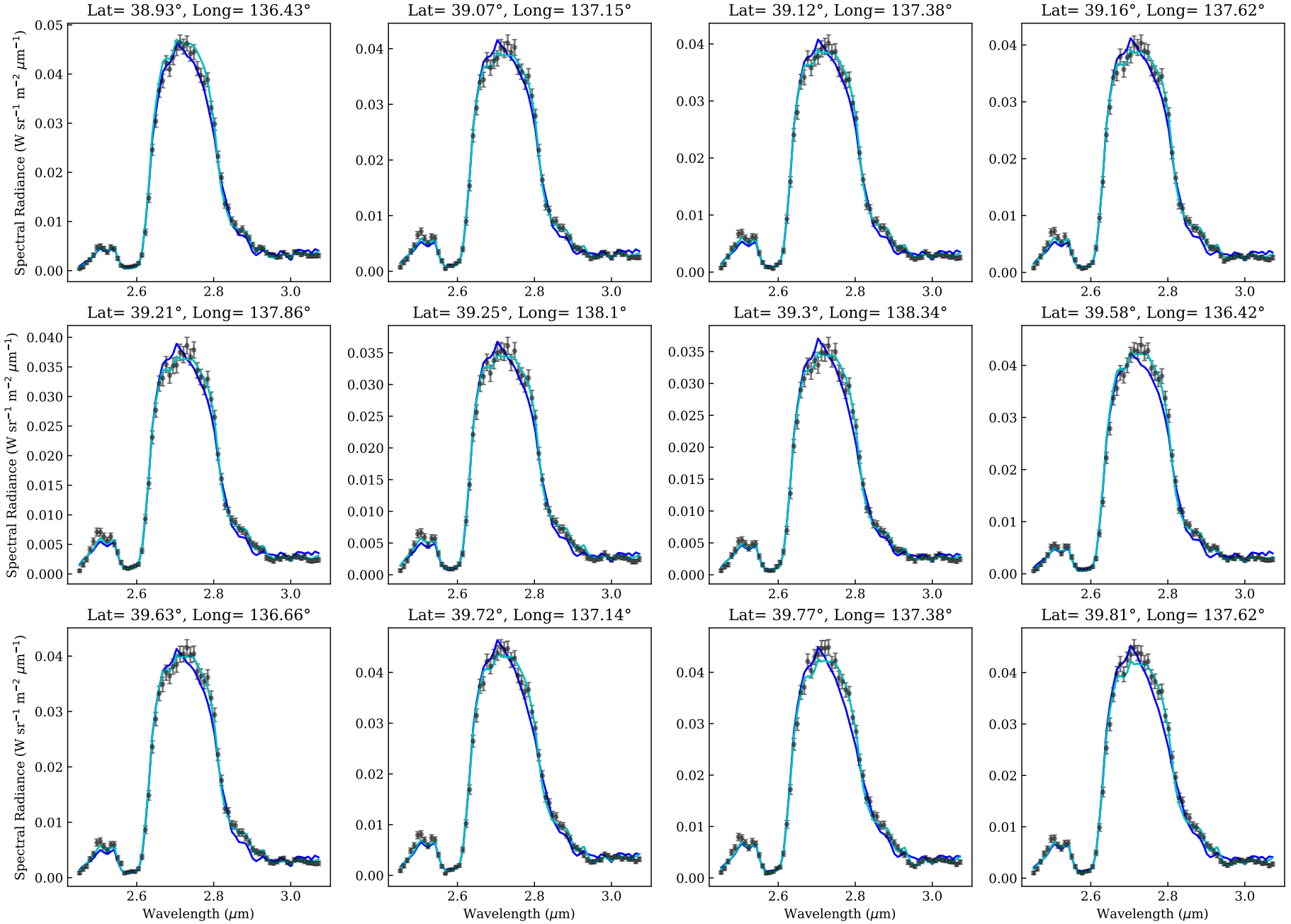


Figure 7.14: JIRAM spectra best-fitted by Model 2 atmospheres, i.e. considering pure ammonia ice main clouds. The color legend is the same of Fig. 7.11.

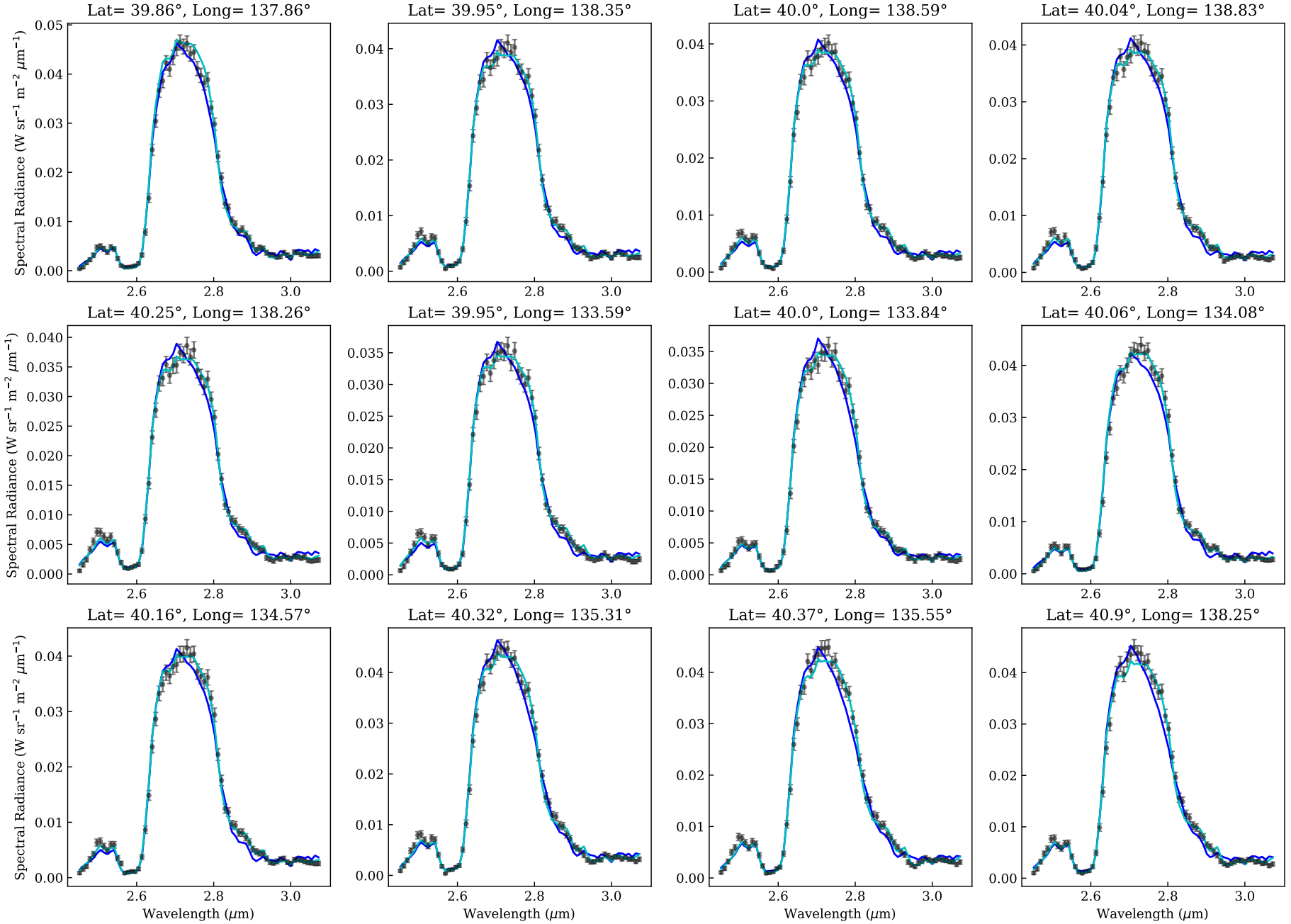


Figure 7.15: JIRAM spectra best-fitted by Model 2 atmospheres, i.e. considering pure ammonia ice main clouds. The color legend is the same of Fig. 7.11.

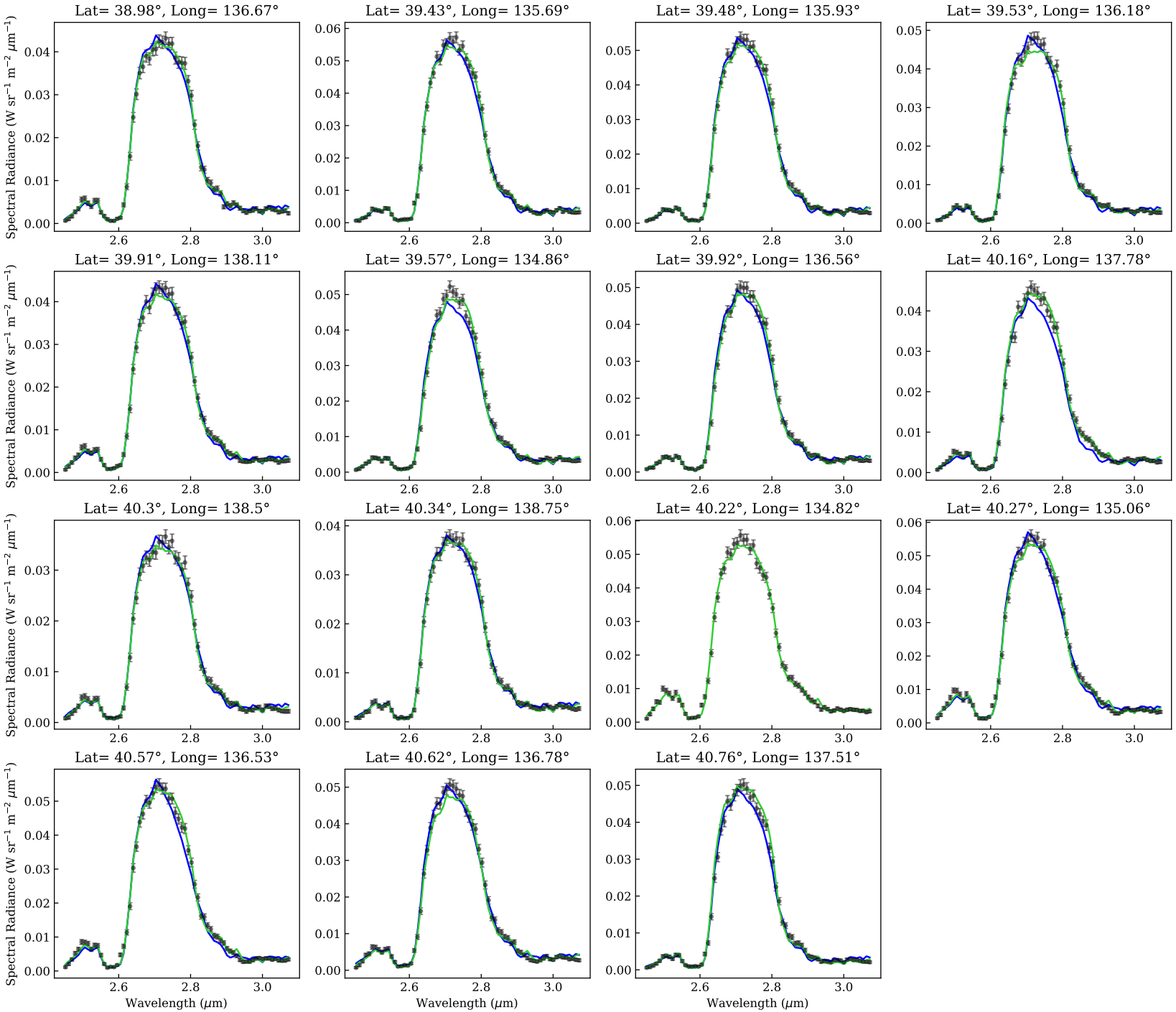


Figure 7.16: JIRAM spectra best-fitted by Model 3 atmospheres, i.e. considering $\gamma = 0.5$ ammonia-coated tholins. The color legend is the same of Fig. 7.11.

Longitude (°)	Latitude (°)	Model	r_h (μm)	r_C (μm)	NH_{3VMR} (ppm)	NH_{3RH} (%)	p_h (bar)	w_h (bar)	N_h (part./cm^3)	p_C (bar)	N_C (part./cm^3)	p_D (bar)	N_D (part./cm^3)
135.95	38.83	2	0.32 ± 0.1	2.6 ± 0.45	329 ± 74	39.17 ± 10.64	0.32 ± 0.06	0.22 ± 0.08	160 ± 299	0.62 ± 0.03	19 ± 10		
136.19	38.88	3	0.3 ± 0.09	3.39 ± 0.29	328 ± 75	45.93 ± 12.86	0.29 ± 0.06	0.22 ± 0.08	209 ± 377	0.63 ± 0.03	26 ± 10		
136.43	38.93	2	0.25 ± 0.06	3.23 ± 0.74	330 ± 75	51.47 ± 14.48	0.27 ± 0.05	0.22 ± 0.08	470 ± 854	0.62 ± 0.03	13 ± 6	1.33 ± 0.55	190 ± 123
136.67	38.98	2	0.24 ± 0.07	3.34 ± 0.76	331 ± 75	54.15 ± 15.2	0.27 ± 0.05	0.22 ± 0.08	581 ± 1088	0.6 ± 0.03	12 ± 5	1.41 ± 0.55	231 ± 225
137.15	39.07	2	0.24 ± 0.07	3.45 ± 0.72	330 ± 75	52.84 ± 14.66	0.26 ± 0.05	0.22 ± 0.08	533 ± 1014	0.6 ± 0.03	12 ± 5	1.35 ± 0.54	231 ± 190
137.38	39.12	2	0.24 ± 0.07	3.72 ± 0.83	330 ± 75	53.78 ± 15.26	0.26 ± 0.05	0.22 ± 0.08	565 ± 1059	0.6 ± 0.03	9 ± 4	1.36 ± 0.56	178 ± 159
137.62	39.16	2	0.24 ± 0.06	3.76 ± 0.85	330 ± 75	50.77 ± 14.72	0.26 ± 0.05	0.22 ± 0.08	498 ± 896	0.6 ± 0.03	8 ± 3	1.28 ± 0.54	143 ± 68
137.86	39.21	2	0.27 ± 0.08	3.37 ± 0.79	331 ± 75	48.49 ± 14.11	0.27 ± 0.05	0.22 ± 0.08	277 ± 514	0.61 ± 0.03	9 ± 4	1.29 ± 0.44	215 ± 82
138.1	39.25	4	0.31 ± 0.1	3.37 ± 0.34	325 ± 73	42.22 ± 12.99	0.3 ± 0.06	0.23 ± 0.09	130 ± 242	0.63 ± 0.04	12 ± 4	1.4 ± 0.37	291 ± 220
134.97	39.28	3	0.31 ± 0.11	2.25 ± 0.11	330 ± 75	41.22 ± 12.01	0.29 ± 0.06	0.23 ± 0.09	113 ± 223	0.64 ± 0.03	52 ± 11		
135.21	39.33	3	0.31 ± 0.1	2.22 ± 0.09	327 ± 74	38.24 ± 11.11	0.28 ± 0.06	0.23 ± 0.09	113 ± 220	0.65 ± 0.03	61 ± 12		
135.45	39.38	3	0.37 ± 0.13	2.84 ± 0.63	320 ± 73	33.8 ± 9.0	0.34 ± 0.06	0.23 ± 0.09	94 ± 175	0.67 ± 0.03	25 ± 12		
135.69	39.43	2	0.33 ± 0.1	3.88 ± 1.06	324 ± 74	39.11 ± 11.07	0.3 ± 0.06	0.22 ± 0.08	127 ± 230	0.62 ± 0.03	8 ± 4	1.21 ± 0.36	309 ± 209
135.93	39.48	2	0.28 ± 0.08	3.65 ± 0.92	327 ± 74	45.14 ± 12.76	0.27 ± 0.05	0.23 ± 0.09	225 ± 401	0.61 ± 0.03	10 ± 4	1.37 ± 0.5	251 ± 232
136.18	39.53	2	0.23 ± 0.07	2.67 ± 0.36	332 ± 75	56.05 ± 14.95	0.25 ± 0.04	0.22 ± 0.08	666 ± 1320	0.57 ± 0.03	18 ± 7		
136.42	39.58	2	0.24 ± 0.07	2.71 ± 0.4	332 ± 75	51.63 ± 14.69	0.24 ± 0.05	0.23 ± 0.08	389 ± 779	0.56 ± 0.03	18 ± 7		
136.66	39.63	2	0.24 ± 0.07	2.94 ± 0.49	331 ± 75	49.46 ± 14.18	0.24 ± 0.05	0.23 ± 0.08	380 ± 750	0.55 ± 0.03	15 ± 6		
137.14	39.72	2	0.23 ± 0.07	2.68 ± 0.35	332 ± 75	52.17 ± 14.0	0.25 ± 0.05	0.23 ± 0.08	499 ± 977	0.57 ± 0.03	18 ± 6		
137.38	39.77	3	0.26 ± 0.08	3.38 ± 0.31	330 ± 75	48.95 ± 14.56	0.26 ± 0.05	0.23 ± 0.09	298 ± 586	0.61 ± 0.04	25 ± 12		
137.62	39.81	2	0.26 ± 0.07	2.89 ± 0.57	330 ± 75	48.63 ± 13.85	0.27 ± 0.05	0.23 ± 0.08	288 ± 540	0.61 ± 0.03	14 ± 7	1.29 ± 0.5	185 ± 79
137.86	39.86	2	0.3 ± 0.09	3.28 ± 1.07	329 ± 75	46.28 ± 14.3	0.29 ± 0.05	0.22 ± 0.09	196 ± 359	0.62 ± 0.04	8 ± 6	1.33 ± 0.57	135 ± 84
138.11	39.91	2	0.36 ± 0.11	2.94 ± 0.82	328 ± 73	40.22 ± 12.15	0.32 ± 0.06	0.23 ± 0.09	99 ± 176	0.63 ± 0.04	9 ± 6	1.43 ± 0.36	391 ± 265
133.16	39.2	3	0.29 ± 0.09	2.16 ± 0.09	329 ± 72	39.87 ± 12.22	0.28 ± 0.06	0.23 ± 0.09	136 ± 264	0.63 ± 0.03	39 ± 10		
133.89	39.36	4	0.29 ± 0.1	2.28 ± 0.09	317 ± 71	35.4 ± 10.32	0.28 ± 0.06	0.23 ± 0.09	112 ± 221	0.66 ± 0.03	46 ± 9		
134.13	39.42	4	0.25 ± 0.09	2.23 ± 0.06	317 ± 71	33.97 ± 9.99	0.25 ± 0.07	0.25 ± 0.09	123 ± 256	0.65 ± 0.03	52 ± 10		
134.62	39.52	4	0.26 ± 0.09	2.13 ± 0.05	313 ± 70	32.28 ± 9.56	0.26 ± 0.07	0.24 ± 0.09	117 ± 247	0.65 ± 0.03	79 ± 17		
135.11	39.62	3	0.29 ± 0.09	2.19 ± 0.09	324 ± 73	38.47 ± 11.58	0.27 ± 0.06	0.23 ± 0.09	133 ± 258	0.64 ± 0.03	48 ± 11		
135.35	39.67	4	0.24 ± 0.07	3.34 ± 0.17	320 ± 73	44.52 ± 12.99	0.25 ± 0.05	0.23 ± 0.08	373 ± 734	0.61 ± 0.03	26 ± 6		
135.59	39.72	4	0.23 ± 0.08	3.4 ± 0.2	323 ± 73	43.32 ± 13.08	0.23 ± 0.07	0.26 ± 0.08	225 ± 449	0.58 ± 0.03	15 ± 3		
135.84	39.77	4	0.29 ± 0.08	2.4 ± 0.34	325 ± 74	40.34 ± 11.16	0.28 ± 0.05	0.23 ± 0.09	174 ± 324	0.62 ± 0.03	23 ± 8		
136.08	39.82	3	0.26 ± 0.08	2.45 ± 0.71	327 ± 74	42.37 ± 12.73	0.26 ± 0.05	0.23 ± 0.09	224 ± 432	0.61 ± 0.03	28 ± 10		
136.56	39.92	2	0.26 ± 0.08	2.6 ± 0.42	329 ± 75	44.99 ± 12.41	0.26 ± 0.05	0.23 ± 0.09	246 ± 470	0.61 ± 0.03	18 ± 9		
136.81	39.97	3	0.28 ± 0.09	3.5 ± 0.43	329 ± 75	46.27 ± 14.08	0.27 ± 0.05	0.23 ± 0.09	196 ± 377	0.62 ± 0.03	17 ± 10		
137.29	40.06	3	0.3 ± 0.1	2.32 ± 0.21	330 ± 75	42.46 ± 13.25	0.29 ± 0.05	0.23 ± 0.09	133 ± 256	0.64 ± 0.03	29 ± 6		
137.53	40.11	4	0.34 ± 0.12	3.26 ± 0.28	324 ± 73	38.59 ± 11.66	0.3 ± 0.07	0.23 ± 0.09	83 ± 158	0.63 ± 0.04	15 ± 5		
131.13	39.39	4	0.31 ± 0.1	2.56 ± 0.29	327 ± 74	40.59 ± 10.32	0.28 ± 0.05	0.23 ± 0.09	148 ± 274	0.6 ± 0.03	21 ± 7		
131.37	39.45	2	0.24 ± 0.07	2.88 ± 0.39	329 ± 75	57.78 ± 14.62	0.26 ± 0.05	0.22 ± 0.08	534 ± 1001	0.59 ± 0.03	20 ± 6		
131.87	39.56	2	0.23 ± 0.07	3.15 ± 0.55	330 ± 75	57.59 ± 15.1	0.26 ± 0.05	0.21 ± 0.08	694 ± 1317	0.6 ± 0.03	15 ± 5		
132.11	39.62	2	0.24 ± 0.07	2.63 ± 0.38	331 ± 75	56.19 ± 14.44	0.26 ± 0.05	0.22 ± 0.08	556 ± 1040	0.62 ± 0.03	27 ± 10		
132.36	39.68	2	0.24 ± 0.07	2.64 ± 0.4	331 ± 75	51.98 ± 14.39	0.24 ± 0.05	0.23 ± 0.08	458 ± 892	0.58 ± 0.03	23 ± 9		
132.61	39.73	3	0.24 ± 0.06	3.87 ± 0.4	332 ± 75	51.61 ± 13.8	0.25 ± 0.04	0.21 ± 0.08	618 ± 1116	0.59 ± 0.03	16 ± 3		
132.85	39.79	3	0.22 ± 0.07	3.44 ± 0.2	338 ± 75	56.68 ± 14.68	0.23 ± 0.05	0.22 ± 0.08	761 ± 1473	0.58 ± 0.03	24 ± 6		
133.1	39.84	2	0.23 ± 0.07	2.4 ± 0.25	341 ± 76	62.27 ± 15.64	0.24 ± 0.05	0.22 ± 0.08	607 ± 1195	0.56 ± 0.03	27 ± 9		
133.59	39.95	2	0.23 ± 0.07	3.2 ± 0.15	340 ± 76	57.48 ± 14.38	0.24 ± 0.05	0.22 ± 0.08	493 ± 930	0.58 ± 0.03	38 ± 9		
134.08	40.06	3	0.22 ± 0.07	3.47 ± 0.21	335 ± 75	57.17 ± 14.87	0.23 ± 0.05	0.22 ± 0.08	582 ± 1146	0.57 ± 0.03	24 ± 7		
134.57	40.16	3	0.25 ± 0.07	2.39 ± 0.36	334 ± 74	48.44 ± 15.32	0.25 ± 0.05	0.23 ± 0.08	352 ± 669	0.6 ± 0.03	23 ± 4		
134.82	40.22	3	0.32 ± 0.1	3.27 ± 0.21	323 ± 73	41.14 ± 9.98	0.27 ± 0.06	0.24 ± 0.09	70 ± 133	0.66 ± 0.03	58 ± 18		
135.55	40.37	2	0.27 ± 0.08	3.52 ± 0.7	329 ± 75	46.97 ± 13.45	0.27 ± 0.05	0.23 ± 0.09	209 ± 398	0.6 ± 0.03	7 ± 3	1.33 ± 0.48	179 ± 94

Table 7.4: Retrieved parameters for the JIRAM spectra best-fitted by Models 2,3, and 4 in regions inside the white vortex.

Longitude (°)	Latitude (°)	Model 1 (Contaminant - Tholins)		Model 2 (Pure Ammonia Ice)		Model 3 (NH_3 coated tholins, γ=0.50)		Model 4 (NH_3 coated tholins, γ=0.85)		Δ BIC
		χ^2/N	BIC	χ^2/N	BIC	χ^2/N	BIC	χ^2/N	BIC	(Model 1 - Best Fit)
136.67	38.98	2.57	226.84	1.53	153.87	1.44	147.46	2.0	173.14	79.38
135.69	39.43	2.75	239.12	1.97	184.39	1.89	178.83	2.0	184.39	60.29
135.93	39.48	2.76	240.04	-	-	1.74	168.25	2.0	179.11	71.79
136.18	39.53	2.73	237.8	1.98	185.55	1.98	185.55	5.0	408.84	52.25
138.11	39.91	2.17	198.45	1.31	138.72	1.12	125.05	1.0	138.72	73.4
134.86	39.57	3.02	258.25	-	-	1.94	182.22	-	-	76.03
136.56	39.92	2.83	245.05	-	-	1.56	156.03	2.0	181.84	89.02
137.78	40.16	4.2	340.5	2.01	187.14	1.79	172.1	2.0	175.66	168.4
138.5	40.3	2.25	204.27	1.05	120.37	1.01	117.47	7.0	539.48	86.8
138.75	40.34	1.56	155.62	0.98	115.11	0.91	110.54	1.0	115.11	45.08
134.82	40.22	-	-	2.34	210.62	2.25	204.03	3.0	264.38	-204.03
135.06	40.27	4.09	333.07	-	-	2.55	224.99	3.0	267.03	108.08
136.53	40.57	4.17	338.45	-	-	2.21	201.25	-	-	137.2
136.78	40.62	2.91	250.58	-	-	2.43	216.82	-	-	33.76
137.51	40.76	2.6	228.58	-	-	2.55	225.36	-	-	3.22
138.58	39.34	1.12	124.95	1.34	140.61	0.98	115.09	1.0	109.84	15.11
135.35	39.67	3.05	260.17	-	-	2.05	190.49	2.0	185.99	74.18
135.59	39.72	3.63	300.77	-	-	-	-	2.0	197.52	103.25
135.84	39.77	-	-	-	-	-	-	2.0	218.58	-218.58
136.81	39.97	2.78	241.44	2.23	202.84	6.93	531.99	2.0	186.07	55.37
137.29	40.06	2.96	253.79	-	-	3.03	258.69	2.0	215.71	38.08
137.53	40.11	-	-	2.35	211.47	-	-	2.0	211.47	-211.47
138.99	40.39	1.19	130.3	1.24	133.7	1.21	131.65	1.0	126.89	3.41
133.1	39.84	-	-	6.16	478.11	6.16	478.11	6.0	478.11	-478.11
136.43	38.93	2.16	197.73	1.57	156.43	1.57	156.43	4.0	302.3	41.3
137.15	39.07	2.73	237.87	1.06	120.77	1.17	128.94	2.0	172.34	117.1
137.38	39.12	2.56	225.7	0.93	112.1	1.09	123.19	2.0	153.93	113.6
137.62	39.16	3.09	263.31	1.01	117.3	1.07	121.93	2.0	175.51	146.01
137.86	39.21	3.39	284.11	1.24	133.26	1.49	151.11	1.0	133.26	150.85
138.1	39.25	2.62	230.39	1.14	126.19	1.18	129.2	1.0	126.19	104.2
138.34	39.3	2.12	194.96	0.9	109.97	0.92	111.24	1.0	149.29	84.99
136.42	39.58	3.56	296.28	1.5	151.4	1.5	151.4	1.0	151.4	144.88
136.66	39.63	3.11	264.35	1.04	119.62	1.5	151.85	2.0	180.58	144.73
137.14	39.72	3.21	271.54	1.74	168.68	1.97	184.63	2.0	168.68	102.86
137.38	39.77	3.74	308.56	1.62	160.25	2.18	199.56	2.0	218.21	148.31
137.62	39.81	3.91	320.53	1.67	163.33	-	-	2.0	182.8	157.2
137.86	39.86	3.28	276.21	1.67	163.8	1.88	178.49	2.0	163.8	112.41
138.35	39.95	2.21	201.67	0.93	112.13	1.01	117.16	2.0	188.92	89.54
138.59	40.0	1.87	177.28	0.84	105.55	0.9	109.5	2.0	187.41	71.73
138.83	40.04	1.46	148.78	1.1	123.43	-	-	1.0	127.25	25.35
138.26	40.25	2.05	189.99	1.08	122.08	1.29	137.31	7.0	504.15	67.91
133.59	39.95	5.67	443.53	2.39	214.36	2.61	229.36	-	-	229.17
133.84	40.0	4.23	342.84	1.49	151.22	1.69	165.07	2.0	219.0	191.62
134.08	40.06	4.26	344.64	2.11	194.7	2.15	197.52	3.0	237.86	149.94
134.57	40.16	5.25	414.03	2.66	232.75	-	-	-	-	181.28
135.31	40.32	4.66	372.7	2.81	243.2	-	-	-	-	129.5
135.55	40.37	4.65	371.91	3.03	258.91	3.11	264.26	-	-	113.0
138.25	40.9	2.27	205.39	0.75	99.25	-	-	1.0	99.25	106.14

Table 7.5: Statistical indicators χ^2 and BIC given for all the retrievals of the JIRAM spectra inside the white vortex, varying the Model atmosphere.

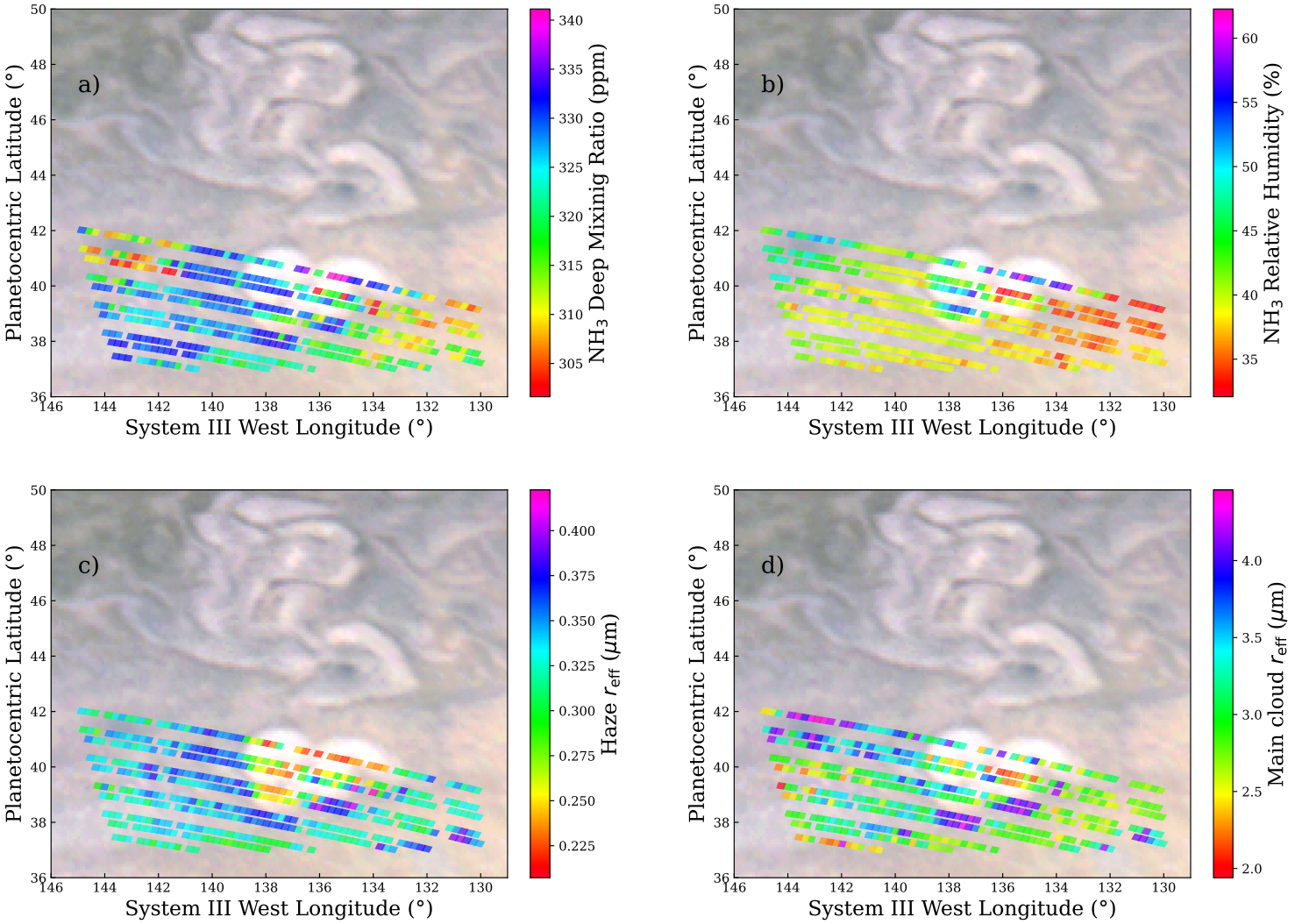


Figure 7.17: Retrieved parameters maps for: (a) gaseous ammonia deep volume mixing ratio, (b) gaseous ammonia relative humidity, (c) haze particles effective radius, and (d) main cloud particles effective radius. For all the panels, the background is a global map created from visible images acquired by the JunoCam.

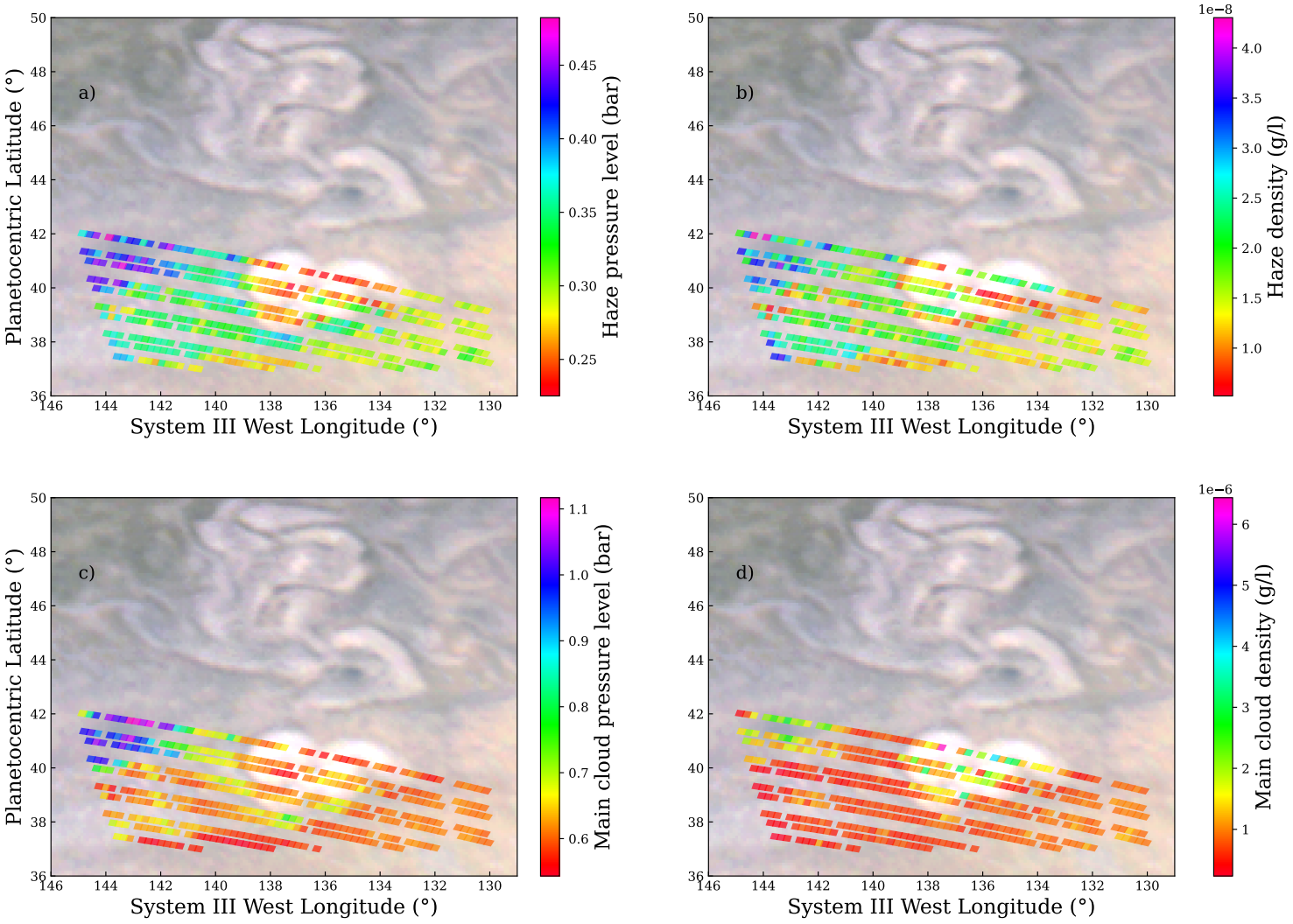


Figure 7.18: Retrieved parameters maps for: (a) haze's pressure levels, (b) haze's density, (c) main cloud's pressure levels, and (d) main cloud's density. For all the panels, the background is a global map created from visible images acquired by the JunoCam.

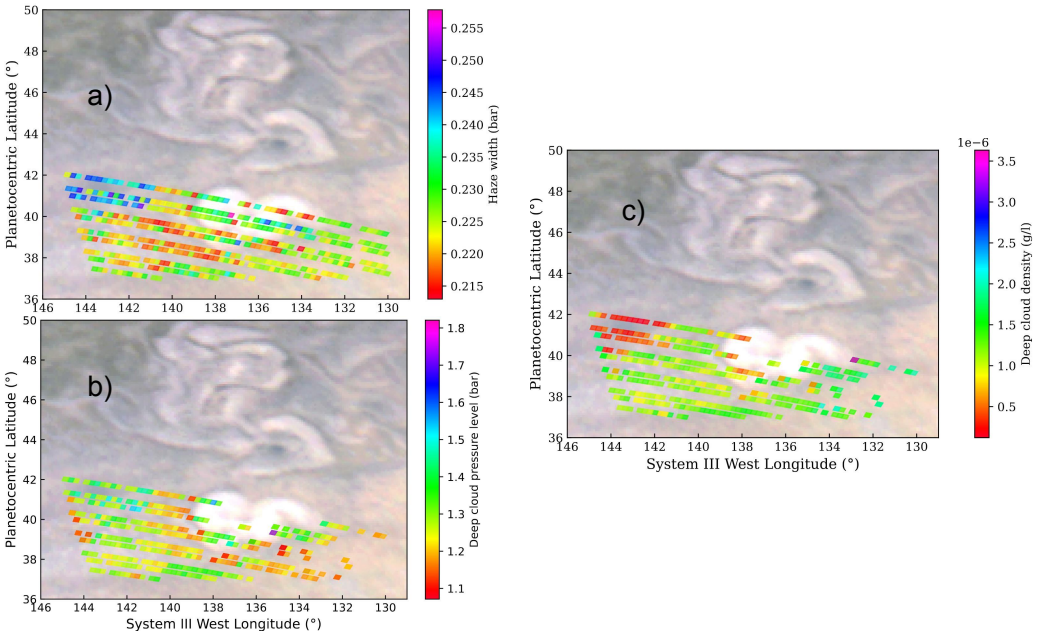


Figure 7.19: Retrieved parameters maps for: (a) haze's width, (b) deep cloud's pressure levels, and (c) deep cloud's density. For all the panels, the background is a global map created from visible images acquired by the JunoCam.

7.4.2 Haze and main cloud particles effective radii

Fig. 7.17c presents the distribution of the haze's effective radii. The values vary from a minimum of 0.21 ± 0.06 μm to a maximum of 0.42 ± 0.15 μm, in agreement with other remote sensing observations both in the infrared (Sromovsky & Fry, 2010a) and in the optical (Simon-Miller et al., 2001a), even if these were performed over regions of lower latitude. The mean uncertainty value is 0.1 μm. It is possible to observe a clear correlation with the vortex, in the proximity of which small ($\simeq 0.2 - 0.25\,\mu$m) effective radii are derived. Outside the vortex it is possible to observe two regions in the map: (i) a 'ring' around the vortex in which the radii are large (0.35-0.4 μm), and (ii) an outer 'halo' in which the radii are close to the median value (0.3 μm). On the contrary, the main cloud's effective radii distribution, shown in 7.17d, does not show any clear correlation with the vortex nor with latitude or longitude. The median value is 3 ± 0.7 μm, in agreement with the values found by Sromovsky & Fry (2018) in the regions where SIACs were detected. However, these results are not in agreement with the works of Dahl et al. (2021); Braude et al. (2020) that retrieved smaller radii ($\simeq 1\,\mu$m) in the visible. It is worth to remark, that the above cited works used discrete and very extended cloud decks to perform the retrievals. The multiple degeneracies discussed in Chapters 3 and 5 may be the reason for the found discrepancy in the values of the retrieved radii.

7.4.3 Haze pressure level and width

The haze pressure level and width maps are shown respectively in Fig. 7.18a and 7.19a. The haze's pressure levels vary from a minimum of 0.23 ± 0.07 bar to a maximum of 0.48 ± 0.05 bar The mean uncertainty value is 0.06 bar. These results are in good agreement with other remote sensing observations both in the infrared

(Sromovsky & Fry, 2010a) and in the optical (Simon-Miller et al., 2001a), over regions of lower latitude. Also, in this case, it is possible to observe a correlation with the vortex, where the hazes are located at lower pressures (i.e. higher altitudes). It is possible to observe a ring where the hazes seem to be lower and which appears to be in correspondence with the same region where larger effective radii are retrieved. Outside the ring, the behavior is not clear. Particularly interesting is a region at approximately $\simeq$ 42 N° and $\simeq$ 143 W°, where the hazes seem to be considerably lower than in the region of the vortex and the nearby regions. In the same location, the JunoCam images reveal a relatively dark oval, Fig. 7.1b, that infrared observations suggest as a zone of relative cloud clearance. However, I note from Fig. 7.3 that this region was observed by JIRAM at large incidence angle values, making it difficult to discern between a real downwelling or a geometry effect.
The widths of the haze's vertical distribution vary from a minimum of 0.21 $\pm$ 0.08 bar to a maximum of 0.26 $\pm$ 0.08 bar The mean uncertainty value is 0.08 bar. These values combined with the pressure levels confirm the fact that an extended layer of small particles that covers the 0.5-0.08 bar levels is needed to fit the JIRAM reflected sunlight spectra. A clear correlation with the vortex is not as evident as for the pressure levels, though in correspondence with the vortex the hazes seem to be slightly more vertically extended than in the nearby surroundings. Interestingly, also in this case, the largest width's values are in correspondence with the dark oval where the hazes seem to be lower in altitude (i.e. at higher pressures).

7.4.4 Main cloud pressure levels

The main cloud's pressure level and deep cloud's pressure levels maps are shown respectively in Fig. 7.18c and 7.19b. The main cloud's pressure levels vary from a minimum of 0.54 $\pm$ 0.05 bar to a maximum of 1.12 $\pm$ 0.08 bar. The mean uncertainty value is 0.04 bar. The comparison with previous works that studied regions at lower latitudes is made difficult by the non-uniformity of the chosen aerosol parametrization. For example both Sromovsky & Fry (2010a), Sromovsky & Fry (2010b), and Sromovsky & Fry (2018) used very wide single layers that extend from a few bars to the haze level. These clouds are too wide for a comparison, since they encompass both the main and deep clouds that I considered in my models. More useful is the comparison with the results from the visible spectral range. The main cloud levels that I found are either close to the 0.6 bar level or near the 0.85 bar level, in good agreement with the ones retrieved by Simon-Miller et al. (2001a), which did not report main clouds deeper than 1 bar level. The retrieved values show a clear correlation with the vortex, where higher clouds (0.6 bar) are detected. However, differently from the haze's levels case, here we do not observe a ring of lower clouds in the nearby region. We observe lower clouds (0.85 bar) only on the west of the vortex (39-42 °N and 141-139 °W). On the east regions that surround the vortex clouds near the 0.6-0.7 bar level are observed. This difference between the east and west sides of the vortex can be the cause of the shadow that was noted in the JunoCam images and discussed in Section 7.2. This may suggest that the vortex does not extend vertically at all longitudes. Interestingly, the main cloud's pressure levels retrieved in correspondence with the dark oval discussed above are much larger than the ones retrieved for the vortex and the nearby regions, suggesting

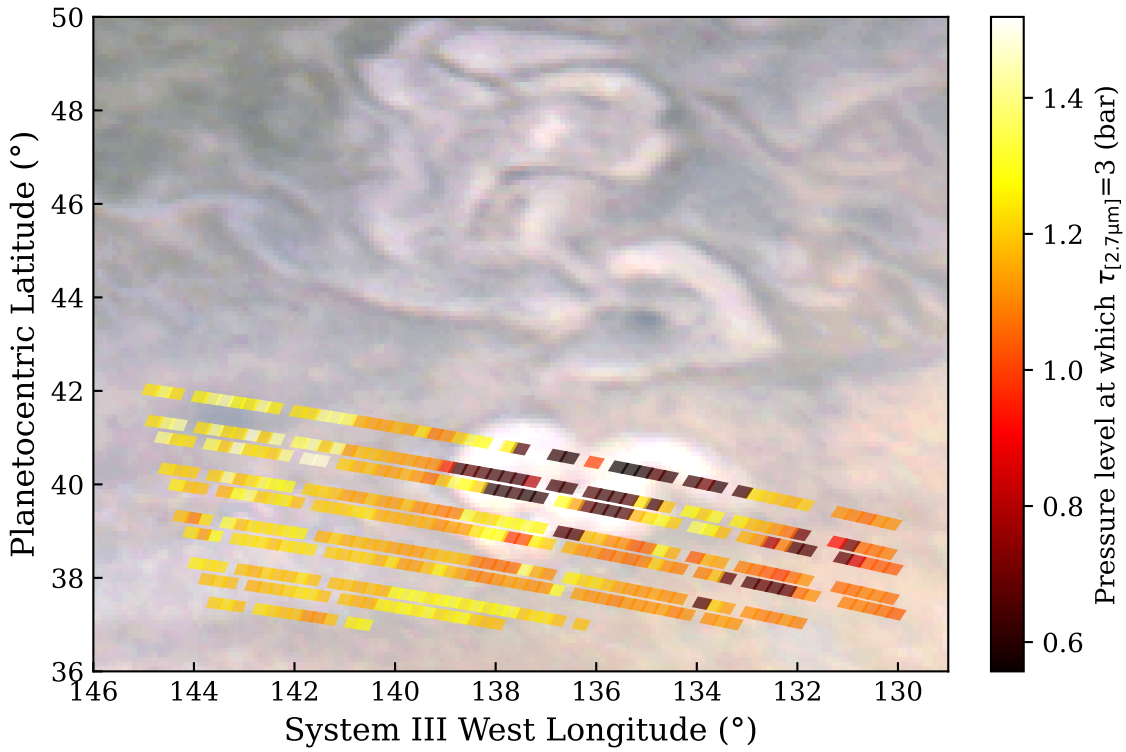


Figure 7.20: JIRAM coverage of the #1 ROI where the color of each pixel represents the pressure level at which a value of 3 in the optical depth at 2.73 μm is reached.

again that this region may be connected to a possible downwelling event.
The deep cloud's pressure levels vary from a minimum of 1.1 ± 0.2 bar to a maximum of 1.8 ± 0.4 bar. The mean uncertainty value is 0.24 bar. The maps in Fig. 7.19b consist only of pixels where the deep clouds can be sounded, i.e. where the main cloud did not become optically thick (see next section). The median deep cloud level retrieved in my analysis is 1.23 ± 0.2 bar. This is consistent with the work of Braude et al. (2020) which found the peak in optical depth to be lower (in altitudes) than the 1 bar level in order to fit the MUSE/VLT visible spectra of the SEB, NEB, and NTBs.

7.4.5 Aerosol layers densities and optical depth

The haze and main cloud density maps are represented respectively in Fig. 7.18b and 7.18d. The deep cloud density map is shown instead in Fig. 7.19c. The values in the maps are given in grams per liter (g/l) to facilitate the comparison between my results and previous and future works. The conversion from densities given in particles per unit of volume is possible once the radius of the particle are known and a fair assumption on density of aerosols is adopted. The retrieved haze's density values can vary from a minimum of (0.5 ± 1.0) $\times 10^{-8}$ g/l (50 ± 40 part./cm^3) to a maximum of (4.3 ± 3.2) $\times 10^{-8}$ g/l (750 ± 250 part./cm^3). The mean uncertainty value is 220 part./cm^3. Even if these values are less constrained by the retrievals, I obtained reasonable results. In fact, I find an extended deck of small particles that are far from becoming optically thick. It is not possible to observe a clear correlation neither with the vortex nor with latitude or longitude. The main cloud's

density can vary from a minimum of (2.4 ± 2.0) $\times 10^{-7}$ g/l (3 ± 2 part./cm^3) to a maximum of (6.4 ± 2.0) $\times 10^{-6}$ g/l (79 ± 18 part./cm^3). The mean uncertainty value is 3 part./cm^3. When the main cloud did not become optically thick it was possible also to retrieve the values of the deep cloud's density. These vary from from a minimum of (1.2 ± 2.5) $\times 10^{-7}$ g/l (40 ± 30 part./cm^3) to a maximum of (3.6 ± 2.0) $\times 10^{-6}$ g/l (1100 ± 900 part./cm^3). Both these values are consistent with previous observational (Braude et al., 2020) and theoretical (Zuchowski et al., 2009) works. These values confirm that observations seem to be far from the predictions of Atreya et al. (1999), even for a folded filamentary region at high latitudes. However, it is worth keeping in mind that densities computed with ECCMs must be intended as upper limits, while the lifting condensation levels (cloud bases) are more robust. The main cloud's densities are clearly correlated with the vortex, where higher values can be found. These values can easily make the cloud optically thick. Outside the vortex, the values are lower and mostly uniform. The only exception is again the dark oval where they become comparable with the vortex in terms of g/l but not in part./cm^3, as in this region the retrieved effective radii are larger than the ones retrieved inside the vortex. This can be a consequence of the above discussed correlation, see Fig. 7.9. On the contrary, the deep cloud's densities inside the vortex are not constrained, given the high optical thickness of the main cloud. Outside the vortex deep clouds seem to be uniform, except in correspondence with the dark oval, where the lowest values are reached.
Using all the values presented in the previous subsections, it is possible to produce a map of the pressure level at which a value of 3 in optical depth is reached at 2.73 μm, the wavelength value where the gas opacity is lowest. This is shown in Fig. 7.20 and was obtained using the following relation:

$$\tau_{2.73\,\mu m}(p_\star) = \sum_{i=h,\,C,\,D} \int_0^{p_\star} [N_i \cdot r^2_{\text{eff},i} \cdot Q_{\text{ext,i}} + \tau_{\text{gas}}] \cdot \Delta H, \tag{7.6}$$

where N must be expressed in part./cm^3, Q_{ext} is the estimate at 2.73 μm and is expressed as a non-dimensional number (i.e. independent of atmospheric properties), and ΔH represents the integration step that follows the considered pressure-temperature profile. τ_{gas} represents the optical depth per km and it is estimated from PSG cloud-free simulations. Fixing $\tau_{2.73\,\mu m} = 3$ it is possible to solve Eqn. (7.6) for $p_\star$ and obtain the values presented in Fig. 7.20. The map shows that the atmosphere tends to become optically thick at the deep cloud level outside the vortex, and optically thick at the main cloud level inside the vortex. This is also a hint that the vortex feature is elevated and more dense than the background clouds. The depth (in pressure) to which it is possible to view into the vortex is only about half the depth it is possible to probe outside the vortex.

7.5 Discussion

7.5.1 Explanation of the observed 2.73 μm shift

In Fig. 7.4 it is possible to observe how, for the spectra inside the vortex, the peak of maximum reflected sunlight seems to be shifted with respect to the spectra outside

the vortex. The shape of this radiation peak is a very important diagnostic of the aerosol properties as it corresponds to a zone of high transmittance, i.e. low gas opacity (an atmospheric window). As a consequence, two aerosol layers different in altitude, vertical extension, and/or composition will produce different radiation peaks in shape and intensity. Differences in altitude and vertical extension should produce the effect of broadening the peak maintaining however the position of the maximum, and this was noted studying the GRS, whose clouds are thought to be higher than the surroundings (Carlson et al., 2016a). There is no obvious relation that connects the Q_{ext}, single scattering albedo, and the HG asymmetry parameter to the resulting shape of the reflectance peak. However, referring to the zoom panel presented in Fig. 7.8 for a radius of 3 μm, it is possible to note that the single scattering albedo spectra of tholins and pure ammonia are very different from each other. All the spectra tend to decrease in this spectral region. However, the pure ammonia and $\gamma = 50\,\%$ ammonia-coated tholins profiles decay with wavelength more slowly than $\gamma = 85\,\%$ ammonia-coated tholins and pure tholins. In particular, the former starts decreasing for $\lambda > 2.8\,\mu$m, while the latter already for $\lambda > 2.74\,\mu$m. The same behavior is observed for optical properties computed considering $r_{\text{eff}} = 2\,\mu$m, Fig. 7.7, while it becomes negligible towards $r_{\text{eff}} = 1\,\mu$m, Fig. 7.6.
As from the JunoCam images there is a clear difference in color from the vortex (mostly white) and the outside (mostly grayish-brown), it is reasonable to suppose that this change is caused by the single-scattering albedo. This hypothesis is consistent with the retrieval results, as inside the vortex the majority of the spectra are best-reproduced by main clouds composed of either pure ammonia ice or $\gamma = 50\,\%$ ammonia-coated tholins, as the single scattering albedo of these two species (computed for $r_{\text{eff}} = 2-3\,\mu$m) can easily provide the shift of the reflection peak observed in JIRAM data.

7.5.2 Detection of ammonia clouds

I detected a total of 25 spectra that are best-reproduced by main clouds composed of pure ammonia ice particles and 15 spectra that are best-reproduced by main clouds composed of $\gamma = 50\,\%$ ammonia-coated tholins. Based on a Bayesian model comparison framework thanks to the BIC indicator, it is possible to claim that, in total, I detected 38 pixels covering spectrally identifiable ammonia clouds (SIACs). All the detections are in the proximity of the white turbulent vortex observed in JunoCam images, that can be considered to be a folded filamentary region (FFR). This kind of vortices are formed commonly at latitudes $> 35°$, and due to their color and thanks to the high-resolution JunoCam images, the presence of ammonia clouds was proposed and theorized (Fletcher et al., 2022; Guillot et al., 2024a). With this work, spectroscopic evidence of the presence of ammonia clouds in high-latitude FFRs on Jupiter has been established.
I want to stress that this detection was driven by finding the best cloud model that can explain the reflectance peak and the 2.95 μm absorption feature. This was possible thanks to the use of a fast and efficient radiative transfer code such as PSG, which does not sacrifice accuracy in performing precise multiple scattering calculations. Trying different models it is fundamental to claim a strong detection and to explore efficiently the parameter space. In fact, multiple combinations of the

physical properties and composition of the clouds can give similar shapes of the reflectance peak, but I found that only pure ammonia ice and heavily ammonia-coated tholin particles with effective radii between 2 and 3.5 μm can simultaneously provide a redshifted peak and an absorption dip at 2.95 μm, and so accurately fit the spectra inside the vortex. The spectra outside the vortex do not need ammonia clouds to be accurately reproduced, but pure tholins. These tholins should be understood as an approximation (in the 2.5-3.1 μm range) for the real - unknown - material that composes the Jovian clouds. Some possibilities for tholins on Jupiter are discussed in Section 7.6.

It is worth underlining that if I only focused on the 2.95 μm region, which is embedded in the gaseous-ammonia high opacity range, it would have been more difficult to determine which cloud model best explains the spectra inside and the outside of the vortex. Lastly, I stress that this detection was also feasible thanks to the spectral and spatial resolution of JIRAM. It would have been a lot more difficult observing different reflection peak shapes at a resolution similar to NIMS (after the High Gain Antenna failure).

In the light of these results I propose studying both the absorption features and the change in reflectance in low gaseous opacity regions as an efficient method to retrieve aerosol and cloud's properties of a planetary atmosphere. The 2.73 μm peak will be within the range of the MAJIS spectrometer on board the JUICE mission (Fletcher et al., 2023). This instrument will have a better and improved spectral resolution with respect to JIRAM, and will also cover the 5.1-5.4 μm range where ammonia hydrosulfide absorption features are expected. A similar 2.73 μm reflectance peak caused by ammonia or contaminated clouds is present also on Saturn (Coulter et al., 2022; Sromovsky et al., 2018) and should be considered as an important proxy for the search of ammonia ice clouds for future direct imaged Jupiter-like exoplanets (Robinson et al., 2016). On Uranus and Neptune, the same wavelength window can be used to infer the composition of the ice giants' planets aerosols (Roman et al., 2023).

The detection of these SIACs in a turbulent region confirms the trend that ammonia clouds are rare on Jupiter and connected to uplifting events, while on the rest of the Jovian disk they are absent or at least masked through a contaminant coating. This trend was established in the past 40 years thanks to NASA's Galileo, Cassini, and New Horizon missions, and to ground-based observations. This detection is the first one made thanks to the data from the Juno mission and places it in continuity with previous missions and literature works.

7.5.3 Interpretation of the vortex's nature

The retrieved physical parameters presented in Section 4 and in Table 7.2 can be used to give an interpretation of the nature of the white snail-like vortex identified as a folded filamentary region. I propose that this white feature is the result of a moist convection storm similar to the ones described in Hueso & Sánchez-Lavega (2001), Hueso & Sánchez-Lavega (2004), and Fletcher et al. (2017b), see Fig. 7.22. These storms can bring fresh ammonia from the deep troposphere (2-8 bar) up to the upper troposphere (1-0.1 bar). Successively, this ammonia can either condense and form pure filamentary ice white clouds or become a coating material for the

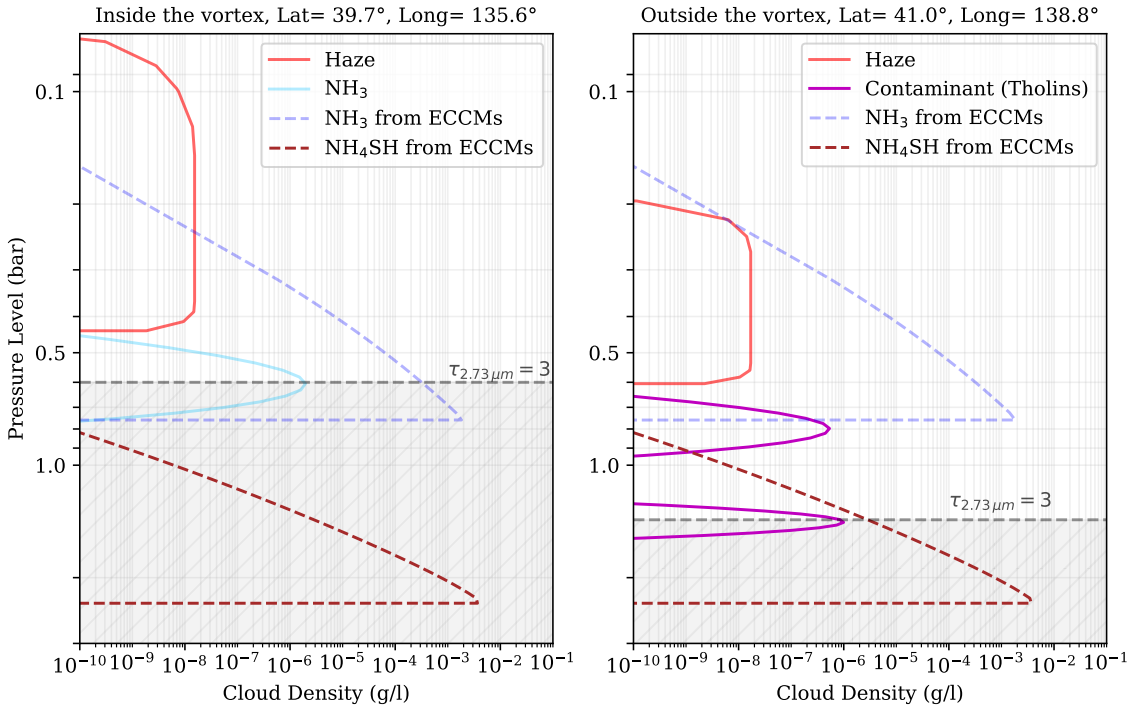


Figure 7.21: Best-fitting aerosol profiles for two JIRAM spectra, respectively outside and inside the white vortex. ECCM results are also shown here. The calculation assume 3× solar NH_3 and H_2S. Cloud densities are upper limits, the lifting condensation levels (cloud bases) are robust, however (Atreya et al., 1999). Gray dashed lines highlight the pressure levels at which $\tau_{[2.73\,\mu m]} = 3$ is reached.

previously existing haze or main cloud's particles. The presence of these storms at mid and high latitudes is not unusual on Jupiter. Juno data showed the presence of lightning caused by liquid $NH_3{\cdot}H_2O$ between 1 and 2 bars (Becker et al., 2020), and that ammonia is depleted down to at least several bars at mid-latitudes (Bolton et al., 2017b; Li et al., 2017). Both the findings can be explained by frequent large convective storms capable of lifting water and ammonia at the 1 bar level and inducing the formation of the so-called mushballs (Guillot et al., 2020a,b). Such an upwelling of ammonia (as well as water) clouds was observed in Saturn's Great Storm of 2010-2011 by Sromovsky et al. (2013).
In this work, the convection storm hypothesis is supported by four observations:

1. I found differences of 0.08-0.15 bars in the haze pressure levels between the regions inside the vortex and the ones surrounding it. These differences are larger than the median uncertainties (0.05 bar) on the retrieved parameters and translate into differences of 5-10 km in altitude;

2. I found higher gaseous ammonia relative humidity values inside the vortex with respect to the outside. Inside the vortex, the values are systematically larger than 45 % and reach a maximum of (63 ± 13) %. Outside the vortex the values are systematically lower than 45 %, reaching a minimum of (32 ± 12) %. This indicates that, above the condensation level, inside the vortex, there is a higher concentration of (presumably cold) gaseous ammonia than outside the vortex;

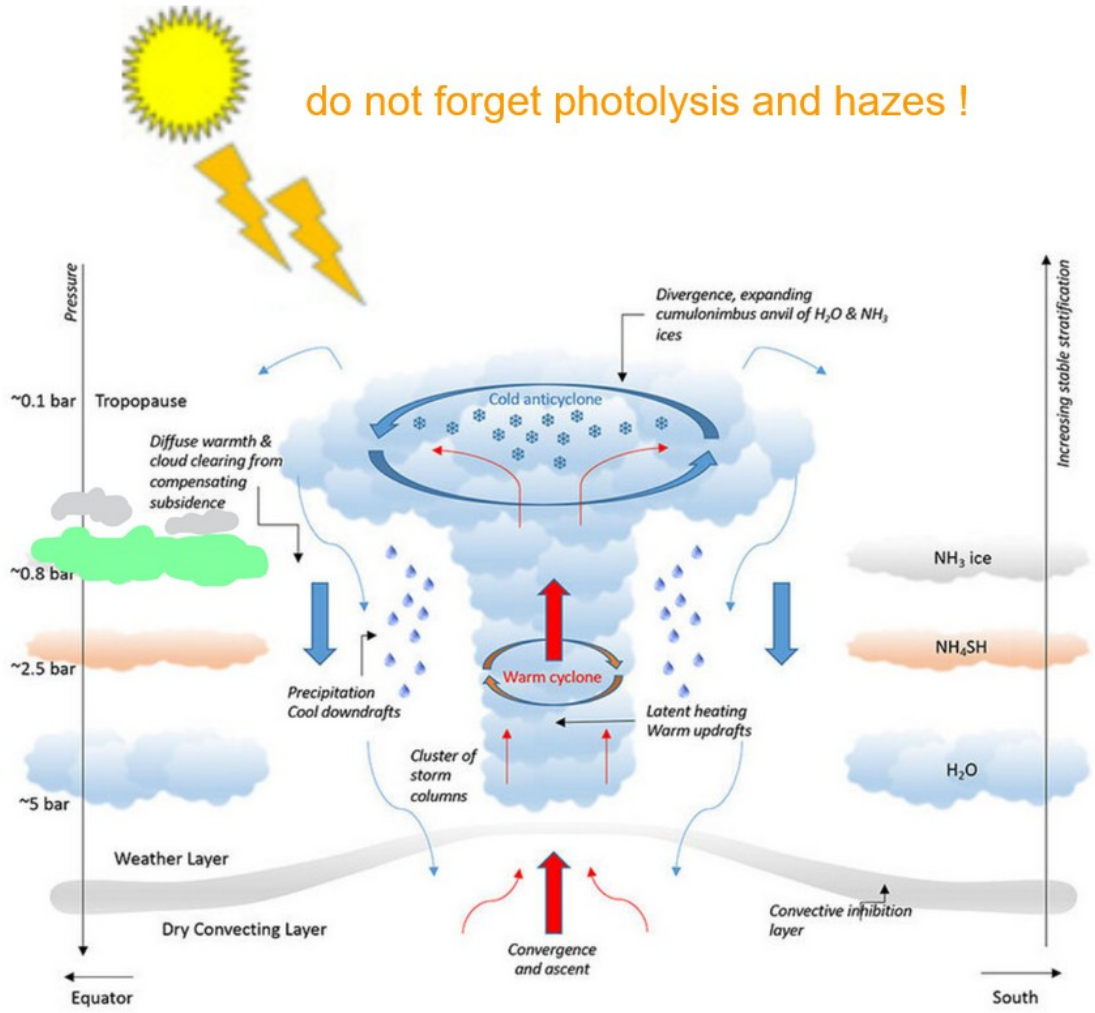


Figure 7.22: Sketch of a convective uplifting event in the Jupiter's atmosphere. A large amount of fresh ammonia is brought up in the upper troposphere where later it can condense and precipitate. The action of photochemistry can produce contaminant materials (green clouds) that can mix and react swith pre-existing ammonia ice particles.

3. I found differences of 0.10-0.20 bars in the main cloud pressure levels between the regions inside the vortex and the ones surrounding it on the west (System III West Longitudes $> 138°$). These differences are larger than the median uncertainties (0.03) on the retrieved parameters and translate into differences of 5-10 km in altitude. Having observed this difference only with the region on the west of the vortex may indicate that the moist convection storm was not uniform in longitude but that is slightly inclined westward. In turn, these values can also provide an explanation for the putative shadow observed in the JunoCam images (Fig. 7.1).

4. I found smaller haze particles' effective radii in the regions inside the vortex. As explained before, I found the haze particles' effective radius to be strongly correlated with the haze's density. However I found differences of $\simeq$ 0.1-0.12 μm in the retrieved parameters between the regions inside the vortex and the ones surrounding it, and these values are slightly larger than the median retrieved uncertainties of 0.08-0.10 μm. This can be a hint of the microphysics of the haze formation, as higher hazes (and clouds) tend to be constituted by smaller and less complex particles.

The obliquity of the storm (point 3) is only a conjecture based on the retrieved parameters because the information about the deep ($p > 1$ bar) vertical structure of the clouds is not accessible, see Fig. 7.20. I found that inside the vortex, where pure ammonia ice or ammonia-coated tholins clouds are detected, values of 3 in the optical depth are reached at the main cloud level. This is consistent with the fact that the vortex, and the folded filamentary regions in general, are highly turbulent making the formation of optically thick clouds statistically favored.
Outside the vortex the main clouds, composed of putative tholins, tend to be optically thin, and high values in optical depth are reached only at the deep cloud level, i.e. 1.1-1.4 bar level. This is consistent with the most recent findings from VLT/MUSE (Braude et al., 2020). The found cloud vertical structures in regions inside and outside the vortex are represented in Fig 7.21, together with results from ECCMs calculations that assume a 3$\times$ solar NH_3 and H_2S. I make several observations: (i) the same value in optical depth is reached approximately at 0.6 bar inside the vortex, and at 1.3 bar outside, which translates into a difference of $\simeq$20 km; (ii) the ECCMs can efficiently predict the pressure level at which the SIACs have been detected; (iii) the ECCMs cannot efficiently predict the inferred density values. In particular, the retrieved density values of the main cloud are at least three orders of magnitudes lower than the ones predicted by Atreya et al. (1999). In Chapter 2 we saw that more sophisticated models such as the one of Wong et al. (2015) predicted cloud densities between 1 and 2 orders of magnitude lower than the ones of Atreya et al. (1999). This finding hints that cloud condensation models need to be refined in order to explain JIRAM data. I propose that photochemistry may be the key process that causes this discrepancy as I will explain in the next section.

7.6 Possible origin of Titan-like tholin material on Jupiter

Titan-like tholins contain complex C,N containing organic compounds. Whereas Titan's atmosphere is dominated by nitrogen and contains ample methane, N_2 has not been detected in Jupiter's atmosphere, but it does contain other forms of nitrogen such as NH_3 and HCN. This allows for the possibility of forming N-C bearing coating material that may resemble Titan tholins. The source could be in the stratosphere or upper troposphere. Carlson et al. (2016a) demonstrated from laboratory experiments that reactions between the photolysis products of ammonia and acetylene resulted in brownish chromophores resembling the color of the Great Red Spot (GRS). Ammonia normally condenses at 0.5-0.7 bar, but in the GRS, it can be upwelled to the upper troposphere, where it can undergo photolysis. SIACs may also represent regions where ammonia is uplifted, allowing for its photolysis. The hypothesis that the Titan's tholins-like material "detected" by JIRAM in the near-infrared (2-3.5 μm) correspond to the material that Sromovsky et al. (2017b) found fitting the visual spectrum of clouds throughout the disk of Jupiter using Cassini/VIMS data is quite intriguing. However, the spectral properties of the used NH_3-C_2H_2 material were only measured in the 0.4-0.9 μm range (Carlson et al., 2016a). Therefore future laboratory measurements are needed to test this hypothesis.
Another possibility for the formation of Titan-like tholins involves HCN. The detection of HCN on Jupiter (Tokunaga et al., 1981) provides an evidence of "N" of NH_3 combining with "C" of CH_4. Models show that HCN is formed by coupled photochemistry of acetylene (C_2H_2, from CH_4) and ammonia in Jupiter's upper troposphere (Kaye & Strobel, 1983). HCN was also detected following the impact of comet Shoemaker-Levy 9 and then distributed planetwide over time (Moreno et al., 2003). HCN was likely the result of thermochemistry between CH_4 and NH_3. Once formed, HCN can undergo polimerization (Matthews, 1997). Complex polymers synthesized from HCN potentially make up a significant portion of Titan-like tholins invoked in this Chapter. Yet, another potential candidate is in the form of nitrogen-bearing polycyclic aromatic hydrocarbon haze (PANH, Atreya (2010)) and associated complex polymers from the upper atmosphere. PANHs require the insertion of nitrogen into PAHs synthesized from benzene (Atreya & Wong, 2005). HCN may provide the nitrogen, either directly or through its dissociation products.

In any case if Jovian tholins exist they should be different from Titan's ones. To test this hypothesis I derived a mean spectrum from JIRAM PJ1 data with the aim of performing one single MCMC full range retrieval and derive global properties and insights on the cloud composition. In order to do so we:

- masked the GRS that represents a very peculiar region
- retained -50 <latitude< 50 spectra due to limb darkening
- retained spectra that satisfy: $40 < \epsilon < 60$ and $60 < i < 80$ to reproduce similar viewing conditions of the future hypothetical LIFE mission that will observe cold exoplanets in direct imaging (Quanz et al., 2022). I decided to

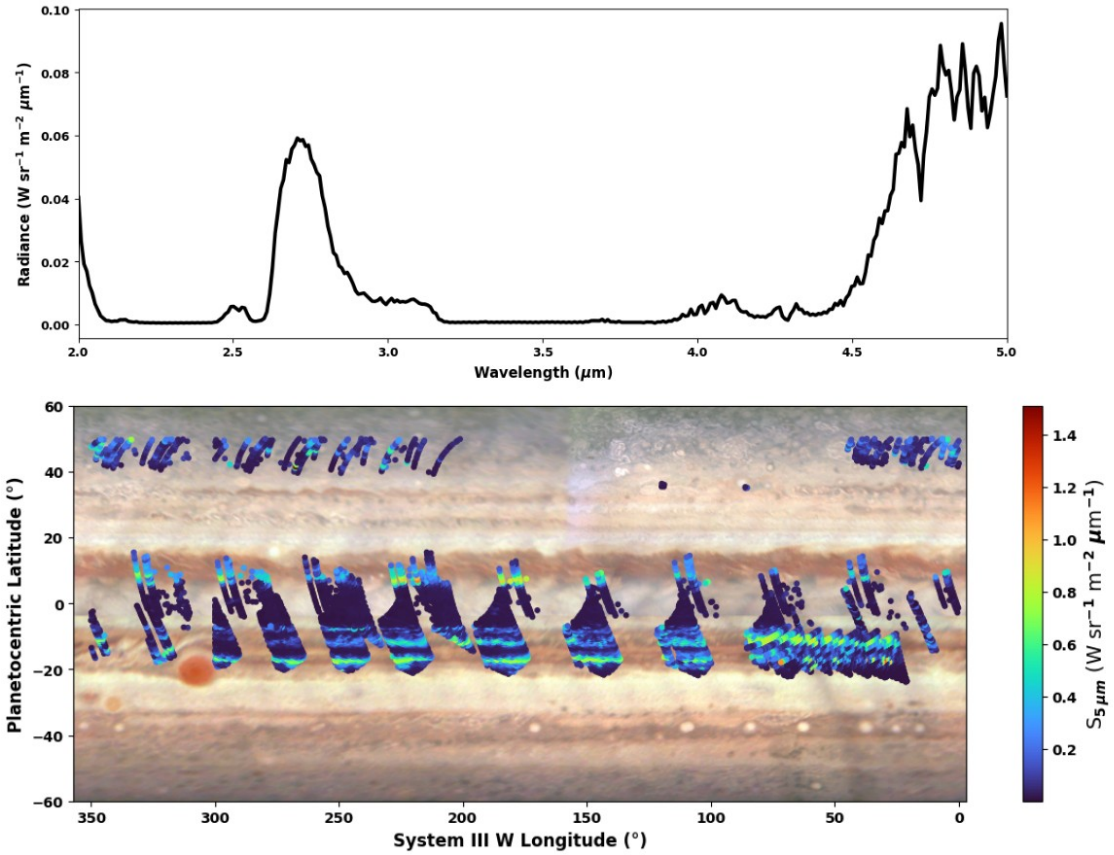


Figure 7.23: Above: JIRAM PJ1 mean spectrum. Below: representation of the selection criteria used to obtain it.

proceed in this way in order to obtain results that can be extended to warm and cold gaseous exoplanets.

The obtained mean spectrum is represented in Fig. 7.23. It is possible to note that the radiance levels are consistent in magnitudes with the full disk spectrum measured by ISO (Encrenaz et al., 1996).
In order to perform the retrieval I used the methods previously described in Section 6.6. After a series of preliminary test I found that the best deep cloud composition is a material with a refractive index of $n = (1.4, 0i)$, i.e. a gray cloud. Said that I performed three set of different MCMC retrievals using 5000 steps and 40 walkers. For each set of retrievals I used a different main cloud composition, as shown in Fig. 7.24,:

- pure ammonia ice as measured by Hudson et al. (2022)
- Titan's tholins as measured by Imanaka et al. (2012)
- Titan's tholins as measured by Imanaka et al. (2012) but removed of the strong 4.7 μm feature in the imaginary refractive index. I refer to this custom material as custom "modified" tholins

While the 2.7 μm peak in k values is induced by the N-H bond, as discussed in Section 7.3, the 4.7 μm feature is induced by C-N bonds (Gautier et al., 2012; Sciamma-O'Brien et al., 2017). I removed the 4.7 μm feature as we expect that Jovian tholins

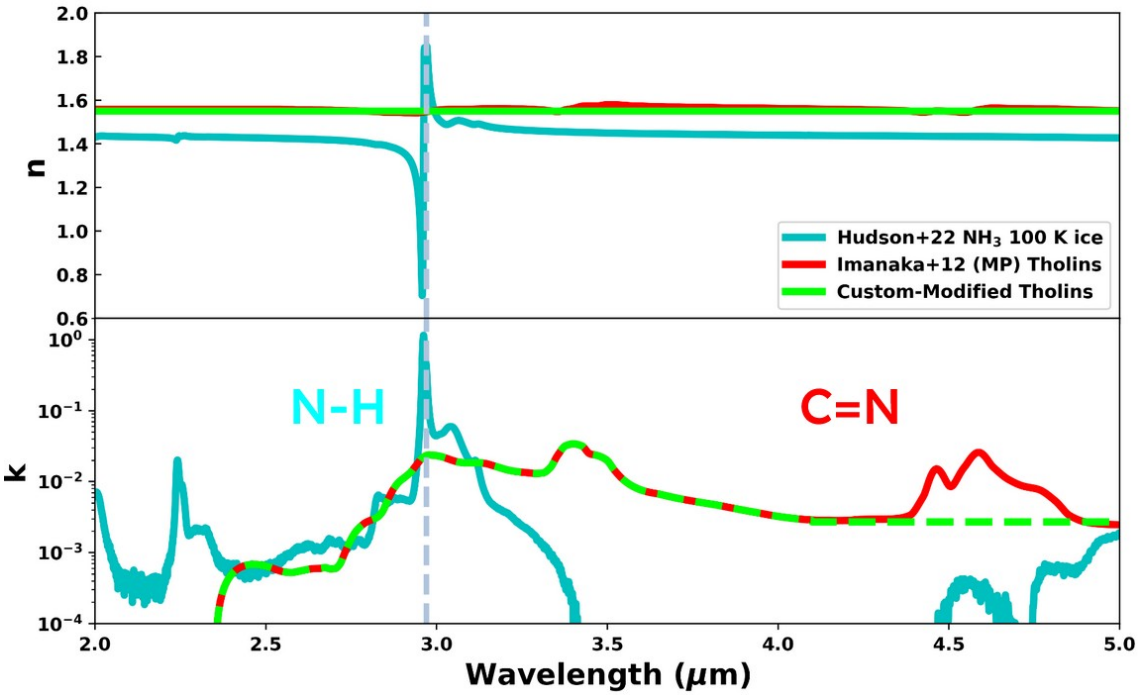


Figure 7.24: Refractive indexes of the main cloud species used to fit the JIRAM PJ1 mean spectrum.

to be different from Titan's ones. On Titan the main atmospheric components are N_2 and methane, with a N_2/CH_4 ratio close to 10. On the other hand, on Jupiter the main atmospheric species is H_2. The most abundant minor species, however, are indeed methane and ammonia with a NH_3/CH_4 ratio close to 0.1. Therefore the amount of available free nitrogen (not in its hydrogenated form) on Jupiter should be order of magnitudes lower with respect to the Titan's one. Laboratory works (Sciamma-O'Brien et al., 2017) showed that an increase in both the methane and hydrogen concentrations act to lower and dim the 4.7 μm feature. This increas have a less prominent impact on the strength of the N-H bonds. Therefore, we can think of the "modified" tholins as a first simple estimate of Jovian "adapted" tholins.
The results of the retrievals are shown in Fig. 7.25. In Fig. 7.26 I report the posterior probability distributions of the retrieved parameters and in Fig. 7.27 the best-fitting aerosol structure.
It is possible to derive important conclusions from this analysis:

- As expected pure ammonia ice clouds provide the worst fit to the JIRAM PJ1 mean spectrum.
- Imanaka et al. (2012) tholins provide a good fit of the solar range, as expected, but a poor fit of the thermal range, because of the 4.7 μm k-feature due to C-N bonds.
- The best fit is obtained when modified (Jovian adapted) tholins are invoked
- The retrieved parameters of the three spearate set of retrievals are consistent with each other at the 1-σ level. The only exception are the haze effective radius and density retrieved using ammonia clouds. However, this is induced

by the degeneracy previously discussed in this Chapter. This result implies that using pure ammonia ice as cloud component can be a reasonable choice to obtain rule of thumb estimates of physical parameters.

- The retrieved densities of the upper cloud are far from the ones estimated by theory (Atreya et al., 1999; Wong et al., 2015)
- Retrieved deep cloud density is consistent with the top of the theoretical NH_4SH cloud (Atreya et al., 1999; Wong et al., 2015)
- Tholins (of any kind) and hazes are not predicted by theory but can easily be explained by photochemistry and photolysis

Therefore I propose that on Jupiter aerosols are globally strictly connected to photochemistry, similarly to what happens on Titan. I propose a formation pathway for this Jovian-adapted tholins that occurs at the interface of the upper troposphere, as illustrated in Figure 7.28.

I hypothesize that these "modified" tholins are synthesized near the apical layer of freshly generated ammonia ice clouds. While the general presence of ammonia clouds is ensured by convective vertical motions, their effective lifetime is posited to be transient. As demonstrated by Sromovsky & Fry (2018), penetrating ultraviolet (UV) radiation is capable of reaching pressure levels up to 1.3 bar. At these altitudes, UV photons can dissociate larger ice particles, which subsequently engage in chemical reactions with the existing haze (likely comprised of small hydrocarbons) and the gaseous photolysis products of ammonia that migrate downwards from the tropopause.This scenario is particularly compelling as it provides a unified framework for several key observational constraints:

- It is consonant with the chromophore model detailed in Chapter 5.
- It is in agreement with the inferred low densities of the main cloud deck.
- It accounts for the observation that pure ammonia ice is detectable exclusively within vigorous storms and intense convective events on the Jovian disk. Only under such strong convective uplift is the deleterious effect of photolysis sufficiently mitigated.
- It is consistent with the spectroscopic signature indicating the presence of ammonia-coated tholins in correspondance of the vortex studied in Section 7.4.

While these observational constraints lend credence to my hypothesis, definitive validation of this scenario necessitates future laboratory investigations and numerical simulations. Moreover, recent results from the James Webb Space Telescope (JWST) underscore the fundamental role of photochemistry in the atmospheres of diverse exoplanets, including hot Jupiters (Tsai et al., 2023) and hazy sub-Neptunes (Kreidberg et al., 2014; Lavvas et al., 2019; Huang et al., 2024), further supporting the relevance of atmospheric photochemical processing in large-scale planetary systems.

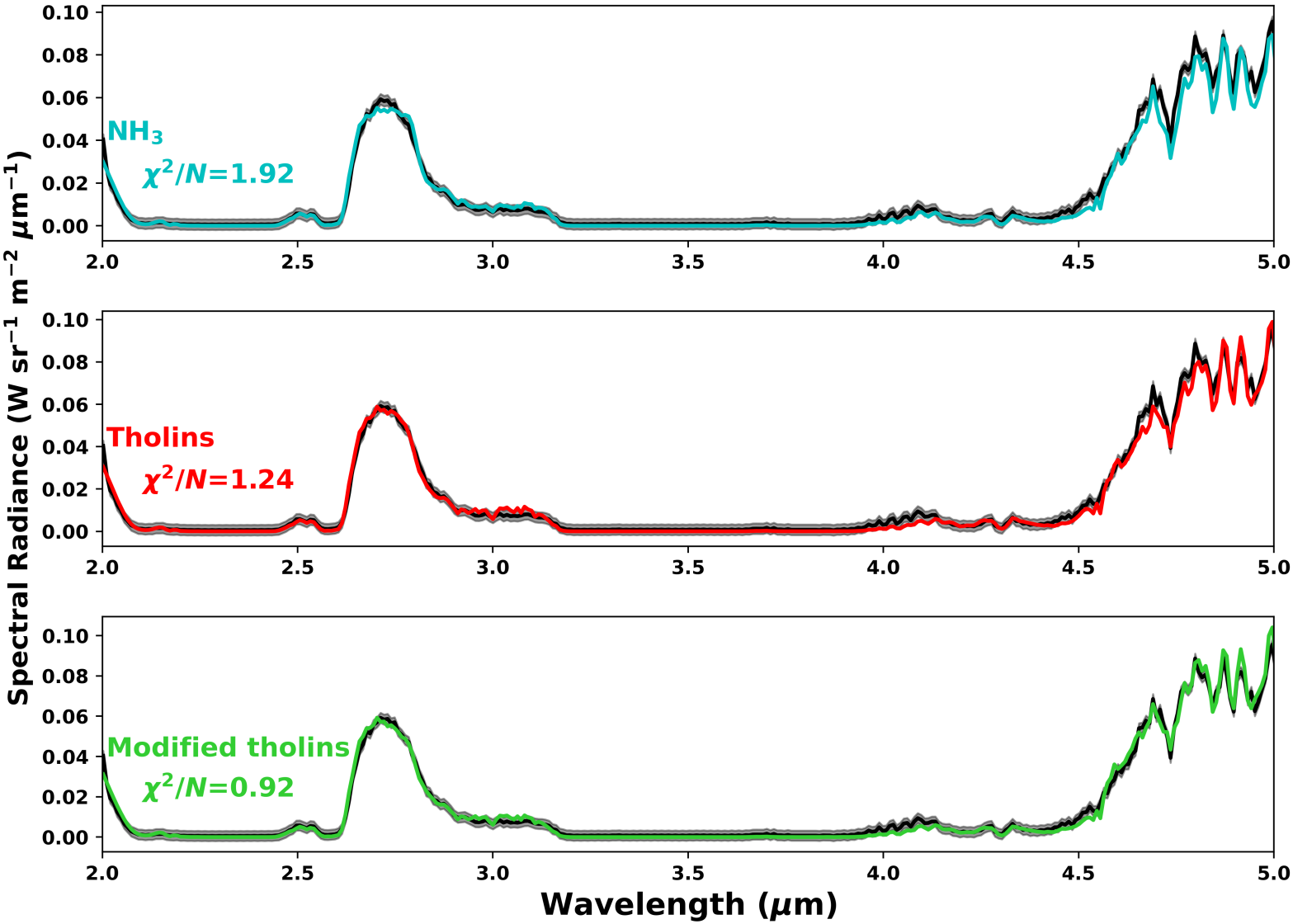


Figure 7.25: Comparison between the JIRAM PJ1 mean spectrum and the best-fitting retrievals.

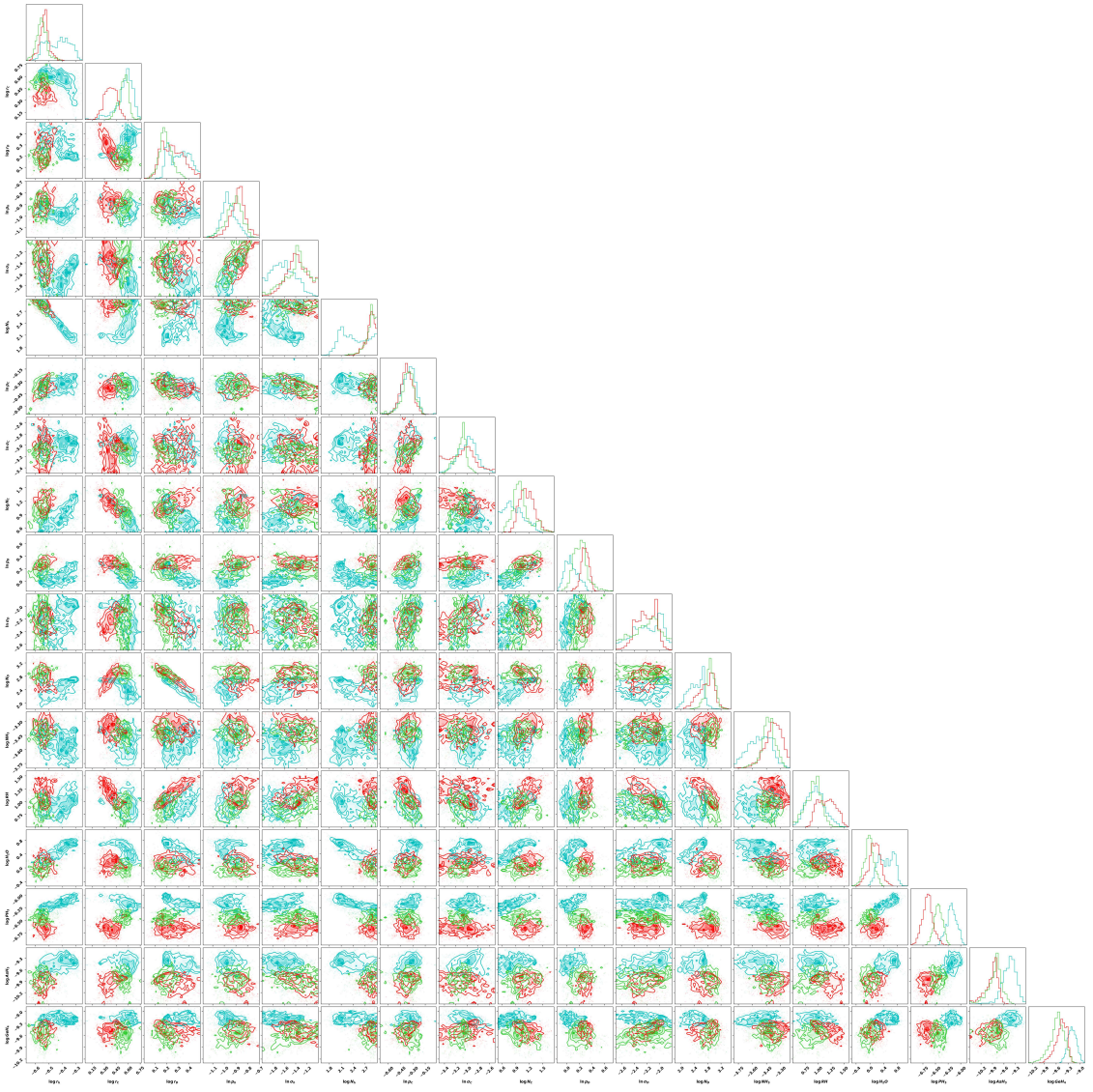


Figure 7.26: Retrieved parameters of the three set of retrievals performed on JIRAM PJ1 data.

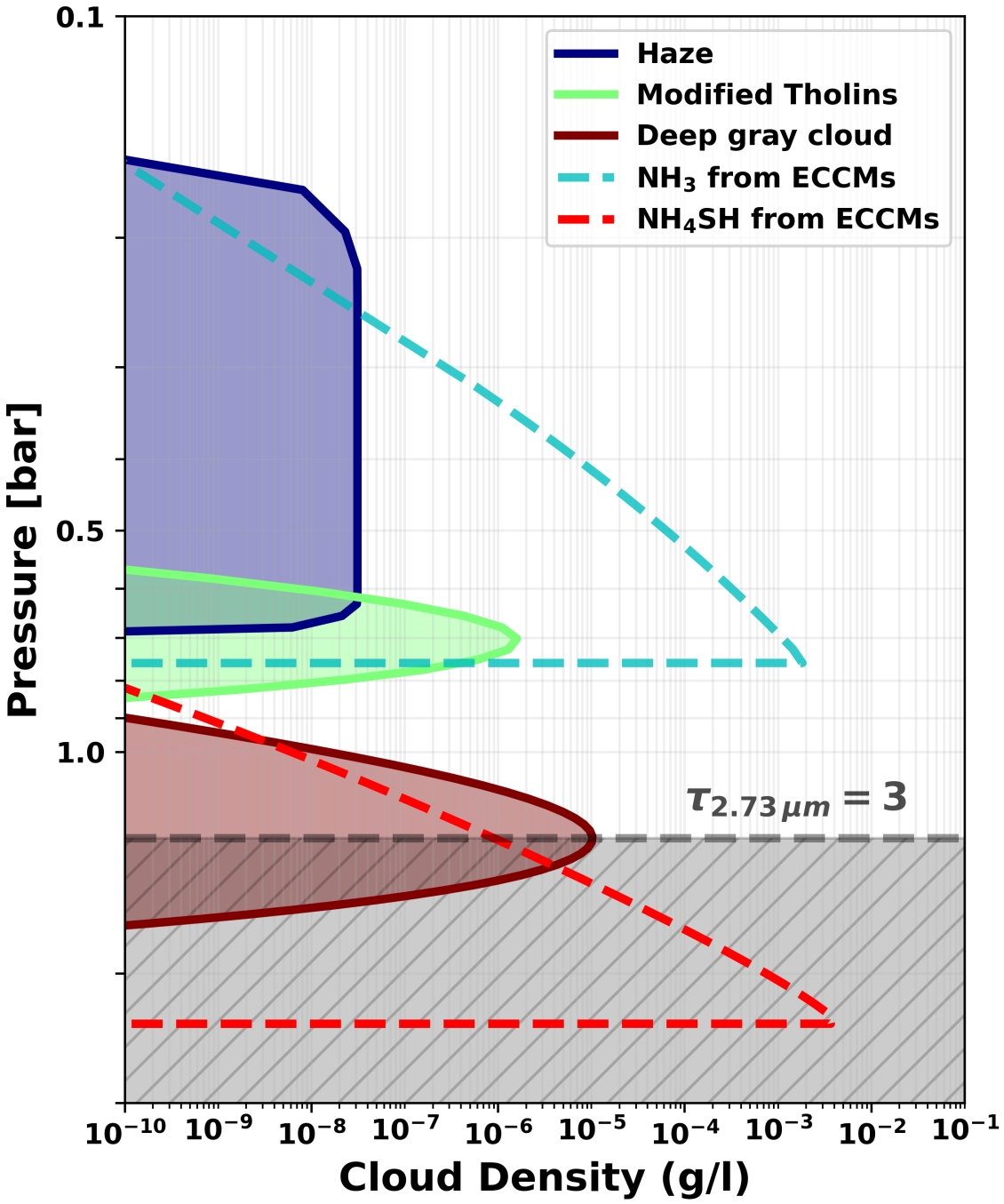


Figure 7.27: Best-fitting retrieved profiles in the case of modified tholins clouds.

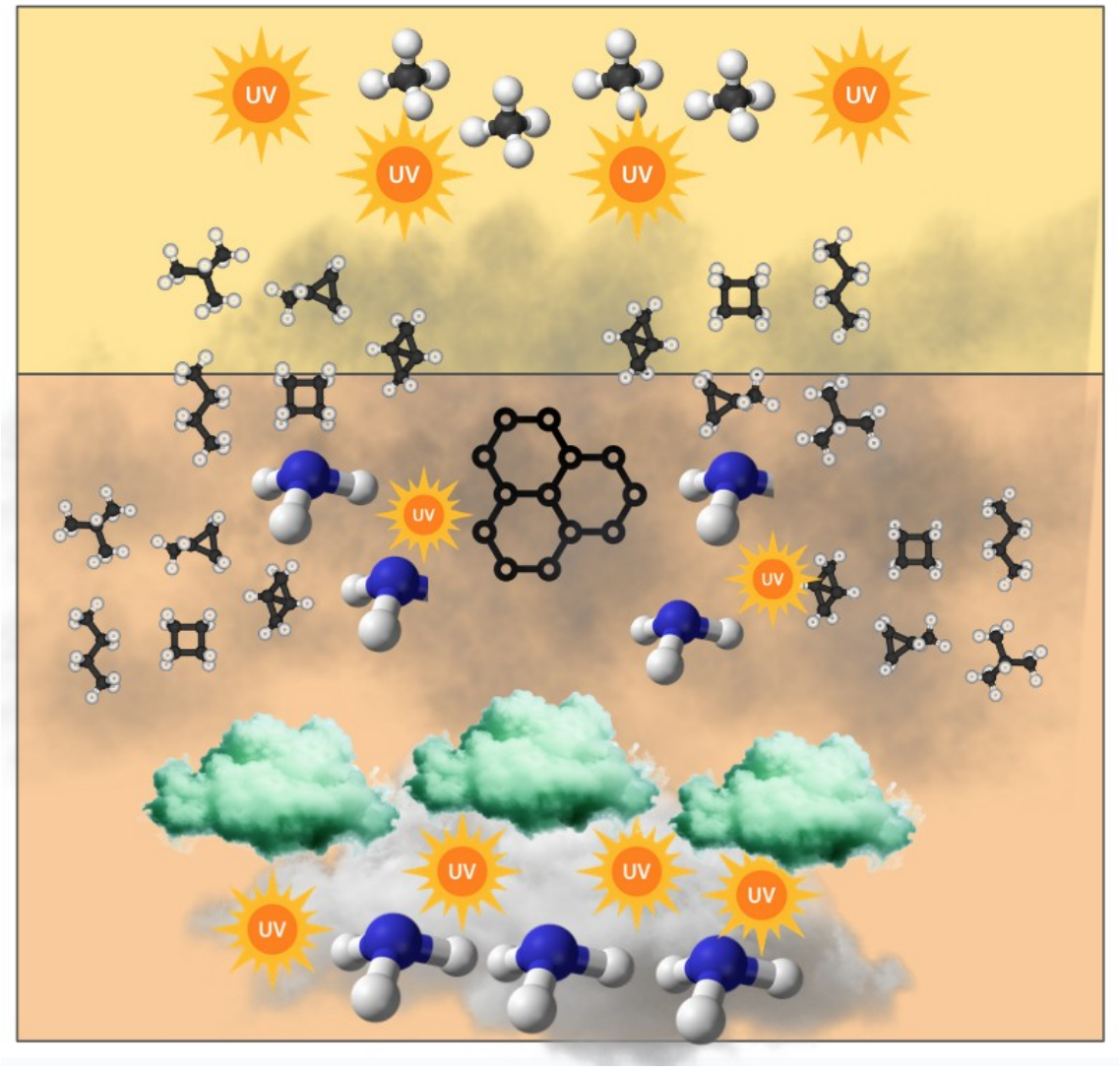


Figure 7.28: Sketch of my hypothesis regarding the formation and origin of modified tholins. The yellow box represents the lower stratosphere, while the orange one the troposphere. With white clouds I represent the fresh-formed ammonia clouds, while with green ones the Jovian-adapted tholins (to keep consistency with the other figures in the section).

Chapter 8

Unveil the origin of the GRS's wake ripples using JIRAM spectral data

8.1 Rationale

As seen in Chapter 2 that on Jupiter we should expect condensation of water clouds approximately close to the 5 bar level. In Chapter 7, however, it was quite clear that usually a value of 3 in optical depth is easily reached around 1-2 bar when cloud decks are present, making impossible to probe the atmosphere deeper. This explains why in literature there are no clear detections of liquid water clouds on Jupiter at the predicted condensation level, a discovery that could have an important astrobiological potential. The only tentative detection is represented by the work of Bjoraker et al. (2015) that hypothesized the presence of an extra opacity near 5 bar by looking at differences in the intensity of high resolution resolved lines of CH_3D with ground based telescopes. The spectral features of water ice have been detected near the 1 bar level using Voyager/IRIS measurements on less than 1 % of the entire dataset (Simon-Miller et al., 2000). This rate is consistent with convective storms (Guillot et al., 2020a) that brought water and ammonia up near the 1 bar level (as seen in Chapter 7) and with the observations of lightning events in the upper atmosphere Becker et al. (2020).
Jupiter atmosphere however is also quite dynamical, as already described in Chapter 2 and 5. Near the GRS, turbulent phenomena (known simply as ripples) have been frequently observed. This turbulent flows can in turn induce the formation of uplifting or downwelling events. The latter are particular interesting in the context of the search for water clouds as they can remove the optical barrier represented by upper clouds. Moreover, they represent unique transient events in the Jovian atmosphere that is known to be fully covered of clouds, with the exception of the exceptionally dry and small regions named hotspots (see Chapter 5). A clever way to easily find these downwellings or "particularly cloud-free" regions is to consider the Irwin anti-correlation relation presented in Chapter 5. Cloud free regions should appear extremely dim in the solar range, dark in the visible, and extremely bright in the 5 μm thermal atmospheric window. In this chapter I investigate the presence of these particular regions in the JIRAM dataset focusing in the latitudes range close to the GRS in order to look closely and physically characterize (for the first time) its ripples.

8.2 Observations

As in the previous chapter, I considered the spectra acquired by the JIRAM instrument during the first Juno perijove passage (PJ1) in August 2016. In Fig. 8.1 it is possible to observe two maps of the Jupiter disk during the PJ1 passage in which I represent the measured radiance by JIRAM at two different wavelengths: (a) at 5 micron, and (b) at 2.7 micron. These JIRAM maps confirm the anticorrelation previously observed between signals measured in the thermal region and those at shorter wavelengths dominated by solar scattering (Irwin et al., 1998). As already explained in Chapter 5, this behavior can simply be explained by the presence of clouds that can both reflect the solar radiation and block the radiation coming from the interiors. Therefore we expect black regions in the visible to present low signals at 2.7 micron and high signals at 5 microns as they lack of strong cloud opacity. The opposite holds true for regions that appear gray/white/yellow/orange in the visible. The main oval of the Great Red Spot and the surrounding dark filaments (named as such for their visible appearance and because they distribute in filamentary structures) are two straightforward examples, as it is possible to note in Fig. 8.1. However, on the west of the GRS, in correspondence of its ripples, it is possible to note at least four regions of interest (ROI) that present unusually low solar reflected signal values and are highlighted with white arrows and an identifier number in Fig. 8.1b and c. They present thermal signal values similar to the ones of the dark filaments, but solar signals way lower (between a factor 2 and 5). This behavior is not expected by the aforementioned anti-correlation. In the optical JunoCam images the ROIs appear as dark black ovals or filaments that are in contrast to the white/reddish surroundings of the GRS. The visible appearance of these regions suggest that they may be areas of unusual cloud clearance. In order to characterize these ROIs in more detail I considered a subset of the whole PJ1 data. The subset spatial coverage is presented in Fig. 8.1d, together with the signal at 2.73 micron measured by JIRAM for each pixel. The subset was selected in order to encompass together: (i) a part of the GRS main oval, (ii) a part of the GRS's hollow, i.e. its solar-bright collar, (iii) part of the GRS's ripples, (iv) the northernmost dark filaments, and (v) the ROIs labelled as 1,2, 3, 4, and 5. To simplify the discussion I will consider the regions different from the ROIs and the dark filaments as control regions. In the selection, the pixels span more than 30° (from 350° W to 320° W) in longitude and $\simeq$ 10° (from 20° S to 10° S) in latitude. The pixels have been selected to have similar incidence, emission, and phase angles as in the previous Chapter. This procedure ensures that the variance in the dataset is driven by different physical conditions rather than by different geometrical viewing conditions. This subset will be the object of this Chapter; in total it contains 420 spectra.

From the maps presented in Fig. 8.1d the ROIs display an unusually low value of the reflected sunlight radiation. I computed bidirectional reflectance distribution function (see Chapter 3) as prescribed by Irwin et al. (1998) in order to investigate deeper the implication on the anticorrelation previously observed by NIMS between signals measured in the thermal and solar wavelength regions. The obtained BDRF values computed at 2.73 and 5 micron are presented in Fig. 8.2. The majority of the data points clearly follow a straight line with a negative slope. The pixels of the control regions and of the dark filaments have been highlighted with red and black,

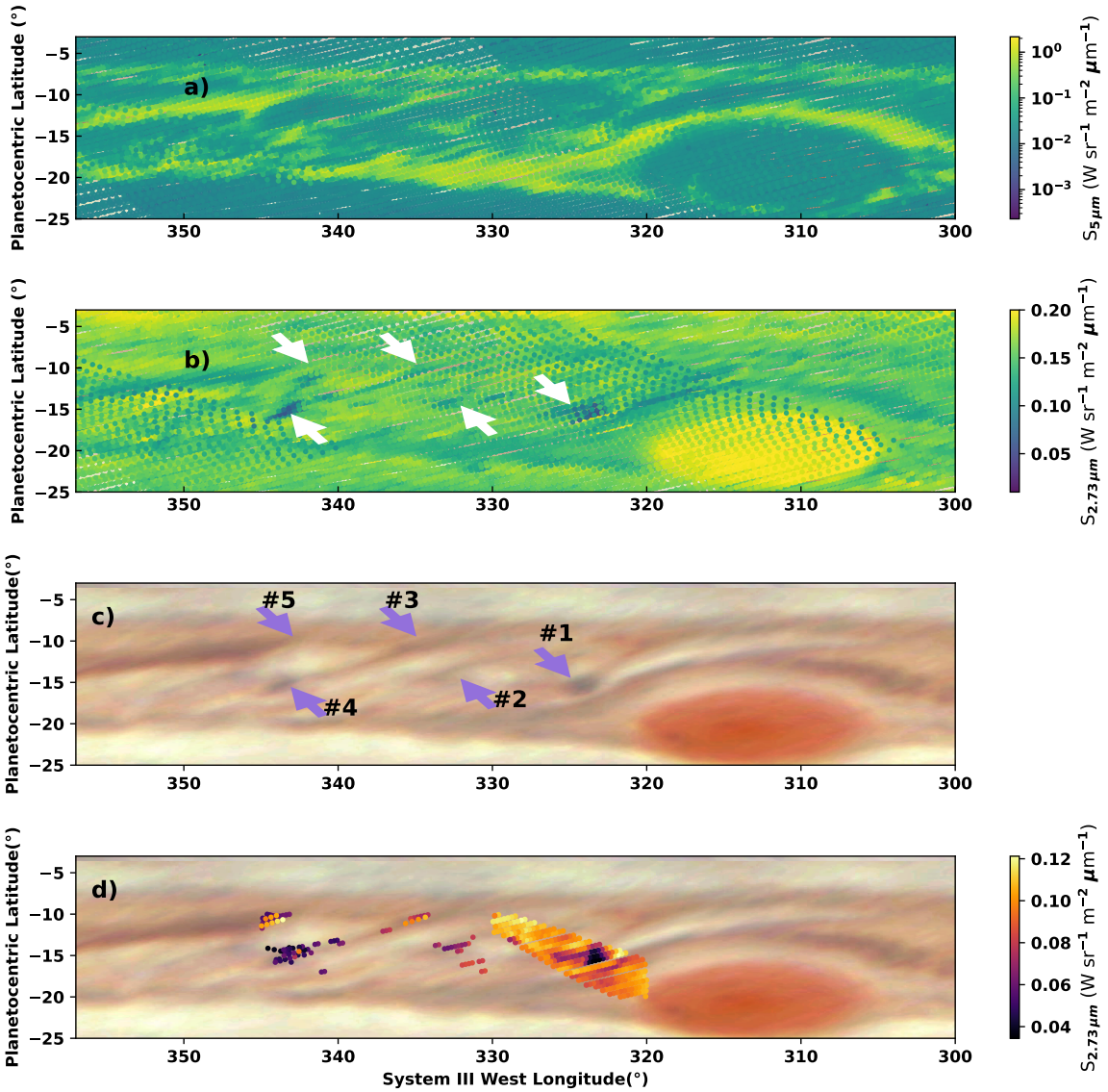


Figure 8.1: (a) 2.7 μm JIRAM maps of the PJ1 data. (b) 5 μm JIRAM maps of the PJ1 data (c) The same region descirbed shown in panel a and b as seen by JunoCam. (d) The subset analyzed in this Chapter.

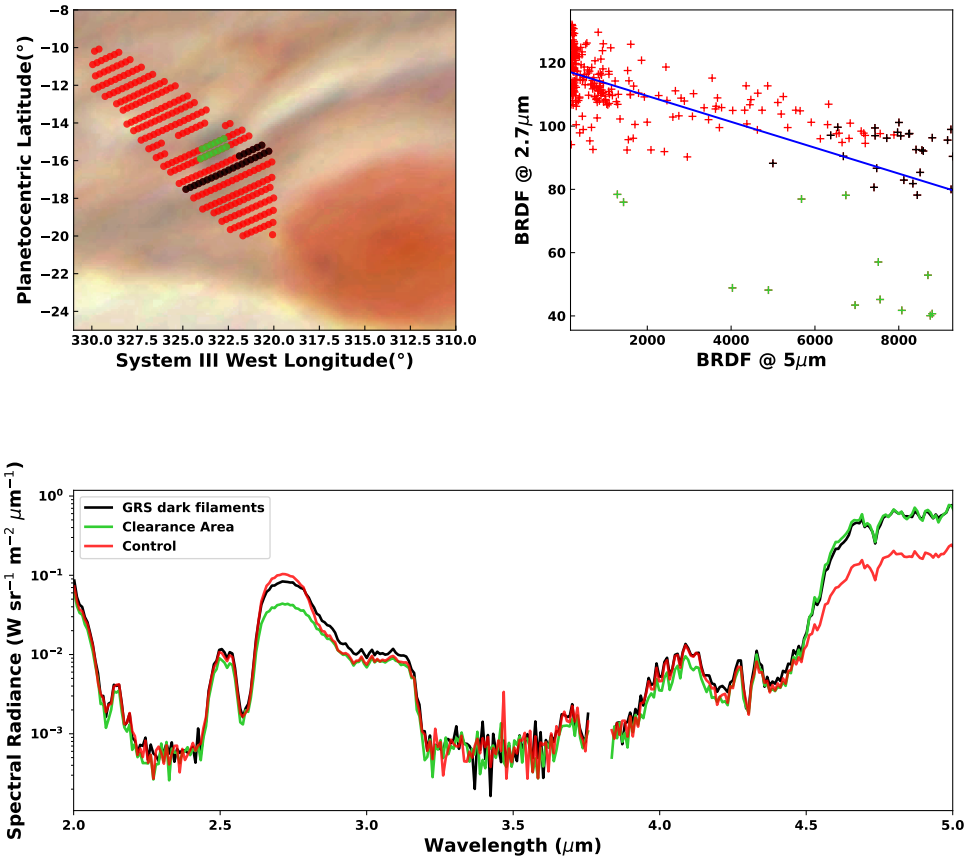


Figure 8.2: Top Left: a zoom on the northwest region of the GRS as seen by JIRAM. The pixels are colored in a way to discriminate: the #1 ROI (green), the dark filaments (black), and the control regions (red). Top Right: BDRF values compute at 2.7 and 5 micron for the JIRAM pixels represented in the Top Left panel. Bottom panel: The mean spectra of the regions highlighted in the Top Left panel. Note the logarithmic y scale.

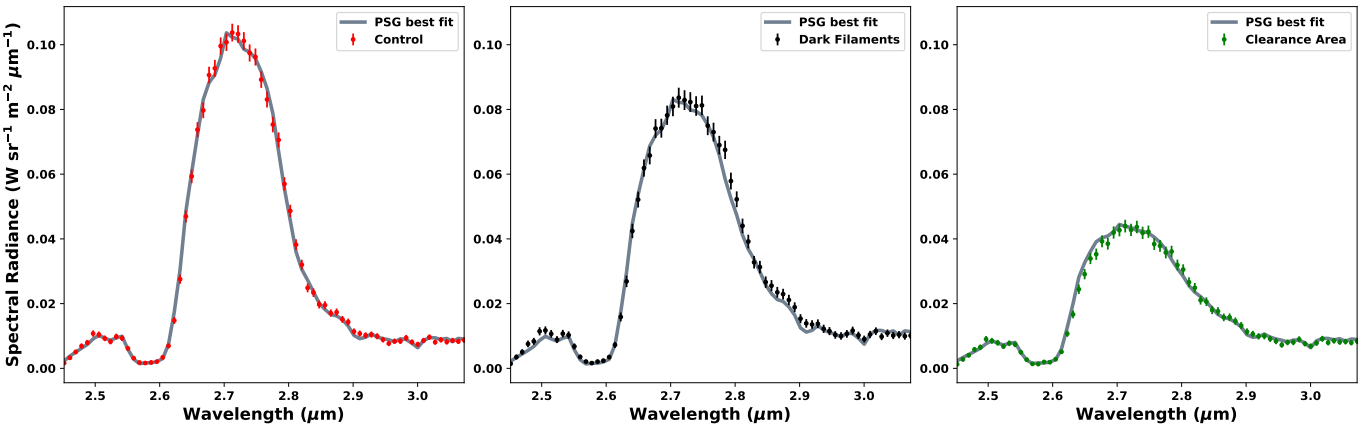


Figure 8.3: Best fitting solar retrievals of three different spectra belonging to: a control region, the dark filaments, and the #1 ROI.

and it is possible to observe that they respect the Irwin anticorrelation. However, a small fraction of the data, highlighted in green, occupy a different location in the parameter space. These points correspond to the pixels of the ROIs as it is possible to observe in Fig. 8.2 in the case of ROI #1. In Fig. 8.2 also three different JIRAM spectra are shown. The green curve represents a spectrum of a pixel inside the #1 ROI, the black one the spectrum of a dark filament, and the red one the spectrum of a control region. It is possible to note that the spectrum of the ROI has a thermal signal level and shape similar to that of the dark filaments. As expected, the solar signal value of the dark filaments is lower than the one of the control regions. However, the solar reflection peak of the ROI is considerably lower in signal than the other two spectra, by a factor between 2 and 5.

8.3 Methods

In order to estimate quantitatively the atmospheric properties of the selected ROIs I performed both solar and thermal retrievals as described in Chapter 6. I decided to first perform the solar retrievals and then the thermal ones. The thermal retrievals, in turn, are constrained to give ammonia concentration and cloud parameters consistent to the solar retrieved values, as explained in Chapter 6. This strategy is usually referred in the field as "snippet" retrievals, and can be advantagious as it is computationally more convenient with respect to full range MCMC retrievals. As I do not suspect the presence of particular cloud species I used Titan's tholins as the composition of the main cloud during the solar retrievals. Also the deep cloud was supposed to be composed of Titan's tholins with a fixed effective radius of 1 μm. For the solar retrievals the convergence criterion was set as $\chi^2/N < 2$. For the thermal retrievals the convergence criterion was $q < 0.12$ (Grassi et al., 2020).

8.4 Results

In Fig. 8.3 three examples of solar retrievals on JIRAM spectra of the control region, the dark filaments, and the #1 ROI are shown. Similarly, in Fig. 8.4 the resulting

Parameter	σ_a	$\bar{\sigma}_{\text{ret}}$
$\log r_h$	0.5	0.4
$\log r_C$	0.5	0.15
$\ln p_h$	0.5	0.12
$\ln w_h$	0.4	0.23
$\log N_h$	1	0.5
$\ln p_C$	0.5	0.075
$\log N_C$	1	0.1
$\ln p_D$	0.5	0.07
$\log N_D$	1	0.1
$\log \mathrm{NH}_{3VMR}$	0.1	0.04
$\log \mathrm{NH}_{3RH}$	0.20	0.09
$\log \mathrm{H_2O}_{VMR}$	0.5	0.5
$\log \mathrm{H_2O}_{RH}$	0.5	0.28
$\log \mathrm{PH}_{3VMR}$	1	0.1
$\log \mathrm{AsH}_{3VMR}$	1	0.27
$\log \mathrm{GeH}_{4VMR}$	1	0.12

Table 8.1: Retrieval parameters and their relative standard deviation of the a priori (σ_a). In the last columns the median retrieved uncertainties are given. The median was obtained considering all the 420 spectra in the collection.

Parameter	Unit	Control	Dark Filaments	ROIs #1 and #4
r_h	μm	0.27 ± 0.2	0.31 ± 0.2	0.29 ± 0.2
r_C	μm	2.8 ± 1.3	3.1 ± 1.4	2.9 ± 1.5
p_h	bar	0.27 ± 0.04	0.29 ± 0.04	0.25 ± 0.04
w_h	bar	0.27 ± 0.08	0.25 ± 0.08	0.26 ± 0.08
N_h	part./cm^3	165 ± 100	151 ± 100	142 ± 100
p_C	bar	0.75 ± 0.10	0.70 ± 0.10	0.6 ± 0.10
N_C	part./cm^3	9 ± 1	9 ± 1	5 ± 1
p_D	bar	1.49 ± 0.15	1.55 ± 0.11	1.39 ± 0.17
N_D	part./cm^3	200 ± 80	195 ± 93	45 ± 30
NH_{3VMR}	ppm	300 ± 45	203 ± 27	193 ± 26
NH_{3RH}	%	12 ± 3	8 ± 2	9 ± 2
$\mathrm{H_2O}_{RH}$	%	5 ± 4	3 ± 4	3 ± 4
PH_{3VMR}	ppm	0.66 ± 0.13	0.34 ± 0.03	0.31 ± 0.03
AsH_{3VMR}	ppb	0.47 ± 0.31	0.16 ± 0.09	0.30 ± 0.08
GeH_{4VMR}	ppb	0.94 ± 0.31	0.72 ± 0.10	0.71 ± 0.09

Table 8.2: Retrieved mean parameters corresponding to: the control regions, the dark filaments, and the ROIs.

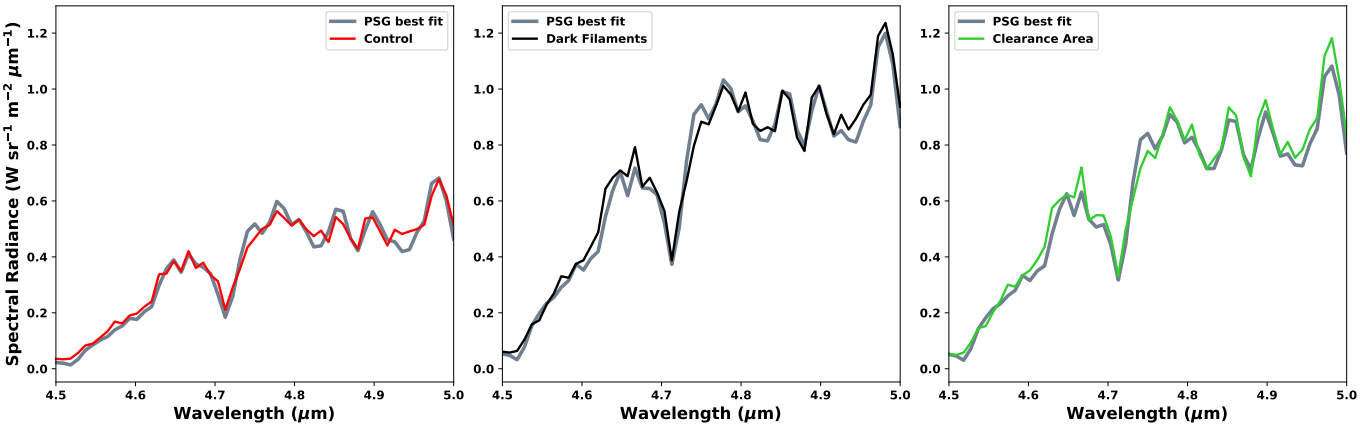


Figure 8.4: Best fitting thermal retrievals of three different spectra belonging to: a control region, the dark filaments, and the #1 ROI

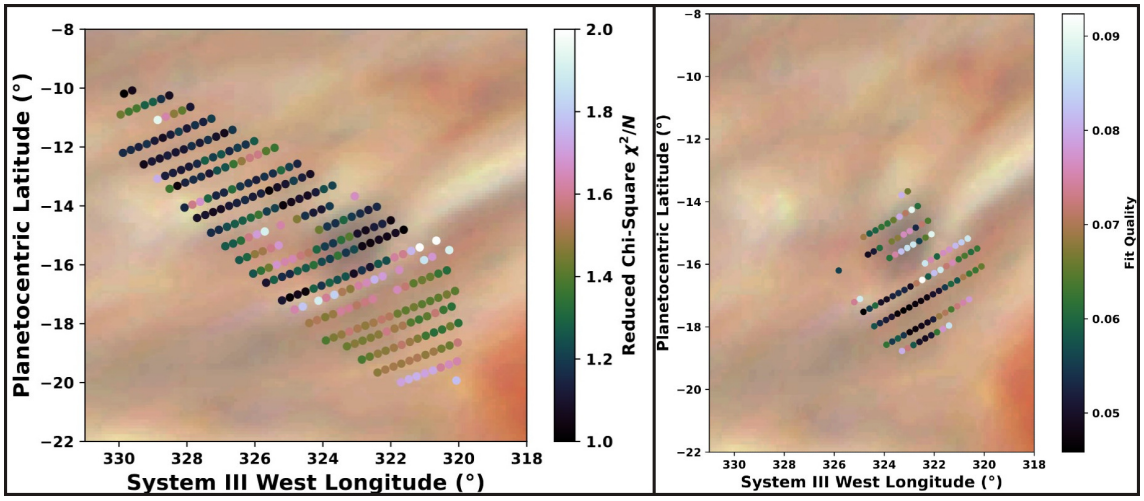


Figure 8.5: χ^2 and q maps for the solar and thermal retrievals of the #1 ROI.

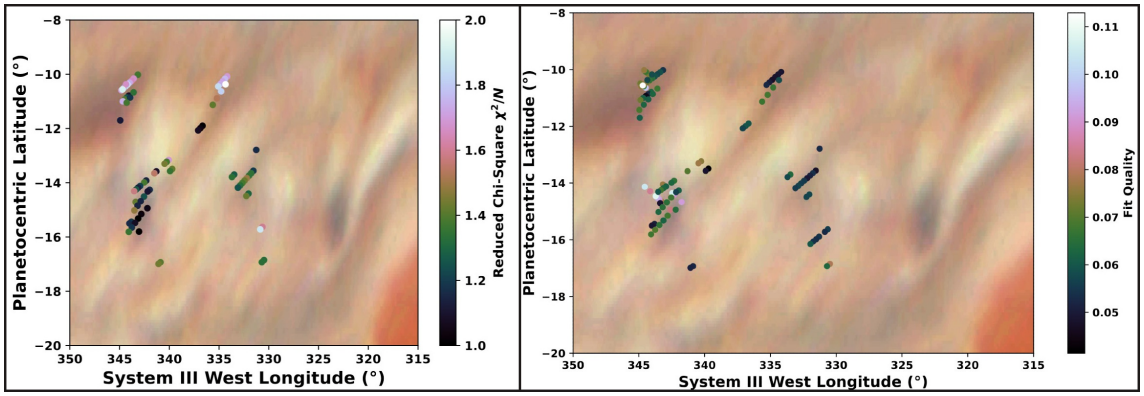


Figure 8.6: χ^2 and q maps for the solar and thermal retrievals of the #2, #3, #4, and #5 ROIs.

best-fitting thermal retrievals are shown considering the same spectra presented in Fig. 8.3. In Fig. 8.5 and 8.6 it is possible to observe the maps of the two used fit-quality indicators. It is possible to observe from the right panel of Fig. 8.5 that the thermal retrievals converged only for the spectra that showed a thermal signal greater than 0.1 W / sr m^2 μm and not for each spectrum in the dataset, a behavior already observed by Drossart et al. (1998), Irwin et al. (1998), and Grassi et al. (2020). However, with the converged thermal retrievals I still have optimal spatial coverage of the ROIs and their surroundings. From Table 8.1 it is possible to observe that the retrieved parameters are weel constrained as their posterior retrieved uncertainties are far below the a priori ones. The only exception is the water deep mixing ratio. This was already noted by Grassi et al. (2020). I stil note the strong degeneracy between the haze radius and its density.
In Fig. 8.7, 8.8, 8.9 and 8.10 the maps of the retrieved clouds and aerosol properties are given, while in Fig. 8.11 and 8.12 the maps of the retrieved gaseous mixing ratios are shown. The mean retrieved values for the control regions, the dark filaments, and the ROIs #1 and #4 are given in Table 8.2. In Fig. 8.13 I present the retrieved values for gaseous ammonia derived both from solar and thermal retrievals. From it, it is possible to observe the consistency between the two separate retrievals.

From the values represented in the above cited figures we can observe that:

- There is not a correlation between the ROIs and water relative humidity. The retrieved values are consistent with previous works of Grassi et al. (2020) and Li et al. (2020a).

- In correspondence with the ROIs and the dark filaments ammonia, phosphine, arsine, and germane appear to be depleted with respect to control regions. Phosphine is depleted of a factor > 2, ammonia by a factor between 1 and 2, while germane and arsine are depleted by a factor between 1.4 and 1.6. However, even if depleted with respect to control regions, retrieved values lie in the range probed by previous studies (Grassi et al., 2020; Fletcher et al., 2016b) and cannot be considered as anomalous. The only exception is depletion of arsine in correspondence with the GRS dark filaments. The retrieved value is a factor 1.5-2 smaller than the one from Grassi et al. (2020). It is also possible to note that arsine concentrations just seem to follow the latitudinal trend already noted both by Grassi et al. (2020) and Fletcher et al. (2016b).

- The haze pressure level and effective radius maps are consistent with previous results in the visible (Simon-Miller et al., 2001a; Baines et al., 2019) and confirm that near the GRS particles are found higher in altitude and are slightly smaller in radius with respect to nominal regions.

- There is not a correlation between the maps of the cloud's effective radii and the ROIs. The same holds for the maps of clouds pressure levels. These are consistent with the previous works of Grassi et al. (2021), Braude et al. (2020), and and Irwin et al. (2025) that place the main source of reflectivity between 0.9 and 0.5 bar, and the optical thick cloud around 1.2-1.5 bar.

- I found a strong correlation between the density of both main and deep clouds and the presence of some ROIs. Namely, in correspondence with the #1

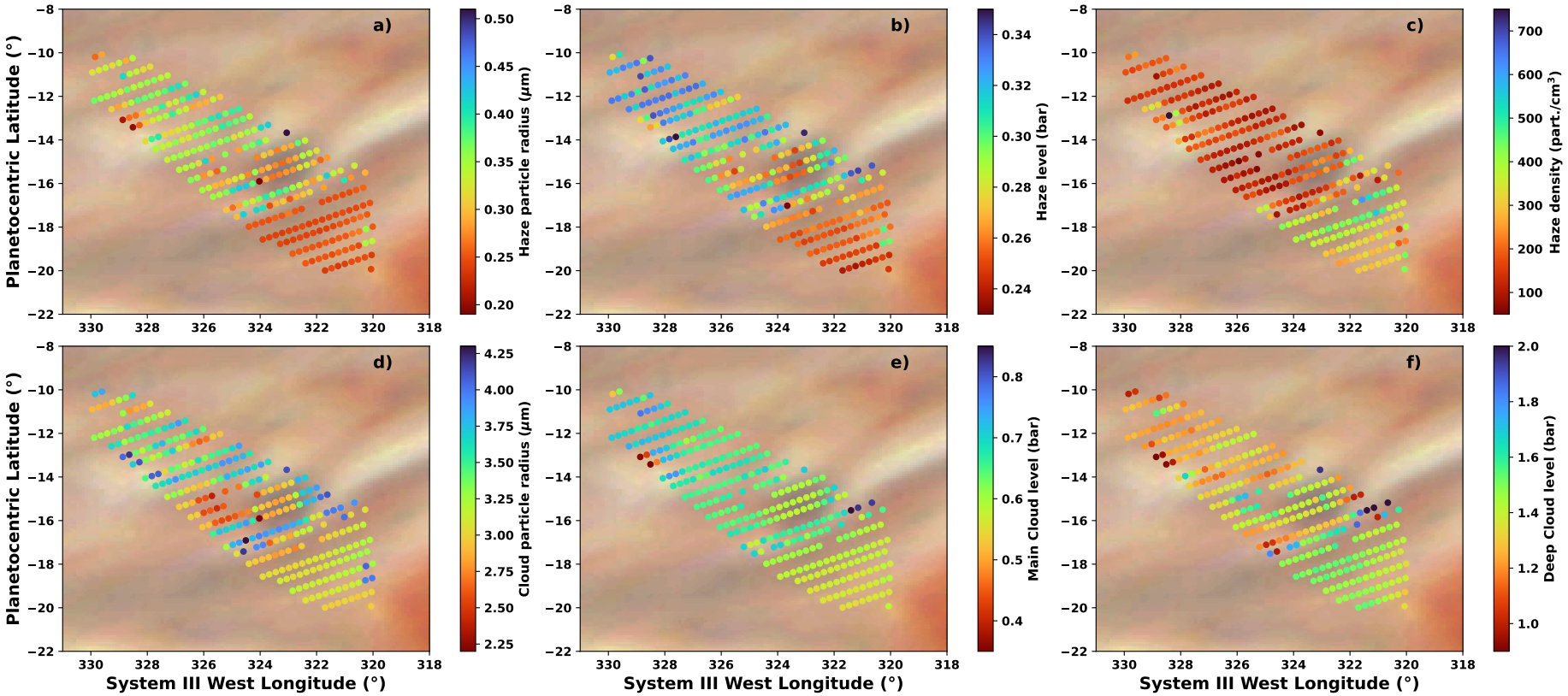


Figure 8.7: Retrieved aerosol parameters maps from the solar retrievals of the #1 ROIs.

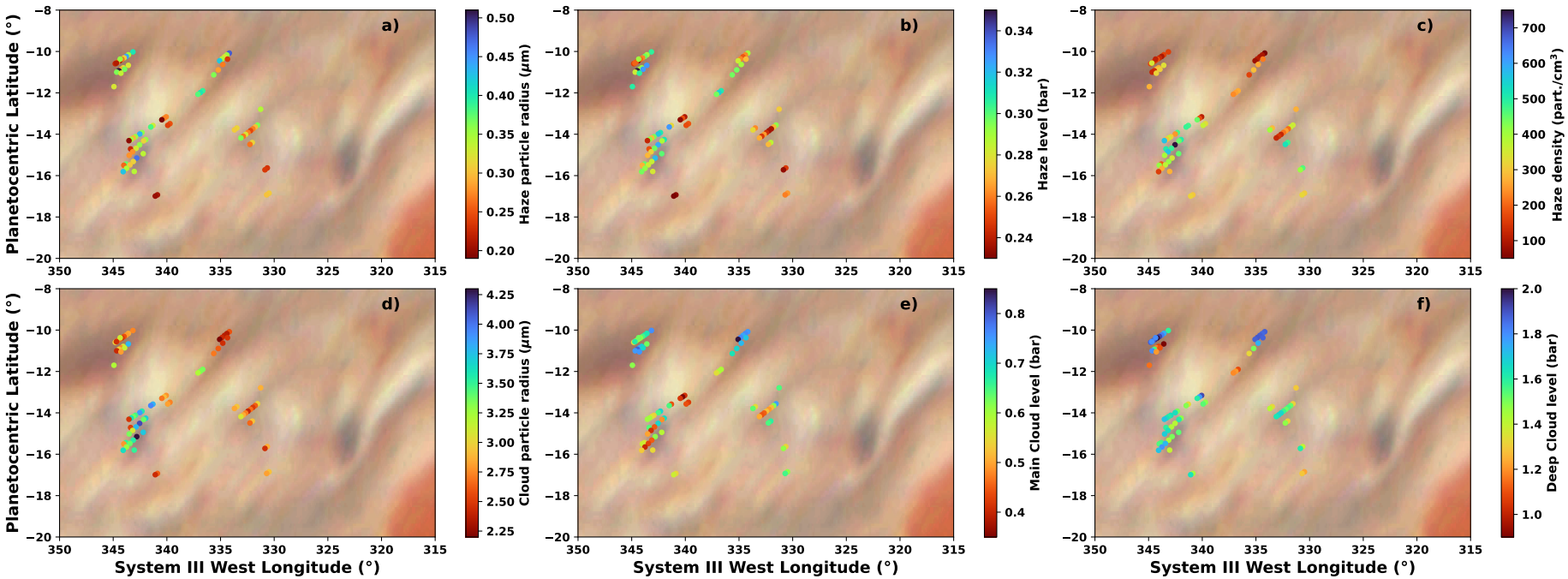


Figure 8.8: Retrieved cloud density maps from the solar retrievals of the #1 ROIs.

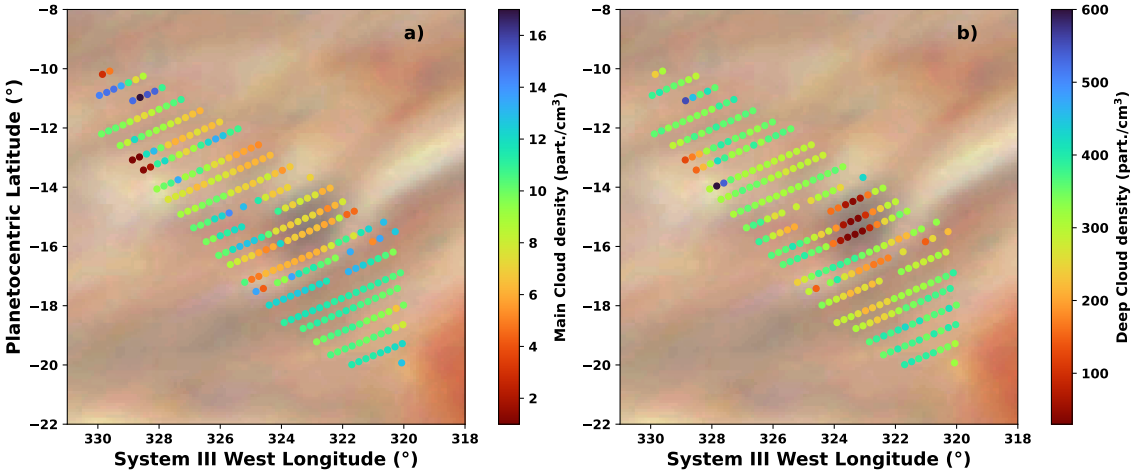


Figure 8.9: Retrieved aerosol parameters maps from the solar retrievals of the #2, #3, #4, and #5 ROIs.

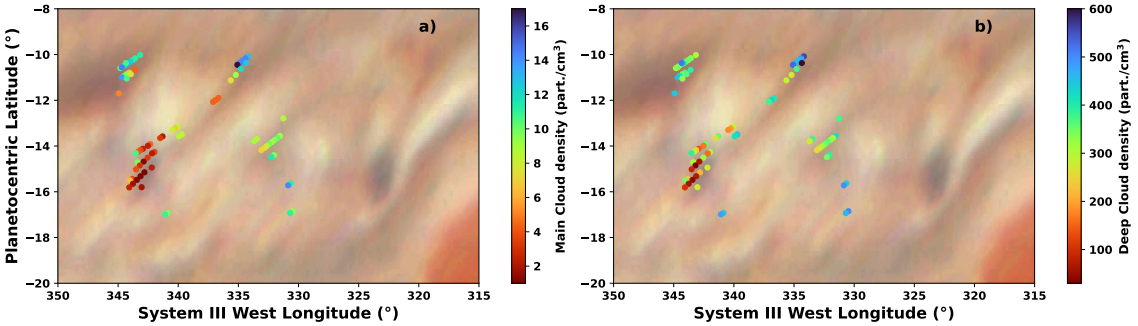


Figure 8.10: Retrieved clouds density maps from the solar retrievals of the #2, #3, #4, and #5 ROIs.

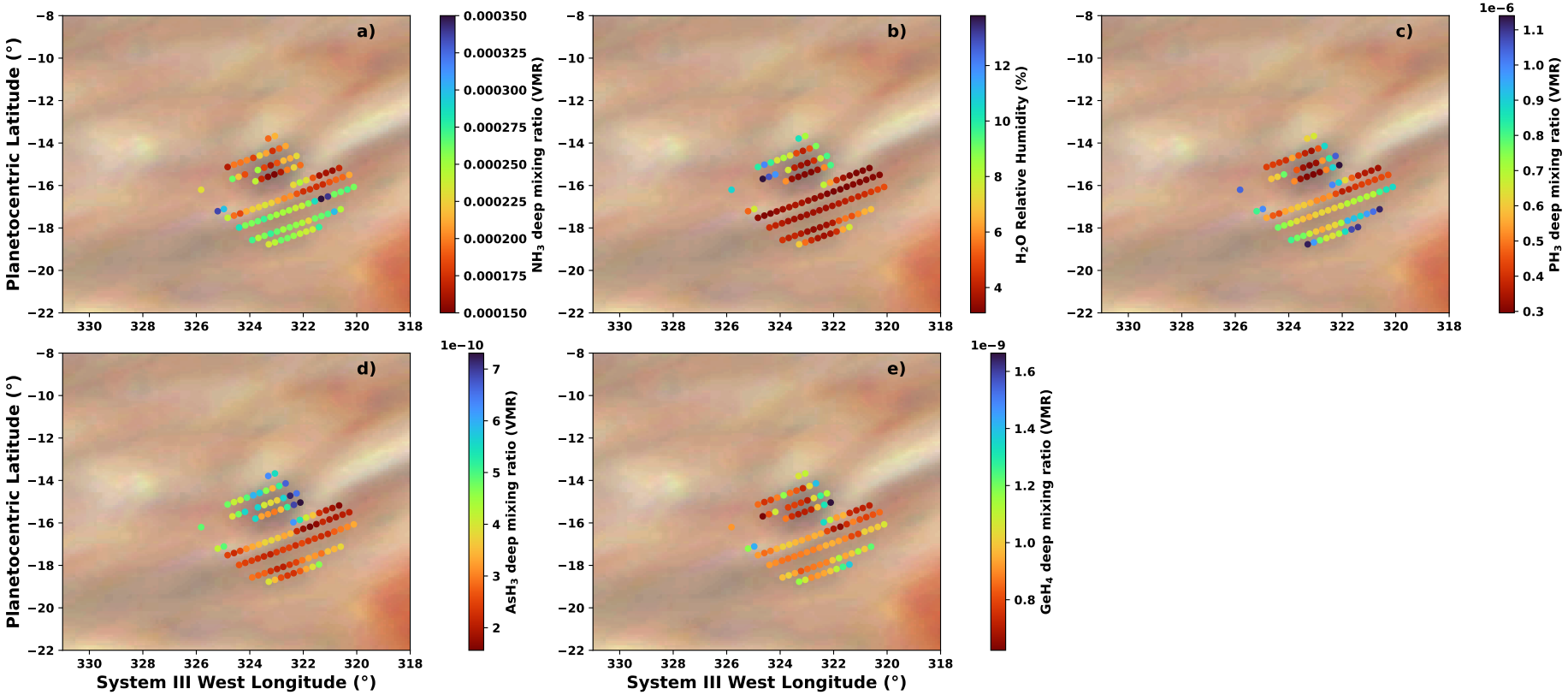


Figure 8.11: Retrieved gases concentration maps from the solar and thermal retrievals of the #1 ROIs.

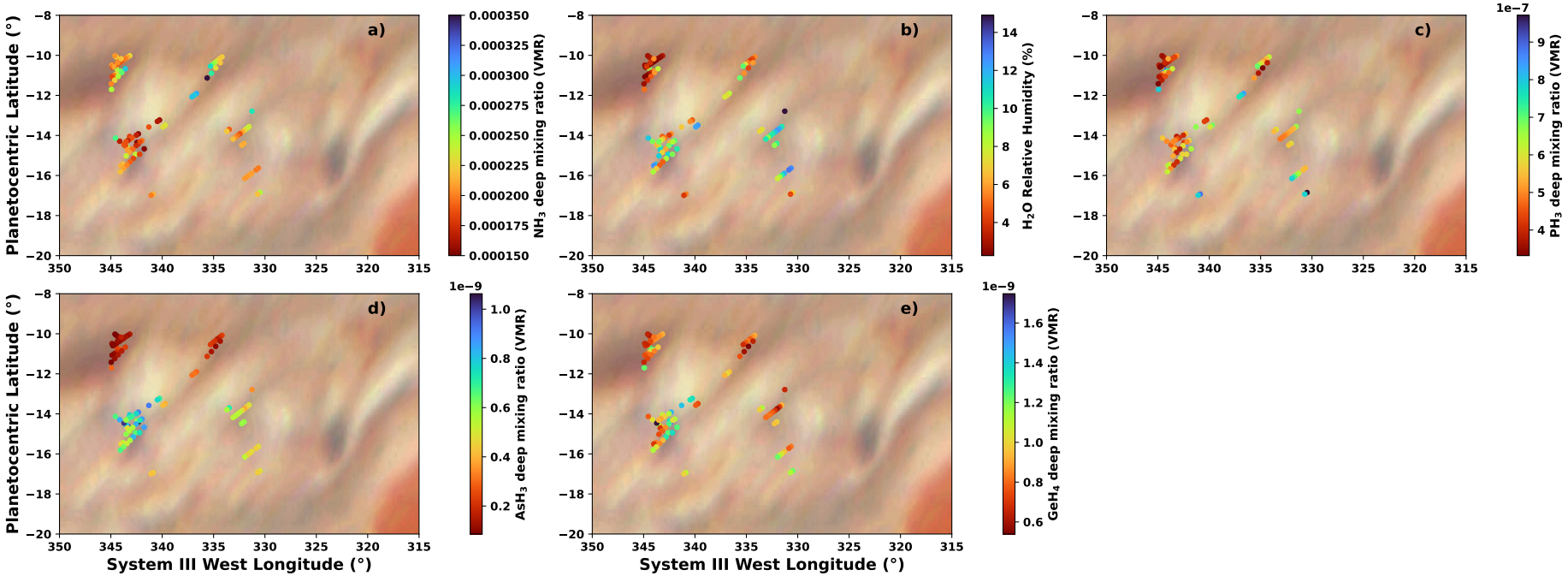


Figure 8.12: Retrieved gases concentration maps from the solar and thermal retrievals of the #2, #3, #4, and #5 ROIs.

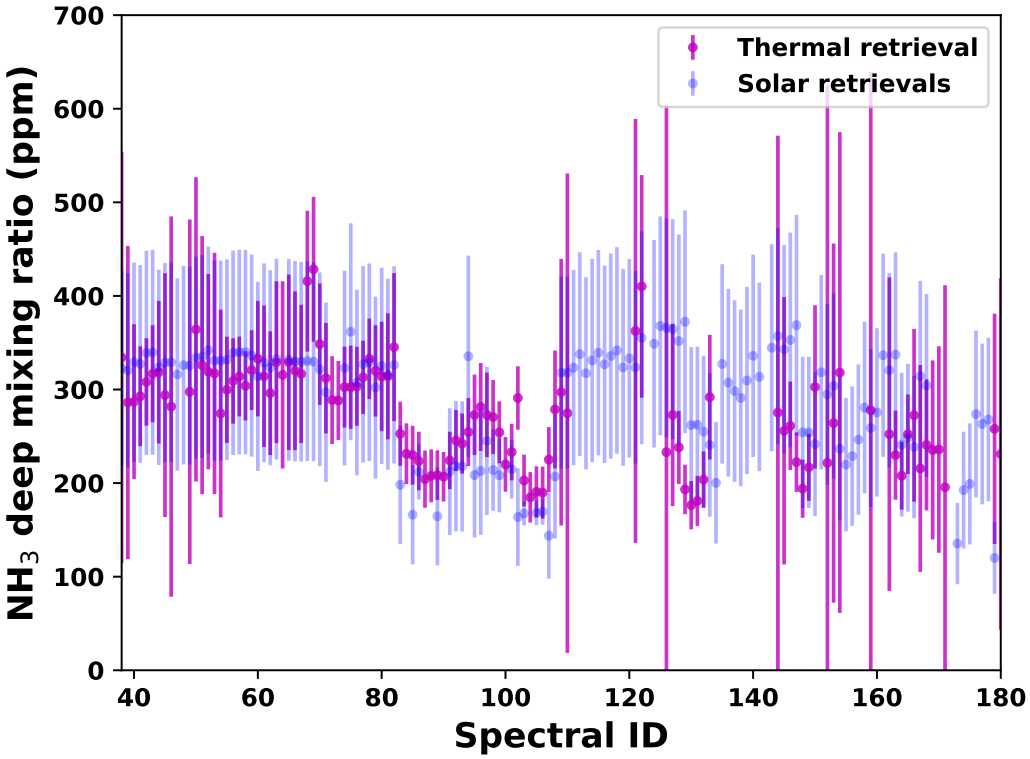


Figure 8.13: Retrieved ammonia deep VMR values from both solar and thermal retrievals.

and #4 ROIs, lower number density values are retrieved. Regarding the deep clouds the retrieved densities are an order of magnitude smaller than the values found for control regions.

In Fig. 8.14 and 8.14 it is possible to observe three different maps: (a) the retrieved total aerosol (haze+ main cloud + deep cloud) colum optical depth (computed at 2.73 micron), (b) the pressure levels at which a value of e in optical depth (computed at 2.73 micron considering both gases and aerosols) is reached, and (c) the pressure levels at which a value of 10 in optical depth (computed at 2.73 micron considering both gases and aerosols) is reached. In the previous Chapter I described how it is possible to derive these pressure levels. To obtain the maps, the results of the solar retrievals were considered. A value equal to the Euler number in optical depth means that the atmosphere becomes - for practical purposes - optically thick. A value of 10, on the other hand, can be useful in discriminating dense clouds to more disperse ones. If a cloud is very dense and compact we expect that the pressure level at which a value of e in optical depth is reached should be close to the one at which a value of 10 is reached. In paticular, the difference should be close to the vertical extension of the cloud, in this case 0.05-0.1 bar. If a cloud is not very dense a value of 10 in optical depth can only be reached deeper in atmosphere, where gas opacities contributions become more important. It is possible to derive several important conclusions from Fig. 8.14 and 8.15:

- In the #1 and #4 ROIs I retrieved lower aerosol column masses

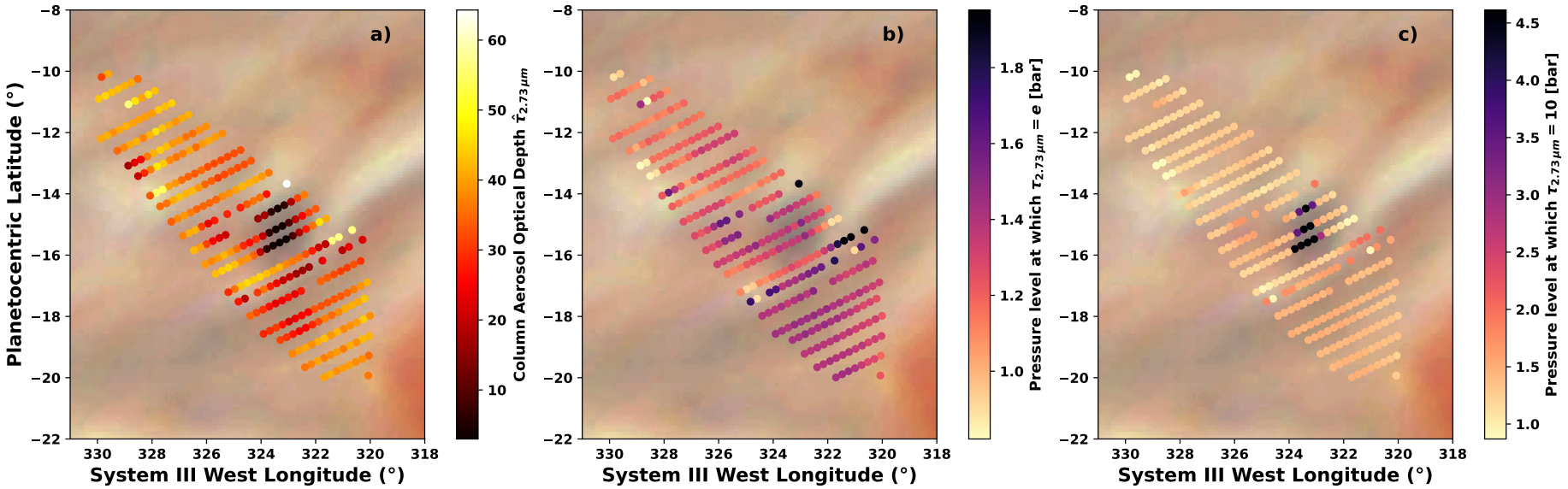


Figure 8.14: Column total aerosol optical depth (a) derived from the retrieved aerosol parameters from the solar retrievals of the #1 ROI. Also the pressure levels at which a value of e (b) and 10 (c) is reached in 2.73 μm optical depth are shown.

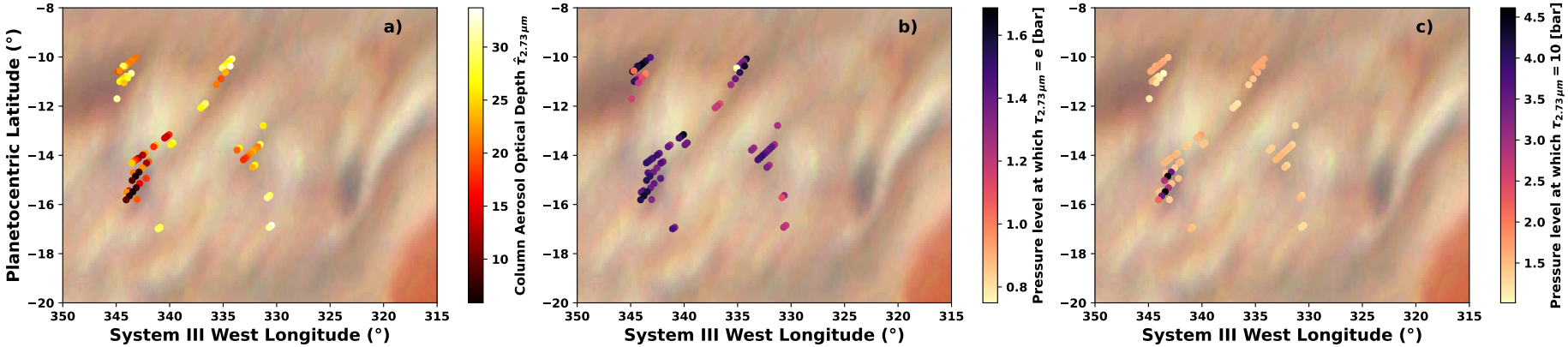


Figure 8.15: Column total aerosol optical depth (a) derived from the retrieved aerosol parameters from the solar retrievals of the #2, #3, #4, and #5 ROIs. Also the pressure levels at which a value of e (b) and 10 (c) is reached in 2.73 μm optical depth are shown.

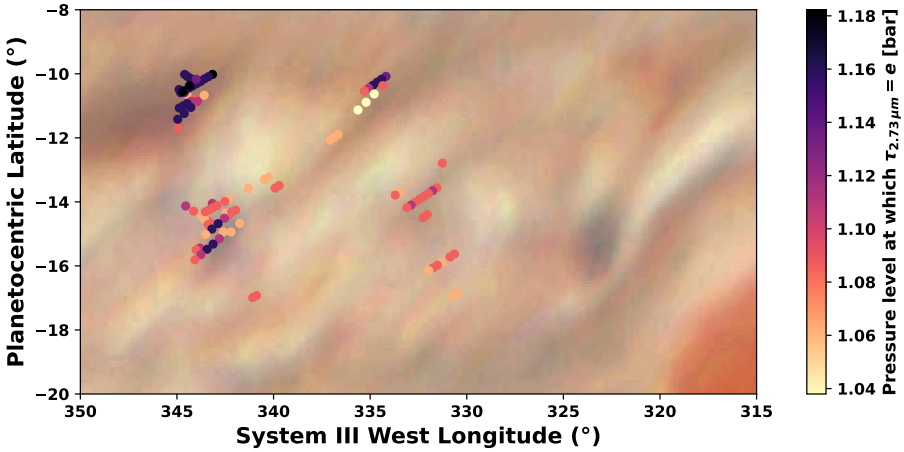


Figure 8.16: Pressure levels at which the 2.73 μm total optical depth is equal to e. The maps are obtained considering the cloud parameters obtained from the thermal retrievals of the #1 ROI.

- The atmosphere becomes optically thick (optical depth equal to the Euler's number) around the 1.1-1.3 bar level almost everywhere, both in ROIs and control regions. This in agreement with Braude et al. (2020) and Irwin et al. (2025).
- A value of 10 in optical depth is reached near the deep cloud level for control regions, the dark filaments, and ROIs #2, #3, and #5. On the contrary in ROIs #1 and #4 this value is reached only deep in the atmosphere around 4 bar.

Lastly, I also derived maps of the pressure level at which a value equal to the Euler's number is reached in optical depth using the results of thermal retrievals, see Fig. 8.16 and 8.17. The comparison with 8.14 and 8.15 can be considered as a further confirm of the consistency between the snippet separate retrievals in the two spectral ranges.

8.5 Discussion

8.5.1 ROIs as clearance regions

The retrieved deep cloud density values and the optical depth ones derived in 8.14 and 8.15, indicate clearly the ROIs #1 and #4 as zones of relative cloud clearance. On Jupiter, clouds are ubiquitous from 1000 bar to the stratosphere (West et al., 2007). Therefore, I am not claiming that the ROIs in the GRS wake detected in this Chapter are cloud free regions. They are zones on the Jovian disk where the uppermost cloud layers (at 0.7 and 1.2 bars) are characterized by an exceptionally low density. Similar regions of exceptional cloud clearance were detected in the past notably in the Hot Spots (Grassi et al., 2017a). They were detected at different latitudes and longitudes, and thanks to the measurements of the Galileo Probe, NIMS (Irwin et al., 1998; Roos-Serote et al., 1998) and of JIRAM (Grassi et al., 2024b), they were demonstrated to be particularly dry, presenting exceptionally low values of water relative humidity and phosphine. On the other hand my retrieval show that

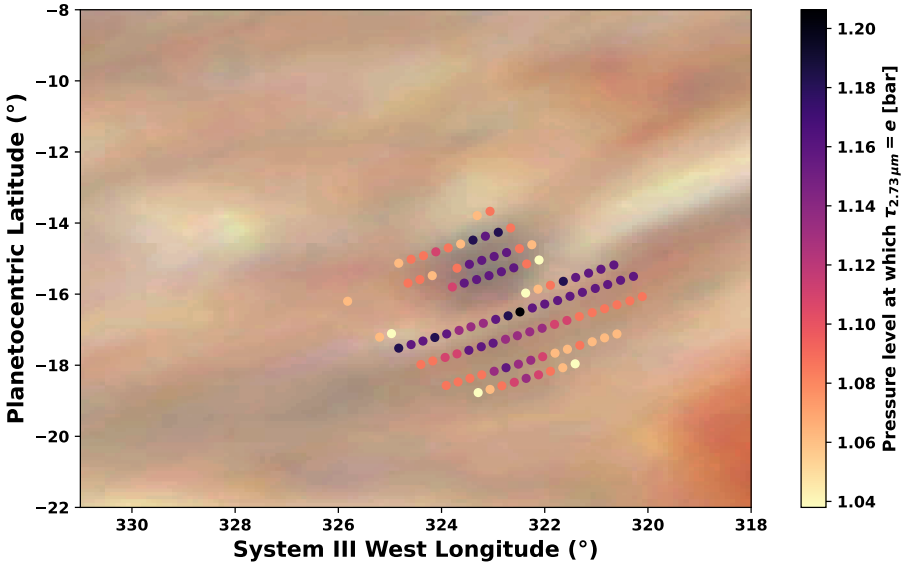


Figure 8.17: Pressure levels at which the 2.73 μm total optical depth is equal to e. The maps are obtained considering the cloud parameters obtained from the thermal retrievals of the #2, #3, #4, and #5 ROIs.

the ROIs are not particularly dry as their retrieved water relative humidity values are similar both to the ones of dark filaments and of control regions. Concentration of ammonia and minor species appear to be depleted with respect to control regions but similar to the values found in the dark filaments. These fundamental findings rule out the ROIs identified in this Chapter to be Jovian hotspots.

8.5.2 Connection to Jovian fluid dynamics

As reported in Chapter 5, different measurements from different instruments showed that the north-western region of the GRS is a highly turbulent region. In its nearby regions strong upwelling events were recorded, together with the detection of Spectrally Identifiable Ammonia Clouds (SIACs) (Baines et al., 2002). These white bright storms were detected also in the visible images (Vasavada et al., 1998) accompanied by dark oval regions. The same was detected by JWST/MIRI (Harkett et al., 2024) in the infrared. Therefore, observational data showed that in the proximity of the GRS the presence of upwelling and downwelling events is quite common and persistent in time. Therefore, I suggest that the cause of the cloud clearance detected by JIRAM in the #1 and #4 ROI can be induced by a turbulent downwelling event. This dynamical process could have inhibited the cloud formation process, and caused a depletion of the trace species such as ammonia, phosphine, and germane, as observed by JIRAM. The origin of these ROIs is more puzzling to explain. From the visible images by the Junocam , also the white/reddish rippled structures that start from the wake appear to be extremely turbulent, see 8.18. The patterns are very similar to the turbulent phenomena known as Von Karman vortices, which are frequently observed in Earth's atmosphere, Fig. 8.18. Von Karman vortices are formed anytime a fluid flows past an obstacle. In our case the fluids are the air masses in the South Equatorial Belt (SEB) and in the South Tropical Zone (STrZ) and the obstacle can be identified in the GRS. This is plausible in the

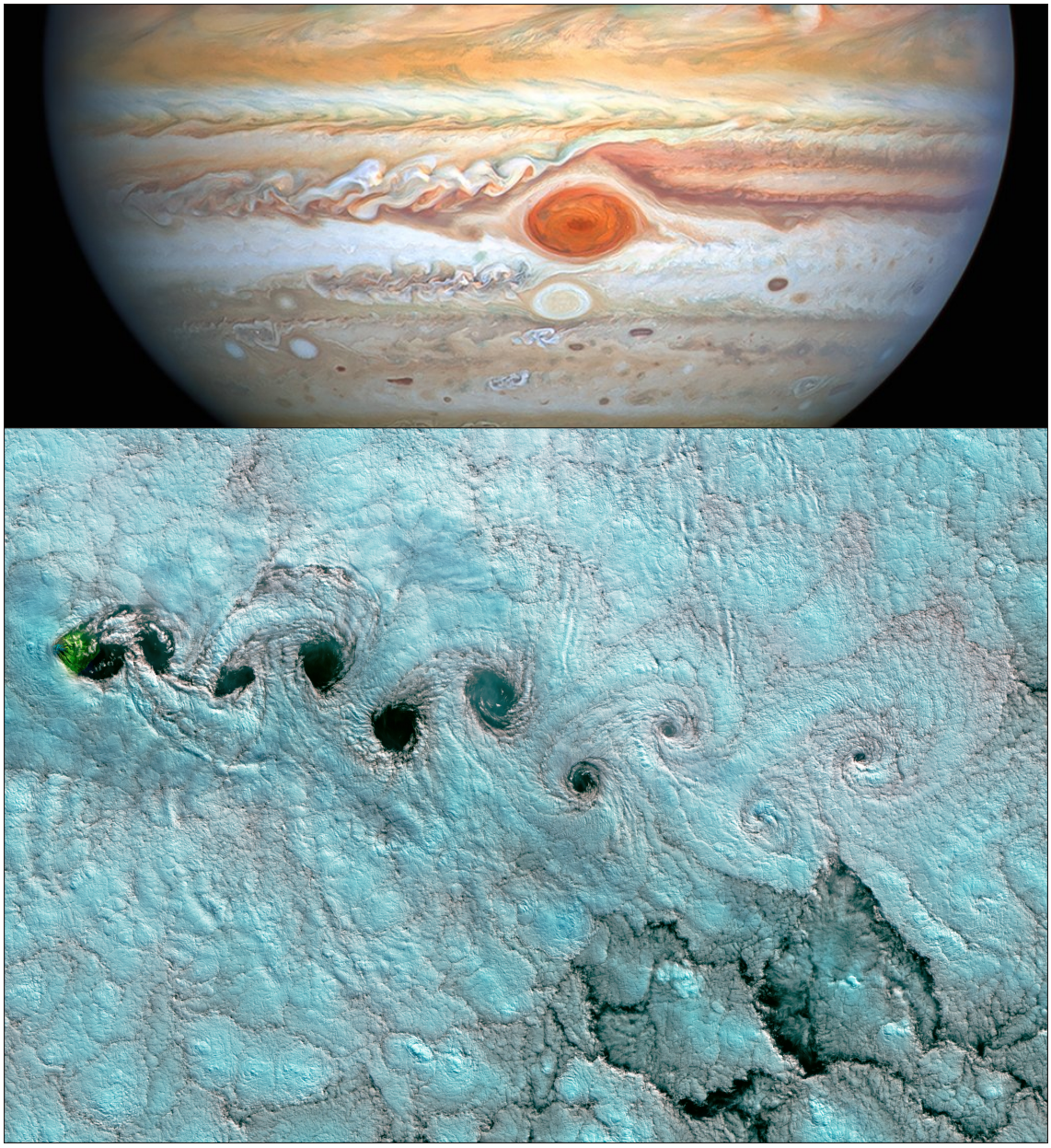


Figure 8.18: The upper panel is a visibleimage of the GRS and its ripples in 2020 taken by HST within the OPAL program (credits to A. Simon, NASA, and M. Wong, Berkeley). In the bottom panel the phenomenon of Von Karman vortices is captured by NASA Earth Observatory in 2017 while observing the Tristan da Cunha island.

light of the latest results from Simon et al. (2024), from which it is clear that the width, aspect ratio, and core UV brightness of the GRS oscillate within a 90 days period. The Simon et al. (2024) observations demonstrate that the GRS is shrunk by the stress induced by zonal jets, but that it can regain its original shape after an oscillation period. If Von Karman vortices form in the GRS extended wake then it is plausible to think that the clearance regions are their natural consequence. In fact, when a fluid encounters an obstacle, it is forced to move around it. This disruption in the flow leads to areas of alternating pressure that are the driving force behind the formation of vortices. There is a pressure gradient within each vortex, with the lowest pressure at the core and gradually increasing towards the outer edges. This can cause the downwelling that in turn inhibits cloud formation and trace gases depletion. Differently from the Earth case, on Jupiter it is not possible however to form entirely cloud-free regions due to the lack of a solid surface. My observations and retrieval of the ripples structures represent the first tentative of modeling quantitatively these ripples. In this context the identification of the #1 and #4 ROIs as both dark visible spots and as cloud clearance regions can be considered as a first proof that Von Karman vortices are present in the Jovian atmosphere. I suggest this since both the #1 and #4 ROIs are found at the same latitude as the GRS. In the other ROIs cloud clearances have not been detected.
However, this picture must be verified both by (1) continuous observations ($<$ 1 day cadence) in the visible of the ripples, and (2) full consistent 3D hydrodynamical models, such as the ones Zhang & Marcus (2024). However, these tasks remain beyond the scope of this thesis work.

8.5.3 Possibility of detecting water clouds

The presence of cloud clearance regions in the ripples is quite intriguing in the context of detecting water clouds. As saw in the first section and in Chapter 2, both equilibrium condensation models (Atreya et al., 1999) and Ackerman & Marley (2001)models both predict the presence of a cloud composed of water ice around the 5 bar level. This is confirmed by GCM models based on Juno results (Ge et al., 2025) that place a water cloud upper limit around 5.5 bar. We saw that the clouds in the clearance regions is less dense than the control ones, by an order of magnitude. However, they are dense enough to make the atmospehre reach a value equal to the Euler's number around 1.1-1.3 bar level making impossible to probe deeper and investigate the presence of hypothetical water clouds. In any case, the clearance regions identified in this thesis work represent the best candidate to observe and find water clouds in the future. In fact, these dark regions on the Jovian disk are known to be very dynamical. The wake of the GRS, here named the #1 ROI, is known to have had several changes in just 25 years. It is possible to simply observe this by comparing the measurements of Vasavada et al. (1998), this thesis work, and of Harkett et al. (2024). Observing constantly the ripples of the GRS with ground-based and space telescopes is the most promising approach towards the detection of water clouds on Jupiter. The Juice mission that will arrive in the Jovian system in 2030s, will be an optimal occasion. Thanks to its instruments suite, and in particular thanks to the MAJIS image spectrometer (Poulet et al., 2024), it will be possible to map a large fraction of the Jovian disk, including the GRS and its ripples. MAJIS

has a spectral range from 0.5 to 5.5 μm with a sampling step of few nanometers and it will be optimal to search also for spectral signatures connected to ammonia ice clouds both in the visible and for wavelengths > 5 μm.

Chapter 9

Using machine learning techniques to study Jovian clouds' global properties and the 3D structure of the GRS

9.1 Rationale

With the advent of state-of-the-art technology, data volumes acquired by astronomy surveys and space missions have increased exponentially. In planetary sciences, the technological development of new propulsion systems, materials, and designs increases the number and quality of scientific instruments on board space missions. An example can be seen in the exploration of the Jovian system as described in Chapter 4. Also the exploration of the Martian system[1] follows a similar trend. In the first decade of the 21th century, three NASA missions orbit Mars: Mars Global Surveyor (Bandfield et al., 2000; Malin & Edgett, 2001; Christensen et al., 2001; Malin et al., 2007), Mars Odyssey Orbiter (Christensen et al., 2004), and Mars Reconnaissance Orbiter (McEwen et al., 2007; Murchie et al., 2007; Mustard et al., 2008). The respective data volumes from each instrument processed on board and throughout the primary and extended missions are: $\simeq$ 1.2 TB, $>$ 2.5 TB, and 3 PB. The increasing complexity and dimension of the datasets have a huge impact on the required data analysis procedures. In the context of multiple scattering atmospheric retrievals, for example, it is fundamental to use very efficient radiative transfer solvers to reach convergence as quickly as possible to analyze the maximum number of spectra. However, radiative transfer simulations execution times scale with the number of wavelength sampling points (or channels) and the number of parameters. This can result in execution times on the orders of minutes (or seconds in the best scenario), which translates into retrieval convergence times on the order of several hours for a single spectrum (or tens of minutes in the best scenario). This makes it very difficult to use all the collected spectra, which often translates into a loss of information and leads to a sub-optimal exploitation of the dataset. Therefore, to tackle the increase in complexity and scale of the data volumes, it is mandatory

[1] https://pds-geosciences.wustl.edu/missions/mep/

to develop efficient techniques that are based on Astrostatistics, Astroinformatics, machine learning (ML), or artificial intelligence (AI) and explored in across a range of studies (Lebofsky et al., 2019; Brzycki et al., 2020; Gajjar et al., 2022; Ma et al., 2023; Baumeister et al., 2020; Nixon & Madhusudhan, 2020; Ardévol Martínez et al., 2024; Hayes et al., 2020).

Jupiter's atmosphere is an excellent example of a rich and ever-expanding dataset and there have been some previous attempts to reduce the dimensionality of the data. The work from Simon-Miller et al. (2001b) is one of the first to have applied dimensionality reduction methods such as Principal Component Analysis (PCA) (see Section 9.3) to the multispectral pixels of the images acquired by HST/WFPC2. Dyudina et al. (2001) used the same methods to analyze the optical and infrared (IR) images collected by SSI and NIMS on board NASA's Galileo mission, respectively. Wong et al. (2023) applied PCA to HST/WFC3 methane-band imaging data and found that components attributed to cloud opacity predicted the observed intensity in simultaneous 5 μm IR images. Studies such as those by Ordonez-Etxeberria et al. (2016), Anguiano-Arteaga et al. (2021), and Anguiano-Arteaga et al. (2023) used PCA on images acquired by HST and Cassini, combining it with clustering techniques (e.g., k-means or nearest neighbors) to identify zones of physical interest. The main rationale behind these works is to perform PCA on the two-dimensional (2D) image arrays taken at different wavelengths to find principal components that are connected to physical properties (e.g., different cloud altitudes, composition, etc.). This is conceptually different from working directly on spectra. The clustering of high-dimensional datasets, such as spectra, is usually a complex and degenerate task but is becoming more important with modern advancements in multi-object spectroscopy (Ellis et al., 2017; Yang et al., 2022). To the best of my knowledge, the only work that applied PCA directly to Jovian spectra is that of Irwin & Dyudina (2002), who analyzed Galileo/NIMS spectral cubes. Similarly, clustering based on deep learning algorithms has been applied to Cassini/VIMS data of the 2008 storm on Saturn (Waldmann & Griffith, 2019). Deep learning algorithms have also been recently used to efficiently and robustly model and characterize Jupiter's interior structure starting from gravity, wind fields, and isotopic composition measurements (Ziv et al., 2024b,a).

In this Chapter I will focus on a new approach based on machine learning techniques, that combines PCA with Gaussian mixture models (GMMs) to automatically identify groups of similar spectra. For this purpose, a fully Pythonic code, `chopper.py`, has been developed (Biagiotti, 2025)[2,3]. The code is completely generic, however, I applied it to Jupiter observations collected during the first perijove passage by Juno/JIRAM (August 2016) and by JWST/NIRSpec during its Early Release Science phase (July 2022). The main focus of my work is the study of clouds and haze properties, namely, altitudes, optical depth, and effective radii. A special focus is placed the great red spot (GRS), the largest and longest-lived vortex in the solar system (Sánchez-Lavega et al., 2024b). I demonstrate that this method can immensely reduce the computational effort during the multiple-scattering retrieval stage by identifying subsets of self-similar spectra in advance. I also show that the technique can identify clusters of spectra that correlate with known structures from

[2]https://github.com/astro-francy/chopper
[3]https://doi.org/10.5281/zenodo.15731419

visible images, along with new ones that had gone previously undetected at optical wavelengths.

9.2 Observations

In this Chapter I will analyze data both from Juno/JIRAM and JWST/NIRSpec. In particular I focus on two subsets of the JIRAM PJ1 data, represented in panels b and c of Fig. 9.1, namely:

- *G+21 subset*: a subset of the data presented in Grassi et al. (2021), as shown in panel b at 2.7 μm. These spectra cover a large longitude span of the southern hemisphere, including: (i) a fraction of the GRS and of the oval BA (Sanchez-Lavega et al., 2001; Wong et al., 2011b); (ii) a fraction of the equatorial zone (EZ); (iii) the south equatorial belt (SEB); (iv) a large fraction of the south tropical zone (STrZ); and (v) the south temperate belt (STeB). I retained only the spectra whose incidence (i) and emission (ε) angles range between 40° and 50°. This selection criterion is the primary cause of the gaps in longitude coverage. However, retaining only spectra with similar viewing angles ensures that the variance in the dataset is driven by the physical properties of clouds instead of geometry. This is a fundamental step to take before using techniques such as PCA, which are largely dependent on the covariance matrix of the data.

- *GRS subset*: a mosaic of spectra of the GRS and its surrounding region is shown in panel c at 2.7 μm. Since the constraint on viewing conditions imposed on the previous dataset would result in a very limited spatial coverage, I decided to expand the selection in order to satisfy the condition $40° < i < 50°$. This condition would result in emission angles between 55° and 80°.

Regarding NIRSpec I used the dataset already introduced in Chapter 4, and I considered both gratings G235H and G395H. Each of the spectra collected with the G235H grating (solar mosaics) consists of 3814 spectral points that span the 1.66-3.17 μm range. With the G395H grating (thermal mosaics) a total of 3610 spectral points were obtained, spanning the 2.87-5.27 μm range. NIRSpec data were reduced and navigated using the JWST pipeline and custom Solar System processing (King et al., 2023), mitigating the effects of spikes, of saturation in reflectivity peaks near $\simeq$ 2 µm, along with the strong thermal emission at 5 μm by subdividing long integrations into shorter durations (known as groups). The reduced mosaics acquired with the two gratings have been later combined. As the acquisitions vary over time, they do not precisely point at the same region on the Jovian disk. In order to combine them, I first performed a manual alignment keeping only the spaxels (pixels on the map where the spectrum was acquired) that satisfy the conditions: $\text{lat}_{\text{G235H}} - \text{lat}_{\text{G395H}} < 0.2°$ and $\text{lon}_{\text{G235H}} - \text{lon}_{\text{G395H}} < 0.2°$. Here, $\text{lat}_{\text{G235H}}$ and $\text{lon}_{\text{G235H}}$ represent the latitude and longitude of the spaxels contained in the solar mosaics, while $\text{lon}_{\text{G235H}}$ and $\text{lon}_{\text{G395H}}$ are the latitude and longitude of the spaxels contained in the thermal mosaics. The chosen threshold of 0.2° was selected because it represents one-third of the mean distance of adjacent spaxels. The results of this manual alignment are shown in Fig. 9.2. The spectra of the spaxels (i.e. NIRSpec IFU pixel, see Chapter 4) that satisfy the condition are retained and merged.The mosaic

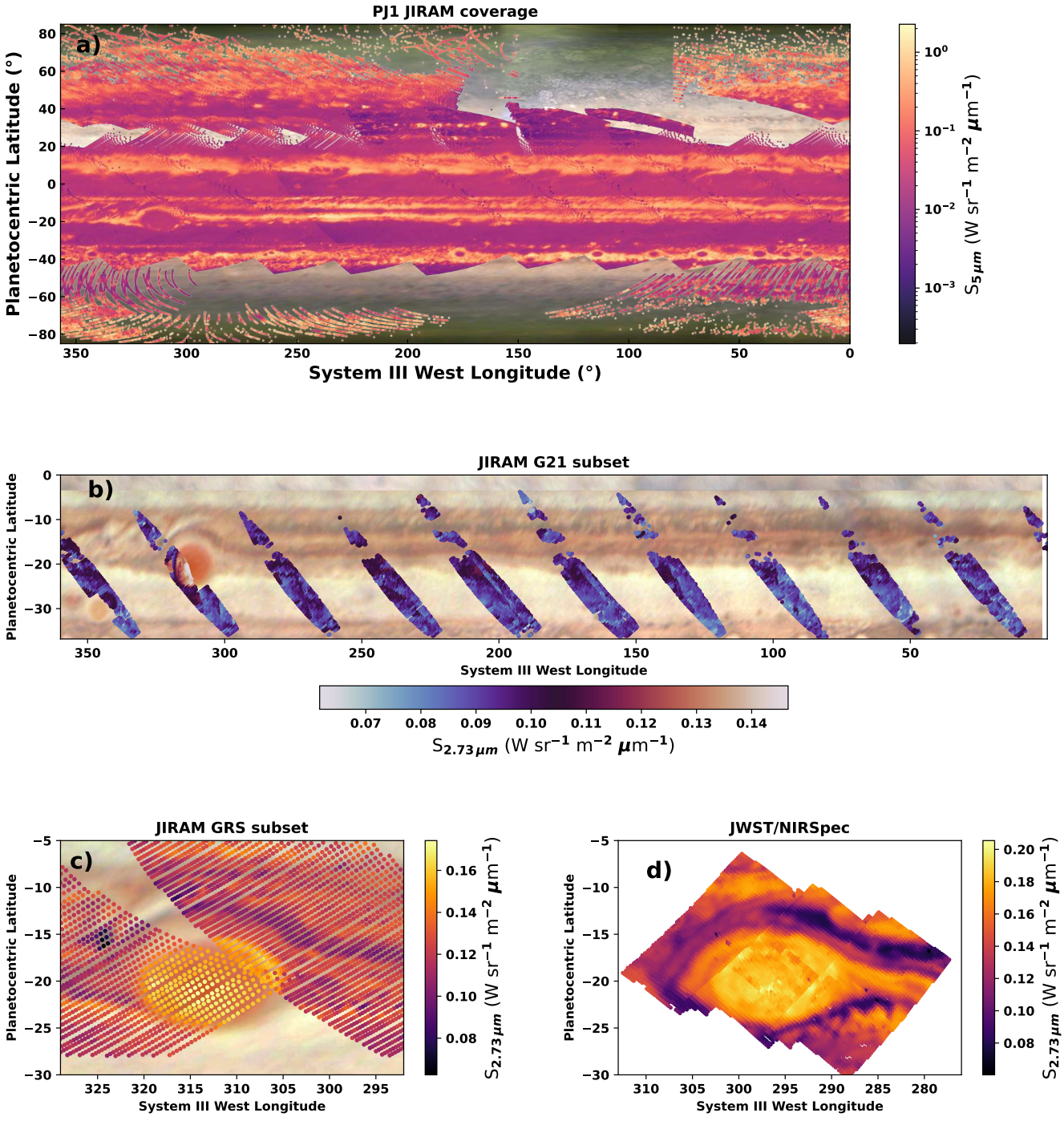


Figure 9.1: (a) Spatial distribution of all the JIRAM PJ1 collected spectra. (b) Spatial map of radiance measured at 2.73 μm for the G21 susbset of PJ1 data considered in this work. (c) Spatial map of radiance measured at 2.73 μm for the GRS susbset of PJ1 data. (d) Spatial maps of radiance measured by JWST/NIRSpec at 2.73 μm.

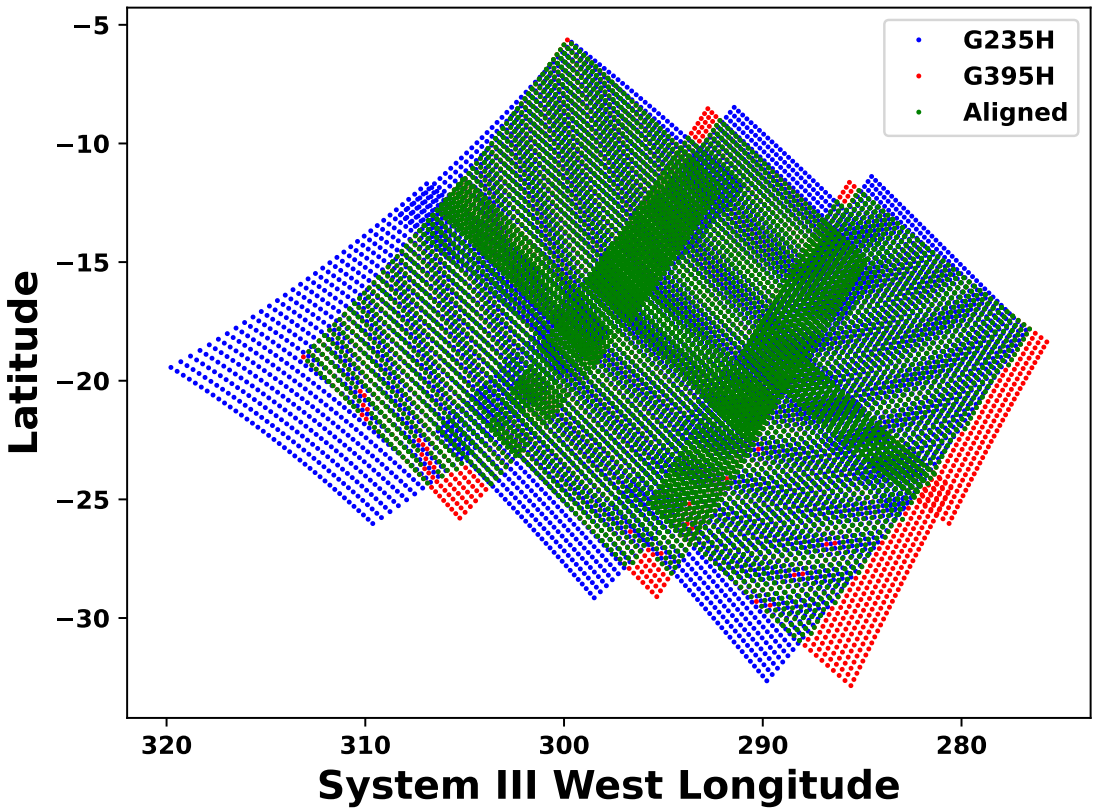


Figure 9.2: Manual alignement performed to combine the G235H and G395H NIRSpec mosaics.

of the GRS as observed by NIRSpec at 2.7 μm is shown in panel d of Fig. 9.1. NIRSpec observations were acquired at viewing angles that satisfy these conditions: 20°$< i <$40° and 20°$< \varepsilon <$40°. Figure 9.3 shows a comparison between a spectrum of the inner regions of the GRS as seen by JIRAM (top panel) and NIRSpec (bottom panel). NIRSpec's spectral and spatial resolution is superior than JIRAM. The disadvantage of NIRSpec is the small coverage of the planet, the small variation of phase angle in the data and the scarcity of Jupiter data that has been obtained from JWST. Unfortunately, the JIRAM and NIRSpec datasets were not close in time (with a difference of eight years) but JIRAM represents the best set of spectra collected by a space mission orbiting Jupiter to compare against the JWST observations.

Before applying techniques that are sensitive to the data variance and covariance such as PCA, it is mandatory to perform a further cleaning step in addition to the reduction. Spikes, corrupted spectra, and missing values can all add instrumental spectral effects that will bias the result of the PCA. Therefore, I performed two different data cleaning procedures on JIRAM and NIRSpec data, discussed in the next subsections.

9.2.1 JIRAM data cleaning

The most significant source of instrumental-induced variance in JIRAM data is the occurrence of frequent spikes in the spectra. They are both caused by cosmic rays

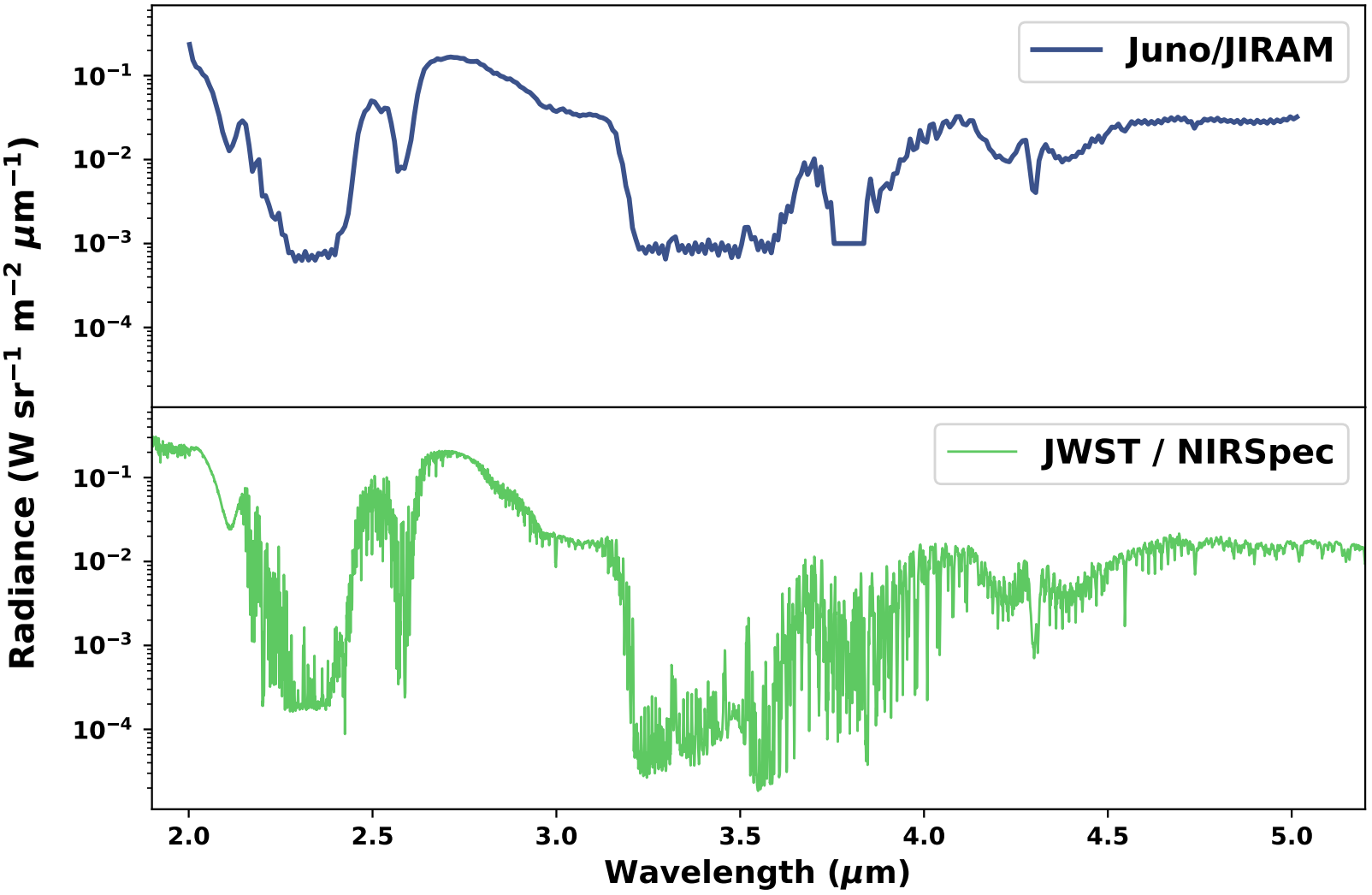


Figure 9.3: Comparison between two spectra of the GRS captured, respectively, by Juno/JIRAM (top panel) and JWST/NIRSpec (bottom panel). It is possible to note the higher spectral resolution of NIRSpec, which must not be confused with noise. Note that the JIRAM spectrum is contaminated by straylight, as discussed in Chapter 6.

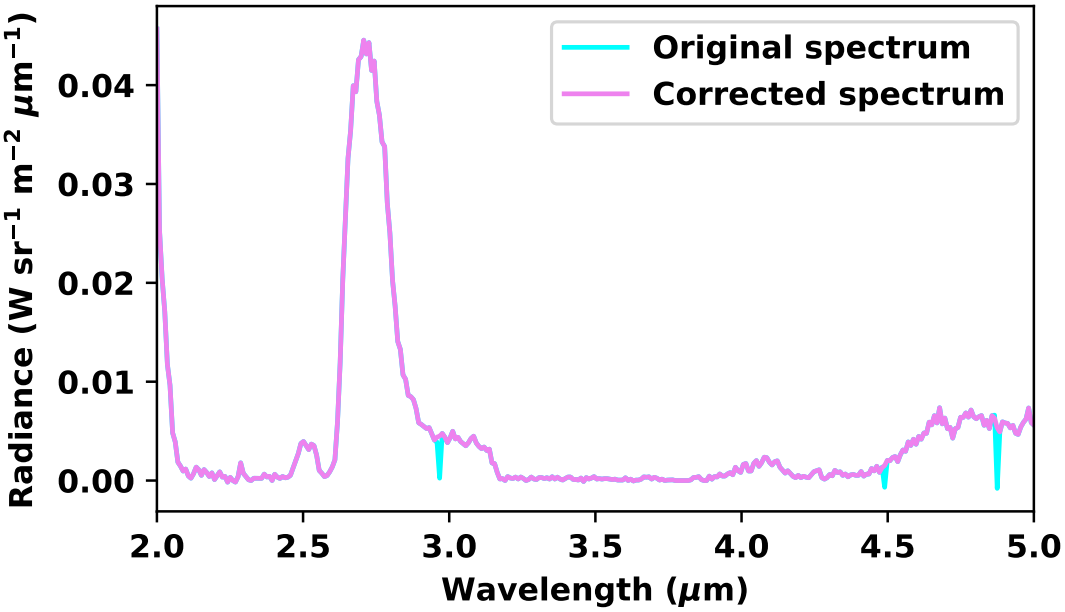


Figure 9.4: Example of a JIRAM spectrum in the G21 subset before (cyan) and after (orchid) being corrected for the presence of spikes.

and energetic particles in the Jovian magnetosphere. To remove them I applied a modified version of the algorithm presented in Whitaker & Hayes (2018). The method is very efficient in correcting Raman spectra, but it can be detrimental if the spectra present reflectance peaks and absorption dips larger than the median signal. Therefore, I did not apply the Whitaker & Hayes (2018) algorithm to the whole JIRAM spectrum at once and, instead, I used it separately on three different regions of the spectrum:

- the solar reflectance peaks between 2 and 2.1 μm, and 2.6 and 2.8 μm, approximately;
- the 5-μm region, masking the absorption features of deuterated methane (CH_3D), phosphine (PH_3), ammonia (NH_3), water (H_2O), germane (GeH_4), and arsine (AsH_3);
- the remaining spectral regions.

Following (Whitaker & Hayes, 2018), I selected threshold value of five. With this approach, it was possible to remove the majority of the spurious spikes present in the JIRAM spectra as shown in Fig. 9.4, where a representative spectrum is shown before and after the correction. After the spike correction, the G+21 subset contains 11180 spectra, each of them constituted by 336 spectral points, while the GRS subset contains 3763 spectra.

9.2.2 NIRSpec data cleaning

As the NIRSpec data were already reduced using the methods in King et al. (2023), I did not apply the spike correction method mentioned in the previous section. In

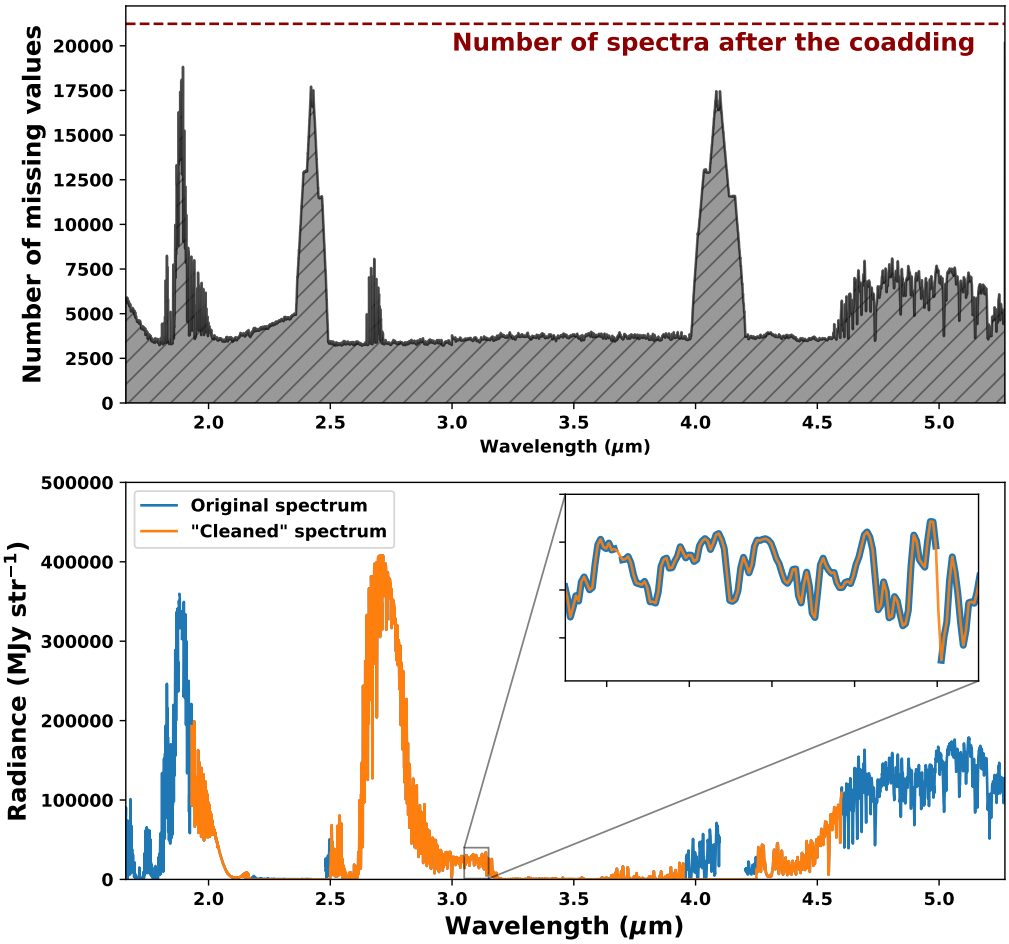


Figure 9.5: *Top panel*: Wavelength distribution of missing values in the Jovian spectra collected by JWST/NIRSpec. *Bottom panel*: Example of an original NIRSpec spectrum (blue) and the correction made to perform an accurate and unbiased PCA+GMM analysis (orange). Zoom-in panel shows the results of the applied imputation methods for missing values.

this case, the most significant source of possible instrumental-induced variance is the occurrence of missing values in the individual spectra. These missing values can arise because of gaps between the gratings and/or residual saturation. The top panel of Fig. 9.5 represents the distribution of missing values as a function of wavelength. The missing values reach a number comparable to the number of total spectra (dashed red line) in the following wavelength windows:

1. from 1.66 μm to 1.8 μm;
2. between 2.17 and 2.5 μm;
3. between 3.95 and 4.25 μm;
4. from 4.73 μm to 5.2 μm.

These windows will be referred to as "contaminated." The second and third windows are caused by the physical gaps between the two NIRSpec detectors. The 1.8 μm window is instead caused by the very bright reflection of solar radiation by clouds. The GRS and its surroundings are well known to be one of the most cloudy regions of the Jovian disk. Lastly, the remaining window is caused by saturation induced by the planet's internal radiation. The 4.5-5.5 μm region is generally known to be an atmospheric window, which probes deep and warm atmospheric layers whose thermal emission reaches high, saturating, radiances. The number of missing values in the 2.6-2.8 μm and 4.-4.6 μm windows is much lower than the number of total spectra. This is proof of the overall excellent work done by the reduction pipeline (King et al., 2023). These two windows are very interesting since they are related to the second brightest reflection peak and to the transition region between the solar and thermal dominated regions of the Jovian spectrum. Once the distribution of the missing values was known, I proceeded as follows:

- I removed all the spectra that present a number of missing values larger than 2,000;
- I cut the four windows listed above that presented the highest number of counts in missing values;
- I imputed by interpolation the remaining few missing values.

Removing the "contaminated" wavelength windows potentially implies the loss of information. On the other hand, missing values interpolation is not efficient if the number of missing points is much larger than the number of "physically sounding" points. Too many imputed missing values can induce non-physical biases into the data. The procedure is also complicated by the nature of the 5-μm window, which is particularly difficult to impute by interpolation because of the numerous absorption dips.
In any case, after the filtering and the removal of the contaminated windows the number of missing values largely decreases, and so the interpolation of missing values becomes feasible. I used a simple cubic spline interpolator in the wavelength space, as implemented by the `scipy` Python package (Virtanen et al., 2020). It is worth stressing that the interpolation involved few and sparse points (on the order of

dozens) with respect to the full NIRSpec wavelength range. After the cleaning process, each spectrum features 6,798 wavelength channels, and there are more than 8,000 spectra in the dataset over all the tiles and dithers in the NIRSpec data.
A comparison between an original NIRSpec spectrum and the corresponding cleaned version is given in the bottom panel of Fig. 9.5. The NIRSpec cleaned data have been used to perform the PCA+GMM analysis, but the results of the clustering can also be extended to the original data.

9.3 Methods

In this thesis work, I present a new clustering approach that uses a PCA combined with the unsupervised clustering technique known as GMM. I developed a simple python code called `chopper.py` (Biagiotti, 2025)[4][5], that applies together the `scikit-learn` (Pedregosa et al., 2011) and `astroML` (VanderPlas et al., 2012b, 2014) PCA and GMM routines to an arbitrary collection of spectra. The architecture of the code will be detailed in this Section and is summarized in Fig. 9.6. `chopper.py` generalizes the methods presented in Irwin & Dyudina (2002), and can be considered its extension. They used PCA to obtain a series of principal component spectra that are used to decompose all of the spectra in the collection. In this way, spectra that are similar in shape and intensity will have similar decomposition coefficients and occupy contiguous spaces in the coefficients' distribution space. Once this space is manually discretized, it is possible to greatly reduce the number of retrievals to be performed considering only one typical spectrum for each region of the coefficients' parameter space. The focus of the Irwin & Dyudina (2002) work was not the identification of the principal components and their connection to physical properties of the troposphere; instead, PCA was used mainly as a tool to simplify the retrieval procedure. `chopper.py` generalizes this approach using PCA on a generic collection of spectra to obtain a series of decomposition coefficients on which an unsupervised clustering (GMMs) is performed. The use of PCA greatly simplifies and stabilizes the clustering procedure. I stress that while it is certainly possible to perform clustering directly on the spectra instead of on the PCA decomposition results, this will increase the complexity of the required algorithm. For example, it is possible to use convolutional neural networks and deep learning algorithms to solve clustering problems (Leon-Dasi et al., 2023; Waldmann & Griffith, 2019), as well as the so-called self-organizing maps algorithms (Horton et al., 2015).
First, `chopper.py` consists of two main steps. The only essential input file is the one containing the N M-dimensional spectra that constitute the collection. In the case of collections acquired by space missions, a correction for the viewing angle is often considered when the spectra were taken over large ranges of incidence or emission angles. In my case, I selected the JIRAM datasets in such a way that all the spectra have similar viewing geometries, and the same holds for the mosaics captured by NIRSpec. Otherwise, it is convenient to transform the collected spectra in bidirectional reflectance distribution functions (BRDF) or I/F, as done by Irwin & Dyudina (2002). `chopper.py` can account for this using a specific flag. I note

[4]https://github.com/astro-francy/chopper
[5]https://doi.org/10.5281/zenodo.15731419

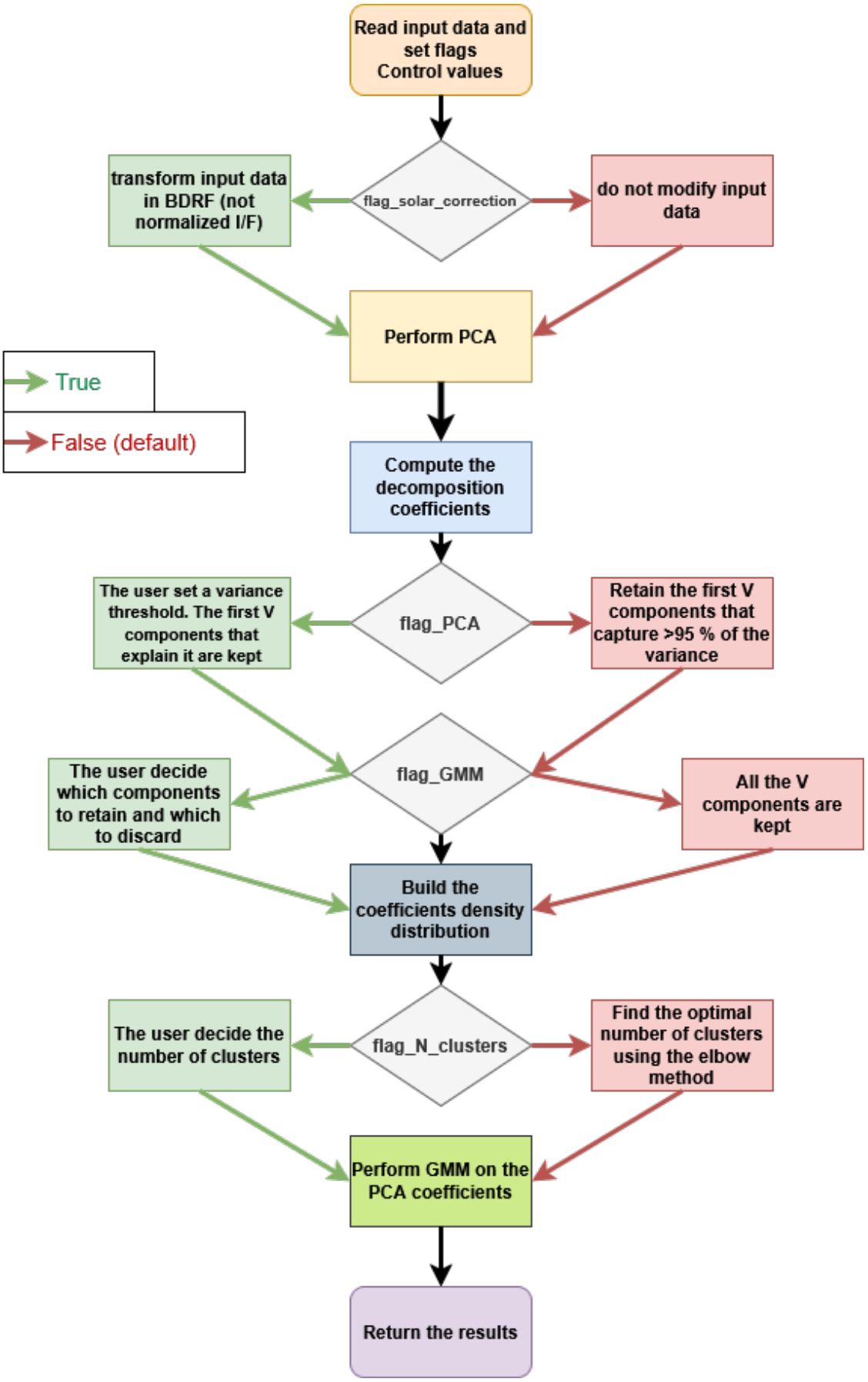


Figure 9.6: Flowchart diagram for the `chopper.py` code.

that my code does not include the reduction and data-cleaning procedures, since this step is strongly dependent on the input data, as discussed in the previous section.

9.3.1 PCA step

This code segment leverages `scikit-learn` (Pedregosa et al., 2011) to perform the PCA on the spectral data. Before describing the details of what `chopper.py` does, I briefly summarize some theoretical basis on how PCA works (Pearson, 1901; Ivezić et al., 2014b). I consider a dataset as a series of N observations, each one with M observed features. In my case N spectra sampled in M wavelength points. The observations are the variables of the dataset and form a vectorial space. They can be stored in a $N \times M$ matrix X, once they are centered for the mean. PCA essentially aims to find a series of $\mathrm{N_{PC}}$ ($\mathrm{N_{PC}}$ <<N) orthogonal functions called the principal components (they are essentially eigenvectors, i.e. a new set of variables) looking at the directions of maximal variance of the observation covariance matrix $C_X = \frac{1}{N-1} X^T X$. To find the directions of maximal variation of C_X, PCA identifies a rotation R to apply to X ($Y = RX$), which has the following characteristics (Ivezić et al., 2014b):

$$C_Y = R^T X^T X R = R^T C_X R. \tag{9.1}$$

Using linear algebra it can be shown that the principal components are the eigenvectors of R, and each eigenvector is associated with the respective eigenvalue of C_Y. These are by definition smaller than one and explain the amount of variance contained within each component.
As the principal components are a set of orthogonal functions obtained from the data matrix, it is possible to decompose (or reconstruct) each spectrum in the dataset through the mean of a simple dot product:

$$x = \mu + \sum_{j=0}^{N_{\mathrm{PC}}} c_j \cdot \mathrm{PC}_j \tag{9.2}$$

where x represents a random spectrum in the collection, μ the mean spectrum, PC_j the j-th used principal components, N_{PC} the number of principal components used in the decomposition, and c the set of N_{PC} coefficients associated with the x spectrum. Similar spectra will have similar PCA decomposition coefficients which can be used - in turn - to perform the clustering phase. At this point `chopper.py` only retains the first V principal components that respect the following criterion:

$$\sum_{i=0}^{V} \lambda_i > 0.95, \tag{9.3}$$

where λ_i is the eigenvalue associated with PC_i. When the 95 % threshold is reached, it means that the V chosen PCs account for more than the 95 % of variance present in the input dataset. This underlines the fact that in my code PCA is principally used to simplify the clustering step. I am interested in the components that explain most of the variance maintaining the condition $V << N$. As the threshold is, in principle, completely arbitrary, a flag inside `chopper.py`, can make this number an

user-inserted parameter. Even if it is not the main goal of my method, it is possible to connect a physical meaning to the principal components' intensities or spectral shape. However, in some cases, it is also possible that some principal components may capture physically degenerate or noise-induced variance. Therefore, I tend to associate a meaning only to principal components that are clearly connected to physical phenomena.

9.3.2 Clustering step

The `chopper.py` code performs clustering on the results of the PCA, instead of performing it on the input spectra. The clustering is performed using GMMs (Kelly, 2007). A GMM is an unsupervised clustering technique that models an underlying density of points, $\rho(x)$, as a weighted sum of K Gaussians (Ivezić et al., 2014b):

$$\rho(x) = \sum_{j=0}^{K} \alpha_j \mathcal{N}\left(m_j, \Sigma_j\right), \tag{9.4}$$

where $\mathcal{N}$ represents the normal distribution, m and Σ the mean and covariance of the j-th gaussian, and α_j are normalization factors. These parameters are updated by GMM on the base of the likelihood of the data, thanks to the so-called expectation-maximization (EM) algorithm (Moon, 1996). Eventually, each point is assigned to a Gaussian distribution based on the likelihood of belonging to that distribution. In my case, the points are the PCA decomposition coefficients, and the density is therefore V-dimensional. It is this use of probabilities that makes GMM stands out from clustering algorithms such as nearest neighbors (Goldberger et al., 2004) or k-means (Jain, 2010), which find similarities based on the minimization of distance between points. It is also different from DBSCAN-like algorithms (Ester et al., 1996; Campello et al., 2013), which finds similarity through density-connectedness, where clusters are defined as dense regions of data points separated by low-density regions. As a caveat, I note that when the dataset is either large or very high-dimensional, GMM will take a considerable time to run.
The application of GMM is dependent on two factors: the input data (different PCA coefficients density distributions lead to different results), as well as the number of clusters, K. Since, in principle, a potential user might also be interested in performing the clustering only using certain principal components of interest, `chopper.py` presents a flag that lets the user choose which coefficients to use and which not. If the flag is not used, `chopper.py` uses the V-dimensional density distribution as input. Regarding the second factor, I use the so-called elbow method, that is a heuristic method used to identify the best number of clusters to use. It consists of running the k-means clustering algorithm multiple times, each time with a different K. Then, it looks for the point where the rate of increase in explained variance starts to slow down significantly, which is typically considered the "elbow" point. In `chopper.py` I decided to use the WCSS, i.e. Within-Cluster Sum of Squares, metric to find the elbow point. WCSS is simply defined as the sum of the squared distances between each data point and the centroid (mean) of the cluster it belongs to. It is a standard metric used to measure variance for K-means clustering. If a further user flag is set, it is possible to insert manually the desired value of K. If

the flag is not used, the value of K resulting from the elbow method is used. By its construction, the developed code is not expected to work well on datasets that

- are not cleaned for spikes or missing values;
- are strongly imbalanced. Imbalanced dataset in machine learning refers to a classification problem where the number of data points for each class is not equally distributed. Specifically, one class (the majority class) has a significantly higher number of observations than the other class(es) (the minority class). A common rule of thumb is that if the minority class constitutes less than 10-20% of the total data, the dataset is often considered imbalanced enough to cause issues;
- balanced datasets containing anomalous spectra.

9.4 Results

In the following subsections, I present the results obtained applying `chopper.py` to the two selected subsets from the JIRAM PJ1 data and to the NIRSpec mosaic of the GRS. This represents the first analysis of the full-range JWST/NIRSpec Jupiter's data.

9.4.1 Application to G+21 data

Figure 9.7a shows the results of the PCA analysis performed on the JIRAM spectra of the G21 subset. More than 90 % of the variance is captured using the first two principal components (see panel e). These components are also anti-correlated, as shown in Fig. 9.7 (subpanels b, c, and d), where the decomposition coefficients' latitude versus longitude maps are shown superimposed on a mosaic of JunoCam images. An example of the PCA decomposition is shown in Fig. 9.8. The quality of the reconstruction after the decomposition is given by the parameter $1 - \chi^2$ (see Chapter 3 and 7), which should be close to unity. The first component is correlated to dark regions on the Jovian disk (and therefore to the thermal signal maps, Fig. 9.1a), and the second to bright regions (and therefore to the solar reflected signal maps, Fig. 9.1b). This is consistent with previous works by Simon-Miller et al. (2001b), Ordonez-Etxeberria et al. (2016), Dyudina et al. (2001), and Irwin & Dyudina (2002), and reflect the "natural" correlation between visible-dark and IR-bright zones on Jupiter found also by Irwin et al. (2001). The main driver of variance in the Jovian spectra (in the 2-5 μm range) is the occurrence of clouds. Depending on their optical thickness we will observe brighter or darker regions. Dense clouds tend both to block radiation coming from the deep troposphere and to enhance the reflection of solar radiation. This becomes immediately evident in my results from PCA analysis. To capture more than the 95 % of the variance also the third component is needed. The physical interpretation of this eigenvector is more complicated, even if it may be connected to second order effects of aerosols on the Jovian spectrum. In fact, the spectral shape of PC3, see Fig. 9.1a, it is characterized by a positive 2 μm rise in signal, usually connected to hazes and high altitude clouds, and by a negative dip that resembles the 2.6-2.8 μm reflection peak flipped upside down. If

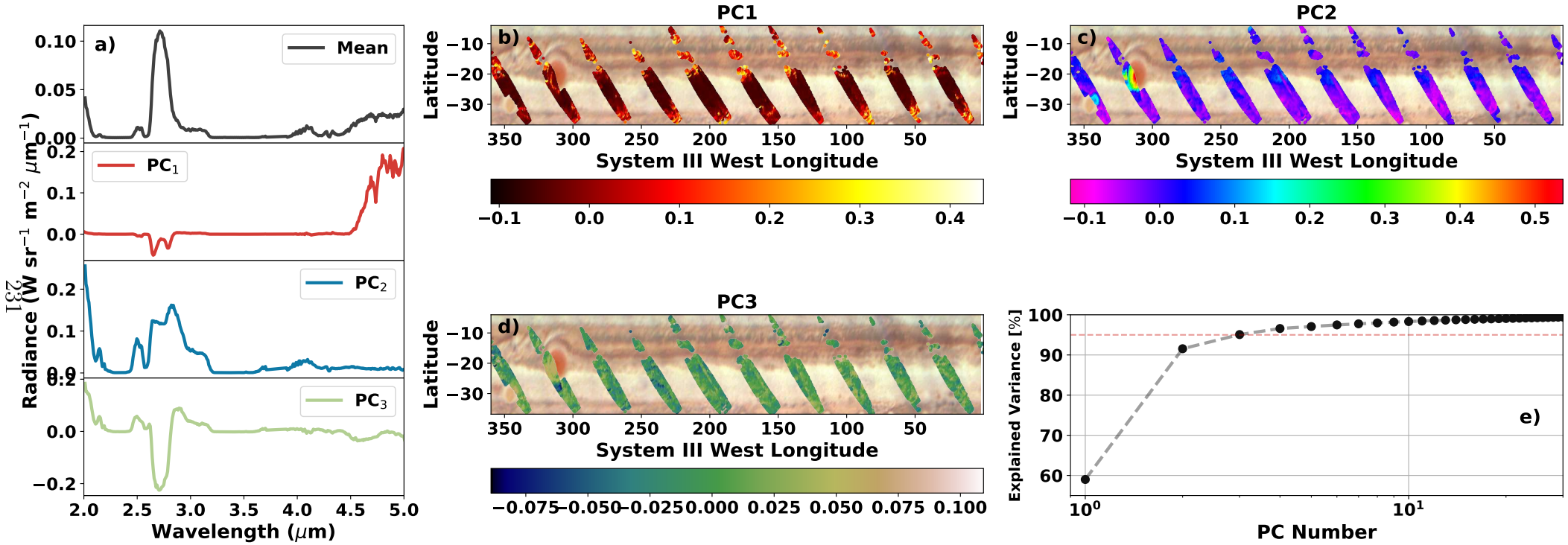


Figure 9.7: (a) Mean and principal components computed using `chopper.py` and considering the PJ1 G21 subset. (b, c, and d) Spatial maps of the first three principal components decomposition coefficients. (e) Cumulative PCA eigenvalues.

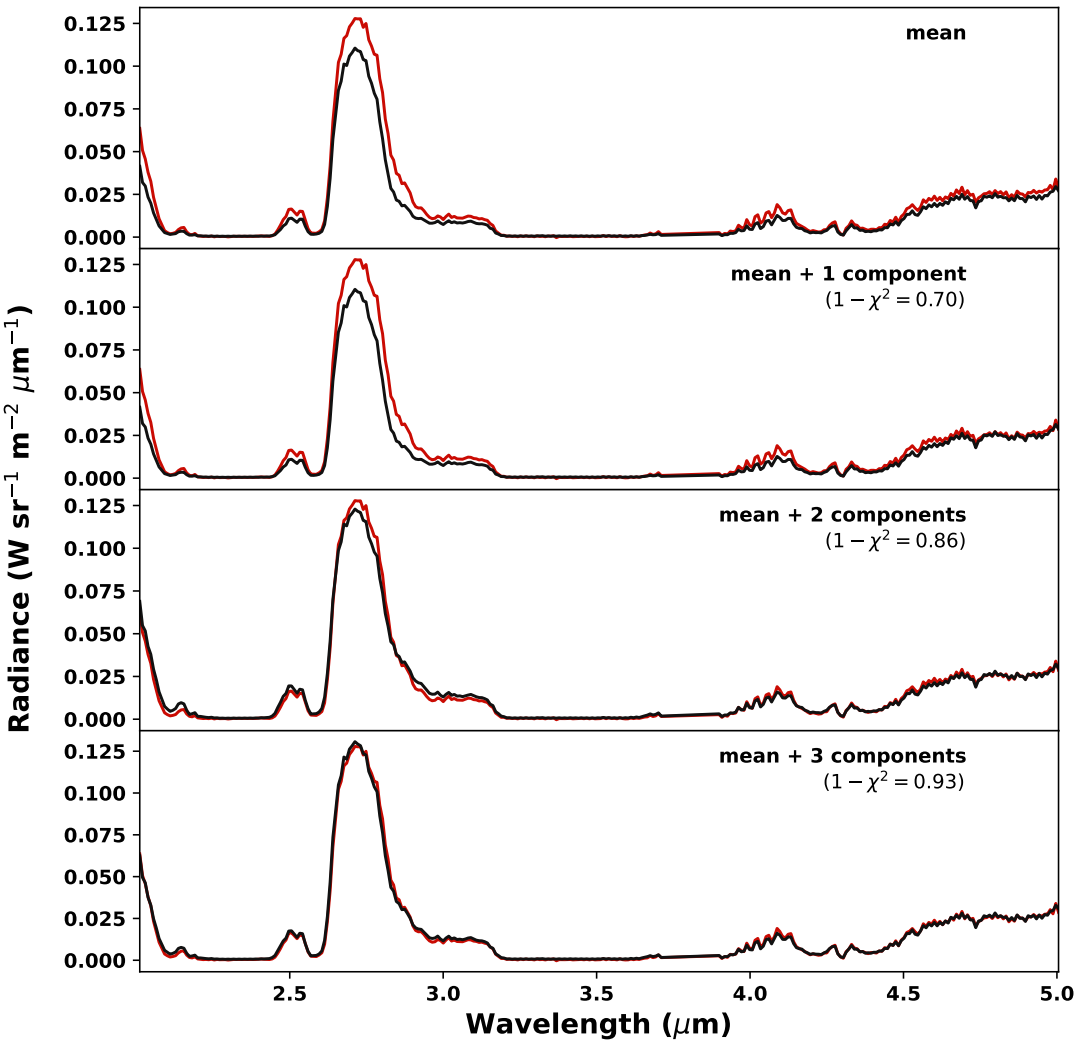


Figure 9.8: Example of the results of the PCA decomposition (black curves, at various stages), cf. Eqn. (9.2), applied to a random spectrum of the PJ1 G21 subset (red curve). The quality of the reconstruction after the decomposition is given by the parameter $1 - \chi^2$, which should be close to unity.

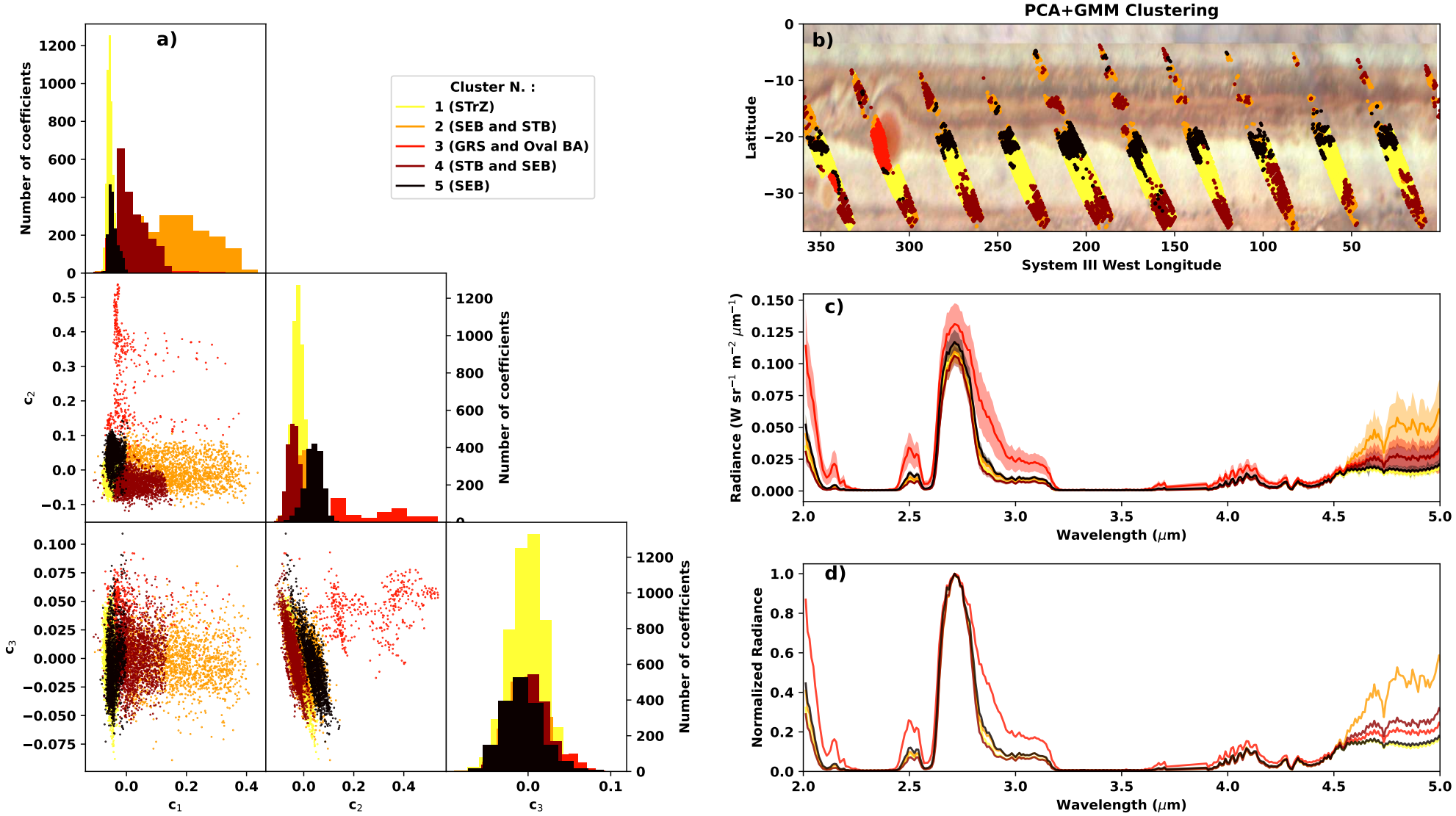


Figure 9.9: (a) Results of the `chopper.py` GMM analysis on the PCA-decomposition coefficients presented in Fig. 9.7. The resulting clusters are represented using different colors in the corner plot of the distribution of the coefficients. (b) Spatial maps of the resulting PCA+GMM clusters found by `chopper.py`. (c) Mean spectra of the clusters found by `chopper.py`. (d) Same as panel c but the spectra are normalized for the radiance measured at 2.73 μm.

PC3 was connected just to the reflection, both the 2 μm and 2.6-2.8 μm contributions should have been positive, as in PC2. Therefore, the physical interpretation is not obvious, as aerosol properties are known to be degenerate. It can be interpreted as a correction for excessive or insufficient spectral broadening or reflection induced by PC2 (see Fig. 9.8).
I decided to keep only three components to use for the GMM clustering. The elbow method suggested the number of clusters to be five and Fig. 9.9 shows the PCA decomposition coefficient distributions and the result of the clustering analysis together with the mean spectra resulting from each cluster and the relative latitude-longitude maps. my code can automatically identify and group together the spectra belonging to: the STrZ (cluster 1, yellow curves and points), the GRS and the Oval BA (cluster 3, red curves and points), the STB (cluster 4, dark red curves and points), and the different regions in cloud opacity comprising the SEB (clusters 2 and 5, orange and black curves and points). It is worth reminding the reader that the clustering was performed on the PCA decomposition coefficients which are derived from IR spectra. Therefore, my finding that clusters correlate with visible maps was not an a-priori guaranteed conclusion.
The spectra associated with the darker region in the SEB (cluster 2) represent the highest thermal signals, while the ones associated with the GRS, the highest solar reflected contribution. That is why they occupy opposite regions in the c_1-c_2 diagram in Fig. 9.9a. The spectra of the GRS also emerge in the c_2-c_3 diagram due to their distorted ("enlarged") solar reflected peak. This is a well-known phenomenon connected to the presence of higher-altitude optically thick clouds (Carlson et al., 2016b; Baines et al., 2002) (pressure levels around 0.4 bar) with respect to the surroundings (unity in optical depth usually reached around 1.3 bar, Braude et al. (2020)). Moreover, when grouping the spectra of the GRS and of the Oval BA together, the clustering is suggesting either a common vertical structure of the aerosols or the presence of similar chromophores. The clusters labeled with 5, 1, and 4, represent regions where cloud density progressively decreases. Cluster 5 seems to group the spectra that belong to particularly cloudy regions, clusters 1 and 4 group together spectra that belong, respectively, to the STrZ and STB.Having five mean cluster spectra that with their associated standard deviation capture more than 95 % of the variance in the original dataset can be very useful in order to improve the efficiency of the retrieval stage. In this way, it is possible to perform just five multiple scattering retrievals to obtain maps of global cloud properties instead of more than 10000 retrievals. This greatly improves the execution time, requiring hours instead of weeks.
To assess the performance of this method, I performed atmospheric retrievals on the mean cluster spectra, considering only the 2.5-3.1 μm range where most of the information regarding solar reflection by the clouds is contained. I used the same methods already described in Chapter 6 and Chapter 7. Tholin main clouds were considered to perform retrievals.

Figure 9.10 shows the results of the PSG retrievals, while the best-fitting parameters are listed in Table 9.1. The results of the retrievals are in a good quantitative agreement with the ones presented both in Grassi et al. (2021) and Harkett et al. (2024). Using the results of the retrievals it is possible to compute two different ancillary parameters as defined in Grassi et al. (2021): the effective cloud altitude

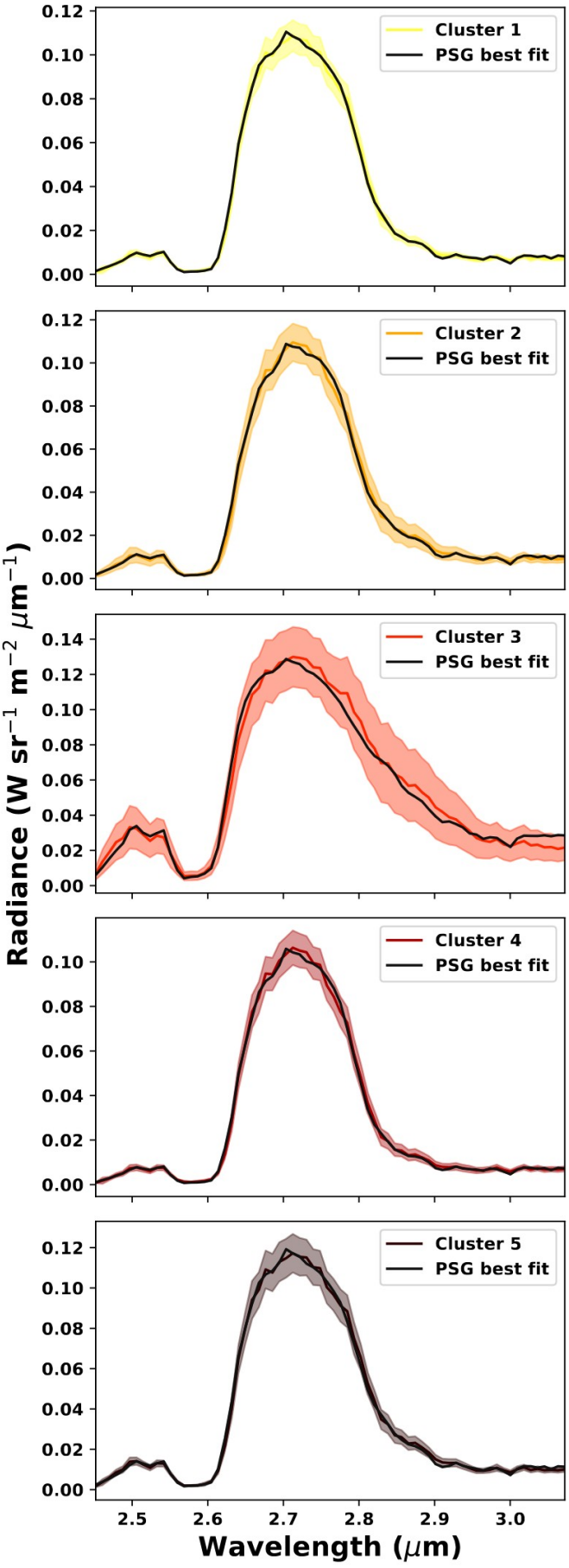


Figure 9.10: Results of the PSG multiple scattering retrievals performed on the five cluster mean spectra identified in Fig. 9.7.

Parameter	Unit	Meaning	Cluster 1 (STrZ)	Cluster 2 (SEB and STB)	Cluster 3 (GRS and Oval BA)	Cluster 4 (STB and SEB)	Cluster 5 (SEB)
NH_3 VMR	ppm	Gaseous ammonia profile deep mixing ratio	254 ± 103	219 ± 65	-	243 ± 84	204 ± 75
NH_3 RH	%	Gaseous ammonia profile relative humidity	24 ± 7	22 ± 6	10 ± 6	23 ± 6	24 ± 7
r_h	μm	Haze particles effective radius	0.38 ± 0.13	0.36 ± 0.15	0.35 ± 0.20	0.48 ± 0.15	0.29 ± 0.11
p_h	bar	Central pressure level of the haze layer	0.30 ± 0.06	0.27 ± 0.07	0.27 ± 0.07	0.33 ± 0.06	0.25 ± 0.07
w_h	bar	Width of the haze layer	0.22 ± 0.08	0.23 ± 0.08	0.27 ± 0.07	0.22 ± 0.10	0.23 ± 0.09
N_h	part./cm^3	Number density of the haze layer	85 ± 140	65 ± 117	135 ± 150	32 ± 52	158 ± 200
r_C	μm	Main cloud particles effective radius	3.3 ± 0.4	3.1 ± 0.4	2.2 ± 0.9	3.7 ± 0.6	3.1 ± 0.3
p_C	bar	Central pressure level of the main cloud	0.64 ± 0.05	0.58 ± 0.04	0.48 ± 0.12	0.64 ± 0.05	0.57 ± 0.04
w_C	bar	Width of the main cloud	0.043 ± 0.020	0.045 ± 0.020	0.082 ± 0.021	0.044 ± 0.021	0.043 ± 0.021
N_C	part./cm^3	Number density of the main cloud	7.5 ± 4.3	6.7 ± 3.9	11 ± 13	5 ± 3	9 ± 5
p_D	bar	Central pressure level of the deep cloud	1.03 ± 0.07	1.26 ± 0.08	-	1.15 ± 0.07	1.09 ± 0.07
N_D	part./cm^3	Number density of the deep cloud	224 ± 26	346 ± 47	-	288 ± 33	295 ± 27

Table 9.1: Results of the PSG retrieval on the mean cluster spectra presented in Fig. 9.9. When missing values are present in the table it does mean that the retrieval was not able to move from its initial guess. This happened only for the ammonia deep mixing ratio and the deep cloud parameters in the case of the GRS spectra retrieval. In that case, in fact, the main cloud deck became optically thick higher in the troposphere. The results presented in this table were used to obtain the maps presented in Fig. 9.11.

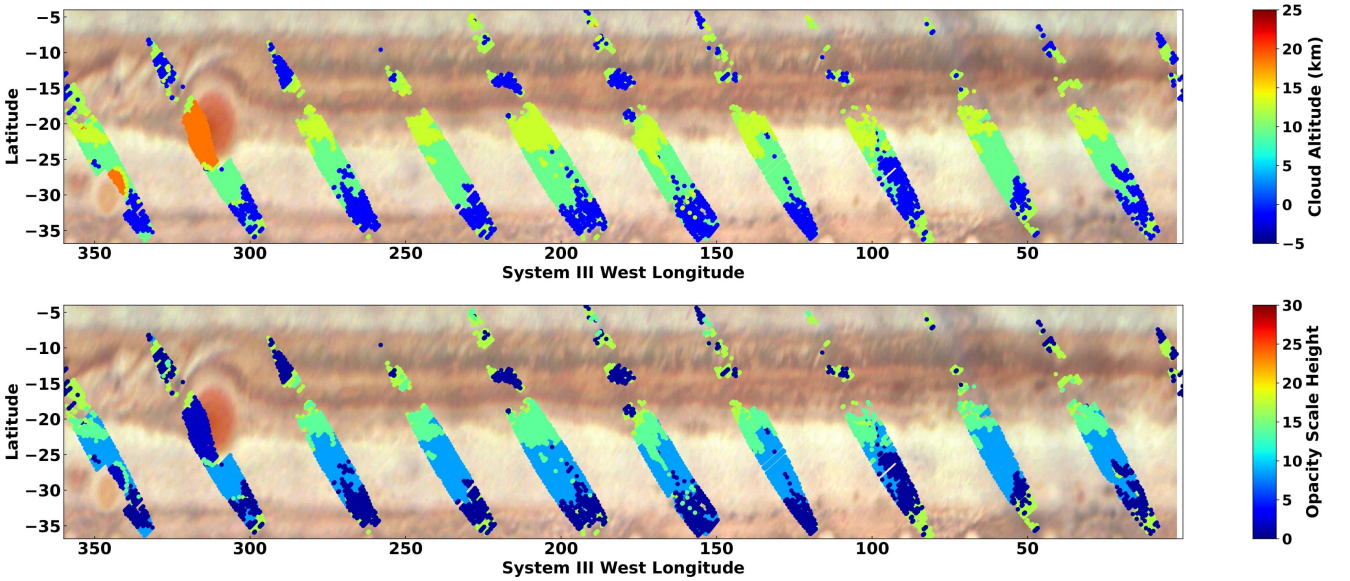


Figure 9.11: Results derived from the atmospheric retrievals in the 2.5-3.1 μm range performed on the mean spectra presented in Fig. 9.9. In the top panel, the effective cloud altitude (see text for the definition) is represented, while in the bottom one the opacity scale height (see text for the definition).

and the opacity scale height. The first parameter is defined as the altitude (with respect to the 1-bar level) where τ@3650 cm^{-1} (2.74 μm) = 1 is achieved. The second parameter is defined as the difference between the retrieved cloud altitude level (given by the retrieved pressure level) and the altitude (with respect to the 1-bar level) where τ@3650 cm^{-1} (2.74 μm) = e (Euler's number) is achieved. The maps of the two ancillary parameters are presented in Fig. 9.11. Comparing them to Fig. 8 and 9 of (Grassi et al., 2021) it is possible to observe a very good agreement, both qualitatively and quantitatively. The quality of correspondence is tuned by the quantization imposed by the number of clusters chosen during the GMM stage. A larger number of clusters will lead to more homogeneous regions being identified and displaying a better agreement.

9.4.2 Application to NIRSpec observations of the GRS

Figure 9.12 shows the results of the PCA analysis performed on the NIRSpec mosaic of the GRS. Also in this case, see Fig. 9.12f, more than 90 % of the variance is captured using the first two principal components which still appear anticorrelated, as deduced by Irwin et al. (2001). In this case, my code found the first component to be correlated to the solar reflected signal, and the second to the thermal one. This is also visible in subpanels b,c,d, and e of Fig. 9.12, where the coefficients' maps are presented. The first component map correlates to the solar reflected signal map presented in Fig. 9.1d. To reach a value larger than 95 % in this case I need to use also the third and fourth eigenvectors. The physical interpretation of these components is not immediately clear. PC3 is similar in spectral shape and intensity to the PC3 derived in the case of the analysis of the JIRAM G21 subset, Fig. 9.7a. Therefore, I can extend the interpretation of PC3 obtained from JIRAM also to NIRSpec. On the other hand, looking at Fig. 9.12e, PC4 varies

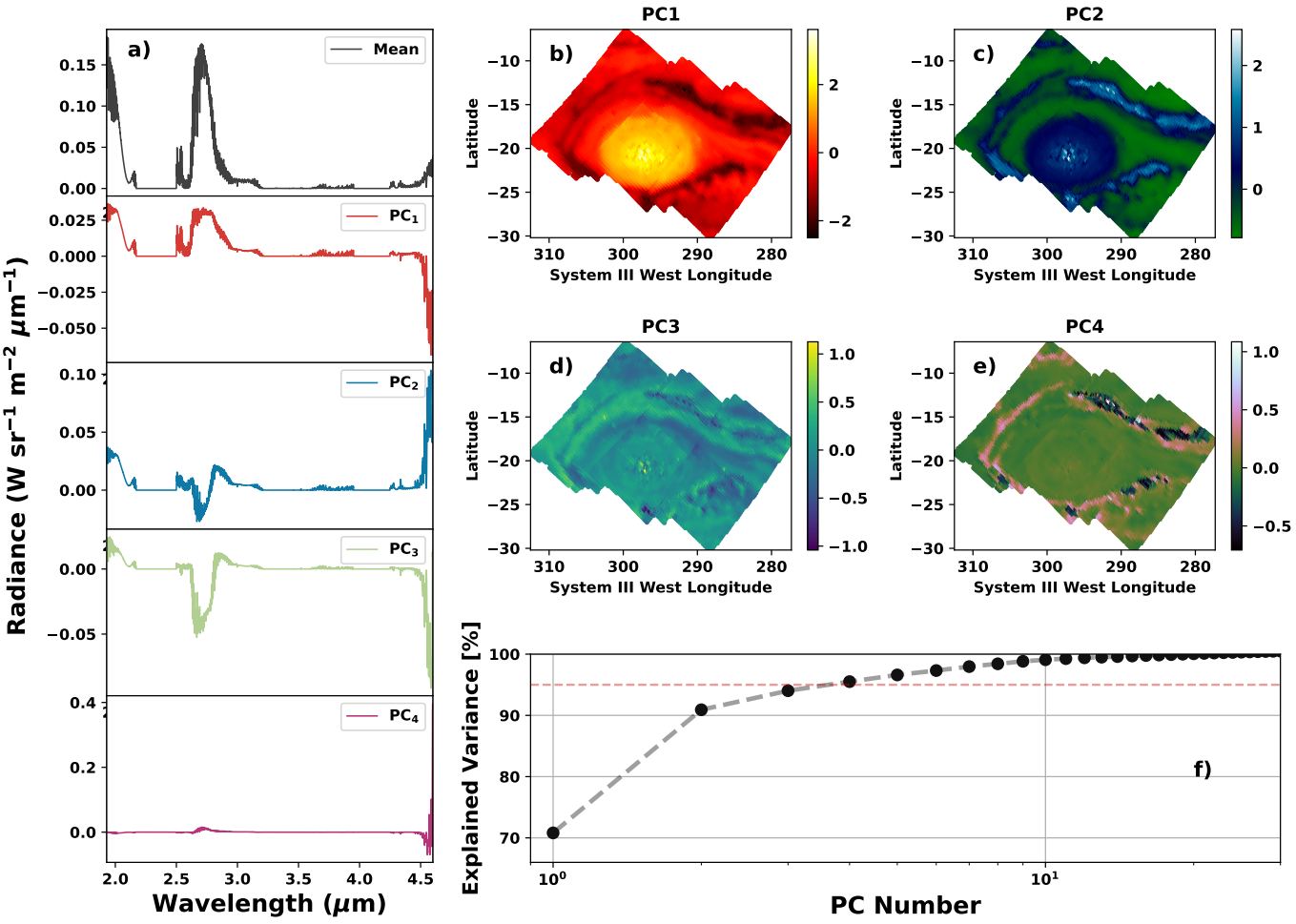


Figure 9.12: (a) Mean and principal components computed considering the JWST/NIRSpec dataset. (b, c, d, and e) Spatial maps of the first four principal components decomposition coefficients. (f) Cumulative PCA eigenvalues.

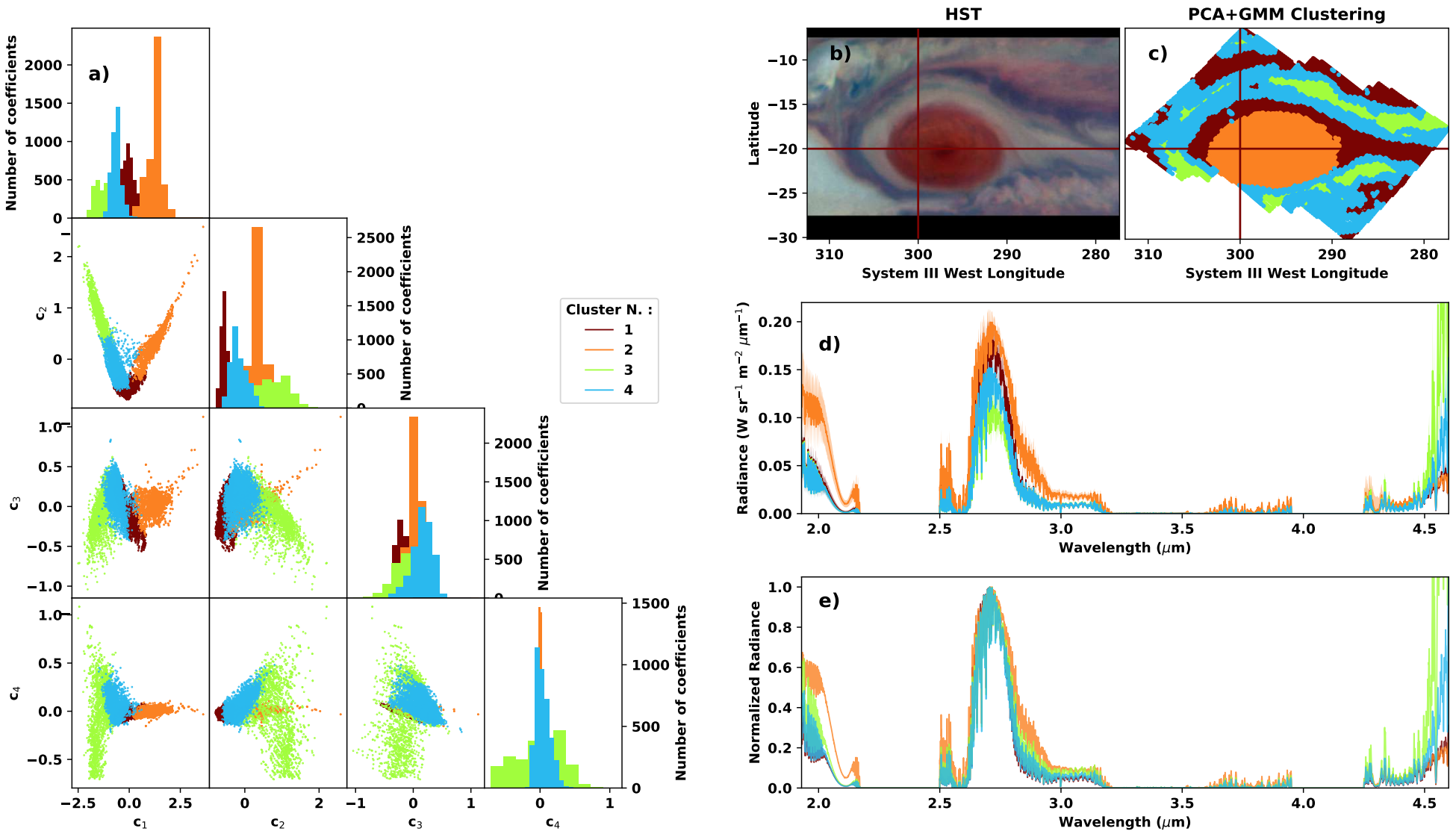


Figure 9.13: (a) Results of the `chopper.py` GMM analysis on the PCA-decomposition coefficients presented in Fig. 9.12 using a value of K=4. The resulting clusters are represented using different colors in the corner plot of the distribution of the coefficients. (b and c) Spatial maps of the resulting PCA+GMM clusters found by `chopper.py` compared to HST images. (d) Mean spectra of the clusters found by `chopper.py`. (e) Same as panel d but the spectra are normalized for the radiance measured at 2.73 μm.

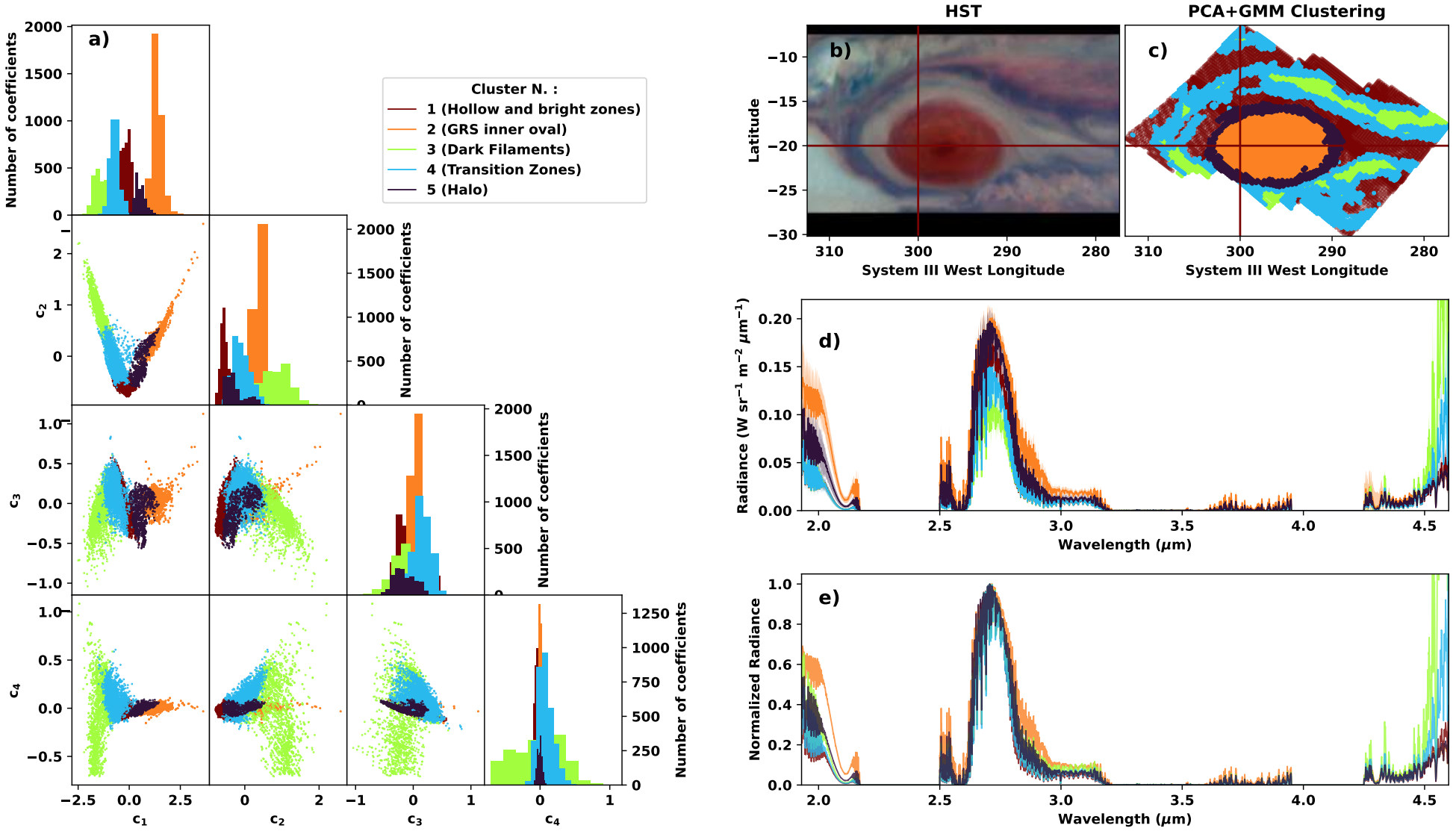


Figure 9.14: (a) Results of the `chopper.py` GMM analysis on the PCA-decomposition coefficients presented in Fig. 9.12 using a value of K=5. The resulting clusters are represented using different colors in the corner plot of the distribution of the coefficients. (b and c) Spatial maps of the resulting PCA+GMM clusters found by `chopper.py` compared to HST images. (d) Mean spectra of the clusters found by `chopper.py`. (e) Same as panel d but the spectra are normalized for the radiance measured at 2.73 μm.

mostly in the dark filaments. Therefore it may be associated with variations in the spectral shape and intensity of the 4.4-4.7 μm region. I decided to retain only the first four components and therefore `chopper.py` performed the GMM clustering on the respective four-dimensional coefficients distribution. In this case, the elbow method suggests the best number of clusters to be four but I also tried to perform the clustering using five of them, as the difference in WCSS score between the two cases was small. Figure 9.13 shows the PCA decomposition coefficient distributions and the result of the clustering analysis in the case of K=4. Figure 9.14 shows the PCA decomposition coefficient distributions and the result of the clustering analysis in the case of K=5. In both scenarios, my code can automatically identify and group together the spectra belonging to: the GRS (cluster 2, orange curves and points), the GRS hollow (cluster 1, dark red curves and points), the dark filaments that surround the GRS (cluster 3, green curves and points), and a transition zone between the hollow and the characteristic Jovian reddish-grayish regions (cluster 4, sky blue curves and points). Once again, the clustering of IR spectra returns results that correlate with the visible images.
In both cases, as pointed out in the previous subsection, the spectra associated with the dark filaments present the highest thermal signals, while the ones associated with the GRS have the highest solar reflected one. Therefore they tend to occupy opposite regions in the c_1-c_2 diagram, with the spectra of the GRS also emerging in the c_2-c_3 diagram. This underlines the consistency between the JIRAM and NIRSpec observations.
However, in the scenario with K=5 an additional group emerges without changing the distribution and shapes of the ones found in the K=4 scenario. This cluster seems to group a series of spectra that distribute geographically forming a halo that surrounds and include the outer rim of GRS. Differently from the other clusters, this halo is not evident from the optical HST or JunoCam images, and therefore they are unlikely to be related to differences in cloud optical depth and/or to the presence of chromophores (Carlson et al., 2016b). If I consider the mean spectra, the solar reflected and thermal signals are almost identical. However, the mean spectrum of the halo presents a less broadened and distorted reflectance peak with respect to the mean spectrum of the inner GRS oval (see Fig. 9.14d). This may be caused by differences in altitude, vertical extension, particle effective radii, and/or composition. I will investigate this in the next section.
The detection of this halo highlights the fact that the use of PCA+GMM on IR spectral data is both useful to get global and mean physical properties of regions of interest known from visible images, but it also may lead to the detection of areas that are identifiable only at non-optical wavelengths.

9.4.3 Application to JIRAM PJ1 GRS subset

I applied my code also to the JIRAM observation of the GRS region during PJ1. The main goal is to verify whether the clustering analysis can identify the halo found using NIRSpec data, and under which combination of parameters. Figure 9.15 shows the obtained principal components. They are very similar - but not identical - to the ones presented in Fig. 9.7. Also in this case, the first component is correlated to the thermal signal, while the second correlates to the solar reflected one. The

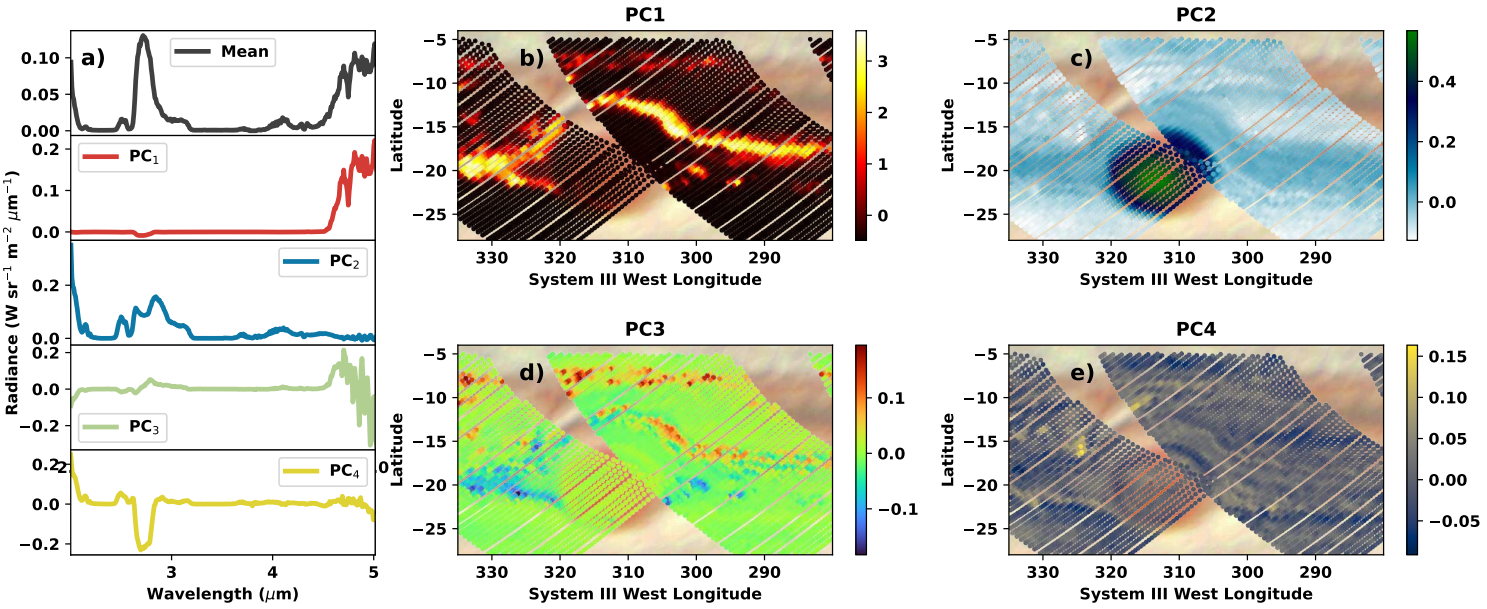


Figure 9.15: (a) Mean and principal components computed considering the Juno/JIRAM PJ1 GRS subset. (b, c, d, and e) Spatial maps of the first four principal components decomposition coefficients.

physical explanation of the third component is not trivial, and may be connected to intrinsic differences observed in the thermal spectra of the dark filaments, similarly to the PC4 derived in the NIRSpec case. The fourth component, instead, is almost identical to PC3 found in Fig. 9.7a and to PC3 found in Fig. 9.14a. Therefore it seems to be connected to second order effects in intensity and spectral shape induced by the presence of clouds and hazes. It can also be interpreted as a a correction for excessive/insufficient spectral broadening or reflection induced by PC2. More than 95 % of variance is captured using only the first two components. However, since I suspected that the halo differs from the GRS because of cloud properties, I decided to perform the clustering twice: first using the c_1 and c_2 coefficients and then the c_2 and c_4 coefficients. In both scenarios, the elbow method suggested the best number of clusters to be four and I proceeded accordingly. The results of the clustering using only the decomposition coefficients relative to the first two components are given in Fig. 9.16, while the results using the c_2 and c_4 coefficients are presented in Fig. 9.17. The first figure shows that when c_1-c_2 coefficients are used, `chopper.py` can automatically identify and group together the spectra belonging to the GRS, the hollow, the dark filaments, and the surroundings. In the end, I found the same results of the G21 subset, as the c_1-c_2 coefficients are basically identical. However, even if K >4 clusters are used, the code is not able to detect any halos surrounding the GRS inner oval. When c_2-c_4 coefficients are used, the spectra belonging to the inner GRS oval and the halo easily emerge and they are distinguished by the code. This underlines the fact that clustering can be very powerful also if one can identify principal components of interest from a physical point of view. Therefore `chopper.py` can be used both in an unsupervised or supervised fashion, depending on the scientific case of interest. It is worth to remark that in the case of identifying

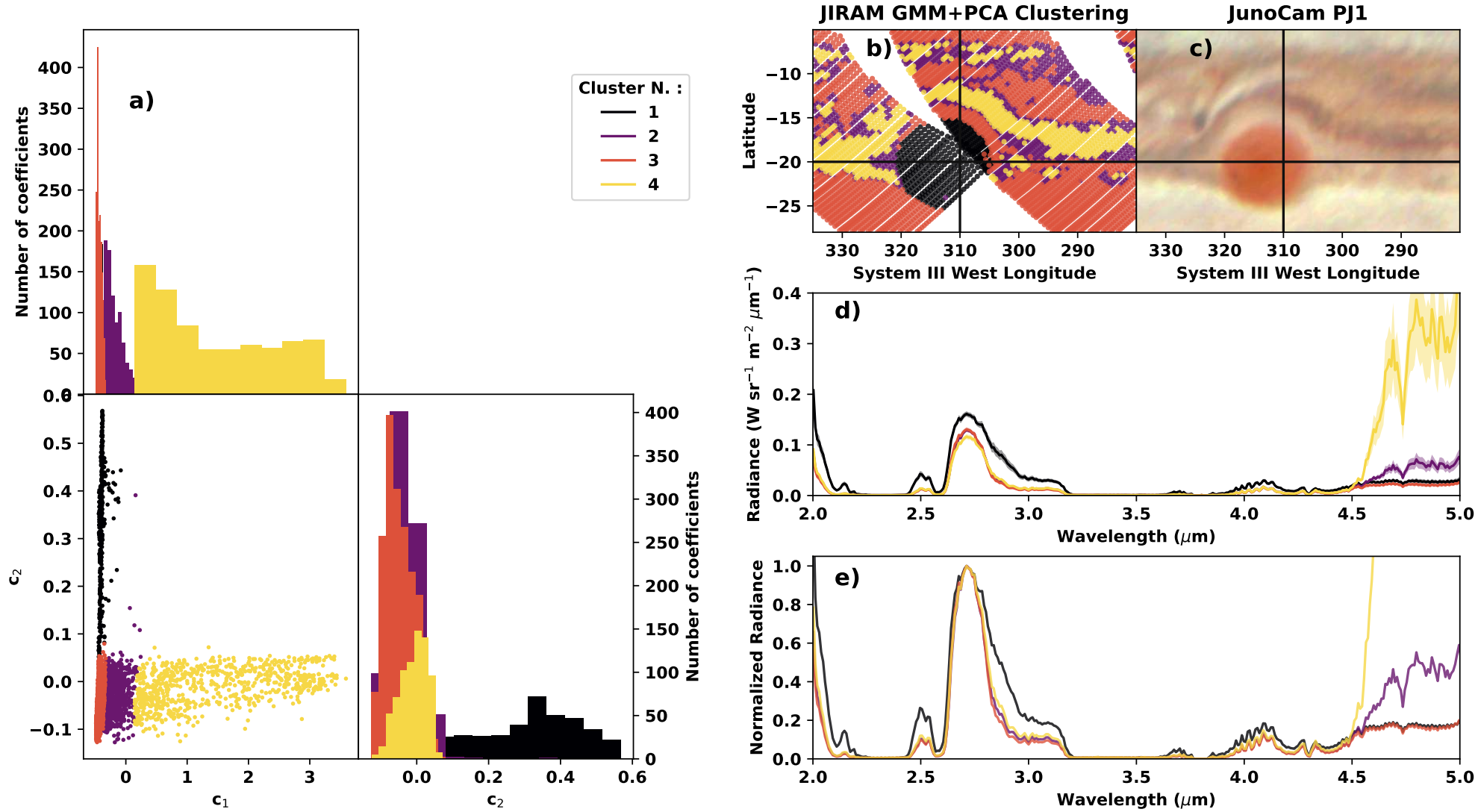


Figure 9.16: (a) Results of the `chopper.py` GMM analysis on the first and second PCA-decomposition coefficients presented in Fig. 9.15. The resulting clusters are represented using different colors in the corner plot of the distribution of the coefficients. (b) Spatial maps of the resulting PCA+GMM clusters found by `chopper.py`. (c) Mean spectra of the clusters found by `chopper.py`. (d) Same as panel c but the spectra are normalized for the radiance measured at 2.73 μm.

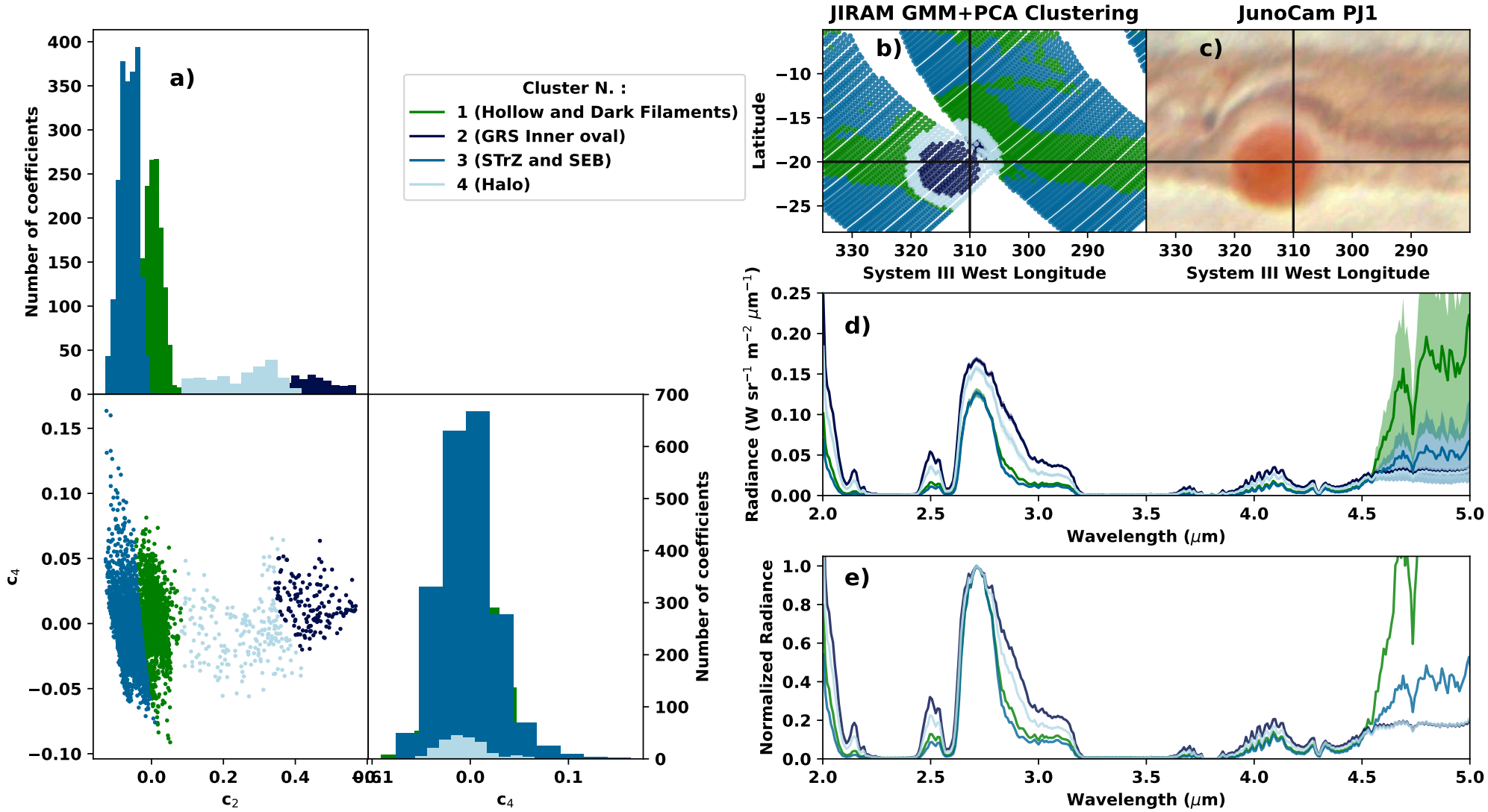


Figure 9.17: (a) Results of the `chopper.py` GMM analysis on the second and fourth PCA-decomposition coefficients presented in Fig. 9.15. The resulting clusters are represented using different colors in the corner plot of the distribution of the coefficients. (b and c) Spatial maps of the resulting PCA+GMM clusters found by `chopper.py` compared to JunoCam image. (d) Mean spectra of the clusters found by `chopper.py`. (e) Same as panel d but the spectra are normalized for the radiance measured at 2.73 μm.

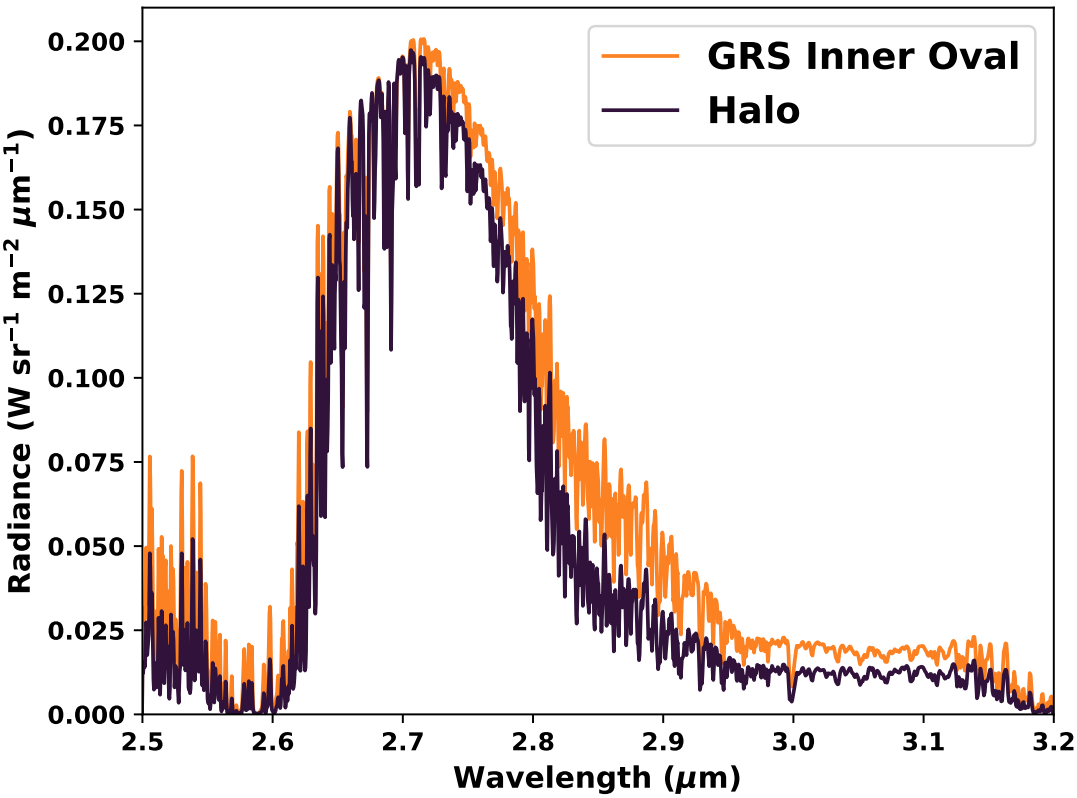


Figure 9.18: JWST/NIRSpec mean spectrum of the inner GRS oval (orange) and of the halo (burgundy) found thanks to the `chopper.py` code.

the halo in JIRAM data a supervised approach in the form of a selection of the PCA coefficients parameter space is mandatory. In fact, as the first two PCs capture more than 95 % of the variance they also dominate the clustering process. This is not true in the JWST case because of the higher spectral and spatial resolution of NIRSpec. Therefore, as the spectra of the halo and of the inner oval seems to exhibit similar solar and thermal signals, they can never be disentangled in the c_1-c_2 space.
The spectra of the hollow and the dark filaments are grouped in one cluster as they both belong to the SEB, while the remaining group joins together the spectra belonging to the EZ and the STrZ. The coefficients of the halo and the inner GRS occupy a very distinct space in the c_2-c_4 parameter space with respect to the coefficients of the GRS surroundings region. This is consistent with the GRS having clouds different from the other Jovian regions, both in composition, vertical distribution, and dynamical origin. Noteworthy, the coefficients of the halo seem to occupy a transition zone between the typical Jovian clouds and the GRS ones, and this is perhaps the reason why it was not possible to detect the halo from the visible images. Also in the JIRAM case, the mean spectra of the GRS and the halo have similar solar and thermal radiation levels. The JIRAM mean spectrum of the halo presents a less broadened and distorted reflectance peak with respect to the JIRAM mean spectrum of the inner GRS oval.

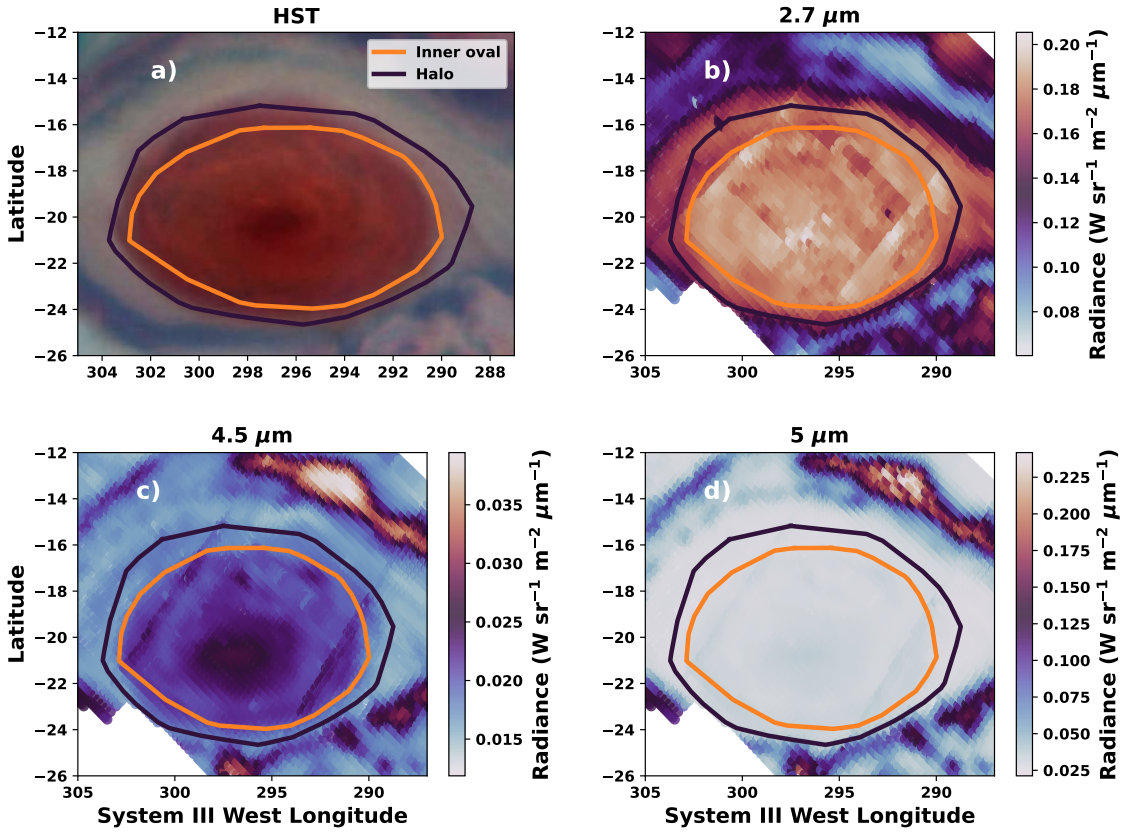


Figure 9.19: Contours of the of the inner GRS oval (orange) and of the halo (burgundy) clusters identified in Fig. 9.14 superimposed to: (a) HST visible image, (b, c, and d) NIRSpec radiance maps at respectively 2.7, 4.5, and 5 μm.

9.5 Discussion: Identification of the GRS "halo"

The main conclusion of my PCA+GMM clustering is the detection of a group of spectral pixels that seem to form a halo corresponding to the outer rim of the GRS, Fig. 9.19. The GRS inner oval pixels on the other hand were classified in a different cluster. The mean spectra extracted from the halo and the inner GRS oval have the same values for solar-reflected and thermal emitted radiation. However, they differ principally in the shape of the 2.73 μm reflection peak, see Fig. 9.18, which for the inner GRS appears to be more broadened with respect to the halo. The detection was made using both JWST/NIRSpec and Juno/JIRAM data. In the case of JWST/NIRSpec, the detection was completely unsupervised. For Juno/JIRAM, I needed to follow a supervised approach and select manually the PCA coefficients parameter space on which the clustering was performed. While the GRS appears quite uniform from visible and NIR maps (see Fig. 9.19a and 9.19b), the IR spectra suggest that the GRS is not uniform but consists of two main concentric structures. This is evident from the radiance maps at wavelengths where both solar and thermal contributions become important, like the 4.5 μm channel (see Fig. 9.19c).
While the presence of rings or bright regions around the outer rim of Jovian anticyclones was noted before at 5 μm (de Pater et al., 2010b) and radio wavelengths (de Pater et al., 2016, 2019c,b) the halo detected here is interior to these rings, see Fig. 9.19d and has not been detected before. de Pater et al. (2010b) proposed that air

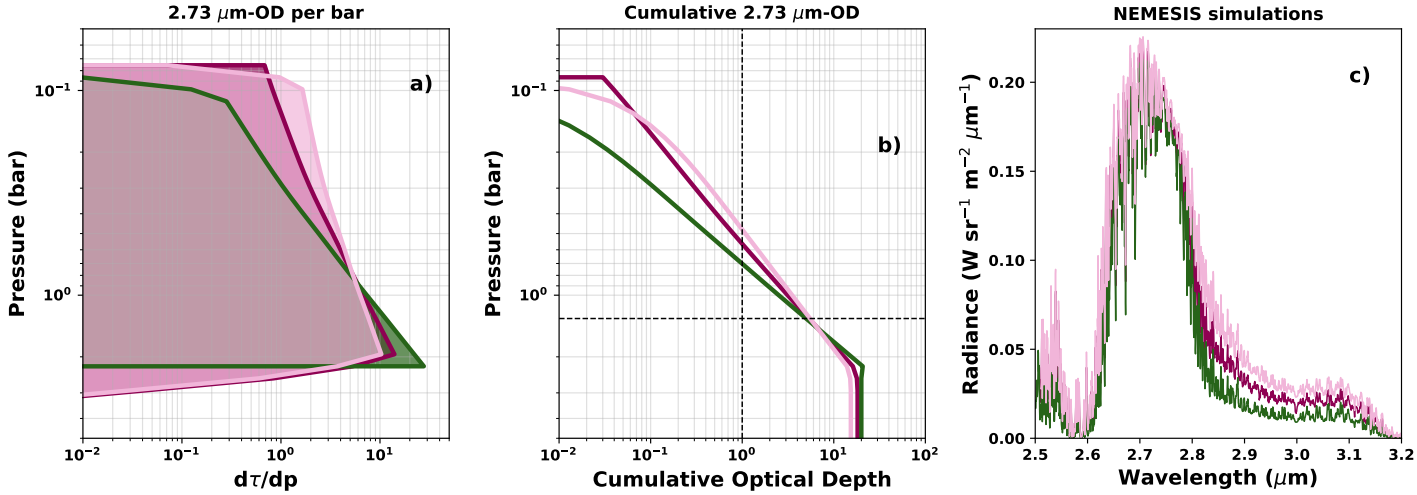


Figure 9.20: (a) Cloud profiles (given as 2.73 μm optical depth per bar) of the three different model atmospheres used to perform NEMESIS simulations. (b) computed cumulative 2.73 μm optical depth for each of the model atmospheres. (c) NEMESIS simulations of three different model atmospheres that differ for the vertical extension of the main cloud layer.

is (baroclinically) rising along the center of Jovian anticyclones in a subadiabatic atmosphere, then descending at a distance not exceeding twice the local Rossby deformation radius. For the GRS, they proposed that the air rises in a ring around the center of the GRS, descending inside that ring (explaining the slight elevation in temperature at the center of the GRS, observed by Fletcher et al. (2010)) and presumably also outside that ring.

As the visible images and the NIR maps in Fig. 9.19b do not suggest the presence of two main concentric structures inside the GRS, I suspect that the halo and the inner oval share the same chromophore upper layer in the Crème Brulée model (Baines et al., 2002; Carlson et al., 2016b) and similar 1-bar cumulative optical depth values. The broadening of the 2.73 μm reflection peak is a hint that the main difference between the halo and the inner oval may lie in the vertical extension of the main cloud layer, and therefore in the pressure level at which a value of 1 in optical depth is reached in the upper troposphere.

To verify this hypothesis, I run different forward simulations using the NEMESIS radiative transfer suite (Irwin et al., 2008), focusing on the 2.5-3.2 μm range. The spectral database, the abundances of H_2, He, CH_4, and its isotopologues are the same as those described in Harkett et al. (2024). I assumed Voigt broadening for all wavelengths with a line wing cut-off of 350 cm^{-1} generating pre-tabulated correlated-k tables using the spectral range and resolution of the NIRSpec instrument. The pressure-temperature profile was fixed to the one measured by Cassini/CIRS (Flasar et al., 2004). NH_3 and PH_3 gaseous volume mixing ratio (VMR) profiles have a fixed single value from a "knee" pressure and extend down to 10 bar. At altitudes above the knee pressure, the profiles decrease with a Fractional Scale Height (FSH). I decided to fix the ammonia knee pressure at 860 mbar, and the phosphine knee pressure at 500 mbar, according to Harkett et al. (2024).

I use a value of 230 ppm for the NH_3 deep VMR, and of 0.8 ppm for PH_3 deep VMR, as derived from the MIRI data (Harkett et al., 2024). The chosen FSH are

0.13 for ammonia and 0.25 for phosphine.
The main ingredient of my forward simulations is the aerosols. In the NIRSpec range we are not sensitive to any tropospheric or stratospheric blue-absorbing species like the Carlson et al. (2016b) and Baines et al. (2002) chromophores. The Jovian spectrum in the NIR, in fact, is more sensitive to the main cloud layer that lies below the chromophore layer. The work of Grassi et al. (2021) and Biagiotti et al. (2025c) have shown that tholins are a good approximation for the optical properties of the unknown material that compose the Jovian clouds. I therefore used Imanaka et al. (2012) tholins with optical properties computed using Mie theory for spherical particles of 2 μm radius. I used three different cloud profiles to perform the forward simulation, as shown in Fig. 9.20 panel a. They are represented by a base pressure level, an optical depth normalized at 2.73 μm, and a cloud fractional scale height. All the profiles have a base pressure level of 2 bar (Irwin et al., 2025), consistent with Baines et al. (2002). The optical depth is adjusted manually to ensure that all the profiles have a cumulative optical depth at 1.2 bar (panel b) equal to five, consistent with Braude et al. (2020). This is also consistent with the observed solar and thermal signal values of the halo and the inner GRS. The only variable that discriminates between the profiles is the fractional scale height (CFSH). The green profile has a CFSH=0.4, the violet profile a CFSH=0.55, and the pink profile a CFSH=0.7. A larger CSFH translates in a larger vertical extension of the cloud layer, i.e. more cloud particles at higher altitudes. It is possible to note this from Fig. 9.20b, where the cumulative optical depths are shown. As a consequence, the profiles with larger CFSH reach a value of unity in optical depth higher in the troposphere (at lower pressures). In Table 9.2 I resume the used parameters for each NEMESIS simulation. The results of the NEMESIS simulations are presented in 9.20 panel c. I draw two main conclusions from Fig. 9.20. The first is that NEMESIS used together with tholin-like clouds can reproduce quite well the spectral shape observed by NIRSpec in the 2.5-3.1 μm range. Secondly, a difference in cloud fractional scale height (and therefore in cloud vertical extension) can explain the broadening of the solar reflection peak observed with NIRSpec. This in turn may suggest that clouds closer to the center of the GRS at the time of the NIRSpec observations were reaching higher altitudes than the ones near the outer rim. Therefore, the halo detected with NIRSpec may be a consequence of increasing transparency of the GRS aerosols with radial distance. In other words, the halo can be a region where reflection from the deeper clouds is blending with the chromophore layer. This would be consistent with some optical and UV HST images, where the colour and the measured radiances change subtly towards the GRS edge and are more intense at the center (Simon et al., 2024).
Quantitatively, NEMESIS simulations suggest that between the center of the GRS and its outer rim may exist a difference in altitude of 10-20 km regarding the level at which the clouds become optically thick. These kinds of differences in altitude are consistent with recent fluid dynamics simulations by Zhang & Marcus (2024) for which a "spinning-top"-like shape for the GRS should be more stable than the classical cylinder shape proposed previously in literature (Parisi et al., 2021b), see Fig. 9.21. Moreover, the formation of higher clouds is highly favored by the low temperatures found in the GRS inner oval (Fletcher et al., 2010; Harkett et al., 2024).

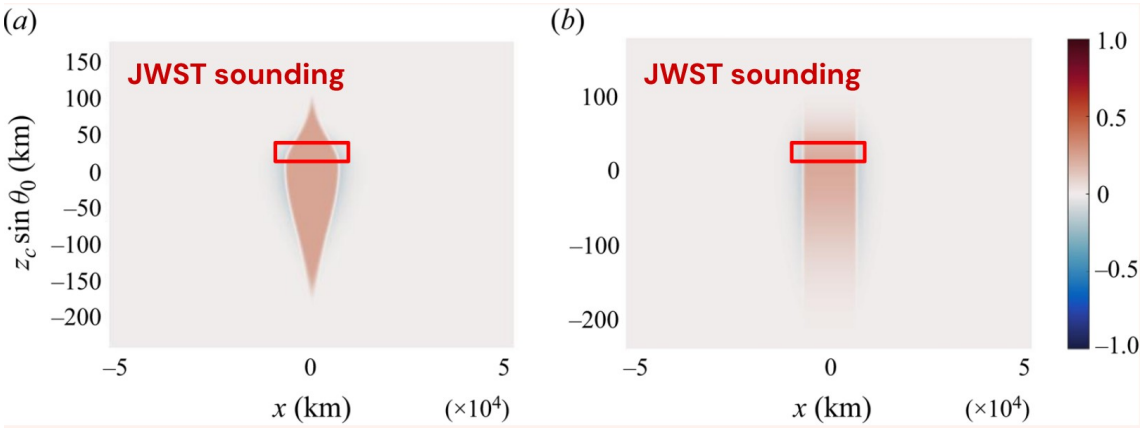


Figure 9.21: The two major fluid-dynamical hypothesis regarding the structure and shape of the GRS. The colorbar is the same of Fig. 5.6. In red I highlight the sounding level of JWST/NIRSpec (from this Thesis work).

In any case, the modeling of a cloudy atmosphere is a very degenerate task. This means that similar variations in the resulting synthetic spectrum can be obtained with different combinations of the input parameters. Therefore, multiple scattering atmospheric retrievals of the NIRSpec spectra over a broader spectral range (to break some of these degeneracies) are needed to verify the hypothesis presented in this Thesis and to obtain quantitative results. However, this is beyond the scope of the present analysis.

The halo spectral cluster seems to align closely with the outer edge of the GRS red ellipse in visible-wavlength HST data (see panels b and c in 9.14). This location is close to two key features of the velocity field of the vortex: the high-speed ring of maximum azimuthal velocities, and the associated region of cyclonic shielding (Valcke & Verron, 1997; Brueshaber et al., 2019; Li et al., 2020b) just outside this high-speed ring. An accurate comparison between the position of the halo spectral cluster and specific velocity field features is not possible because the GRS velocity field is variable on both short and long timescales (Wong et al., 2021b; Simon et al., 2024), but the wind field was not measured at the time of the JWST/NIRSpec observations nor at the time of the JIRAM PJ1 observations. The edge of the visible red area of the GRS and Oval BA typically lies just outside the high-speed ring (Wong et al., 2011b; Simon et al., 2024), with the cyclonic shielding just outside the high-speed ring (Wong et al., 2021b). Thus the halo spectral cluster may align better with the cyclonic shielding region of the velocity field, which is qualitatively consistent with the reduced cloud opacity interpretation, because cyclonic shear is often associated with subsidence, warming, and evaporation/sublimation of cloud material. Future observations with simultaneous near-IR resolved spectra and visible-wavelength velocity fields are needed for a detailed comparison.

Parameter Name	Model 1 (Green)	Model 2 (Magenta)	Model 3 (Pink)
Base pressure (bar)	2.30	2.12	2.11
Optical depth at the base ($\tau_{2.73\,\mu m}$)	21.3	17.2	14.8
Cumulative optical depth at 1.2 bar ($\tau_{2.73\,\mu m}$)	1	1	1
Cloud fractional scale height (CFSH)	0.4	0.55	0.7
Cloud effective radius (μm)	2	2	2
Cloud composition	Imanaka et al. (2012)	Imanaka et al. (2012)	Imanaka et al. (2012)
NH_3 deep VMR (ppm)	230	230	230
PH_3 deep VMR (ppm)	0.8	0.8	0.8

Table 9.2: Physical parameters used to perform the NEMESIS simulations displayed in Fig. 9.20. $\tau_{2.73\,\mu m}$ refers to optical depth normalized at the 2.73 μm wavelength, the center of the Jovian reflection peak.

Chapter 10

Conclusions

The major results of this thesis can be summarized as follows:

- I successfully applied the NASA Planetary Spectrum Generator to model Jovian spectra collected by JIRAM. This represents a significant leap, as far as I know, since PSG was never used in previous works to model the near-infrared spectra of Jupiter. I successfully created three fully Pythonic retrieval codes that use PSG to model the solar, thermal, and full range of JIRAM. The retrievals can be performed either according the Optimal Estimation Method (thanks to the `PyOE` package), or according the MCMC technique with the `emcee` package. This thesis represents the first successful attempt to perform a full-range retrieval from JIRAM data.

- I developed a new tool able to greatly reduce the execution time of retrieval analysis by means of an automatic clustering of spectral collection. The methods are condensed in the open source Python code `chopper.py`. This result is not trivial, since performing clustering of high-dimensional datasets such as spectral collection can be extremely degenerate. In order to avoid this, `chopper.py` first performs a Principal Component Analysis (PCA) on the collection and then a Gaussian Mixture Model (GMM) Machine Learning (ML) clustering on the results of the PCA decomposition. I validated the code using JIRAM data already presented in (Grassi et al., 2021). I found that the code is able to successfully automatically group together similar spectra belonging to known regions such as the belts, the zones, and the GRS. I extracted the mean spectrum for each cluster and performed solar retrievals with PSG. I compared these results with the ones obtained by (Grassi et al., 2021), who performed a separate retrieval for each individual spectrum in the dataset. The agreement was found to be optimal both qualitatively as well as quantitatively. In order to perform this task, I developed a technique able to clean JIRAM spectra from spurious features such as spikes, which can compromise the PCA stage of the analysis.

- I identified the spectral features of ammonia ice clouds in the data collected by JIRAM during the first perijove passage, PJ1. I established a new method of searching for ammonia ice clouds on Jupiter that is based on the shape of the 2.6-2.8 μm reflection peak rather than the expected absorption feature at 2.97 μm. I also proposed two new indicators (see Section 7.2), in order to

efficiently find ammonia ice clouds in future and/or archive data. The method is completely general since the shape of the reflection peak is strongly correlated to variations induced by the single scattering albedo due to the relatively low gaseous opacity in the 2.6-2.8 μm window. Therefore, the method can be generalized to other planets and exoplanets once a fixed gaseous composition and candidate materials for the main cloud deck are assumed.

- I detected a total of 25 Spectrally Identifiable Ammonia Clouds (or SIACs) that are located in correspondence with the central regions of a white vortex in the Northern Temperate Domain, thought to be a FFR. The detection was made by performing different atmospheric retrievals with variable main cloud compositions. In proximity of the SIACs, I observed that the best-fit is achieved when the clouds are assumed to be composed of Titan's tholins as measured by Imanaka et al. (2012) coated with ammonia ice. Outside the vortex, the best fit is reached invoking Titan's tholins as measured by Imanaka et al. (2012). This result represents the first detection of pure ammonia ice clouds in the Juno data. Detecting the presence of pure ammonia ice was one of the main goals of the JIRAM instrument science team, as stated by Adriani et al. (2017).

- Performing solar retrievals from JIRAM data, I was able to quantitatively characterize the aerosol and atmospheric properties in correspondence with the vortex. I found that, with respect to its surroundings, the vortex region presented: (i) lower haze's effective radii, (ii) lower haze's pressure levels (therefore higher altitude hazes), (iii) higher values of ammonia relative humidity, (iv) lower main cloud's pressure levels, and (v) denser clouds. These results are consistent with the vortex being the result of a strong uplifting convective event that brought up in the upper troposphere fresh ammonia from the deep atmosphere. This effort represents the first quantitative spectral analysis of a candidate FFR on Jupiter. These results and the detection of 25 SIACs can be considered in continuity with previous literature works (Baines et al., 2002; Sromovsky & Fry, 2018) that claimed that on Jupiter, pure ammonia ice clouds are present only in correspondence with vortex and strong convective events. In other regions, Jupiter clouds are not composed of ammonia ice but dominated by an unknown contaminant material that I approximated to be similar to Titan's tholins as measured by Imanaka et al. (2012). I also found that the retrieved cloud densities of the main cloud are orders of magnitude lower than the values predicted by ECCM models.

- I explored the putative origin of the unknown contaminant material described in the previous point. I extracted a mean spectrum from the JIRAM PJ1 data, considering viewing conditions close to future missions that will observe exoplanets in reflected light. I performed full range MCMC atmospheric retrievals on the full range JIRAM spectrum using different compositions for the main cloud. I found that the best fit is achieved when Imanaka et al. (2012)'s tholins removed from their 4.7 μm feature are invoked. This material can be considered as an adaptation of the Titan's tholins to the Jovian case. In particular, in order to adequately fit JIRAM data, a material that bears the NH

bond (between 2 and 3.2 μm, i.e., the solar range) and that bears weak CN bonds (around 4.7 μm) is required. This is consistent with the photochemical pathways on Jupiter, that are different from the ones on Titan. I proposed that on Jupiter the chromophore material is created via coagulation of UV dissociation products of freshly formed ammonia ice particles and photolysis products of methane and ammonia in the lower stratosphere and upper troposphere. This work will be further expanded and can have huge implications for Saturn, Uranus, Neptune, and warm and cold gaseous exoplanets.

- Performing solar and thermal retrievals on JIRAM data, I was able to quantitatively characterize for the first time the turbulent regions surrounding the Great Red Spot. I focused in particular on the wake and four dark ovals in correspondence with the ripples of the GRS. I identified them as regions of interest (ROIs) since they presented unusually low values of the solar reflected radiance at 2.73 μm. As a comparison, I also performed retrievals of nearby nominal regions and of the dark filaments that surround the GRS. The results of the thermal retrievals showed that the ROIs present lower VMR values for ammonia, phosphine, arsine, and germane. However, these values were closer to the ones retrieved in the dark filaments, ruling out the possibility of the ROIs being Hot Spots. The depletion of minor species, however, identifies these regions as downdrifting events. The result of the solar retrievals, on the other hand, showed that in the ROIs at the same latitude of the GRS, the retrieved deep clouds' densities are an order of magnitude lower than expected. On the basis of this measure I therefore claimed the detection of two cloud clearance areas in correspondence of the turbulent regions near the GRS. I computed optical depth profiles and verified that, despite lower cloud densities, a value of 3 in optical depth is reached around the 1.5 bar level, precluding the probing of the water cloud level. I propose that these cloud clearance areas are the result of Von Karman vortices induced by the presence of the GRS that acts as a solid body with respect to the SEB. This hypothesis requires however further confrimations by precise 3D fluid dynamical simulations.

- I analyzed the unpublished JWST/NIRSpec 2022 observations of the Great Red Spot region. Since the dataset is extremely high dimensional, I decided to apply to it the `chopper.py` code. In order to do so, I first developed a technique that is able to clean the already pre-processed NIRSpec data from missing values induced by saturation. The application of `chopper.py` to NIRSpec maps sdemonstrated that the code is able to group together the pixels and extract the JWST spectra belonging to the GRS, the GRS's hollow, the dark filaments, and the surrounding regions. This can enormously reduce the time of the analysis since it is possible to perform a single retrieval on a representative spectrum instead of a single retrieval for each NIRSpec pixel. Moreover, `chopper.py` was able to identify two new regions that went undetected using visible images and spectra. Namely, I found that the GRS seems to be composed of two substructures: a low-reflectivity halo and a bright inner oval. Comparing them to HST visible images, it is possible to note that the halo corresponds to the outer rim of the GRS. The spectra of these two substructures present similar values of the solar and thermal signals. However, the

halo spectrum reflection peak (2.6-2.8 μm) appears to be less broadened with respect to the main oval. In order to verify this finding, I also performed the same analysis on JIRAM PJ1 data of the GRS and its surroundings. Also in this new scenario `chopper.py` was able to identify both the halo and the main oval and to confirm the spectroscopic findings of NIRSpec. I then performed a series of NEMESIS multiple scattering radiative transfer simulations in order to explain the observed differences in the reflection peak between the halo and the main oval. As a result, I inferred that such behaviour can be explained by differences in the vertical extension of the cloud layers. In particular, a more vertically-extended cloud will produce a broader reflection peak. This finding is in agreement with recent 3D fluid dynamics simulations by Zhang & Marcus (2024) that claim that the GRS, in order to maintain its secular stability, should be shaped as a spinning-top instead of a more classical cylinder (Parisi et al., 2021a). I consider my finding of more extended clouds towards the center of the GRS with respect to the outer rim to be a supporting evidence of the Zhang & Marcus (2024) hypothesis.

In conclusion, the substantial body of work and novel findings detailed throughout this thesis are positioned not as an endpoint, but, hopefully, as a valuable launchpad for the next decade of research into Jovian and gas giant aerosols. The analytical framework and methods pioneered herein represent an applicable toolset for tackling the vast, still largely unexplored archive of JIRAM data. Furthermore, this work arrives at a truly timely moment for planetary science. The James Webb Space Telescope (JWST) is set to revolutionize our understanding of giant planet atmospheres; the increasing allocation of observation time—such as the three distinct Jovian campaigns accepted for JWST Cycle 4 (Fletcher et al., 2025; Wong et al., 2025; Tiranti et al., 2025)—signals a sustained commitment to this area of study. The future promises even richer data with the arrival of the JUpiter ICy moons Explorer (JUICE) spacecraft in July 2031. Jupiter observations will be performed at each perijove passage, exploiting instruments such as MAJIS, an image spectrometer with a spectral range of 0.5-5.5 μm, and a spectral resolution between 4 and 9 nm. MAJIS will offer an unparalleled vantage point to survey the Jovian atmosphere, improving significantly the performances of JIRAM.
The models and methodologies developed in this thesis can hopefully represent valuable resources that will directly inform observational strategy, refine data reduction, and ensure that these future missions yield the maximum possible scientific return, propelling our understanding of planetary atmospheres.

Tears and fears and feeling proud
To say "I love you" right out loud
Dreams and schemes and circus crowds
I've looked at life that way

But now old friends are acting strange
They shake their heads, they say I've changed
Well, something's lost, but something's gained
In living every day

I've looked at life from both sides now
From win and lose and still somehow
It's life's illusions I recall
I really don't know life at all

- Joni Mitchell

Appendix

In this Appendix the `cfg.txt` file used to perform the best-fitting PSG simulations described in Section 7.6 is given.

```
<OBJECT>Planet
<OBJECT-NAME>Jupiter
<OBJECT-DATE>2018/09/15 12:54
<OBJECT-DIAMETER>142693
<OBJECT-GRAVITY>23.32
<OBJECT-GRAVITY-UNIT>g
<OBJECT-STAR-DISTANCE>5.2
<OBJECT-STAR-VELOCITY>0.0
<OBJECT-SOLAR-LONGITUDE>0.0
<OBJECT-SOLAR-LATITUDE>0.0
<OBJECT-SEASON>0.00
<OBJECT-STAR-TYPE>G
<OBJECT-STAR-TEMPERATURE>5778
<OBJECT-STAR-RADIUS>1.00
<OBJECT-OBS-LONGITUDE>0.00
<OBJECT-OBS-LATITUDE>77.0
<OBJECT-OBS-VELOCITY>0.0
<OBJECT-PERIOD>0.41345
<OBJECT-PERIAPSIS>0.00
<OBJECT-ECCENTRICITY>0.00000
<OBJECT-INCLINATION>18.53
<GEOMETRY>Nadir
<GEOMETRY-OFFSET-NS>0.0
<GEOMETRY-OFFSET-EW>0.0
<GEOMETRY-OFFSET-UNIT>arcsec
<GEOMETRY-OBS-ALTITUDE>10000
<GEOMETRY-ALTITUDE-UNIT>km
<GEOMETRY-USER-PARAM>49.0
<GEOMETRY-STELLAR-TYPE>G
<GEOMETRY-STELLAR-TEMPERATURE>5777
<GEOMETRY-STELLAR-MAGNITUDE>0
<GEOMETRY-STAR-DISTANCE>-1.000000e+00
<GEOMETRY-STAR-FRACTION>0.000000e+00
<GEOMETRY-REF>User
<GEOMETRY-DISK-ANGLES>1
<GEOMETRY-ROTATION>0.00,0.00
<GEOMETRY-SOLAR-ANGLE>77.0
<GEOMETRY-OBS-ANGLE>49.0
<GEOMETRY-PLANET-FRACTION>2.031199e-06
<GEOMETRY-AZIMUTH>101.57734965538987
<GEOMETRY-BRDFSCALER>1.0
<ATMOSPHERE-DESCRIPTION>Jupiter atmosphere ars
<ATMOSPHERE-STRUCTURE>Equilibrium
<ATMOSPHERE-WEIGHT>2.30661
<ATMOSPHERE-PRESSURE>22.372
<ATMOSPHERE-PUNIT>bar
<ATMOSPHERE-NGAS>7
<ATMOSPHERE-NAERO>3
<ATMOSPHERE-AEROS>miev,cloud2,Cloud
<ATMOSPHERE-AABUN>1,1,1
<ATMOSPHERE-AUNIT>scl,scl,scl
```

```
<ATMOSPHERE-ASIZE
   >0.2783146825143455,3.5163228777479807,1.5445155730144462
<ATMOSPHERE-ASUNI>um,um,um
<ATMOSPHERE-LAYERS-MOLECULES>Altitude,miev,cloud2,Cloud,gastly,CH4,
   NH3,H2O,PH3,germane,arsine
<ATMOSPHERE-LAYERS>171
<ATMOSPHERE-TEMPERATURE>100
<ATMOSPHERE-NMAX>5
<ATMOSPHERE-LMAX>99
<ATMOSPHERE-ASIZE
   >0.2783146825143455,3.5163228777479807,1.5445155730144462
<ATMOSPHERE-LAYER-1>2.237E+1,4.168E+2,0.000E+0,0.000E+0,0.000E
   +0,0.000E+0,1.000E-2,1.810E-3,3.749E-4,1.829E-3,3.611E-7,2.752E
   -10,1.568E-10
<ATMOSPHERE-LAYER-2>2.154E+1,4.131E+2,2.427E+0,0.000E+0,0.000E
   +0,0.000E+0,1.000E-2,1.810E-3,3.749E-4,1.707E-3,3.611E-7,2.752E
   -10,1.568E-10
<ATMOSPHERE-LAYER-3>2.074E+1,4.094E+2,4.833E+0,0.000E+0,0.000E
   +0,0.000E+0,1.000E-2,1.810E-3,3.749E-4,1.590E-3,3.611E-7,2.752E
   -10,1.568E-10
<ATMOSPHERE-LAYER-4>1.997E+1,4.057E+2,7.218E+0,0.000E+0,0.000E
   +0,0.000E+0,1.000E-2,1.810E-3,3.749E-4,1.478E-3,3.611E-7,2.752E
   -10,1.568E-10
<ATMOSPHERE-LAYER-5>1.922E+1,4.020E+2,9.581E+0,0.000E+0,0.000E
   +0,0.000E+0,1.000E-2,1.810E-3,3.749E-4,1.371E-3,3.611E-7,2.752E
   -10,1.568E-10
<ATMOSPHERE-LAYER-6>1.851E+1,3.983E+2,1.192E+1,0.000E+0,0.000E
   +0,0.000E+0,1.000E-2,1.810E-3,3.749E-4,1.268E-3,3.611E-7,2.752E
   -10,1.568E-10
<ATMOSPHERE-LAYER-7>1.782E+1,3.946E+2,1.424E+1,0.000E+0,0.000E
   +0,0.000E+0,1.000E-2,1.810E-3,3.749E-4,1.171E-3,3.611E-7,2.752E
   -10,1.568E-10
<ATMOSPHERE-LAYER-8>1.716E+1,3.909E+2,1.654E+1,0.000E+0,0.000E
   +0,0.000E+0,1.000E-2,1.810E-3,3.749E-4,1.078E-3,3.611E-7,2.752E
   -10,1.568E-10
<ATMOSPHERE-LAYER-9>1.652E+1,3.872E+2,1.882E+1,0.000E+0,0.000E
   +0,0.000E+0,1.000E-2,1.810E-3,3.749E-4,9.904E-4,3.611E-7,2.752E
   -10,1.568E-10
<ATMOSPHERE-LAYER-10>1.590E+1,3.835E+2,2.107E+1,0.000E+0,0.000E
   +0,0.000E+0,1.000E-2,1.810E-3,3.749E-4,9.074E-4,3.611E-7,2.752E
   -10,1.568E-10
<ATMOSPHERE-LAYER-11>1.531E+1,3.797E+2,2.331E+1,0.000E+0,0.000E
   +0,0.000E+0,1.000E-2,1.810E-3,3.749E-4,8.291E-4,3.611E-7,2.752E
   -10,1.568E-10
<ATMOSPHERE-LAYER-12>1.474E+1,3.760E+2,2.552E+1,0.000E+0,0.000E
   +0,0.000E+0,1.000E-2,1.810E-3,3.749E-4,7.556E-4,3.611E-7,2.752E
   -10,1.568E-10
<ATMOSPHERE-LAYER-13>1.419E+1,3.723E+2,2.771E+1,0.000E+0,0.000E
   +0,0.000E+0,1.000E-2,1.810E-3,3.749E-4,6.865E-4,3.611E-7,2.752E
   -10,1.568E-10
<ATMOSPHERE-LAYER-14>1.367E+1,3.686E+2,2.988E+1,0.000E+0,0.000E
   +0,0.000E+0,1.000E-2,1.810E-3,3.749E-4,6.220E-4,3.611E-7,2.752E
   -10,1.568E-10
<ATMOSPHERE-LAYER-15>1.316E+1,3.649E+2,3.203E+1,0.000E+0,0.000E
   +0,0.000E+0,1.000E-2,1.810E-3,3.749E-4,5.618E-4,3.611E-7,2.752E
   -10,1.568E-10
```

```
<ATMOSPHERE-LAYER-16>1.267E+1,3.612E+2,3.415E+1,0.000E+0,0.000E+0,0.000E+0,1.000E-2,1.810E-3,3.749E-4,5.059E-4,3.611E-7,2.752E-10,1.568E-10
<ATMOSPHERE-LAYER-17>1.220E+1,3.575E+2,3.626E+1,0.000E+0,0.000E+0,0.000E+0,1.000E-2,1.810E-3,3.749E-4,4.540E-4,3.611E-7,2.752E-10,1.568E-10
<ATMOSPHERE-LAYER-18>1.174E+1,3.538E+2,3.834E+1,0.000E+0,0.000E+0,0.000E+0,1.000E-2,1.810E-3,3.749E-4,4.061E-4,3.611E-7,2.752E-10,1.568E-10
<ATMOSPHERE-LAYER-19>1.131E+1,3.501E+2,4.040E+1,0.000E+0,0.000E+0,0.000E+0,1.000E-2,1.810E-3,3.749E-4,3.620E-4,3.611E-7,2.752E-10,1.568E-10
<ATMOSPHERE-LAYER-20>1.088E+1,3.464E+2,4.244E+1,0.000E+0,0.000E+0,0.000E+0,1.000E-2,1.810E-3,3.749E-4,3.215E-4,3.611E-7,2.752E-10,1.568E-10
<ATMOSPHERE-LAYER-21>1.048E+1,3.427E+2,4.446E+1,0.000E+0,0.000E+0,0.000E+0,1.000E-2,1.810E-3,3.749E-4,2.845E-4,3.611E-7,2.752E-10,1.568E-10
<ATMOSPHERE-LAYER-22>1.009E+1,3.390E+2,4.645E+1,0.000E+0,0.000E+0,0.000E+0,1.000E-2,1.810E-3,3.749E-4,2.508E-4,3.611E-7,2.752E-10,1.568E-10
<ATMOSPHERE-LAYER-23>9.714E+0,3.353E+2,4.843E+1,0.000E+0,0.000E+0,0.000E+0,1.000E-2,1.810E-3,3.749E-4,2.202E-4,3.611E-7,2.752E-10,1.568E-10
<ATMOSPHERE-LAYER-24>9.353E+0,3.316E+2,5.038E+1,0.000E+0,0.000E+0,0.000E+0,1.000E-2,1.810E-3,3.749E-4,1.925E-4,3.611E-7,2.752E-10,1.568E-10
<ATMOSPHERE-LAYER-25>9.005E+0,3.279E+2,5.232E+1,0.000E+0,0.000E+0,0.000E+0,1.000E-2,1.810E-3,3.749E-4,1.676E-4,3.611E-7,2.752E-10,1.568E-10
<ATMOSPHERE-LAYER-26>8.670E+0,3.242E+2,5.423E+1,0.000E+0,0.000E+0,0.000E+0,1.000E-2,1.810E-3,3.749E-4,1.452E-4,3.611E-7,2.752E-10,1.568E-10
<ATMOSPHERE-LAYER-27>8.347E+0,3.205E+2,5.611E+1,0.000E+0,0.000E+0,0.000E+0,1.000E-2,1.810E-3,3.749E-4,1.253E-4,3.611E-7,2.752E-10,1.568E-10
<ATMOSPHERE-LAYER-28>8.036E+0,3.168E+2,5.798E+1,0.000E+0,0.000E+0,0.000E+0,1.000E-2,1.810E-3,3.749E-4,1.075E-4,3.611E-7,2.752E-10,1.568E-10
<ATMOSPHERE-LAYER-29>7.737E+0,3.133E+2,5.983E+1,0.000E+0,0.000E+0,0.000E+0,1.000E-2,1.810E-3,3.749E-4,9.270E-5,3.611E-7,2.752E-10,1.568E-10
<ATMOSPHERE-LAYER-30>7.449E+0,3.098E+2,6.165E+1,0.000E+0,0.000E+0,0.000E+0,1.000E-2,1.810E-3,3.749E-4,7.985E-5,3.611E-7,2.752E-10,1.568E-10
<ATMOSPHERE-LAYER-31>7.172E+0,3.063E+2,6.346E+1,0.000E+0,0.000E+0,0.000E+0,1.000E-2,1.810E-3,3.749E-4,6.847E-5,3.611E-7,2.752E-10,1.568E-10
<ATMOSPHERE-LAYER-32>6.905E+0,3.029E+2,6.524E+1,0.000E+0,0.000E+0,0.000E+0,1.000E-2,1.810E-3,3.749E-4,5.842E-5,3.611E-7,2.752E-10,1.568E-10
<ATMOSPHERE-LAYER-33>6.648E+0,2.994E+2,6.701E+1,0.000E+0,0.000E+0,0.000E+0,1.000E-2,1.810E-3,3.749E-4,4.959E-5,3.611E-7,2.752E-10,1.568E-10
<ATMOSPHERE-LAYER-34>6.401E+0,2.960E+2,6.875E+1,0.000E+0,0.000E+0,0.000E+0,1.000E-2,1.810E-3,3.749E-4,4.187E-5,3.611E-7,2.752E-10,1.568E-10
```

```
<ATMOSPHERE-LAYER-35>6.163E+0,2.926E+2,7.048E+1,0.000E+0,0.000E+0,0.000E+0,1.000E-2,1.810E-3,3.749E-4,3.540E-5,3.611E-7,2.752E-10,1.568E-10
<ATMOSPHERE-LAYER-36>5.934E+0,2.893E+2,7.218E+1,0.000E+0,0.000E+0,0.000E+0,1.000E-2,1.810E-3,3.749E-4,2.992E-5,3.611E-7,2.752E-10,1.568E-10
<ATMOSPHERE-LAYER-37>5.713E+0,2.861E+2,7.387E+1,0.000E+0,0.000E+0,0.000E+0,1.000E-2,1.810E-3,3.749E-4,2.514E-5,3.611E-7,2.752E-10,1.568E-10
<ATMOSPHERE-LAYER-38>5.500E+0,2.828E+2,7.554E+1,0.000E+0,0.000E+0,0.000E+0,1.000E-2,1.810E-3,3.749E-4,2.102E-5,3.611E-7,2.752E-10,1.568E-10
<ATMOSPHERE-LAYER-39>5.296E+0,2.795E+2,7.718E+1,0.000E+0,0.000E+0,0.000E+0,1.000E-2,1.810E-3,3.749E-4,1.747E-5,3.611E-7,2.752E-10,1.568E-10
<ATMOSPHERE-LAYER-40>5.098E+0,2.762E+2,7.881E+1,0.000E+0,0.000E+0,0.000E+0,1.000E-2,1.810E-3,3.749E-4,1.443E-5,3.611E-7,2.752E-10,1.568E-10
<ATMOSPHERE-LAYER-41>4.909E+0,2.731E+2,8.042E+1,0.000E+0,0.000E+0,0.000E+0,1.000E-2,1.810E-3,3.749E-4,1.195E-5,3.611E-7,2.752E-10,1.568E-10
<ATMOSPHERE-LAYER-42>4.726E+0,2.700E+2,8.202E+1,0.000E+0,0.000E+0,0.000E+0,1.000E-2,1.810E-3,3.749E-4,9.906E-6,3.611E-7,2.752E-10,1.568E-10
<ATMOSPHERE-LAYER-43>4.550E+0,2.669E+2,8.359E+1,0.000E+0,0.000E+0,0.000E+0,1.000E-2,1.810E-3,3.749E-4,8.164E-6,3.611E-7,2.752E-10,1.568E-10
<ATMOSPHERE-LAYER-44>4.381E+0,2.639E+2,8.515E+1,0.000E+0,0.000E+0,0.000E+0,1.000E-2,1.810E-3,3.749E-4,6.688E-6,3.611E-7,2.752E-10,1.568E-10
<ATMOSPHERE-LAYER-45>4.218E+0,2.608E+2,8.669E+1,0.000E+0,0.000E+0,1.488E-312,1.000E-2,1.810E-3,3.749E-4,5.445E-6,3.611E-7,2.752E-10,1.568E-10
<ATMOSPHERE-LAYER-46>4.061E+0,2.578E+2,8.821E+1,0.000E+0,0.000E+0,4.293E-281,1.000E-2,1.810E-3,3.749E-4,4.403E-6,3.611E-7,2.752E-10,1.568E-10
<ATMOSPHERE-LAYER-47>3.910E+0,2.548E+2,8.971E+1,0.000E+0,0.000E+0,2.081E-252,1.000E-2,1.810E-3,3.749E-4,3.564E-6,3.611E-7,2.752E-10,1.568E-10
<ATMOSPHERE-LAYER-48>3.764E+0,2.519E+2,9.119E+1,0.000E+0,0.000E+0,2.819E-226,1.000E-2,1.810E-3,3.749E-4,2.891E-6,3.611E-7,2.752E-10,1.568E-10
<ATMOSPHERE-LAYER-49>3.624E+0,2.491E+2,9.266E+1,0.000E+0,0.000E+0,1.698E-202,1.000E-2,1.810E-3,3.749E-4,2.330E-6,3.611E-7,2.752E-10,1.568E-10
<ATMOSPHERE-LAYER-50>3.489E+0,2.462E+2,9.412E+1,0.000E+0,0.000E+0,7.038E-181,1.000E-2,1.810E-3,3.749E-4,1.865E-6,3.611E-7,2.752E-10,1.568E-10
<ATMOSPHERE-LAYER-51>3.360E+0,2.433E+2,9.555E+1,0.000E+0,0.000E+0,2.992E-161,1.000E-2,1.810E-3,3.749E-4,1.482E-6,3.611E-7,2.752E-10,1.568E-10
<ATMOSPHERE-LAYER-52>3.235E+0,2.405E+2,9.697E+1,0.000E+0,0.000E+0,1.890E-143,1.000E-2,1.810E-3,3.749E-4,1.169E-6,3.611E-7,2.752E-10,1.568E-10
<ATMOSPHERE-LAYER-53>3.114E+0,2.377E+2,9.837E+1,0.000E+0,0.000E+0,2.497E-127,1.000E-2,1.810E-3,3.749E-4,9.215E-7,3.611E-7,2.752E-10,1.568E-10
```

```
<ATMOSPHERE-LAYER-54>2.998E+0,2.350E+2,9.976E+1,0.000E+0,0.000E+0,9.443E-113,1.000E-2,1.810E-3,3.749E-4,7.283E-7,3.611E-7,2.752E-10,1.568E-10
<ATMOSPHERE-LAYER-55>2.887E+0,2.323E+2,1.011E+2,0.000E+0,0.000E+0,1.368E-99,1.000E-2,1.810E-3,3.749E-4,5.713E-7,3.611E-7,2.752E-10,1.568E-10
<ATMOSPHERE-LAYER-56>2.779E+0,2.296E+2,1.025E+2,0.000E+0,0.000E+0,9.938E-88,1.000E-2,1.810E-3,3.749E-4,4.448E-7,3.611E-7,2.752E-10,1.568E-10
<ATMOSPHERE-LAYER-57>2.676E+0,2.269E+2,1.038E+2,0.000E+0,0.000E+0,4.628E-77,1.000E-2,1.810E-3,3.749E-4,3.436E-7,3.611E-7,2.752E-10,1.568E-10
<ATMOSPHERE-LAYER-58>2.576E+0,2.242E+2,1.051E+2,0.000E+0,0.000E+0,1.738E-67,1.000E-2,1.810E-3,3.749E-4,2.631E-7,3.611E-7,2.752E-10,1.568E-10
<ATMOSPHERE-LAYER-59>2.480E+0,2.215E+2,1.065E+2,0.000E+0,0.000E+0,6.507E-59,1.000E-2,1.810E-3,3.749E-4,2.008E-7,3.611E-7,2.752E-10,1.568E-10
<ATMOSPHERE-LAYER-60>2.388E+0,2.189E+2,1.077E+2,0.000E+0,0.000E+0,2.947E-51,1.000E-2,1.810E-3,3.749E-4,1.535E-7,3.611E-7,2.752E-10,1.568E-10
<ATMOSPHERE-LAYER-61>2.299E+0,2.163E+2,1.090E+2,0.000E+0,0.000E+0,1.930E-44,1.000E-2,1.810E-3,3.749E-4,1.163E-7,3.611E-7,2.752E-10,1.568E-10
<ATMOSPHERE-LAYER-62>2.214E+0,2.138E+2,1.103E+2,0.000E+0,0.000E+0,2.159E-38,1.000E-2,1.810E-3,3.749E-4,8.736E-8,3.611E-7,2.752E-10,1.568E-10
<ATMOSPHERE-LAYER-63>2.131E+0,2.112E+2,1.115E+2,0.000E+0,0.000E+0,4.807E-33,1.000E-2,1.810E-3,3.749E-4,6.501E-8,3.611E-7,2.752E-10,1.568E-10
<ATMOSPHERE-LAYER-64>2.052E+0,2.086E+2,1.128E+2,0.000E+0,0.000E+0,2.446E-28,1.000E-2,1.810E-3,3.749E-4,4.791E-8,3.611E-7,2.752E-10,1.568E-10
<ATMOSPHERE-LAYER-65>1.976E+0,2.061E+2,1.140E+2,0.000E+0,0.000E+0,3.241E-24,1.000E-2,1.810E-3,3.749E-4,3.535E-8,3.611E-7,2.752E-10,1.568E-10
<ATMOSPHERE-LAYER-66>1.902E+0,2.038E+2,1.152E+2,0.000E+0,1.116E-311,1.259E-20,1.000E-2,1.810E-3,3.749E-4,2.642E-8,3.611E-7,2.752E-10,1.568E-10
<ATMOSPHERE-LAYER-67>1.831E+0,2.015E+2,1.164E+2,0.000E+0,1.081E-276,1.601E-17,1.000E-2,1.810E-3,3.749E-4,1.958E-8,3.611E-7,2.752E-10,1.568E-10
<ATMOSPHERE-LAYER-68>1.763E+0,1.991E+2,1.175E+2,0.000E+0,5.158E-245,7.369E-15,1.000E-2,1.810E-3,3.749E-4,1.437E-8,3.611E-7,2.752E-10,1.568E-10
<ATMOSPHERE-LAYER-69>1.698E+0,1.968E+2,1.187E+2,0.000E+0,2.241E-216,1.346E-12,1.000E-2,1.810E-3,3.749E-4,1.044E-8,3.611E-7,2.752E-10,1.568E-10
<ATMOSPHERE-LAYER-70>1.634E+0,1.945E+2,1.199E+2,0.000E+0,1.581E-190,1.063E-10,1.000E-2,1.810E-3,3.749E-4,7.509E-9,3.611E-7,2.752E-10,1.568E-10
<ATMOSPHERE-LAYER-71>1.574E+0,1.922E+2,1.210E+2,0.000E+0,3.073E-167,3.924E-9,1.000E-2,1.810E-3,3.749E-4,5.357E-9,3.611E-7,2.752E-10,1.568E-10
<ATMOSPHERE-LAYER-72>1.515E+0,1.900E+2,1.221E+2,0.000E+0,2.686E-146,7.285E-8,1.000E-2,1.810E-3,3.749E-4,3.857E-9,3.611E-7,2.752E-10,1.568E-10
```

```
<ATMOSPHERE-LAYER-73>1.459E+0,1.878E+2,1.232E+2,0.000E+0,1.651E-127,7.259E-7,1.000E-2,1.810E-3,3.749E-4,2.748E-9,3.611E-7,2.752E-10,1.568E-10
<ATMOSPHERE-LAYER-74>1.404E+0,1.856E+2,1.243E+2,0.000E+0,1.079E-110,4.125E-6,1.000E-2,1.810E-3,3.749E-4,1.936E-9,3.611E-7,2.752E-10,1.568E-10
<ATMOSPHERE-LAYER-75>1.352E+0,1.834E+2,1.254E+2,0.000E+0,1.104E-95,1.414E-5,1.000E-2,1.810E-3,3.749E-4,1.350E-9,3.611E-7,2.752E-10,1.568E-10
<ATMOSPHERE-LAYER-76>1.302E+0,1.812E+2,1.265E+2,0.000E+0,2.505E-82,3.075E-5,1.000E-2,1.810E-3,3.749E-4,9.295E-10,3.611E-7,2.752E-10,1.568E-10
<ATMOSPHERE-LAYER-77>1.253E+0,1.790E+2,1.275E+2,0.000E+0,1.765E-70,4.448E-5,1.000E-2,1.810E-3,3.749E-4,6.323E-10,3.611E-7,2.752E-10,1.568E-10
<ATMOSPHERE-LAYER-78>1.207E+0,1.768E+2,1.286E+2,0.000E+0,5.158E-60,4.468E-5,1.000E-2,1.810E-3,3.749E-4,4.276E-10,3.611E-7,2.752E-10,1.568E-10
<ATMOSPHERE-LAYER-79>1.162E+0,1.746E+2,1.296E+2,0.000E+0,8.252E-51,3.241E-5,1.000E-2,1.810E-3,3.749E-4,2.855E-10,3.611E-7,2.752E-10,1.568E-10
<ATMOSPHERE-LAYER-80>1.119E+0,1.725E+2,1.306E+2,0.000E+0,9.390E-43,1.759E-5,1.000E-2,1.810E-3,3.749E-4,1.881E-10,3.611E-7,2.752E-10,1.568E-10
<ATMOSPHERE-LAYER-81>1.077E+0,1.703E+2,1.316E+2,0.000E+0,9.518E-36,7.389E-6,1.000E-2,1.810E-3,3.749E-4,1.222E-10,3.611E-7,2.752E-10,1.568E-10
<ATMOSPHERE-LAYER-82>1.037E+0,1.682E+2,1.326E+2,0.000E+0,1.075E-29,2.473E-6,1.000E-2,1.810E-3,3.179E-4,7.817E-11,3.611E-7,2.752E-10,1.568E-10
<ATMOSPHERE-LAYER-83>9.984E-1,1.660E+2,1.336E+2,0.000E+0,1.640E-24,6.781E-7,1.000E-2,1.810E-3,2.470E-4,4.936E-11,3.593E-7,2.739E-10,1.560E-10
<ATMOSPHERE-LAYER-84>9.612E-1,1.640E+2,1.346E+2,0.000E+0,4.075E-20,1.564E-7,1.000E-2,1.810E-3,1.959E-4,3.218E-11,3.207E-7,2.444E-10,1.393E-10
<ATMOSPHERE-LAYER-85>9.254E-1,1.621E+2,1.355E+2,0.000E+0,1.947E-16,3.099E-8,1.000E-2,1.810E-3,1.543E-4,2.069E-11,2.862E-7,2.181E-10,1.243E-10
<ATMOSPHERE-LAYER-86>8.910E-1,1.601E+2,1.365E+2,0.000E+0,2.086E-13,5.388E-9,1.000E-2,1.810E-3,1.207E-4,1.310E-11,2.554E-7,1.947E-10,1.109E-10
<ATMOSPHERE-LAYER-87>8.579E-1,1.582E+2,1.374E+2,0.000E+0,5.781E-11,8.375E-10,1.000E-2,1.810E-3,9.380E-5,8.177E-12,2.279E-7,1.737E-10,9.899E-11
<ATMOSPHERE-LAYER-88>8.259E-1,1.562E+2,1.383E+2,0.000E+0,4.717E-9,1.184E-10,1.000E-2,1.810E-3,7.235E-5,5.020E-12,2.034E-7,1.551E-10,8.834E-11
<ATMOSPHERE-LAYER-89>7.952E-1,1.543E+2,1.392E+2,0.000E+0,1.277E-7,1.547E-11,1.000E-2,1.810E-3,5.539E-5,3.031E-12,1.816E-7,1.384E-10,7.885E-11
<ATMOSPHERE-LAYER-90>7.656E-1,1.525E+2,1.401E+2,0.000E+0,1.282E-6,1.895E-12,1.000E-2,1.810E-3,4.331E-5,1.894E-12,1.620E-7,1.235E-10,7.037E-11
<ATMOSPHERE-LAYER-91>7.371E-1,1.507E+2,1.410E+2,0.000E+0,5.272E-6,2.203E-13,1.000E-2,1.810E-3,3.367E-5,1.168E-12,1.446E-7,1.102E-10,6.280E-11
```

```
<ATMOSPHERE-LAYER-92>7.097E-1,1.490E+2,1.419E+2,0.000E+0,9.736E-6,2.460E-14,1.000E-2,1.810E-3,2.600E-5,7.089E-13,1.291E-7,9.837E-11,5.605E-11
<ATMOSPHERE-LAYER-93>6.833E-1,1.472E+2,1.428E+2,0.000E+0,8.786E-6,2.663E-15,1.000E-2,1.810E-3,1.993E-5,4.231E-13,1.152E-7,8.780E-11,5.002E-11
<ATMOSPHERE-LAYER-94>6.579E-1,1.454E+2,1.436E+2,0.000E+0,4.186E-6,2.824E-16,1.000E-2,1.810E-3,1.516E-5,2.483E-13,1.028E-7,7.835E-11,4.464E-11
<ATMOSPHERE-LAYER-95>6.334E-1,1.436E+2,1.445E+2,0.000E+0,1.130E-6,2.956E-17,1.000E-2,1.810E-3,1.145E-5,1.431E-13,9.174E-8,6.993E-11,3.984E-11
<ATMOSPHERE-LAYER-96>6.098E-1,1.421E+2,1.453E+2,2.606E-8,1.848E-7,3.084E-18,1.000E-2,1.810E-3,8.949E-6,8.757E-14,8.188E-8,6.241E-11,3.556E-11
<ATMOSPHERE-LAYER-97>5.871E-1,1.406E+2,1.462E+2,2.096E-7,1.938E-8,3.223E-19,1.000E-2,1.810E-3,6.997E-6,5.346E-14,7.307E-8,5.570E-11,3.173E-11
<ATMOSPHERE-LAYER-98>5.653E-1,1.391E+2,1.470E+2,3.843E-7,1.376E-9,3.395E-20,1.000E-2,1.810E-3,5.439E-6,3.217E-14,6.522E-8,4.971E-11,2.832E-11
<ATMOSPHERE-LAYER-99>5.442E-1,1.376E+2,1.478E+2,4.442E-7,6.945E-11,3.623E-21,1.000E-2,1.810E-3,4.200E-6,1.905E-14,5.820E-8,4.436E-11,2.528E-11
<ATMOSPHERE-LAYER-100>5.240E-1,1.361E+2,1.486E+2,4.564E-7,2.608E-12,3.936E-22,1.000E-2,1.810E-3,3.222E-6,1.110E-14,5.194E-8,3.959E-11,2.256E-11
<ATMOSPHERE-LAYER-101>5.045E-1,1.346E+2,1.494E+2,4.688E-7,7.583E-14,4.371E-23,1.000E-2,1.810E-3,2.455E-6,6.358E-15,4.636E-8,3.534E-11,2.013E-11
<ATMOSPHERE-LAYER-102>4.857E-1,1.334E+2,1.502E+2,4.828E-7,1.778E-15,4.993E-24,1.000E-2,1.810E-3,2.008E-6,4.162E-15,4.137E-8,3.154E-11,1.797E-11
<ATMOSPHERE-LAYER-103>4.676E-1,1.324E+2,1.510E+2,4.974E-7,3.468E-17,5.875E-25,1.000E-2,1.810E-3,1.664E-6,2.787E-15,3.693E-8,2.815E-11,1.604E-11
<ATMOSPHERE-LAYER-104>4.502E-1,1.313E+2,1.517E+2,5.125E-7,5.802E-19,7.135E-26,1.000E-2,1.810E-3,1.373E-6,1.849E-15,3.295E-8,2.512E-11,1.431E-11
<ATMOSPHERE-LAYER-105>4.335E-1,1.302E+2,1.525E+2,5.280E-7,8.555E-21,8.965E-27,1.000E-2,1.810E-3,1.130E-6,1.215E-15,2.941E-8,2.242E-11,1.277E-11
<ATMOSPHERE-LAYER-106>4.174E-1,1.292E+2,1.533E+2,5.440E-7,1.140E-22,1.168E-27,1.000E-2,1.810E-3,9.254E-7,7.901E-16,2.625E-8,2.001E-11,1.140E-11
<ATMOSPHERE-LAYER-107>4.018E-1,1.281E+2,1.540E+2,5.603E-7,1.406E-24,1.580E-28,1.000E-2,1.810E-3,7.552E-7,5.087E-16,2.343E-8,1.786E-11,1.017E-11
<ATMOSPHERE-LAYER-108>3.869E-1,1.274E+2,1.548E+2,5.786E-7,1.639E-26,2.230E-29,1.000E-2,1.810E-3,6.594E-7,3.739E-16,2.091E-8,1.594E-11,9.079E-12
<ATMOSPHERE-LAYER-109>3.725E-1,1.267E+2,1.555E+2,5.979E-7,1.839E-28,3.278E-30,1.000E-2,1.810E-3,5.882E-7,2.864E-16,1.866E-8,1.422E-11,8.103E-12
<ATMOSPHERE-LAYER-110>3.586E-1,1.261E+2,1.563E+2,6.178E-7,2.016E-30,5.023E-31,1.000E-2,1.810E-3,5.240E-7,2.186E-16,1.665E-8,1.269E-11,7.232E-12
```

```
<ATMOSPHERE-LAYER-111>3.453E-1,1.254E+2,1.570E+2,6.383E-7,2.193E-32,8.029E-32,1.000E-2,1.810E-3,4.659E-7,1.660E-16,1.486E-8,1.133E-11,6.454E-12
<ATMOSPHERE-LAYER-112>3.324E-1,1.248E+2,1.577E+2,6.595E-7,2.397E-34,1.339E-32,1.000E-2,1.810E-3,4.137E-7,1.256E-16,1.326E-8,1.011E-11,5.760E-12
<ATMOSPHERE-LAYER-113>3.201E-1,1.241E+2,1.585E+2,6.815E-7,2.665E-36,2.332E-33,1.000E-2,1.810E-3,3.666E-7,9.459E-17,1.184E-8,9.023E-12,5.141E-12
<ATMOSPHERE-LAYER-114>3.081E-1,1.235E+2,1.592E+2,7.046E-7,3.048E-38,4.245E-34,1.000E-2,1.810E-3,3.318E-7,7.425E-17,1.056E-8,8.053E-12,4.588E-12
<ATMOSPHERE-LAYER-115>2.967E-1,1.230E+2,1.599E+2,7.288E-7,3.617E-40,8.070E-35,1.000E-2,1.810E-3,3.033E-7,5.939E-17,9.429E-9,7.187E-12,4.095E-12
<ATMOSPHERE-LAYER-116>2.856E-1,1.225E+2,1.606E+2,7.537E-7,4.492E-42,1.602E-35,1.000E-2,1.810E-3,2.769E-7,4.737E-17,8.415E-9,6.414E-12,3.654E-12
<ATMOSPHERE-LAYER-117>2.750E-1,1.220E+2,1.614E+2,7.796E-7,5.874E-44,3.321E-36,1.000E-2,1.810E-3,2.525E-7,3.766E-17,7.510E-9,5.724E-12,3.261E-12
<ATMOSPHERE-LAYER-118>2.648E-1,1.215E+2,1.621E+2,8.063E-7,8.145E-46,7.186E-37,1.000E-2,1.810E-3,2.299E-7,2.984E-17,6.702E-9,5.109E-12,2.911E-12
<ATMOSPHERE-LAYER-119>2.549E-1,1.210E+2,1.628E+2,8.310E-7,1.204E-47,1.622E-37,1.000E-2,1.810E-3,2.092E-7,2.358E-17,5.982E-9,4.559E-12,2.598E-12
<ATMOSPHERE-LAYER-120>2.454E-1,1.205E+2,1.635E+2,8.261E-7,1.906E-49,3.821E-38,1.000E-2,1.810E-3,1.931E-7,1.918E-17,5.339E-9,4.069E-12,2.318E-12
<ATMOSPHERE-LAYER-121>2.363E-1,1.201E+2,1.642E+2,7.645E-7,3.246E-51,9.385E-39,1.000E-2,1.810E-3,1.799E-7,1.590E-17,4.764E-9,3.632E-12,2.069E-12
<ATMOSPHERE-LAYER-122>2.275E-1,1.197E+2,1.649E+2,6.559E-7,5.963E-53,2.402E-39,1.000E-2,1.810E-3,1.675E-7,1.316E-17,4.252E-9,3.241E-12,1.847E-12
<ATMOSPHERE-LAYER-123>2.190E-1,1.192E+2,1.656E+2,5.198E-7,1.185E-54,6.400E-40,1.000E-2,1.810E-3,1.559E-7,1.086E-17,3.795E-9,2.893E-12,1.648E-12
<ATMOSPHERE-LAYER-124>2.109E-1,1.188E+2,1.663E+2,3.693E-7,2.555E-56,1.774E-40,1.000E-2,1.810E-3,1.449E-7,8.945E-18,3.387E-9,2.582E-12,1.471E-12
<ATMOSPHERE-LAYER-125>2.031E-1,1.184E+2,1.670E+2,2.166E-7,5.983E-58,5.116E-41,1.000E-2,1.810E-3,1.346E-7,7.354E-18,3.023E-9,2.304E-12,1.313E-12
<ATMOSPHERE-LAYER-126>1.955E-1,1.181E+2,1.677E+2,8.621E-8,1.524E-59,1.533E-41,1.000E-2,1.810E-3,1.270E-7,6.237E-18,2.698E-9,2.056E-12,1.172E-12
<ATMOSPHERE-LAYER-127>1.882E-1,1.177E+2,1.684E+2,1.350E-8,4.231E-61,4.773E-42,1.000E-2,1.810E-3,1.209E-7,5.394E-18,2.408E-9,1.835E-12,1.046E-12
<ATMOSPHERE-LAYER-128>1.812E-1,1.174E+2,1.691E+2,7.335E-11,1.280E-62,1.541E-42,1.000E-2,1.810E-3,1.151E-7,4.662E-18,2.149E-9,1.638E-12,9.331E-13
<ATMOSPHERE-LAYER-129>1.745E-1,1.171E+2,1.698E+2,0.000E+0,4.219E-64,5.161E-43,1.000E-2,1.810E-3,1.096E-7,4.023E-18,1.918E-9,1.462E-12,8.328E-13
```

```
<ATMOSPHERE-LAYER-130>1.680E-1,1.168E+2,1.705E+2,0.000E+0,1.516E-65,1.789E-43,1.000E-2,1.810E-3,1.042E-7,3.467E-18,1.711E-9,1.305E-12,7.432E-13
<ATMOSPHERE-LAYER-131>1.617E-1,1.165E+2,1.712E+2,0.000E+0,5.939E-67,6.423E-44,1.000E-2,1.810E-3,9.906E-8,2.984E-18,1.527E-9,1.164E-12,6.633E-13
<ATMOSPHERE-LAYER-132>1.557E-1,1.162E+2,1.718E+2,0.000E+0,2.536E-68,2.385E-44,1.000E-2,1.810E-3,9.478E-8,2.603E-18,1.363E-9,1.039E-12,5.920E-13
<ATMOSPHERE-LAYER-133>1.499E-1,1.159E+2,1.725E+2,0.000E+0,1.179E-69,9.151E-45,1.000E-2,1.810E-3,9.165E-8,2.321E-18,1.217E-9,9.273E-13,5.283E-13
<ATMOSPHERE-LAYER-134>1.443E-1,1.156E+2,1.732E+2,0.000E+0,5.967E-71,3.625E-45,1.000E-2,1.810E-3,8.859E-8,2.068E-18,1.086E-9,8.276E-13,4.715E-13
<ATMOSPHERE-LAYER-135>1.390E-1,1.154E+2,1.739E+2,0.000E+0,3.283E-72,1.482E-45,1.000E-2,1.810E-3,8.561E-8,1.840E-18,9.690E-10,7.386E-13,4.208E-13
<ATMOSPHERE-LAYER-136>1.338E-1,1.151E+2,1.746E+2,0.000E+0,1.962E-73,6.242E-46,1.000E-2,1.810E-3,8.272E-8,1.637E-18,8.648E-10,6.592E-13,3.756E-13
<ATMOSPHERE-LAYER-137>1.288E-1,1.149E+2,1.752E+2,0.000E+0,1.272E-74,2.708E-46,1.000E-2,1.810E-3,7.989E-8,1.455E-18,7.718E-10,5.883E-13,3.352E-13
<ATMOSPHERE-LAYER-138>1.240E-1,1.146E+2,1.759E+2,0.000E+0,8.941E-76,1.209E-46,1.000E-2,1.810E-3,7.730E-8,1.297E-18,6.888E-10,5.250E-13,2.991E-13
<ATMOSPHERE-LAYER-139>1.194E-1,1.144E+2,1.766E+2,0.000E+0,6.800E-77,5.554E-47,1.000E-2,1.810E-3,7.544E-8,1.178E-18,6.148E-10,4.686E-13,2.670E-13
<ATMOSPHERE-LAYER-140>1.150E-1,1.142E+2,1.773E+2,0.000E+0,5.590E-78,2.621E-47,1.000E-2,1.810E-3,7.359E-8,1.069E-18,5.487E-10,4.182E-13,2.383E-13
<ATMOSPHERE-LAYER-141>1.107E-1,1.140E+2,1.779E+2,0.000E+0,4.957E-79,1.270E-47,1.000E-2,1.810E-3,7.179E-8,9.696E-19,4.897E-10,3.732E-13,2.126E-13
<ATMOSPHERE-LAYER-142>1.066E-1,1.138E+2,1.786E+2,0.000E+0,4.736E-80,6.311E-48,1.000E-2,1.810E-3,7.000E-8,8.783E-19,4.370E-10,3.331E-13,1.898E-13
<ATMOSPHERE-LAYER-143>1.026E-1,1.135E+2,1.793E+2,0.000E+0,4.867E-81,3.215E-48,1.000E-2,1.810E-3,6.825E-8,7.956E-19,3.900E-10,2.973E-13,1.694E-13
<ATMOSPHERE-LAYER-144>9.879E-2,1.135E+2,1.799E+2,0.000E+0,5.382E-82,1.680E-48,1.000E-2,1.810E-3,0.000E+0,0.000E+0,0.000E+0,0.000E+0,0.000E+0
<ATMOSPHERE-LAYER-145>9.511E-2,1.136E+2,1.806E+2,0.000E+0,6.395E-83,9.008E-49,1.000E-2,1.810E-3,0.000E+0,0.000E+0,0.000E+0,0.000E+0,0.000E+0
<ATMOSPHERE-LAYER-146>9.157E-2,1.138E+2,1.813E+2,0.000E+0,8.136E-84,4.940E-49,1.000E-2,1.810E-3,0.000E+0,0.000E+0,0.000E+0,0.000E+0,0.000E+0
<ATMOSPHERE-LAYER-147>8.816E-2,1.140E+2,1.819E+2,0.000E+0,1.106E-84,2.769E-49,1.000E-2,1.810E-3,0.000E+0,0.000E+0,0.000E+0,0.000E+0,0.000E+0
<ATMOSPHERE-LAYER-148>8.488E-2,1.142E+2,1.826E+2,0.000E+0,1.605E-85,1.586E-49,1.000E-2,1.810E-3,0.000E+0,0.000E+0,0.000E+0,0.000E+0,0.000E+0
```

```
<ATMOSPHERE-LAYER-149>8.172E-2,1.144E+2,1.833E+2,0.000E+0,2.482E-86,9.268E-50,1.000E-2,1.810E-3,0.000E+0,0.000E+0,0.000E+0,0.000E+0,0.000E+0
<ATMOSPHERE-LAYER-150>7.868E-2,1.146E+2,1.839E+2,0.000E+0,4.646E-88,5.432E-50,1.000E-2,1.810E-3,0.000E+0,0.000E+0,0.000E+0,0.000E+0,0.000E+0
<ATMOSPHERE-LAYER-151>0.075756,115.072,184.625,0.0,7.150598842816971e-88,3.3701921671968427e-50,0.01,0.00181,0.0,0.0,0.0,0.0,0.0
<ATMOSPHERE-LAYER-152>0.0729371,115.531,185.303,0.0,1.3272211502204933e-88,2.0925908120027597e-50,0.01,0.00181,0.0,0.0,0.0,0.0,0.0
<ATMOSPHERE-LAYER-153>0.070223,115.99,185.983,0.0,2.6074877901430842e-89,1.323004207267378e-50,0.01,0.00181,0.0,0.0,0.0,0.0,0.0
<ATMOSPHERE-LAYER-154>0.06761,116.449,186.667,0.0,5.414340474930114e-90,8.512277576309743e-51,0.01,0.00181,0.0,0.0,0.0,0.0,0.0
<ATMOSPHERE-LAYER-155>0.0650942,116.907,187.353,0.0,1.1862985780010367e-90,5.57026431731841e-51,0.01,0.00181,0.0,0.0,0.0,0.0,0.0
<ATMOSPHERE-LAYER-156>0.06267199999999999,117.367,188.042,0.0,2.7385121157727186e-91,3.7052926926142446e-51,0.01,0.00181,0.0,0.0,0.0,0.0,0.0
<ATMOSPHERE-LAYER-157>0.0603399,117.83,188.733,0.0,6.650406920263065e-92,2.5041114092390167e-51,0.01,0.00181,0.0,0.0,0.0,0.0,0.0
<ATMOSPHERE-LAYER-158>0.058094700000000006,118.293,189.428,0.0,1.6965894282495115e-92,1.718467145592195e-51,0.01,0.00181,0.0,0.0,0.0,0.0,0.0
<ATMOSPHERE-LAYER-159>0.055932899999999994,118.757,190.125,0.0,4.539375822388015e-93,1.1968709494561571e-51,0.01,0.00181,0.0,0.0,0.0,0.0,0.0
<ATMOSPHERE-LAYER-160>0.0538516,119.22,190.825,0.0,1.2721271610985714e-93,8.455993491576343e-52,0.01,0.00181,0.0,0.0,0.0,0.0,0.0
<ATMOSPHERE-LAYER-161>0.0518478,119.684,191.527,0.0,3.728842353036104e-94,6.057464750854465e-52,0.01,0.00181,0.0,0.0,0.0,0.0,0.0
<ATMOSPHERE-LAYER-162>0.049918500000000005,120.157,192.23200000000003,0.0,1.1416296854825002e-94,4.39788052102919e-52,0.01,0.00181,0.0,0.0,0.0,0.0,0.0
<ATMOSPHERE-LAYER-163>0.048061,120.717,192.941,0.0,3.648368915939196e-95,3.2367649288747142e-52,0.01,0.00181,0.0,0.0,0.0,0.0,0.0
<ATMOSPHERE-LAYER-164>0.0462726,121.278,193.653,0.0,1.2145129736108621e-95,2.4120644121120177e-52,0.01,0.00181,0.0,0.0,0.0,0.0,0.0
<ATMOSPHERE-LAYER-165>0.0445508,121.838,194.368,0.0,4.2061866062832565e-96,1.81923836645158e-52,0.01,0.00181,0.0,0.0,0.0,0.0,0.0
<ATMOSPHERE-LAYER-166>0.042893,122.398,195.086,0.0,1.5135004893237078e-96,1.388124913170308e-52,0.01,0.00181,0.0,0.0,0.0,0.0,0.0
<ATMOSPHERE-LAYER-167>0.041297,122.958,195.807,0.0,5.651992711285492e-97,1.0711373351912632e-52,0.01,0.00181,0.0,0.0,0.0,0.0,0.0
```

```
<ATMOSPHERE-LAYER-168>0.0397603,123.519,196.532,0.0,2.1876373322275692e-97,8.355258150349008e-53,0.01,0.00181,0.0,0.0,0.0,0.0,0.0
<ATMOSPHERE-LAYER-169>0.0382808,124.094,197.261,0.0,8.767454863674623e-98,6.586625546028239e-53,0.01,0.00181,0.0,0.0,0.0,0.0,0.0
<ATMOSPHERE-LAYER-170>0.036856299999999995,124.67,197.992,0.0,3.633614401125237e-98,5.245000012270294e-53,0.01,0.00181,0.0,0.0,0.0,0.0,0.0
<ATMOSPHERE-LAYER-171>0.0354849,125.245,198.72700000000003,0.0,1.5556994304534405e-98,4.2175295447736715e-53,0.01,0.00181,0.0,0.0,0.0,0.0,0.0
<ATMOSPHERE-CONTINUUM>Refraction,Layering
<ATMOSPHERE-ATYPE>miev_T5_USER,cloud2_T5_USER,Simple_GSFC
<ATMOSPHERE-GAS>gastly,CH4,NH3,H2O,PH3,arsine,germane
<ATMOSPHERE-TYPE>gastly_T3_USER,HIT[6],HIT[11],HIT[1],HIT[28],arsine_T3_USER,germane_T3_USER
<ATMOSPHERE-ABUN>100,1,1,1,1,1,1,1
<ATMOSPHERE-UNIT>scl,scl,scl,scl,scl,scl,scl
<ATMOSPHERE-TAU>0.07,0.07,0.07,0.07,0.07,0.07,0.07
<SURFACE-TEMPERATURE>416.784
<SURFACE-ALBEDO>00
<SURFACE-EMISSIVITY>1.000
<SURFACE-GAS-RATIO>1.0000
<SURFACE-NSURF>0
<SURFACE-GAS-UNIT>ratio
<SURFACE-MODEL>Lambert
<SURFACE-PHASEMODEL>ISO
<GENERATOR-BEAM>2.5
<GENERATOR-BEAM-UNIT>mrad
<GENERATOR-GAS-MODEL>Y
<GENERATOR-CONT-MODEL>Y
<GENERATOR-RANGE1>1950
<GENERATOR-RANGE2>5050
<GENERATOR-RANGEUNIT>nm
<GENERATOR-RESOLUTION>900
<GENERATOR-RESOLUTIONUNIT>RP
<GENERATOR-RADUNITS>Wsrm2um
<GENERATOR-DIAMTELE>6.5
<GENERATOR-LOGRAD>N
<GENERATOR-CONT-STELLAR>Y
<GENERATOR-TRANS-APPLY>N
<GENERATOR-TRANS-SHOW>N
<GENERATOR-TRANS>02-01
<GENERATOR-NOISE>NO
<GENERATOR-NOISE2>1
<GENERATOR-NOISETIME>0.2
<GENERATOR-NOISEOTEMP>300
<GENERATOR-NOISEOEFF>1
<GENERATOR-NOISEOEMIS>1
<GENERATOR-NOISEFRAMES>40
<GENERATOR-NOISEPIXELS>1
<GENERATOR-NOISE1>1
<GENERATOR-TELESCOPE>SINGLE
<GENERATOR-TELESCOPE1>1
<GENERATOR-TELESCOPE2>0.0
<GENERATOR-TELESCOPE3>1.0
```

```
<GENERATOR-INSTRUMENT>user
<GENERATOR-RESOLUTIONKERNEL>N
<RETRIEVAL-FLUXLABELS>Data,Noise,Model
<RETRIEVAL-GAMMA>1.0
<RETRIEVAL-RESOLUTION>100
<RETRIEVAL-RESOLUTIONUNIT>RP
<RETRIEVAL-FLUXSCALER>1.0
<RETRIEVAL-FITTELLURIC>N
<RETRIEVAL-FITGAIN>-1
<RETRIEVAL-FITGAIN-PHOTOMETRIC>Y
<RETRIEVAL-REMOVEOFFSET>-1
<RETRIEVAL-REMOVEFRINGE>0
<RETRIEVAL-FITSTELLAR>N
<RETRIEVAL-FITFREQ>N
<RETRIEVAL-FITRESOLUTION>N
<RETRIEVAL-NVARS>1
<RETRIEVAL-VARIABLES>AEROSOL-Haze
<RETRIEVAL-VALUES>1.7621e-01
<RETRIEVAL-MIN>0
<RETRIEVAL-MAX>1
<RETRIEVAL-UNITS>scl
<RETRIEVAL-STATUS>OK
<RETRIEVAL-SIGMAS>1.4956e-03
<OBJECT-STAR-LONGITUDE>0.00
<OBJECT-STAR-LATITUDE>0.00
<SURFACE-MIXING>
<SURFACE-SURF>
<SURFACE-TYPE>
<SURFACE-ABUN>
<SURFACE-UNIT>
<SURFACE-THICK>
</SPEC>
```

So if you care to find me
Look to the western sky
As someone told me lately
"Everyone deserves the chance to fly"
And if I'm flying solo
At least I'm flying free
To those who'd ground me
Take a message back from me
Tell them how I am defying gravity
I'm flying high, defying gravity
And soon I'll match them in renown

- Stephen Schwartz, author of the musical "Wicked: The Untold Story of the Witches of Oz"

Bibliography

ALMA Partnership et al., 2015, *The 2014 ALMA Long Baseline Campaign: First Results from High Angular Resolution Observations toward the HL Tau Region*, ApJL, 808, L3

Abel M., Frommhold L., Li X., Hunt K. L. C., 2011, *Collision-Induced Absorption by H2 Pairs: From Hundreds to Thousands of Kelvin*, Journal of Physical Chemistry A, 115, 6805

Abel M., Frommhold L., Li X., Hunt K. L. C., 2012, *Infrared absorption by collisional H_2-He complexes at temperatures up to 9000 K and frequencies from 0 to 20 000 cm^{-1}*, JCP, 136, 044319

Achterberg R. K., Conrath B. J., Gierasch P. J., 2006, *Cassini CIRS retrievals of ammonia in Jupiter's upper troposphere*, Icarus, 182, 169

Ackerman A. S., Marley M. S., 2001, *Precipitating Condensation Clouds in Substellar Atmospheres*, apj, 556, 872

Adriani A., et al., 2017, *JIRAM, the Jovian Infrared Auroral Mapper*, SSR, 213, 393

Adriani A., et al., 2018, *Clusters of cyclones encircling Jupiter's poles*, Nat, 555, 216

Adriani A., et al., 2020, *Two-Year Observations of the Jupiter Polar Regions by JIRAM on Board Juno*, Journal of Geophysical Research (Planets), 125, e06098

Andrews D. G., 2000, *An Introduction to Atmospheric Physics*

Andrews D. G., Holton J. R., Leovy C. B., 1987, *Middle atmosphere dynamics.*

Anguiano-Arteaga A., Pérez-Hoyos S., Sánchez-Lavega A., Sanz-Requena J. F., Irwin P. G. J., 2021, *Vertical Distribution of Aerosols and Hazes Over Jupiter's Great Red Spot and Its Surroundings in 2016 From HST/WFC3 Imaging*, Journal of Geophysical Research (Planets), 126, e06996

Anguiano-Arteaga A., Pérez-Hoyos S., Sánchez-Lavega A., Sanz-Requena J. F., Irwin P. G. J., 2023, *Temporal Variations in Vertical Cloud Structure of Jupiter's Great Red Spot, Its Surroundings and Oval BA From HST/WFC3 Imaging*, Journal of Geophysical Research (Planets), 128, e2022JE007427

Ardévol Martínez F., Min M., Huppenkothen D., Kamp I., Palmer P. I., 2024, *FlopPITy: Enabling self-consistent exoplanet atmospheric retrievals with machine learning*, aap, 681, L14

Armstrong B., 1967, *Spectrum line profiles: The Voigt function*, JQSRT, 7, 61

Atreya S. K., 1986, *Atmospheres and ionospheres of the outer planets and their satellites*, doi:10.1007/978-3-642-71394-1.

Atreya S. K., 2010, *The significance of trace constituents in the solar system*, Faraday Discussions, 147, 9

Atreya S. K., Wong A.-S., 2005, *Coupled Clouds and Chemistry of the Giant Planets— A Case for Multiprobes*, SSR, 116, 121

Atreya S. K., Wong M. H., Owen T. C., Mahaffy P. R., Niemann H. B., de Pater I., Drossart P., Encrenaz T., 1999, *A comparison of the atmospheres of Jupiter and Saturn: deep atmospheric composition, cloud structure, vertical mixing, and origin*, planss, 47, 1243

Atreya S. K., Mahaffy P. R., Niemann H. B., Wong M. H., Owen T. C., 2003, *Composition and origin of the atmosphere of Jupiter - an update, and implications for the extrasolar giant planets*, PLANSS, 51, 105

Baines K. H., Carlson R. W., Kamp L. W., 2002, *Fresh Ammonia Ice Clouds in Jupiter. I. Spectroscopic Identification, Spatial Distribution, and Dynamical Implications*, Icarus, 159, 74

Baines K. H., et al., 2007, *Polar Lightning and Decadal-Scale Cloud Variability on Jupiter*, Science, 318, 226

Baines K. H., Sromovsky L. A., Carlson R. W., Momary T. W., Fry P. M., 2019, *The visual spectrum of Jupiter's Great Red Spot accurately modeled with aerosols produced by photolyzed ammonia reacting with acetylene*, Icarus, 330, 217

Bandfield J. L., Hamilton V. E., Christensen P. R., 2000, *A Global View of Martian Surface Compositions from MGS-TES*, Science, 287, 1626

Banfield D., Dissly R., Mishchenko M., Muñoz O., Roos-Serote M., Stam D., Volten H., 2004, in Wilson A., ed., ESA Special Publication Vol. 544, Planetary Probe Atmospheric Entry and Descent Trajectory Analysis and Science. pp 287–294

Barnard E. E., 1885, *Changes in the length of the Great Red Spot on Jupiter*, The Observatory, 8, 244

Barstow J. K., 2020, *Unveiling cloudy exoplanets: the influence of cloud model choices on retrieval solutions*, MNRAS, 497, 4183

Batalha N. E., Marley M. S., Lewis N. K., Fortney J. J., 2019, *Exoplanet Reflected-light Spectroscopy with PICASO*, apj, 878, 70

Baumeister P., Padovan S., Tosi N., Montavon G., Nettelmann N., MacKenzie J., Godolt M., 2020, *Machine-learning Inference of the Interior Structure of Low-mass Exoplanets*, ApJ, 889, 42

Bayes M., Price M., 1763, *An Essay towards Solving a Problem in the Doctrine of Chances. By the Late Rev. Mr. Bayes, F. R. S. Communicated by Mr. Price, in a Letter to John Canton, A. M. F. R. S.*, Philosophical Transactions of the Royal Society of London Series I, 53, 370

Becker H. N., et al., 2020, *Small lightning flashes from shallow electrical storms on Jupiter*, Nature, 584, 55

Bell T. J., et al., 2024, *Nightside clouds and disequilibrium chemistry on the hot Jupiter WASP-43b*, Nature Astronomy, 8, 879

Biagiotti F., 2025, *astro-francy/chopper: chopper_v1.0, https://doi.org/10.5281/zenodo.15731420*, doi:10.5281/zenodo.15731420, https://doi.org/10.5281/zenodo.15731420

Biagiotti F., et al., 2024a, in European Geosciences Union General Assembly 2024 (EGU24). EGU General Assembly Conference Abstracts. p. 12950, doi:10.5194/egusphere-egu24-12950

Biagiotti F., et al., 2024b, in AGU Fall Meeting Abstracts. pp P51A–03

Biagiotti F., et al., 2025a, in EPSC-DPS Joint Meeting 2025. Helsinki, Finland, pp EPSC–DPS2025–1656, doi:10.5194/epsc-dps2025-1656, https://meetingorganizer.copernicus.org/EPSC-DPS2025/EPSC-DPS2025-1656.html

Biagiotti F., et al., 2025b, in EGU General Assembly 2025. Vienna, Austria, pp EGU25–17760, doi:10.5194/egusphere-egu25-17760, https://meetingorganizer.copernicus.org/EGU25/EGU25-17760.html

Biagiotti F., et al., 2025c, *Evidence of pure ammonia clouds in Jupiter's Northern Temperate domain from Juno/JIRAM infrared spectral data*, Monthly Notices of the Royal Astronomical Society, p. staf381

Biagiotti F., et al., 2025d, *Evidence of pure ammonia clouds in Jupiter's Northern Temperate domain from Juno/JIRAM infrared spectral data*, MNRAS, 538, 1535

Biagiotti F., et al., 2025e, *Machine learning spectral clustering techniques: Application to Jovian clouds from Juno/JIRAM and JWST/NIRSpec*, AA, 701, A247

Bjoraker G. L., Wong M. H., de Pater I., Ádámkovics M., 2015, *Jupiter's Deep Cloud Structure Revealed Using Keck Observations of Spectrally Resolved Line Shapes*, ApJ, 810, 122

Blum J., Wurm G., 2008, *The growth mechanisms of macroscopic bodies in protoplanetary disks.*, ARAA, 46, 21

Bohren C. F., Huffman D. R., 1983, *Absorption and scattering of light by small particles*

Bolton S. J., et al., 2017a, *The Juno Mission*, SSR, 213, 5

Bolton S. J., et al., 2017b, *Jupiter's interior and deep atmosphere: The initial pole-to-pole passes with the Juno spacecraft*, Science, 356, 821

Bolton S. J., et al., 2021, *Microwave observations reveal the deep extent and structure of Jupiter's atmospheric vortices*, Science, 374, 968

Borucki W. J., Levin Z., Whitten R. C., Keesee R. G., Capone L. A., Summers A. L., Toon O. B., Dubach J., 1987, *Predictions of the electrical conductivity and charging of the aerosols in Titan's atmosphere*, icarus, 72, 604

Borysow A., 2002, *Collision-induced absorption coefficients of H_2 pairs at temperatures from 60 K to 1000 K*, AA, 390, 779

Boss A. P., Keiser S. A., 2010, *Who Pulled the Trigger: A Supernova or An Asymptotic Giant Branch Star?*, ApJL, 717, L1

Bourda G., Capitaine N., 2004, *Precession, nutation, and space geodetic determination of the Earth's variable gravity field*, AandA, 428, 691

Braude A. S., Irwin P. G. J., Orton G. S., Fletcher L. N., 2020, *Colour and tropospheric cloud structure of Jupiter from MUSE/VLT: Retrieving a universal chromophore*, Icarus, 338, 113589

Brooke T. Y., Knacke R. F., Encrenaz T., Drossart P., Crisp D., Feuchtgruber H., 1998, *Models of the ISO 3-μm Reflection Spectrum of Jupiter*, Icarus, 136, 1

Brown R. H., et al., 2004, *The Cassini Visual And Infrared Mapping Spectrometer (Vims) Investigation*, SSR, 115, 111

Brown L. R., et al., 2013, *Methane line parameters in the HITRAN2012 database*, JQSRT, 130, 201

Brueshaber S. R., Sayanagi K. M., Dowling T. E., 2019, *Dynamical regimes of giant planet polar vortices*, Icarus, 323, 46

Brzycki B., et al., 2020, *Narrow-band Signal Localization for SETI on Noisy Synthetic Spectrogram Data*, pasp, 132, 114501

Campello R. J. G. B., Moulavi D., Sander J., 2013, in Pei J., Tseng V. S., Cao L., Motoda H., Xu G., eds, Advances in Knowledge Discovery and Data Mining. Springer Berlin Heidelberg, Berlin, Heidelberg, pp 160–172

Carissimo A., De Feis I., Serio C., 2005, *The physical retrieval methodology for IASI: the δ-IASI code*, Environmental Modelling and Software, 20, 1111

Carlson B. E., Lacis A. A., Rossow W. B., 1993, *Tropospheric gas composition and cloud structure of the Jovian North Equatorial Belt*, JGR, 98, 5251

Carlson R. W., Baines K. H., Anderson M. S., Filacchione G., Simon A. A., 2016a, *Chromophores from photolyzed ammonia reacting with acetylene: Application to Jupiter's Great Red Spot*, Icarus, 274, 106

Carlson R. W., Baines K. H., Anderson M. S., Filacchione G., Simon A. A., 2016b, *Chromophores from photolyzed ammonia reacting with acetylene: Application to Jupiter's Great Red Spot*, Icarus, 274, 106

Carter A. L., et al., 2024, *A benchmark JWST near-infrared spectrum for the exoplanet WASP-39 b*, Nature Astronomy, 8, 1008

Castagnoli C., et al., 2025, *Characterization and Sensitivity Analysis of JIRAM Spectra for Optimizing CH_4 and H3+ Retrieval*, PSJ, 6, 93

Chandrasekhar S., 1950, *Radiative Transfer*. Oxford University Press, Oxford

Chang X., et al., 2024, *Theoretical evidence of H-He demixing under Jupiter and Saturn conditions*, Nature Communications, 15, 8543

Charbonneau D., Brown T. M., Latham D. W., Mayor M., 2000, *Detection of Planetary Transits Across a Sun-like Star*, ApJL, 529, L45

Christensen U. R., 2002, *Zonal flow driven by strongly supercritical convection in rotating spherical shells*, Journal of Fluid Mechanics, 470, 115

Christensen P. R., et al., 2001, *Mars Global Surveyor Thermal Emission Spectrometer experiment: Investigation description and surface science results*, JGR, 106, 23823

Christensen P. R., et al., 2004, *The Thermal Emission Imaging System (THEMIS) for the Mars 2001 Odyssey Mission*, SSR, 110, 85

Clapp M. L., Miller R. E., 1996, *Complex Refractive Indices of Crystalline Hydrazine from Aerosol Extinction Spectra*, Icarus, 123, 396

Clough S. A., Kneizys F. X., Davies R. W., 1989, *Line shape and the water vapor continuum*, Atmospheric Research, 23, 229

Connerney J. E. P., et al., 2017, *The Juno Magnetic Field Investigation*, SSR, 213, 39

Coradini A., et al., 2007, *Virtis: An Imaging Spectrometer for the Rosetta Mission*, SSR, 128, 529

Cornish N. J., Littenberg T. B., 2007, *Tests of Bayesian model selection techniques for gravitational wave astronomy*, prd, 76, 083006

Coulter D. J., Barnes J. W., Fortney J. J., 2022, *Jupiter and Saturn as Spectral Analogs for Extrasolar Gas Giants and Brown Dwarfs*, ApJL, 263, 15

Czerny M., Turner A. F., 1930, *Über den Astigmatismus bei Spiegelspektrometern*, Zeitschrift fur Physik, 61, 792

Dahl E. K., et al., 2021, *Vertical Structure and Color of Jovian Latitudinal Cloud Bands during the Juno Era*, PSJ, 2, 16

Dahlback A., Stamnes K., 1991, *A new spherical model for computing the radiation field available for photolysis and heating at twilight*, planss, 39, 671

Dalgarno A., Williams D. A., 1962, *Rayleigh Scattering by Molecular Hydrogen.*, ApJ, 136, 690

Dirac P. A. M., 1927, *The Quantum Theory of the Emission and Absorption of Radiation*, Proceedings of the Royal Society of London Series A, 114, 243

Drossart P., et al., 1998, *The solar reflected component in Jupiter's 5-μm spectra from NIMS/Galileo observations*, JGR, 103, 23043

Dyudina U. A., Ingersoll A. P., Danielson G. E., Baines K. H., Carlson R. W., The Galileo NIMS SSI Teams 2001, *Interpretation of NIMS and SSI Images on the Jovian Cloud Structure*, Icarus, 150, 219

Einstein A., 1917, *Zur Quantentheorie der Strahlung*, Physikalische Zeitschrift, 18, 121

Eisberg R., Resnick R., 1985, *Quantum Physics of Atoms, Molecules, Solids, Nuclei, and Particles, 2nd Edition*

Ellis R. S., et al., 2017, *The Future of Multi-Object Spectroscopy: a ESO Working Group Report*, arXiv e-prints, p. arXiv:1701.01976

Encrenaz T., et al., 1996, *First results of ISO-SWS observations of Jupiter.*, AA, 315, L397

Enriquez J. E., et al., 2017, *The Breakthrough Listen Search for Intelligent Life: 1.1-1.9 GHz Observations of 692 Nearby Stars*, ApJ, 849, 104

Ester M., Kriegel H.-P., Sander J., Xu X., 1996, in Pfitzner D. W., Salmon J. K., eds, Second International Conference on Knowledge Discovery and Data Mining (KDD'96). Proceedings of a conference held August 2-4. pp 226–331

Evans K. F., 1998, *The Spherical Harmonics Discrete Ordinate Method for Three-Dimensional Atmospheric Radiative Transfer*, Journal of the Atmospheric Sciences, 55, 429

Fan E., 2000, *Extended tanh-function method and its applications to nonlinear equations*, Physics Letters A, 277, 212

Fegley Jr. B., Lodders K., 1994, *Chemical Models of the Deep Atmospheres of Jupiter and Saturn*, Icarus, 110, 117

Ferraro J. R., Sill G., Fink U., 1980, *Infrared Intensity Measurements of Cryodeposited Thin Films of NH_3, NH_4HS, H_2S, and Assignments of Absorption Bands*, Applied Spectroscopy, 34, 525

Flasar F. M., et al., 2004, *Exploring The Saturn System In The Thermal Infrared: The Composite Infrared Spectrometer*, SSR, 115, 169

Fletcher L. N., et al., 2010, *Thermal structure and composition of Jupiter's Great Red Spot from high-resolution thermal imaging*, Icarus, 208, 306

Fletcher L. N., Greathouse T. K., Orton G. S., Sinclair J. A., Giles R. S., Irwin P. G. J., Encrenaz T., 2016a, *Mid-infrared mapping of Jupiter's temperatures, aerosol opacity and chemical distributions with IRTF/TEXES*, Icarus, 278, 128

Fletcher L. N., Greathouse T. K., Orton G. S., Sinclair J. A., Giles R. S., Irwin P. G. J., Encrenaz T., 2016b, *Mid-infrared mapping of Jupiter's temperatures, aerosol opacity and chemical distributions with IRTF/TEXES*, Icarus, 278, 128

Fletcher L. N., et al., 2017a, *Jupiter's North Equatorial Belt expansion and thermal wave activity ahead of Juno's arrival*, GRL, 44, 7140

Fletcher L. N., Orton G. S., Rogers J. H., Giles R. S., Payne A. V., Irwin P. G. J., Vedovato M., 2017b, *Moist convection and the 2010-2011 revival of Jupiter's South Equatorial Belt*, Icarus, 286, 94

Fletcher L., et al., 2022, in European Planetary Science Congress. pp EPSC2022–475, doi:10.5194/epsc2022-475

Fletcher L. N., et al., 2023, *Jupiter Science Enabled by ESA's Jupiter Icy Moons Explorer*, SSR, 219, 53

Fletcher L. N., et al., 2024, in European Planetary Science Congress. pp EPSC2024–801, doi:10.5194/epsc2024-801

Fletcher L., et al., 2025, *Jupiter's Stripes: Testing the Canonical View of Banded Circulation Patterns on Giant Planets*, JWST Proposal. Cycle 4, ID. #6865

Foreman-Mackey D., Hogg D. W., Lang D., Goodman J., 2013, *emcee: The MCMC Hammer*, pasp, 125, 306

Fouchet T., Lellouch E., Feuchtgruber H., 2003, *The hydrogen ortho-to-para ratio in the stratospheres of the giant planets*, Icarus, 161, 127

Friedson A. J., Wong A.-S., Yung Y. L., 2002, *Models for Polar Haze Formation in Jupiter's Stratosphere*, icarus, 158, 389

Fritts D. C., Alexander M. J., 2003, *Gravity wave dynamics and effects in the middle atmosphere*, Reviews of Geophysics, 41, 1003

Fulchignoni M., et al., 2005, *In situ measurements of the physical characteristics of Titan's environment*, Nature, 438, 785

Funke B., López-Puertas M., García-Comas M., Kaufmann M., Höpfner M., Stiller G. P., 2012, *GRANADA: A Generic RAdiative traNsfer AnD non-LTE population algorithm*, JQSRT, 113, 1771

Gajjar V., et al., 2022, *Searching for Broadband Pulsed Beacons from 1883 Stars Using Neural Networks*, ApJ, 932, 81

Galanti E., Kaspi Y., 2021, *Combined magnetic and gravity measurements probe the deep zonal flows of the gas giants*, MNRAS, 501, 2352

Gardner J. P., et al., 2006, *The James Webb Space Telescope*, SSR, 123, 485

Gautier T., et al., 2012, *Mid- and far-infrared absorption spectroscopy of Titan's aerosols analogues*, Icarus, 221, 320

Ge H., Li C., Zhang X., Moeckel C., 2024, *Heat-flux-limited Cloud Activity and Vertical Mixing in Giant Planet Atmospheres with an Application to Uranus and Neptune*, PSJ, 5, 101

Ge H., Li C., Zhang X., Ingersoll A. P., Chen S., 2025, *Nonuniform Water Distribution in Jupiter's Mid Latitudes: Influence of Precipitation and Planetary Rotation*, arXiv e-prints, p. arXiv:2509.25610

Gelaro R., et al., 2017, *The Modern-Era Retrospective Analysis for Research and Applications, Version 2 (MERRA-2)*, Journal of Climate, 30, 5419

Gierasch P. J., 1996, *Atmospheric Dynamics on the Outer Planets*, Science, 273, 320

Gierasch P. J., Conrath B. J., Magalhães J. A., 1986, *Zonal mean properties of Jupiter's upper troposphere from voyager infrared observations*, Icarus, 67, 456

Giles R. S., Fletcher L. N., Irwin P. G. J., 2017, *Latitudinal variability in Jupiter's tropospheric disequilibrium species: GeH_4, AsH_3 and PH_3*, Icarus, 289, 254

Gladstone G. R., Allen M., Yung Y. L., 1996, *Hydrocarbon Photochemistry in the Upper Atmosphere of Jupiter*, Icarus, 119, 1

Goldberger J., Hinton G. E., Roweis S., Salakhutdinov R. R., 2004, in Saul L., Weiss Y., Bottou L., eds, Vol. 17, Advances in Neural Information Processing Systems. MIT Press, https://proceedings.neurips.cc/paper_files/paper/2004/file/42fe880812925e520249e808937738d2-Paper.pdf

Gomes R., Levison H. F., Tsiganis K., Morbidelli A., 2005, *Origin of the cataclysmic Late Heavy Bombardment period of the terrestrial planets*, Nature, 435, 466

Goody R. M., Yung Y. L., 1989, *Atmospheric radiation : theoretical basis*

Goody R., West R., Chen L., Crisp D., 1989, *The correlated-k method for radiation calculations in nonhomogeneous atmospheres.*, JQSRT, 42, 539

Gordon I. E., et al., 2017, *The HITRAN2016 molecular spectroscopic database*, JQSRT, 203, 3

Gordon I. E., et al., 2022, *The HITRAN2020 molecular spectroscopic database*, JQSRT, 277, 107949

Grassi D., 2018, *Atmospheric physics and Atmospheres of Solar-System bodies*, arXiv e-prints, p. arXiv:1804.08340

Grassi D., et al., 2010, *Jupiter's hot spots: Quantitative assessment of the retrieval capabilities of future IR spectro-imagers*, planss, 58, 1265

Grassi D., et al., 2017a, *Preliminary results on the composition of Jupiter's troposphere in hot spot regions from the JIRAM/Juno instrument*, GRL, 44, 4615

Grassi D., et al., 2017b, *Analysis of IR-bright regions of Jupiter in JIRAM-Juno data: Methods and validation of algorithms*, JQSRT, 202, 200

Grassi D., et al., 2020, *On the Spatial Distribution of Minor Species in Jupiter's Troposphere as Inferred From Juno JIRAM Data*, Journal of Geophysical Research (Planets), 125, e06206

Grassi D., et al., 2021, *On the clouds and ammonia in Jupiter's upper troposphere from Juno JIRAM reflectivity observations*, MNRAS, 503, 4892

Grassi D., Biagiotti F., Mura A., Piccioni G., Plainaki C., Sindoni G., Bolton S., 2024a, in European Planetary Science Congress. pp EPSC2024–28, doi:10.5194/epsc2024-28

Grassi D., et al., 2024b, *Jupiter's Hot Spots as observed by JIRAM-Juno: limb-darkening in thermal infrared*, Monthly Notices of the Royal Astronomical Society, p. stae1858

Grassi D., Biagiotti F., Mura A., Piccioni G., Plainaki C., Sindoni G., Bolton S. J., 2025, in EGU General Assembly 2025. Vienna, Austria, pp EGU25–4098, doi:10.5194/egusphere-egu25-4098, https://meetingorganizer.copernicus.org/EGU25/EGU25-4098.html

Grevesse N., Asplund M., Sauval A. J., 2007, *The Solar Chemical Composition*, SSR, 130, 105

Griffith C. A., Bézard B., Greathouse T. K., Kelly D. M., Lacy J. H., Noll K. S., 1997, *Thermal Infrared Imaging Spectroscopy of Shoemaker-Levy 9 Impact Sites: Spatial and Vertical Distributions of NH3, C2H4, and 10-micron Dust Emission*, Icarus, 128, 275

Griffiths D. J., Schroeter D. F., 2018, *Introduction to Quantum Mechanics*, doi:10.1017/9781316995433.

Guillot T., 1999a, *A comparison of the interiors of Jupiter and Saturn*, PSSJ, 47, 1183

Guillot T., 1999b, *Interiors of giant planets inside and outside the Solar System.*, Science, 296, 72

Guillot T., 2004, *Probing the giant planets.*, Physics Today, 57, 4.63

Guillot T., Hueso R., 2006, *The composition of Jupiter: sign of a (relatively) late formation in a chemically evolved protosolar disc*, MNRAS, 367, L47

Guillot T., Chabrier G., Gautier D., Morel P., 1995, *Effect of Radiative Transport on the Evolution of Jupiter and Saturn*, ApJ, 450, 463

Guillot T., et al., 2018, *A suppression of differential rotation in Jupiter's deep interior*, Nature, 555, 227

Guillot T., Stevenson D. J., Atreya S. K., Bolton S. J., Becker H. N., 2020a, *Storms and the Depletion of Ammonia in Jupiter: I. Microphysics of "Mushballs"*, Journal of Geophysical Research (Planets), 125, e06403

Guillot T., et al., 2020b, *Storms and the Depletion of Ammonia in Jupiter: II. Explaining the Juno Observations*, Journal of Geophysical Research (Planets), 125, e06404

Guillot T., et al., 2023, in EGU General Assembly Conference Abstracts. EGU General Assembly Conference Abstracts. pp EGU–17178, doi:10.5194/egusphere-egu23-17178

Guillot T., et al., 2024a, in EGU General Assembly Conference Abstracts. EGU General Assembly Conference Abstracts. p. 17351, doi:10.5194/egusphere-egu24-17351

Guillot T., et al., 2024b, in European Geosciences Union General Assembly 2024 (EGU24). EGU General Assembly Conference Abstracts. p. 17351, doi:10.5194/egusphere-egu24-17351

Gurnett D. A., Shaw R. R., Anderson R. R., Kurth W. S., Scarf F. L., 1979, *Whistlers observed by Voyager 1: Detection of lightning on Jupiter*, GRL, 6, 511

Hammel H. B., et al., 1995, *HST Imaging of Atmospheric Phenomena Created by the Impact of Comet Shoemaker-Levy 9*, Science, 267, 1288

Hanel R. A., Conrath B. J., Jennings D. E., Samuelson R. E., 2003, *Exploration of the Solar System by Infrared Remote Sensing: Second Edition*

Hansen J. E., 1971, *Multiple Scattering of Polarized Light in Planetary Atmospheres. Part I. The Doubling Method.*, Journal of the Atmospheric Sciences, 28, 120

Hansen J. E., Travis L. D., 1974, *Light scattering in planetary atmospheres*, SSR, 16, 527

Hansen C. J., Caplinger M. A., Ingersoll A., Ravine M. A., Jensen E., Bolton S., Orton G., 2017, *Junocam: Juno's Outreach Camera*, SSR, 213, 475

Harkett J., et al., 2024, *The Thermal Structure and Composition of Jupiter's Great Red Spot From JWST/MIRI*, Journal of Geophysical Research (Planets), 129, e2024JE008415

Harrington J., Dowling T. E., Baron R. L., 1996, *Jupiter's Tropospheric Thermal Emission. I. Observations and Techniques*, Icarus, 124, 22

Hartmann J. M., Boulet C., Brodbeck C., van Thanh N., Fouchet T., Drossart P., 2002, *A far wing lineshape for H2 broadened CH4 infrared transitions*, JQSRT, 72, 117

Hastings W. K., 1970, *Monte Carlo Sampling Methods using Markov Chains and their Applications*, Biometrika, 57, 97

Hayes J. J. C., et al., 2020, *Optimizing exoplanet atmosphere retrieval using unsupervised machine-learning classification*, MNRAS, 494, 4492

He C., et al., 2024, *Optical properties of organic haze analogues in water-rich exoplanet atmospheres observable with JWST*, Nature Astronomy, 8, 182

Heimpel M., Aurnou J., Wicht J., 2005, *Simulation of equatorial and high-latitude jets on Jupiter in a deep convection model*, Nature, 438, 193

Helled R., 2023, *The mass of gas giant planets: Is Saturn a failed gas giant?*, AA, 675, L8

Helled R., Stevenson D., 2017, *The Fuzziness of Giant Planets' Cores*, ApJL, 840, L4

Henyey L. G., Greenstein J. L., 1941, *Diffuse radiation in the Galaxy.*, ApJ, 93, 70

Hogan R. J., 2010, *The Full-Spectrum Correlated-kMethod for Longwave Atmospheric Radiative Transfer Using an Effective Planck Function*, Journal of the Atmospheric Sciences, 67, 2086

Holton J. R., 1992, *An introduction to dynamic meteorology*

Horton D. E., Johnson N. C., Singh D., Swain D. L., Rajaratnam B., Diffenbaugh N. S., 2015, *Contribution of changes in atmospheric circulation patterns to extreme temperature trends*, Nature, 522, 465

Howard S., Müller S., Helled R., 2024, *Evolution of Jupiter and Saturn with helium rain*, AA, 689, A15

Howell S. B., 2000, *Handbook of CCD Astronomy*

Howett C. J. A., Carlson R. W., Irwin P. G. J., Calcutt S. B., 2007, *Optical constants of ammonium hydrosulfide ice and ammonia ice*, Journal of the Optical Society of America B Optical Physics, 24, 126

Huang K., 1987, *Statistical Mechanics, 2nd Edition*

Huang Z., Yu X., Tsai S.-M., Moses J. I., Ohno K., Krissansen-Totton J., Zhang X., Fortney J. J., 2024, *Probing Cold-to-temperate Exoplanetary Atmospheres: The Role of Water Condensation on Surface Identification with JWST*, ApJ, 975, 146

Hudson R. L., Gerakines P. A., Yarnall Y. Y., 2022, *Ammonia Ices Revisited: New IR Intensities and Optical Constants for Solid NH_3*, ApJ, 925, 156

Hueso R., Sánchez-Lavega A., 2001, *A Three-Dimensional Model of Moist Convection for the Giant Planets: The Jupiter Case*, Icarus, 151, 257

Hueso R., Sánchez-Lavega A., 2004, *A three-dimensional model of moist convection for the giant planets II: Saturn's water and ammonia moist convective storms*, Icarus, 172, 255

Hueso R., et al., 2017, *Jupiter cloud morphology and zonal winds from ground-based observations before and during Juno's first perijove*, GRL, 44, 4669

Hueso R., et al., 2023, *An intense narrow equatorial jet in Jupiter's lower stratosphere observed by JWST*, Nature Astronomy, 7, 1454

Iess L., et al., 2018, *Measurement of Jupiter's asymmetric gravity field*, Nature, 555, 220

Ignatiev N. I., Grassi D., Zasova L. V., 2005, *Planetary Fourier spectrometer data analysis: Fast radiative transfer models*, planss, 53, 1035

Imanaka H., Cruikshank D. P., Khare B. N., McKay C. P., 2012, *Optical constants of Titan tholins at mid-infrared wavelengths (2.5-25 μm) and the possible chemical nature of Titan's haze particles*, Icarus, 218, 247

Ingersoll A. P., 1990, *Atmospheric Dynamics of the Outer Planets*, Science, 248, 308

Ingersoll A. P., Gierasch P. J., Banfield D., Vasavada A. R., Galileo Imaging Team 2000, *Moist convection as an energy source for the large-scale motions in Jupiter's atmosphere*, Nature, 403, 630

Irwin P. G. J., 2009, *Giant Planets of Our Solar System*, doi:10.1007/978-3-540-85158-5.

Irwin P. G. J., Dyudina U., 2002, *The Retrieval of Cloud Structure Maps in the Equatorial Region of Jupiter Using a Principal Component Analysis of Galileo/NIMS Data*, Icarus, 156, 52

Irwin P. G. J., et al., 1998, *Cloud structure and atmospheric composition of Jupiter retrieved from Galileo near-infrared mapping spectrometer real-time spectra*, JGR, 103, 23001

Irwin P. G. J., Weir A. L., Taylor F. W., Calcutt S. B., Carlson R. W., 2001, *The Origin of Belt/Zone Contrasts in the Atmosphere of Jupiter and Their Correlation with 5-μm Opacity*, Icarus, 149, 397

Irwin P. G. J., et al., 2008, *The NEMESIS planetary atmosphere radiative transfer and retrieval tool*, JQSRT, 109, 1136

Irwin P. G. J., Hill S. M., Fletcher L. N., Alexander C., Rogers J. H., 2025, *Clouds and Ammonia in the Atmospheres of Jupiter and Saturn Determined From a Band-Depth Analysis of VLT/MUSE Observations*, Journal of Geophysical Research (Planets), 130, 2024JE008622

Israël G., et al., 2005, *Complex organic matter in Titan's atmospheric aerosols from in situ pyrolysis and analysis*, Nature, 438, 796

Ivezić Ž., Connolly A. J., VanderPlas J. T., Gray A., 2014a, *Statistics, Data Mining, and Machine Learning in Astronomy: A Practical Python Guide for the Analysis of Survey Data*, doi:10.1515/9781400848911.

Ivezić Ž., Connolly A. J., VanderPlas J. T., Gray A., 2014b, *Statistics, Data Mining, and Machine Learning in Astronomy: A Practical Python Guide for the Analysis of Survey Data*, doi:10.1515/9781400848911.

Jackson J. D., Fox R. F., 1999, *Classical Electrodynamics, 3rd ed.*, American Journal of Physics, 67, 841

Jain A. K., 2010, *Data clustering: 50 years beyond K-means*, Pattern Recognition Letters, 31, 651

Jakobsen P., et al., 2022, *The Near-Infrared Spectrograph (NIRSpec) on the James Webb Space Telescope. I. Overview of the instrument and its capabilities*, AA, 661, A80

Janssen M. A., et al., 2017, *MWR: Microwave Radiometer for the Juno Mission to Jupiter*, SSR, 213, 139

Johnson T. V., Yeates C. M., Young R., 1992, *Space science reviews volume on Galileo Mission overview*, SSR, 60, 3

Judge D. L., Carlson R. W., 1974, *Pioneer 10 Observations of the Ultraviolet Glow in the Vicinity of Jupiter*, Science, 183, 317

Kalogerakis K. S., Marschall J., Oza A. U., Engel P. A., Meharchand R. T., Wong M. H., 2008, *The coating hypothesis for ammonia ice particles in Jupiter: Laboratory experiments and optical modeling*, Icarus, 196, 202

Kaspi Y., et al., 2018, *Jupiter's atmospheric jet streams extend thousands of kilometres deep*, Nature, 555, 223

Kasting J. F., 1988, *Runaway and moist greenhouse atmospheres and the evolution of Earth and Venus*, Icarus, 74, 472

Kattawar G. W., 1975, *A three-parameter analytic phase function for multiple scattering calculations*, JQSRT, 15, 839

Kaye J. A., Strobel D. F., 1983, *HCN formation on Jupiter: The coupled photochemistry of ammonia and acetylene*, Icarus, 54, 417

Kelly B. C., 2007, *Some Aspects of Measurement Error in Linear Regression of Astronomical Data*, ApJ, 665, 1489

Kempton E. M. R., Lupu R., Owusu-Asare A., Slough P., Cale B., 2017, *Exo-Transmit: An Open-Source Code for Calculating Transmission Spectra for Exoplanet Atmospheres of Varied Composition*, PASP, 129, 044402

Kessler M. F., et al., 1996, *The Infrared Space Observatory (ISO) mission.*, AA, 315, L27

Khare B. N., Sagan C., Arakawa E. T., Suits F., Callcott T. A., Williams M. W., 1984, *Optical constants of organic tholins produced in a simulated Titanian atmosphere: From soft x-ray to microwave frequencies*, icarus, 60, 127

Khurana K. K., Kivelson M. G., Stevenson D. J., Schubert G., Russell C. T., Walker R. J., Polanskey C., 1998, *Induced magnetic fields as evidence for subsurface oceans in Europa and Callisto*, Nature, 395, 777

King O., Fletcher L. N., 2022, *Global Modeling of Ganymede's Surface Composition: Near-IR Mapping From VLT/SPHERE*, Journal of Geophysical Research (Planets), 127, e2022JE007323

King O. R. T., Fletcher L. N., Harkett J., Roman M. T., Melin H., 2023, *Custom JWST NIRSpec/IFU and MIRI/MRS Data Reduction Pipelines for Solar System Targets*, Research Notes of the American Astronomical Society, 7, 223

Kitchin C. R., 2013, *Astrophysical Techniques*

Kochanov R. V., Gordon I. E., Rothman L. S., Wcisło P., Hill C., Wilzewski J. S., 2016, *HITRAN Application Programming Interface (HAPI): A comprehensive approach to working with spectroscopic data*, JQSRT, 177, 15

Kohlhase C. E., Penzo P. A., 1977, *Voyager Mission Description*, SSR, 21, 77

Kramers H. A., de L. Kronig R., 1928, *Zur Theorie der Absorption und Dispersion in den Röntgenspektren*, Zeitschrift für Physik, 48, 174

Kreidberg L., et al., 2014, *Clouds in the atmosphere of the super-Earth exoplanet GJ1214b*, Nat, 505, 69

Kronig R. D. L., 1926, *On the theory of dispersion of x'rays*, Journal of the Optical Society of America (1917-1983), 12, 547

Kunde V., et al., 1982, *The tropospheric gas composition of Jupiter's north equatorial belt /NH3, PH3, CH3D, GeH4, H2O/ and the Jovian D/H isotopic ratio*, ApJ, 263, 443

Lange J. U., 2023, *nautilus: boosting Bayesian importance nested sampling with deep learning*, Monthly Notices of the Royal Astronomical Society, 525, 3181

Lange N. A., Forker G. M., 1953, *Handbook of Chemistry. Eighth Edition*, Soil Science, 75, 82

Laplace P.-S., 1796, *Exposition du systeme du monde*. Imprimerie du Cercle-Social, Paris

Lavvas P., Koskinen T., Steinrueck M. E., García Muñoz A., Showman A. P., 2019, *Photochemical Hazes in Sub-Neptunian Atmospheres with a Focus on GJ 1214b*, ApJ, 878, 118

Lebofsky M., et al., 2019, *The Breakthrough Listen Search for Intelligent Life: Public Data, Formats, Reduction, and Archiving*, pasp, 131, 124505

Lellouch E., Bézard B., Fouchet T., Feuchtgruber H., Encrenaz T., de Graauw T., 2001, *The deuterium abundance in Jupiter and Saturn from ISO-SWS observations*, AA, 370, 610

Leon-Dasi M., Besse S., Doressoundiram A., 2023, *Deep Learning Investigation of Mercury's Explosive Volcanism*, Remote Sensing, 15, 4560

Levenberg K., 1944, *A Method for the Solution of Certain Non-Linear Problems in Least Squares*, Quarterly of Applied Mathematics, 2, 164

Lewis J. S., 1969, *The clouds of Jupiter and the NH3-H2O and NH3-H2S systems*, Icarus, 10, 365

Li C., et al., 2017, *The distribution of ammonia on Jupiter from a preliminary inversion of Juno microwave radiometer data*, GRL, 44, 5317

Li C., et al., 2020a, *The water abundance in Jupiter's equatorial zone*, Nature Astronomy, 4, 609

Li C., Ingersoll P. A., Klipfel P. A., Brettle H., 2020b, *Modeling the stability of polygonal patterns of vortices at the poles of Jupiter as revealed by the Juno spacecraft*, Proceedings of the National Academy of Science, 117, 24082

Liddle A. R., 2007, *Information criteria for astrophysical model selection*, MNRAS, 377, L74

Lightsey P. A., Atkinson C., Clampin M., Feinberg L. D., 2012, *James Webb Space Telescope: large deployable cryogenic telescope in space*, Optical Engineering, 51, 011003

Lindal G. F., Sweetnam D. N., Eshleman V. R., 1985, *The atmosphere of Saturn - an analysis of the Voyager radio occultation measurements*, AJ, 90, 1136

Liou K. N., 1980, *An introduction to atmospheric radiation.*

Lodders K., 2010, in Barnes R., ed., , Formation and Evolution of Exoplanets. p. 157, doi:10.1002/9783527629763.ch8

Lodge M. G., Wakeford H. R., Leinhardt Z. M., 2024, *Aerosols are not spherical cows: using discrete dipole approximation to model the properties of fractal particles*, MNRAS, 527, 11113

Lohmann U., Feichter J., 2005, *Global indirect aerosol effects: a review*, Atmospheric Chemistry & Physics, 5, 715

López-Puertas M., Taylor F. W., 2001, *Non-LTE Radiative Transfer in the Atmosphere*. World Scientific Publishing Company

Lorenz R. D., et al., 2007a, *Titan's young surface: Initial impact crater survey by Cassini RADAR and model comparison*, grl, 34, L07204

Lorenz R. D., Zarnecki J. C., Towner M. C., Leese M. R., Ball A. J., Hathi B., Hagermann A., Ghafoor N. A. L., 2007b, *Descent motions of the Huygens probe as measured by the Surface Science Package (SSP): Turbulent evidence for a cloud layer*, planss, 55, 1936

Lovas F. J., Tiemann E., 1974, *Microwave Spectral Tables I. Diatomic Molecules*, Journal of Physical and Chemical Reference Data, 3, 609

Lunine J. I., Hubbard W. B., Burrows A., Wang Y. P., Garlow K., 1989, *The Effect of Gas and Grain Opacity on the Cooling of Brown Dwarfs*, apj, 338, 314

Ma P. X., et al., 2023, *A deep-learning search for technosignatures from 820 nearby stars*, Nature Astronomy, 7, 492

Maahn M., Turner D. D., Löhnert U., Posselt D. J., Ebell K., Mace G. G., Comstock J. M., 2020, *Optimal Estimation Retrievals and Their Uncertainties: What Every Atmospheric Scientist Should Know*, Bulletin of the American Meteorological Society, 101, E1512

MacDonald R. J., Madhusudhan N., 2017, *HD 209458b in new light: evidence of nitrogen chemistry, patchy clouds and sub-solar water*, MNRAS, 469, 1979

Malin M. C., Edgett K. S., 2001, *Mars Global Surveyor Mars Orbiter Camera: Interplanetary cruise through primary mission*, JGR, 106, 23429

Malin M. C., et al., 2007, *Context Camera Investigation on board the Mars Reconnaissance Orbiter*, Journal of Geophysical Research (Planets), 112, E05S04

Markham S., Guillot T., 2024, *Stable Stratification of the Helium Rain Layer Yields Vastly Different Interiors and Magnetic Fields for Jupiter and Saturn*, PSJ, 5, 269

Marquardt D. W., 1963, *An Algorithm for Least-Squares Estimation of Nonlinear Parameters*, SIAM Journal on Applied Mathematics, 11, 431

Martonchik J. V., Orton G. S., Appleby J. F., 1984, *Optical properties of NH_3 ice from the far infrared to the near ultraviolet.*, AO, 23, 541

Matson D. L., Spilker L. J., Lebreton J.-P., 2002, *The Cassini/Huygens Mission to the Saturnian System*, ssr, 104, 1

Matthews C. N., 1997, *Hydrogen cyanide polymers from the impact of comet P/Shoemaker-Levy 9 on Jupiter*, Advances in Space Research, 19, 1087

Mayor M., Queloz D., 1995, *A Jupiter-mass companion to a solar-type star*, Nature, 378, 355

McEwen A. S., et al., 1998, *Active Volcanism on Io as Seen by Galileo SSI*, Icarus, 135, 181

McEwen A. S., et al., 2007, *Mars Reconnaissance Orbiter's High Resolution Imaging Science Experiment (HiRISE)*, Journal of Geophysical Research (Planets), 112, E05S02

McKay C. P., Pollack J. B., Courtin R., 1989, *The thermal structure of Titan's atmosphere*, icarus, 80, 23

Meadows V. S., Crisp D., 1996, *Ground-based near-infrared observations of the Venus nightside: The thermal structure and water abundance near the surface*, JGR, 101, 4595

Melin H., Fletcher L., Irwin P., Grassi D., Mura A., 2022, in European Planetary Science Congress. pp EPSC2022–817, doi:10.5194/epsc2022-817

Melin H., et al., 2024a, *Ionospheric irregularities at Jupiter observed by JWST*, Nature Astronomy, 8, 1000

Melin H., et al., 2024b, *Ionospheric irregularities at Jupiter observed by JWST*, Nature Astronomy, 8, 1000

Menzel D. H., Coblentz W. W., Lampland C. O., 1926, *Planetary Temperatures Derived from Water-Cell Transmissions*, ApJ, 63, 177

Metropolis N., Rosenbluth A. W., Rosenbluth M. N., Teller A. H., Teller E., 1953, *Equation of State Calculations by Fast Computing Machines*, JCP, 21, 1087

Mie G., 1908, *Beiträge zur Optik trüber Medien, speziell kolloidaler Metallösungen*, Annalen der Physik, 330, 377

Militzer B., Hubbard W. B., 2023, *Relation of Gravity, Winds, and the Moment of Inertia of Jupiter and Saturn*, PSJ, 4, 95

Mlawer E. J., Cady-Pereira K. E., Mascio J., Gordon I. E., 2023, *The inclusion of the MT_CKD water vapor continuum model in the HITRAN molecular spectroscopic database*, JQSRT, 306, 108645

Moon T. K., 1996, *The expectation-maximization algorithm*, IEEE Signal Processing Magazine, 13, 47

Morbidelli A., Marchi S., Bottke W. F., Kring D. A., 2012, *A sawtooth-like timeline for the first billion years of lunar bombardment*, Earth and Planetary Science Letters, 355, 144

Moreno R., Marten A., Matthews H. E., Biraud Y., 2003, *Long-term evolution of CO, CS and HCN in Jupiter after the impacts of comet Shoemaker-Levy 9*, planss, 51, 591

Moses J. I., Fouchet T., Bézard B., Gladstone G. R., Lellouch E., Feuchtgruber H., 2005, *Photochemistry and diffusion in Jupiter's stratosphere: Constraints from ISO observations and comparisons with other giant planets*, Journal of Geophysical Research (Planets), 110, E08001

Müller H. S. P., Thorwirth S., Roth D. A., Winnewisser G., 2001, *The Cologne Database for Molecular Spectroscopy, CDMS*, AA, 370, L49

Mura A., et al., 2018, *Juno observations of spot structures and a split tail in Io-induced aurorae on Jupiter*, Science, 361, 774

Mura A., et al., 2024, *The temporal variability of Io's hotspots*, Frontiers in Astronomy and Space Sciences, 11, 1369472

Murchie S., et al., 2007, *Compact Reconnaissance Imaging Spectrometer for Mars (CRISM) on Mars Reconnaissance Orbiter (MRO)*, Journal of Geophysical Research (Planets), 112, E05S03

Mustard J. F., et al., 2008, *Hydrated silicate minerals on Mars observed by the Mars Reconnaissance Orbiter CRISM instrument*, Nature, 454, 305

Nettelmann N., Cano Amoros M., Tosi N., Helled R., Fortney J. J., 2024, *Atmospheric Helium Abundances in the Giant Planets*, SSR, 220, 56

Newville M., Stensitzki T., Allen D. B., Ingargiola A., 2014, *LMFIT: Non-Linear Least-Square Minimization and Curve-Fitting for Python*, doi:10.5281/zenodo.11813

Niemann H. B., et al., 1996, *The Galileo Probe Mass Spectrometer: Composition of Jupiter's Atmosphere*, Science, 272, 846

Niraula P., de Wit J., Gordon I. E., Hargreaves R. J., Sousa-Silva C., Kochanov R. V., 2022, *The impending opacity challenge in exoplanet atmospheric characterization*, Nature Astronomy, 6, 1287

Nixon M. C., Madhusudhan N., 2020, *Assessment of supervised machine learning for atmospheric retrieval of exoplanets*, MNRAS, 496, 269

O'Hirok W., Gautier C., 1998, *A Three-Dimensional Radiative Transfer Model to Investigate the Solar Radiation within a Cloudy Atmosphere. Part I: Spatial Effects.*, Journal of the Atmospheric Sciences, 55, 2162

Ordonez-Etxeberria I., Hueso R., Sánchez-Lavega A., Pérez-Hoyos S., 2016, *Spatial distribution of jovian clouds, hazes and colors from Cassini ISS multi-spectral images*, Icarus, 267, 34

Ortiz J. L., Orton G. S., Friedson A. J., Stewart S. T., Fisher B. M., Spencer J. R., 1998, *Evolution and persistence of 5-μm hot spots at the Galileo probe entry latitude*, JGR, 103, 23051

Orton G. S., Appleby J. F., Martonchik J. V., 1982, *The effect of ammonia ice on the outgoing thermal radiance from the atmosphere of Jupiter*, Icarus, 52, 94

Orton G., et al., 1995, *Collision of Comet Shoemaker-Levy 9 with Jupiter Observed by the NASA Infrared Telescope Facility*, Science, 267, 1277

Orton G. S., et al., 2017, *The first close-up images of Jupiter's polar regions: Results from the Juno mission JunoCam instrument*, GRL, 44, 4599

Orton G. S., Gustafsson M., Fletcher L. N., Roman M. T., Sinclair J. A., 2025, *Improved H2-He and H2-H2 Collision-Induced Absorption Models and Application to Outer-Planet Atmospheres*, arXiv e-prints, p. arXiv:2506.09257

Palotai C., Brueshaber S., Sankar R., Sayanagi K., 2022, *Moist Convection in the Giant Planet Atmospheres*, Remote Sensing, 15, 219

Parisi M., et al., 2021a, *The depth of Jupiter's Great Red Spot constrained by Juno gravity overflights*, Science, 374, 964

Parisi M., et al., 2021b, *The depth of Jupiter's Great Red Spot constrained by Juno gravity overflights*, Science, 374, 964

Park J., Kim S. J., Jeon M., Sim C. K., Melin H., Courtin R., Seon J. H., 2024, *Spatial and spectral characteristics of the Jovian polar haze inferred from 2-μm Juno/JIRAM spectro-images*, Icarus, 420, 116139

Patra K. C., Winn J. N., Holman M. J., Yu L., Deming D., Dai F., 2017, *The Apparently Decaying Orbit of WASP-12b*, AJ, 154, 4

Pearson K., 1901, *LIII. On lines and planes of closest fit to systems of points in space*, The London, Edinburgh, and Dublin Philosophical Magazine and Journal of Science, 2, 559

Pedregosa F., et al., 2011, *Scikit-learn: Machine Learning in Python*, Journal of Machine Learning Research, 12, 2825

Peek B. M., 1958, *The Planet Jupiter*. Faber and Faber, London

Piazzi G., 1802, *Della scoperta del nuovo pianeta Cerere Ferdinandea, ottavo tra i primari del nostro sistema solare*, doi:10.3931/e-rara-2902.

Piccioni G., et al., 2007, *South-polar features on Venus similar to those near the north pole*, Nature, 450, 637

Plass G. N., Kattawar G. W., Catchings F. E., 1973, *Matrix operator theory of radiative transfer. 1: Rayleigh scattering.*, AO, 12, 314

Porco C. C., et al., 2003, *Cassini Imaging of Jupiter's Atmosphere, Satellites, and Rings*, Science, 299, 1541

Porco C. C., et al., 2005, *Imaging of Titan from the Cassini spacecraft*, Nature, 434, 159

Poulet F., et al., 2024, *Moons and Jupiter Imaging Spectrometer (MAJIS) on Jupiter Icy Moons Explorer (JUICE)*, SSR, 220, 27

Prahl S., 2023, *miepython: Pure python implementation of Mie scattering*, doi:10.5281/zenodo.8218010

Prandtl L., 1925, *7. Bericht über Untersuchungen zur ausgebildeten Turbulenz*, Zeitschrift Angewandte Mathematik und Mechanik, 5, 136

Prinn R. G., Barshay S. S., 1977, *Carbon Monoxide on Jupiter and Implications for Atmospheric Convection*, Science, 198, 1031

Prinn R. G., Lewis J. S., 1975, *Phosphine on Jupiter and Implications for the Great Red Spot*, Science, 190, 274

Quanz S. P., et al., 2022, *Large Interferometer For Exoplanets (LIFE). I. Improved exoplanet detection yield estimates for a large mid-infrared space-interferometer mission*, AA, 664, A21

Ragent B., Colburn D. S., Rages K. A., Knight T. C. D., Avrin P., Orton G. S., Yanamandra-Fisher P. A., Grams G. W., 1998, *The clouds of Jupiter: Results of the Galileo Jupiter mission probe nephelometer experiment*, JGR, 103, 22891

Randles C. A., et al., 2017, *The MERRA-2 Aerosol Reanalysis, 1980 Onward. Part I: System Description and Data Assimilation Evaluation*, Journal of Climate, 30, 6823

Rannou P., McKay C. P., Lorenz R. D., 2003, *A model of Titan's haze of fractal aerosols constrained by multiple observations*, planss, 51, 963

Raymond S. N., Boulet T., Izidoro A., Esteves L., Bitsch B., 2018, *Migration-driven diversity of super-Earth compositions*, MNRAS, 479, L81

Reuter D. C., et al., 2008, *Ralph: A Visible/Infrared Imager for the New Horizons Pluto/Kuiper Belt Mission*, SSR, 140, 129

Rex A., Finn C., 2017, *Finn's Thermal Physics*. CRC Press, https://books.google.it/books?id=iuneDwAAQBAJ

Robbins-Blanch N., Kataria T., Batalha N. E., Adams D. J., 2022, *Cloudy and Cloud-free Thermal Phase Curves with PICASO: Applications to WASP-43b*, apj, 930, 93

Robinson T. D., Stapelfeldt K. R., Marley M. S., 2016, *Characterizing Rocky and Gaseous Exoplanets with 2 m Class Space-based Coronagraphs*, PASP, 128, 025003

Rodgers C. D., 2000, *Inverse Methods for Atmospheric Sounding: Theory and Practice*, doi:10.1142/3171.

Rodríguez-Ovalle P., et al., 2024, *Temperature and Composition Disturbances in the Southern Auroral Region of Jupiter Revealed by JWST/MIRI*, Journal of Geophysical Research (Planets), 129, e2024JE008299

Rodríguez-Ovalle P., et al., 2025, *JWST observations of exogenic species on Jupiter: HCN, H_2O, and CO_2*, AA, 696, A173

Rogers J. H., 1995, *The giant planet Jupiter*

Rogers J. H., Adamoli G., Mettig H. J., 2011, *Jupiter' high-latitude storms: a Little Red Spot tracked through a Jovian year*, Journal of the British Astronomical Association, 121, 19

Rogers J., et al., 2022a, in European Planetary Science Congress. pp EPSC2022–16, doi:10.5194/epsc2022-16

Rogers J. H., et al., 2022b, *Flow patterns of Jupiter's south polar region*, Icarus, 372, 114742

Roman N. G., 2019, *Nancy Grace Roman and the Dawn of Space Astronomy*, ARAA, 57, 1

Roman M. T., 2023, *Mid-Infrared Observations of the Giant Planets*, Remote Sensing, 15, 1811

Roman M. T., et al., 2023, in AGU Fall Meeting Abstracts. pp P41C–03

Rooney C. M., Batalha N. E., Gao P., Marley M. S., 2022, *A New Sedimentation Model for Greater Cloud Diversity in Giant Exoplanets and Brown Dwarfs*, apj, 925, 33

Roos-Serote M., et al., 1998, *Analysis of Jupiter North Equatorial Belt hot spots in the 4-5-μm range from Galileo/near-infrared mapping spectrometer observations: Measurements of cloud opacity, water, and ammonia*, JGR, 103, 23023

Rosner D. E., Khalil Y. F., 2000, *Particle and Knudsen Transition-Effects on Thermophoretically Dominated Total Mass Deposition Rates from COAGULATION-AGED Aerosol Population*, Journal of Aerosol Science, 31, 273

Rothenberg D., Hisch T., 2016, *darothen/py-mie: py-mie 0.4.0*, doi:10.5281/zenodo.192510, https://doi.org/10.5281/zenodo.192510

Rothman L. S., et al., 2009, *The HITRAN 2008 molecular spectroscopic database*, JQSRT, 110, 533

Safronov V. S., 1972, *Evolution of the protoplanetary cloud and formation of the earth and planets.*

Sagan C., Khare B. N., 1979, *Tholins: organic chemistry of interstellar grains and gas*, Nature, 277, 102

Sagan C., Thompson W. R., 1984, *Production and condensation of organic gases in the atmosphere of Titan*, icarus, 59, 133

Sakurai J. J., 1985, *Modern quantum mechanics*

Salvatier J., Wiecki T. V., Fonnesbeck C., 2016, *PyMC3: Python probabilistic programming framework*, Astrophysics Source Code Library, record ascl:1610.016

Sanchez-Lavega A., Quesada J. A., 1988, *Ground-based imaging of Jovian cloud morphologies and motions II. The northern hemisphere from 1975 to 1985*, Icarus, 76, 533

Sanchez-Lavega A., et al., 2001, *NOTE: The Merger of Two Giant Anticyclones in the Atmosphere of Jupiter*, Icarus, 149, 491

Sánchez-Lavega A., Hueso R., Pérez-Hoyos S., García-Melendo E., Rojas J. F., 2004, in Ulla A., Manteiga M., eds, , Vol. 1, Lecture Notes and Essays in Astrophysics. pp 63–86

Sánchez-Lavega A., García-Melendo E., Legarreta J., Miró A., Soria M., Ahrens-Velásquez K., 2024a, *The Origin of Jupiter's Great Red Spot*, GRL, 51, e2024GL108993

Sánchez-Lavega A., García-Melendo E., Legarreta J., Miró A., Soria M., Ahrens-Velásquez K., 2024b, *The Origin of Jupiter's Great Red Spot*, GRL, 51, e2024GL108993

Saumon D., Guillot T., 2004, *Shock Compression of Deuterium and the Interiors of Jupiter and Saturn*, ApJ, 609, 1170

Schwarzschild M., 1958, *Structure and evolution of the stars.*

Sciamma-O'Brien E., Upton K. T., Salama F., 2017, *The Titan Haze Simulation (THS) experiment on COSmIC. Part II. Ex-situ analysis of aerosols produced at low temperature*, Icarus, 289, 214

Seager S., Bains W., Petkowski J. J., 2016, *Toward a List of Molecules as Potential Biosignature Gases for the Search for Life on Exoplanets and Applications to Terrestrial Biochemistry*, Astrobiology, 16, 465

Segelstein D., 1981, M.s. thesis, University of Missouri–Kansas City

Seiff A., Knight T. C. D., 1992, *The Galileo Probe Atmosphere Structure instrument*, SSR, 60, 203

Seiff A., et al., 1996, *Structure of the Atmosphere of Jupiter: Galileo Probe Measurements*, Science, 272, 844

Seiff A., et al., 1997, *Thermal structure of Jupiter's upper atmosphere derived from the Galileo probe*, Science, 276, 102

Showman A. P., Ingersoll A. P., 1998, *Interpretation of Galileo Probe Data and Implications for Jupiter's Dry Downdrafts*, Icarus, 132, 205

Siebenaler L., Miguel Y., de Regt S., Guillot T., 2025, *Conditions for radiative zones in the molecular hydrogen envelope of Jupiter and Saturn: The role of alkali metals*, AandA, 693, A308

Simon A. A., 1999, *The Structure and Temporal Stability of Jupiter's Zonal Winds: A Study of the North Tropical Region*, Icarus, 141, 29

Simon A. A., Wong M. H., 2024, *Zonal and Regional Jupiter Brightness Trends from the Hubble Outer Planet Atmospheres Legacy Program*, PSJ, 5, 259

Simon-Miller A. A., Conrath B., Gierasch P. J., Beebe R. F., 2000, *A Detection of Water Ice on Jupiter with Voyager IRIS*, Icarus, 145, 454

Simon-Miller A. A., Banfield D., Gierasch P. J., 2001a, *Color and the Vertical Structure in Jupiter's Belts, Zones, and Weather Systems*, Icarus, 154, 459

Simon-Miller A. A., Banfield D., Gierasch P. J., 2001b, *Color and the Vertical Structure in Jupiter's Belts, Zones, and Weather Systems*, Icarus, 154, 459

Simon-Miller A. A., Banfield D., Gierasch P. J., 2001c, *Color and the Vertical Structure in Jupiter's Belts, Zones, and Weather Systems*, Icarus, 154, 459

Simon A. A., Wong M. H., Marcus P. S., Irwin P. G. J., 2024, *A Detailed Study of Jupiter's Great Red Spot over a 90-day Oscillation Cycle*, PSJ, 5, 223

Sinclair J. A., et al., 2023, *Long-term variability of Jupiter's northern auroral 8-micron CH4 emissions*, Icarus, 406, 115740

Sindoni G., et al., 2017, *Characterization of the white ovals on Jupiter's southern hemisphere using the first data by the Juno/JIRAM instrument*, GRL, 44, 4660

Sing D. K., et al., 2016, *A continuum from clear to cloudy hot-Jupiter exoplanets without primordial water depletion*, Nat, 529, 59

Sirianni M., et al., 2005, *The Photometric Performance and Calibration of the Hubble Space Telescope Advanced Camera for Surveys*, PASP, 117, 1049

Smith P. H., Tomasko M. G., 1984a, *Photometry and polarimetry of Jupiter at large phase angles II. Polarimetry of the South Tropical Zone, South Equatorial Belt, and the polar regions from the Pioneer 10 and 11 missions*, Icarus, 58, 35

Smith P. H., Tomasko M. G., 1984b, *Photometry and polarimetry of Jupiter at large phase angles II. Polarimetry of the South Tropical Zone, South Equatorial Belt, and the polar regions from the Pioneer 10 and 11 missions*, Icarus, 58, 35

Smith B. A., et al., 1979, *The Jupiter System Through the Eyes of Voyager 1*, Science, 204, 951

Smith M. D., Wolff M. J., Clancy R. T., Murchie S. L., 2009, *Compact Reconnaissance Imaging Spectrometer observations of water vapor and carbon monoxide*, Journal of Geophysical Research (Planets), 114, E00D03

Speedie J., et al., 2024, *Gravitational instability in a planet-forming disk*, Nature, 633, 58

Spencer J. R., et al., 2007, *Io Volcanism Seen by New Horizons: A Major Eruption of the Tvashtar Volcano*, Science, 318, 240

Sromovsky L. A., Fry P. M., 2010a, *The source of 3-μm absorption in Jupiter's clouds: Reanalysis of ISO observations using new NH_3 absorption models*, Icarus, 210, 211

Sromovsky L. A., Fry P. M., 2010b, *The source of widespread 3-μm absorption in Jupiter's clouds: Constraints from 2000 Cassini VIMS observations*, Icarus, 210, 230

Sromovsky L. A., Fry P. M., 2018, *Composition and structure of fresh ammonia clouds on Jupiter based on quantitative analysis of Galileo/NIMS and New Horizons/LEISA spectra*, Icarus, 307, 347

Sromovsky L. A., Baines K. H., Fry P. M., 2013, *Saturn's Great Storm of 2010-2011: Evidence for ammonia and water ices from analysis of VIMS spectra*, Icarus, 226, 402

Sromovsky L. A., Baines K. H., Fry P. M., Carlson R. W., 2017a, *A possibly universal red chromophore for modeling color variations on Jupiter*, Icarus, 291, 232

Sromovsky L. A., Baines K. H., Fry P. M., Carlson R. W., 2017b, *A possibly universal red chromophore for modeling color variations on Jupiter*, Icarus, 291, 232

Sromovsky L. A., Baines K. H., Fry P. M., 2018, *Models of bright storm clouds and related dark ovals in Saturn's Storm Alley as constrained by 2008 Cassini/VIMS spectra*, Icarus, 302, 360

Stamnes K., Tsay S. C., Jayaweera K., Wiscombe W., 1988, *Numerically stable algorithm for discrete-ordinate-method radiative transfer in multiple scattering and emitting layered media*, AO, 27, 2502

Stern S. A., 2008, *The New Horizons Pluto Kuiper Belt Mission: An Overview with Historical Context*, SSR, 140, 3

Stern S. A., et al., 2015, *The Pluto system: Initial results from its exploration by New Horizons*, Science, 350, aad1815

Stiller G. P., et al., 1998, in Wang J., Wu B., Ogawa T., Guan Z.-H., eds, Society of Photo-Optical Instrumentation Engineers (SPIE) Conference Series Vol. 3501, Optical Remote Sensing of the Atmosphere and Clouds. pp 257–268, doi:10.1117/12.317754

Stone E. C., Lane A. L., 1979, *Voyager 1 Encounter with the Jovian System*, Science, 204, 945

Stratton J. A., Chu L. J., 1941, *Steady-State Solutions of Electromagnetic Field Problems. II. Forced Oscillations of a Conducting Sphere*, Journal of Applied Physics, 12, 236

Strobel D. F., 1973, *The Photochemistry of Hydrocarbons in the Jovian Atmosphere.*, Journal of the Atmospheric Sciences, 30, 489

Tamminen J., KyröLä E., 2001, *Bayesian solution for nonlinear and non-Gaussian inverse problems by Markov chain Monte Carlo method*, JGR, 106, 14,377

Tennyson J., et al., 2016, *The ExoMol database: Molecular line lists for exoplanet and other hot atmospheres*, Journal of Molecular Spectroscopy, 327, 73

Tinetti G., et al., 2018, *A chemical survey of exoplanets with ARIEL*, Experimental Astronomy, 46, 135

Tiranti P., Knowles K. L., Melin H., Moore L., O'Donoghue J., Roberts K., Stallard T., Thomas E. M., 2025, *Chasing the Great Red Spot: Exploring Coupling Between Jupiter's Atmospheric Layers*, JWST Proposal. Cycle 4, ID. #8147

Tokunaga A. T., Beck S. C., Geballe T. R., Lacy J. H., Serabyn E., 1981, *The detection of HCN on Jupiter*, Icarus, 48, 283

Tonkov M. V., Filippov N. N., Timofeyev Y. M., Polyakov A. V., 1996, *A simple model of the line mixing effect for atmospheric applications: theoretical background and comparison with experimental profiles.*, JQSRT, 56, 783

Toon O. B., Ackerman T. P., 1981, *Algorithms for the calculation of scattering by stratified spheres*, AO, 20, 3657

Toon O. B., Turco R. P., Pollack J. B., 1980, *A physical model of Titan's clouds*, icarus, 43, 260

Tosi F., et al., 2024, *Salts and organics on Ganymede's surface observed by the JIRAM spectrometer onboard Juno*, Nature Astronomy, 8, 82

Tran H., Flaud P. M., Fouchet T., Gabard T., Hartmann J. M., 2006, *Model, software and database for line-mixing effects in the ν 3 and ν 4 bands of CH4 and tests using laboratory and planetary measurements – II: H2 (and He) broadening and the atmospheres of Jupiter and Saturn*, JQSRT, 101, 306

Tsai S.-M., et al., 2023, *Photochemically produced SO_2 in the atmosphere of WASP-39b*, Nature, 617, 483

Tsubota T. K., Wong M. H., Stallard T., Zhang X., Simon A. A., 2025, *UV-dark polar ovals on Jupiter as tracers of magnetosphere-atmosphere connections*, Nature Astronomy, 9, 221

Turner D. D., Löhnert U., 2014, *Information Content and Uncertainties in Thermodynamic Profiles and Liquid Cloud Properties Retrieved from the Ground-Based Atmospheric Emitted Radiance Interferometer (AERI)*, Journal of Applied Meteorology and Climatology, 53, 752

Twomey S., 1974, *Pollution and the planetary albedo*, Atmospheric Environment, 8, 1251

Valcke S., Verron J., 1997, *Interactions of Baroclinic Isolated Vortices: The Dominant Effect of Shielding*, Journal of Physical Oceanography, 27, 524

VanderPlas J., Connolly A. J., Ivezic Z., Gray A., 2012a, in Proceedings of Conference on Intelligent Data Understanding (CIDU. pp 47–54 (arXiv:1411.5039), doi:10.1109/CIDU.2012.6382200

VanderPlas J., Connolly A. J., Ivezic Z., Gray A., 2012b, in Proceedings of Conference on Intelligent Data Understanding (CIDU. pp 47–54 (arXiv:1411.5039), doi:10.1109/CIDU.2012.6382200

VanderPlas J., Fouesneau M., Taylor J., 2014, *AstroML: Machine learning and data mining in astronomy*, Astrophysics Source Code Library, record ascl:1407.018

Vasavada A. R., et al., 1998, *Galileo Imaging of Jupiter's Atmosphere: The Great Red Spot, Equatorial Region, and White Ovals*, Icarus, 135, 265

Villanueva G. L., Milam S. N., 2023a, *A new era in solar system astronomy with JWST*, Nature Communications, 14, 7444

Villanueva G. L., Milam S. N., 2023b, *A new era in solar system astronomy with JWST*, Nature Communications, 14, 7444

Villanueva G. L., et al., 2015, *Strong water isotopic anomalies in the martian atmosphere: Probing current and ancient reservoirs*, Science, 348, 218

Villanueva G. L., Smith M. D., Protopapa S., Faggi S., Mandell A. M., 2018, *Planetary Spectrum Generator: An accurate online radiative transfer suite for atmospheres, comets, small bodies and exoplanets*, JQSRT, 217, 86

Villanueva G. L., Liuzzi G., Faggi S., Protopapa S., Kofman V., Fauchez T., Stone S. W., Mandell A. M., 2022, *Fundamentals of the Planetary Spectrum Generator*

Villanueva G. L., et al., 2024, *Modeling Atmospheric Lines by the Exoplanet Community (MALBEC) Version 1.0: A CUISINES Radiative Transfer Intercomparison Project*, PSJ, 5, 64

Virtanen P., et al., 2020, *SciPy 1.0: fundamental algorithms for scientific computing in Python*, Nature Methods, 17, 261

Vitali F., Stefani S., Piccioni G., Snels M., Grassi D., Biondi D., Boccaccini A., 2025, *New experimental measurements of the Collision Induced Absorptions of H_2-H_2 and H_2-He in the 3600-5500 cm^{-1} spectral range from 120 to 500 K*, JQSRT, 330, 109255

Wahl S. M., et al., 2017, *Comparing Jupiter interior structure models to Juno gravity measurements and the role of a dilute core*, JGRL, 44, 4649

Waite J. H., Young D. T., Cravens T. E., Coates A. J., Crary F. J., Magee B., Westlake J., 2007, *The Process of Tholin Formation in Titan's Upper Atmosphere*, Science, 316, 870

Waldmann I. P., Griffith C. A., 2019, *Mapping Saturn using deep learning*, Nature Astronomy, 3, 620

Warren S. G., 1984, *Optical constants of ice from the ultraviolet to the microwave*, AO, 23, 1206

Welbanks L. C., 2021, PhD thesis, University of Cambridge, Institute of Astronomy

West R. A., 1979, *Spatially Resolved Methane Band Photometry of Jupiter. II. Analysis of the Southern Equatorial Belt and South Tropical Zone Reflectivity*, Icarus, 38, 34

West R. A., Baines K. H., Friedson A. J., Banfield D., Ragent B., Taylor F. W., 2007, in Bagenal F., Dowling T. E., McKinnon W. B., eds, , Jupiter. p. 79

Whitaker D. A., Hayes K., 2018, *A Simple Algorithm for Despiking Raman Spectra*, Chemometrics and Intelligent Laboratory Systems, 179, 82

White K. O., Watkins W. R., Bruce C. W., Meredith R. E., Smith F. G., 1978, *Water vapor continuum absorption in the 3.5-4.0-μm region*, AO, 17, 2711

Wiechert U., Halliday A. N., Lee D. C., Snyder G. A., Taylor L. A., Rumble D., 2001, *Oxygen Isotopes and the Moon-Forming Giant Impact*, Science, 294, 345

Wildt R., 1932, *Methan in den Atmosphären der großen Planeten*, Naturwissenschaften, 20, 851

Williams J. P., Cieza L. A., 2011, *Protoplanetary Disks and Their Evolution*, ARAA, 49, 67

Wong M. H., de Pater I., 2005, in AAS - Division for Planetary Sciences Meeting Abstracts - 37. p. 22.03

Wong M. H., Bjoraker G. L., Smith M. D., Flasar F. M., Nixon C. A., 2004a, *Identification of the 10-μm ammonia ice feature on Jupiter*, planss, 52, 385

Wong M. H., Mahaffy P. R., Atreya S. K., Niemann H. B., Owen T. C., 2004b, *Updated Galileo probe mass spectrometer measurements of carbon, oxygen, nitrogen, and sulfur on Jupiter*, Icarus, 171, 153

Wong M. H., Mahaffy P. R., Atreya S. K., Niemann H. B., Owen T. C., 2004c, *Updated Galileo probe mass spectrometer measurements of carbon, oxygen, nitrogen, and sulfur on Jupiter*, Icarus, 171, 153

Wong M. H., de Pater I., Asay-Davis X., Marcus P. S., Go C. Y., 2011a, *Vertical structure of Jupiter's Oval BA before and after it reddened: What changed?*, Icarus, 215, 211

Wong M. H., de Pater I., Asay-Davis X., Marcus P. S., Go C. Y., 2011b, *Vertical structure of Jupiter's Oval BA before and after it reddened: What changed?*, Icarus, 215, 211

Wong M. H., Atreya S. K., Kuhn W. R., Romani P. N., Mihalka K. M., 2015, *Fresh clouds: A parameterized updraft method for calculating cloud densities in one-dimensional models*, icarus, 245, 273

Wong M. H., Marcus P. S., Simon A. A., de Pater I., Tollefson J. W., Asay-Davis X., 2021a, *Evolution of the Horizontal Winds in Jupiter's Great Red Spot From One Jovian Year of HST/WFC3 Maps*, GRL, 48, e93982

Wong M. H., Marcus P. S., Simon A. A., de Pater I., Tollefson J. W., Asay-Davis X., 2021b, *Evolution of the Horizontal Winds in Jupiter's Great Red Spot From One Jovian Year of HST/WFC3 Maps*, GRL, 48, e93982

Wong M. H., Bjoraker G. L., Goullaud C., Stephens A. W., Luszcz-Cook S. H., Atreya S. K., de Pater I. d., Brown S. T., 2023, *Deep Clouds on Jupiter*, Remote Sensing, 15, 702

Wong M. H., et al., 2025, *Jupiter's Oval BA: Trends in Space and Time*, JWST Proposal. Cycle 4, ID. #6840

Woodgate B. E., et al., 1998, *The Space Telescope Imaging Spectrograph Design*, PASP, 110, 1183

Yang H., Shi C., Cai J., Zhou L., Yang Y., Zhao X., He Y., Hao J., 2022, *Data mining techniques on astronomical spectra data - I. Clustering analysis*, MNRAS, 517, 5496

Young R. M. B., Read P. L., Wang Y., 2019, *Simulating Jupiter's weather layer. Part II: Passive ammonia and water cycles*, icarus, 326, 253

Yung Y. L., Demore W. B., eds, 1999, *Photochemistry of planetary atmospheres*

Zambon F., et al., 2023, *Io Hot Spot Distribution Detected by Juno/JIRAM*, GRL, 50, e2022GL100597

Zhang A., Marcus P. S., 2024, *Stable three-dimensional vortex families consistent with Jovian observations including the Great Red Spot*, Journal of Fluid Mechanics, 984, A61

Ziv M., Galanti E., Sheffer A., Howard S., Guillot T., Kaspi Y., 2024a, *NeuralCMS: A deep learning approach to study Jupiter's interior*, aap, 686, L7

Ziv M., Galanti E., Howard S., Guillot T., Kaspi Y., 2024b, *Characterizing Jupiter's interior using machine learning reveals four key structures*, aap, 692, A251

Zuchowski L. C., Yamazaki Y. H., Read P. L., 2009, *Modeling Jupiter's cloud bands and decks. 1. Jet scale meridional circulations*, icarus, 200, 548

de Pater I., Dunn D., Romani P., Zahnle K., 2001, *Reconciling Galileo Probe Data and Ground-Based Radio Observations of Ammonia on Jupiter*, Icarus, 149, 66

de Pater I., et al., 2010a, *A multi-wavelength study of the 2009 impact on Jupiter: Comparison of high resolution images from Gemini, Keck and HST*, Icarus, 210, 722

de Pater I., Wong M. H., Marcus P., Luszcz-Cook S., Ádámkovics M., Conrad A., Asay-Davis X., Go C., 2010b, *Persistent rings in and around Jupiter's anticyclones - Observations and theory*, Icarus, 210, 742

de Pater I., Sault R. J., Butler B., DeBoer D., Wong M. H., 2016, *Peering through Jupiter's clouds with radio spectral imaging*, Science, 352, 1198

de Pater I., et al., 2017, *ERS observations of the Jovian System as a Demonstration of JWST's Capabilities for Solar System Science*, JWST Proposal ID 1373. Cycle 0 Early Release Science

de Pater I., et al., 2019a, *First ALMA Millimeter-wavelength Maps of Jupiter, with a Multiwavelength Study of Convection*, AJ, 158, 139

de Pater I., et al., 2019b, *First ALMA Millimeter-wavelength Maps of Jupiter, with a Multiwavelength Study of Convection*, AJ, 158, 139

de Pater I., Sault R. J., Wong M. H., Fletcher L. N., DeBoer D., Butler B., 2019c, *Jupiter's ammonia distribution derived from VLA maps at 3-37 GHz*, Icarus, 322, 168

de Sanctis M. C., et al., 2011, *The VIR Spectrometer*, SSR, 163, 329

von Zahn U., Hunten D. M., Lehmacher G., 1998, *Helium in Jupiter's atmosphere: Results from the Galileo probe helium interferometer experiment*, JGR, 103, 22815

Of course, none of you have come to this point all by yourself. Each of you is part of a much greater community. Think of all the people over the last thirty years who worked to build the Space Telescope and its instruments, and those who worked to develop the scientific ideas that it was designed to test.Along with the contribution of your fellow scientists, engineers and mathematicians, it was also with the support of your families and so many of your friends that you have been able to appreciate and take part in this wonderful enterprise, which has enabled us to see the world around us in a new way.

Never forget, then, that what you are doing is meant to benefit all of us. Be generous in sharing what you learn and what you experience, as best you can and however you can. Do not hesitate to share the joy and the amazement born of your contemplation of the "seeds" that, in the words of Saint Augustine, God has sown in the harmony of the universe (cf. De Genesis ad Litteram, V, 23, 44-45). The more joy you share, the more joy you create, and in this way, through your pursuit of knowledge, each of you can contribute to building a more peaceful and just world.

- Address of Pope Leo XIV to the participants of the VOSS25 summer school promoted by the Vatican Observatory

Acknowledgements

Ringrazio l'INAF-IAPS, l'Università di Roma La Sapienza, e l'Agenzia Spaziale Italiana (accordo 2016-23-H.0) per aver finanziato e supportato la mia attività di ricerca in questi tre anni.

Prima di tutto sento il bisogno di ringraziare le due persone a cui è dedicata questa tesi e che purtroppo non hanno potuto vedermi mentre la difendevo, Nonna Teresa e Zia Betta. Ve ne siete andate durante questi tre anni senza potervi dirvi addio e quindi lo farò qua. Mi mancate ogni giorno e non potrò mai ringraziarvi abbastanza per tutto l'amore che mi avete donato. Un amore immenso e incondizionato. Quel tipo di amore gratuito che alcune volte ti fa dubitare di meritarlo. Ricordo ogni regalo, ogni telefonata, ogni abbraccio, ogni storia, ogni sorriso, e ogni risata insieme, e li custodirò gelosamente. Avete sempre creduto in me e mi avete donato immensa forza. Ma più di tutto siete state un modello. Molto della persona che sono oggi, l'ho imparato da voi. Sarete sempre con me, come un'impronta indelebile sul mio cuore.

Ringrazio Davide, il mio supervisor, per tutto l'aiuto ricevuto, la pazienza, e per essere stato una guida in questi tre anni. Come un mastro artigiano mi hai insegnato tutti i trucchi del mestiere, dall'arrivare in fretta ai coffee break, fino agli ultimi consigli su come scrivere la tesi (che ammetto di non aver seguito in pieno !). Sei stato un supervisor sempre disponibile e attento, ma che comunque mi ha sempre dato fiducia e spazio per crescere. Questo è estremamente raro. Nonostante il tuo aspetto "burbero", ogni tuo gesto mi ha dimostrato affetto e cura, soprattutto nei momenti più bui. Ma soprattutto vorrei ringraziarti per gli insegnamenti non accademici di cui ho fatto tesoro. Sicuramente in questi tre anni ho imparato tanto sulle nubi e i retrieval, ma il mio bagaglio è stato arricchito anche con qualche parola in arzân, nuovi consigli culinari e cinematografici, e storie su Reggio Emilia e dintorni.

Vorrei ringraziare Giuseppe e Alessandro, i miei co-supervisor, per tutti i consigli, il supporto, e l'aiuto costante. Vi ringrazio per la fiducia sempre garantita fin dal primo giorno e dalla prima riunione esplorativa.
Vorrei ringraziare tutti i ricercatori e i tecnici dell'INAF-IAPS che mi sono stati vicini soprattutto durante i primi anni: Roberto Sordini, Christina Plainaki, Giuseppe Sindoni, John Scige Liu, Stefania Stefani, Fabrizio Oliva, Emiliano D'Aversa, Giovanna Rinaldi, Federico Tosi, Francesca Zambon, Enrico Bruschini, Marco Ferrari, Alessandro Moirano, Pietro Scarica, Simone Benella, Federica Duras, Giacomo Carrozzo, Sergio Fonte, Francesco Carraro, e molti altri !
Ringrazio soprattutto Giulia, Elisa, Francesca (FraV), Chiara, Matteo, Federico, Edoardo, Pier Paolo, Martina, Francesca (FraF), Francesco (FraC), Stefano, Beatrice, Samuel, Lorenzo, Alessandro e Gabriele. Siete stati dei compagni di viaggio per questi tre anni. Con voi ho girato l'Europa, condiviso innumerevoli coffee break sia al bar "Da Serena" che alle macchinette, e parlato di meme, trash (comprese Roma e Lazio), film, tiramisù al matcha e aperitivi. Oltre ovviamente a ricoprire il prestigioso ruolo di giudice per la prima edizione di "Benvenuti nella mia CucINAF" ! Grazie mille !

Vorrei ringraziare con affetto il prof. Giuliano Liuzzi dell'Università della Basilicata. Grazie per avermi aiutato a imparare le vie di PSG e per i preziosissimi consigli.

I would like to express my sincere gratitude to Prof. Leigh N. Fletcher of Leicester University and Prof. Tristan Guillot of the Côte d'Azur Observatory. Thank you for granting me the opportunity to be a visiting PhD student at your institutions. That journey allowed me to grow not only as a researcher, but most importantly, as a human being. Exploring the world and meeting new people is one of the brightest sides of our job, and I am delighted to have spent months in Leicester and Nice. The UK universities and the Côte d'Azur Observatory have been fundamental to planetary sciences in general, and I still cannot believe that I was able to visit both of them while sharing my research work. During my PhD journey, it was immensely important to have tangible proof that experienced researchers like you could be interested in (and supportive of!) the work of a student like me. Thank you for your hospitality, patience, guidance, and help. It was truly significant. When I was a Master's student, I remember studying and admiring your work (it was everywhere in my textbooks!). Meeting you in person was an honor, and it confirmed my high opinion of you.
I would also like to thank all the people I met both in the UK and in Nice: Mike, Oliver, Jake, Henrik, Simon, Nishil, and Vivien. Similarly, my thanks go out to all the people I met at conferences and PhD Schools across Europe and the US: Yana Markus, Paula Gorrini, Glenn Orton, Sushil Atreya, Imke dePater, Thierry Fouchet, Cheng Li, Geronimo Villanueva, Eleonora Alei, and many, many others. I would like to particularly thank Prof. Ricardo Hueso of the University of the Basque Country. Everything I have said about Leigh and Tristan also applies to you. Thank you for your kindness and your steadfast support throughout these three years.
A special thank goes to the whole VOSS25 family (in alphabetical order): Ana Maria, Akash, Bor, Candela, Dalale, Dario, Delvin, Emma, Hugo, Ignas, Isabella, Jerry, Joao, Maria, Mia, Mirley, Miguel, Rebecca, Renzo, Rodrigo, Rojas, Sean, Simon, Shahd, and Stella. I would also like to thank all the staff of the Specola Vaticana, Br. Guy Consolmagno, Br. David Brown, Eiichi Egami, Almudena Alonso-Herrero, and the whole VOSS25 faculty. Thank you for the wonderful summer that I will always remember. Hope to see you again for another pizza and tiramisù !

Con questa tesi si conclude anche il mio percorso di studi universitari lungo ben 8 anni. Non posso non ringraziare tutti gli amici che ho conosciuto e che mi sono stati a fianco dal primo giorno in cui ho varcato i cancelli di quel luogo ameno chiamato Sogene, fino alla difesa di questa tesi al Marconi. Ringrazio Antonio, Paolo, Marco, Lollo, Flavia, Daniele, Alessandro, Tessa, Simone, Edo (per la seconda volta, sì), Frap, Stefano, Arianna, PPP, Valerio, Adriano, Shahid, Giovanni, Sakshi, Roberta, Matteo, Simone (Filomeno), e Lorenzo. Grazie per aver parlato insieme pochissimo di fisica e astrofisica, preferendo DnD, anime, libri, film, Meme, Magic, Star Wars, Cina, Meme sulle scimmie, e molto moltissimo altro. Grazie per tutte le serate alle cantine e sulla Tuscolana e per essermi stati accanto dai primi esami fino ai giorni dei workshop. Vorrei ringraziare anche tutti gli altri studenti del 38° ciclo con cui

ho condiviso questi ultimi tre anni tra gioie e dolori.

Ringrazio di cuore Daniele, Matteo, Sara, Luca, Emiliano, Alessia, Loris, Giovanni, Lorenzo, Mattia ed Andrea. Non è facile mantenere un'amicizia per più di 10 anni. Eppure noi ci siamo riusciti a colpi di giochi da tavola, videogiochi, Risiko, dingo pictures, film trash, Barony, Freestyle Football, cartonati di Cristante, meme, yaoi, DnD, Wicked e Jannik Sinner. Non so se sia un pro o un contro. Quello che so è che devo ringraziarvi per i tantissimi bei momenti passati insieme in allegria e spensieratezza. E per dirmi di sì anche quando vi propongo film irlandesi o ungheresi in cinema sconosciuti.

Ringrazio tutta la mia famiglia, Zia Pia, Cristina, Zio Memmo, Zio Mariano, Zia Patrizia, Emanuele, Elena, Gianluca, Manuela, Adriano, Eleonora e i nuovi arrivati Edoardo, Ottavia e Futura. Grazie per il supporto in questi anni e per aver sempre, sempre, creduto in me e nel mio lavoro.
Desidero esprimere la mia gratitudine più profonda ai miei genitori Fulvio e Maria Consiglia. Mi supportate e accettate ogni giorno, con affetto e amore. Siete sempre stati la mia roccia, la mia certezza, nonostante le discussioni e i momenti difficili, che in questi tre anni sono stati molti. A voi devo non solo l'opportunità di poter studiare, ma la convinzione che, con impegno, tenacia e onestà, ogni obiettivo è raggiungibile. Il vostro esempio di dedizione è la vera ispirazione dietro queste pagine. Mamma, sei tu che hai innescato, mettendo la mia gioia sempre al primo posto, la mia passione per i libri, la scienza, ed il cinema, che poi sono stati fondamentali per scegliere astrofisica ed arrivare fino ad oggi. Spero che ogni tuo sforzo sia stato ripagato e che lo sarà in futuro.
Papà, anche se alcune volte non lo dici a parole, so che tu sei felice se anche io lo sono. Ogni tuo gesto verso di me ha sempre avuto questo obiettivo, con cura e impegno costante.
Ringrazio con tutto il mio cuore Jack, il mio fratellino peloso. Anche se non può leggere queste parole spero che sappia che da più di 13 anni lui è il mio rifugio, il mio migliore amico. Sa tutto di me e mi è stato vicino nei momenti più duri. Ha il super potere di farmi tornare il sorriso anche dopo una giornata terribile. Ringrazio Dio, o qualsiasi cosa ci sia là fuori, per ogni giorno passato insieme e per tutti gli altri che spero di passare ancora insieme a te.
Vorrei citare Carl Sagan, che è stato fondamentale per convincermi a continuare il mio percorso di studi. "Dopo tutte le nostre ricerche, l'unica cosa che abbiamo trovato che rende il vuoto sopportabile è l'amore che ci lega". E voi, Mamma, Papà, e Jack me lo avete dimostrato ogni giorno.

Infine voglio ringraziare me, cercando di sembrare il meno narcisista possibile. Quando avevo 10 anni volevo essere come Indiana Jones e cercare dinosauri. Alla fine ho girato una bella parte di questo pazzo mondo e cerco di capire di cosa sono fatte le nuvole in pianeti che potrebbero essere benissimo in Star Wars. Non credo sia andata così male, alla fine come dice Ariana Grande "I'm still the same, but only entirely different". Però vorrei dire alla mia versione di 10 anni che molti dei suoi sogni sono stati esauditi. Che molti di quegli ostacoli che sembravano invalicabili sono stati superati, e che le cose sono cambiate per il meglio. Che ce l'ha fatta ad

andare in America prima di Natale, e ce l'ha fatta solo grazie ai suoi impegni e la sua bravura. Purtroppo deve ancora vedere uno scudetto della Roma, ma volesse il cielo, quest'anno forse è quello buono. Con questa tesi si chiude un periodo importante della mia vita, il periodo della mia formazione. Ho imparato e vissuto tantissimo. Ma la cosa più bella forse è che ho ancora più domande, dubbi, e sogni di prima. E spero che la mia versione tra 10 anni sia fiera di me.

A sense of calm came over me. More and more often I found myself thinking, "This is where I belong. This is what I came into this world to do."

Only if we understand, can we care. Only if we care, we will help. Only if we help, we shall be saved.

- Jane Goodall